Pt in the latter, which is further diminished by the adsorbed gas. The electron density acquired from NH_3 hardly moves to SWCNT as is shown by the accumulation of electron density on the Pt atom (Δq_{Pt}, $-0.17e$) after interacting with NH_3. Up until this point, $SWCNT_{Vac}$/Pt adequately satisfies the basic sensitivity requirements and induces more electronic change in terms of both the energy gap and partial charge transfer to the SWCNT than to the SWCNT/Pt.

4. Conclusion

We tried to study qualitatively the sensing performance of Pt–SWCNT with defective and pristine SWCNTs for NO_2 and NH_3 by means of first principle calculations. Overall, in both Pt-deposited and Pt-doped SWCNTs, platinum increases the charge transfer and other calculated properties. For the adsorption of NO_2, the Pt-doped SWCNT shows slightly smaller binding energies and gap changes than both the pristine SWCNT and the Pt-deposited SWCNT. Its electronic structure modulations are greater than that of the pristine SWCNT and its electron densities in the SWCNT unit are more disturbed than the ones of the Pt-deposited SWCNT. The binding of Pt to the SWCNT in the doped case is much stronger than if it is deposited on the surface. For NH_3 adsorption, the Pt-doped SWCNT shows the largest electron transfers to the SWCNT. We further compared the Pt-doped SWCNT with the well-known reactive defected SWCNT. Their abilities for capturing a NO_2 molecule are similar but for NH_3 the Pt-doped SWCNT is far better. The sensitivity of Pt-doped SWCNT is superior for both the detection of NO_2 and NH_3, because it exhibits larger energy gap changes and a larger charge transfer. These findings should be useful for the development of SWCNT-based nanosensor devices.

Acknowledgements

This research was supported by grants from the Thailand Research Fund to PP (Royal Golden Jubilee Ph.D. fellowship 3.C.KU/50/A.1) and to JL, the National Science and Technology Development Agency (NSTDA Chair Professor and NANOTEC Center of Excellence and CNC Consortium), the Kasetsart University Research and Development Institute (KURDI), and the Commission on Higher Education (Postgraduate Education and Research Programs in Petroleum, Petrochemicals and Advanced Materials). Support for CPU time on the Tera cluster of the Thai National Grid Center is also acknowledged.

Appendix A. Supplementary data

Supplementary data associated with this article can be found, in the online version, at doi:10.1016/j.jmgm.2009.04.005.

References

[1] J. Kong, N.R. Franklin, C. Zhou, M.G. Chapline, S. Peng, K. Cho, H. Dailt, Nanotube molecular wires as chemical sensors, Science 287 (5453) (2000) 622–625.
[2] H. Chang, J.D. Lee, S.M. Lee, Y.H. Lee, Adsorption of NH_3 and NO_2 molecules on carbon nanotubes, Appl. Phys. Lett. 79 (23) (2001) 3863–3865.
[3] S. Peng, K. Cho, P. Qi, H. Dai, Ab initio study of CNT NO_2 gas sensor, Chem. Phys. Lett. 387 (4–6) (2004) 271–276.
[4] S. Santucci, S. Picozzi, F. Di Gregorio, L. Lozzi, C. Cantalini, L. Valentini, J.M. Kenny, B. Delley, NO_2 and CO gas adsorption on carbon nanotubes: experiment and theory, J. Chem. Phys. 119 (20) (2003) 10904–10910.
[5] J. Lu, S. Nagase, Y. Maeda, T. Wakahara, T. Nakahodo, T. Akasaka, D. Yu, Z. Gao, R. Han, H. Ye, Adsorption configuration of NH_3 on single-wall carbon nanotubes, Chem. Phys. Lett. 405 (1–3) (2005) 90–92.
[6] L. Valentini, F. Mercuri, I. Armentano, C. Cantalini, S. Picozzi, L. Lozzi, S. Santucci, A. Sgamellotti, J.M. Kenny, Role of defects on the gas sensing properties of carbon nanotubes thin films: experiment and theory, Chem. Phys. Lett. 387 (4–6) (2004) 356–361.
[7] J. Andzelm, N. Govind, A. Maiti, Nanotube-based gas sensors—role of structural defects, Chem. Phys. Lett. 421 (1–3) (2006) 58–62.
[8] F. Mercuri, A. Sgamellotti, L. Valentini, I. Armentano, J.M. Kenny, Vacancy-induced chemisorption of NO_2 on carbon nanotubes. A combined theoretical and experimental study, J. Phys. Chem. B 109 (27) (2005) 13175–13179.
[9] L. Bai, Z. Zhou, Computational study of B- or N-doped single-walled carbon nanotubes as NH_3 and NO_2 sensors, Carbon 45 (10) (2007) 2105–2110.
[10] S. Peng, K. Cho, Ab initio study of doped carbon nanotube sensors, Nano Lett. 3 (4) (2003) 513–517.
[11] R. Wang, D. Zhang, W. Sun, Z. Han, C. Liu, A novel aluminum-doped carbon nanotubes sensor for carbon monoxide, Theochem 806 (1–3) (2007) 93–97.
[12] R. Wang, D. Zhang, Y. Zhang, C. Liu, Boron-doped carbon nanotubes serving as a novel chemical sensor for formaldehyde, J. Phys. Chem. B 110 (37) (2006) 18267–18271.
[13] A. Star, V. Joshi, S. Skarupo, D. Thomas, J.-C.P. Gabriel, Gas sensor array based on metal-decorated carbon nanotubes, J. Phys. Chem. B 110 (42) (2006) 21014–21020.
[14] M. Penza, G. Cassano, R. Rossi, M. Alvisi, A. Rizzo, M.A. Signore, T. Dikonimos, E. Serra, R. Giorgi, Enhancement of sensitivity in gas chemiresistors based on carbon nanotube surface functionalized with noble metal (Au, Pt) nanoclusters, App. Phys. Lett. 90 (17) (2007) 173123/1–173123/3.
[15] S. Mubeen, T. Zhang, B. Yoo, M.A. Deshusses, N.V. Myung, Palladium nanoparticles decorated single-walled carbon nanotube hydrogen sensor, J. Phys. Chem. C 111 (17) (2007) 6321–6327.
[16] M.K. Kumar, S. Ramaprabhu, Nanostructured Pt functionlized multiwalled carbon nanotube based hydrogen sensor, J. Phys. Chem. B 110 (23) (2006) 11291–11298.
[17] S.J. Kim, Y.J. Park, E.J. Ra, K.K. Kim, K.H. An, Y.H. Lee, J.Y. Choi, C.H. Park, S.K. Doo, M.H. Park, C.W. Yang, Defect-induced loading of Pt nanoparticles on carbon nanotubes, App. Phys. Lett. 90 (2) (2007) 023114/1–023114/3.
[18] C. Zhou, J. Wu, A. Nie, R.C. Forrey, A. Tachibana, H. Cheng, On the sequential hydrogen dissociative chemisorption on small platinum clusters: a density functional theory study, J. Phys. Chem. C 111 (34) (2007) 12773–12778.
[19] L.C. Grabow, A.A. Gokhale, S.T. Evans, J.A. Dumesic, M. Mavrikakis, Mechanism of the water gas shift reaction on Pt: first principles, experiments, and microkinetic modeling, J. Phys. Chem. C 112 (12) (2008) 4608–4617.
[20] Y. Wang, P.B. Balbuena, Roles of proton and electric field in the electroreduction of O_2 on Pt(1 1 1) surfaces: results of an ab-initio molecular dynamics study, J. Phys. Chem. B 108 (14) (2004) 4376–4384.
[21] H. Orita, Y. Inada, DFT investigation of CO adsorption on Pt(2 1 1) and Pt(3 1 1) surfaces from low to high coverage, J. Phys. Chem. B 109 (47) (2005) 22469–22475.
[22] B. Delley, An all-electron numerical method for solving the local density functional for polyatomic molecules, J. Chem. Phys. 92 (1) (1990) 508–517.
[23] B. Delley, From molecules to solids with the $DMol^3$ approach, J. Chem. Phys. 113 (18) (2000) 7756–7764.
[24] T. Strassner, M.A. Taige, Evaluation of functionals O3LYP, KMLYP, and MPW1K in comparison to B3LYP for selected transition-metal compounds, J. Chem. Theory Comput. 1 (5) (2005) 848–855.
[25] Z. Slanina, P. Pulay, S. Nagase, H_2, Ne, and N_2 energies of encapsulation into C60 evaluated with the MPWB1K functional, J. Chem. Theory Comput. 2 (2006) 782–785.
[26] S.G. Stepanian, M.V. Karachevtsev, A.Yu. Glamazda, V.A. Karachevtsev, L. Adamowicz, Stacking interaction of cytosine with carbon nanotubes: MP2, DFT and Raman spectroscopy study, Chem. Phys. Lett. 459 (2008) 153–158.
[27] J.P. Perdew, Y. Wang, Accurate and simple analytic representation of the electron-gas correlation energy, Phys. Rev. B 45 (23) (1992) 13244–13249.
[28] B. Delley, Hardness conserving semilocal pseudopotentials, Phys. Rev. B: Condens. Matter Mater. Phys. 66 (15) (2002) 155125/1–155125/9.
[29] H.J. Monkhorst, J.D. Pack, Special points for Brillouin-zone integrations, Phys. Rev. B 13 (12) (1976) 5188–5192.
[30] O. Gulseren, T. Yildirim, S. Ciraci, Systematic ab initio study of curvature effects in carbon nanotubes, Phys. Rev. B: Condens. Matter Mater. Phys. 65 (15) (2002) 153405/1–153405/4.
[31] X. Blase, L.X. Benedict, E.L. Shirley, S.G. Louie, Hybridization effects and metallicity in small radius carbon nanotubes, Phys. Rev. Lett. 72 (12) (1994) 1878–1881.
[32] D. Vanderbilt, Soft self-consistent pseudopotentials in a generalized eigenvalue formalism, Phys. Rev. B 41 (11) (1990) 7892–8795.
[33] V. Milman, B. Winkler, J.A. White, C.J. Pickard, M.C. Payne, E.V. Akhmatskaya, R.H. Nobes, Electronic structure, properties, and phase stability of inorganic crystals: a pseudopotential plane-wave study, Int. J. Quantum Chem. 77 (5) (2000) 895–910.
[34] E. Durgun, S. Dag, V.M.K. Bagci, O. Gulseren, T. Yildirim, S. Ciraci, Systematic study of adsorption of single atoms on a carbon nanotube, Phys. Rev. B: Condens. Matter Mater. Phys. 67 (20) (2003) 201401/1–201401/4.
[35] G. Chen, Y. Kawazoe, Interaction between a single Pt atom and a carbon nanotube studied by density functional theory, Phys. Rev. B: Condens. Matter Mater. Phys. 73 (12) (2006) 125410/1–125410/6.
[36] L.Y. Chiang, J.B. Bhonsle, L. Wang, S.F. Shu, T.M. Chang, J.R. Hwu, Efficient one-flask synthesis of water-soluble [60]fullerenols, Tetrahedron 52 (14) (1996) 4963–4972.
[37] Z. Slanina, X. Zhao, L.Y. Chiang, E. Osawa, Biologically active fullerene derivatives: computations of structures, energetics, and vibrations of C60(OH)X and $C60(NO_2)Y$, Int. J. Quantum Chem. 74 (3) (1999) 343–349.
[38] The National Institute of Standards and Technology (NIST): Standard Reference Data Program (Chemistry WebBook, http://webbook.nist.gov).
[39] Y. Zhang, C. Suc, Z. Liu, J. Li, Carbon nanotubes functionalized by NO_2: coexistence of charge transfer and radical transfer, J. Phys. Chem. B 110 (45) (2006) 22462–22470.

Structure and Dynamics of Water Confined in Single-Wall Nanotubes

Tanin Nanok,[†,‡,§] Nongnuch Artrith,[†,‡,||] Piboon Pantu,[†,‡] Philippe A. Bopp,[⊥] and Jumras Limtrakul*[,†,‡]

Laboratory for Computational and Applied Chemistry, Department of Chemistry, Faculty of Science and Center of Nanotechnology, Kasetsart University, Bangkok 10900, Thailand, NANOTEC Center of Excellence, National Nanotechnology Center, Kasetsart University, Bangkok 10900, Thailand, and Department of Chemistry, Université Bordeaux 1, 351 Cours de la Libération, Building A12, F-33405 Talence cedex, France

Received: October 7, 2008; Revised Manuscript Received: November 28, 2008

The structure and dynamics of water confined in model single-wall carbon- and boron-nitride nanotubes (called SWCNT and SWBNNT, respectively) of different diameters have been investigated by molecular dynamics (MD) simulations at room temperature. The simulations were performed on periodically extended nanotubes filled with an amount of water that was determined by soaking a section of the nanotube in a water box in an *NpT* simulation (1 atm, 298 K). All MD production simulations were performed in the canonical (*NVT*) ensemble at a temperature of 298 K. Water was described by the extended simple point charge (SPC/E) model. The wall−water interactions were varied, within reasonable limits, to study the effect of a modified hydrophobicity of the pore walls. We report distribution functions for the water in the tubes in spherical and cylindrical coordinates and then look at the single-molecule dynamics, in particular self-diffusion. While this motion is slowed down in narrow tubes, in keeping with previous findings (Liu et al. *J. Chem. Phys.* **2005**, *123*, 234701−234707; Liu and Wang. *Phys. Rev.* **2005**, *72*, 085420/1−085420/4; Liu et al. *Langmuir* **2005**, *21*, 12025−12030) bulk-water like self-diffusion coefficients are found in wider tubes, more or less independently of the wall−water interaction. There may, however, be an anomaly in the self-diffusion for the SWBNNT.

I. Introduction

Carbon nanotubes (CNTs) have gained recognition as prominent building blocks of nanomaterials; they are used in a variety of nanotechnology applications due to their exceptional mechanical and electrical properties.[1,2] The transport of molecules in these nanoporous media could also exhibit interesting characteristics, different from the ones of transport in ordinary bulk media, since the interactions between the pore wall and the molecules become rather strong when the dimensions of the pore approach the size of the transported molecule. Although the mechanical and electrical properties of CNTs can be measured explicitly in experiments,[3] the understanding of the transport and conduction mechanisms through their pores is still incomplete. This is partly due to the difficulty of preparing CNTs with uniform pore sizes and distributions and of tracing the diffusive behavior inside. Computational studies thus play an important role in the interpretation of experimental data and provide predictive information on molecular transport through nanopores.

Because of the simplicity and hydrophobicity of their interior, CNTs are recognized as promising prototype models. They are frequently used as models for systems such as water transport in aquaporin water channels,[4] water migration in xylem vessels of plants,[5] the delivery of beneficial molecules to target cells[6−8] and other biological nanofluidic systems.

A previous molecular dynamics (MD) simulation study[9] on water conduction through the channel of single-walled carbon nanotubes (SWCNTs) showed that under normal conditions of pressure and temperature the filling of an empty (6,6)-CNT channel (8.1 Å in diameter and 13.4 Å in length) with water takes place within a few ten picoseconds. The channel then remained filled during the entire simulation time of 66 ns. The water molecules constrained in such a narrow space form a one-dimensionally ordered hydrogen-bond network that is not observed in bulk water. It was shown[10] that the channel occupancy and conductivity are dramatically decreased by a reduction of the attractive nanotube−water interactions. A 25% reduction leads to fluctuations between filled and empty sections in the tube and a 40% reduction to an emptying of the CNT channel.[9] This filling and conducting behavior has also been observed in an isoelectronic nanotube (a subnanometer boron nitride nanotube (BNNT)[11]) and other hydrophobic nanopores.[12,13]

Recently, several MD simulation studies have been performed on the diameter dependence of the CNT hydration. It was, for example, found that water confined in a critical-size armchair-(9,9) CNT can undergo a transition into a state having an ice-like mobility with an average number of hydrogen bonds close to that in bulk water under ambient temperature and pressure.[14] Unusual features, not seen in bulk ice, can also be observed with other CNT diameters under conditions of high water densities[15] and extremely high axial pressures (50 Mpa to 500 Mpa).[16] The radial distribution functions reveal highly ordered layered water structures in this case. For the dynamic properties, the radial and axial diffusivities of water encapsulated in SWCNTs are smaller than those of bulk water; both components

* Corresponding author. E-mail: fscijrl@ku.ac.th.
[†] Faculty of Science, Kasetsart University.
[‡] NANOTEC Center of Excellence, Kasetsart University.
[§] Present address: Institut für theoretische Physik, Universität Leipzig, Vor dem Hospitaltore, D-04103 Leipzig, Germany.
[||] Present address: Lehrstuhl für Theoretische Chemie, Ruhr-Universität Bochum, D-44780 Bochum, Germany.
[⊥] Université Bordeaux 1.

10.1021/jp8088676 CCC: $40.75
Published on Web 12/30/2008

TABLE 1: Details for the MD Simulation Runs of Water in Carbon- and Boron-Nitride Nanotubes in This Work[a]

tube	effective inner diameter (Å)	no. of water molecules	simulation time (ns)
(9,9)-nanotubes	8.86	77	4
(10,10)-nanotubes	10.22	102	4
(12,12)-nanotubes	12.92	162	1
(14,14)-nanotubes	15.62	237	1
(16,16)-nanotubes	18.34	327	1
(20,20)-nanotubes	23.74	547	1

[a] The length is 36.89 Å in all cases.

decrease as the diameter of the SWCNTs decreases.[15,17,18] In other tubes with similar diameters, the flow of water was found to be strongly influenced by the hydrophilicity of the wall.[19,20] The strong interfacial water−nanotube attraction causes a significant reduction of the water flow rate.

Even though the structure and dynamics of water confined in SWCNTs have been extensively studied by MD simulations, most efforts have been directed toward small diameter tubes, in which the characteristics of bulk water cannot be attained even at the tube center. Thus, a more comprehensive understanding of the structural and dynamic properties of water confined in larger diameter SWCNTs seems to be desirable. Here, we study tubes with effective diameters (see below) between 8.86 to 23.74 Å and report on the influences of the attractive interactions between the wall and the confined water at an average density of 1.0 g/cm^3 under ambient conditions.

In the next section, the models and simulation details will be presented. Then, we will investigate the structure of the water in the tubes in terms of radial and cylindrical distribution functions. A study of the self-diffusion will then be presented.

II. Models and Simulation Details

The armchair type SWCNTs considered in this study are modeled as rigid networks of uncharged Lennard-Jones (LJ) carbon atoms with C−C bond distances of 1.42 Å and a fixed nanotube length of 36.89 Å. To study the diameter dependence of the structural and dynamic properties of the confined water, the "effective diameter" (i.e., the diameter after excluding the van der Waals radius of a C atom, 1.70 Å) is varied from 8.86 to 23.74 Å, corresponding to the (*m*,*m*)-armchair SWCNTs with $m = 9$, 10, 12, 14, 16 and 20, respectively. *m* is an integer in the chiral vector $\mathbf{A} = m\mathbf{a}_1 + m\mathbf{a}_2$ of the hexagonal honeycomb

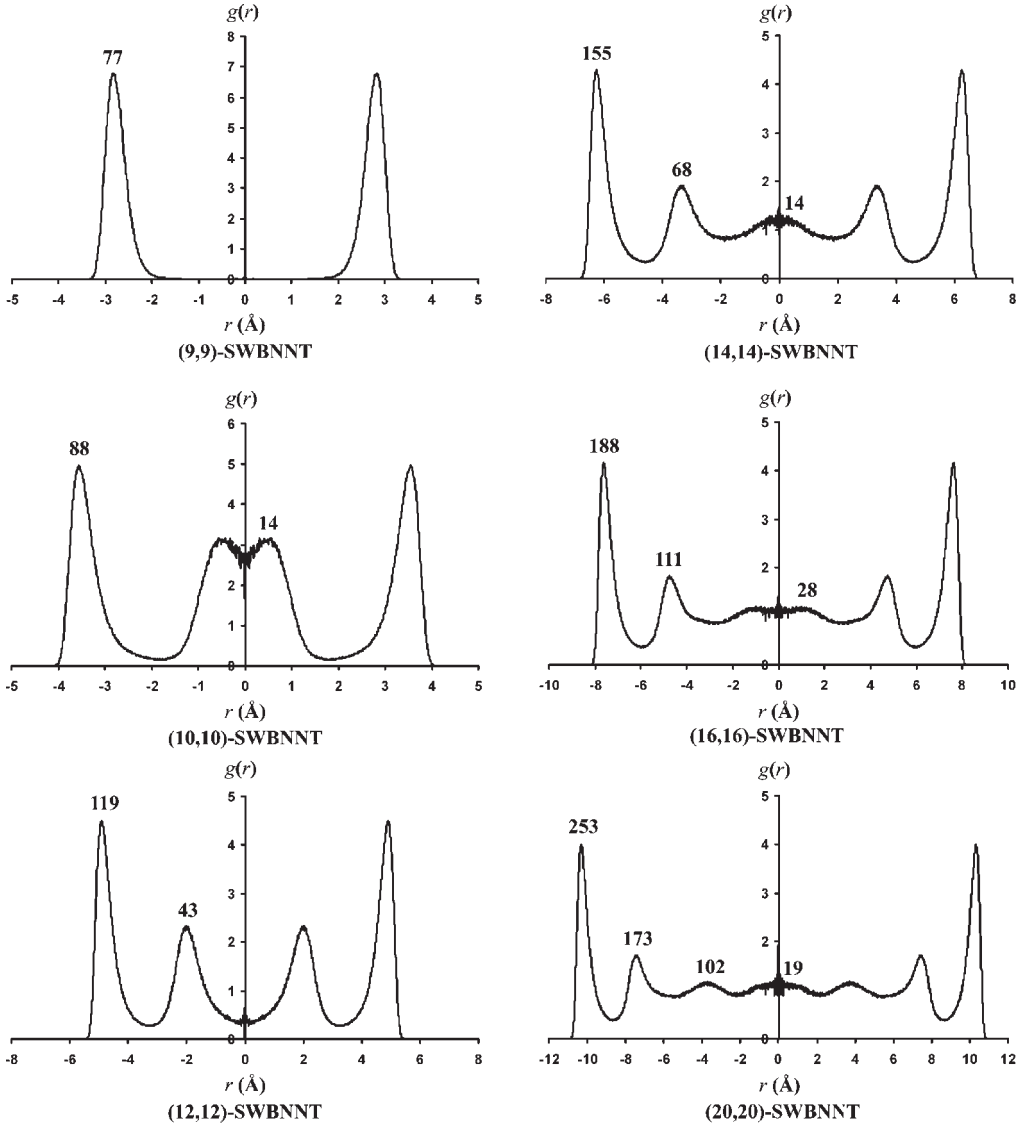

Figure 1. Local density distribution functions, in cylindrical coordinates, for the water molecules in the SWBNNTs. The numbers above the curves indicate the number of molecules present, on the average, in the various regions.

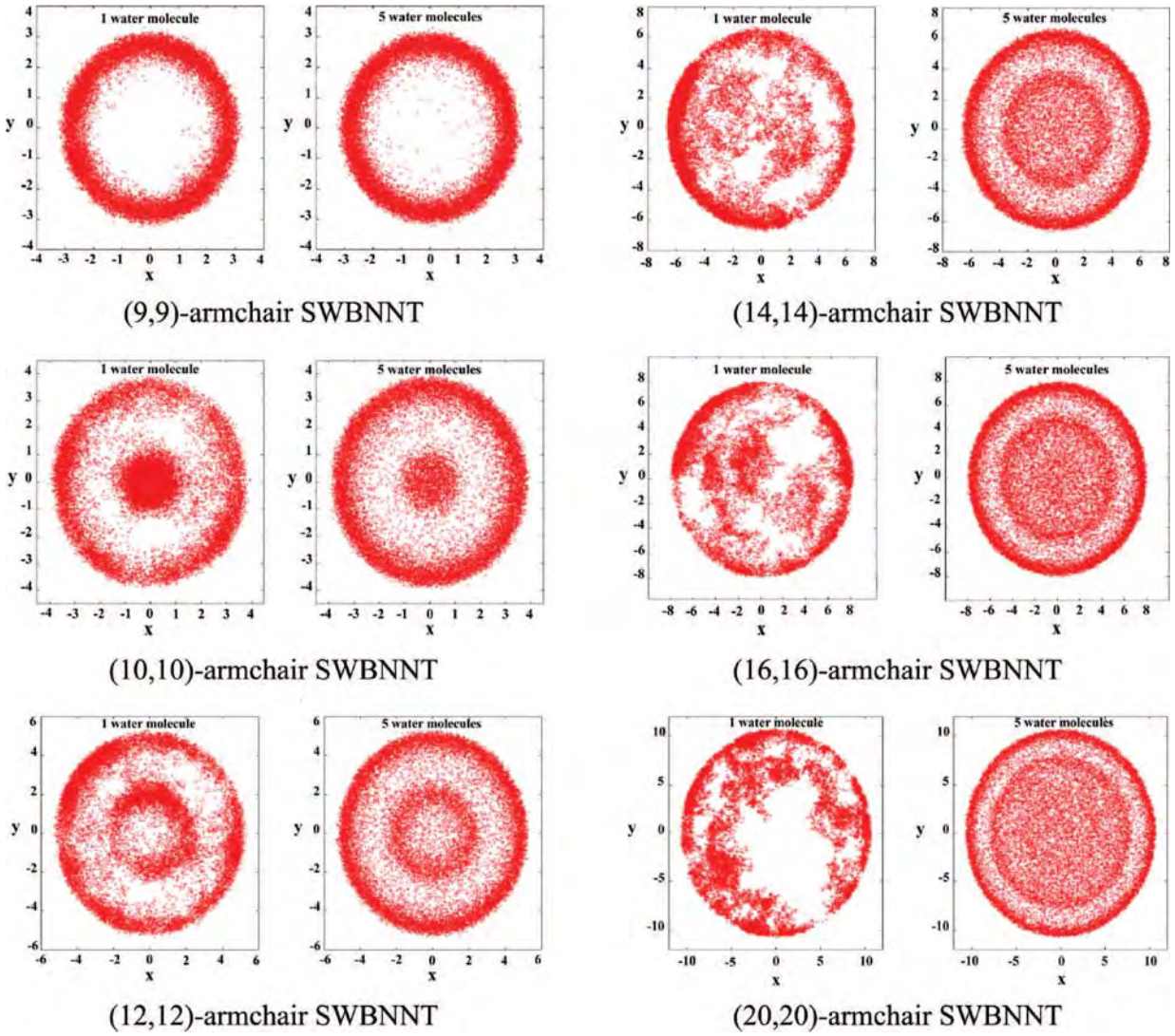

Figure 2. Trajectories of 1 (left) and 5 (right) arbitrarily selected water molecules in the SWBNNTs, corresponding to Figure 1, monitored during 1 ns. Note that the scale is not the same for all tubes.

lattice, where $\mathbf{a}_1$ and $\mathbf{a}_2$ are unit vectors. These nanotubes are filled with a total number of 77, 102, 162, 237, 327, and 547 water molecules, respectively, which leads to an average water density of 1.0 g/cm^3 in the tube.

Water is described by the extended simple point charge (SPC/E) model ($\varepsilon_{O-O} = 0.1554$ kcal/mol and $\sigma_{O-O} = 3.16$ Å).[21,22] The geometry of each water molecule is kept rigid using the SHAKE algorithm. The two hydrogen atoms are located at 1.0 Å from the oxygen with an H−O−H angle of 109.5°. Atomic charges of $-0.8476e$ and $+0.4238e$ are assigned to the oxygen and hydrogen sites, respectively.

The interactions between water and the nanotube wall are described by a 12-6 LJ potential. The LJ parameters for carbon ($\varepsilon_{C-C} = 0.0970$ kcal mol^{-1} and $\sigma_{C-C} = 3.36$ Å) are taken from ref 14. The water−nanotube interaction parameters are derived by using the Lorentz−Berthelot combining rules i.e., $\varepsilon_{ij} = (\varepsilon_i\varepsilon_j)^{1/2}$ and $\sigma_{ij} = (\sigma_i + \sigma_j)/2$, where ε_{ij} and σ_{ij} symbolize the strength and size of the LJ potential parameters between sites i and j.

The degree of "nanotube hydrophobicity" is varied for all tubes by changing the strength of the LJ potential parameter (ε_{O-C}) between water and wall as an independent parameter, keeping the size parameter (σ_{C-C}) unchanged. Hydrophobicity is said to increase when ε_{O-C} is reduced. We study the case $\varepsilon_{O-C} = 0.1143$ kcal/mol, a 7% reduction compared to the full value $\varepsilon_{O-C} = 0.1230$ kcal/mol. These simulations are labeled a, e.g. (9,9)-SWCNTa; simulations with the full potential are labeled b. Furthermore, we study a case which models boron nitride nanotubes (SWBNNT) isostructural to the carbon tubes. Still keeping the σ-value constant, we set $\varepsilon = 0.1216$ and 0.1502 kcal/mol for the oxygen−boron and oxygen−nitrogen interactions, respectively, as in ref 11. Already the 7% decrease in hydrophobicity is found to lead to a loss of water conductivity in the small (5,5)-SWCNT.[11] Similarly, it is found that in (5,5)-armchair SWBNNT attractive interactions between water and nitrogen sites are primarily accountable for the good water conduction. Therefore, it seemed interesting to look at the diffusion and structural properties of water confined in large diameter tubes also of this type. Further details of the nanotube-simulations are given in Table 1. A pure SPC/E-water box at 298 K was also run for comparison.

The coordinates for the wall atoms of the nanotubes are generated by using the Materials Studio Visualizer program.[23] Short pieces of tube are then surrounded by about 2,000 SPC/E water molecules in a simulation box, *NpT* simulations are started with $p = 1$ atm and the temperature is lowered from high values to $T = 298$ K. In a few 10 ps, depending on tube size, the small sections of the tubes are filled with water. Several of these

pieces, for details see below, are then put together in a periodic box and equilibrated before starting the production runs.

All MD production simulations are performed in the canonical (*NVT*) ensemble at a temperature of 298 K using the Nosé-Hoover thermostat implemented in the DL_POLY program package,[24] version 2.17. The dimensions of the periodic simulation box for each system are twice the nanotube diameter in the *x*- and *y*-directions and the length of the tube in the *z*-direction. The principal axis of the nanotube is the *z*-axis of the simulation box. Periodic boundary conditions are applied to all three directions. The long-range electrostatic interactions between water molecules are computed using the Ewald method, and the short-range van der Waals interactions are computed up to a cutoff radius equal to the nanotube diameter for $m = 9$, 10, and 12, and equal to 18.44 Å for $m = 14$, 16, and 20. The equations of motion are integrated with a 0.25-fs time step. The production runs are conducted for at least 1 ns following the equilibration period of 0.25 ns. During the production runs, the coordinates and velocities are stored, usually every 50 fs, for further analyses.

III. Results and Discussion

(a) Structure. Figure 1 shows the so-called cylindrical $g(r)$-functions across the boron-nitride nanotubes. The numbers above the curves refer to the average number of water molecules present in the various regions; the total number of molecules is listed in Table 1. In the (9,9) case only one peak appears, in keeping with the results by Mashl et al.[14] for their (9,9) single-wall nanotube, while starting from the (10,10) and in the larger tubes, the cylindrical RDF shows two peaks indicating layering. The distance between these two peaks is 2.89, 2.89, 2.91 and 2.92 Å in the (12,12), (14,14), (16,16), and (20,20) tubes, respectively, larger than the r_{OO} distance of the first maximum of the $g(r_{OO})$-function in bulk water (2.76 Å). In the tubes with diameters above 18 Å the water density at the interior layer is very close to bulk density; inside a cylinder of 2.2 Å radius around the *z*-axis of the (20,20) tube it is exactly 1.0 g/cm^3.

Figure 2 gives a visual impression of the water arrangements (and motions) by showing the *x*- and *y*-coordinates of one (left) and five (right) arbitrarily selected water molecules plotted at regular time intervals during the simulations. The functions for the other two cases, SWCNTa and SWCNTb, are very similar to Figures 1 and 2 and are, therefore, not shown here. The boundary-layer peaks are only slightly enhanced with increasing wall−water interactions, as expected. As an example, we find an average of 250, 252, and 253 water molecules in the boundary layer in the cases of (20,20) SWCNTa, SWCNTb, and SWBNNT, respectively. The motions of the water molecules will be analyzed below.

When water molecules are confined in nanotubes, their neighborhoods differ from those in the bulk phase. A molecule is said here to have *n* neighbors if at a given time there are simultaneously *n* oxygen atoms with distances of r_{OO} < the first minimum of the bulk $g(r_{OO})$ (i.e., 3.33 Å) from the central oxygen atom. This definition does of course not imply that the coordination of the central oxygen is necessarily tetrahedral. Figure 3 shows the distributions of the number of neighbors, as defined above, for the SWBNNTs, separately for water molecules in the center and near the wall of the tubes, and in pure water. In the (9,9) tube all water molecules are located close to the wall and there is no water in the center of the pore, see Figures 1 and 2. The water structure in this tube is indeed peculiar with an extremely strong preference for four neighbors. For the wider nanotubes, a regular pattern emerges with a more or less invariable distribution of neighbors in the outermost layer and distributions in the interior converging with increasing tube diameter toward the one for pure water.

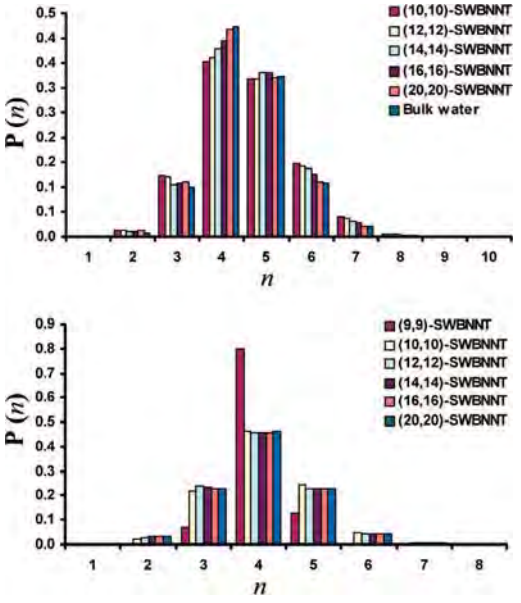

Figure 3. Distributions of the number of water neighbors of a water molecule in the interior (top) and in the outermost layer (bottom) in SWBNNT and, for comparison, in pure SPC/E water (top).

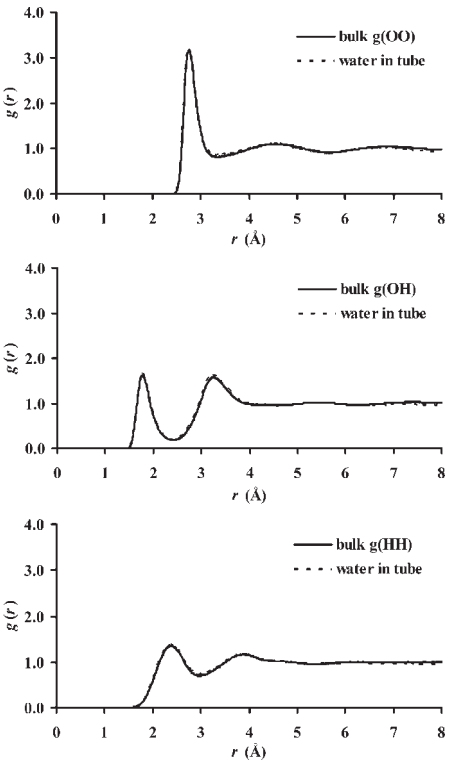

Figure 4. Radial distribution functions g_{OO}, g_{OH}, and g_{HH} for pure water (solid) and for water molecules in the center (−2.2 Å < *r* < 2.2 Å) of the (20,20) SWBNNT (dashed).

In order to further analyze the water structure in the center of a large tube, Figure 4 compares the three radial distribution functions (rdf) $g(r_{OO})$, $g(r_{OH})$, and $g(r_{HH})$ obtained in our pure bulk water reference run (see Table 1) with the ones obtained for molecules in the center of the (20,20) SWBNNT. Only sites inside a cylinder of 2.2 Å radius around the *z*-axis (see Figure 1) are selected as centers for this function. Since the number

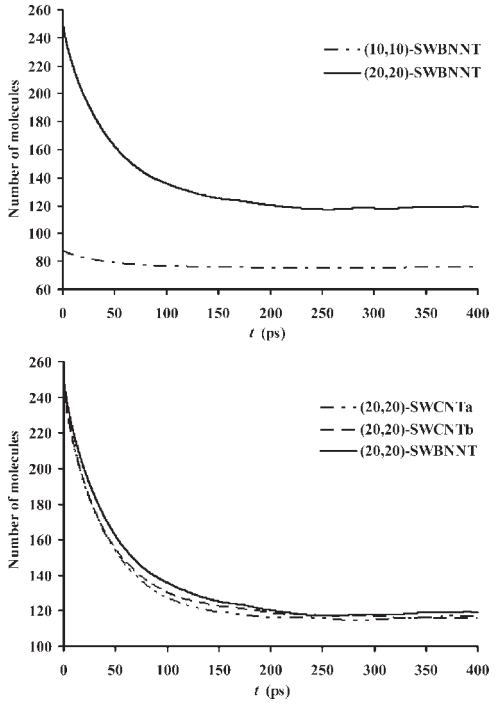

Figure 5. Average number of water molecules present in the outermost water layer at time 0 and still present there at later times, from simulation of (10,10) and (20,20) SWBNNT (top), and additionally, for comparison, for SWCNTa and SWCNTb (bottom).

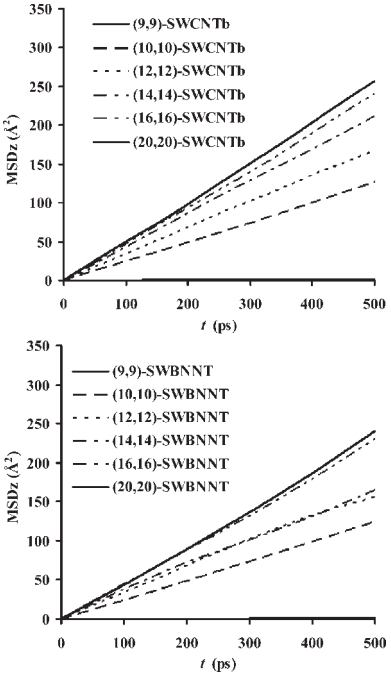

Figure 6. Mean square displacements of the oxygen atoms of water in the SWCNTbs (top) and SWBNNTs (bottom). For the self-diffusion coefficients, see Table 2 and Figure 7.

density is not constant across the tube, the normalization of these functions is somewhat arbitrary. The zone of roughly constant density inside the tube is about 8-Å wide, we thus selected to set $g(r \approx 6\ \text{Å}) = 1$ to ease comparisons. The figure shows that the three g-functions inside the tube are almost indistinguishable from the bulk ones. Thus, even with the strongest of our three wall−water interaction models, the water inside the larger tubes is, at least as far as the radial structure is concerned, very close to bulk water.

(b) Dynamics. Figure 5 shows the decay of the number of water molecules present in the boundary layer of the tube wall [defined as the water molecules with $r = \sqrt{(x^2 + y^2)}$ values larger than the minima in the distribution functions shown in Figure 1] at an initial time t_0, as a function of time. This figure shows, as examples, the results for a large and a small tube and also for a large tube with different interactions strengths (hydrophobicities) between water and wall. They confirm the visual impression obtained from Figure 2, namely that a given water molecules samples more or less the entire tube interior during the duration of our simulations.

The long time limit of these correlation functions is the expectation value of the initial molecules being present in the boundary layer when the system is totally mixed. It is seen that this value is reached, within the fluctuations, in all cases after about 150 ps. Functions of type

$$f(t) = a + b \cdot \exp(-t/\tau) \tag{1}$$

describe the correlation very well in all cases; the correlation times τ are all between 40 and 50 ps with the higher values for the stronger wall−water interactions. The sum $a + b$ obtained from the fits is, as it should be, close to the average total number of water molecules present in the boundary layer, which is also reported in Figure 1 from integrations of the distribution functions plotted there.

Figure 6 shows the averaged mean-square displacements of the oxygen atoms of the water molecules, corrected for the random drifts induced by the thermostat. The translational self-diffusion coefficients reported in Table 2 and Figure 7 have been obtained by fitting expressions

$$\left\langle (z - z_0)^2(t) \right\rangle = A + 2D_z t \tag{2}$$

to the mean-square displacement curves in z-direction at long times. We obtained a value of $D = 2.5 \pm 0.1 \times 10^{-5}$ cm^{2}s^{-1} from our pure water simulation. This D-value is intermediate between the values reported by Mashl[14] (2.69×10^{-5} cm^{2}s^{-1}) and by experimental diffusion coefficient of water (2.30×10^{-5} cm^2 s^{-1}).[25] In passing, we also take good note of the remarks in these papers that the fact that the experimental D is well reproduced by a given model for the pure liquid at a given state point does not necessarily mean that it will also do so in solutions, at an interface, or under different thermodynamic conditions. We nevertheless expect systematic trends (e.g., size dependences, or when the wall−water interactions are modified) to be reasonably well mirrored.

Figure 7 shows that no self-diffusion can be detected in the narrowest tubes during our simulation runs of a few nanoseconds. D_z increases with increasing tube diameter and comes close to its bulk value in our widest tubes with diameters of about 24 Å, the convergence toward this value being faster for smaller wall−water interactions. In the case of the boron-nitride tubes the convergence is not monotonous. We were not able to pinpoint the particular structural features that may explain the plateau in D_z observed between the (10,10) and (14,14) tubes (which we think is outside our uncertainties) in a convincing way. Even larger irregular variations of the self-diffusion have been observed by Mashl et al.[14] in narrower CNTs. No influence of the wall−water interactions can be distinguished in tubes wider than about 20 Å.

It is seen in Figure 6 that the linear regime of the mean-square displacement is reached typically after about 10 ps. Comparing this time with the typical time for water molecules to stay in the boundary layer discussed above (viz. 40 to 50 ps, see Figure 5), indicates that a separation of the total self-

TABLE 2: Axial Self-Diffusion Coefficients D_z ($cm^2\ s^{-1}$) of Water in Nanotubes at the Average Temperature of 298 K and the Water Density of 1.0 g/cm^3[a]

model	D_z ($cm^2\ s^{-1}$)	model	D_z ($cm^2\ s^{-1}$)	model	D_z ($cm^2\ s^{-1}$)
bulk water	2.50×10^{-5}				
(9,9)-SWCNTa	3.00×10^{-8}	(9,9)-SWCNTb	9.80×10^{-8}	(9,9)-SWBNNT	8.60×10^{-8}
(10,10)-SWCNTa	1.20×10^{-5}	(10,10)-SWCNTb	1.30×10^{-5}	(10,10)-SWBNNT	1.20×10^{-5}
(12,12)-SWCNTa	2.00×10^{-5}	(12,12)-SWCNTb	1.70×10^{-5}	(12,12)-SWBNNT	1.60×10^{-5}
(14,14)-SWCNTa	2.30×10^{-5}	(14,14)-SWCNTb	2.10×10^{-5}	(14,14)-SWBNNT	1.60×10^{-5}
(16,16)-SWCNTa	2.40×10^{-5}	(16,16)-SWCNTb	2.40×10^{-5}	(16,16)-SWBNNT	2.40×10^{-5}
(20,20)-SWCNTa	2.70×10^{-5}	(20,20)-SWCNTb	2.60×10^{-5}	(20,20)-SWBNNT	2.50×10^{-5}

[a] The uncertainties are estimated to be of the order of $\pm 0.1 \times 10^{-5}$ $cm^2\ s^{-1}$.

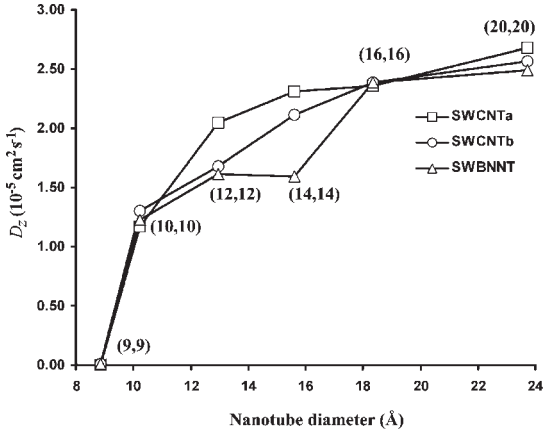

Figure 7. Axial self-diffusion coefficients D_z (10^{-5} $cm^2\ s^{-1}$) of water in nanotubes as a function of tube size.

diffusion into a component originating in the boundary layer molecules and a second one originating in the bulk would be justified. This work is presently ongoing.

IV. Summary and Conclusions

Molecular dynamics computer simulations at room temperature of water-filled single-wall model nanotubes with diameters ranging from about 9 Å to about 24 Å have shown that, by and large, the influence of the wall on the local density of the water and on its self-diffusion does not extend much beyond the layer of molecules directly adsorbed to the wall. In particular circumstances, probably when the geometrical constraints by and the interactions with the wall favor the formation of particular water structures, anomalies cannot be ruled out even in tubes of intermediate widths.

Varying the strength of the wall−water interactions within reasonable limits for carbon or boron-nitride tubes does not alter these conclusions. The adsorbed water layer, on the other hand, is very strongly affected both in its structure and in its dynamics. The characteristic time for the exchange dynamics between the adsorbed layer and the rest of the water is of the order of about 40 to 50 ps, i.e. relatively long compared to the time needed for the diffusive regime to be reached in normal, unconfined water at the same thermodynamic conditions.

Acknowledgment. This work was supported in part by Grants from the Thailand Research Fund (to J.L. and P.A.B.) and the Kasetsart University Research and Development Institute (KURDI), the National Nanotechnology Center (NANOTEC Center of Excellence and CNC Consortium), the National Research Council of Thailand (NRCT), and the Commission on Higher Education (Postgraduate Education and Research Programs in Petroleum and Petrochemicals, and Advanced Materials to J.L. as well as Postdoctoral Research Scholar to T.N.). The support from the Graduate School Kasetsart University (to N.A.) is also acknowledged.

References and Notes

(1) O'Connell, M. J. *Carbon Nanotubes: Properties and Applications*; CRC Press: Boca Raton, FL, 2006.
(2) Iijima, S. *Nature* **1991**, *354*, 56–58.
(3) Wang, Z. L.; Poncharal, P.; De Heer, W. A. *J. Phys. Chem. Solids* **2000**, *61*, 1025–1030.
(4) Sui, H.; Han, B. G.; Lee, J. K.; Walian, P.; Jap, B. K. *Nature* **2001**, *414*, 872–878.
(5) Kolesnikov, A. I.; Zanotti, J.-M.; Loong, C.-K.; Thiyagarajan, P.; Moravsky, A. P.; O. Loutfy, R. O.; Burnham, C. J. *Phys. Rev. Lett.* **2004**, *93*, 035503/1–035503/4.
(6) Chou, C.-C.; Hsiao, H.-Y.; Hong, Q.-S.; Chen, C.-H.; Peng, Y.-W.; Chen, H.-W.; Yang, P.-C. *Nano Lett.* **2008**, *8*, 437–445.
(7) Tajkhorshid, E.; Nollert, P.; Jensen Morten, O.; Miercke Larry, J. W.; O'Connell, J.; Stroud Robert, M.; Schulten, K. *Science (New York)* **2002**, *296*, 525–530.
(8) Bianco, A.; Kostarelos, K.; Prato, M. *Curr. Opin. Chem. Biol.* **2005**, *9*, 674–679.
(9) Hummer, G.; Rasaiah, J. C.; Noworyta, J. P. *Nature* **2001**, *414*, 188–190.
(10) Waghe, A.; Rasaiah, J. C.; Hummer, G. *J. Chem. Phys.* **2002**, *117*, 10789–10795.
(11) Won, C. Y.; Aluru, N. R. *J. Am. Chem. Soc.* **2007**, *129*, 2748–2749.
(12) Beckstein, O.; Biggin, P. C.; Sansom, M. S. P. *J. Phys. Chem. B* **2001**, *105*, 12902–12905.
(13) Allen, R.; Hansen, J.-P.; Melchionna, S. *J. Chem. Phys.* **2003**, *119*, 3905–3919.
(14) Mashl, R. J.; Joseph, S.; Aluru, N. R.; Jakobsson, E. *Nano Lett.* **2003**, *3*, 589–592.
(15) Liu, Y.; Wang, Q.; Wu, T.; Zhang, L. *J. Chem. Phys.* **2005**, *123*, 234701–234707.
(16) Koga, K.; Tanaka, H.; Zeng, X. C. *Nature* **2000**, *408*, 564–567.
(17) Liu, Y.; Wang, Q. *Phys. Rev.* **2005**, *72*, 085420/1–085420/4.
(18) Liu, Y.; Wang, Q.; Zhang, L.; Wu, T. *Langmuir* **2005**, *21*, 12025–12030.
(19) Joseph, S.; Aluru, N. R. *Nano Lett.* **2008**, *8*, 452–458.
(20) Won, C. Y.; Aluru, N. R. *J. Phys. Chem. C* **2008**, *12*, 1812–1818.
(21) Berendsen, H. J. C.; Grigera, J. R.; Straatsma, T. P. *J. Phys. Chem.* **1987**, *91*, 6269–6271.
(22) Guillot, B. *J. Mol. Liq.* **2002**, *101*, 219–260.
(23) Accelrys, Inc. *Materials Studio, 4.2 V*; Accelrys, Inc.: San Diego, CA, 2007.
(24) Smith, W.; Forester, T. R.; Todorov, I. T.; Leslie, M. *The DL_POLY 2.0, User Manual, Version 2.17*; CCLRC, Daresbury Laboratory: Daresbury, U.K., 2006.
(25) Price, W. S.; Ide, H.; Arata, Y. *J. Phys. Chem. A* **1999**, *103*, 448–450.

JP8088676

Stable nanoporous alkali halide polymorphs: a first principles bottom-up study

W. Sangthong,[abc] J. Limtrakul,[bc] F. Illas[a] and S. T. Bromley*[ad]

Received 29th May 2008, Accepted 2nd October 2008
First published as an Advance Article on the web 7th November 2008
DOI: 10.1039/b809129c

The stability of nanoclusters and nanocluster-based polymorphs of a large range of alkali halides were investigated using state-of-the-art plane wave density functional theory (DFT) calculations. Specifically, the most energetically stable cluster isomers of $(MX)_{12}$ (M = Li, Na, K, Rb, Cs, X = F, Cl, Br, I) were considered (*i.e.* the slab and cage) with respect to two bulk polymorphs: rock-salt (rs-MX) and a nanoporous analogue of the zeolite sodalite (SOD-MX). In both cases, these bulk materials can be regarded as being assembled from their respective cluster building block (slab → rs, cage → SOD). For all alkali halides the dense rs-MX phase was found to be more stable than the low-density nanoporous SOD-MX phase. For the $(MX)_{12}$ clusters, the dense slab cluster isomers were also generally found to be the most stable cluster type except, however, for the LiX series where the cage isomer was energetically preferred. The energy difference between the rs-MX and the SOD-MX bulk polymorphs (per MX unit) was found to follow the same trend as that between the respective $(MX)_{12}$ slab and cage clusters. Correspondingly, the cage-based SOD-LiX phases were all found to be only marginally metastable with respect to the rs-LiX forms ($\Delta E_{\text{SOD-rs}} \leq 0.05$ eV per LiX). From DFT calculations on the low enthalpy landscape of LiF polymorphs, the energy *versus* volume equations of state of rs-LiF and SOD-LiF were compared with those of a number of other LiF polymorphs showing SOD-LiF to be stable with respect to compression and expansion and very competitive energetically with a number of denser phases. Classical molecular dynamics calculations were also performed to confirm the thermal stability of the SOD-LiF phase, further strengthening our prediction as to the viability of these novel low density nanoporous ionic materials.

Introduction

The modification of the structure of inorganic crystalline solids through varying the external pressure is now a widely used experimental technique that has led to the discovery of a number of new phases with potential applications.[1,2] Theoretical methods have also been widely used to study the behavior of experimentally known ground-state phases of numerous materials under pressure.[3] Although experiments are now able to effectively maintain negative pressure conditions to explore the possibility of phases lower in density than the ground state, this technique does not yet allow one to investigate a wide class of very low density porous crystalline materials (*e.g.* zeolites[4]), which are regularly synthesised *via* bottom-up routes in solution. In order to theoretically explore the feasibility of new crystalline polymorphs, other than those obtained through pressure-induced transformations of the most stable phase, global optimisation algorithms may be employed to study the energy landscape of materials.[5–7] In relation to the present work on alkali halide polymorphs, we note in particular the recent careful investigations of a range of known and new hypothetical polymorphs of the alkali halides by Schön and co-workers[8,9] based on empirical potential based global optimisation followed by refined energy evaluation by DFT calculations. Crystal global optimisations generally start from the assumption of a bulk periodic crystal cell occupied by atoms, and make use of different algorithms to modify the atomic positions and cell dimensions towards possible minima. Such approaches may be described as top-down approaches. Increasing evidence indicates that the atomic structure of materials at the nanoscale, where the assumption of long-range crystalline periodicity breaks down, can be significantly different from that exhibited by bulk materials. Recent work, for instance, provides evidence that materials exhibiting the well-known wurtzite structure such as AlN, GaN, and SiC may exhibit a new graphitic phase as nanofilms.[10] Likewise, ZnO nanostructures have been predicted to experience different types of structural transformations specific to the nanoscale.[11,12] Compelling evidence that both SiO_2 and MgO may exhibit different stable alternative phases in thin films grown on metal substrates has also been reported.[13,14]

Recently, some of us reported on the prediction of low density nanoporous polymorphs of MgO, ZnO[15] and SiO_2[16] based on the assembly of highly stable nanoclusters. In contrast to top-down global optimisations, this approach follows the ideas contained in the ground-breaking work of Jena and co-workers on metal clusters[17] and can be regarded as a bottom-up means to materials prediction. Although both top-down and bottom-up approaches aim to find new stable polymorphs the former directly searches through the space of possible polymorphs whereas the latter aims first to find stable building blocks (*e.g.* through global optimisation

[a]*Departament de Química Física & Institut de Química Teòrica i Computacional (IQTCUB), Universitat de Barcelona, C/Martí i Franquès 1, E-08028 Barcelona, Spain*
[b]*Center of Nanotechnology, Kasetsart University, Bangkok 10900, Thailand*
[c]*Department of Chemistry, Kasetsart University, Bangkok 10900, Thailand*
[d]*Institució Catalana de Recerca i Estudis Avançats (ICREA), 08010 Barcelona, Spain*

of cluster isomers[15,16]) and then materials that may be regarded as arising from their assembly. Although both approaches are quite complementary, the focus on those materials which can be regarded as formed from stable cluster building blocks may provide more insight into ways in which these materials maybe fabricated *via* bottom-up routes. The prediction of stable polymorphs of MgO and ZnO as low density zeolitic analogues, derived from the bottom-up assembly of highly stable $(MO)_{12}$ cluster building blocks,[15] strongly suggests that similar nanoporous phases are likely to be stable for different types of materials.

In this work, we explore a wide range of ionic alkali halides for which, in many cases, small clusters have been experimentally generated.[18–20] Following the work of Carrasco *et al.*,[15] we use DFT calculations to study the relative stability of energetically lowest lying $(MX)_{12}$ (X = halogen, M = alkali metal) cluster isomers with respect to that of two polymorphs, which can be considered as formed from the assembly of these clusters: the rock-salt (rs-MX), and SOD-MX (the latter phase having strong topological similarity with the silicate zeolite sodalite[4,15]) phases. We compare the energetic trends of the cluster isomers and their respective bulk phases, throughout the full range of materials which reveals an intriguing link between nanoscale and macroscopic stabilities. The Li-based materials are shown, in particular, to be most likely to exhibit new viable low density nanoporous phases.

II. Computational details

In order to explore low density phases of the alkali halides, two different sets of DFT calculations were carried out. In the first, the differences between the most energetically stable cluster isomers were calculated, and in the second we obtained the energy *versus* volume equation of state (EOS) of the extended bulk polymorphs. In the case of the clusters, for all alkali halides we considered three low energy $(MX)_{12}$ isomers: (i) a $4 \times 2 \times 1$ slab, (ii) a tube formed from four stacked X_3M_3 hexagons, and (iii) a discrete SOD cage. In order to attain a balanced description of both discrete and extended systems, it is convenient to use the same computational approach and, whenever possible, the same basis set. This can be achieved by first choosing a reliable exchange-correlation functional that can be used in molecular and periodic calculations and, secondly, by expanding the total electron density in a plane wave basis using an appropriate unit cell. A plane wave basis is computationally efficient and for which the quality can be conveniently and generally defined by a single parameter. The Perdew–Wang (PW91) form[21,22] of the generalised gradient approach (GGA), as implemented in the VASP code,[23–25] has been chosen for the exchange-correlation potential. Due to its formulation, the PW91 functional is known to be particularly suitable for solids.[26] Furthermore, for the comparison of the stabilities of solids of the same composition but with significantly different densities and ionic coordination environments (especially relevant for comparing rs-MX and SOD-MX polymorphs) the PW91 functional has also been shown to perform extremely well for other materials.[27] Specifically for the alkali halides other work has shown that the PW91 can reproduce experimental data with high accuracy[28] (see also Table 2).

For the discrete systems, using a plane wave basis set requires simply placing the clusters inside a large enough box, which is periodically repeated. The box chosen has to be large enough so that the distance between repeated $(MX)_{12}$ clusters is sufficient to make inter-cluster interactions negligible (in our calculations >1 nm). For the solids, although in principle we may use the same $(MX)_{12}$ units and reduce the vacuum space between the periodically repeated units in such a way that a bulk structure is created, it was computationally more convenient to use the typical cubic unit cell for rs-MX and a cubic unit cell containing 12 atoms of a cage for SOD-MX. For the bulk systems, it is also necessary to carry out appropriate integrations in reciprocal space, this is accomplished by using a Monkhorst–Pack grid of special *k*-points ($7 \times 7 \times 7$ for the rock-salt structure and $3 \times 3 \times 3$ for the low density phases). In the present work, we included plane waves with kinetic energies up to 415 eV in the basis set. The effect of core electrons on the valence density was taken into account through the plane augmented wave method[29] as implemented by Kresse and Joubert.[30] For all MX bulk structures, density functional optimisations of atomic positions and cell shape were carried out for different volumes of the unit cell and the volume *versus* energy data fitted using the Birch–Murnaghan EOS[31] in order to obtain the minimum energy and optimum cell parameters. For all calculations (both solids and clusters) no explicit use of symmetry was employed.

III. Relative stability of $(MX)_{12}$ alkali halide clusters

The main purpose of the present work is to analyse the possibility of low density bulk phases of alkali halides and their relative stability with respect to the face-centered cubic (fcc) structure, which is almost always the most stable alkali halide polymorph. We note that for the most voluminous cation (Cs^+) with the three larger anions: Cl^-, Br^-, I^-, the body-centered cubic (bcc) phase is the ground state bulk phase. With relation to our bottom-up approach, however, the clusters $(CsCl)_{12}$, $(CsBr)_{12}$, $(CsI)_{12}$, all appear to be most stable as $4 \times 3 \times 2$ fcc slab isomers. For each alkali halide, we energy minimised the slab, the cage and tube (see Fig. 1) as $(MX)_{12}$ isomers. In all cases the $(MX)_{12}$ tube was never found to be the most stable isomer, with the lowest energy

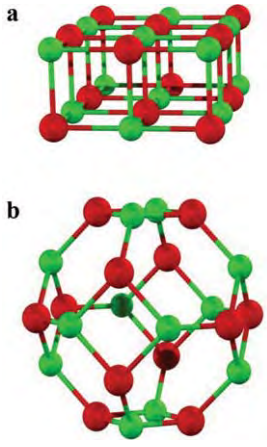

Fig. 1 Schematic representation of the structure of the slab (a) and cage (b) structures of the $(MX)_{12}$ alkali halide clusters. Red spheres represent the fluoride anion whereas the green spheres represent the lithium cations.

Table 1 Total energy (binding energy with respect to constituent spherical non spin-polarised atoms) per MX unit (in eV) of the slab and cage isomers of the $(MX)_{12}$ alkali halide clusters

MX	Slab	Cage
LiF	−9.25	−9.28
LiCl	−7.16	−7.18
LiBr	−6.46	−6.48
LiI	−5.70	−5.72
NaF	−8.14	−8.09
NaCl	−6.43	−6.38
NaBr	−5.81	−5.76
NaI	−5.14	−5.09
KF	−7.86	−7.79
KCl	−6.39	−6.31
KBr	−5.83	−5.74
KI	−5.22	−5.13
RbF	−7.76	−7.69
RbCl	−6.32	−6.23
RbBr	−5.77	−5.68
RbI	−5.17	−5.08
CsF	−7.73	−7.69
CsCl	−6.34	−6.25
CsBr	−5.80	−5.72
CsI	−5.22	−5.13

isomers being either the cage or slab only. Results for the relative energy of the slabs and cages for the series (M = Li–Cs and X = F–I) are reported in Table I.

For both slab and cage isomers, it is found that with the same alkali cation (M^+) and varying the halide anion (X^-), the optimised energies increase with decreasing ionic radius ratio (r_{M^+}/r_{X^-}) and follow an almost linear correlation (see Fig. 2a,b). Correspondingly, the most stable clusters are those of $(MF)_{12}$ type while the least stable are those of $(MI)_{12}$ composition. In contrast along each series: $(MF)_{12}$, $(MCl)_{12}$, $(MBr)_{12}$, $(MI)_{12}$ (*i.e.* fixing the halide type and varying the alkali metal ion) we see that, although for $(MCl)_{12}$, $(MBr)_{12}$, $(MI)_{12}$ the energy varies very little, for $(MF)_{12}$ both the cages and slabs clusters are significantly more stabilised (see Fig. 2a,b). Of all alkali halides, LiF is found to provide the most stable clusters for both slab and cage structures with energies (per MX unit) of −9.25 and −9.28 eV per LiF, respectively. This result together with the energetic preference of LiF for the cage isomer over the slab already provides an indication that LiF can be regarded as a special case.

In Fig. 3 we report the energy difference (per MX unit) between the cage and the slab isomers for each fixed halide (X) while varying the metal type (M). In most cases we find that the cubic slab isomer is most stable. This concurs with previous work showing an energetic preference for cubic isomers in alkali halide clusters containing Na, K, and Rb using a variety of theoretical methods including global optimisation techniques with empirical potentials, *ab initio* Hartree–Fock and Møller–Plesset second-order perturbation theory.[32–36] These works also often found

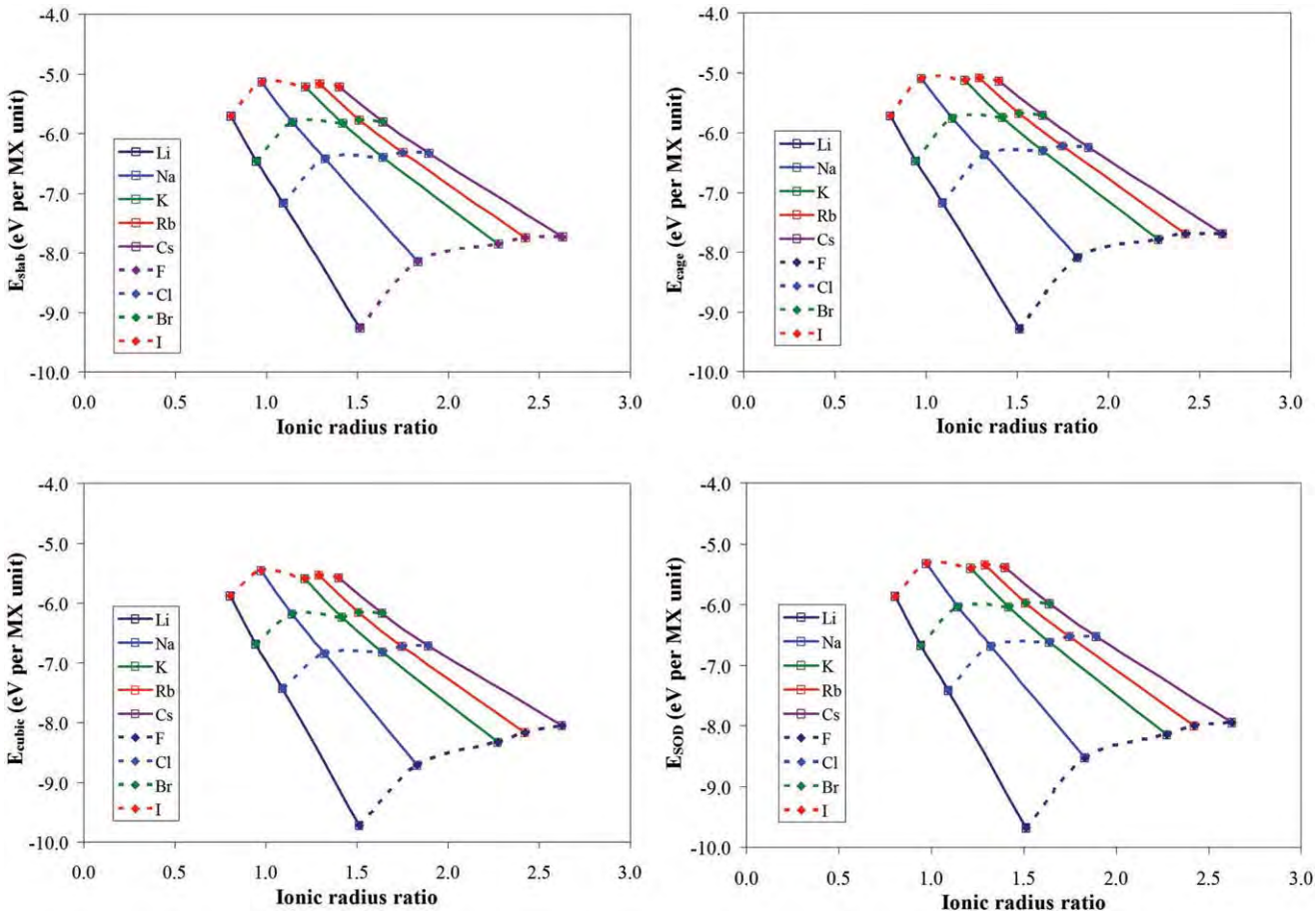

Fig. 2 Total energy of the alkali halides as clusters (left-top: slab; right-top: cage) and materials (left-bottom: RS; right-bottom: SOD) as a function of the cation and anion type with respect to cation-to-anion radius.

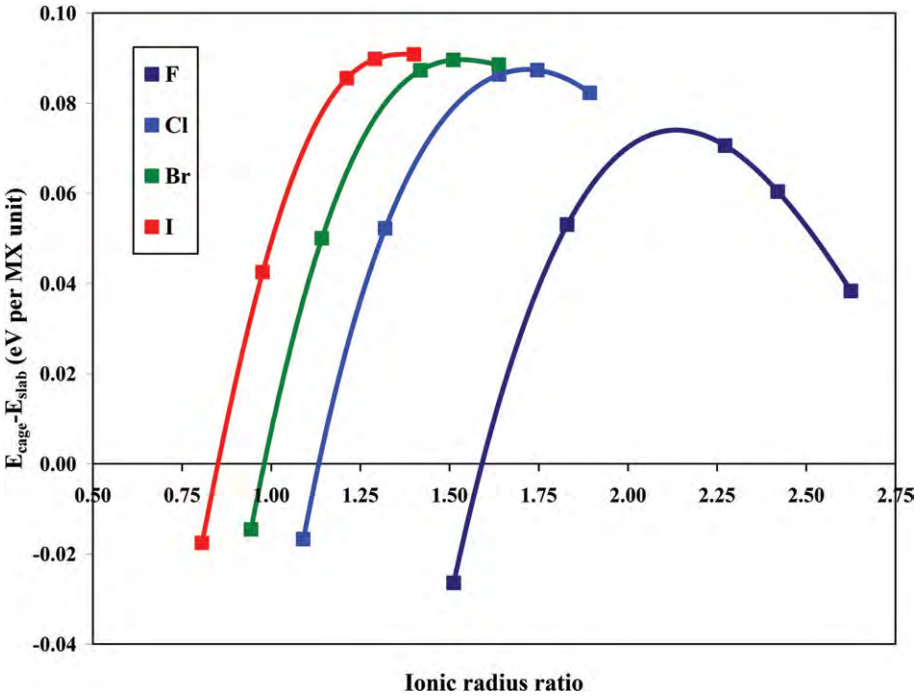

Fig. 3 Energy difference (eV per MX) between the slab and cage structure of the $(MX)_{12}$ alkali halide clusters as a function of the cation-to-anion ionic radius ratio. Each set of points relates to a series maintaining the halide and varying the alkali metal from Li^+ to Cs^+ from left to right (the lines are parabolic fits to the points to guide the eye).

evidence for competition between the energetic stability between rock-salt and tubular hexagonal ring-based structures with the latter being generally favoured for Li-containing clusters. On idealised ionic packing grounds, it has been argued that the relative energy between the dense cubic and more open tubular structures may be rationalised by consideration of the ratio between the cationic and anionic radii.[33,37] Essentially, the argument is analogous to that used in the approximate rationalisation of dense crystal structures[38] whereby increasing differences in cation and anion radii leads to the inability of the ions to pack as closely as when of similar size, thus leading to more open crystal structures. In clusters, as there are no restrictions on periodicity, we may expect that the respective ions when of significantly different size may use non-bulk-like means to optimise their ionic packing. The reported emergence of non-bulk-like tubular low energy cluster isomers is in line with such packing rationalisations for the LiX series due to the very small relative size of the Li^+ ion with respect to all the halide ions. However, as noted above, for the size $(MX)_{12}$ we find tubular clusters are not the ground state isomer for any alkali halide and further that for the $(LiX)_{12}$ series the more open SOD cage structure appears to be the optimal manner to "pack" Li^+ and X^- ions. Specifically, the cage structure is found to be more stable than both the slab and tubular cluster isomers for all the $(LiX)_{12}$ clusters, and for the remainder the cubic slab is the $(MX)_{12}$ ground state. For $(LiX)_{12}$ the energy differences between cubic slab and cage isomers are rather small, lying in the range between -0.015 to -0.026 eV per LiX. However, from Li to Cs for a fixed halide, the energy difference between the two clusters increases steeply with increasing cation *versus* anion ionic radius ratio up to a maximum difference. For I the energy difference increase stops at this maximum point for CsI, whereas for Br-, Cl- and F-containing clusters the energy difference maximises and then starts to reduce again. For the F series this effect is most notable with an energy difference between slab and cage reaching a maximum for KF and then decreasing significantly for RbF and CsF. Again, we can rationalise this trend with respect to ionic radii ratios, whereby at the maximum of the curves in Fig. 3 we have ions of a very similar size (and thus a preference for close-packed slabs) and away from these maxima such packing is not possible and the more open cage isomer becomes progressively more competitive.

Although ionic packing arguments are useful, they are only general idealised guides to structural preferences that omit many details (*e.g.* polarisation-induced ion distortions) of the bonding in real systems, which is governed by the electronic structure. To gain some more detailed insight into the bonding and ionic polarisation in the cage and slab clusters, we have also analysed the changes in the electronic structure upon increasing the formal cation–anion radius ratio using the electron localisation function (ELF). The ELF was introduced by Becke and Edgecombe[39] and has been extensively used to analyse chemical bonding in a range of systems.[40–42] The topological analysis of the ELF allows one to distinguish between core and valence electrons and, in this last case, between lone pairs, covalent bonding between two atoms or multi-centered bonds. In the case of the alkali halide clusters, the chemical bonding is highly ionic as is reflected in the ELF maps shown in Fig. 4. When going from the extremes of LiF to CsF, through KF as an intermediate case, one can note interesting changes in the ELF maps for both cage and slab cluster isomers. The ELF maps for the slab cluster show rather spherical ELF basins, which are indicative of a highly ionic character, although

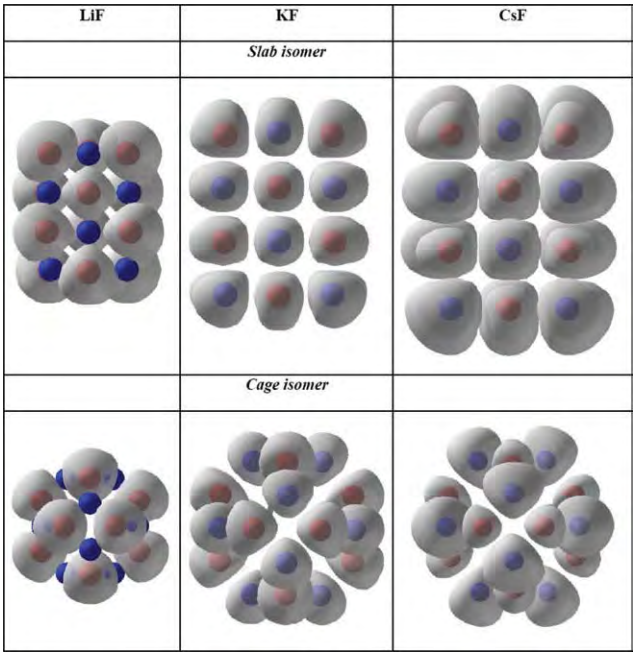

Fig. 4 ELF maps for the slab and cage structures of LiF, KF and CsF. The red centres indicate the positions of the alkali metal ions and the blue centres the halide ion positions. The grey area shows the form of the ELF basins for each ion.

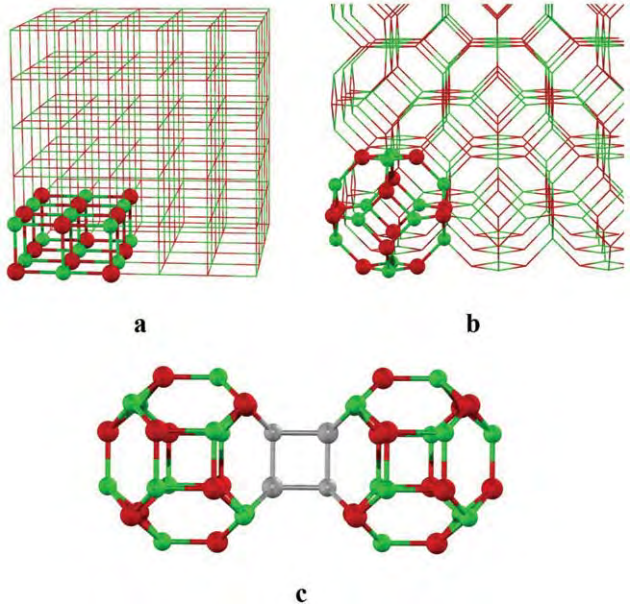

Fig. 5 rs-MX and SOD-MX structures of alkali halides viewed as the assembling of $(MX)_{12}$ slabs (a) and $(MX)_{12}$ cage clusters (b). In (c) we highlight (in grey) one of the 12 linkages per cage involved in the assembly of the cage cluster into the SOD-MX material. Red spheres represent the fluoride anion whereas the green spheres represent the cations.

with an increasing and noticeable deformation when going from LiF to CsF. For the cage clusters the situation is rather different, the ELF maps are largely deformed from the symmetric spherical shape, even for LiF. This is a clear indication that, in spite of similar stability, the chemical bond between the alkali metal and the halogen atom in the slab and cage clusters is different, with a more marked polarised and directional character in the cage structures. The directional character of the chemical bond in the cage structures is enhanced when going from LiF to CsF. This may seem counter-intuitive since one would expect the ionic character to increase along the series in response to the decrease of the alkali atom ionisation potential. However, one must also consider the different polarisation of the electron density upon increasing the cation atomic radius. In any case, the ELF maps in Fig. 4 show that a clear difference exists in the chemical bond of alkali halides in the slab and cage structures.

IV. Rock-salt structure *versus* sodalite structure of bulk alkali halides

Two types of bulk structures have been considered for the alkali halide materials (rs-MX and SOD-MX) both of which may be thought of as arising from assembling slab or cage clusters, respectively (see Fig. 5c). SOD-MX may be constructed by assembling twelve $(MX)_{12}$ cages by square links in such a way that an equivalent empty cage is created in the center of the resulting unit (see Fig. 4c). In the SOD-MX phase, the alkali and halide atoms are four-coordinated centers whereas in the rs-MX, the usual octahedral coordination is maintained. It should be noted that the sodalite (SOD) is not the only low density phase that may be generated by using $(MX)_{12}$ clusters as building blocks. Other low density nanoporous zeolite-like materials (*e.g.* LTA or faujasite[4]) can also be constructed from this simple building block,[15] however, these structures are generally less stable than SOD and have not been further considered.

For all the alkali halides series, the energy minimum for the SOD-MX structure has a volume per MX unit, which is significantly larger than that of the rs-MX structure with a concomitant lower density. Moreover, the SOD-MX phase is always higher in energy than the rs-MX polymorph, which is qualitatively different from the $(MX)_{12}$ slab and cage clusters where the cage structure was predicted to be more stable for the lithium halides. Nevertheless, as with the clusters, LiF is found to be the most stable compound in both rs-MX and SOD-MX phases with the calculated total energies being rather close: −9.73 and −9.68 eV per LiF, respectively. In order to investigate energetic trends, following the above analysis of the clusters, we have considered the dependence of the total energy of the rs-MX and SOD-MX phases with respect to the ionic radii ratio of the respective alkali metal and halide. For both phases, the total energy of the most stable polymorph, for a given cation while varying the anion, increases almost linearly with decreasing the ionic radii ratio (see Fig. 2c,d) in line with the trend observed for the clusters. Following the variation in cluster energetics, we also observe relatively little change in the energy of either bulk phase with the MCl, MBr, or MI composition, whereas the SOD-MF and rs-MF phases are particularly stable.

Examining the energy difference between rs-MX and SOD-MX phases at their corresponding optimised geometries, Fig. 6 shows that the energy difference between the rs-MX and SOD-MX phases also follows the same trend as the energy difference between the slab and cage $(MX)_{12}$ clusters (Fig. 3). This interesting finding strongly suggests that the relative energy

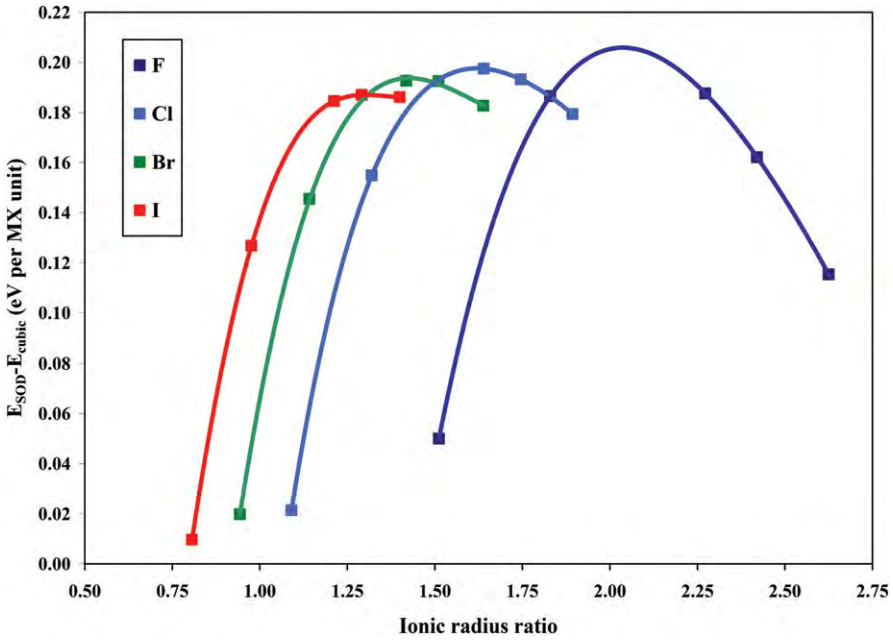

Fig. 6 Energy difference (eV per MX) between the rs-MX and SOD-MX alkali halide materials as a function of the cation–anion ionic radius ratio. Each set of points relates to a series maintaining the halide and varying the alkali metal from Li^+ to Cs^+ from left to right (the lines are parabolic fits to the points to guide the eye).

of the rs-MX and SOD-MX crystal structures is largely determined by the same driving forces that cause the energy difference between the slab and cage building blocks. Contrary to the cluster energetics, the SOD-MX phase is always less stable than the rs-MX phase. However, for the most stable SOD-MX materials (*i.e.* those containing the smallest cation, Li) the minimum energies of the SOD-LiX phases (LiF, LiCl, LiBr and LiI) are only 0.01–0.05 eV per LiX above the ground state rs-LiX structure. These very small energy differences suggest that for these compositions the SOD-LiX structure could be a viable synthesis target. Furthermore, in line with the behavior observed in Fig. 3 for the clusters, we also find the SOD-CsF phase (exhibiting a significant difference between anion and cation radius) is only 0.12 eV per CsF higher than the rs-CsF phase.

V. Stability of SOD-LiF

In order to compare the present results with previous work, we have calculated the energy *versus* volume EOS for rs-LiF and SOD-LiF together with a range of other reported phases in the literature. In particular we compare our bottom-up generated LiF-SOD phase with three new LiF phases predicted by Doll *et al.*[8] by global optimisation. These authors have also carried out periodic Hartree–Fock and LDA calculations for the different polymorphs predicted from their global optimisation studies. Interestingly, the low density SOD-LiF structure was not located by this method although it is very competitive in energy with respect to their newly predicted low energy LiF-phases (*i.e.* LiF-I, LiF-II and LiF-III). The probable reason for this omission is not due to any failure in the global optimisation methodology employed but rather due to the concentration on relatively dense materials with typically smaller unit cells. Whereas periodic Hartree–Fock calculations incorrectly predict wurtzite as the most stable LiF polymorph, both LDA calculations by Doll *et al.*[8] and the present GGA calculations correctly predict rs-LiF to be the most stable structure, in agreement with experiment. The energetic stability order of the remaining polymorphs predicted by LDA and GGA is, however, rather different. This is not so surprising since LDA is known to overestimate binding energies. Consequently, polymorphs with different crystal structures and variable coordination environments around each atom are affected differently by the LDA error. The GGA energies are likely to be considerably more accurate[26–28] and it is likely that the phase diagram in Fig. 7 provides a more realistic picture of the energy landscape of LiF polymorphs. In Table 2 we also compare the present GGA calculations for rs-LiF with other reported DFT calculations and experimental data also showing that the present PW91 calculations give a good account of the cell volume and bulk modulus.

The GGA calculated energy *versus* volume EOS curves predict that the SOD-LiF structure is marginally lower in energy than the LiF-I phase and significantly lower in energy than the LiF-II and LiF-III phases generated by Doll *et al.*[8] Only four phases appear to lie lower in energy than the SOD-LiF phase: rs-LiF, 5-5-LiF, wz-LiF (wurtzite), and zb-LiF (zincblende), all of which are significantly denser than SOD-LiF. The 5-5 phase (also known as the hexagonal phase in other studies[43,15]) was first proposed by Schön in the context of global optimisation of alkali metal oxide phases.[5] Interestingly, from a bottom-up perspective, the 5-5 phase can also be regarded as being generated from the assembly of hexagonal tubular clusters. Structurally, the 5-5 phase lies between wurtzite and rocksalt and is thought to be a relatively unstable phase with respect to its collapse into rocksalt, and, thus, 5-5-LiF is probably only viable as a real material at very low temperatures and low pressures.[5,8,43] Although the EOS curve of SOD-LiF shows that the structure is

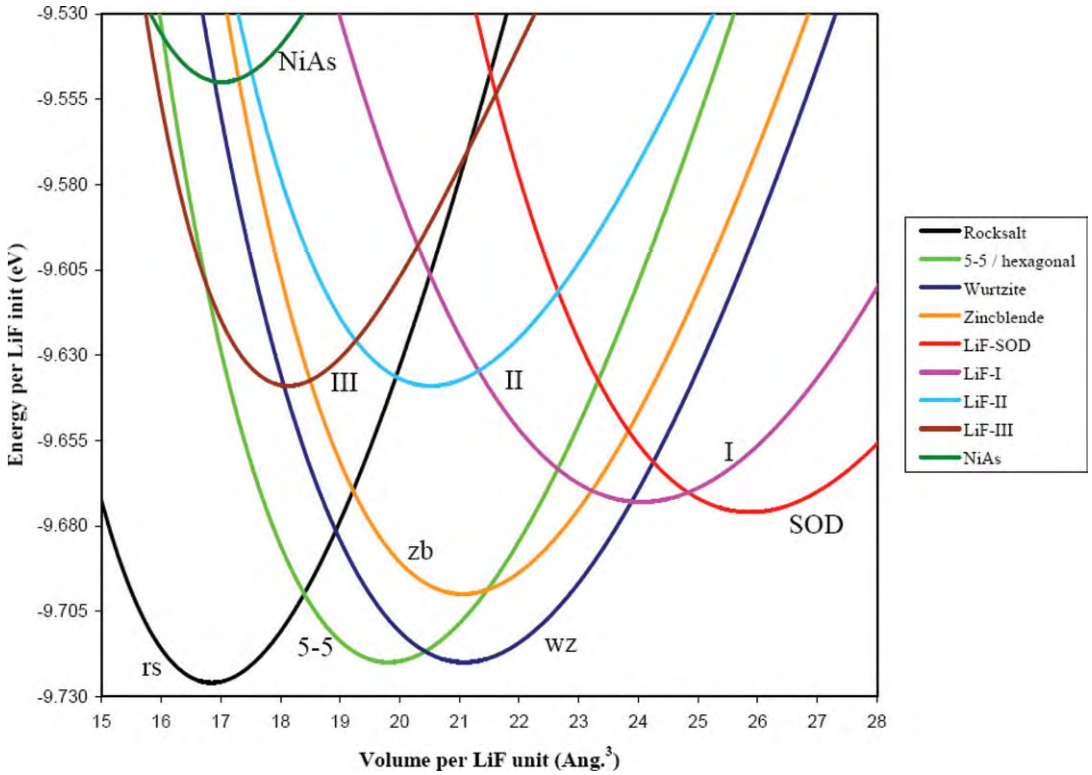

Fig. 7 Energy *versus* volume phase diagram for various polymorphs of LiF. The legend entries are ordered from top to bottom with respect to increasing minimum total energy (E_o).

Table 2 Properties of a range of LiF polymorphs calculated from the EOS fits to the GGA-DFT calculated data shown in Fig. 6: (i) E_0, minimum total energy (eV per LiF), (ii) ΔE_0, total energy differences (eV per LiF), (iii) V_0, volume at minimum energy (Å^3 per LiF), (iv) B_0, the bulk modulus (GPa per LiF). The equilibrium volume and bulk modulus (where available) of rs-LiF are compared with experimental values and other reported DFT calculations in the first five rows

	E_0	ΔE_0	V_0	B_0
rs-LiF (exp.)			16.32[47]	69.9[48]
rs-LiF (present work)	−9.726	0.000	16.85 (+3.2%)	68.6 (−1.9%)
rs-LiF (BPW91-GGA)[49]			17.48 (+7.1%)	63.9 (−8.6%)
rs-LiF (LDA)[49]			14.38 (−11.9%)	71.4 (+2.1%)
rs-LiF (LDA)[8]			15.29 (−6.3%)	—
wz-LiF	−9.720	0.006	21.08	48.3
5-5-LiF	−9.701	0.025	16.94	60.4
zb-LiF	−9.700	0.026	21.06	51.8
SOD-LiF	−9.676	0.050	25.87	41.7
LiF-I	−9.673	0.054	24.05	36.0
LiF-II	−9.639	0.087	20.52	48.6
LiF-III	−9.639	0.087	18.13	72.5

stable with respect to a range of pressures (both negative and positive in relation to the ground state) this only strictly applies at 0 K. Considering that SOD-LiF is one of the lowest density phases yet predicted for a purely ionic material, it is of interest as to whether the structure would be also stable to collapse to a denser more stable phase at finite temperatures.

In order to test the finite temperature stability of LiF-SOD we have employed constant pressure and temperature (NPT) molecular dynamics (MD). Due to the current unavailability of NPT-MD simulations within the VASP code and the very high computational expense of performing such simulations in a fully *ab initio* manner, we employed classical MD. For these simulations we employed the GULP code[44] and the interionic potentials of Catlow *et al.*[45] with a 3 Å cut-off and a 0.25 Å smoothing taper to avoid discontinuities in the energy and first and second derivatives. Importantly, considering the ELF analysis in section II, the potentials account for ionic polarisation *via* the shell model of Dick and Overhauser.[46] Firstly, we note that energy minimisations of atomic position and cell parameters using these potentials confirm that the SOD-LiF phase is metastable (by 0.03–0.17 eV per LiF) with respect to the lower energy denser phases (rs-LiF, wz-LiF, zb-LiF, 5-5-LiF) in qualitative agreement with the GGA-DFT optimisations, which confirms that the SOD-MX phase is not artificially stabilised by the

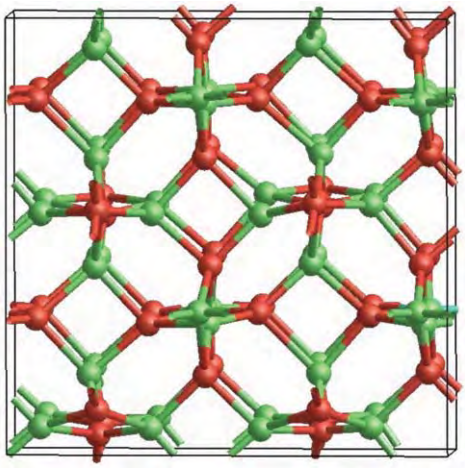

Fig. 8 Snapshot from the MD simulation of the SOD-LiF phase showing a typical configuration of the $2 \times 2 \times 2$ super cell at 300K. Red spheres represent the fluoride anions and green spheres represent the lithium cations.

potentials. Furthermore, although fitted with respect to rs-LiF, the potentials also give optimised SOD-LiF cell parameters (a, b, $c = 5.17$ Å; α, β, $\gamma = 90°$) in reasonable agreement with the GGA-DFT results (a, b, $c = 5.37$Å; α, β, $\gamma = 90°$). After first equilibrating the SOD-LiF system for 30 ps, we simulated the behaviour of a SOD-LiF $2 \times 2 \times 2$ supercell at 300 K at zero external pressure for over 2 nanoseconds. Throughout the MD simulation we found that the bonding topology of the SOD-LiF structure remained fully intact with the root mean squared deviations from the optimal cell parameters being only 0.12 Å with respect to unit cell dimensions and 1.44 degrees with respect to unit cell angles (see typical MD snapshot in Fig. 8). Surprisingly, unlike the 5-5-LiF phase, which is probably unstable, these calculations suggest that the SOD-LiF phase, if synthesised, would be stable under ambient conditions.

V. Conclusions

The possible existence of low density phases of bulk alkali halides has been investigated using a bottom-up approach together with state-of-the-art plane wave DFT calculations. To this end, the relative energies of the lowest energy cluster isomers of $(MX)_{12}$ have been studied throughout the MX series. The slab form of the $(MX)_{12}$ cluster may be viewed as the precursor of the rock-salt (rs-MX) structure while the assembling of $(MX)_{12}$ cages can lead to a low density phase reminiscent of the sodalite zeolite (SOD-MX). The slab $(MX)_{12}$ isomer is found to be energetically more stable than the cage, except for the LiX (X = F, Cl, Br, I) series where the cage is the most stable $(MX)_{12}$ cluster isomer. For a given halide series the energy difference between slab and cage isomers increases up until a maximum is reached and then decreases towards CsX. In the bulk analogues, the same behaviour with respect to the energy difference between rs-MX and SOD-MX is also observed. In both cases, the trends may be approximately rationalised in terms of ionic packing. In all alkali halides the SOD-MX phase was found to be stable with respect to compression and expansion at 0 K through calculation of their volume *versus* energy EOS. Furthermore, in the LiX (X = F, Cl, Br, I) series, where the cage is the ground state $(LiX)_{12}$ cluster, the SOD-LiX material is found to be particularly low in energy with respect to the lowest energy rs-LiX phase ($E_{\text{SOD-rs}}$ energy differences ranging between 0.01–0.05 eV per LiX). Taking the LiF-SOD phase as a case study, we have further employed MD simulations to confirm that the structure of this nanoporous alkali halide is thermally stable at 300 K. Considering that the lowest energy cluster for $(LiX)_{12}$ is a cage, together with the demonstration that for LiF, a nanoporous phase based upon its assembly, is stable with respect to 0 K pressure variation and at finite temperature, we suggest that these highly ionic yet low density materials may be realistic, yet challenging, synthesis targets through an appropriate bottom-up route.

Acknowledgements

This study has been supported in part by the Spanish Ministry of Education and Science (grants CTQ2005-08459-CO2-01 and UNBA05-33-001) by the Generalitat de Catalunya (grants 2005SGR00697, 2005PEIR0051/69). This work was further supported in part by grants from the Thailand Research Fund (to W.S. and J.L.) and the Commission on Higher Education, Ministry of Education under Postgraduate Education and Research Programs in Petroleum and Petrochemicals, and Advanced Materials. Support from the National Nanotechnology Center (NANOTEC Center of Excellence) under the National Science and Technology Development Agency and KURDI is also acknowledged.

References

1 L. Liu, W. A. Bassett, *Elements, Oxides, and Silicates. High-Pressure Phases with Implications for the Earth's Interior*, Oxford University Press, New York, 1986.
2 R. J. Hemley, *Ultrahigh-Pressure Mineralogy: Physics and Chemistry of the Earth's Deep Interior, vol. 37 of Reviews in Mineralogy*, The Mineralogical Society of America, Washington, DC, 1998.
3 A. Schleife, F. Fuchs, J. Furthmüller and F. Bechstedt, *Phys. Rev. B*, 2006, **73**, 245212.
4 *Atlas of Zeolite Framework Types, Sixth Edition*, ed. Ch. Baerlocher, LynneB. McCuskerand D. H. Olson, 6th revised edition, Elsevier, Amsterdam, 2007.
5 J. C. Schön, *Z. Anorg. Allg. Chem.*, 2004, **630**, 2354.
6 S. M. Woodley, P. D. Battle, J. D. Gale and C. R. A. Catlow, *Phys. Chem. Chem. Phys.*, 1999, **1**, 2535.
7 A. R. Oganov and C. W. Glass, *J. Chem. Phys.*, 2006, **124**, 244704.
8 K. Doll, J. C. Schön and M. Jansen, *Phys. Chem. Chem. Phys.*, 2007, **9**, 6127.
9 Z. P. Cancarevic, J. C. Schön and M. Jansen, *Chem.–Asian J.*, 2008, **3**, 561.
10 C. L. Freeman, F. Claeyssens, N. L. Allan and J. H. Harding, *Phys. Rev. Lett.*, 2006, **96**, 066102.
11 L. Zhang and H. Huang, *Appl. Phys. Lett.*, 2007, **90**, 023115.
12 A. J. Kulkarni, M. Zhou, K. Sarasamak and S. Limpijumnong, *Phys. Rev. Lett.*, 2006, **97**, 105502.
13 J. Weissenrieder, S. Kaya, J. L. Lu, H. J. Gao, S. Shaikhutdinov, H. J. Freund, M. Sierka and J. Sauer, *Phys. Rev. Lett.*, 2005, **95**, 076103.
14 J. Goniakowski, C. Noguera and L. Giordano, *Phys. Rev. Lett.*, 2004, **93**, 215702.
15 J. Carrasco, F. Illas and S. T. Bromley, *Phys. Rev. Lett.*, 2007, **99**, 235502.
16 J. C. Wojdel, M. A. Zwijnenburg and S. T. Bromley, *Chem. Mater.*, 2006, **18**, 1464.
17 S. N. Khanna and P. Jena, *Phys. Rev. Lett.*, 1992, **69**, 1664.

18 J. E. Campana, T. M. Barlak, R. J. Colton, J. J. DeCorpo, J. R. Wyatt and B. I. Dunlap, *Phys. Rev. Lett.*, 1981, **47**, 1046.
19 R. Pflaum, P. Pfau, K. Sattler and E. Recknagel, *Surf. Sci.*, 1985, **156**, 165.
20 Y. J. Twu, C. W. S. Conover, Y. A. Yang and L. A. Bloomfield, *Phys. Rev. B*, 1990, **42**, 5306.
21 J. P. Perdew, J. A. Chevary, S. H. Vosko, K. A. Jackson, M. R. Pederson, D. J. Singh and C. Fiolhais, *Phys. Rev. B*, 1992, **46**, 6671.
22 J. A. White and D. M. Bird, *Phys. Rev. B*, 1994, **50**, 4954.
23 G. Kresse and J. Hafner, *Phys. Rev. B*, 1993, **47**, 558.
24 G. Kresse and J. Furthmüller, *Comput. Mater. Sci.*, 1996, **6**, 15.
25 G. Kresse and J. Furthmüller, *Phys. Rev. B*, 1996, **54**, 11169.
26 J. P. Pedew and K. Burke, *Int. J. Quantum Chem.*, 1996, **57**, 309.
27 D. R. Hamann, *Phys. Rev. Lett.*, 1996, **76**, 660.
28 E. Apra, M. Causa, M. Príncipe, R. Dovesi and V. R. Saunders, *J. Phys.: Condens. Matter*, 1993, **5**, 2969.
29 P. E. Blöchl, *Phys. Rev. B*, 1994, **50**, 17953.
30 G. Kresse and D. Joubert, *Phys. Rev. B*, 1999, **59**, 1758.
31 F. Birch, *Phys. Rev.*, 1947, **71**, 809.
32 J. P. K. Doye and D. J. Wales, *Phys. Rev. B*, 1999, **59**, 2292.
33 A. Aguado, A. Ayuela, J. M. Lopez and J. A. Alonso, *Phys. Rev. B*, 1997, **56**, 15353.
34 T. Croteau and J. Patey, *J. Chem. Phys.*, 2006, **124**, 244506.
35 C. Ochsenfeld and R. Alrichs, *Ber. Der Bunsen-Gesellschaft*, 1994, **98**, 34.
36 M. Lintuluoto, *J. Mol. Struct. (Theochem)*, 2002, **540**, 177.
37 A. Wootton and P. Harrowell, *J. Chem. Phys.*, 2004, **121**, 7440.
38 D. Pettifer, *Bonding and Structure of Molecules and Solids*, Clareden, Oxford, 1995.
39 A. D. Becke and K. E. Edgecombe, *J. Chem. Phys.*, 1990, **92**, 5397.
40 B. Silvi and A. Savin, *Nature*, 1994, **371**, 683.
41 A. Savin, R. Nesper, S. Wengert and T. P. Fässler, *Angew. Chem., Int. Ed. Engl.*, 1992, **36**, 1809.
42 X. Krokidis, S. Noury and B. Silvi, *J. Phys. Chem. A*, 1997, **101**, 7277.
43 S. Limpijumnong and W. R. L. Lambrecht, *Phys. Rev. B*, 2001, **63**, 104103.
44 J. D. Gale, *J. Chem. Soc., Faraday Trans.*, 1997, **93**, 629.
45 C. R. A. Catlow, K. M. Diller and M. J. Norgett, *J. Phys. C: Solid State Phys.*, 1977, **10**, 1395.
46 B. G. Dick and A. W. Overhauser, *Phys. Rev.*, 1958, **112**, 90.
47 V. A. Streltsov, V. G. Tsirelson, R. P. Ozerov and O. A. Golovanov, *Kristallografiya*, 1987, **33**, 90.
48 C. V. Briscoe and C. F. Squire, *Phys. Rev.*, 1957, **1175**, 106.
49 G. Sandrone and D. A. Dixon, *J. Phys. Chem. A*, 1998, **102**, 10310.

Predicting transition pressures for obtaining nanoporous semiconductor polymorphs: oxides and chalcogenides of Zn, Cd and Mg

Winyoo Sangthong,[abc] Jumras Limtrakul,[bc] Francesc Illas[a] and Stefan T. Bromley*[ad]

Received 22nd March 2010, Accepted 29th May 2010
First published as an Advance Article on the web 6th July 2010
DOI: 10.1039/c0cp00002g

The energy *versus* volume equations of state are calculated for seven known and hypothetical polymorphic forms of ZnX, CdX, and MgX (where X = O, S, Se, Te). From these data the phases of lowest enthalpy are extracted with respect to decreasing pressure starting at the ground state for all compositions. Following these paths of minimum enthalpy, with respect to the polymorphs considered, we predict the transition pressures required to convert the ground-state phase into the novel, as yet hypothetical, nanoporous SOD phase (an analogue of the silicate zeolite sodalite). Our results suggest that the SOD phase would be thermodynamically stable for all compositions considered under suitable negative pressures. Of all the compositions considered CdX and MgX with relatively large anions (*i.e.* Se and Te) are specifically predicted to be the most amenable materials for the experimental preparation of the SOD phase.

Introduction

Binary ionic insulating materials of composition AB are known to exhibit only a small number of dense ground-state phases and are perhaps expected to be the least likely type of system in which to find new low-density polymorphs. Detailed theoretical explorations of the energy and enthalpy landscape of a number of such materials (*e.g.* the alkali halides and oxides) have, however, predicted that some moderately low-density phases should be only slightly metastable at standard pressure, and thermodynamically stable at slightly negative pressures.[1–3] Closely following these predictions, low-temperature atomic deposition on specially prepared substrates, causing conditions of effective negative pressure *via* lattice mismatch effects, has led to the production of LiBr and LiCl in the wurtzite structure (wz-LiBr and wz-LiCl) rather than the denser rocksalt (rs-LiBr and rs-LiCl) polymorph;[4,5] the latter being the ground-state phase under ambient pressure and temperature conditions. Although these are remarkable steps forward in the synthesis of new low-density inorganic polymorphs, potentially more exciting is the possibility of negative pressure conditions leading to new relatively low-density solid phases that are not known to be exhibited by any existing material. The so-called 5–5 or hexagonal phase (referred to hereafter by the abbreviation "hex-AB", where the AB is a 1 : 1 binary compound) consisting of aligned A_3B_3 hexagonal tubes, with density lower than rocksalt but higher than wurtzite, for example, was independently theoretically proposed as a metastable polymorph of NaCl[3] and later of MgO.[6] Although a hex-AB bulk phase has not yet been stabilized experimentally, it has been predicted to be potentially stable under suitable negative pressures (typically in the range −1 to −5 GPa) and low temperatures for a number of alkali halides[1] and alkali oxides.[2] Additionally, hex-MgO has been predicted to be formed in localized regions upon mechanically induced buckling of rs-MgO nanotubes.[7]

Other than AB insulators the binary wide-bandgap semiconductor ZnO has attracted significant recent attention with respect to its possible novel low-density polymorphism. ZnO can be prepared in small quantities as the rs-ZnO structure,[8] and can exist as both zinc blende (zb-ZnO) and wz-ZnO (the ground state) structural forms under standard conditions. Density functional (DF) calculations have also predicted that hex-ZnO may be stablised in unstrained ultra-thin nanorods and nanowires,[9] and in thicker nanorods under tensile strain.[10] A phase very similar to hex-ZnO but expanded in the crystallographic *c*-direction so as to make it closely analogous to the layered *h*-BN phase, with a density very similar to wz-ZnO, was also predicted by DFT calculations to be stable in thin films of ZnO.[11] We note that this phase, although often referred to as a graphitic ZnO phase, strictly does not have the same layer ordering as in graphite. Following Limpijumnong *et al.*[10] we will thus refer to this phase as "layered". Experimental deposition of monolayers of ZnO on Ag substrates confirmed that the layered-ZnO phase was stable up to three monolayers where upon the denser wz-ZnO phase appeared to form.[12] More recent DF calculations have predicted that another polymorph, the BCT (Body Centred Tetragonal) phase (also known as the β-BeO phase due to its existence as a high-temperature stable polymorph of BeO[13]), having a lower density than wurtzite, may be stabilized in slightly thicker nanoscale films of ZnO.[14] Other DF calculations have further predicted that BCT-ZnO may be stabilised

[a] *Departament de Química Física & Institut de Química Teòrica i Computacional (IQTCUB), Universitat de Barcelona, C/Martí i Franquès 1, E-08028 Barcelona, Spain*
[b] *Center of Nanotechnology, Kasetsart University Research and Development Institute (KURDI), Kasetsart University, Bangkok 10900, Thailand*
[c] *Department of Chemistry, Faculty of Science, Center of Nanotechnology, Kasetsart University, Bangkok 10900, Thailand*
[d] *Institució Catalana de Recerca i Estudis Avançats (ICREA), 08010 Barcelona, Spain*

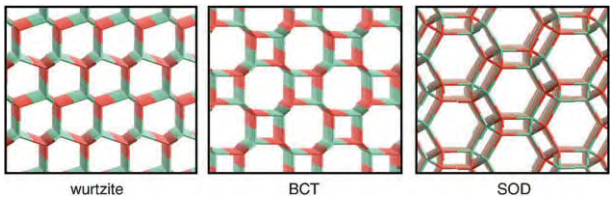

Fig. 1 Views of the three lowest density polymorphs considered. Left: wurtzite along the *a*-axis, middle: BCT along the *a*-axis, and right: SOD along the [111] direction.

in wz-ZnO nanorods under a tensile strain of 7 GPa (*i.e.* −7 GPa uniaxial pressure) in the [0001] direction.[15] We note that the BCT phase has also been predicted as a polymorphic phase potentially accessible under conditions of negative pressure greater (*i.e.* more negative) than that required to obtain the hexagonal phase for a range of alkali halides and oxides.[1,2] Searches of the low-energy landscape of the insulator boron nitride (BN) have also found BCT-BN as a possible metastable phase.[16] The BCT structure is shown in Fig. 1.

Having an even lower density than BCT, the SOD polymorph (with an analogous structure to the silicate sodalite structure[17]), has also been predicted by DF calculations to be only moderately metastable under conditions of zero pressure and temperature for both ZnO[18] and many alkali halides.[19] The SOD structure (see Fig. 1) is particularly interesting due to its nanoporous structure consisting of interlinked cages, and, surprisingly for such a low density structure, shows high thermal stability.[19] Recently, it has also been suggested that SOD-ZnO may form the structural basis for the most energetically stable nanoparticles for $(ZnO)_N$ for $N \geq 60$.[20] Although the SOD structural type is, as yet, experimentally unknown in any AB material, if its synthesis is viable, it would be particularly interesting for semiconductor materials where it immediately suggests the possibility of introducing dopant atoms into the cages to enable tailoring of physical and chemical properties for a range of applications (*e.g.* opto-electronics, sensors).

In the present work, we considerably extend the exploration of predictive polymorphism in AB materials by studying the oxides and chalcogenides (sulfides, selenides, and tellurides) of Mg, Zn and Cd. Apart from MgO and MgS, it is of note that the remaining members of this set of materials are semiconductors with experimentally determined bandgaps ranging between 1.4 eV (CdTe) and 3.6 eV (MgSe). In particular, we explore the relative energetic and enthalpic stability of the low-density nanoporous SOD polymorph with respect to seven other polymorphic forms: (i) rs, (ii) hex, (iii) layered, (iv) wz, (v) zb, (vi) NiAs, and (vii) BCT. We note that the layered phase is only considered when the hex polymorph is unstable to spontaneous "de-layering" for a particular composition. For all polymorphs in all compositions we use DF calculations to assess the viability of forming the SOD phase under negative pressure conditions *via* calculating the transition pressures for obtaining the SOD phase from the respective ground state phase. Trends in the transition pressures are used to predict the semiconductor materials for which the SOD polymorph could be most easily prepared.

Computational details

The energies and structures of all considered phases of MgX, ZnX and CdX (where X = O, S, Se, Te) were calculated using DFT employing the GGA (Generalised Gradient Approximation) PW91 exchange–correlation potential[21] as implemented in the VASP code.[22] Integrations in reciprocal space were accomplished by using Monkhorst–Pack[23] grids of special *k*-points (rs: 7 × 7 × 7, wz: 7 × 7 × 7, zb: 3 × 3 × 3, hex: 7 × 7 × 7, NiAs: 7 × 7 × 7, 3 × 3 × 3: BCT, 3 × 3 × 3: SOD). The effect of core electrons on the valence density was taken into account through the projector augmented wave method[24] with a 415 eV plane wave energy cut-off for valence states. All reported calculated energies refer to constituent spherical non-spin-polarised atoms in eV per formula unit. Calculated volume *versus* energy data was fitted using the third-order Birch–Murnaghan equation of state (EOS).[25] The corresponding expression for the enthalpy with respect to pressure was then used to calculate the transition pressures (taken to be the pressure where the enthalpies of two phases were equal). In some cases where there are transitions to intermediate phases going from the ground-state phase to the SOD phase, the pressure of the final transition (*i.e.* the one at the most negative pressure) is reported.

Results and discussion

ZnX series

Figs. 2a–d show the calculated total energy *versus* volume plots for the ZnX series. All EOS fitting parameters of the various considered phases of ZnX are given in Tables 1(a–d). The predicted series of ground-state phases are found to vary as wz-ZnO, zb-ZnS, zb-ZnSe and zb-ZnTe following the experimentally observed stability trend.[26] The energy difference between wz-ZnX and zb-ZnX is always found to be very small ($\leq$0.017 eV/ZnX) indicating that both phases are likely to be found as ZnX polymorphs under non-extreme thermodynamic conditions, also matching with the experimentally observed phases. Other than the wz-ZnX to zb-ZnX crossover, the trends in energetic stability with respect to wz-ZnX upon changing the anion from O to Te are very similar. For all phases apart from zb-ZnS, the change of anion from O to S results in an energetic destabilisation with respect to wz-ZnS. The largest O-to-S energetic shift is found for rs-ZnS (+0.33 eV/ZnX) and the smallest for BCT-ZnS (+0.03 eV/ZnX). Going along the series ZnS, ZnSe, ZnTe, there are few further changes in relative energetic stability with the order of energetic stability maintained throughout the set of considered polymorphs. The relatively lower density BCT-ZnX and SOD-ZnX phases are particularly unaffected by the anion change from S through to Te, with both only varying by up to a maximum of 0.017 eV/ZnX with respect to wz-ZnX. Throughout the same anion variation the denser phases, rs-ZnX and NiAs-ZnX, both become slightly more energetically stable with respect to wz-ZnX by 0.055 eV/ZnX.

The evolution of stability of the hex-ZnO phase with increase in anion size is subtlety different from the other considered phases in that it is also mechanically destabilized

upon the ZnO-to-ZnS compositional change. Although hex-ZnO is truly the bonded tubular hexagonal phase, lying at a density between that of wz-ZnO and rs-ZnO, for ZnX (with X = S, Se, Te) the hexagonal phase has an energetic preference to form the layered-ZnX phase. This tendency can be seen in the EOS plots in Figs. 2b–d where the energetic minimum of the layered-ZnX phase EOS lies at almost the same volume as that for wz-ZnX. Also the shape of the EOS curves for the layered-ZnX phases are distinctly asymmetrical about the energetic minima with the higher volume side of the curves being flatter due to the relative energetic ease of de-layering (also reflected in the relatively low fitted B0 values in Tables 1b–d).

A more general mechanical instability is shown by the BCT phase. In all cases considered the low volume (high pressure)

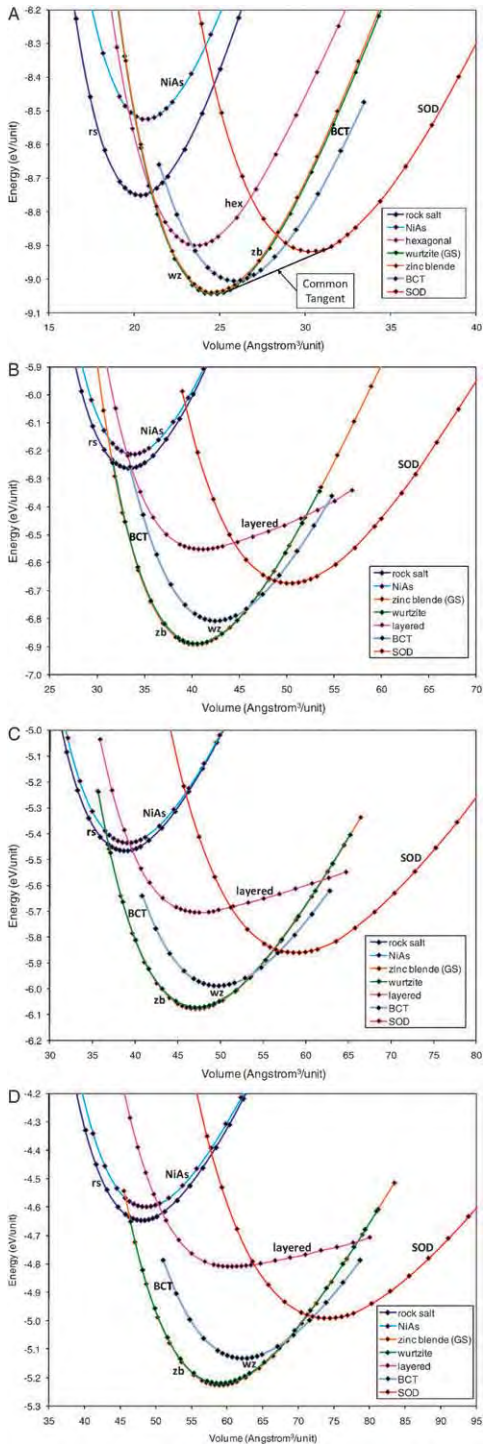

Fig. 2 (a) Energy *versus* volume plots for the seven considered phases of ZnO. GS in the legend denotes the experimental ground-state phase. An example of the common tangent construction between the EOS curves of wz-ZnO and SOD-ZnO is also shown. (b) Energy *versus* volume plots for the seven considered phases of ZnS. GS in the legend denotes the experimental ground-state phase. (c) Energy *versus* volume plots for the seven considered phases of ZnSe. GS in the legend denotes the experimental ground-state phase. (d) Energy *versus* volume plots for the seven considered phases of ZnTe. GS in the legend denotes the experimental ground-state phase. Note that for (a)–(d) (*i.e.* S–Te) the hex-ZnTe is found to be unstable to spontaneous transformation to the layered phase which is reflected in the figure labelling—see also main text.

Table 1 (a–d) Fitted parameters to the EOS data of the ZnX series polymorphs: total energy ($E0$, eV/ZnX), volume per unit ($V0$, Å^3/ZnX), bulk modulus ($B0$, GPa), and the pressure derivative (B'). Bold entries indicate the experimental ground-state phases

(a) ZnO

	$E0$	$V0$	$B0$	B'
rs-ZnO	−8.75	20.35	166.2	4.57
NiAs-ZnO	−8.52	20.69	159.5	4.55
zb-ZnO	−9.04	24.68	130.7	4.52
wz-ZnO	−9.05	24.68	129.6	4.57
hex-ZnO	−8.90	23.60	130.5	5.15
BCT-ZnO	−9.00	25.82	113.5	3.52
SOD-ZnO	−8.92	30.26	105.1	4.51

(b) ZnS

	$E0$	$V0$	$B0$	B'
rs-ZnZ	−6.26	33.33	86.1	4.55
NiAs-ZnZ	−6.21	33.74	86.5	4.62
zb-ZnS	−6.89	40.40	69.7	4.48
wz-ZnS	−6.89	40.46	69.4	4.40
hex-ZnS	−6.56	41.75	32.3	7.91
BCT-ZnS	−6.81	42.73	60.9	3.18
SOD-ZnS	−6.67	50.28	54.6	4.39

(c) ZnSe

	$E0$	$V0$	$B0$	B'
rs-ZnSe	−5.46	38.75	70.6	4.72
NiAs-ZnSe	−5.43	39.15	70.6	4.65
zb-ZnSe	−6.08	47.15	57.1	4.60
wz-ZnSe	−6.07	47.21	56.7	4.55
hex-ZnSe	−5.70	47.96	27.6	9.54
BCT-ZnSe	−5.99	49.70	51.0	4.00
SOD-ZnSe	−5.86	58.75	44.4	4.59

(d) ZnTe

	$E0$	$V0$	$B0$	B'
rs-ZnTe	−4.65	48.09	53.9	4.85
NiAs-ZnTe	−4.60	48.61	53.3	4.72
zb-ZnTe	−5.23	58.98	43.6	4.73
wz-ZnTe	−5.22	58.99	43.3	4.72
hex-ZnTe	−4.81	61.73	16.9	9.87
BCT-ZnTe	−5.13	62.22	38.5	4.44
SOD-ZnTe	−4.99	73.89	33.2	4.69

points on the EOS for each BCT-AB phase considered could only be continued up to a limited lower volume bound before a spontaneous transition occurred to the respective rock salt phase. Due to this transition to BCT-rs the EOS for BCT was fitted only for those points before the transition occurred, explaining the somewhat truncated appearance of the EOS curves for some BCT compositions.

CdX series

The calculated total energy *versus* volume plots for the polymorphs of the CdX series are shown in Figs. 3a–d. Tables 2(a–d) gives all EOS fitting parameters of the various considered phases of CdX. Unlike the ZnX series, the ground state for CdO is found to be rock salt, as also observed in experiment.[26] Upon traversing the series of anions from O toTe, the trend in energetic stabilities with respect to wz-CdX is quite similar to that of the ZnX series. Again, apart from zb-CdX all other phases are relatively destabilized with respect to wz-CdS in increasing anion size. Contrasting with the ZnX series trend, this continues in a monotonically increasing fashion for all the relatively dense phases (rs-CdX, NiAs-CdX, hex-CdX). Note that, unlike ZnX, although the hex-CdX phase has a tendency to delayer (as seen in the asymmetric EOS curves) their energetic minima correspond to the hexagonal phase and not the layered-CdX phase. The lower density phases of BCT-CdX and SOD-CdX, after their initial destabilization upon going from the CdO to CdS, maintain fairly constant energy differences (0.06 ± 0.01 eV/CdX and 0.15 ± 0.01 eV/CdX, respectively) with wz-CdX. For CdS and CdSe, the wurtzite phase is the ground state. The relative stabilization of the zb-CdX phase upon increasing anion size, however, causes zb-CdTe to become the predicted ground-state phase. The ground-state trend with anion variation (*i.e.* rs-CdO, wz-CdS, wz-CdSe, zb-CdTe) matches the observed trend in experiment.[26]

MgX series

The calculated total energy *versus* volume curves of the considered polymorphs of the MgX series are shown in Figs. 4a–d. All corresponding EOS fitting parameters are documented in Tables 3(a–d). Following experiment, for the relatively smaller O and S anions rs-MgO and rs-MgS are found to be the most stable phases. With increasing anion size from O to Te, we note a number of changes in the relative energetic stability of the considered polymorphs. For consistency with our previous discussions and taking wz-MgX as a reference point, we find the dense rs-MX and hex-MgX phases become continually and rapidly destabilized going through the series (with an overall relative shift of 0.28 eV/unit and 0.24 eV/unit, respectively). Conversely, the two other relatively dense polymorphs (NiAs-MgX and zb-MgX) become more stabilized with respect to wz-MgX (although with NiAs-MgTe becoming slightly destabilized again going from X = Se to Te). At the same time, the least dense phases of BCT-MgX and SOD-MgX change little in their relative energetic stability with respect to wz-MgX (between 0.04–0.06 eV/unit for BCT-MgX and 0.13–0.17 for SOD-MgX), similar to that found for the ZnX and CdX series. The relative destabilization of the rs-MgX phase with increasing anion size results in the emergence of wz-MgX as a new predicted ground-state phase upon going from X = S to X = Se, and subsequently Te. The concurrent

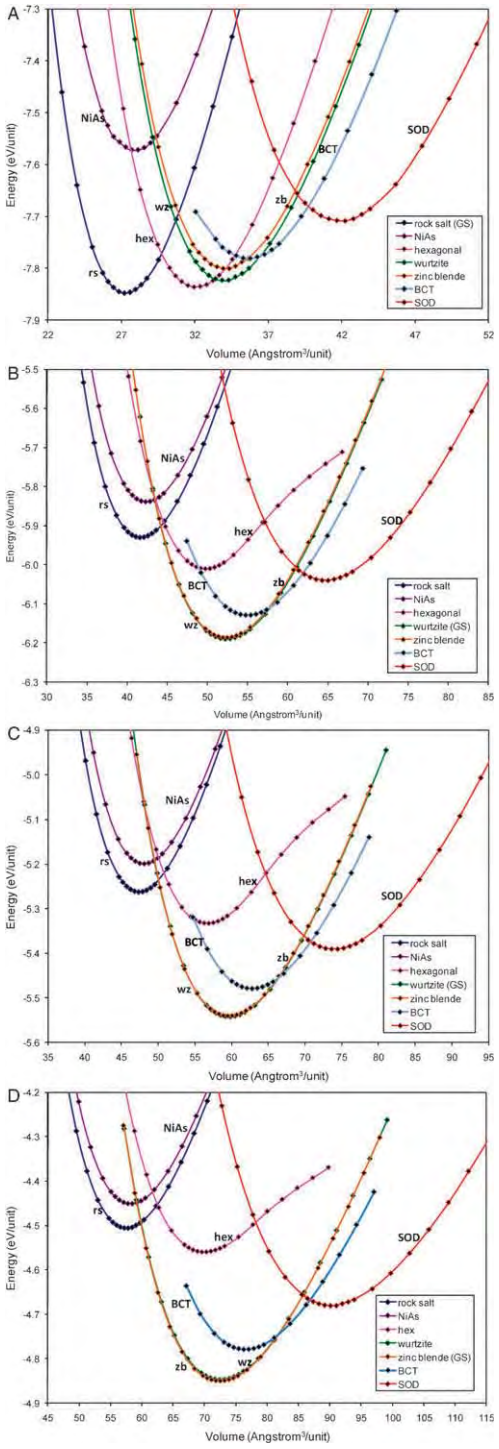

Fig. 3 (a) Energy *versus* volume plots for the seven considered phases of CdO. GS in the legend denotes the experimental ground-state phase. (b) Energy *versus* volume plots for the seven considered phases of CdS. GS in the legend denotes the experimental ground-state phase. (c) Energy *versus* volume plots for the seven considered phases of CdSe. GS in the legend denotes the experimental ground-state phase. (d) Energy *versus* volume plots for the seven considered phases of CdTe. GS in the legend denotes the experimental ground-state phase.

Table 2 (a–d) Fitted parameters to the EOS data of the CdX series polymorphs: total energy ($E0$, eV/CdX), volume per unit ($V0$, Å^3/CdX), bulk modulus ($B0$, GPa), and the pressure derivative (B'). Bold entries indicate the experimental ground-state phases

(a) CdO

	$E0$	$V0$	$B0$	B'
rs-CdO	−7.85	27.25	128.6	4.89
NiAs-CdO	−7.57	27.86	120.5	4.85
hex-CdO	−7.83	31.89	103.6	5.58
wz-CdO	−7.82	33.99	93.2	4.84
zb-CdO	−7.80	34.10	93.2	4.73
BCT-CdO	−7.78	35.60	74.8	2.92
SOD-CdO	−7.71	41.80	75.5	4.72

(b) CdS

	$E0$	$V0$	$B0$	B'
rs-CdS	−5.93	41.67	72.6	4.81
NiAs-CdS	−5.84	42.38	71.0	4.77
hex-CdS	−6.01	49.92	52.9	5.21
zb-CdS	−6.19	52.29	53.8	4.65
wz-CdS	−6.19	52.33	53.6	4.63
BCT-CdS	−6.13	55.03	48.1	3.91
SOD-CdS	−6.04	64.71	42.8	4.66

(c) CdSe

	$E0$	$V0$	$B0$	B'
rs-CdSe	−5.26	47.37	60.8	4.87
NiAs-CdSe	−5.20	48.07	60.1	4.83
hex-CdSe	−5.33	56.92	43.0	5.68
zb-CdSe	−5.54	59.63	45.2	4.76
wz-CdSe	−5.54	59.68	45.0	4.72
BCT-ZnSe	−5.48	62.76	40.4	4.30
SOD-ZnSe	−5.39	73.92	35.8	4.77

(d) CdTe

	$E0$	$V0$	$B0$	B'
rs-CdTe	−4.51	57.51	47.2	5.00
NiAs-CdTe	−4.45	58.20	46.6	4.97
hex-CdTe	−4.56	70.24	30.6	6.06
zb-CdTe	−4.85	72.49	35.4	4.87
wz-CdTe	−4.85	72.54	35.2	4.83
BCT-CdTe	−4.78	76.58	30.7	3.88
SOD-CdTe	−4.68	90.29	27.6	4.89

stabilization of zb-MgX and NiAs-MgX also results in a complicated competition for the ground state. Experimentally, it is found that both MgS and MgSe can be crystallized in three polymorphs (rocksalt, zinc blende and wurtzite)[27,28] implying that the crossover in stability is very gradual and that competition between these three phases is particularly close for MgS and MgSe. Although experimentally the rs-to-wz crossover has not quite occurred for MgSe (where rs-MgSe is found to be the ground state), in our calculations we find that zb-MgSe and wz-MgSe are slightly more stable than rs-MgSe, by only 0.03 eV/MgSe and 0.04 eV/MgSe, respectively. For MgTe, the experimental ground state is still not fully decided between NiAs-MgTe and wz-MgTe.[29] Our prediction of a wz-MgTe ground state is thus currently not possible to unambiguously confirm but matches well with other GGA-based DF calculations.[29] In comparable situations GGA DF calculations have proved to be superior to calculations using local density approximation based functionals;[30] the latter predicting NiAs-MgTe as the ground state.[31]

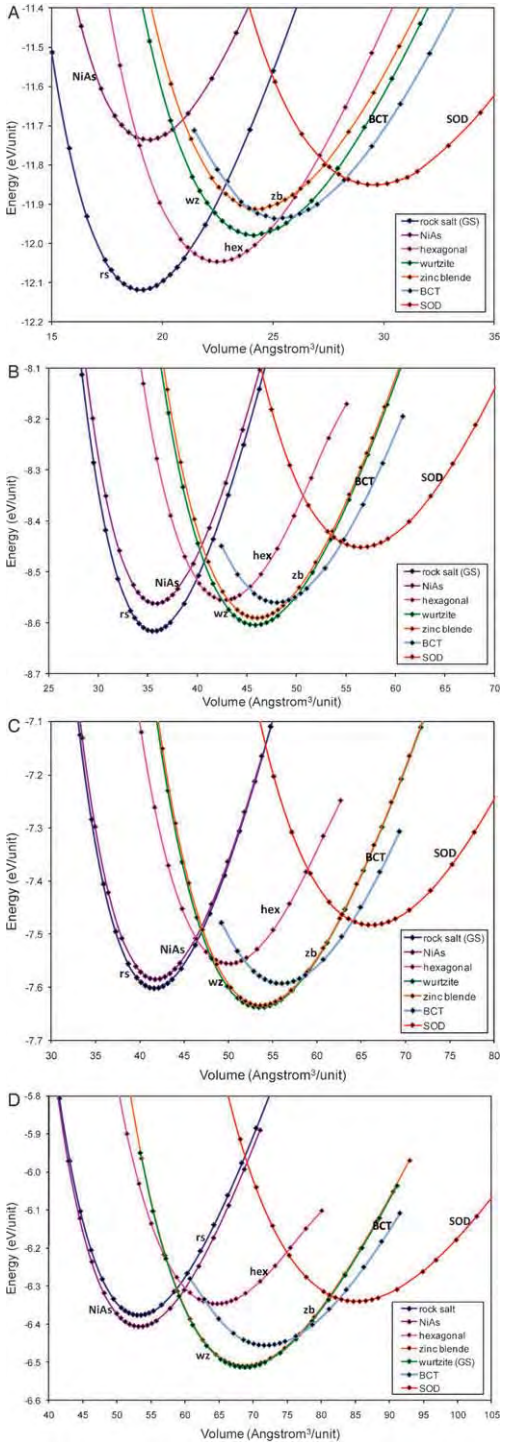

Fig. 4 (a) Energy *versus* volume plots for the seven considered phases of MgO. GS in the legend denotes the experimental ground-state phase. (b) Energy *versus* volume plots for the seven considered phases of MgS. GS in the legend denotes the experimental ground state phase. (c) Energy *versus* volume plots for the seven considered phases of MgSe. GS in the legend denotes the experimental ground-state phase. (d) Energy *versus* volume plots for the seven considered phases of MgTe. GS in the legend denotes the experimental ground-state phase. Note that for MgTe both wz-MgTe and NiAs-MgTe have been proposed as the possible experimental ground state[29]—see also main text.

Table 3 (a–d) Fitted parameters to the EOS data of the MgX series polymorphs: total energy ($E0$, eV/MgX), volume per unit ($V0$, Å^3/MgX), bulk modulus ($B0$, GPa), and the pressure derivative (B'). Bold entries indicate the experimental ground-state phases.

(a) MgO

	$E0$	$V0$	$B0$	B'
rs-MgO	−12.12	19.03	153.1	4.17
NiAs-MgO	−11.74	19.34	147.4	4.18
hex-MgO	−12.05	22.45	126.0	4.50
wz-MgO	−11.98	24.15	117.8	4.12
zb-MgO	−11.91	24.31	117.6	4.12
BCT-MgO	−11.93	25.25	102.2	3.17
SOD-MgO	−11.85	29.53	95.6	4.11

(b) MgS

	$E0$	$V0$	$B0$	B'
rs-MgS	−8.62	35.58	74.6	4.10
NiAs-MgS	−8.56	35.77	73.9	4.13
hex-MgS	−8.55	42.81	57.6	4.34
zb-MgS	−8.60	45.84	55.6	4.14
wz-MgS	−8.59	45.99	55.9	4.11
BCT-MgS	−8.56	47.99	47.8	2.88
SOD-MgS	−8.45	56.53	44.57	4.08

(c) MgSe

	$E0$	$V0$	$B0$	B'
rs-MgSe	−7.60	41.64	61.2	4.15
NiAs-MgSe	−7.59	41.80	60.9	4.16
hex-MgSe	−7.55	50.08	47.5	4.49
zb-MgSe	−7.64	53.51	45.2	4.16
wz-MgSe	−7.63	53.63	45.5	4.13
BCT-MgSe	−7.59	55.97	38.2	2.89
SOD-MgSe	−7.48	66.12	36.2	4.11

(d) MgTe

	$E0$	$V0$	$B0$	B'
rs-MgTe	−6.38	53.25	46.4	4.27
NiAs-MgTe	−6.41	53.30	46.5	4.25
hex-MgTe	−6.35	64.65	33.7	4.99
zb-MgTe	−6.51	68.74	34.3	4.21
wz-MgTe	−6.51	78.73	34.3	4.18
BCT-MgTe	−6.45	71.74	27.9	2.63
SOD-MgTe	−6.34	85.16	27.1	4.18

Although our DF calculations failed to predict that wz-MgSe is the ground state, we stress that the general experimental trend in ground-state MgX polymorphic stability with change in anion type is reproduced. This small energetic preference for wz-MgSe over rs-MgSe, is unlikely to affect our predicted transition pressures to obtain SOD-MgSe as the transition would almost certainly proceed indirectly *via* wz-MgSe in any case (as for CdO and MgS).

Further, considering: (i) the likely sensitive energetic balance of factors determining the ground-state crossover point for the MgX series, (ii) the success of our methodology with respect to the relative stabilities of the ground states of the corresponding ZnX and CdX series, and (iii) that the main objective of this study is concerned with predicting trends in (energetic and enthalpic) stability, rather than to try to achieve an exactingly accurate match to experimental data, we feel that the computational set-up employed is more than adequate for our present purposes.

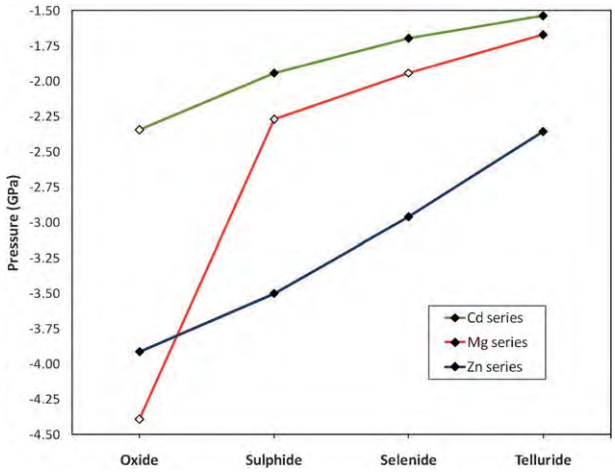

Fig. 5 Transition pressures going from the ground state to the respective SOD phase. Solid data points denote direct ground-state-to-SOD transitions and open data points denote indirect transitions *via* other phases—see main text for details.

SOD phase transition pressures

Based upon the Birch–Murnaghan fitted EOS data in Tables 1, 2 and 3, for every considered phase and composition we have derived the corresponding expression for the enthalpy. For each composition we started from the ground state and decreased the pressure while extracting a path following the phases with the lowest enthalpy. In all cases the aim was to find the pressure at which the SOD phase may possibly be stabilized, and for which compositions this was relatively most facile.

For the full ZnX series, CdS, CdSe, CdTe and MgTe, the lowest enthalpy path only included the ground-state phase and the corresponding SOD phase. In other words, for these compositions, no other phase competes with SOD on enthalpic grounds when applying negative pressures to the ground state at 0 K. The calculated pressure required for this transition varies greatly from −3.93 GPa for wz-ZnO to SOD-ZnO to −1.54 GPa for zb-CdTe to SOD-CdTe (see solid data points in Fig. 5 for a graph of all calculated direct transition pressures). The fact that this transition is predicted to be direct is perhaps less surprising when we consider that in all these cases the ground-state phase is either zinc blende or wurtzite and thus the only real competitor to SOD in our considered series could be the BCT phases (having a density intermediate between wurtzite/zinc blende and SOD). We further note that even in the cases where the lowest enthalpy transition from the ground state to the SOD phase is *via* other phases, this is always either *via* wurtzite for CdO, MgS, and MgSe or *via* the hexagonal phase for MgO, and never *via* BCT (transition pressures from an intermediate phase are shown as open data points in Fig. 5). That BCT is never enthalpically more stable than SOD is a strong indication that SOD may be the most thermodynamically stable phase under suitable negative pressures. The enthalpic stability of SOD over BCT with respect to negative pressure can also be seen graphically *via* the common tangent construction. This construction finds points on two EOS curves with: (i) the same gradient, and

(ii) which can be joined by a single tangent line. This common tangent line then corresponds to one of equal pressure and enthalpy respectively with the gradient of the line equating to the negative of the transition pressure between the two phases. Evidently the shallower the common tangent line connecting two EOS curves the lower the magnitude of the transition pressure and the more thermodynamically favoured it is over transitions to phases with EOS curves above the tangent line. In Fig. 2a we show the common tangent between the EOS curves of wz-ZnO and SOD-ZnO clearly passing under the EOS of BCT-ZnO. We note that very recent work has predicted that many polymorphs lie in the density region between wurtzite and SOD for a number of materials including ZnO, ZnS and CdS.[32] In all cases however none of these phases were found to lie below the common tagnet line between wurtzite and SOD, which further confirms our proposition that SOD is likely to be thermodynamically stable under conditions of negative pressure.

Apart from the relatively large negative pressure required to traverse from rs-MgO to SOD-MgO *via* hex-MgO, the overall trend in transition pressures follows the trend CdX, MgX, and ZnX in terms of decreasing relative ease in obtaining the SOD phase from the ground state. In each series it can also be seen that the SOD phase may be obtained more easily with increasing anion size. These trends result in CdTe (−1.54 GPa), MgTe (−1.68 GPa) and CdSe (−1.70 GPa) being the most promising candidates for obtaining the SOD phase *via* application of negative pressure. Considering that it has been estimated that effective negative pressures of about −1 GPa can be achieved in low temperature deposition solid state syntheses,[2] we are thus hopeful that the SOD phase may soon be experimentally prepared.

Summary and conclusions

We systematically survey the low-energy and enthalpic polymorphic landscape of the oxides and chalcogenides of Zn, Cd, and Mg in order to establish pressure conditions under which the novel nanoporous SOD phase may be stabilised. Specifically, for all compositions we use gradient corrected DF calculations to derive the EOS of eight AB polymorphs: (i) rs, (ii) NiAs, (iii) hex, (iv) layered (v) zb, (vi) wz, (vii) BCT, and (viii) SOD. The extracted enthalpies of each phase allow us to follow the lowest enthalpy path for each composition and thus the transition pressures under which SOD may be obtained. We find that in all cases the low-density SOD phase is thermodynamically stable under conditions of negative pressure. Conversely, the potentially competing BCT phase is never thermodynamically stable. Transition pressures to obtain the SOD phase are predicted to be most facile for the CdX series and the MgS, MgSe, MgTe set. Due to the decrease in the magnitude of the negative pressure required to obtain the SOD phase with increasing anion size the most favourable candidates (of those compositions considered) for SOD formation are predicted to be CdTe, MgTe and CdSe with transition pressures calculated to be in the range −1.54 to −1.70 GPa.

Acknowledgements

This study has been supported in part by the Spanish Ministry of Education and Science (grants FIS2008-02238) and by the Generalitat de Catalunya (grants 2009SGR1041 and XRQTC). This work was further supported in part by grants from the National Science and Technology Development Agency (2009 NSTDA Chair Professor funded by the Crown Property Bureau under the management of the National Science and Technology Development Agency and NANOTEC Center of Excellence funded by the National Nanotechnology Center), The Thailand Research Fund, The Commission of Higher Education, Ministry of Education (“National Research University of Thailand” and “Postgraduate Education and Research Programs in Petroleum and Petrochemicals, and Advanced Materials”). Support from the Kasetsart University Research and Development Institute (KURDI) is also acknowledged. The Barcelona Supercomputer Center is gratefully acknowledged for time on the Marenostrum supercomputer. Alexey Sokol is kindly acknowledged for useful discussions.

References

1 Ž. Čančarević, J. C. Schön and M. Jansen, *Chem.–Asian J.*, 2008, **3**, 561.
2 J. C. Schön, *Z. Anorg. Allg. Chem.*, 2004, **630**, 2354.
3 J. C. Schön and M. Jansen, *Comput. Mater. Sci.*, 1995, **4**, 43.
4 Y. Liebold-Ribeiro, D. Fischer and M. Jansen, *Angew. Chem., Int. Ed.*, 2008, **47**, 4428.
5 A. Bach, D. Fischer and M. Jansen, *Z. Anorg. Allg. Chem.*, 2009, **635**, 2406.
6 W. R. L. Lambrecht, S. Limpijumnong and B. Segall, *MRS Internet J. Nitride Semicond. Res.*, 1999, **4S1**, p. G6.8.
7 A. N. Enyashin, I. R. Shein and A. L. Ivanovskii, *Phys. Rev. B: Condens. Matter Mater. Phys.*, 2007, **75**, 193408.
8 F. Decremps, J. Pellicer-Porres, F. Datchi, J. P. Itie, J. P. A. Polian, F. Baudelet and J. Z. Jiang, *Appl. Phys. Lett.*, 2002, **81**, 4820.
9 L. Zhang and H. Huang, *Appl. Phys. Lett.*, 2007, **90**, 023115.
10 A. J. Kulkarni, M. Zhou, K. Sarasamak and S. Limpijumnong, *Phys. Rev. Lett.*, 2006, **97**, 105502.
11 C. L. Freeman, F. Claeyssens, N. L. Allen and J. Harding, *Phys. Rev. Lett.*, 2006, **96**, 066102.
12 C. Tusche, H. L. Meyerheim and J. Kirschner, *Phys. Rev. Lett.*, 2007, **99**, 026102.
13 D. K. Smith and C. F. Cline, *Acta Crystallogr.*, 1965, **18**, 393.
14 B. J. Morgan, *Phys. Rev. B: Condens. Matter Mater. Phys.*, 2009, **80**, 174105.
15 J. Wang, A. J. Kulkarni, K. Sarasamak, S. Limpijumnong, M. J. Ke and M. Zhou, *Phys. Rev. B: Condens. Matter Mater. Phys.*, 2007, **76**, 172103.
16 K. Doll, J. C. Schön and M. Jansen, *Phys. Rev. B: Condens. Matter Mater. Phys.*, 2008, **78**, 144110.
17 Ch. Baerlocher, L. B. McCusker and D. H. Olson, *Atlas of Zeolite Framework types*, Elsevier, Amsterdam, 6th edn, 2007.
18 J. Carrasco, F. Illas and S. T. Bromley, *Phys. Rev. Lett.*, 2007, **99**, 235502.
19 W. Sangthong, J. Limtrakul, F. Illas and S. T. Bromley, *J. Mater. Chem.*, 2008, **18**, 5871.
20 B. Wang, X. Wang and J. Zhao, *J. Phys. Chem. C*, 2010, **114**, 5741.
21 J. Perdew, K. Burke and Y. Wang, *Phys. Rev. B: Condens. Matter*, 1996, **54**, 16533.
22 G. Kresse and D. Joubert, *Phys. Rev. B: Condens. Matter Mater. Phys.*, 1999, **59**, 1758.
23 H. J. Monkhorst and J. D. Pack, *Phys. Rev. B: Solid State*, 1976, **13**, 5188.
24 P. E. Blöchl, *Phys. Rev. B: Condens. Matter*, 1994, **50**, 17953.
25 F. Birch, *Phys. Rev.*, 1947, **71**, 809.

26 C.-Y. Yeh, W. Lu, S. Froyen and A. Zunger, *Phys. Rev. B: Condens. Matter*, 1992, **46**, 10086.
27 T. Li, H. Luo, R. G. Greene, A. L. Ruoff, S. S. Trail and F. J. DiSalvo, *Phys. Rev. Lett*., 1995, **74**, 5232.
28 L. Konczenwicz, P. Bigenwal, T. Cloitre, M. Chibane, R. Ricou, P. Testuo, O. Briot and R. L. Aulombard, *J. Cryst. Growth*, 1996, **117**, 159.
29 Y. Cai, S. Wu, J. Yu and R. Xu, *Phys. Rev. B: Condens. Matter Mater. Phys*., 2006, **74**, 214112.
30 D. R. Hamann, *Phys. Rev. Lett*., 1996, **76**, 660.
31 S. Duman, S. Bağcı, H. M. Tütüncü and G. P. Srivastava, *Phys. Rev. B: Condens. Matter Mater. Phys*., 2006, **73**, 205201.
32 M. A. Zwijnenburg, F. Illas and S. T. Bromley, *Phys. Rev. Lett*., 2010, **104**, 175503.

Electrochimica Acta 55 (2010) 8116–8120

Contents lists available at ScienceDirect

Electrochimica Acta

journal homepage: www.elsevier.com/locate/electacta

Single point electrodeposition of nickel for the dissymmetric decoration of carbon tubes

G. Loget[a], G. Larcade[a], V. Lapeyre[a], P. Garrigue[a], C. Warakulwit[b], J. Limtrakul[b], M.-H. Delville[c], V. Ravaine[a], A. Kuhn[a,*,1]

[a] Université Bordeaux, ISM, ENSCBP, 33607 Pessac Cedex, France
[b] Center of Nanotechnology and Chemistry Department, Kasetsart University, Bangkok 10900, Thailand
[c] CNRS, UPR-9048, Université de Bordeaux, ICMCB, 87 Avenue du Dr. A. Schweitzer, 33608 Pessac Cedex, France

ARTICLE INFO

Article history:
Received 3 December 2009
Received in revised form 12 January 2010
Accepted 15 January 2010
Available online 25 January 2010

Keywords:
Janus particles
Bipolar electrochemistry
Single point electrodeposition
Carbon tubes
Capillary electrophoresis

ABSTRACT

Dissymmetric micro- and nanoobjects are of enormous interest in many areas ranging from molecular electronics to targeted drug delivery. So far it has been quite difficult to synthesize dissymmetric objects at these scales and most approaches are based on using interfaces to break the symmetry. Only a few bulk procedures are known so far to produce the so-called Janus-type objects. We report here a simple approach for the bulk generation of dissymmetric micro- and nanoobjects, especially carbon tubes (CTs), based on a known, but so far underestimated electrochemical principle, namely bipolar electrodeposition. A suspension of CTs is introduced in a capillary containing an aqueous nickel salt solution and a high electric field is applied to orientate and polarize the individual tubes. During their transport through the capillary under sufficient polarization, each tube is the site of water oxidation at one end, and of Ni^{2+} reduction at the other one. The resulting nickel deposit at one end of the tube allows manipulation of the objects with the help of a magnetic field.

1. Introduction

Dissymmetric functionalization of micro- and nanoobjects is of major importance for many applications, ranging for example from directed self-assembly and electronic paper to sensing and catalysis. Various approaches to generate dissymmetric particles, also called Janus-type particles, have been reported in the recent literature. They have been obtained either by protection/deprotection mechanisms [1], focused laser-induced reactions [2], co-jetting of parallel polymer solutions under the influence of an electrical field [3], anisotropic electroless deposition [4], or with microfluidic techniques [5]. However, so far, most of the methods used to generate such objects need to break the symmetry by introducing interfaces like in the case of sputtering [6,7], stamp coating [8,9], and Langmuir–Blodgett-based techniques [10]. This makes the preparation of large quantities rather difficult because the majority of the techniques usually lead to monolayer equivalents of material as the modification occurs in a two-dimensional reaction space.

Thus, there is an increasing interest in developing truly three-dimensional techniques, in order to replace the two-dimensional approaches, and thus allowing a scale-up of the production of Janus objects to larger quantities by using bulk procedures [11]. Examples for such kind of approaches are based on the dissymmetric generation of charge carriers in semiconductors such as TiO_2 by using light [12] or antenna chemistry based on the irradiation of carbon nanotubes with microwaves [13]. However, in these cases a fine tuning of the driving force of the reactions is not possible.

In this context, an attractive way to break the symmetry in a three-dimensional reaction space is based on the concept of bipolar electrochemistry described by Fleischmann et al. [14]. This appealing approach relies on the fact that when a conducting object is placed in a strong electric field between two electrodes a polarization occurs that is proportional to the electric field E and the characteristic dimension r of the object as illustrated in Fig. 1. This concept has recently found interesting applications as driving force in electrochemiluminescent reactions [15], as detection mode in capillary electrophoresis [16] and for bipolar patterning [17,18]. In the present study we are using the approach to trigger point selective nickel electrodeposition on carbon tubes (CT) in analogy to our earlier work on the dissymmetric decoration of carbon nanotubes with gold nanoparticles [19]. In comparison to this previous work we want to demonstrate here that it is possible to generalize the approach by using another substrate (carbon microtubes)

* Corresponding author. Tel.: +33 5 40 00 65 73; fax: +33 5 40 00 27 17.
E-mail address: kuhn@enscbp.fr (A. Kuhn).
[1] ISE member.

0013-4686/$ – see front matter © 2010 Elsevier Ltd. All rights reserved.
doi:10.1016/j.electacta.2010.01.070

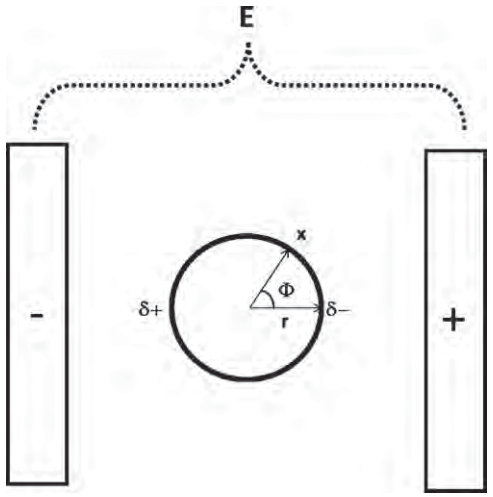

Fig. 1. Schematic illustration of the polarization of a conducting spherical particle in an electric field between two electrodes.

and another metal (Ni) which is much more difficult to reduce than the gold ions. In addition, we wanted to deposit a ferromagnetic metal in order to be able to manipulate the resulting objects with a magnetic field.

The simple equation [14] governing this polarization also immediately illustrates the practical problems that will arise when applying this concept to small objects.

$$\eta_x = Er\cos\Phi \quad (1)$$

With η_x being the polarization at a given point x at the surface of the object, E the total electric field and r the radius of the particle, one can easily calculate that the maximum potential difference ΔV_{max} between the two opposite sides of the object is given by:

$$\Delta V_{max} = 2Er \quad (2)$$

In order to carry out two different redox reactions at the opposite sides of the object ΔV_{max} has to be in a first order approximation equal to the difference of the formal potentials of the two redox reactions. In the present case, the redox reactions that should take place in an aqueous environment are the following ones:

$$Ni^{2+} + 2e^- \rightarrow Ni_{(s)}{}^0 \quad E^\circ = -0.26\,V \quad vs \quad NHE$$

$$2H_2O_{(l)} \leftrightarrow 4H_{(aq)}{}^+ + O_{2(g)} + 4e^- \quad E^\circ = +1.23\,V \quad vs \quad NHE$$

It immediately follows that the polarization has to generate a potential difference of approximately 1.5 V. This becomes an intrinsic problem of the approach when dealing with micro- or nanometer sized objects, as in this case E needs to achieve values of up to MV/m, conditions that seem to be incompatible with a normal laboratory environment and especially with aqueous solutions because of the inherent side reactions accompanied by macroscopic bubble formation at both electrodes that disturbs the orientation of the objects in the electric field. Bradley et al. could partly circumvent the problem by using organic solvents in order to enlarge the potential window of the electrolyte and thus it was possible to generate metal layers in a dissymmetric way on different objects in the micrometer and sub-micrometer range [20,21]. However it was also necessary to immobilize the objects on a substrate in order to prevent them from rotating, which means that it is again a 2D and not a bulk process. Recently we could demonstrate that it is possible to get around these problems and to extend the approach to truly nanosized objects by using a capillary electrophoresis set-up to apply the high electric field [19]. With this capillary assisted bipolar electrodeposition (CABED) process we were able to generate a nanosized gold cluster selectively on one end of multiwall carbon nanotubes. This spatially controlled single point electrodeposition is extended in the present contribution to nickel as a metal and a different type of carbon tubes in order to demonstrate the possibility to generalize this attractive approach as an alternative to generate dissymmetric micro- and nanoobjects of different compositions in a straight forward and well-controlled way.

2. Experimental

2.1. Preparation of carbon tube suspensions

The carbon tubes used in this study were produced by chemical vapor deposition with a porous aluminum oxide membrane serving as a template [22]. After acid digestion of the template (Fig. 2a) the quite homogeneous tubes were recovered as a powder (Fig. 2b).

Suspensions of CTs can be produced in a different way compared to the procedure that we have used in former studies for other types of carbon [23–25]. About 0.1 mg of CTs was added to absolute ethanol (1.5 mL). To accelerate the formation of a suspension the mixture was sonicated, but only for a short time (1 min) in order to avoid excessive breaking of the tubes. After 3 h of sedimentation, 0.5 mL of the supernatant was taken and added to a solution of 10 mM $NiSO_4$ in ultrapure water.

2.2. Bipolar nickel deposition on carbon nanotubes

For CE experiments, all solutions or suspensions were introduced into the capillary by filling it manually with a syringe. The capillary used here is a fused silica capillary with a length of 30 cm and an inner diameter of 100 μm. The distance from the capil-

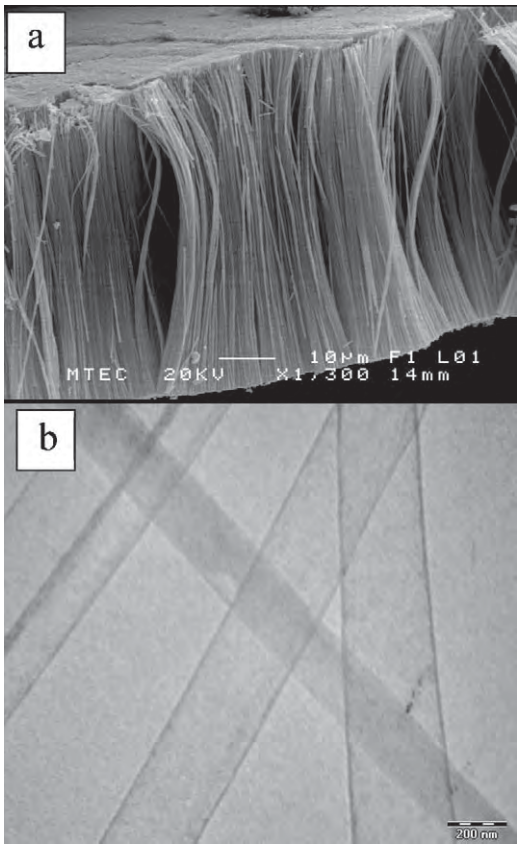

Fig. 2. (a) Scanning electron micrograph of the CT sample after dissolution of the Al_2O_3 template and (b) transmission electron micrograph of typical tubes obtained after suspension in water.

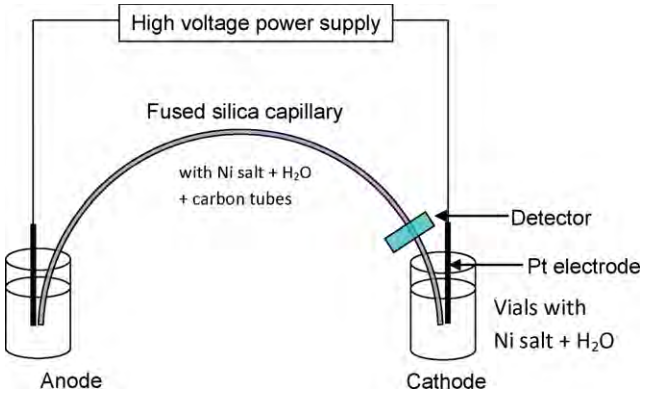

Fig. 3. Schematic illustration of the capillary electrophoresis set-up used in this study.

lary inlet (left side in Fig. 3) to the detection window (right side) was 24 cm in this case. The applied voltage was 30 kV whilst the temperature was maintained at 25 °C. The CE experiment was first performed by rinsing the capillary with ultrapure water. Then the diluted aqueous suspension of the carbon tubes was introduced into the capillary. The reason for using a diluted suspension for the CE experiment is due to the narrow capillary (100 μm). Introducing suspensions that are too concentrated leads to clogging of the capillary. The combination of electrophoretic migration and electroosmotic flow determines the transport of the CTs through the capillary. The flow characteristics were determined by recording the absorbance variations in the UV detector (254 nm) as a function of time.

The bipolar electrochemical nickel deposition on CTs is achieved by introducing the CT/$NiSO_4$ (10 mM) suspension into the capillary at the anodic side. No buffer solution was used in order to keep the conductivity of the medium as low as possible. Because the addition of the nickel salt increases the ionic strength it can result in the aggregation of the CTs, and, therefore, the suspension has to be sonicated for a short time in an ultrasound bath in order to maintain the CTs well dispersed just before introduction into the capillary. For such salt concentrations the typical currents in the electrophoresis set-up were around 1 μA.

The sample leaving the capillary at the cathodic side was collected directly at the outlet. This collected sample was put on a TEM grid or another substrate and dried. Because the suspension still contains nickel salt, drying of the suspension leads to salt crystallization which extremely disturbs the further microscopic analysis. Therefore, after the suspension was dropped onto the TEM grid, the solution, still containing salt, was soaked through the grid by placing a cleaning tissue under the grid. After that, the remaining particles on the grid were washed three times with ultrapure water using the same procedure. The washed objects were then characterized by optical microscopy, scanning electron microscopy or transmission electron microscopy.

3. Results and discussion

The potentials given in the above redox equations are standard potentials and, as the experiment is carried out far from standard conditions in terms of concentrations and partial gas pressures, large deviations from the theoretical threshold value of 1.5 V can be expected. This also means that the calculated electric fields might be different, especially when somewhat longer objects like the CTs are used. Using carbon tubes instead of carbon nanotubes for this experiment also has the advantage that the obtained objects can be easily visualized directly under the optical microscope and their movement, due to the presence of a magnetic field, can be followed in real time. The anisotropic tube structure results in a stronger polarization that induces at the same time an orientation of the tubes parallel to the electric field, which is preserved during their whole journey through the capillary. Thus, it is easier to perform such a bipolar electrochemical deposition with CTs compared to spherical objects that might change their orientation during the experiment and in this way lead to random metal deposition at the object's surface.

The experiment has been carried out at the maximum potential difference that could be delivered by the capillary electrophoresis set-up, which is 30 kV. When this potential difference is applied between the two ends of a capillary with a total length of 30 cm, an electric field of roughly 100 kV/m is generated in the capillary. For CTs with a typical length of 20 μm the maximum polarization that can be obtained between the two ends of the carbon tube is of the order of 2 V. This value is higher than the minimum potential difference required for driving the two redox reactions when the calculation is based on the standard potentials, and therefore the bipolar electrodeposition should occur under these conditions. The experiment shows indeed striking evidence for a dissymmetric deposition of nickel at one end of the tubes (see Fig. 4a) and the counter reaction at the other side of the tubes involves the formation of oxygen bubbles which dissolve in the surrounding medium.

The picture in Fig. 4b is representative of the majority of the tubes reaching the capillary outlet; however, in a more general sense, not 100% are always modified. The percentage of modified tubes obviously depends on the experimental parameters and there are several possible origins for a non-quantitative modification. First of all, the nickel deposit can detach from the tube during the collection and rinsing procedure. Second, the tubes can be more or less conducting depending on their morphology and defects. In

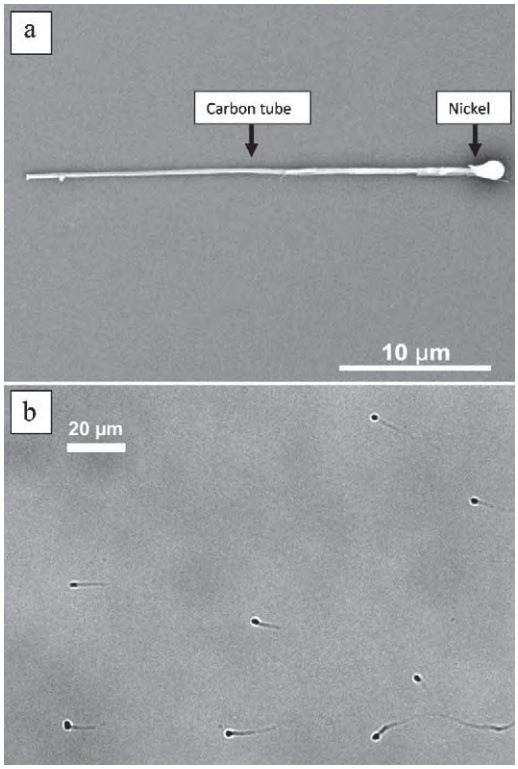

Fig. 4. Site selective bipolar electrodeposition of nickel at one end of a carbon tube (a) electron microscope image of a selected tube from a diluted sample and (b) optical microscope image of an ensemble of nickel modified tubes still suspended in the aqueous solution.

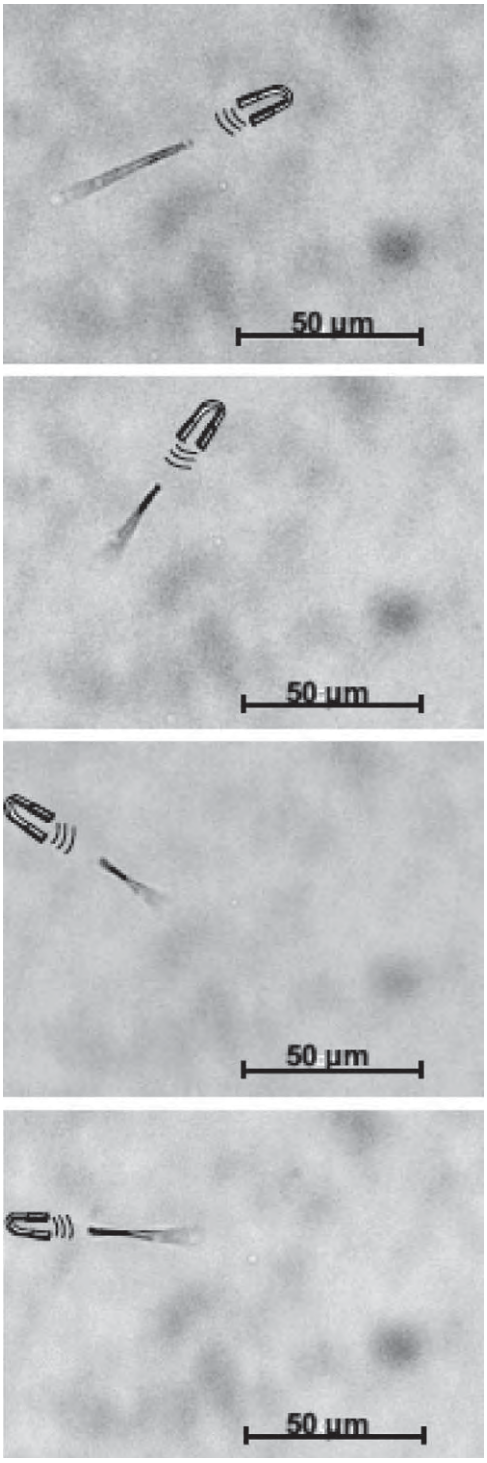

Fig. 5. Manipulation of a nickel modified carbon tube suspended in water by using an anti-clockwise rotating magnetic field.

the extreme case of an insulating tube, no deposition can occur and even for conducting tubes the conductivity has to be better than that of the surrounding electrolyte to induce a sufficient potential difference. The third reason is that the polarization scales with the length of the tube, and therefore shorter tubes might experience a potential difference between the two ends that is below the threshold value necessary to achieve metal deposition on one side and water oxidation on the other side. In order to approach 100% of modification the experiment should be carried out with tubes as long as possible and an external potential as high as possible. When optimizing these parameters one can achieve in a routine experiment that more than half of the tubes are modified (see, for example, Fig. 4b).

It is important to note that, in contrast to the former experiments [20,21], in this set-up the high voltage is not a problem, although we do not use organic solvents but water, because the electrodes are positioned at the outside of the capillary. This means that an eventual macroscopic hydrogen or oxygen evolution at the cathode or anode respectively does not disturb the experiment as it takes place in the bulk solution reservoirs and not in the capillary. Furthermore the currents are in the µA range because there is no added supporting electrolyte present and thus the total amount of developed gas is rather small.

In contrast to our former study using site selective deposition of gold on carbon nanotubes [19] we have used in this study on purpose a ferromagnetic metal. This allows us to manipulate the modified tubes with a magnetic field. Fig. 5 illustrates the possibility to turn the tube around an axis perpendicular to the tube's main axis. Such picture sequences are rather difficult to obtain because during application of the rotating magnetic field the object has to be followed simultaneously in the *x*, *y* and *z* direction with the additional problem that not the entire object is in the same focal plane. Triggering a well controlled rotation of the object would be difficult when using homogeneously modified tubes, but can be easily carried out with the present objects due to their dissymmetric nature. Therefore one can imagine using this process of single point electrodeposition for the generation of nano- and microobjects playing a crucial role in the construction of miniaturized mechanical devices such as motors.

4. Conclusions

The concept of bipolar electrochemistry has been adapted to modify in a dissymmetric way carbon tubes with a ferromagnetic nickel cap. The method employed to create these Janus-type objects is based on a slightly modified capillary electrophoresis experiment, (i) allowing the application of the mandatory high voltages, (ii) without having to use organic solvents and (iii) especially avoiding gas bubble formation in the reaction chamber, which otherwise would completely prevent the alignment of the tubes in the electric field. In contrast to the majority of literature processes used for the generation of dissymmetric objects the present process does not need any interface or surface to break the symmetry, but is a bulk process which allows one to easily imagine a scale-up of the production.

Looking into the future, the CABED process can be generalized to other types of nanoobjects and also deposits of a very different nature such as other metals, semiconductors, or polymers. The approach therefore opens up the way to a whole new family of experiments leading to complex nanoobjects with a sophisticated design allowing original applications, among others for example in the area of autonomous micro- and nanoswimmers [26–28]. In addition, the procedure reported here could also be adapted to sort conducting, semiconducting, and insulating carbon tubes, as the latter ones will not be modified with metal, whereas the first two categories of species will undergo a potential-dependent metal modification.

Acknowledgments

This work is part of the CUBIHOLE project funded by the European NanoSci-Era+ action under contract ANR-08-NSCI-008-01 and has also been supported by the French Ministry of Research, CNRS, and ENSCBP. C.W. and J.L. thank the National Science and Technology Development Agency (NSTDA Chair Professor and National

Nanotechnology Center) and the Thailand Research Fund for support. We also thank P. Pannopard for providing us with CT samples.

References

[1] A. Perro, S. Reculusa, F. Pereira, M.-H. Delville, C. Mingotaud, E. Duguet, E. Bourgeat-Lami, S. Ravaine, Chem. Commun. 44 (2005) 5542.
[2] E. Hugonnot, M.-H. Delville, J.-P. Delville, Appl. Surf. Sci. 248 (2005) 470.
[3] K.-H. Roh, D.C. Martin, J. Lahann, Nat. Mater. 4 (2005) 759.
[4] J.-Q. Cui, I. Kretzschmar, Langmuir 22 (2006) 8281.
[5] T. Nisisako, T. Torii, T. Takahashi, Y. Takizawa, Adv. Mater. 18 (2006) 1152.
[6] H. Takei, N. Shimizu, Langmuir 13 (1997) 1865.
[7] Y. Lu, H. Xiong, X. Jiang, Y. Xia, M. Prentiss, G.M. Whitesides, J. Am. Chem. Soc. 125 (2003) 12724.
[8] O. Cayre, V.N. Paunov, O.D. Velev, J. Mater. Chem. 13 (2003) 2445.
[9] V.N. Paunov, O.J. Cayre, Adv. Mater. 16 (2004) 788.
[10] K. Fujimoto, K. Nakahama, M. Shidara, H. Kawaguchi, Langmuir 15 (1999) 4630.
[11] L. Hong, A. Cacciuto, E. Luijten, S. Granick, Nano Lett. 6 (2006) 2510.
[12] H. Reiche, W.W. Dunn, A.J. Bard, J. Phys. Chem. 83 (1979) 2248.
[13] J.G. Duque, M. Pasquali, H.K. Schmidt, J. Am. Chem. Soc. 130 (2008) 15340.
[14] M. Fleischmann, J. Ghoroghchian, D. Rolison, S. Pons, J. Phys. Chem. 90 (1986) 6392.
[15] F. Mavré, K.-F. Chow, E. Sheridan, B.-Y. Chang, J.A. Crooks, R.M. Crooks, Anal. Chem. 81 (2009) 6218.
[16] O. Ordeig, N. Godino, J. Del Campo, F.X. Muñoz, F. Nikolajeff, L. Nyholm, Anal. Chem. 80 (2008) 3622.
[17] C. Ulrich, O. Andersson, L. Nyholm, F. Björefors, Anal. Chem. 81 (2009) 453.
[18] C. Ulrich, O. Andersson, L. Nyholm, F. Björefors, Angew. Chem. Int. Ed. 47 (2008) 3034.
[19] C. Warakulwit, T. Nguyen, J. Majimel, M.-H. Delville, V. Lapeyre, P. Garrigue, V. Ravaine, J. Limtrakul, A. Kuhn, Nano Lett. 8 (2008) 500.
[20] J.-C. Bradley, H.-M. Chen, J. Crawford, J. Eckert, K. Ernazarova, T. Kurzeja, M. Lin, M. McGee, W. Nadler, S.G. Stephens, Nature 389 (1997) 268.
[21] J.-C. Bradley, M. Zhongming, Angew. Chem. Int. Ed. 38 (1999) 1663.
[22] C. Warakulwit, Ph.D. Thesis, Kasetsart University Bangkok and University Bordeaux 1, 2007.
[23] P. Garrigue, M.-H. Delville, C. Labrugère, E. Cloutet, P.J. Kulesza, J.P. Morand, A. Kuhn, Chem. Mater. 16 (2004) 2984.
[24] D. Fattakhova-Rohlfing, A. Kuhn, Carbon 44 (2006) 1942.
[25] C. Warakulwit, J. Majimel, M.-H. Delville, P. Garrigue, J. Limtrakul, A. Kuhn, J. Mater. Chem. 18 (2008) 4056.
[26] N. Mano, A. Heller, J. Am. Chem. Soc. 127 (2005) 11574.
[27] U.K. Demirok, R. Laocharoensuk, K.M. Manesh, J. Wang, Angew. Chem. Int. Ed. 47 (2008) 9349.
[28] D. Pantarotto, W.R. Browne, B.L. Feringa, Chem. Commun. (2008) 1533.

Persistence of magic cluster stability in ultra-thin semiconductor nanorods

Winyoo Sangthong,[abcd] Jumras Limtrakul,[bcd] Francesc Illas[a] and Stefan T. Bromley*[ae]

Received (in Zürich, Switzerland) 28th September 2009, Accepted 23rd November 2009
First published as an Advance Article on the web 14th December 2009
DOI: 10.1039/b9nr00282k

The progression from quasi zero-dimensional (Q0D) nanoclusters to quasi one-dimensional (Q1D) nanorods, and, with increasing length, to nanowires, represents the most conceptually fundamental transition from the nanoscale to bulk-like length scales. This dimensionality crossover is particularly interesting, both scientifically and technologically, for inorganic semiconducting (ISC) materials, where striking concomitant changes in optoelectronic properties occur.[1,2] Such effects are most pronounced for ultra-thin[3] ISC nanorods/nanowires, where the confining and defective nature of the atomic structure become key. Although experiments on ISC materials in this size regime have revealed especially stable (or "magic") non-bulk-like Q0D nanoclusters,[4,5] all ISC Q1D nanostructures have been reported as having structures corresponding to bulk crystalline phases. For two important ISC materials (CdS and CdSe) we track the Q0D-to-Q1D transition employing state-of-the-art electronic structure calculations demonstrating an unexpected persistence of magic cluster stability over the bulk-like structure in ultra-thin nanorods up to >10 nm in length. The transition between the magic-cluster-based and wurtzite nanorods is found to be accompanied by a large change in aspect ratio thus potentially providing a route to nano-mechanical transducer applications.

The impressive scientific and technological advances resulting from the intense research effort into inorganic semiconducting (ISC) nanosystems is exemplified by the continuing developments based on nanoscale CdS. Inspired by the technological promise of its tunable (opto)electronic properties,[1,2] recent work on 1D nano-CdS has given rise to a wide range of device applications such as lasers,[6] transistors[7] and waveguides.[8] Enhancement of finite size effects in 1D nano-CdS systems such as defect-induced optical response and quantum confinement,[9] can be achieved through restricting the length to form a nanorod and/or by reducing the diameter of nanowires or nanorods to the ultra-thin, or strongly-confined regime. For ISC Q1D nanosystems this size range can be defined as that where the dimensions of a nanorod or nanowire are significantly below the Bohr exciton radius (~3 nm for CdS and ~5 nm for CdSe) where one expects the greatest deviation from bulk properties. A number of recent experimental studies have reported the preparation of 1D CdS[10,11] and CdSe[12,13] nanorods with diameters <5 nm. Thus far, however, all such ultra-thin CdS and CdSe nanorods have had reported diameters >1.5 nm and, where measured (*e.g.* by high-resolution transmission electron microscopy (HRTEM) and X-ray diffraction), seemed to possess the bulk wurtzite (wz) atomic structure with the (001) direction aligned along the length of the rods. Relatively thick CdS and CdSe nanorods and nanowires (≥30 nm diameter) can be grown directly from the vapour phase from pure material powders,[14] but typically ultra-thin Q1D nanosystems are made from colloidal growth and assembly of ligated clusters in solution (*i.e.* oriented attachment[3]). Although ligands are important for shape and size control, they can also affect the atomic structure of ISC nanosystems[15] and thus for studying the intrinsic size-dependent behaviour of pure ISC materials it is desirable that they should be removed. Below, we concentrate our discussion mainly on ligand-free Q0D and Q1D nanosystems of CdS, although we note that strongly analogous results are also found for the corresponding CdSe systems.

Considering the wealth of experimental studies and, further, the role of 1D nano-CdS as a model system for studying the fundamental physics of anisotropic quantum confinement, surprisingly few detailed calculations have been performed on infinite CdS nanowires,[16–18] and, as far as we are aware, none on CdS nanorods. In contrast, computational modelling studies of Q0D CdS nanosystems are relatively abundant and have tended to proceed *via* two distinct routes: (i) top-down, where nanoparticle atomic structures are derived from cutting fragments from either the wz or zincblende (zb) bulk phases,[19,20] or (ii) bottom-up, where the most energetically stable nanocluster structures are sought without recourse to bulk crystalline structural stabilities.[5,21] Largely due to the use of its simplifying structural assumption, the former approach has permitted studies of size-dependent optical and electronic properties of wz- or zb-structured $(CdS)_N$ nanoparticles over a wide size range.[19,20] Technically, due to the explosion in the number of possible structures with increasing size, the bottom-up approach to modelling CdS nanoclusters is significantly more difficult and the ground-state energy minimum structures of $(CdS)_N$ nanoclusters are reasonably well established up to only $N = 16$ with some suggestions for $28 < N < 35$.[4,5] Unlike the assumed crystalline structures adopted in the top-down approach none of the reported ground-state nanocluster structures in this latter size regime are found to be wz-like or zb-like. Recent work has also suggested that wz-structured CdS nanoparticles up 2 nm in diameter are unstable with respect to amorphisation.[22] In Q1D nanowires and high-aspect-ratio nanorods the surface/volume ratio is significantly lower than in Q0D systems of the same composition and we may expect a more rapid convergence to bulk-like crystalline structures. That this may not be the case for ultra-thin nanowires was first proposed in 1998 by Tosatti *et al.* for elemental metal systems using simple atomistic models.[23] For

[a]*Departament de Química Física & Institut de Química Teòrica i Computacional (IQTCUB), Universitat de Barcelona, C/Martí i Franquès 1, E-08028 Barcelona, Spain*
[b]*Department of Chemistry, Kasetsart University, Bangkok 10900, Thailand*
[c]*Center of Nanotechnology, Kasetsart University, Bangkok 10900, Thailand*
[d]*NANOTEC Center of Excellence, National Nanotechnology Center, Kasetsart University, Bangkok 10900, Thailand*
[e]*Institució Catalana de Recerca i Estudis Avançats (ICREA), 08010 Barcelona, Spain*

compound materials of nanotechnological interest, such as the numerous types of ISC, however, neither experiment nor theory has reported any tendency for ultra-thin Q1D nanosystems to deviate from bulk-like structures.

In an effort to bridge the gap between experiment and theory, with respect to the inherent behaviour of ultra-thin Q1D nanosystems of pure ISC materials, we employed large state-of-the-art scale density functional theory (DFT) calculations to follow the Q0D-to-Q1D transition for ultra-thin CdS. In order to tackle both ends of this range we have combined both bottom-up and top-down modelling approaches by calculating the stability of both small nanoclusters and infinite nanowires. The main feature of our approach, however, is that we explicitly follow the transition between these extremes by computing how the stabilities of cluster-assembled nanorods vary with increasing length. Specifically, we have investigated the energetic stability and atomistic and electronic structure of ultra-thin nanorods and nanowires assembled from experimentally detected $(CdS)_{13}/(CdSe)_{13}$ magic clusters (*i.e.* clusters exhibiting pronounced abundance peaks in cluster beams[4,5]) with a diameter 1.0–1.2 nm, with respect to the corresponding bulk-like wz-structured Q1D systems. Of note is that the prominent high abundance of clusters with 13 units is observed both in laser ablation experiments producing ligand-free clusters,[4,5] and in solution-based nucleation experiments[4] where the clusters are ligated. Although the structure of the magic cluster(s) corresponding to these peaks cannot, as yet, be directly ascertained from experiment, following previous studies,[4,5] we assume that it most likely corresponds to the bare $(CdS)_{13}/(CdSe)_{13}$ isomer with the lowest energy.

To calculate the relative stabilities and properties of nanorods and nanowires built from wz and magic nanocluster building blocks we employed periodic density functional (DF) theory using the PW91 implementation[24] of the Generalized Gradient Approach (GGA) form of the exchange–correlation potential using the VASP code.[25] A plane wave basis set with a kinetic energy cut-off of 415 eV was used, with the effect of the atomic core on the valence electron density taken into account by the projector augmented wave (PAW) approach.[26,27] The calculations for all cluster isomers and nanorods were carried out by placing each system inside a large enough box so as to make the interaction between repeated images negligible in all directions (10 Å was found to be sufficient). The infinite nanowires, similarly spaced in all directions perpendicular to the axes of the wires, were also considered. For the infinite nanowire a $1 \times 1 \times 9$ Monkhorst–Pack mesh[28] of special k-points was employed, whereas for the finite nanorods and clusters Γ-point calculations were performed. In all cases the atomic structure of the system was fully relaxed until the forces were smaller than 0.01 eV $Å^{-1}$. In constructing the infinite nanowires, a magic cluster or wz cluster was initially placed in a periodic cell such that the axis of symmetry was aligned along the z-direction with a z-spacing of a suitable bond length. In order to prevent artificial geometric constraints due to the use of only one cluster as a repeat unit in the subsequent structural optimisations of the nanowires a two-cluster supercell (*i.e.* 52 atoms) was employed. Firstly, the nanowires were optimised (both the internal atomic structure and supercell length) to their closest energy minimum to the as-constructed structure (cluster-assembled nanowires). Subsequently, we mechanically annealed the cluster-assembled nanowires by gradually compressing and stretching them (by up to 30% of their original length) by appropriately varying the z-dimension of the supercell of the initial cluster-assembled nanowires; for every fixed z-value optimising the nanowire structure. Every time a structural change occurred (causing a new minimum energy atomic configuration), the annealing procedure was again performed around the minimum energy configuration of the newly obtained structure. This process was repeated until stretching and compressing the nanowires did not change their minimum energy structure. The resulting nanowires are referred to as annealed nanowires below.

In Fig. 1 we show the structures and calculated relative energetic stabilities of three selected $(CdS)_{13}/(CdSe)_{13}$ cluster isomers: a) the likely ground-state "magic" cluster, b) a cage-like cluster, and c) a wz cluster fragment. The $(CdS)_{13}$ magic cluster has been predicted by calculations to have the form of a distorted cage filled by a single 4-coordinated sulfur atom bonded to four 4-coordinated cadmium atoms giving rise to a C_3 structure.[4,5] Particularly interesting for the present study is the fact that the magic cluster structure lies ~1 eV below the wz nanocluster. Our calculations further confirm that the magic cluster structure is also the likely ground state for CdSe with a very similar energetic stability over the corresponding wz-structured isomer. The cage-like cluster isomer is an example of the numerous cluster isomers having energetic stabilities between that of the wz cluster and the likely ground-state magic cluster.[5,21] Although, in principle, one could consider many Q1D nanosystems based on these isomers, herein, we concentrate on comparing arguably the most important clusters (i) the wz cluster (giving rise to wz-structured Q1D nanosystems as observed for many Q1D CdS/CdSe nanosystems experimentally), (ii) the most stable cluster isomer, assumed to correspond to the magic-cluster abundance peak in experiments.

In previous studies we showed that stable clusters of other materials (*e.g.* ZnO, LiF) when considered as nanosized building blocks, can, when appropriately assembled, lead to predictions of novel stable bulk polymorphs.[29,30] Here, although the symmetry of the magic $(CdS)_{13}$ cluster does not easily lend itself to assembly in three dimensions, we may take advantage of its axial C_3 symmetry to form ultra-thin 1D nanowires and nanorods by forming Q1D stacks of axially aligned clusters. The wz $(CdS)_{13}$ isomer also has three-fold

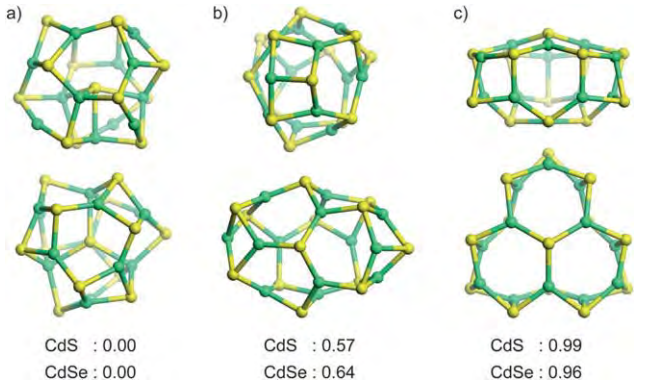

Fig. 1 Optimised structures of three $N = 13$ nanocluster isomers, where the upper and lower rows correspond to different views of the same three clusters: a) magic-, b) cage-, and c) wurtzite-based clusters. Below each cluster the relative energy (in eV) is given for both CdS and CdSe compositions with respect to the energy of the magic-cluster. As for all figures yellow balls represent sulfur or selenium atom positions and green balls cadmium atom positions. All reported energies of clusters, nanorods and nanowires refer to binding energies with respect to constituent spherical non spin-polarised atoms.

symmetry allowing us to also construct axially aligned ultra-thin nanowires and nanorods with the wz structure (with their long axis aligned with the (001) direction in the wz crystal as found in experiments) of exactly the same atomic composition as in the magic-cluster case for direct comparison. It was found in both cases considered that annealed nanowires were significantly more stable than cluster-assembled wires. The wz cluster-assembled nanowire was found to be a shallow, relatively high lying, energy minimum having a layered hexagonal structure (see Fig. 2) analogous to that found in bulk boron nitride (*h*-BN) which has also been predicted theoretically to be stable for ultra-thin nanorods and nanowires of ZnO[31] and in thicker ZnO nanorods under tensile strain.[32] We note that this relatively dense phase should be differentiated from a similar low-density hexagonal phase with larger interlayer spacing,[33,34] which was not observed in our investigation. Upon annealing, the hexagonal layered nanowire transforms into new structure with a deeper lying energetic minimum having a more bulk-like wz structure with a correspondingly longer (+28%) unit cell length (Figs. 2, 3a1 and 3b1). For the magic-cluster-assembled nanowire, the annealing procedure proceeds *via* an intermediate nanowire structure and finally leads to a more stable nanowire structure having a slightly shorter (-6%) unit cell length (Figs. 2, 3a2 and 3b2) but which is still significantly longer (+20%) than the annealed wz nanowire. Unlike for $(CdS)_{13}$ nanoclusters, but following experimental observations for thicker CdS nanowires and nanorods, Fig. 2 clearly shows that the wz structure is the most stable structure for $(CdS)_{13}$-based nanowires. The comparable diameters of the wz and magic-cluster-based ultra-thin nanowires results in similarly strong quantum confinement with an increase in the band gap with respect to the bulk wz band gap by a factor of 2.5 (see Fig. 4). In contrast, the absolute energy levels of the annealed wz nanowire are deeper than for the magic-cluster-based nanowire probably due to the energetically preferred atomic structure of the former.

In order to analyze the transition from the most stable 01D nanosystem for $(CdS)_{13}$ (*i.e.* the magic-cluster structure) to the most stable infinite nanowire (*i.e.* bulk-like wz-structured) we considered

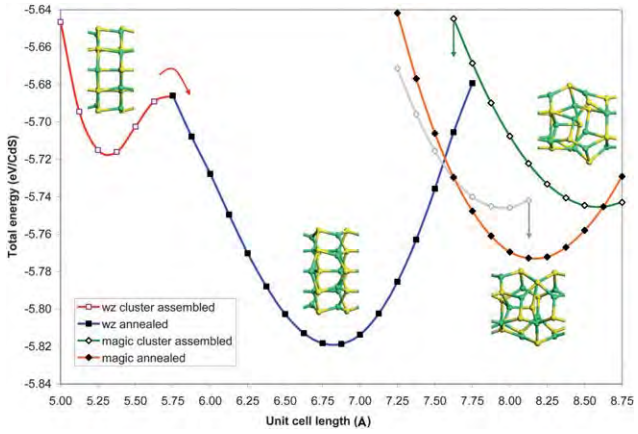

Fig. 2 Energy (in eV/CdS) *versus* length curves for the infinite CdS nanowires. Total energy of the cluster-assembled and annealed nanowires constructed from the $(CdS)_{13}$ wz and magic clusters as a function of the unit cell length (half the super cell length used in the calculations) along the nanowire *z*-direction. The arrows indicate the energetically downhill annealing path. The inset figures show the structure of a unit cell of the cluster-assembled and final annealed nanowires.

$[(CdS)_{13}]_n$ nanorods of all four CdS nanowire structures considered above (*i.e.* wz- and magic-cluster-based, both annealed and cluster-assembled) from the size of a one-cluster unit ($n = 1$ or 26 atoms) to a six-cluster unit ($n = 6$ or 156 atoms). In Fig. 5 we show the change in total energy of the four nanorods per CdS unit with increasing length. Interestingly, unlike for the nanowires, for up to $n = 3$, the cluster-assembled wz nanorod was found to be more stable than the nanorod with the annealed wz structure. For all considered sizes, however, the annealed magic-cluster nanorod was found to be most energetically stable. As the length of the nanorods increases, the energy difference between the annealed wz and magic-cluster-based nanorod structures gradually reduces implying that a transition to the wz structure occurs for larger *n*. In order to predict at what length this transition occurs, we have extrapolated the energy *versus* length trends of the magic-cluster-based and wz nanorods by fitting the data points to an inverse power law (see inset to Fig. 5, fitted with $R^2 > 0.99$). We find that the persistence of the excess stability of the annealed magic nanorods with respect to the annealed wz nanorods lasts until approximately 13 cluster units; equating to 338 atoms and to more than 10 nm length with respect to the length of the annealed magic nanorod. We have also calculated the energy difference between annealed wz and magic-cluster-based $[(CdSe)_{13}]_6$ nanorods which is very similar to that found for CdS indicating analogous behaviour in both Q1D systems. Relative energies of all nanorods and nanowires are given in Table 1. To understand these trends we have examined the atomic and electronic structure of the nanorods.

The higher crystallinity of the annealed wz $[(CdS)_{13}]_6$ nanorod is clear from the radial distribution function (RDF) taken with respect to the position of a central sulfur atom showing prominent peaks at well-determined distances (see RDF for the annealed wz $[(CdS)_{13}]_6$ in Fig. 3c1 with respect to the structure shown in Fig. 3d1). In contrast, the corresponding RDF of the annealed magic-cluster-based $[(CdS)_{13}]_6$ nanorod (see Fig. 3c2 with respect to structure shown in Fig. 3d2). This lower crystallinity is also manifested in the oscillatory diameter of the annealed magic-cluster-based Q1D nanosystems (Fig. 3b2) due to the recognisable magic-cluster $(CdS)_{13}$ repeat units (see highlighted segment in Fig. 3d1). In contrast, the annealed wz Q1D nanosystems have a much more regular stacked structure with a uniform diameter (see Fig. 3d1). This crystalline layering has been observed by HRTEM in CdS and CdSe nanorods of larger diameters than those studied here.[10,13] Based upon our results we predict that such layering will be absent in well-annealed bare CdS and CdSe nanorods of diameters <1.5 nm and lengths <13 nm. Of potential technological importance, such annealed magic-cluster-based nanorods would also have significantly higher aspect ratios than wz nanorods of the same composition (~50% higher in the case of $[(CdS)_{13}]_6$). Under pressure cycling, ultra-thin CdSe nanorods have previously been shown to exhibit dramatic structural transitions between the six-fold coordinated rocksalt phase and the four-fold coordinated wz phase[35] often leading to fracturing. In the present case, although accompanied by a large aspect ratio change, the atomic-level transition is much more subtle and may thus be more robust for repetitive utilization in nano-mechanical transducers. We also note that we have confirmed the experimental observation that rocksalt nanorods are only stable under external pressure for the ultra-thin regime by attempts to optimise ultra-thin rocksalt-structured nanorods. We found in all cases that the such nanorods spontaneously relaxed into distorted non-cubic structures

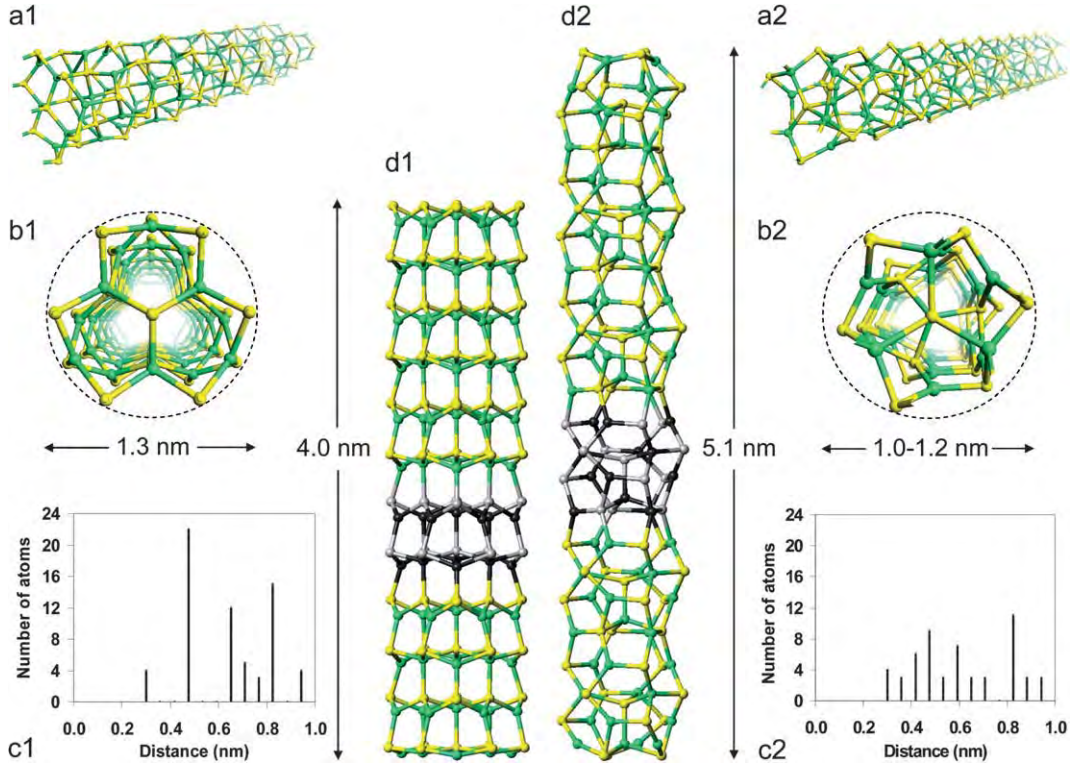

Fig. 3 Summary of the structural features of annealed wz and magic-cluster-based CdS nanowires and nanorods. Perspective views of the annealed wz- (a1) and magic-cluster-based (a2) nanowires, cross-section of the of the annealed wz (b1) and the magic-cluster-based (b2) nanowire/nanorod, radial distribution function of the annealed wz (c1) and magic-cluster-based (c2) $[(CdS)_{13}]_6$ nanorod, atomic structure of the annealed wz (d1) and the magic-cluster-based (d2) $[(CdS)_{13}]_6$ nanorods (the $(CdS)_{13}$ repeat unit is highlighted in each case). Quoted distances include the radii of two sulfur ions to better compare with estimates made by HRTEM. The two distances in b2 indicate the maximum and minimum of the oscillatory diameter of the annealed magic-cluster-based nanorods and nanowires.

(usually with final structures similar to wz) which were always significantly less stable than the other nanorods considered herein.

Experimentally, CdS and CdSe nanorods possessing a layered wz structure oriented along the (001) direction are known to have very large electric dipole moments along the length of the rod[36] which are thought to be important for their self-assembly.[37] Maintaining a large dipole is not energetically favourable and it is known in similarly structured infinite 2D wz nanoslabs (where such a dipole is unsustainable) in other materials, that the atomic structure can reconstruct in ways to drastically reduce the moment across the slab.[33,34] In our case we estimate the dipole moment in the annealed wz CdS nanorods to be reduced by approximately 5% when going to the annealed magic-cluster-based CdS nanorods indicating that dipole reduction is not a significant structure-directing influence in the ultra-thin Q1D systems considered.

Along their length, both magic-cluster and wz annealed nanorods have the same atomic nearest neighbour coordination per $(CdS)_{13}$ unit: four four-coordinated and nine three-coordinated sulfur atoms and four four-coordinated and nine three-coordinated cadmium atoms. At their ends, termination induces three two-coordinated cadmium atoms in both annealed nanorod types and a further three two-coordinated sulfur atoms in the annealed wz nanorods only. Two-coordinated sulfur atoms appear to be an inherent terminating structural feature of bare annealed wz nanorods which cannot be repaired by local reconstruction. In order to retain a wz-like structure, while avoiding such under-coordination of the sulfur atoms, wholesale reconstruction seems to be the only option. Such a reconstruction leads to nanorods with a hexagonal layered structure and the resulting lower under-coordination of the sulfur atoms is a likely reason why such nanorods are more stable than annealed wz nanorods for n <4 (see Fig. 5). Electronically, both the wz- and magic-cluster-based nanorods have a large number of states in the region of the gap of their respective infinite nanowire counterparts due to their defective end terminations. In line with the higher under-coordination in the annealed wz nanorods, the energy level spectrum is destabilised with respect to that of the annealed magic-cluster-based nanorods (see Fig. 4). We can view the annealed magic-cluster nanorods as structurally reconstructed versions of the annealed wz nanorods which helps to heal the less energetically favourable sulfur terminations in the latter. This reconstruction, although stabilising with respect to the nanorod ends also causes the internal atomic structure of the nanorod to be non-wz-like. Thus, with increasing length, a greater and greater percentage of the atoms in the annealed magic-cluster nanorods will be found in a structure known to be energetically less stable than the wz structure in the infinite limit and the percentage of atoms involved in an energetically preferable terminating reconstruction will become correspondingly lower. Evidently, at some length this situation will no longer be more stable than an annealed wz structure with a less favourable terminating end reconstruction. At this point, structural transition between the annealed magic-cluster structure and the annealed wz nanorod will be energetically favourable (at a length of ~10 nm, as predicted by our

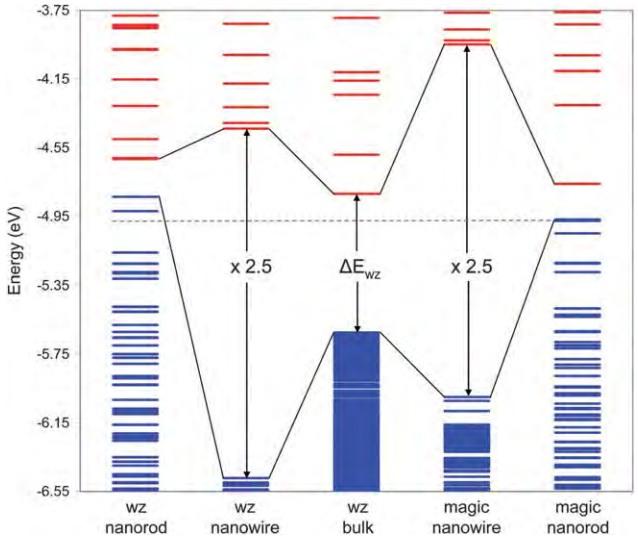

Fig. 4 Summary of the electronic structure of annealed wz- and magic-cluster-based CdS nanowires and nanorods. Calculated energy levels (eV) of CdS systems (from left to right): annealed wz $[(CdS)_{13}]_n$ nanorod, infinite annealed wz nanowire, wz bulk crystal, infinite annealed magic-cluster-based nanowire, annealed magic-cluster-based $[(CdS)_{13}]_n$ nanorod. Blue denotes occupied levels (sulfur s–p states) and red unoccupied levels (cadmium s states). The gaps of the nanowires are shown to be red-shifted by a 2.5× multiplicative factor with respect to the bulk CdS wz bandgap (ΔE_{wz}) due to quantum confinement. We note that, as is typical for DFT calculations, the band gaps are systematically underestimated and thus the figure provides an indication of relative changes in electronic structure (*i.e.* Q1D with respect to bulk) only.

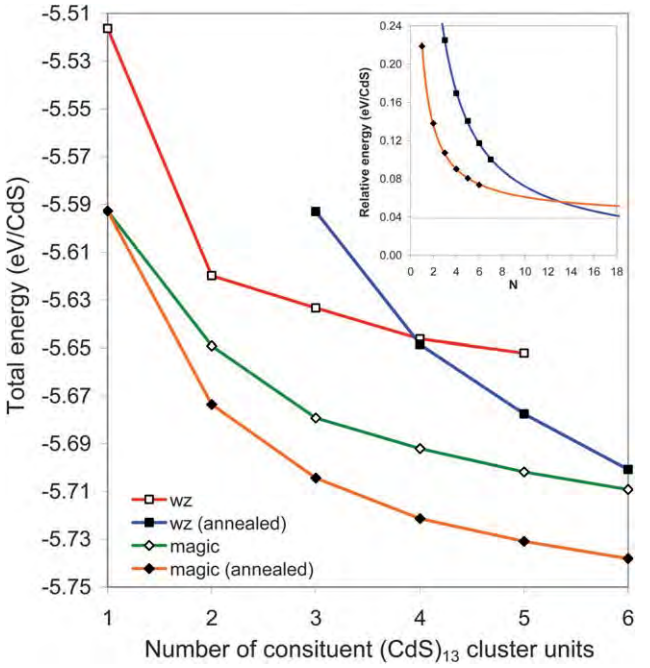

Fig. 5 Energy (eV/CdS) of the cluster-assembled and annealed $[(CdS)_{13}]_n$ nanorods constructed from the $(CdS)_{13}$ wz and magic-cluster units as a function of n. The inset shows extrapolated energetic relative stability of the wz and magic-cluster-based annealed $[(CdS)_{13}]_n$ nanorods as a function of n with respect to the energy of the calculated energy of the infinite annealed wz nanowire. The horizontal grey line shows the energy of the infinite magic-cluster annealed nanowire.

calculations). We note that this strong dependence of the overall CdS/CdSe ultra-thin nanowire structure, and, furthermore, aspect ratio, on the terminating surface atomic/electronic structure may provide a means for influencing the predicted nanorod structural crossover by reversible attachment of suitable ligands.

In summary, we have compared the stability of ultra-thin bare CdS nanowires and nanorods having the bulk wz structure with those based on the assembly of particularly stable $(CdS)_{13}$ magic-cluster building blocks using first principles calculations. Although the wz structure is energetically favoured in relatively thick CdS nanorods and in the limit of infinitely long ultra-thin nanowires, in ultra-thin nanorods the magic-cluster-based structure is found to be persistently more energetically stable than the correspondingly sized bulk-like wz nanorods up to a length of 10 nm. This nanoscale structural transition is also predicted to be found in ultra-thin Q1D CdSe and in both materials should be experimentally verifiable by HRTEM. As the length-dependent transition is also accompanied by a large change in the aspect ratio of the nanorods, if physically realized, this effect may find potential application in nano-mechanical transducers. We believe that our explicit demonstration of the persistence of the stability non-bulk like atomic structures in Q0D nanoclusters to Q1D ultra-thin nanorods in two nanotechnologically important ISC materials is likely to be general to many other materials. We hope that our work may help to encourage experimental efforts in this area to fabricate ultra-thin Q1D nanosytems (particularly with diameters ~1 nm) in a range of materials, many of which we predict will have novel non-bulk-like atomic structures and potentially useful new nanoscale properties.

Table 1 Calculated energies (eV per formula unit) of all considered nanorods and nanowires of CdS and CdSe

Composition	wz cluster assembled	wz cluster annealed	Magic cluster assembled	Magic cluster annealed
$Cd_{13}S_{13}$	−5.516	—	−5.593	—
$Cd_{26}S_{26}$	−5.620	—	−5.649	−5.674
$Cd_{39}S_{39}$	−5.633	−5.593	−5.679	−5.704
$Cd_{52}S_{52}$	−5.646	−5.649	−5.692	−5.721
$Cd_{65}S_{65}$	−5.652	−5.678	−5.702	−5.731
$Cd_{78}S_{78}$	—	−5.701	−5.709	−5.738
$Cd_{91}S_{91}$	—	−5.718	—	—
CdS nanowire	−5.720	−5.818	−5.747	−5.780
$Cd_{13}Se_{13}$	−5.062	—	−4.988	—
$Cd_{78}Se_{78}$	—	−5.177	—	−5.140
CdSe nanowire	—	−5.211	—	−5.246

Acknowledgements

We acknowledge support from the Spanish Ministry of Education and Science (grant FIS2008-02238), time on the *MareNostrum* supercomputer (*Barcelona Supercomputing Center/Centro Nacional de Supercomputación*) and grants from the Thailand Research Fund (to WS and JL) and the National Science and Technology Development Agency (NSTDA Chair Professor and NANOTEC Center of Excellence). Support from the Thai Commission on Higher Education, Ministry of Education under Postgraduate Education and Research Programs in Petroleum and Petrochemicals, and Advanced Materials is also acknowledged.

References

1 L.-S. Li, J. Hu, W. Yang and A. P. Alivisatos, *Nano Lett.*, 2001, **1**, 349–351.
2 H. Yu, J. Li, R. A. Looms, L.-W. Wang and W. Buhro, *Nat. Mater.*, 2003, **2**, 517–520.
3 L. Cademartiri and G. A. Ozin, *Adv. Mater.*, 2008, **20**, A1–8.
4 A. S. R. Kasuya, Y. A. Barnakov, I. M. Dmitruk, T. Nirasawa, V. A. Romanyuk, V. Kumar, S. V. Mamykin, K. Tohji, B. Jeyadevan, K. Shinoda, T. Kudo, O. Terasaki, Z. Liu, R. V. Belosludov, V. Sundararajan and Y. Kawazoe, *Nat. Mater.*, 2004, **3**, 99–102.
5 E. Sanville, A. Burnin and J. BelBruno, *J. Phys. Chem. A*, 2006, **110**, 2378–2386.
6 X. F. Duan, Y. Huang, R. Agarwal and C. M. Lieber, *Nature*, 2003, **421**, 241–245.
7 X. F. Duan, C. M. Niu, V. Sahi, J. Chen, J. W. Parce, S. Empedocles and J. L. Goldman, *Nature*, 2003, **425**, 274.
8 C. J. Barrelet, A. B. Greytak and C. M. Leiber, *Nano Lett.*, 2004, **4**, 1981–1985.
9 Y. Wang and N. Herron, *J. Phys. Chem.*, 1991, **95**, 525–532.
10 W. Cai, Z. Li and J. Sui, *Nanotechnology*, 2008, **19**, 465606(1–6).
11 A. Ghezelbash, B. Koo and B. Korgel, *Nano Lett.*, 2006, **6**, 1832–1836.
12 N. Pradhan, X. Huifang and X. Peng, *Nano Lett.*, 2006, **6**, 720–724.
13 F. S. Riehle, R. Bienert, R. Thomann, G. A. Urban and M. Krüger, *Nano Lett.*, 2009, **9**, 514–518.
14 C. H. Ye, G. W. Meng, Y. H. Wang, Z. Jiang and L. D. Zhang, *J. Phys. Chem. B*, 2002, **106**, 10338–10341.
15 S. D. Elliott, M. P. Moloney and Y. K. Gun'ko, *Nano Lett.*, 2008, **8**, 2452–2457.
16 J. B. Li and L. W. Wang, *Phys. Rev. B: Condens. Matter Mater. Phys.*, 2005, **72**, 125325(1–15).
17 S. –P. Huang, W. –D. Cheng, D.-S. Wu, J.-M. Hu, J. Shen, Z. Xie, H. Zhang and Y.-J. Gong, *Appl. Phys. Lett.*, 2007, **90**, 031904(1–3).
18 H. Pan and Y. P. Feng, *ACS Nano*, 2008, **2**, 2410–2414.
19 S. Datta, M. Kabir, T. Saha-Dasgupta and D. D. Sarma, *J. Phys. Chem. C*, 2008, **112**, 8206–8214.
20 J. Frenzel, J.-O. Joswig and G. Siefert, *J. Phys. Chem. C*, 2007, **111**, 10761–10761.
21 S. M. Woodley, A. A. Sokol and C. R. A. Catlow, *Z. Anorg. Allg. Chem.*, 2004, **630**, 2343–2353.
22 C. E. Junkermeier, J. P. Lewis and G. W. Bryant, *Phys. Rev. B: Condens. Matter Mater. Phys.*, 2009, **79**, 125323(1–8).
23 O. Gülseren, F. Ercolessi and E. Tosatti, *Phys. Rev. Lett.*, 1998, **80**, 3775–3778.
24 J. Perdew, K. Burke and Y. Wang, *Phys. Rev. B: Condens. Matter*, 1996, **54**, 16533–16539.
25 G. Kresse and J. Hafner, *Phys. Rev. B: Condens. Matter*, 1993, **47**, 558–561.
26 P. E. Blöchl, *Phys. Rev. B: Condens. Matter*, 1994, **50**, 17953–17979.
27 G. Kresse and D. Joubert, *Phys. Rev. B: Condens. Matter Mater. Phys.*, 1999, **59**, 1758.
28 H. J. Monkhorst and J. D. Pack, *Phys. Rev. B: Solid State*, 1976, **13**, 5188–5192.
29 J. Carrasco, F. Illas and S. T. Bromley, *Phys. Rev. Lett.*, 2007, **99**, 235502(1–4).
30 W. Sangthong, J. Limtrakul, F. Illas and S. T. Bromley, *J. Mater. Chem.*, 2008, **18**, 5871–5879.
31 L. Zhang and H. Huang, *Appl. Phys. Lett.*, 2007, **90**, 023115(1–3).
32 A. J. Kulkarni, M. Zhou, K. Sarasamak and S. Limpijumnong, *Phys. Rev. Lett.*, 2006, **97**, 105502(1–4).
33 C. L. Freeman, F. Claeyssens and N. L. Allen, *Phys. Rev. Lett.*, 2006, **96**, 066102(1–4).
34 C. Tusche, H. L. Meyerheim and J. Kirschner, *Phys. Rev. Lett.*, 2007, **99**, 026102(1–4).
35 D. Zaziski, S. Prilliman, E. C. Scher, M. Casula, J. Wickham, S. M. Clark and A. P. Alivisatos, *Nano Lett.*, 2004, **4**, 943–946.
36 L.-S. Li and A. P. Alivisatos, *Phys. Rev. Lett.*, 2003, **90**, 097402(1–4).
37 A. V. Titov and P. Král, *Nano Lett.*, 2008, **8**, 3605–3612.

CARBON 48 (2010) 1524–1530

available at www.sciencedirect.com

ScienceDirect

journal homepage: www.elsevier.com/locate/carbon

Density functional theory evidence for an electron hopping process in single-walled carbon nanotube-mediated redox reactions

Teeranan Nongnual [a,b], *Somkiat Nokbin* [a,b], *Pipat Khongpracha* [a,b], *Philippe Anthony Bopp* [c], *Jumras Limtrakul* [a,b,*]

[a] *Laboratory for Computational and Applied Chemistry, Chemistry Department, Faculty of Science, Kasetsart University, Bangkok 10900, Thailand*

[b] *NANOTEC Center of Excellence, National Nanotechnology Center, Kasetsart University, Research and Development Institute, Bangkok 10900, Thailand*

[c] *Department of Chemistry, Université Bordeaux 1, FR-33405 Talence Cedex, France*

ARTICLE INFO

Article history:
Received 18 September 2009
Accepted 18 December 2009
Available online 24 December 2009

ABSTRACT

The electron hopping mechanism in the single-walled carbon nanotube (SWCNT)-mediated redox reaction between anthraquinonyl (AQH_2) and 4-arylhydroxyl amine (4AHA) groups is studied by density functional theory calculations. The (8, 0) SWCNT is used to mimic the real system of interest. It is found that electrons from the oxidized AQH_2 group can be transferred to the oxidizing 4AHA group, at the other end of the nanotube, by a hopping process through the mediating SWCNT. Disparity of electron densities ascribable to non-localized electrons confirms this finding. The disparity, partial electron density difference, and Hirshfeld partial charges analyses show that the SWCNT can hold 87% of the extra electron density of the hypothetical negative intermediate produced from the oxidation of the AQH_2 process. Chemical attachments of these two redox reagents to the SWCNT also cause new impurity states within the band gap, thereby giving more metallic characteristics to the system. These findings provide a detailed understanding of the electron hopping process and agree well with a previous experimental study.

1. Introduction

Among all nanoscale morphologies of carbon, multi-walled carbon nanotubes (MWCNTs) were first observed under transmission electron microscopy (TEM) by Iijima in 1991 [1]. After that, single-walled carbon nanotubes (SWCNTs) were produced independently by Iijima and Ichihashi [2] and Bethune et al. [3] in 1993. Since these discoveries of low-dimensional carbon nanostructures, carbon nanotubes (CNTs) have attracted much interest in modern nanoscience and nanotechnology due to their novel and structure-dependent properties. Over the years, the physical and chemical properties of CNTs have been well-documented with more and more sophisticated methods. The novel properties of these CNTs allow their application as nanoelectronic devices [4], sensors [5], field emission sources [6], and composite materials [7]. The CNTs also function as nanowires to transport electrons between an electrode and electroactive proteins chemically

* *Corresponding author:* Address: NANOTEC Center of Excellence, National Nanotechnology Center, Kasetsart University, Research and Development Institute, Bangkok 10900, Thailand. Fax: +66 2562 5555x2176.
E-mail address: jumras.l@ku.ac.th (J. Limtrakul).

0008-6223/$ - see front matter © 2009 Elsevier Ltd. All rights reserved.
doi:10.1016/j.carbon.2009.12.049

attached on each end of the tube [8]. The transport distances, controlling the rate of electron transfer, are larger than 150 nm from the enzymatic active center to the electrode [9].

The chemical functionalization reactions for CNTs are categorized into three methods, which are: direct attachment to the graphitic surface, ester linkage, and covalent binding using diazonium reagents with high selectivity. The diazonium media method was further developed by Compton's group to initiate chemisorptions of aryl diazonium salts by direct reduction with hypophosphorous acid in the presence of carbon powder [10–12]. The method was further extended to the application on MWCNTs with anthraquinone-1-diazonium chloride and 4-nitrobenzenediazonium tetrafluoroborate, resulting in the synthesis of 1-anthraquinonyl–MWCNTs (AQ–MWCNTs) and 4-nitrophenyl–MWCNTs (NB–MWCNTs) [13].

Recently, Wong and Compton [14] reported a redox reaction on the same MWCNT for the first time. This MWCNT is functionalized with two redox-active species, directly attached by the diazonium salt method. The 4-arylhydroxyl amine (4AHA) and AQH_2 species are generated in the first oxidation cycle from NO_2–C_6H_4–MWCNT and AQ–MWCNT, respectively. This redox reaction consists of a reversible oxidation and an irreversible reduction; it is studied by the cyclic voltammetry technique. These authors proposed a redox reaction mechanism where AQH_2 is the oxidizing agent with the oxidation peak at $E_a = -0.385$ V while NHOH–C_6H_4 is the reducing group lessening the oxidation peak at $E_a = 0.125$ V

$$AQH_2\text{–MWCNT–}C_6H_4\text{–NHOH} \rightarrow AQ\text{–MWCNT–}C_6H_4\text{–}NH_2 + H_2O$$

The pathway of electron transfer from AQH_2 to the 4-arylhydroxyl amine group is investigated to determine whether it is via intermolecular electron tunneling between reagents or by electron hopping via the CNT. The hopping was proposed to be more favorable because of the shorter distance through the tube compared to a process through the solvent. This phenomenon is unique for both oxidizing and reducing groups confined to the same CNT.

Here, we report a theoretical study on the possible processes of electron hopping between two redox reagents functionalized on the same CNT. The mediating MWCNT (in the real system) is simplified to a semiconducting SWCNT for computational efficiency. Periodic calculations are performed to obtain computed electronic properties as realistic as possible. Although time-dependent calculations can yield more details about the electron transfer, such calculations are not practicable for such a large system due to computational limitations. We have thus limited ourselves to static calculation and have tried to overcome the limitations by focusing on six hypothetical subsystems, using static analysis techniques such as the disparity of the electron densities and the nucleophilic Fukui function plot. This yields enough information to establish and characterize the electron transfer process in the whole system.

We also focus only on the redox reaction and not on the chemical attachment and the preparation steps. Thus, the following redox reaction from AQH_2–SWCNT–4AHA, terminated at AQ–SWCNT–4AA, is proposed. It can be subdivided into a reversible oxidation and an irreversible reduction (see Fig. 1), where 4-arylamine is noted as 4AA.

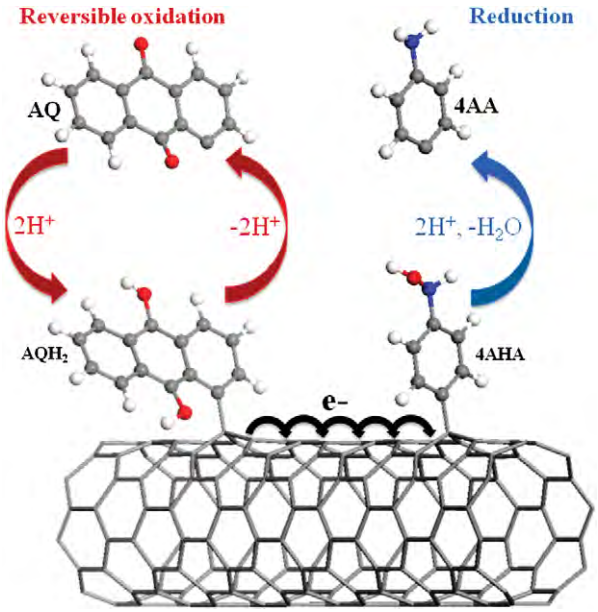

Fig. 1 – Proposed mechanism for the SWCNT-mediated redox reaction, consisting of a reversible oxidation and an irreversible reduction. The SWCNT accepts electrons from the AQH_2 species and donates the electrons to the 4-arylhydroxyl amine.

Total reaction:

$$AQH_2\text{–SWCNT–4AHA} \rightarrow AQ\text{–SWCNT–4AA} + H_2O$$

Oxidation:

$$AQH_2\text{–SWCNT–4AHA} \leftrightarrow AQ\text{–SWCNT–4AHA} + 2H^+ + 2e^-$$

Reduction:

$$AQ\text{–SWCNT–4AHA} + 2H^+ + 2e^- \rightarrow AQ\text{–SWCNT–4AA} + H_2O$$

2. Calibration of the SWCNTs and computational method

The periodic calculations were carried out using the density functional theory (DFT) method as implemented in the DMol3 package [15,16]. For all functionals that we investigated, the generalized gradient approximation (GGA) and an all-electron double numerical basis set with polarized function (DNP) were chosen for these spin-unrestricted computations. These functionals can be applied to large periodic systems and are known to bring about reliable qualitative results. The density functionals used in this work do not include dispersion energy contributions. The DNP basis set corresponds to a double-ζ quality basis set with a p-type polarization function added to hydrogen and d-type polarization functions added to heavier atoms, and is comparable to 6-31G** Gaussian basis sets, providing a better accuracy, particularly for the hydrogen removal step. The real space global cutoff radius was set to be 3.70 Å. For the geometrical optimizations, all atoms were fully optimized until all the forces on the atoms were less than 0.05 eV $Å^{-1}$. The Brillouin zone was sampled using the Monkhorst–Pack scheme [17].

2.1. Calibration of the SWCNTs

In the present approach, a suitably calibrated SWCNT is used to mimic the multi-walled tubes used in the experiments for the computations. The important feature is that the MWCNTs used in the experiments have electronic band gaps like semiconductors. The criterion for the calibration is thus, that the gap of the model-tube should be in the range of 0.5–1.5 eV [18]. The calibration is started with a study of naked (n, 0) zigzag SWCNTs, investigated with three functionals and comparing the energy gaps (E_{gap}) with each other and with the ones obtained in previous studies. Each initial structure is generated in a supercell periodic box of $20 \times 20 \times 8.52$ Å^3, composed of two repeated unit cells of SWCNT along the tube axis. The closest distance between two neighboring SWCNTs is larger than 10 Å in order to be able to ignore intertube interactions in the calculations.

The calibrations are performed in the GGA in the Perdew–Burke–Ernzerhof (PBE) [19], Becke's exchange and Lee, Yang, and Parr's correlation functional (BLYP) [20,21], and non-local exchange–correlation functional (PW91) [22] with the maximum k points of $1 \times 1 \times 50$. The BLYP method is immediately disqualified due to its large average deviation of ±0.079 eV in E_{gap} compared to previous theoretical data [23–28]. The PBE and PW91 methods give the same E_{gap} within a small deviation of ±0.007 eV and a smaller deviation of ±0.044 eV compared to the same data. Although these two methods are very similar, the PBE functional is chosen in our calculations, following the recent theoretical studies [29,30] of periodic systems.

The diameter of the zigzag SWNCTs is then varied systematically and the band gaps studied with the same procedure to find the smallest nanotube representative of the experimental system. Three (n, 0) SWCNTs with n mod 3 = 0 are found to be metallic, obeying the empirical (n, n + 3i) rule for metallic carbon nanotubes, also known as the 1/3 rule: (6, 0) with an E_{gap} of 0.00 eV ($E_{gap,\ calc}$ = 0.00 eV, Ref. [23]); (9, 0) with an E_{gap} of 0.17 eV ($E_{gap,\ expt}$ = 0.080 ± 0.005 eV, Ref. [24] and $E_{gap,\ calc}$ = 0.17 eV, Ref. [25]); and (12, 0) with an E_{gap} of 0.14 eV ($E_{gap,\ expt}$ = 0.042 ± 0.004 eV, Ref. [24] and $E_{gap,\ calc}$ = 0.078 eV, Ref. [23]) (where *expt* is experimental data, *calc* is theoretical data, and i is an integer). The (7, 0) SWCNT also presents a metallic character with an 0.15 eV energy gap (0.21 eV, Ref. [26] and 0.19 eV, Ref. [27]). Thus, the (6, 0), (7, 0), (9, 0), and (12, 0) SWCNTs are certainly not usable as models because of their metallic character.

The (8, 0) SWCNT is found to be the smallest zigzag carbon nanotube that displays a semiconducting behavior with an acceptable energy gap of 0.62 eV. The calculated value is in good agreement with previous data for the E_{gap} (0.643 eV, Ref. [23]; 0.62 eV, Ref. [25]; 0.59 eV, Ref. [27]; and 0.63 eV, Ref. [28]) and confirms that the E_{gap} of n mod 3 = 2 tubes is larger than that n mod 3 = 1 [27]. In order to be able to neglect the intermolecular interaction between the two redox species, the six repeated unit cells along the z-direction of the carbon nanotube are used for the calculations of functionalized tubes. Therefore, the SWCNT-mediated redox models in this work are generated from the validated (8, 0) SWCNT and calculated by periodic calculations with the PBE method.

2.2. Redox systems

As seen above, an (8, 0) SWCNT is chosen. For the full redox system, it is functionalized by two redox groups more than 12 Å apart from each other to minimize, and eventually neglect, the intermolecular interaction between these two species. A supercell with $40 \times 40 \times 24.15$ Å^3, comprising six periodic lengths for the zigzag SWCNT, is adopted in the calculation with the PBE function (see Fig. S3(a)). Each supercell contains two redox groups, which are covalently bonded to the sidewall of the SWCNT. The smallest distance between two neighboring SWCNTs is larger than 30 Å. In order to save computational time, the k points are reduced to be $1 \times 1 \times 10$, following the previous study [30], to calculate the electronic properties of the full redox system. Only the Γ point in the Brillouin zone is also considered for the geometric optimization and orbital analysis.

Even though the individual processes in the overall redox reaction take place concurrently, we simplify the problem by dividing the full redox pathway into six hypothetical states (see Fig. S1), which are: AQH_2–SWCNT–4AHA (substrate: *subs*), $[AQH–SWCNT–4AHA]^{1-}$ (*intermediate-1*), $[AQ–SWCNT–4AHA]^{2-}$ (*intermediate-2*: *int-2*), $[AQ–SWCNT–Ph–NH]^{1-}$ (intermediate-3: *int-3*) and AQ–SWCNT–4AA (product: *prod*) (AQ = anthraquinonyl, 4AHA = 4-arylhydroxyl amine, 4AA = 4-arylamine, SWCNT = (8, 0) zigzag SWCNT). The intermediate-1 state can be considered in two configurations, which are termed intermediate-1-a (*int-1-a*) and intermediate-1-b (*int-1-b*) for the removal of H*a* and H*b*, respectively.

Mimicking a half-cell redox reaction, the singly functionalized tubes with two electrons from the oxidation reaction, $[AQ–SWCNT]^{2-}$ (*AQ-tube*) and $[4AHA–SWCNT]^{2-}$ (*4AHA-tube*), are also investigated to consider the possibility of the transfer of these electrons (see Fig. S2). This half-cell redox system is optimized and investigated using the same parameter as the full redox system described above.

3. Results and discussion

The diazonium method provides a well-defined chemical bond between the molecule and a carbon atom of the tube rather than the less well-defined interaction between an entire group and the tube surface found in the adsorption of π-conjugated molecules. Indeed, the optimized geometry of the functionalized SWCNTs in the full redox system shows that the reacting groups with closing carbon atoms of the nanotube change their geometries with an average displacement of 0.19 Å for the AQ derivatives and 0.22 Å for the 4AHA derivatives. While the remaining atoms, which are far from the reacting species, of the tube remain roughly at the same positions within, on an average, 0.06 Å. These averages are calculated for all atoms of a desired part changing their relative positions in each step of the mechanism. We also found that the phenyl plane of the 4AHA group (including its derivatives: Ph–NH, and 4AA) is parallel to the perpendicular axis (reference line), which is vertical to the tube axis of the SWCNT medium, as shown in Fig. S4. The angle between the anthraquinonyl plane of the AQH_2 group in *subs* and the reference line is sharp, about 30°, due to the steric effect to

the adjacent hydrogen atom (H*b*) of the hydroxyl moiety of the AQH_2 group (see Fig. S3(a)). Whenever this hydrogen atom is cleaved, the repulsive force on the ketone becomes smaller. Thus, a less sharp angle is found, about 10°. However, the AQ group is not exactly sharp to the reference line, because the carbonyl oxygen atom is a hindrance for such an orientation.

The electronic properties of the redox systems are reported in Table 1. The results show that the two configurations of intermediate-1 have relative energy which differs by −0.95 kcal mol^{-1}, the *int-1-b* being more favorable than *int-1-a* due to a smaller steric effect between the hydrogen atom of the AQH group (H*b*) and the nanotube. The proposed mechanism pathway of the redox reaction through *int-2* is presented in snapshots. It starts from the *subs* configuration and goes through *int-1-b*, *int-2*, and *int-3* to *prod*. In more detail: The O–H*b* of the *subs* is first cleaved, as demonstrated in the *int-1-b*, with one electron remaining. Sequentially, the O–H*a* is removed, resulting in the *int-2*. This is a half-cell redox reaction, with, overall, two electrons left. The *int-3* is an intermediate state, corresponding to the *int-2* to *prod* reduction, where a hydroxyl group of the 4AHA is dehydrated by an acidic proton addition, and the Ph–NH group remains. The nucleophilic nitrogen atom of the *int-3* is then also attacked by another electrophilic proton, resulting in the *prod* configuration. The reduction reaction cannot be reversible: A negative −0.26*e* local Hirshfeld charge is found on the nucleophilic nitrogen atom of the Ph–NH part of *int-3*. This makes an attack between this site and an oxygen atom of water highly unlikely.

The chemical attachment of the two redox reagents to the SWCNT creates new impurity states within the band gap. From the pristine SWCNT, E_{gap} = 0.62 eV, the band gap in the redox systems is lowered to less than 0.16 eV, thereby introducing a more metallic character to the system. This eases electron delocalization in the modified system. The electron density difference and Hirshfeld partial charges analyses show that the tube can hold 87% of the extra electron density of the hypothetical negative intermediate produced from the oxidation of the AQH_2 (see entry 5 in Table 1). In addition, the remaining charge at the AQ in the *int-2* is −0.19*e*, leading to a reverse reduction of the AQ to the AQH_2.

The frontier molecular orbitals of the redox system are illustrated in Fig. S5. An electron ionization and reception occurs at the SWCNT, which can be clearly observed at both the HOMO and LUMO for the substrate. In the intermediate steps, an electronic connection between the AQ and the 4AHA molecules is clearly shown at the HOMO level. An electron movement is proposed as a theoretical mechanism pathway. The first electron from the oxidation reaction of the AQH_2 to AQH is initially excited to occupy the LUMO level of the *int-1-b*. In this state, both the AQ group and the nanotube are occupied, as shown in the LUMO level in Fig. S5(b). After that, the second electron is generated from the oxidation of the AQH to AQ, resulting in two excited electrons occupying strongly only in the AQ part in the LUMO level of the *int-2*. This case confirms the reversible reaction of the AQ to AQH_2. These two electrons then transfer to the 4AHA part, resulting in the strong occupation in the 4AHA side (Ph–NH) as shown in the LUMO level in Fig. S5(d). The Ph–NH group is eventually reduced by the extra electron at that level, resulting in the 4AA. The HOMO of the *prod* shows that the electrons are distributed mostly at the 4AA and no longer occupy the AQ side. In addition, an electron in the *int-1-b* and *int-2*, which is strongly localized at the AQ part, confirms that it can reversely reduce. This is the reduction reaction from AQ to AQH_2. On the other hand, an electron is rarely available at the 4AHA group (Ph–NH) in the *int-2* and *int-3*, leading to an irreversible reduction.

The plots of the difference of the Hirshfeld charge are presented in Fig. 2(a). These plots are calculated from the difference of each atomic charge between the negatively-charged structure and its neutralized version, neglecting relaxations, resulting in the charge difference of the negative atomic charge. An electron in the intermediate states has a high probability of presence at the AQH, leading to the reverse reduction of AQH to AQH_2. Two electrons in the *int-2* step have high probabilities at the AQ, 4AHA, and at the bridge in the nanotube, as shown in Fig. 2(a)-2. Therefore, it is clearly verified that the AQ and 4AHA groups can be reduced to AQH_2 and 4AA, respectively.

Fig. 2(b) shows the calculated disparity of the electron densities, following the definition; $\Delta\rho(\mathbf{i} \rightarrow \mathbf{j}) = \rho(\mathbf{j}) - \rho(\mathbf{i})$, where $\Delta\rho(\mathbf{i} \rightarrow \mathbf{j})$ is the change of negative charge densities between the negatively-charged structure, $\rho(\mathbf{j})$, and its neutralized version, $\rho(\mathbf{i})$, resulting in the density of only the negative charge. This plot clearly shows the connection between the reducing

Table 1 – Hirshfeld partial charge (in elementary changes *e*), energy gap (eV), and relative energy (kcal mol^{-1}) calculated with the PBE method and DNP basis set for pristine SWCNT, substrate, intermediate, product, and single-functionalized systems (D = direct, I = indirect energy gap).

Entry	Structure	Hirshfeld charge				Energy gap (eV)	Relative energy (kcal mol^{-1})
		Partial charge			Total		
1	Pristine SWCNT	–	–	–	–	0.62 D	–
2	Substrate	AQH_2 = 0.05	SWCNT = −0.07	4AHA = 0.03	0.01	0.00	–
3	Intermediate-1-a	AQH = −0.06	SWCNT = −0.91	4AHA = −0.02	−0.99	0.04 D	0.00
4	Intermediate-1-b	AQH = −0.16	SWCNT = −0.81	4AHA = −0.02	−0.99	0.04 I	−0.95
5	Intermediate-2	AQ = −0.19	SWCNT = −1.73	4AHA = −0.07	−1.99	0.10 I	–
6	Intermediate-3	AQ = −0.07	SWCNT = −0.77	Ph–NH = −0.16	−1.00	0.16 I	–
7	Product	AQ = −0.01	SWCNT = −0.03	4AA = 0.05	0.01	0.00	–
8	$[AQ–SWCNT]^{2-}$	AQ = −0.27	SWCNT = −1.72	–	−1.99	0.00	–
9	$[4AHA–SWCNT]^{2-}$	–	SWCNT = −1.92	4AHA = −0.07	−1.99	0.00	–

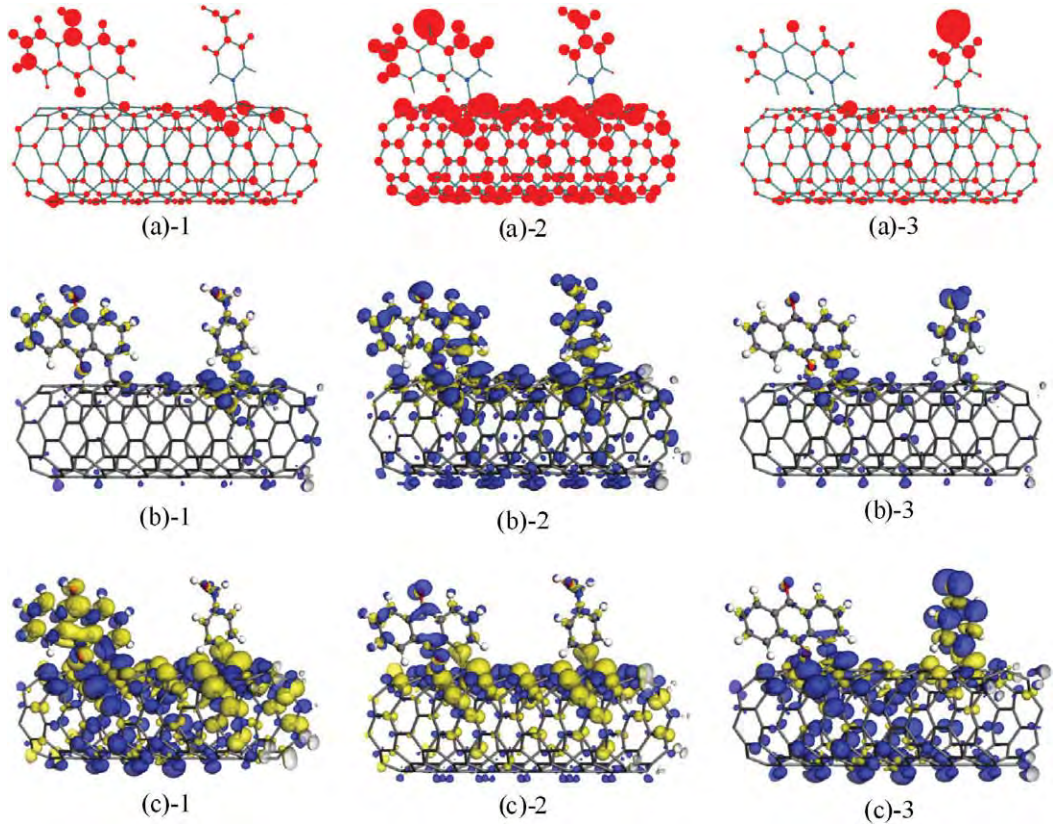

Fig. 2 – Hirshfeld charge difference (a), where the red color represents a negative charge and the blue color a positive charge. Disparity of electron densities (b), where the blue and yellow colors represent electron accumulation and depression zones, respectively. Nucleophilic Fukui function plot (c). (1 stands for *int-1-b*, 2 for *int-2*, and 3 for *int-3*. (b) and (c) are plotted with an isovalue of ±0.004*e* Å^{-3}.) (For interpretation of the references to color in this figure legend, the reader is referred to the web version of this article.)

group and the oxidizing group. The electron density obviously occupies only the redox molecules and their junction to the SWCNT medium.

The nucleophilic Fukui function plots, as demonstrated in Fig. 2(c), confirm the electron hopping process of the redox reaction via the nanotube. The mechanism starts with a high nucleophilic character of the AQ and its connection. Then, the reducing negative behavior at the AQ leads to an increase at 4AHA. However, the two carbon atoms of the nanotube connected to the AQ and 4AHA species are of the non-conjugated sp^3 type. The negative charge density is high at the bridging single bonds of both of the carbon atoms, as depicted in Fig. 2(c)-1–(c)-3, opening a route for the electron transfer from the reducing AQ group to the other. Therefore, the electron transfer between two redox groups can occur by electron hopping via the SWCNT.

The partial electron density difference plots, as shown in Fig. 3, are calculated from the difference of the electron densities between the whole structure and its three divided parts, which are an AQ derivative, a 4AHA derivative, and the tube. The definition; $\Delta\rho(\mathbf{R}) = \rho(\mathbf{R}) - \rho(\mathbf{o}) - \rho(\mathbf{r}) - \rho(\mathbf{m})$ (where $\Delta\rho(\mathbf{R})$ is the partial electron density difference of the redox system; **R** is all redox parts, **o** is the oxidation part, **r** is the reduction part, and **m** is the medium part) is considered and implied to both resonance character and an electron transferable of the system. The plot of *int-1-b* in Fig. 3(b) shows a high electron resonance of the π-conjugated system, covering the electron transfer, after the H*b* is cleaved. In Fig. 3(a) and (e), the electron transfer is observed between the two functionalized groups and the tube, confirming the electron movement possibility. The electron transfer between two redox groups is shown as the linkage at the tube in *int-2* and *int-3*.

In order to show that both functionalized groups must indeed be present on the same tube, the electron transfer of the singly functionalized tubes (known as the half-cell redox system), the *AQ-tube* and the *4AHA-tube*, is calculated and compared to the full redox system. The Hirshfeld partial charges analyses show that the charge density on the tube is virtually the same in the *AQ-tube* (−1.72*e*) and in the full redox system (−1.73*e*), which eases comparison: a more negative charge is left on the AQ group in the single-functionalized tube due to the lack of further electron accepting groups. When the accepting group, 4AHA, is added to the *AQ-tube* to obtain the full redox system, the remaining electron density in the AQ group is lowered by 30% and donated to the 4AHA (see entries 5 and 8 in Table 1). The plots of the deviation of electron densities of these single-functionalized systems are presented in Fig. S6. The plots show that an electron from the single AQ can transfer to the tube in the *AQ-tube*; and an electron in the tube can also transfer to the single 4AHA group in

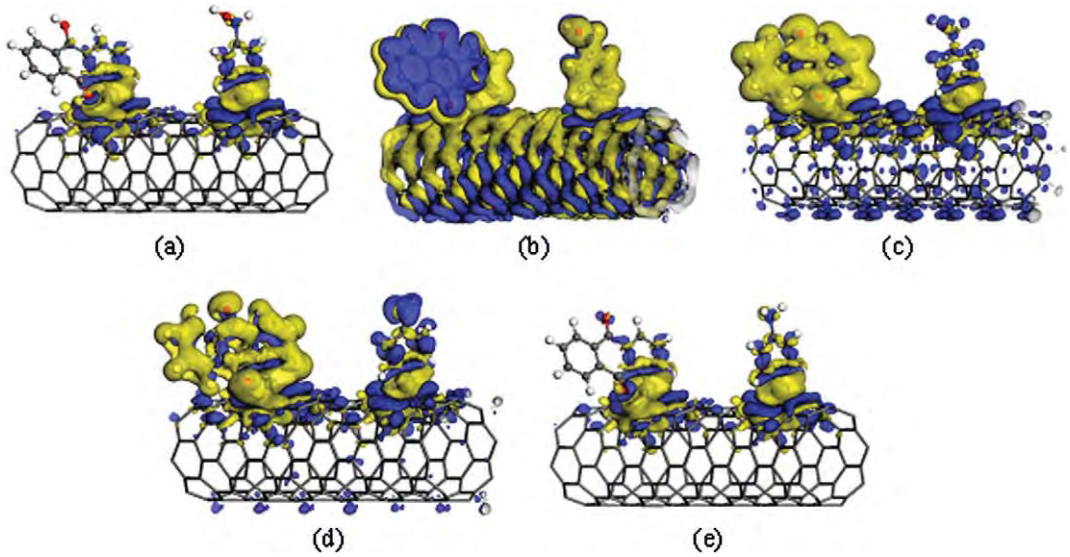

Fig. 3 – Partial electron density difference of *subs* (a), *int-1-b* (b), *int-2* (c), *int-3* (d), and *prod* (e), plotted for an isovalue of ±0.004*e* Å^{-3}.

the *4AHA-tube*. Two electrons in both singly functionalized systems have high probabilities along the tube, but the electronic junction can be observed only in the full redox system, as described above.

4. Conclusions

DFT calculations with the PBE functional are used to investigate the reaction mechanism of electron hopping in the SWCNT-mediated redox reaction of anthraquinonyl (AQH_2) and 4-arylhydroxyl amine (4AHA) groups. Our findings can be summarized into three main points. First, the disparity of electron densities, partial electron density difference, and Hirshfeld partial charges analysis show that the SWCNT can hold 87% of the extra electron density of the hypothetical negative intermediate produced from the oxidation of AQH_2. Second, the chemical attachment of these two redox reagents to the SWCNT also causes new impurity states to appear within the band gap, thereby introducing a more metallic character to the system. Third, the electrons from the oxidized AQH_2 group can be transferred to the oxidizing 4AHA group at the other end of the nanotube by a hopping process through the mediating SWCNT. This mechanism is confirmed by the non-localized distribution of the hopping excited electrons. These findings provide a detailed understanding of the electron hopping process and agree well with previous experimental study. This work is not only complementing experimental study by giving an interpretation in terms of electronic wave functions, but also demonstrates a promising application of the CNT materials in the nanotechnology field.

Acknowledgements

This work was supported in part by Grants from the National Science and Technology Development Agency (2009 NSTDA Chair Professor funded by the Crown Property Bureau under the Management of the National Science and Technology Development Agency and NANOTEC Center of Excellence funded by the National Nanotechnology Center), Kasetsart University Research and Development Institute (KURDI), the Thailand Research Fund (TRF), and the Commission of Higher Education, Ministry of Education under Postgraduate Education and Research Programs in Petroleum and Petrochemicals and Advanced Materials and the Development and Promotion of Science and Technology Talents Project (DPST). The Kasetsart University Graduate School is also acknowledged. PAB particularly thanks the TRF and NSTDA Chair Professor for the generous support of his visits to Thailand and the Memorandum of Understanding between Kasetsart and Bordeaux 1 Universities. The computational calculations are supported by the Thai National Grid Center (TNGC) under the Software Industry Promotion Agency (SIPA).

Appendix A. Supplementary data

Supplementary data associated with this article can be found, in the online version, at doi:10.1016/j.carbon.2009.12.049.

REFERENCES

[1] Iijima S. Helical microtubules of graphitic carbon. Nature 1991;354(6348):56–8.
[2] Iijima S, Ichihashi T. Single-shell carbon nanotubes of 1-nm diameter. Nature 1993;363(6430):603–5.
[3] Bethune DS, Klang CH, de Vries MS, Gorman G, Savoy R, Vazquez J, et al. Cobalt-catalysed growth of carbon nanotubes with single-atomic-layer walls. Nature 1993;363(6430):605–7.
[4] Tans SJ, Verschueren ARM, Dekker C. Room-temperature transistor based on a single carbon nanotube. Nature 1998;393(6680):49–52.
[5] Kong J, Franklin NR, Zhou C, Chapline MG, Peng S, Cho K, et al. Nanotube molecular wires as chemical sensors. Science 2000;287(5453):622–5.

[6] de Heer WA, Châtelain A, Ugarte D. A carbon nanotube field-emission electron source. Science 1995;270(5239):1179–80.
[7] Baughman RH, Zakhidov AA, de Heer WA. Carbon nanotubes – the route toward applications. Science 2002;297(5582):787–92.
[8] Gooding JJ, Wibowo R, Liu JQ, Yang W, Losic D, Orbons S, et al. Protein electrochemistry using aligned carbon nanotube arrays. J Am Chem Soc 2003;125(30):9006–7.
[9] Patolsky F, Weizmann Y, Willner I. Long-range electrical contacting of redox enzymes by SWCNT connectors. Angew Chem Int Edit 2004;43(16):2113–7.
[10] Pandurangappa M, Lawrence NS, Compton RG. Homogeneous chemical derivatisation of carbon particles: a novel method for funtionalising carbon surfaces. Analyst 2002;127(12):1568–71.
[11] Wildgoose GG, Pandurangappa M, Lawrence NS, Jiang L, Jones TGJ, Compton RG. Anthraquinone-derivatised carbon powder: reagentless voltammetric pH electrodes. Talanta 2003;60(5):887–93.
[12] Leventis HC, Streeter I, Wildgoose GG, Lawrence NS, Jiang L, Jones TGJ, et al. Derivatised carbon powder electrodes: reagentless pH sensors. Talanta 2004;63(4):1039–51.
[13] Heald CGR, Wildgoose GG, Jiang L, Jones TGJ, Compton RG. Chemical derivatisation of multiwalled carbon nanotubes using diazonium salts. Chem Phys Chem 2004;5(11):1794–9.
[14] Wong ELS, Compton RG. Chemical reaction of reagents covalently confined to a nanotube surface: nanotube-mediated redox chemistry. J Phys Chem C 2008;112(22):8122–6.
[15] Delley B. An all-electron numerical method for solving the local density functional for polyatomic molecules. J Chem Phys 1990;92(1):508–17.
[16] Delley B. From molecules to solids with the DMol^3 approach. J Chem Phys 2000;113(18):7756–64.
[17] Monkhorst HJ, Pack JD. Special points for Brillouin-zone integrations. Phys Rev B 1976;13(12):5188.
[18] O'Connell MJ, Bachilo SM, Huffman CB, Moore VC, Strano MS, Haroz EH, et al. Band gap fluorescence from individual single-walled carbon nanotubes. Science 2002;297(5581):593–6.
[19] Perdew JP, Burke K, Ernzerhof M. Generalized gradient approximation made simple. Phys Rev Lett 1996;77(18):3865.
[20] Becke AD. Density-functional exchange-energy approximation with correct asymptotic behavior. Phys Rev A 1988;38(6):3098.
[21] Lee C, Yang W, Parr RG. Development of the Colle–Salvetti correlation-energy formula into a functional of the electron density. Phys Rev B 1988;37(2):785.
[22] Perdew JP, Wang Y. Accurate and simple analytic representation of the electron-gas correlation energy. Phys Rev B 1992;45(23):13244.
[23] Gülseren O, Yildirim T, Ciraci S. Systematic ab initio study of curvature effects in carbon nanotubes. Phys Rev B 2002;65(15):1534051–4.
[24] Ouyang M, Huang JL, Cheung CL, Lieber CM. Energy gaps in "metallic" single-walled carbon nanotubes. Science 2001;292(5517):702–5.
[25] Blase X, Benedict LX, Shirley EL, Louie SG. Hybridization effects and metallicity in small radius carbon nanotubes. Phys Rev Lett 1994;72(12):1878–81.
[26] Zólyomi V, Kürti J. First-principles calculations for the electronic band structures of small diameter single-wall carbon nanotubes. Phys Rev B 2004;70(8).
[27] Valavala PK, Banyai D, Seel M, Pati R. Self-consistent calculations of strain-induced band gap changes in semiconducting (n, 0) carbon nanotubes. Phys Rev B 2008;78(23).
[28] Pannopard P, Khongpracha P, Probst M, Limtrakul J. Gas sensing properties of platinum derivatives of single-walled carbon nanotubes: a DFT analysis. J Mol Graph Model 2009;28(1):62–9.
[29] Zhao JX, Ding YH. Chemical functionalization of single-walled carbon nanotubes (SWNTs) by aryl groups: a density functional theory study. J Phys Chem C 2008;112(34):13141–9.
[30] Wu X, Zeng XC. First-principles study of a carbon nanobud. ACS Nano 2008;2(7):1459–65.

J. of Supercritical Fluids 51 (2009) 230–237

Contents lists available at ScienceDirect

The Journal of Supercritical Fluids

journal homepage: www.elsevier.com/locate/supflu

Formation of retinyl palmitate-loaded poly(L-lactide) nanoparticles using rapid expansion of supercritical solutions into liquid solvents (RESOLV)

Amporn Sane[a,b,*], Jumras Limtrakul[a,c]

[a] NANOTEC Center of Excellence, National Nanotechnology Center, Kasetsart University and Center of Nanotechnology, Kasetsart University Research and Development Institute, Kasetsart University, Bangkok 10900, Thailand
[b] Department of Packaging and Materials Technology, Faculty of Agro-Industry, Kasetsart University, Bangkok 10900, Thailand
[c] Department of Chemistry, Faculty of Science, Kasetsart University, Bangkok 10900, Thailand

ARTICLE INFO

Article history:
Received 10 May 2009
Received in revised form 5 September 2009
Accepted 5 September 2009

Keywords:
Poly(L-lactide)
Retinyl palmitate
Nanoparticles
Encapsulation
RESOLV
Supercritical fluids

ABSTRACT

Poly(L-lactide) (PLLA) nanoparticles loaded with retinyl palmitate (RP) were successfully prepared by rapid expansion of a supercritical carbon dioxide (CO_2) solution into an aqueous receiving solution containing a stabilizing agent (RESOLV). Three stabilizing agents, Pluronic F127, Pluronic F68, and sodium dodecyl sulfate (SDS) have been employed and the Pluronic F127 was found to be more effective for stabilizing PLLA/RP nanoparticles than Pluronic F68 and SDS, as RESOLV into a 0.1 wt% Pluronic F127 solution produced a stable nanosuspension consisting mainly of well-dispersed, individual nanoparticles. The effect of rapid expansion processing conditions (i.e., degree of saturation (S), pre-expansion temperature (T_{pre}), and concentrations of PLLA and RP (C_{PLLA}, C_{RP})) on the particle size, form, and RP loading was systematically investigated. It was found that spherical PLLA/RP nanoparticles with an average size range of ~40–110 nm and RP loadings of 0.9–6.2 wt% were consistently produced by RESOLV. The size of PLLA/RP nanoparticles increased from ~30–80 to ~30–160 nm as the solution degree of saturation changed from $S < 1$ to $S > 1$, independent of T_{pre}, C_{PLLA}, and C_{RP}. The entrapment capacity of RP in PLLA nanoparticles was predominantly determined by T_{pre} and C_{RP}. Increasing the T_{pre} from 70 to 100 °C and the C_{RP} from 0.05 to 0.15 wt% increased the encapsulated RP content at least twofold. Our results show that the technique with benign supercritical CO_2 should be generally applicable to nanoparticle fabrications of other important active ingredients, especially in liquid form, in polymeric nanoparticles.

1. Introduction

Encapsulation of active compounds, including drugs, cosmetics, and nutraceuticals, in nanoparticles of biodegradable and biocompatible polymers (e.g., chitosan, poly(D,L-glycolide), poly(D,L-lactide-co-glycolide), and polylactic acid or polylactide) has greatly attracted attention in the pharmaceutical, cosmetic, and food industries for multipurpose delivery applications, especially, controlling release, targeting, and increasing stability of active components [1,2]. Incorporation of such active ingredients in the polymeric nanoparticles with a controllable and narrow size distribution increases therapeutic benefits, leading to the small dosages required and avoiding undesirable side effects. Conventional techniques for encapsulating active substances in polymeric nanoparticles based on nano-emulsion templates [3] still have several limitations, including using organic solvents that need to be removed from the final products, generating broad particle size distributions, and requiring large quantities of surfactants. Rapid expansion of supercritical solutions (RESS) technology is generally recognized as a well-established technique for producing nano to micron-sized particles from a single component, especially from organics and polymers [4–8]. When a supercritical solution containing a dissolved solute is rapidly (10^{-6} s) expanded across a micro-orifice, the solvent density dramatically decreases, leading to precipitation of the solute from the solvent (typically carbon dioxide) [9–11]. Due to very high supersaturation during the rapid expansion in the post-expansion environment, the process favors the formation of small particles with narrow size distributions. Besides single-compound particles, RESS has also been investigated for producing composite particles [12–24]. Tom et al. [12] reported the preparation of composite microparticles (10–100 μm) by co-precipitation of poly(D,L-lactic acid) and lovastatin. Microencapsulation of naproxen in poly(L-lactide) particles with a size range of 10–75 μm was published by Kim et al. [15] and Mishima et al. [16] described the encapsulation of lipase and lysozyme in polymer (e.g., poly(ethylene glycol), poly(methyl methacrylate),

* Corresponding author at: Department of Packaging and Materials Technology, Faculty of Agro-Industry, Kasetsart University, Bangkok 10900, Thailand.
Tel.: +66 2562 5099; fax: +66 2562 5092.
E-mail address: amporn.s@ku.ac.th (A. Sane).

0896-8446/$ – see front matter © 2009 Elsevier B.V. All rights reserved.
doi:10.1016/j.supflu.2009.09.003

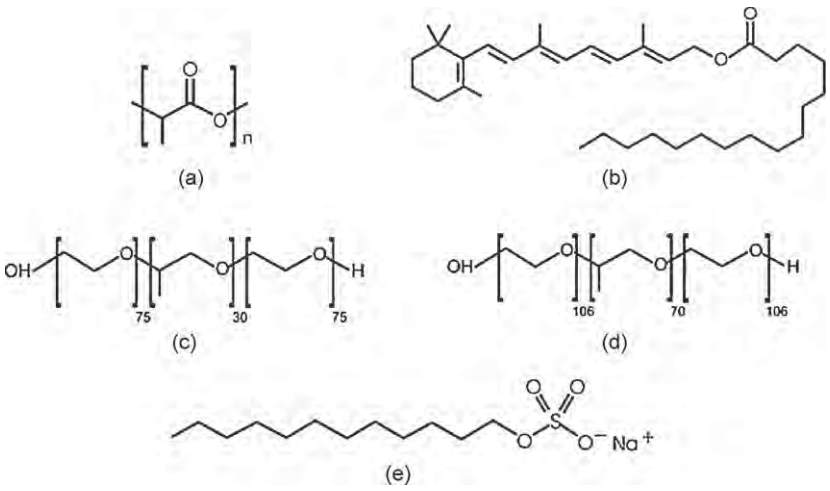

Fig. 1. Chemical structures of chemicals used in this study: (a) poly(L-lactide), (b) retinyl palmitate, (c) Pluronic F68, (d) Pluronic F127, and (e) sodium dodecyl sulfate.

and poly(L-lactic acid)) microparticles. Recently, Türk and Hils [20] were the first to report the feasibility of RESS for producing phytosterol-loaded poly(L-lactic acid) nanoparticles with the size of ~50 nm. This group found that the polymer content of the composite nanoparticles decreased with increasing pre-expansion temperature. Thus far, the RESS technique has been studied for encapsulating only crystalline solid, but not liquid, compounds in polymeric particles.

A modification of conventional RESS is the so-called RESOLV (rapid expansion of supercritical solutions into liquid solvents) process, in which the supercritical solution containing a solute is directly expanded into a liquid receiving solution (typically aqueous solution) that may or may not contain a stabilizing agent [6,25–28]. Organic particles produced using RESOLV were found to be smaller than those prepared by RESS due to expansion of the supercritical solution into a receiving liquid preventing the particles from collision and, hence, coalescence [5,6]. Particles with a bimodal size distribution (5–50 and 120–200 nm) were obtained from β-sitosterol [5], and phytosterol [29], and nanoparticles (~25–90 nm) were produced from ibuprofen, naproxen, fluorinated tetraphenylporphyrin, fluorinated acrylate polymer, poly(L-lactic acid), and poly(methyl methacrylate) [6,26–28]. Unlike RESS, RESOLV has not yet been investigated for encapsulating active components in polymeric nanoparticles. Thus, it remains a challenge to incorporate an active ingredient, especially in liquid form, in polymeric nanoparticles using the RESOLV process.

The aim of this work was to study the feasibility of RESOLV on encapsulation of a liquid active compound in biodegradable polymeric nanoparticles. In this study, retinyl (vitamin A) palmitate and poly(L-lactide) were chosen as a liquid active compound and a particle matrix, respectively. Retinyl palmitate, a vitamin A ester derivative in the retinoid group, is widely used in pharmaceutical and cosmetic applications. However, the therapeutic use of retinoids is still limited due to their light instability and adverse effects at high uptake [30]. Therefore, encapsulation is an alternative to protect retinyl palmitate from photo degradation induced by UVA and UVB radiation. Poly(L-lactide) has been widely used as a matrix material for drug delivery systems due to its biodegradability and biocompatibility [31–33]. In this work, we report on (i) the use of RESOLV to produce retinyl palmitate-loaded poly(L-lactide) nanoparticles and (ii) the effect of RESOLV processing conditions on size, morphology, and retinyl palmitate loading of the obtained particles.

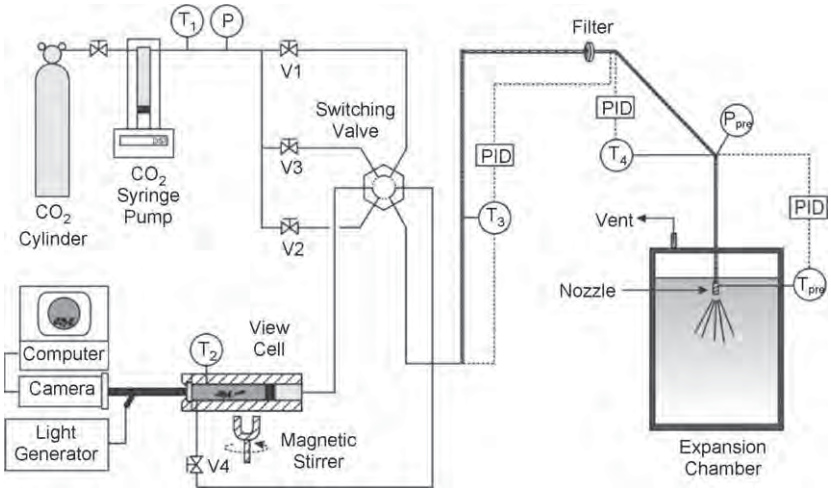

Fig. 2. Schematic of phase-behavior and RESOLV apparatus.

2. Experimental

2.1. Materials

Low-molecular-weight poly(L-lactide) (PLLA) with a number-average molecular weight of 1100 and a polydispersity index of 1.15 was supplied by Polymer Source. Retinyl palmitate (RP), sodium dodecyl sulfate (SDS), Pluronic F68 (F68) and Pluronic F127 (F127) were purchased from Sigma–Aldrich. The chemical structures of these compounds are shown in Fig. 1. Acetonitrile (HPLC grade) was obtained from Lab-Scan Analytical Sciences. Carbon dioxide (CO_2) with high purity grade (≥99.98%) was purchased from Chattakorn Lab Center (Thailand). Water was distilled before using it as a receiving solution.

2.2. Phase-behavior measurements

The phase-behavior measurements of PLLA and PLLA + RP in supercritical CO_2 were performed prior to RESOLV experiments because the phase state of a solute–solvent mixture has been found to be an important variable for RESS [4,7]. A schematic of the apparatus used in this work is shown in Fig. 2. Note that the same apparatus was used for both phase-behavior and RESOLV experiments. The central feature of the apparatus is a variable-volume view cell based on the design of McHugh and co-workers [34]. A syringe pump (Isco, Model 500HP) connected to one end of the view cell used CO_2 as the working fluid and pushed the piston to compress the PLLA or PLLA + RP solution on the other side of the piston. The solution mixture in the cell was observed through a view port with a rigid borescope (Gradient Lens, Model HBR-080-327-100) equipped with a light source (Gradient Lens, Model Luxxor 24), a digital CCD camera (Watec, Model WAT-202D), and a computer (Fig. 2). For a typical cloud-point (i.e., liquid–liquid transition) experiment, the view cell was charged with 0.008–0.023 g of RP and/or 0.015–0.046 g of PLLA, as well as ~15.2 g of CO_2. The cell was pressurized to 340 bar and heated to ~50 °C under continuous mixing using a magnetic stirrer until a homogeneous, clear solution was obtained. To determine the cloud point, the pressure of the solution was slowly decreased during continuous mixing until the transparent solution became cloudy. In this work, the cloud point was defined as the point at which the solution just became hazy. Upon reaching the temperature of ~100 °C, the heating was stopped and the cloud points were remeasured as the solution was slowly cooled down.

2.3. RESOLV experiments

Rapid expansion experiments were carried out by expanding a supercritical solution of PLLA + RP in supercritical CO_2 across a nozzle (50 μm dia., L/D = 4) into an aqueous solution containing a stabilizing agent (Fig. 2). To do an experiment, the variable-volume view cell was loaded with 0.030–0.091 g of PLLA and 0.015–0.046 g of RP. The cell was then sealed and charged with ~30.4 g of CO_2 using the syringe pump. After the mixture was pressurized to the desired pre-expansion pressure (P_{pre}), the cell was heated to 50–60 °C. Next, the mixture was stirred until a homogeneous solution was obtained. CO_2 was then allowed to flow from the syringe pump, bypassing the view cell, and finally expand across the nozzle into air. The fluid in the tubing leading to the nozzle and nozzle assembly was heated to the desired pre-expansion temperature (T_{pre}) using cable heaters. During this step, the pre-expansion temperature and pressure were measured upstream of the nozzle (Fig. 2). After steady-state conditions (as indicated by constant T_{pre} and P_{pre}) were established, the flow of pure CO_2 was diverted via the 6-port switching valve (Valco Instruments, Model 6C6UWEY) to the high pressure cell, indirectly pushing the PLLA + RP solution in supercritical CO_2 out of the cell by means of the movable piston in the cell. The solution was subsequently expanded through the nozzle into 50 mL of aqueous solution containing 0.1 wt% stabilizer (F68, F127, and SDS) by submerging the nozzle ~2 cm below the liquid surface.

2.4. Particle size and morphological characterization

Suspension samples from RESOLV experiments were characterized by the dynamic light scattering (DLS) method using a Zetasizer (Malvern Instruments, Model Nano ZS90) for measuring the hydrodynamic diameter (d_h) of PLLA/RP particles [35,36]. The d_h was computed from the translational diffusion coefficient (D) using the Malvern software package based on the theory of Brownian motion and the Stokes–Einstein equation:

$$d_h = \frac{kT}{3\pi\eta D} \quad (1)$$

where k is the Boltzmann's constant, T the absolute temperature, and η is the suspending medium viscosity. The particle size and morphology were also determined using field emission scanning electron microscopy (FESEM, Hitachi, Model S4700). The FESEM sample was prepared by depositing ~100 μL of the RESOLV suspension onto a conductive carbon tape attached to an aluminum stub and then dried under vacuum (1 bar) at ambient temperature overnight.

2.5. Determination of RP loading

The quantities of RP and PLLA in composite particles obtained by RESOLV were determined via UV/vis spectrophotometry as follows. The suspension was centrifuged (10,000 rpm, 10 °C) in order to separate the particles and dried under vacuum (1 bar) at room temperature for at least 2 days. The dried powder sample was then dissolved in acetonitrile and analyzed by a UV/vis spectrophotometer (Thermo Fisher Scientific, Model HeλIOS Gamma Series). PLLA and RP have well-characterized absorption bands with λ_{max} values of 211 ± 0.5 and 325 ± 0.5 nm, respectively, allowing for the accurate determination of PLLA and RP concentrations. The amounts of individual components in the particles were determined from the corresponding absorbance standard curves generated by known concentrations of PLLA and RP. The percentage of RP encapsulated (RP loading) in the particles was calculated by means of the following equation:

$$\text{RP loading (wt\%)} = \frac{\text{encapsulated RP (g)}}{\text{PLLA (g)} + \text{encapsulated RP (g)}} \times 100 \quad (2)$$

3. Results and discussion

3.1. Phase-behavior experiments of PLLA + RP in CO_2

Cloud-point pressures of PLLA and PLLA + RP in supercritical CO_2 were measured over a temperature range of ~50–100 °C as a function of PLLA and RP concentrations. Results are shown as a pressure–temperature diagram in Fig. 3. Initially, the pressure was taken to 340 bar at ambient temperature, and then the cell was heated at constant pressure until the polymer melted and completely dissolved (at a temperature range of ~50 – 60 °C). The concentrations of PLLA used in this study were 0.1 and 0.3 wt% because it was found that its solubility in supercritical CO_2 was ~0.4 wt% at pressure and temperature up to 340 bar and 100 °C, respectively. Consequently, the RP concentrations of 0.05 and 0.15 wt% were chosen such that the ratios of RP and PLLA ranged between 1:6 and 1:2. It is important to note that PLLA is significantly less soluble in supercritical CO_2 than RP and, therefore, the poly-

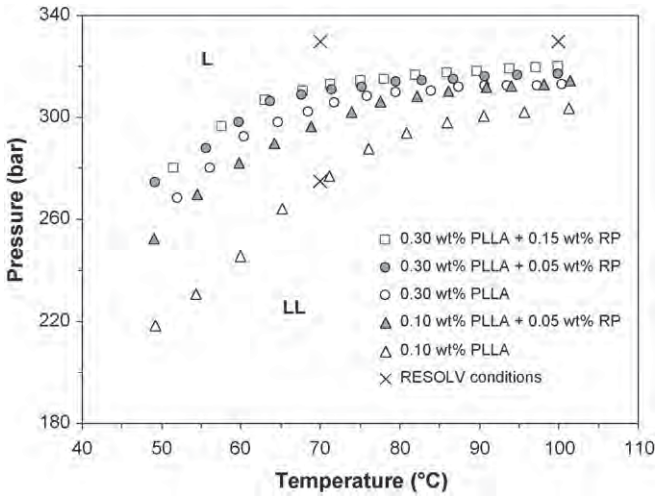

Fig. 3. Cloud-point curves for PLLA and PLLA + RP solutions in supercritical CO_2 and RESOLV experiments for PLLA + RP supercritical solutions in relation to their relevant cloud-point curves.

mer is the major component precipitated during decreasing the system pressures just below the cloud-point curve, whereas the RP remains dissolved within the solvent. As seen in Fig. 3, the measured cloud-point curves show a typical lower critical solution temperature (LCST) behavior, with the cloud-point slopes, $(\delta P/\delta T)_x$, up to 2.8 bar/°C. The LCST curve is interrupted at lower temperatures due to the solidification of PLLA and shifted toward higher pressures when increasing the concentrations of PLLA and RP. It is possible that the phase-behavior of this ternary PLLA + RP + CO_2 system exhibits multi-phase equilibria such as (i) LLV behavior especially in the vicinity of critical point of CO_2 due to the liquid–liquid immiscibility of PLLA-rich and RP-rich phases and (ii) SLLV behavior at low pressures due to the crystallization of PLLA. Therefore, the phase-behavior of this ternary system could be very complicated. Unfortunately, complete phase-behavior measurements of ternary mixtures are rather scarce, and most studies have focused only on portions of the liquid–liquid region. The cloud-point pressures of a 0.1 wt% PLLA solution in supercritical CO_2 increased from 219 to 303 bar as the temperature increased from 49.2 to 101.2 °C. The pressures increased by ~40 bar when increasing the concentration of PLLA to 0.3 wt%. The addition of RP at 0.05 wt% increased the cloud-point pressures of a 0.1 wt% PLLA solution by ~30 bar due to the presence of ternary solubility diminution of PLLA. This depressed solubility could be attributed to (i) the decrease in vapor pressure of low-molecular-weight PLLA due to the presence of liquid RP in CO_2 [37] and (ii) the occurrence of LV phase equilibrium for both PLLA + CO_2 and RP + CO_2 binary systems [38]. However, for 0.3 wt% PLLA, the cloud-point pressures were only slightly affected by the increase in the RP concentration from 0.5 to 0.15 wt%. The cloud-point pressures of a 0.1 wt% PLLA solution in CO_2 obtained in this work are approximately 120 bar higher than those in a mixture of tetrahydrofuran (THF) and CO_2 (20:80, w/w) reported by Sane and Thies [7] due to the cosolvent effect of THF. Significant increases in cloud-point pressures of PLLA in CO_2 solutions containing ~20 wt% of a cosolvent (either chlorodifluoromethane or dichloromethane) up to ~600–700 bar were reported when the polymer molecular weights increased to 2000, 50,000, and 100,000 [39,40]. Additionally, the solubility of low-molecular-weight PLLA in CO_2 is lower than that of higher-molecular-weight fluoropolymer poly(heptadecafluorodecyl acrylate) [4], but still relatively higher when compared to that of other higher-molecular-weight polymers such as poly(D,L-lactide-co-glycolide) [41], poly(methyl acrylate), and poly(vinyl acetate) [42].

3.2. Formation of PLLA/RP nanoparticles using RESOLV

RESOLV experiments were carried out by directly expanding PLLA + RP solutions in supercritical CO_2 at different experimental conditions (see Fig. 3) into liquid receiving solutions containing 0.1 wt% stabilizing agent (F68, F127, SDS). The RESOLV processing conditions included the degree of saturation (S) (varied by adjusting P_{pre}), pre-expansion temperature (T_{pre}), and PLLA and RP concen-

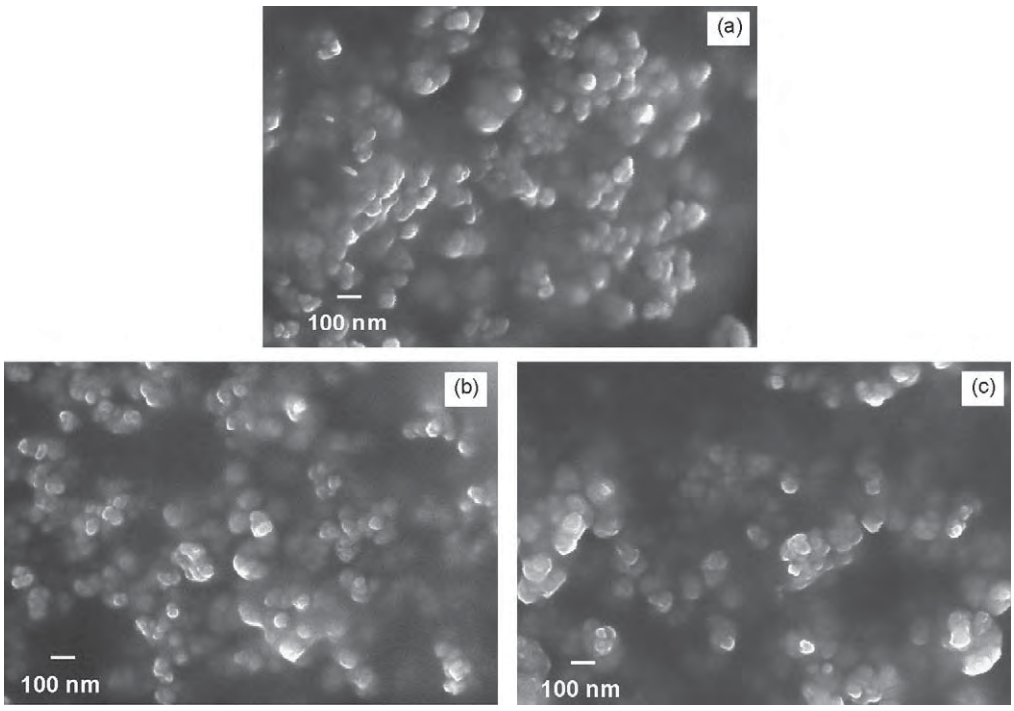

Fig. 4. FESEM micrographs of nanoparticles obtained from RESOLV of a 0.3 wt% PLLA + 0.05 wt% RP solution in CO_2 with T_{pre} = 70 °C, P_{pre} = 330 bar (S < 1) into aqueous receiving solutions containing 0.1 wt% stabilizing agent: (a) F68, (b) F127, and (c) SDS.

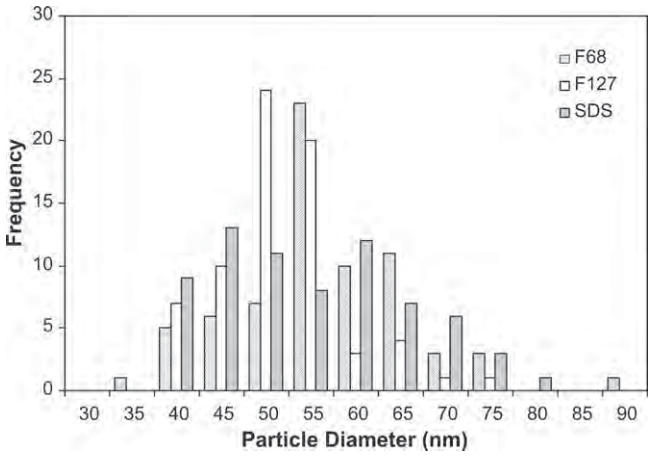

Fig. 5. PSDs measured from FESEM micrographs of nanoparticles obtained by RESOLV of a 0.3 wt% PLLA + 0.05 wt% RP solution in CO_2 with T_{pre} = 70 °C, P_{pre} = 330 bar (S < 1) into aqueous receiving solutions containing 0.1 wt% stabilizing agent (F68, F127, and SDS).

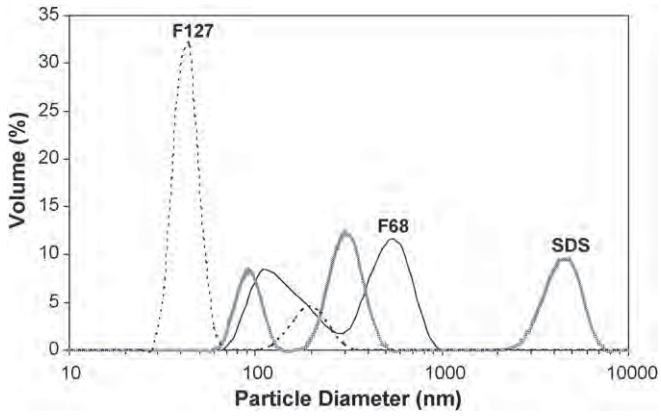

Fig. 6. PSDs from DLS analysis of stabilized nanoparticles prepared by RESOLV of a 0.3 wt% PLLA + 0.05 wt% RP solution in CO_2 with T_{pre} = 70 °C, P_{pre} = 330 bar (S < 1) into aqueous receiving solutions containing 0.1 wt% stabilizing agent (F68, F127, and SDS).

trations (C_{PLLA}, C_{RP}). The S is defined as the ratio of the actual solute concentration to the equilibrium concentration at pre-expansion conditions (T_{pre}, P_{pre}).

3.2.1. Effect of stabilizers on dispersibility of PLLA/RP nanoparticles

Because PLLA and RP are insoluble in water, aqueous solutions were used as the receiving solutions. However, there was a severe agglomeration of PLLA/RP particles in pure water owing to their hydrophobic nature (see Fig. 1a and b). From our previous work, the dispersibility of nanoparticles in a given receiving solution depends on the wettability of the surface of nanoparticles to the receiving solution [6]. The wettability of solid particles is affected by the type of surfactants and surface tension of the aqueous surfactant solutions [43,44]. In addition, decreasing surface tension of aqueous surfactant solutions usually provides improved wetting properties. Therefore, appropriate stabilizing agents for the PLLA/RP particle dispersion in this work had to be identified. F68, F127, and SDS were chosen as stabilizers for RP-encapsulated PLLA particles because F68 and F127 are nonionic, polymeric surfactants, while SDS is a conventional anionic surfactant (Fig. 1c–e). The stabilizer concentration of 0.1 wt% used in RESOLV was chosen based on the typical concentrations used in aqueous dispersions of nanoparticles and submicron-sized particles [25,45–47]. From FESEM characterization, spherical nanoparticles with a diameter (d_p) range of ~35–90 nm and an average size ($\bar{d}_p$) of ~50 ± 10 nm, independent of stabilizer type (Figs. 4 and 5 and Table 1), were reproducibly obtained by RESOLV of a 0.3 wt% PLLA + 0.05 wt% RP solution at T_{pre} = 70 °C, P_{pre} = 330 bar, and S < 1 (i.e., above the cloud-point curve). The obtained nanoparticles were in the forms of individual particles and agglomerates (Fig. 4). Note that all the particle sizes were statistically determined from multiple FESEM images with the same magnification (60,000×) and the sharpness (contrast and focus) of the images were adjusted to enhance the particle–background and particle–particle boundaries before the size measurements. For the sizes of primary particles within the agglomerates, only partially overlapping particles were considered, while those with fully overlapping boundaries or uneven brightness/contrast were manually excluded. When measuring the hydrodynamic diameter (d_h) range and the mean hydrodynamic size ($\bar{d}_h$) using the DLS technique, however, broader particle size distributions (PSDs) were obtained and the size became dependent on the stabilizer type, as shown in Fig. 6 and Table 1. The measured hydrodynamic sizes ranged from 30 nm to 7.5 μm with bimodal and trimodal distributions. The particles stabilized in a 0.1 wt% F127 solution were substantially smaller (30–68 and 106–342 nm) than those suspended in 0.1 wt% F68 (59–300 and 342–800 nm) and 0.1 wt% SDS (59–142, 164–531, and 2000–7460 nm) solutions, indicating that the F127 is more effective for dispersing the PLLA/RP nanoparticles in the aqueous solution. Because DLS cannot be used to distinguish between individual particles and agglomerates, unlike FESEM, the larger measured sizes obtained from DLS were primarily due to the agglomeration of the PLLA/RP nanoparticles. F68 was a less effective stabilizer than F127 because slightly larger submicron-sized agglomerates were still present in the suspensions. This could be explained by the surface tension of receiving solutions, as the surface tension of a 0.1 wt% F68 solution (50 mN/m, 25 °C) is slightly higher than that of a 0.1 wt% F127 solution (41 mN/m, 25 °C) [48], thus providing less wettability and dispersibility to the PLLA/RP nanoparticles. However, this trend was not observed when using SDS as the particle stabilizer even though a 0.1 wt% SDS solution possesses the lowest surface tension of 33 mN/m (25 °C) [49], indicating that steric stabilization provided by nonionic polymeric surfactants is more efficient for stabilizing the PLLA/RP nanoparticles than ionic stabilization by SDS. Accordingly, F127 was chosen and used as the stabilizer for investigating the processing conditions on PLLA/RP particle size, morphology, and RP loading.

Table 1
Particle sizes obtained from DLS and FESEM measurements of nanoparticles prepared by RESOLV of a 0.3 wt% PLLA + 0.05 wt% RP solution in CO_2 with T_{pre} = 70 °C, P_{pre} = 330 bar (S < 1) into aqueous receiving solutions containing 0.1 wt% stabilizing agent.

Receiving solution	DLS		FESEM	
	d_h range (nm)	$\bar{d}_h$ (nm)	d_p range (nm)	$\bar{d}_p$ ± S.D. (nm)
0.1 wt% F68	59–300	148	35–87	54 ± 9
	342–800	531		
0.1 wt% F127	30–68	43	37–72	49 ± 7
	106–342	198		
0.1 wt% SDS	59–142	923	39–77	53 ± 10
	164–531	310		
	2000–7460	4460		

3.2.2. Effect of rapid expansion conditions on PLLA/RP nanoparticles

To determine the effect of RESOLV processing conditions (i.e., S, T_{pre}, C_{RP}, and C_{PLLA}) on size, morphology, and RP loading of PLLA/RP particles, experiments were carried out by expanding PLLA + RP solutions in supercritical CO_2 into 0.1 wt% F127 solu-

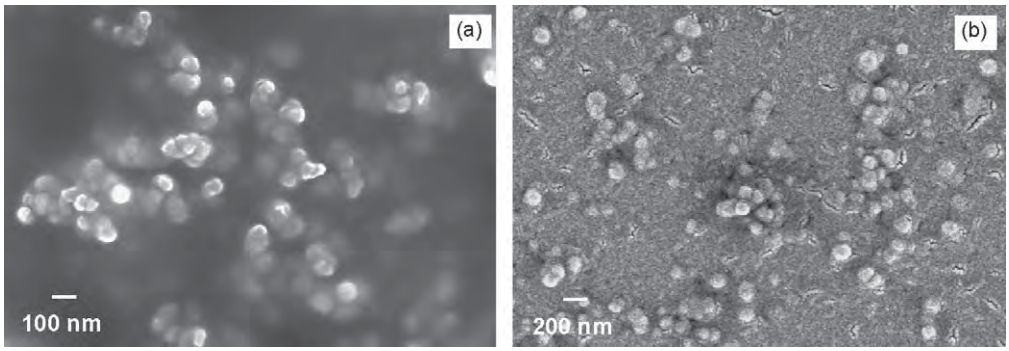

Fig. 7. FESEM micrographs of PLLA/RP nanoparticles prepared by RESOLV of a 0.3 wt% PLLA + 0.05 wt% RP solution in CO_2 with T_{pre} = 70 °C, P_{pre} = 275 bar (S > 1) into a 0.1 wt% F127 solution.

tions at different processing conditions (see Fig. 3). FESEM was used to characterize the size and form of particles while UV/vis spectrophotometry was used to determine the RP loading of the particles. As shown in Table 2, PLLA/RP nanoparticles with the average size ranging from ~40 to ~110 nm were produced. The effect of S was investigated by rapidly expanding PLLA + RP solutions at T_{pre} = 70 °C and two different pressures (275 and 330 bar) such that one solution was initially supersaturated (S > 1) and the other was subsaturated (S < 1), respectively. The nanoparticles with an average size of 49 ± 7 nm (Fig. 4b and Table 2) were obtained when expansion of a 0.3 wt% PLLA + 0.05 wt% RP solution occurred from the unsaturated solution, while the particles with a bimodal size distribution and two average sizes of 45 ± 7 and 106 ± 19 nm (Fig. 7) were obtained when expansion occurred from the supersaturated solution. The significant increase in the particle size with S can be seen in Fig. 8. A similar trend was also obtained in the cases of RESOLV of 0.1 wt% PLLA + 0.05 wt% RP and 0.3 wt% PLLA + 0.15 wt% RP solutions, as shown in Table 2. The obtained results are consistent with both (i) the phase separation kinetics and (2) the classical nucleation theory and growth mechanism [4,50] as follows. Larger nanoparticles (~110 nm) are formed when RESOLV is carried out such that the supercritical solution is supersaturated at pre-expansion conditions because the solution has already phase separated into polymer-rich and solvent-rich phases upstream of the nozzle, leading to (i) the formation of liquid-like droplets and even coalescence of the droplets and (ii) the nucleation of the liquid-like droplets followed by growth process via droplet diffusion and coagulation [9,50] until the solvent diffuses out of the polymer-rich droplets to the continuous phase and the formed structures solidify at sufficient pressure and temperature quenches. Furthermore, the smaller nanoparticles (~40–60 nm) are also present possibly due to the subsequent nucleation from the solvent-rich phase when a sufficient pressure drop has occurred upon expansion. On the other hand, only smaller nanoparticles (~50–60 nm) are formed when the expansion was initiated from unsaturated conditions, suggesting that the nucleation does not occur until a significant pressure drop has reached inside the nozzle or possibly not even until downstream of the nozzle. Our trend is consistent with RESS works reported by Blasig et al. [4] and Sane and Thies [7]. However, the PLLA/RP particles obtained from RESOLV are considerably smaller than those fluoropolymer and PLLA particles prepared by RESS, indicating that expansion into a receiving solution effectively hinders the particle growth in the free jet.

RESOLV of unsaturated solutions of 0.1 wt% PLLA + 0.05 wt% RP at T_{pre} of 70 and 100 °C produced nanoparticles with average sizes of 48 ± 7 and 51 ± 9 nm, respectively (Fig. 9 and Table 2). However, changing the T_{pre} from 70 to 100 °C slightly increased the average sizes of the nanoparticles from 49 ± 7 to 63 ± 10 nm and 56 ± 10 to 62 ± 15 nm when expanding the unsaturated solutions of 0.3 wt% PLLA + 0.05 wt% RP and 0.3 wt% PLLA + 0.15 wt% RP, respectively (Table 2). In addition, increasing C_{PLLA} from 0.1 to 0.3 wt% and C_{RP} from 0.05 to 0.15 wt% also yielded minor increases of particle sizes from 51 ± 9 to 63 ± 10 nm (T_{pre} = 100 °C, P_{pre} = 330 bar) and from 49 ± 7 to 56 ± 10 nm (T_{pre} = 70 °C, P_{pre} = 330 bar), respectively, as shown in Table 2. Both T_{pre} and C_{RP} influenced the extent of nanoparticle agglomeration, as the agglomeration was found to increase with T_{pre} and C_{RP}. Therefore, our results indicate that T_{pre}, C_{PLLA}, and C_{RP} do not play a significant role in the determination of the size of PLLA/RP nanoparticles, consistent with our previous work on RESOLV of fluorinated tetraphenylporphyrin (TBTPP) [6]. However, the average size of those TBTPP nanoparticles (28 ± 9 nm) is considerably smaller than that of PLLA/RP nanoparticles. This could be explained by the collision-coalescence theory

Table 2
Experimental conditions and sizes of PLLA/RP nanoparticles produced by RESOLV of a PLLA + RP solution in supercritical CO_2 into a 0.1 wt% F127 receiving solution.

C_{PLLA} (wt%)	C_{RP} (wt%)	T_{pre} (°C)	P_{pre} (bar)	S	$\bar{d}_p$ ± S.D. (nm)
0.1	0.05	70	330	<1	48 ± 7
		70	275	>1	43 ± 7, 95 ± 17
		100	330	<1	51 ± 9
0.3	0.05	70	330	<1	49 ± 7
		70	275	>1	45 ± 7, 106 ± 19
		100	330	<1	63 ± 10
	0.15	70	330	<1	56 ± 10
		70	275	>1	48 ± 9, 110 ± 20
		100	330	<1	62 ± 15

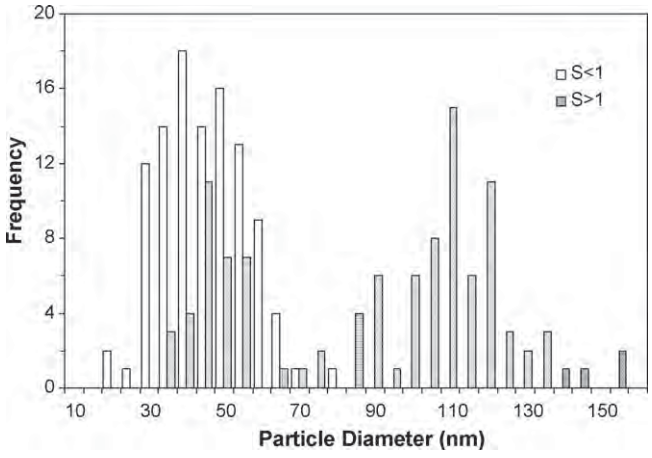

Fig. 8. PSDs of PLLA/RP nanoparticles prepared by RESOLV into a 0.1 wt% F127 solution of a 0.3 wt% PLLA + 0.05 wt% RP solution in CO_2 with T_{pre} = 70 °C: P_{pre} = 275 bar (S > 1) and P_{pre} = 330 bar (S < 1).

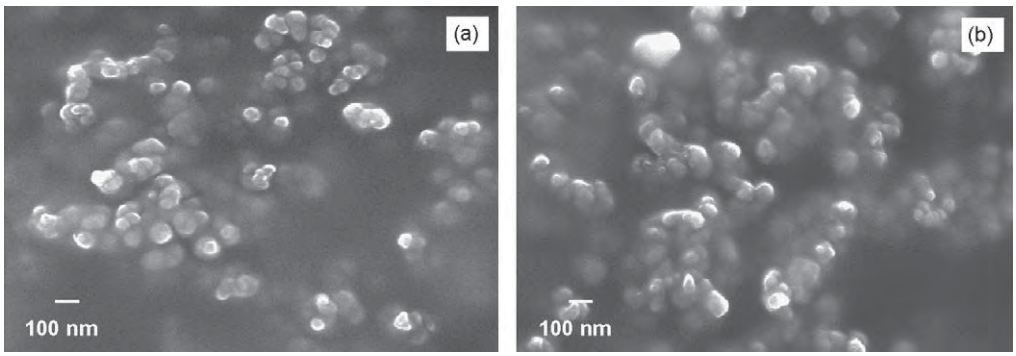

Fig. 9. FESEM micrographs of PLLA/RP nanoparticles produced by RESOLV into a 0.1 wt% F127 solution of a 0.1 wt% PLLA + 0.05 wt% RP solution in CO_2 with P_{pre} = 330 bar (S < 1): (a) T_{pre} = 70 °C and (b) T_{pre} = 100 °C.

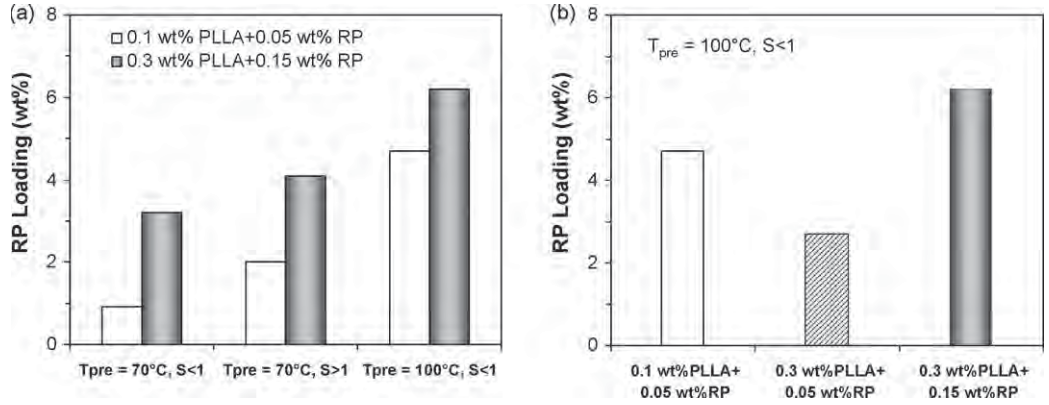

Fig. 10. Influence of RESOLV processing conditions: (a) T_{pre} and S and (b) C_{PLLA} and C_{RP} on RP loading levels of PLLA/RP nanoparticles.

developed by Friedlander and co-workers [51–53] in which the coalescence rate and the size of inorganic nanoparticles strongly increase with the solid-state diffusion coefficient (D_s), as recently applied to describe the growth of TBTPP and PLLA particles during rapid expansion across the nozzle and traveling in the free jet by Sane and Thies [6,7]. Since $D_s \propto \exp(-T_m/T)$ [54], decreasing absolute melting temperature (T_m) at a constant absolute temperature of particles (T) yields a rapid increase of the diffusion coefficient, leading to higher particle coalescence rate and larger particles. Consequently, the particles obtained from lower melting PLLA (120 °C, and lower in the presence of liquid RP) are larger than those of higher melting TBTPP (348 °C) because of the higher coalescence rate of PLLA particles during rapid expansion across the nozzle and traveling in the free jet before submerging under the receiving solution.

The extent of RP encapsulated in PLLA nanoparticles produced by RESOLV ranged from 0.9 to 6.2 wt%, depending on T_{pre}, S, C_{PLLA}, and C_{RP} (Fig. 10). An increase of T_{pre} from 70 to 100 °C during expanding a 0.1 wt% PLLA + 0.05 wt% RP solution at P_{pre} = 330 bar (S < 1) resulted in increasing the RP loading from 0.9 to 4.7 wt% (Fig. 10a). Similar to the case of RESOLV of a 0.3 wt% PLLA + 0.15 wt% RP solution at the same P_{pre}, the RP loading level increased from 3.2 to 6.2 wt% when increasing the T_{pre} from 70 to 100 °C. This indicates that the entrapment of RP in the PLLA nanoparticles is favored when rapid expansion occurs at a higher T_{pre}. The increment of RP loading could be attributed to the decreases in RP and PLLA solubility leading to the solute precipitation initiated at higher pressures during expansion, the enhanced mass transfer between RP and PLLA components, and the small increase in particle size and agglomeration at the higher T_{pre}. The trend of increasing RP loading with increasing T_{pre} agrees with results from RESS of PLLA + phytosterol reported by Türk and Hils [20]. In addition, the RP loading of nanoparticles obtained from RESOLV of a 0.1 wt% PLLA + 0.05 wt% RP solution with T_{pre} = 70 °C slightly increased from 0.9 to 2.0 wt% when increasing the degree of saturation from S < 1 to S > 1 (Fig. 10a). Similar to the case of RESOLV of a 0.3 wt% PLLA + 0.15 wt% RP solution, increasing the S resulted in the slight increase of the RP content from 3.2 to 4.1 wt%. Therefore, the S had less impact on the RP loading than the T_{pre}. The smaller increase in the RP loading with the S probably resulted from the supersaturated solution phase separated (L-LL) before entering the nozzle [4], and PLLA-rich droplets already formed, and even coalesced, within the CO_2-rich phase prior to expansion across the nozzle. As expected, the amount of RP trapped in the PLLA nanoparticles reduced with increasing C_{PLLA} while increased with increasing C_{RP} due to the availability of individual components during the rapid expansion. As shown in Fig. 10b, RESOLV at T_{pre} of 100 °C and P_{pre} of 330 bar (S < 1) with C_{RP} of 0.05 wt%, decreasing C_{PLLA} from 0.3 to 0.1 wt% resulted in increased RP loading from 2.7 to 4.7 wt%. In addition, the encapsulated RP increased from 2.7 to 6.2 wt% when increasing C_{RP} from 0.05 to 0.15 wt%.

4. Conclusions

In this work, PLLA nanoparticles containing RP were successfully produced in a single step using the RESOLV technique. F127 was a more effective stabilizer for dispersing the PLLA/RP nanoparticles than F68 and SDS. RESOLV into 0.1 wt% F127 solutions produced stable nanosuspensions containing mainly well-dispersed, spherical, individual nanoparticles with an average size range of ~40–110 nm and RP loadings of 0.9–6.2 wt%. The size of the PLLA/RP nanoparticles increased with S, relatively independent of T_{pre}, C_{PLLA}, and C_{RP}. The extent of RP encapsulated in the nanoparticles increased with increasing T_{pre}, S, and C_{RP} while decreased with increasing

C_{PLLA}. Theoretical studies based on these results are necessary to better understand the relation between the processing conditions and the RP loaded PLLA nanoparticles. Finally, RESOLV is considered as a promising technique for producing stable suspensions of well-dispersed and uniform polymeric nanoparticles loaded with a liquid compound, with the process being amenable to commercial scale-up.

Acknowledgements

This work was sponsored by the Thailand Research Fund (TRF). The authors would like to acknowledge the National Science and Technology Development Agency (NSTDA Chair Professor and NANOTEC Center of Excellence), Ministry of Science and Technology of Thailand as well as the Kasetsart University Research and Development Institute (KURDI) for financial support. We also acknowledge Dr. Markus Weber (now of Stettemerstrasse, Schaffhausen, Switzerland) and Prof. Mark C. Thies (Clemson University) for designing and supporting, respectively, the rapid expansion nozzles.

References

[1] A.S. Agnihotri, N.N. Mallikarjuna, T.J. Aminabhavi, Recent advances on chitosan-based micro- and nanoparticles in drug delivery, J. Control. Release. 100 (2004) 5–28.
[2] V.J. Mohoraj, Y. Chen, Nanoparticles—a review, Trop. J. Pharm. Res. 5 (2006) 561–573.
[3] N. Anton, J.-P. Benoit, P. Saulnier, Design and production of nanoparticles formulated from nano-emulsion templates—a review, J. Control. Release. 128 (2008) 185–199.
[4] A. Blasig, C. Shi, R.M. Enick, M.C. Thies, Effect of concentration and degree of saturation on RESS of a CO_2-soluble fluoropolymer, Ind. Eng. Chem. Res. 41 (2002) 4976–4983.
[5] M. Türk, P. Hils, B. Helfgen, K. Schaber, H.-J. Martin, M.A. Wahl, Micronization of pharmaceutical substances by the rapid expansion of supercritical solutions (RESS): a promising method to improve bioavailability of poorly soluble pharmaceutical agents, J. Supercrit. Fluids 22 (2002) 75–84.
[6] A. Sane, M.C. Thies, The formation of fluorinated tetraphenylporphyrin nanoparticles via rapid expansion processes: RESS vs. RESOLV, J. Phys. Chem. B 109 (2005) 19688–19695.
[7] A. Sane, M.C. Thies, Effect of material properties and processing conditions on RESS of poly(L-lactide), J. Supercrit. Fluids 40 (2007) 253–263.
[8] M. Türk, Manufacture of submicron drug particles with enhanced dissolution behavior by rapid expansion processes, J. Supercrit. Fluids 47 (2009) 537–545.
[9] M. Weber, M.C. Thies, Understanding the RESS process, in: Y.-P. Sun (Ed.), Supercritical Fluid Technology in Materials Science and Engineering: Syntheses, Properties, and Applications, Marcel Dekker, New York, 2002, pp. 387–437.
[10] B. Helfgen, M. Türk, K. Schaber, Hydrodynamic and aerosol modelling of the rapid expansion of supercritical solutions (RESS-process), J. Supercrit. Fluids 26 (2003) 225–242.
[11] M. Weber, M.C. Thies, A simplified and generalized model for the rapid expansion of supercritical solutions, J. Supercrit. Fluids 40 (2007) 402–419.
[12] J.W. Tom, G.-B. Lim, P.G. Debenedetti, R.K. Prud'homme, Applications of supercritical fluids in the controlled release of drugs, ACS Symp. Ser. 514 (1993) 238–257.
[13] J.W. Tom, P.G. Debenedetti, R. Jerome, Precipitation of poly(L-lactic acid) and composite poly(L-lactic acid)-pyrene particles by rapid expansion of supercritical solutions, J. Supercrit. Fluids 7 (1994) 9–29.
[14] H. Ksibi, P. Subra, Powder coprecipitation by the RESS process, Adv. Powder Technol. 7 (1996) 21–28.
[15] J.-H. Kim, T.E. Paxton, D.L. Tomasko, Microencapsulation of naproxen using rapid expansion of supercritical solutions, Biotechnol. Prog. 12 (1996) 650–661.
[16] K. Mishima, K. Matsuyama, D. Tanabe, S. Yamauchi, T.J. Young, K.P. Johnston, Microencapsulation of proteins by rapid expansion of supercritical solution with a nonsolvent, AIChE J. 46 (2000) 857–865.
[17] J. Jung, M. Perrut, Particle design using supercritical fluids: literature and patent survey, J. Supercrit. Fluids 20 (2001) 179–219.
[18] M. Türk, P. Hils, R. Lizow, K. Schaber, Stabilization of pharmaceutical substances by rapid expansion of supercritical solutions (RESS), in: Proceedings of the Sixth International Symposium on Supercritical Fluids, vol. 3, Versailles, France, April 28–30, 2003, pp. 1911–1922.
[19] S.-D. Yeo, E. Kiran, Formation of polymer particles with supercritical fluids: a review, J. Supercrit. Fluids 34 (2005) 287–308.
[20] M. Türk, P. Hils, Formation of composite drug–polymer particles by co-precipitation during the rapid expansion of supercritical fluids, J. Supercrit. Fluids 39 (2006) 253–263.
[21] M. Bahrami, S. Ranjbarian, Production of micro- and nano-composite particles by supercritical carbon dioxide, J. Supercrit. Fluids 40 (2007) 263–283.
[22] K. Mishima, Biodegradable particle formation for drug and gene delivery using supercritical fluid and dense gas, Adv. Drug Deliv. Rev. 60 (2008) 411–432.
[23] C. Vemavarapu, M.J. Mollan, T.E. Needham, Coprecipitation of pharmaceutical actives and their structurally related additives by the RESS process, Powder Technol. 189 (2009) 444–453.
[24] M.J. Cocero, A. Martín, F. Mattea, S. Varona, Encapsulation and co-precipitation processes with supercritical fluids: fundamentals and applications, J. Supercrit. Fluids 47 (2009) 546–555.
[25] M.J. Meziani, H.W. Rollins, L.F. Allard, Y.-P. Sun, Protein-protected nanoparticles from rapid expansion of supercritical solution into aqueous solution, J. Phys. Chem. B 106 (2002) 11178–11182.
[26] M.J. Meziani, P. Pathak, R. Hurezeaun, M.C. Thies, R.M. Enick, Y.-P. Sun, Supercritical-fluid processing technique for nanoscale polymer particles, Angew. Chem. Int. Ed. 43 (2004) 704–707.
[27] P. Pathak, M.J. Meziani, T. Desai, Y.-P. Sun, Nanosizing drug particles in supercritical fluid processing, J. Am. Chem. Soc. 126 (2004) 10842–10843.
[28] M.J. Meziani, P. Pathak, T. Desai, Y.-P. Sun, Supercritical fluid processing of nanoscale particles from biodegradable and biocompatible polymers, Ind. Eng. Chem. Res. 45 (2006) 3420–3424.
[29] M. Türk, R. Lietzow, Stabilized nanoparticles of phytosterol by rapid expansion from supercritical solution into aqueous solution, AAPS Pharm. Sci. Technol. 5 (2004), Article 56.
[30] M. Cafara, C. Marianecci, A. Codeca, P. Squillaci, M. Scaizo, F. Cerreto, E. Santucci, Retinyl palmitate-loaded vesicles: influence on vitamin light-induced degradation, J. Drug Del. Sci. Technol. 16 (2006) 407–412.
[31] L.Y. Lee, C.H. Wang, K.A. Smith, Supercritical antisolvent of biodegradable micro- and nanoparticles for controlled delivery of paclitaxel, J. Control. Release. 125 (2008) 96–106.
[32] A.-M. Layre, R. Gref, J. Richard, D. Requier, H. Chacun, M. Appel, A.J. Domb, P. Couvreur, Nanoencapsulation of a crystalline drug, Int. J. Pharm. 298 (2005) 323–327.
[33] B. Conti, F. Pavenetto, I. Genta, Use of polylactic acid for the preparation of microparticulate drug delivery system, J. Microencapsulat. 19 (1992) 153–159.
[34] B.M. Hasch, S.-H. Lee, M.A. McHugh, The effect of copolymer architecture on solution behavior, Fluid Phase Equilib. 83 (1993) 341–348.
[35] B. Berne, R. Pecora, Dynamic Light Scattering: With Applications to Chemistry, Biology, and Physics, Dover Publications, Mineola, New York, 2000.
[36] A. Bootz, V. Vogel, D. Schubert, J. Kreuter, Comparison of scanning electron microscopy, dynamic light scattering and analytical ultracentrifugation for the sizing of poly(butyl cyanoacrylate) nanoparticles, Eur. J. Pharm. Biopharm. 57 (2004) 369–375.
[37] Ö. Güçlü-Üstündağ, F. Temelli, Solubility behavior of ternary systems of lipids in supercritical carbon dioxide, J. Supercrit. Fluids 38 (2006) 275–288.
[38] F.P. Lucien, N.R. Foster, Solubilities of solid mixtures in supercritical carbon dioxide: a review, J. Supercrit. Fluids 17 (2000) 111–134.
[39] J.M. Lee, B.-C. Lee, S.-J. Hwang, Phase behavior of poly(L-lactide) in supercritical mixtures of carbon dioxide and chlorodifluoromethane, J. Chem. Eng. Data 45 (2000) 1162–1166.
[40] B.-C. Lee, Y.-M. Kuk, Phase behavior of poly(L-lactide) in supercritical mixtures of dichloromethane and carbon dioxide, J. Chem. Eng. Data 47 (2002) 367–370.
[41] H.-S. Byun, H.-Y. Lee, Cloud-point measurement of the biodegradable poly(D,L-lactide-co-glycolide) solution in supercritical fluid solvents, Korean J. Chem. Eng. 23 (2006) 1003–1008.
[42] F. Rindfleisch, T.P. DiNoia, M.A. McHugh, Solubility of polymers and copolymers in supercritical CO_2, J. Phys. Chem. 100 (1996) 15581–15587.
[43] G.D. Parfitt, Fundamental aspects of dispersion, in: G.D. Parfitt (Ed.), Dispersion of Powder in Liquids, 2nd ed., Wiley & Sons, New York, 1973, pp. 1–43.
[44] M.J. Rosen, Surfactants and Interfacial Phenomena, Wiley & Sons, New York, 1989.
[45] P.E. Luner, S.R. Babu, S.C. Mehta, Wettability of a hydrophobic drug by surfactant solutions, Int. J. Pharm. 128 (1996) 29–44.
[46] E. Lemos-Senna, D. Wouessidjewe, S. Lesieur, D. Duchêne, Preparation of amphiphilic cyclodextrin nanospheres using the emulsification solvent evaporation method: influence of the surfactant on preparation and hydrophobic drug loading, Int. J. Pharm. 170 (1998) 119–128.
[47] Y. Lin, T.W. Smith, P. Alexandridis, Adsorption of a rake-type siloxane surfactant onto carbon black nanoparticles dispersed in aqueous media, Langmuir 18 (2002) 6147–6158.
[48] BASF Corporation, http://www2.basf.us/performancechemical/bcperfpluronic_grid.html (accessed July 2009).
[49] A. Bose, Wetting by solutions, in: J.C. Berg (Ed.), Wettability, Marcel Dekker, New York, 1993, pp. 149–181.
[50] W. Zhuang, E. Kiran, Kinetics of pressure-induced phase separation (PIPS) from polymer solutions by time-resolved light scattering. Polyethylene + n-pentane, Polymer 39 (1998) 2903–2915.
[51] S.K. Friedlander, M.K. Wu, Linear rate law for the decay of the excess surface area of a coalescing solid particle, Phys. Rev. B 49 (1994) 3622–3624.
[52] S.K. Friedlander, Synthesis of submicron solid particles: aerosol reactors, in: Smoke, Dust, and Haze: Fundamentals of Aerosol Dynamics, 2nd ed., Oxford University Press, New York, 2000, pp. 331–358.
[53] K.E.J. Lehtinen, R.S. Windeler, S.K. Friedlander, Prediction of nanoparticle size and the onset of dendrite formation using the method of characteristic times, J. Aerosol Sci. 27 (1996) 883–896.
[54] E.G. Seebauer, C.E. Allen, Estimating surface diffusion coefficients, Prog. Surf. Sci. 49 (1995) 265–330.

Journal of Molecular Liquids 147 (2009) 64–70

Contents lists available at ScienceDirect

Journal of Molecular Liquids

journal homepage: www.elsevier.com/locate/molliq

Potential energy surface and molecular dynamics simulation of gold(I) in liquid nitromethane

Natcha Injan [a,b], Tünde Megyes [c], Tamas Radnai [c], Imre Bako [c], Szabolcz Balint [c], Jumras Limtrakul [b], Daniel Spangberg [d], Michael Probst [a,*]

[a] Institute of Ion Physics and Applied Physics, Innsbruck University, Austria
[b] Chemistry Department and Center of Nanotechnology, Kasetsart University, Bangkok, Thailand
[c] Chemical Research Centre of the Hungarian Academy of Sciences, Budapest, Hungary
[d] Angström Laboratory, Uppsala University, Uppsala, Sweden

ARTICLE INFO

Available online 17 November 2008

Keywords:
Au(I)
Ion solvation
Nitromethane
Potential energy functions
Molecular dynamics simulations
Cluster calculations
Quantum chemistry
Solvation shell

ABSTRACT

Potential energy functions for Au(I)-nitromethane (NM, CH_3NO_2) and NM–NM interactions were calculated by fitting analytical expressions to quantum chemically derived energies. These functions were then used in a molecular dynamics simulation of one Au(I) cation in 499 nitromethane molecules in the NVT ensemble at room temperature. A comparative simulation with a generic NM–NM potential energy function was also performed for comparison and gave the same results with respect to the calculated properties. It was found that the first solvation shell around the gold ion contains 9–10 nitromethane molecules in an environment with no strong symmetry.

Complementary, cluster calculations on $AuNM_n^+$ were performed. The especially strong binding of nitromethane in $AuNM_2^+$ and the validity of the pair approximation are discussed.

1. Introduction

A renewed interest in the properties of gold ions [1] in non-aqueous solution can be noticed and stems from various new applications and problems. New applications of gold solutions in nanotechnology and cluster science deal, for example, with gold nanowires and with the catalytic properties of gold nanoclusters. Many applications utilize the ability of gold to change easily between the oxidation states 0, 1 and 3. Potentially useful nanostructures can also be formed by self-assembly of ligands around gold ions. Gold surfaces in contact with various solvents play an important role in electrochemistry and in technology and, last but not least, gold is a biocompatible metal. On the other side, gold — like other heavy metals are — is an environmental liability. Since it is omnipresent in electronics devices it has to be separated and recovered before dumping or burning outdated boards and other scrap. Optimal processes for retrieving gold under such circumstances are still under investigation [2].

Gold exists in solutions predominantly as colloidal gold and as Au (I) and as Au(III) cations. Au cations in both of these oxidation states are normally complexed in solution and can easily transform or disproportionate into each other with Au(III) being normally the more stable and more strongly complexed oxidation state. Gold ions can also easily be reduced to neutral gold atoms which can form nanoclusters. There exist a large number of experimental works on gold ions in connection to nanotechnology but very few molecular dynamics studies on solutions of gold ions have been performed, however. Farges et al. [3] performed an EXAFS study on aqueous Au(III) chloride and found that gold exists as AuX_4 complexes (X = Cl, OH) at higher and at $AuCl_4^-$ at lower pH values. Bryce et al. [4] studied gold(I) thiosulfate in aqueous solution by means of EXAFS measurements and density functional. They found a linear S–Au(I)–S coordination. Their calculations used a continuum model for the effect of water. Concerning MD simulations of liquid nitromethane (NM) and the resulting properties we refer to a recent paper [5] where classical and Car–Parrinello simulation results are compared with diffraction data. NM is one of the good solvent of gold ions. Therefore this work investigate to study the specific properties of Au(I)–NM_n cluster via quantum chemical calculations and the behaviors of Au(I) in liquid NM by molecular dynamics simulations.

2. Theory

2.1. Quantum chemical calculations

Most of our quantum chemical calculations were performed with the LANL2DZ [6] basis set for Au and the D95V [7] basis set for N, O, C and H. This choice of basis sets was motivated by the necessity of including relativistic effects for Au and the requirement that the LANL2DZ [6] basis set and ECP which is often used successfully for Au

* Corresponding author. Tel.: +43 6643244486.
E-mail address: michael.probst@uibk.ac.at (M. Probst).

0167-7322/$ – see front matter © 2008 Elsevier B.V. All rights reserved.
doi:10.1016/j.molliq.2008.10.016

[2,8] must be combined with a same-quality basis for the lighter elements. This also allows us to perform quantum chemical calculations on the larger clusters. As a method we employed Hartree–Fock (HF) and MP2. Primarily because of the use of an ECP for the Au core electrons, the BSSE (basis set superposition error) of the binding energy at the HF level is small. For calculations at the MP2 level it was found that after correcting for the BSSE, (which is larger than for HF), both HF and MP2 binding energies are very similar, which is typical for systems dominated by electrostatics. The method and basis sets as mentioned above were performed to investigate the geometry, electronic structure, and the binding energy of $AuNM_n^+$ clusters with $n=1$–10. Because NM is a molecule with a high dipole moment (4.6 debye) its electrostatic potential (Fig. 1) is divided into a positive half-space (CH_3) and a negative one (NO_2). This defines the electrostatics qualitatively . The chemical aspects of the coordination of Au(I) to NO_2 are discussed in paragraph 3 in detailed. All quantum chemical calculations were carried out with the Gaussian 03 [9] computer program.

2.2. Au^+–NM and NM–NM potential energy surface

The Au^+–NM and NM–NM intermolecular potential functions were developed for investigating the dynamics of Au(I) in liquid NM. We constructed an analytical pair potential for Au^+–NM by fitting the parameters of functions of the interatomic distances to energies derived from quantum chemical calculations. Details of these calculations were given in Section 2.1 above. Au(I) coordinates (Fig. 2) were generated along straight lines around a rigid NM molecule. In principle, it is not important how the conformation space is sampled unless important parts of it are left out. The subdivision of the sampling coordinates into straight lines only allows for an easy visualization of the potential energy in sets of distinct curves. The q_i partial charges of NM were taken from [10] as shown in Table 3, for reasons of consistency ($q_{Au}=1$ a.u.). The equation and its parameters describing the Au^+–NM potential energy surfaces were obtained by minimizing the least-square deviation between the energies from the analytical formula and their quantum-chemically calculated counterparts.

We also calculated NM–NM energy surfaces at B3LYP/6–31 + G(d) level and constructed a NM–NM potential energy function, in the same way as described above. This served the purpose of providing an independent check since the intermolecular part of the NM potential energy function previously used for simulations of liquid NM [5,10] was derived from physical data of crystals of triazines [11,12]. Its accuracy is therefore difficult to judge and besides the issue of transferability sometimes such potential energy functions are not accurate for liquid state simulations where much more mutual orientations of neighboring molecules play a role than in the crystalline phase. We refer to this potential energy function subsequently as the 'generic NM pair potential'. The charges q_{ij} were fixed at the values given in [10] in order of being able to use the Au–NM energy function described above.

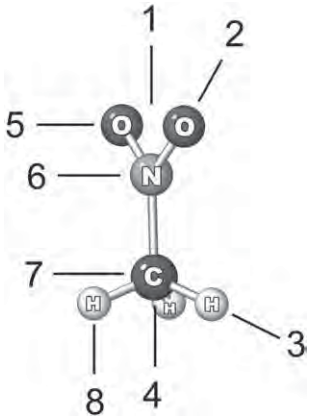

Fig. 2. Positions of Au around NM used for the construction of the Au^+–NM potential energy function. The solid lines refer to movement of Au^+. The numbers of the lines refer to the energy curves in Fig. 5.

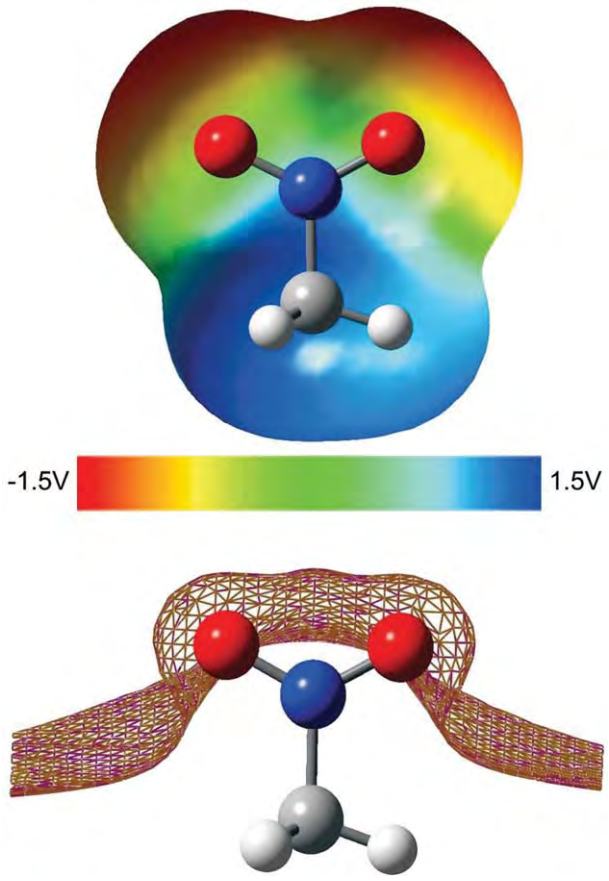

Fig. 1. Electrostatic potential of NM (upper part) and the surface of zero ESP (lower part).

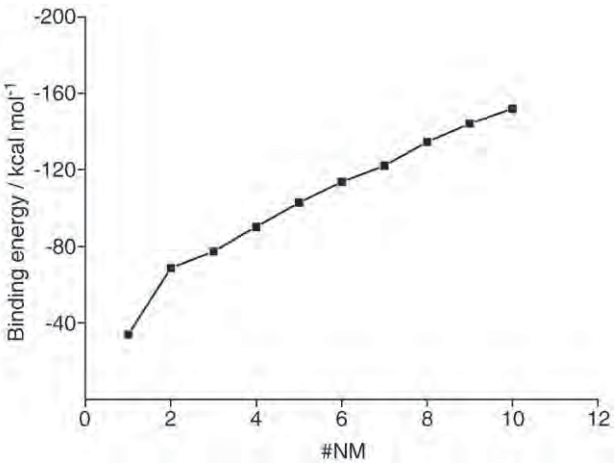

Fig. 3. Total ligand–cation binding energies defined as $E=E(Au(NM)_n^+)-E(Au^+)-nE$ (NM) in the $Au(NM)_n^+$ clusters with $n=1$ to 10. It can be seen that for $n>4$ the binding energies in the tri- to deca-coordinated complexes increase regularly.

Table 1
Atomic partial charge (NPA) and electronic configurations (NEC) of the atoms in NM, $AuNM^+$ and $AuNM_2^+$. See text for details.

	NM					$AuNM^+$					$AuNM_2^+$				
	NPA	NEC				NPA	NEC				NPA	NEC			
Au	1.00	6s	0.00	5d	10.00	0.96	6s	0.08	5d	9.96	0.84	6s	0.4	5d	9.81
N	0.57	2s	1.15	2p	3.25	0.61	2s	1.16	2p	3.20	0.61	2s	1.2	2p	3.20
C	−0.38	2s	1.12	2p	3.25	−0.37	2s	1.13	2p	3.23	−0.37	2s	1.1	2p	3.23
O*	−0.48	2s	1.79	2p	4.67	−0.65	2s	1.77	2p	4.86	−0.63	2s	1.8	2p	4.52
O	−0.40	2s	1.75	2p	4.64	−0.30	2s	1.75	2p	4.54	−0.28	2s	1.8	2p	4.85
H	0.23	1s	0.77			0.25	1s	0.75			0.25	1s	0.8		
H	0.23	1s	0.77			0.25	1s	0.75			0.25	1s	0.8		
H	0.23	1s	0.77			0.25	1s	0.75			0.25	1s	0.8		

2.3. Molecular dynamics

We performed two MD simulations, one with the newly developed potential energy function for the NM–NM interaction and one with a previously published NM–NM potential energy function taken from the literature [11]. The cubic box contained 499 rigid NM molecules and one Au^+ cation. The boxlength of 35.561 Å corresponded to the volume occupied by 500 NM molecules at 300K and atmospheric pressure. A continuous negative charge distribution was neutralizing the box. Periodic boundary conditions were employed, together with the minimal image convention for the short-range forces. For the electrostatic forces the Ewald summation was used. The simulation was performed in the NVT ensemble at 300 K. A timestep of 0.5 fs was chosen and the production run was performed for 77.5 ps after equilibrating the system for 22.5 ps. Before that, several equilibration cycles at high temperature with crude temperature scaling were employed to relax the system.

3. Results and discussions

3.1. The Au–NM interaction

Despite a long history of applying quantum chemical theory and calculations to gold–ligand systems some aspects of the energetics and the bond-directionality of transition metal cation–ligand interactions remain an interesting problem.

In some respect, Au(I)–ligand systems are simpler than most other transition metal–ligand systems because Au(I) has a completely filled d^{10}-shell, like Cu(I) and Ag(I). Even on the Hartree–Fock level, however, orbital effects are encountered: If NM ligands are added subsequently into the solvation shell of Au(I), the second NM molecule is about as strongly (or even slightly stronger, depending on the method of calculation) bound than the first one. Such a behavior is not found for singly charged alkaline ions where saturation effects start right away and in fact the decrease

$$\Delta E_n^{\mathrm{inc}} = E_n^{\mathrm{inc}} - E_{n-1}^{\mathrm{inc}}$$

in the incremental binging energies

$$E_n^{\mathrm{inc}} = E\left(\mathrm{Au(NM)}n^+\right) - E\left(\mathrm{Au(NM)}_{n-1}^+\right) - E(\mathrm{NM})$$

is largest when going from one to two ligands ($\Delta E_1^{\mathrm{inc}}$). In other words, for 'purely electrostatic' systems like alkali cations the binding energy per ligand in the 1:1 complex is always more than the one in 1:2 complexes while for Au(I) the opposite is found, as Fig. 3 shows. The natural bond orbital analysis (NBO, [13]) shows that no chemical bond is formed between Au(I) and the coordinating oxygen atom of NM. The charge transfer from one NM molecule to Au is 0.04*e* for $AuNM^+$ and 0.08*e* for $AuNM_2^+$. The Au 6*s* population in $AuNM_2^+$ is 0.35*e* while the 5*d* population decreases to 9.81*e* as shown in Table 1. A similar small overall charge transfer with a large increase in density of the highest *s* AO has been observed for $Cu(I)/H_2O$ long ago by Rosi and Bauschlicher. In two publications on this subject [14,15], they show (their Tables III and I, respectively) the increase in 4*s* density in $Cu(H2O)_2^+$. These authors already give a probably correct reason for the nonadditive behavior. They state that even without forming a bond, the mixing of s^1–d^9 into the wavefunction reduces the Cu(I)–O repulsion, thus allowing the ligand to approach closer. In the linear O–Cu(I)–O system the cost of the *s*–*d* mixing is shared between two ligands, offsetting the usual saturation effects. The same argument can be applied to Au(I). It is known [8,16] that, due to relativistic effects, the 6*s*–5*d* splitting in Au is much smaller than in Ag or Cu (in fact, the color of gold results from this [16]. These effects cause a lowering of the 6*s* and an increase of the 5*d* energy, thus facilitating the *s*–*d* mixing. The interaction of Au(I) with one and two water molecules

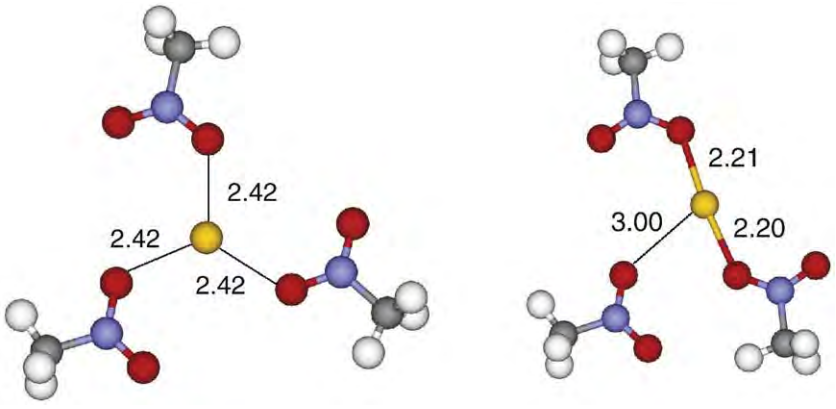

Fig. 4. Geometries of C_3h-symmetric (left) and fully geometry-optimized (right) $AuNM_3^+$, together with Au–O distances (Å).

Table 2
Atomic partial charges (NPA) and 6s and 5d populations (NEC) of Au in $AuNM_3^+$: geometry-optimized (left) and forced C_3h-symmetric structure (right).

$AuNM_3^+$ (opt. geom.)					$AuNM_3^+$ (C_3h geom.)				
NPA	NEC				NPA	NEC			
0.86	6s	0.30	5d	9.83	0.91	6s	0.13	5d	9.94

has also recently been investigated [17] by Lee and coworkers. Their interpretation uses the same arguments but is more involved.

In some sense, therefore, the non-additivity discussed above is a relativistic effect. Non-relativistic quantum chemical calculations on Au are not recommended. Relativistic calculations on Au are not per se a problem, since the main effects like mass-velocity and Darwin are already well dealt with by using an atom-derived relativistic effective core potential like [6] and only for very accurate results high-level calculations that solve the full-electron Dirac equation are necessary.

This situation is further illustrated by comparing the fully geometry-optimized $AuNM_3^+$ complex with one in which C_3h symmetry is enforced. In the former, one O–Au–O angle is nearly linear and the Au–O distance to the third oxygen is considerably longer (Fig. 4). There linear O–Au–O arrangement goes together with a 6*s* population of 0.30*e* compared to 0.13*e* in the C_3h complex (Table 2).

In order to see if this highly nonadditive behavior for low coordination numbers has consequences for larger complexes, we performed geometry optimizations on $AuNM_n$ with $1 \le n \le 10$. From the interaction energies (Fig. 3), it can be seen that for $n>3$, the energetics resemble a low charge-density cation like K^+. Despite of the large value of ΔE_n^{inc} for $n=1$, NM molecules beyond $n=2$ are also bound in the first shell because they increase the overall binding energy. This justifies the construction of a pair potential like normally used for large, singly charged cations without problems. Its construction is outlined in Section 2.2. One might argue that nevertheless it has to be differentiated between the first two NM molecules and the rest in the sense that larger clusters $AuNM_n^+$ consist of $AuNM_2^+$ solvated by $n-2$ more loosely bound NM molecules. However, one sees that in $AuNM_3^+$ the energy of the trigonal planar geometry (Fig. 4) is only slightly higher than the T-shaped one and for $n=4$ the tetrahedral arrangement is already 2 kcal/mol more stable than the square planar one. Therefore $AuNM_2^+$ should not be considered as an 'inert core', dynamical considerations notwithstanding. The $AuNM_n^+$ clusters were all optimized without constraints. Up to $n=8$ they are compact and even the $AuNM_{10}^+$ cluster shows not two solvation shells but eight shorter (4.02 Å) and two longer (~5.11 Å) Au–O distances in a capped double prism typical of coordination number 10. Therefore, even without taking into account the pV term which in condensed phase systems makes 'spongy' structures less favourable, a high coordination number of Au(I) in NM can be expected. We should mention that at least for the gas phase this is different to the $Au(I)/H_2O$ system where calculations indicate that more than two water molecules build a second shell [18], partially due to the larger water–water interaction. Finally it should be mentioned that a recent combined experimental and theoretical study [19] on Cu/H_2O and Ag/H_2O hydration in the gas phase showed that the situation for Cu^+ is similar to the one encountered for Au^+ while the *d*/*s* gap in Ag^+ is much larger.

We can conclude that the quantum chemical cluster calculations indicate that, despite the peculiarities of the Au(I)–NM interaction, MD simulations with pair-additive potentials are justified for the condensed phase.

Table 3
Charges and fitted parameters (kcal/mol and Å) for the Au^+–NM pair potential.

	q	A	B	C	D
C	−0.305	8905.8000	−19,646.0000	166,150.0000	3.1885
H	0.146	650.5703	−149.5139	81.1500	1.0576
N	0.821	0.0044	235.6198	2500.2000	1.8507
O	−0.477	11,814.0000	−10,535.0000	69,080.0000	3.1399

See text for explanations.

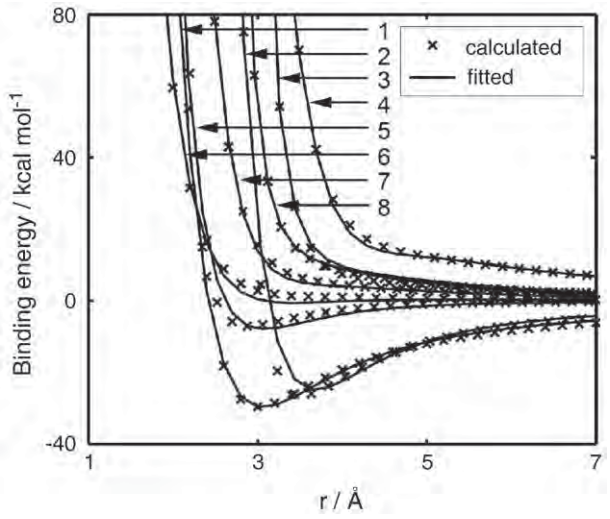

Fig. 5. Au–NM interaction: Quantum chemical (x) and fitted (solid lines) energies. The numbers 1–8 refer to Fig. 2.

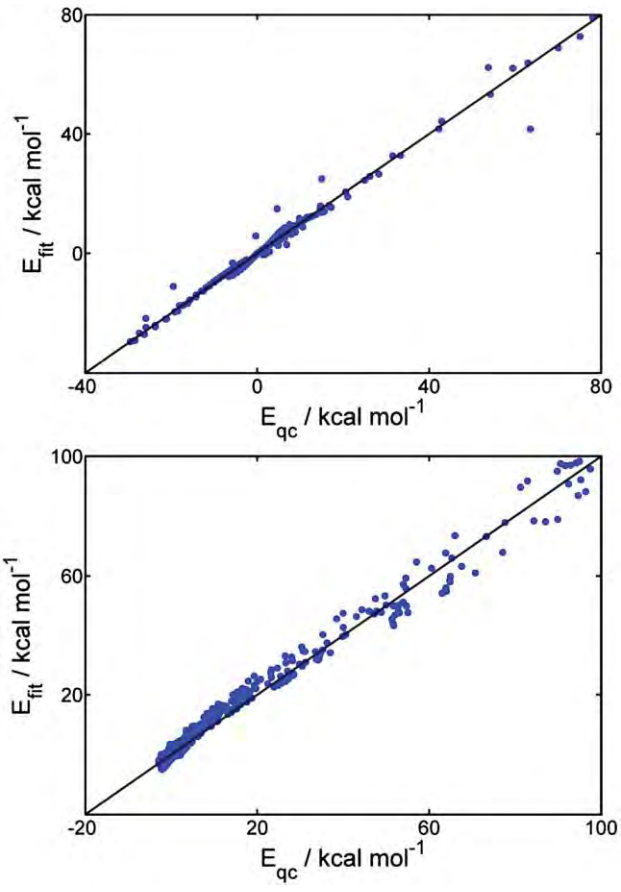

Fig. 6. Fitting accuracy of the Au^+–NM potential (upper part) and the NM–NM potential energy function (lower part).

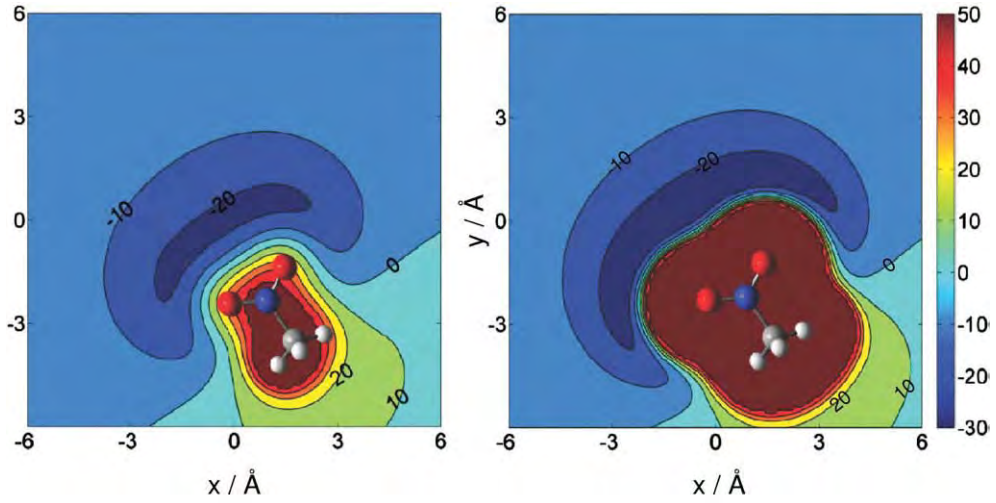

Fig. 7. Au^{+}–NM Potential energy according to Eq. (1) in the C_s plane of NM (right) and 2 Å above (left). Energies in kcal/mol and x/y coordinates in Å.

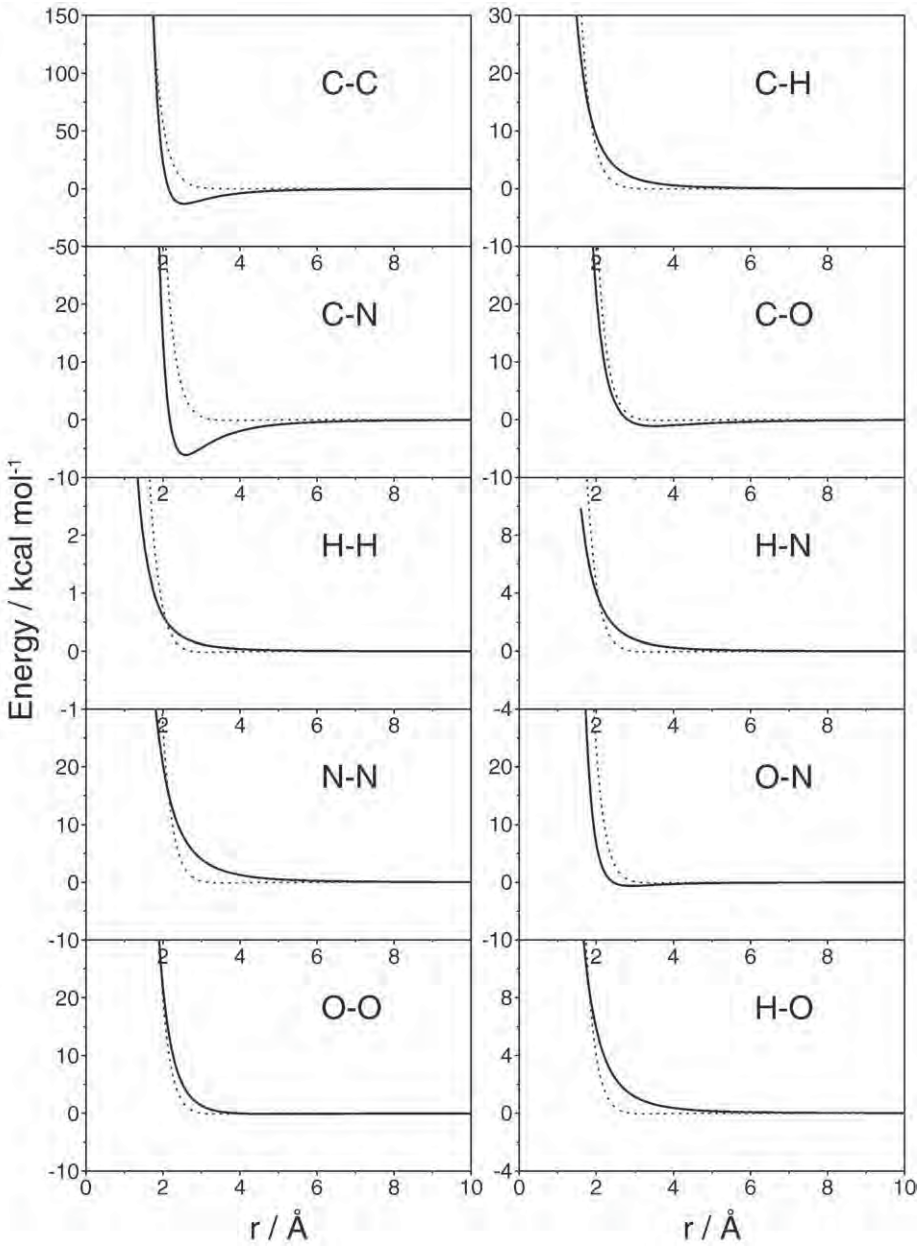

Fig. 8. Comparison of the atom–atom terms of our (solid lines) and the generic (dashed lines) NM–NM potential energy functions.

Table 4
Values of the parameters of the analytical NM–NM pair potential expression (Eq. (2)).

j	k	A	B	C
C	C	23,563.0	0.0	−1112.2000
C	H	0.0	0.0	146.5868
C	N	12,299.0	0.0	−548.6524
C	O	0.0	2375.6	−844.1313
H	H	0.0	0.0	9.7094
H	N	0.8246	0.0	64.1848
H	O	0.0	0.0	93.0748
N	N	0.0	0.0	323.2490
N	O	3104.0	0.0	−87.7924
O	O	270.4317	1366.2	−353.2470

Energies in kcal/mol and distances in Å.

3.2. Au^+–NM potential energy surface

We used the analytical energy expression:

$$V_{\text{fit}}^{CH_3NO_2-Au^+} = \sum_{k\in NM} q_k / r_k + A_k / r_k^8 + B_k / r_k^6 + C\exp(-Dr_k) \quad (1)$$

for explaining the Au^+–NM intermolecular potential. The powers of r of −8 and −6 in Eq. (1) do not have special physical significance but they gave a slightly better fitting than other combinations. These two terms in take care for the steep short-range parts while the exponential term models the shallow potential at medium distances. The values of the parameters A to D were obtained from the fitting calculations as described in Section 2.2. The values of the parameters are given in Table 3.

In Fig. 5, we show the fitted energy together with the ab-initio data. The fitting accuracy (Fig. 6) is generally good.

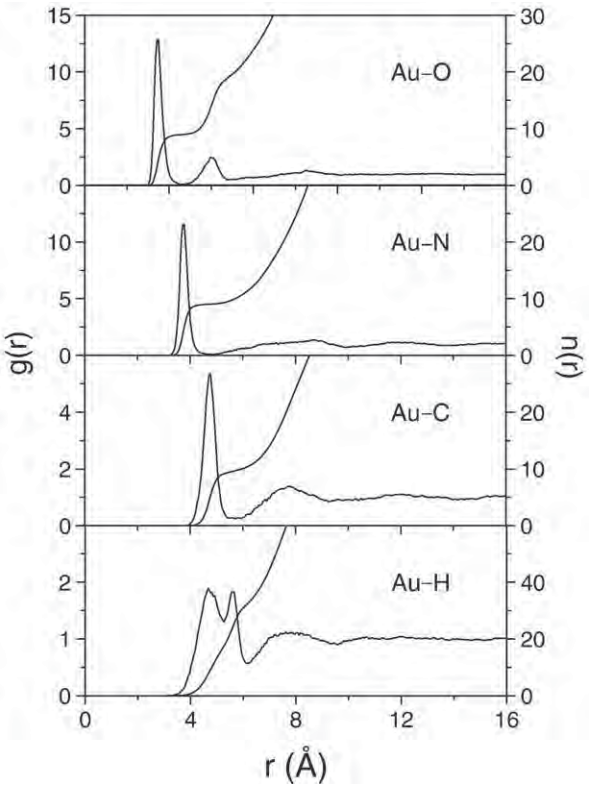

Fig. 9. Au–NM radial distribution functions from the simulation utilizing the newly constructed NM–NM potential energy function.

Table 5
Characteristic values of the radial distribution functions for the Au^+–nitromethane system with the (a) new and (b) generic NM–NM potential energy functions.

Pair	1st shell					2nd shell				
	r_{max}	$g(r_{max})$	r_{min}	$g(r_{min})$	$n(r_{min})$	r_{max}	$g(r_{max})$	r_{min}	$g(r_{min})$	$n(r_{min})$
(a)										
Au–O	2.62	12.86	3.42	0.11	8.96	4.52	2.47	5.07	0.51	18.88
Au–N	3.77	11.57	4.67	0.07	9.01	8.72	1.36	10.06	0.73	49.37
Au–C	4.77	5.35	5.52	0.27	9.44	7.72	1.39	9.26	0.84	37.87
Au–H	4.67	1.89	6.17	0.57	32.43	7.62	1.12	9.56	0.90	121.01
(b)										
Au–O	2.62	13.44	3.52	0.08	9.84	4.62	2.69	5.17	0.37	20.48
Au–N	3.77	12.56	4.92	0.06	10.00	8.47	1.34	9.91	0.69	47.96
Au–C	4.67	5.39	5.92	0.14	10.60	7.67	1.53	10.16	0.72	49.34
Au–H	4.62	1.98	6.17	0.52	33.86	8.22	1.25	9.61	0.89	125.24

Fig. 7 shows a contour plot of two cuts through the analytical Au–NM potential energy surface according to Eq. (1), in the symmetry plane of NM and 2 Å above it.

3.3. NM–NM potential energy surface

Our own pair potential energy expression for the NM–NM interactions is a polynomial in $1/r$

$$V_{\text{fit}}^{CH_3NO_2-CH_3NO_2} = \sum_{j\in NM1}\sum_{k\in NM2} q_{jk} / r_{jk} + A_{jk} / r_k^8 + B_{jk} / r_k^5 + C_{jk} / r_k^4 \quad (2)$$

Fig. 8 shows that Eq. (2) provides a reasonable reproduction of the NM–NM interactions. Due to the higher dimensionality of the NM–NM system compared to the NM–Au system (6 internal degrees of freedom versus 3), much several thousand energy points had to be calculated and we do not show the various potential energy curves here. The number of non-zero parameters (Table 4) for the ten atom pairs is not overwhelming. Again, the atomics charges in the NM molecules were not changed.

A comparison between the two potential energy functions in terms of the various atom–atom pair terms is given in Fig. 8. Since the partial charges are the same in both cases, the electrostatic contributions were excluded. Our potential energy function is given in Eq. (2) while

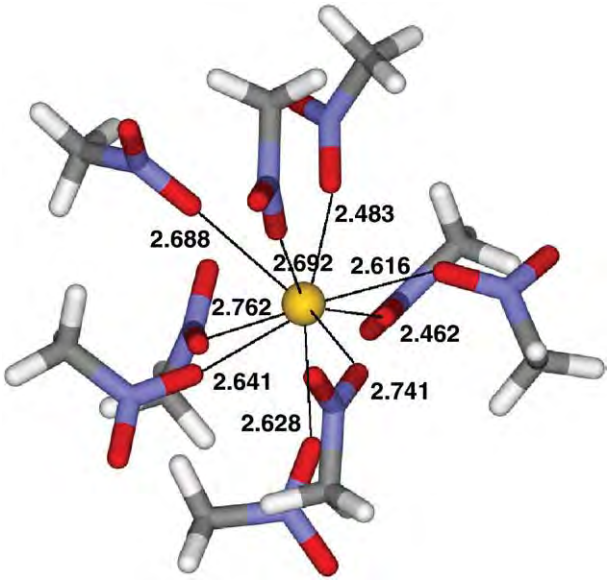

Fig. 10. Typical configuration of NM around Au^+.

the generic one [10] uses an $\exp(-r)$ term for the repulsion and an r^{-6} term for attractive interactions beside the electrostatic terms.

Two main differences are present: In all curves the $\exp(-x)$ term leads to a steeper repulsive part. This is a consequence of the values of the parameters and not of the functional form since r^{-8} is infinite for $r=0$ while $\exp(-r)$ terms are finite. Further, all terms in the generic potential exhibit no or only extremely shallow minima, in contrast to the pronounced minimum for C–N in our potential energy function. Due to the fact of the completely different ways in which both energy expressions were derived, detailed comparisons are difficult but it can be safely stated that the generic expression acts as a 'soft sphere plus coulomb'-type of potential. The largest deviations between both potential energy functions can be seen for C–N and C–C. These centers are, however, shielded by hydrogen atoms and not in close contact with each other.

Since it also turned out (see below) that the MD results from both Sorescu's [10] and our potential energy function are very similar to each other, one can conclude that electrostatic interactions dominate also in our model and the softer repulsive part plays a minor role.

3.4. Molecular dynamics simulation

The trajectory was analyzed in terms of radial distribution functions (RDFs). Fig. 9 shows all Au–NM pair correlation functions. The characteristic values of the RDFs are listed in Table 5. There the running integration numbers n_{xy}, defined according to

$$n_{xy}(r) = 4\pi\rho_0 \int_0^r r^2 g_{xy}(r)\mathrm{d}r \tag{3}$$

are also given. All RDFs with the exception of $g_{\mathrm{Au-H}}$ have one sharp first peak that goes down to near zero after its maximum. The splitting of $g_{\mathrm{Au-H}}$ might be an artifact from the rigidity of our NM model. The number of N atoms under the first peak is about 10 for the generic NM pair potential energy function [11] and 9.01 if our new one is used. Such a difference — even if the Au–NM interactions are the same in both potentials — is not surprising. These respective values for $n_{\mathrm{Au-O}}$ are consistent with the values for $n_{\mathrm{Au-C}}$ and $n_{\mathrm{Au-N}}$. Such a large solvation number is a consequence of the large distance (2.62 Å) at which $g_{\mathrm{Au-O}}$ has its maximum. The second O atom of the NM molecules is found under the second peak of $g_{\mathrm{Au-O}}$ at distances of about 4.62 Å. Consequently, $n_{\mathrm{Au-O}}$ is 18.88 (our potential) and 20.48 after this second peak. This is somewhat remarkable since the attractive potential at the site of one O atom and between two O atoms is similar (Fig. 7) and the quantum chemical details that might lead to a preference of coordination to a single oxygen (Section 3.1) are, of course, absent in our simple pair potential. Looking at the conformations (a typical snapshot is plotted in Fig. 10) one sees, however, that the more distant O atoms can interact favorably with the electropositive methyl groups, thus allowing for the crowded solvation shell. As mentioned above, virtually identical results for RDFs, coordination numbers and typical geometries are obtained if we use the NM–NM potential from [11] instead of the newly constructed one.

4. Summary

Energetic and geometric features of various gold(I)–nitromethane clusters were calculated and discussed in the light of the peculiar properties of Au(I). Ab-initio pair energy surfaces for Au(I)–NM and NM–NM were derived by fitting simple analytical functions to quantum chemically calculated energies. These functions were then used to perform a molecular dynamics simulation of one Au(I) cation in 499 nitromethane molecules in the NVT ensemble at room temperature. A comparative simulation with an older, generic NM–NM potential energy function was also performed and gave nearly identical results with respect to the analyzed quantities. The first solvation shell around the gold ion consists of 9–10 nitromethane molecules with a distance of about 2.6 Å for the first and about 4.6 Å for the second O atom to Au^+.

Acknowledgements

Support from the projects WTZ A13/2006, GVOP-3.2.1.-2004-04-0210/3.0, NAP VENEUS05 OMsFB-00650/2005, OTKA K 68498 and from the organizations NANOTEC Center of Excellence, CNC Consortium, TRF, KURDI and CHE is gratefully acknowledged. NI thanks the University Development Commission (UDC) and the Graduate School of Kasetsart University for financial support.

References

[1] P. Pyykko, Gold Bull. 37 (2004) 136.
[2] P. Pyykko, Inorg. Chim. Acta 358 (2005) 4113–4130.
[3] F. Farges, J.A. Sharps, G.E. Brown, Geochim. Cosmochim. Acta 57 (1993) 1243–1252.
[4] R.A. Bryce, J.M. Charnock, R.A.D. Pattrick, A.R. Lennie, J. Phys. Chem. A 107 (2003) 2516–2523.
[5] T. Megyes, S. Balint, T. Grosz, T. Radnai, I. Bako, L. Almasy, J. Chem. Phys. 126 (2007) 164507.
[6] P.J. Hay, W.R. Wadt, J. Chem. Phys. 82 (1985) 299–310.
[7] T.H. Dunning, P.J. Hay, in: H.F. Schaefer III (Ed.), Modern Theoretical Chemistry, Plenum, New York, 1976, p. 1.
[8] P. Pyykko, Angew. Chem. Int. Ed. 43 (2004) 4412–4456.
[9] M.J. Frisch, G.W. Trucks, H.B. Schlegel, G.E. Scuseria, M.A. Robb, J.R. Cheeseman, J.A. Montgomery Jr., T. Vreven, K.N. Kudin, J.C. Burant, J.M. Millam, S.S. Iyengar, J. Tomasi, V. Barone, B. Mennucci, M. Cossi, G. Scalmani, N. Rega, G.A. Petersson, H. Nakatsuji, M. Hada, M. Ehara, K. Toyota, R. Fukuda, J. Hasegawa, M. Ishida, T. Nakajima, Y. Honda, O. Kitao, H. Nakai, M. Klene, X. Li, J.E. Knox, H.P. Hratchian, J.B. Cross, V. Bakken, C. Adamo, J. Jaramillo, R. Gomperts, R.E. Stratmann, O. Yazyev, A.J. Austin, R. Cammi, C. Pomelli, J.W. Ochterski, P.Y. Ayala, K. Morokuma, G.A. Voth, P. Salvador, J.J. Dannenberg, V.G. Zakrzewski, S. Dapprich, A.D. Daniels, M.C. Strain, O. Farkas, D.K. Malick, A.D. Rabuck, K. Raghavachari, J.B. Foresman, J.V. Ortiz, Q. Cui, A.G. Baboul, S. Clifford, J. Cioslowski, B.B. Stefanov, G. Liu, A. Liashenko, P. Piskorz, I. Komaromi, R.L. Martin, D.J. Fox, T. Keith, M.A. Al-Laham, C.Y. Peng, A. Nanayakkara, M. Challacombe, P.M.W. Gill, B. Johnson, W. Chen, M.W. Wong, C. Gonzalez, J.A. Pople, Gaussian Inc., Wallingford CT.
[10] D.C. Sorescu, B.M. Rice, D.L. Thompson, J. Phys. Chem. A 105 (2001) 9336–9346.
[11] D.C. Sorescu, B.M. Rice, D.L. Thompson, J. Phys. Chem. B 104 (2000) 8406–8419.
[12] D.C. Sorescu, B.M. Rice, D.L. Thompson, J. Phys. Chem. B 101 (1997) 798–808.
[13] J.E. Carpenter, F. Weinhold, J. Mol. Struct.,Theochem. 169 (1988) 41–62.
[14] M. Rosi, C.W. Bauschlicher, J. Chem. Phys. 90 (1989) 7264–7272.
[15] M. Rosi, C.W. Bauschlicher, J. Chem. Phys. 92 (1990) 1876–1878.
[16] H. Schmidbaur, S. Cronje, B. Djordjevic, O. Schuster, Chem. Phys. 311 (2005) 151–161.
[17] H.M. Lee, M. Diefenbach, S.B. Suh, P. Tarakeshwar, K.S. Kim, J. Chem. Phys. 123 (2005) 074328.
[18] J.U. Reveles, P. Calaminici, M.R. Beltran, A.M. Koster, S.N. Khanna, J. Am. Chem. Soc. 129 (2007) 15565–15571.
[19] T. Iino, K. Ohashi, K. Inoue, K. Judai, N. Nishi, H. Sekiya, J. Chem. Phys. 126 (2007) 194302.

Adsorption of M Species and M_2 Dimers (M = Cu, Ag, and Au) on the Pristine and Defective Single-Walled Carbon Nanotubes: A Density Functional Theory Study

Chan Inntam*[,†] and Jumras Limtrakul[‡,§,||]

Chemistry Department, Faculty of Science, Ubon Ratchathani University, Ubon Ratchathani, 34190 Thailand, Chemistry Department and Center of Nanotechnology, Kasetsart University, Bangkok 10900, Thailand, and Center for Advanced Studies in Nanotechnology and Its Applications in Chemical, Food and Agricultural Industries, Kasetsart University, Bangkok 10900, Thailand

Received: September 23, 2010; Revised Manuscript Received: November 3, 2010

We studied the adsorption of neutral M, charged M, and M_2 dimers (M = Cu, Ag, Au) on the pristine single-walled carbon nanotubes (SWNTs) as well as on the Stone−Wales and vacancy sites by means of the B3LYP/6-31G (d,p) hybrid density functional method. Our results for neutral metal atoms on the pristine and defective SWNTs agree very well with previous periodic calculations. The binding affinity trend of metal species toward the pristine and defective SWNTs is in the order of $M^+ > M^- > M$. This implies that the transfer of electron density between metal species and the nanotubes, the electrostatic attraction, and the Pauli repulsion play an important role in the M−SWNT system. From the Mulliken population analysis, the transfer of electron density induces a positive charge of the metal species and a negative charge of the carbon atoms of nanotubes. As far as the adsorption energy is concerned, the metal species are likely to deposit on the defect site, particularly on the vacancy site, rather than on the pristine tube. To explore the reactivity of the M−SWNT complexes which can serve as a gas sensor as well as a catalyst, the interaction between a CO molecule and a metal atom deposited on the atomic vacancy was also examined. We also found that the adsorption energy per atom decreases from the metal atom to metal dimers in line with the fact that metal−metal cohesion dominates over metal−SWNT interaction. Finally, based on calculated interaction energies, dimerization of adsorbed atoms on the defect sites is not particularly favored compared to dimerization on the pristine tube except for that of Ag and Au atoms on the vacancy site.

1. Introduction

Single-walled carbon nanotubes (SWNTs)[1,2] have attracted a great deal of interest due to their unique structural, electrical, and mechanical properties.[3−7] They have been the focus of many recent studies on sensor materials, optics, catalysts, and nanoelectronic devices.[8−19] The electronic properties of the SWNTs depend on the structure and chirality of the nanotubes, resulting in a semiconducting or metallic nature. However, these properties can be modified by metal doping or functionalization of the nanotubes. Recently, various transition metal atoms have been doped and decorated on the sidewall of SWNTs to investigate the reactivity and the characteristic of such complexes[20−23] as well as to developing novel techniques for the decoration of SWNTs with metal nanoparticles.[24−30] These are of particular interest as the metal atom and metal-nanoparticle-decorated SWNTs exhibit high sensitivity, being able to detect the presence of gases at concentrations below the order of parts per million (ppm), and high reactivity materials. For example, Rh-decorated SWNTs were found to bind strongly with the NO_2 molecule at low temperature (200 K).[31] After some modifications, this material can be considered as a CNT-based sensor for detecting NO_2 at room temperature.

The interaction between transition metal atoms and SWNTs has been investigated through experimental and theoretical approaches.[15,18,20−22,32−42] Durgun et al.[22] systematically studied the adsorption of 23 transition metal atoms on the perfect (8,0) and of 4 transition metal atoms on the perfect (6,6) SWNTs. They found that the interaction of two species depends on the hybridization between the p_z orbital of carbon and the d orbitals of transition metals. Also, various kinds of defects found in the SWNTs, e.g., vacancies, Stone−Wales (SW), dangling bonds, and rehybridization,[43−45] can affect the properties of nanotubes and the nature of transition metal adsorption as reported by Yang et al.[46] They studied theoretically the adsorption of the Ni atom on the perfect and defective (5,5) and (10,0) SWNTs. It was reported that the presence of defects enhances the interaction between Ni and SWNTs, especially the single vacancy. Nevertheless, most theoretical studies of SWNTs and transition metals have focused either on the pristine tube or neutral metal atoms. Studies on the interactions of charged metal atoms, both of cation and anion species, as well as the small metal coinages have not been reported. The fundamental knowledge based on the interaction of charged metal species and small metal clusters on the sidewall of SWNTs is crucial. The results can provide an in-depth understanding of the nature of transition metal−nanotube interaction for producing metal nanoparticles with controlled sizes and shapes as well as for fabricating functional nanodevices.

In this article, we study systematically the interactions of the neutral metal atom M, metal M cation, and metal M anion (M = Cu, Ag, and Au) on the sidewall of (5,5) SWNTs using a density functional theory at the B3LYP level of calculation. To

* To whom correspondence should be addressed, inntam@gmail.com.
† Chemistry Department, Faculty of Science, Ubon Ratchathani University.
‡ Chemistry Department and Center of Nanotechnology, Kasetsart University.
§ Center for Advanced Studies in Nanotechnology and Its Applications in Chemical, Food and Agricultural Industries, Kasetsart University.
|| Present address: Laboratory for Computational and Applied Chemistry (LCAC) and Center of Nanotechnology, Kasetsart University.

10.1021/jp109098q
Published on Web 11/19/2010

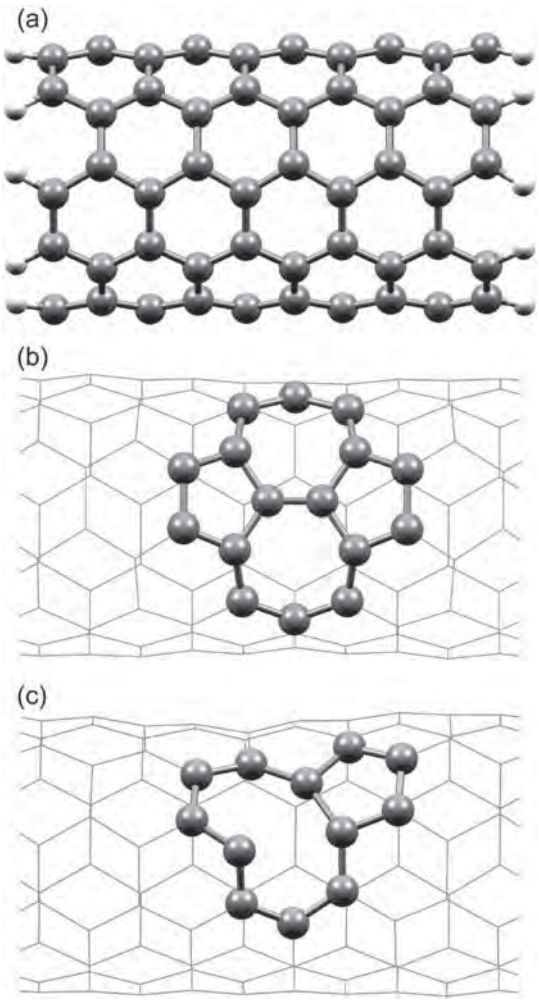

Figure 1. Sketches of the cluster models of SWNTs: (a) the pristine SWNTs ($C_{100}H_{20}$), (b) the Stone−Wales defect ($C_{100}H_{20}$), (c) the vacancy defect ($C_{99}H_{20}$).

elucidate the influence of the defect sites on the adsorption of such metal species, the metal deposition on the pristine and intrinsic defective SWNTs, vacancy, and Stone−Wales (SW), is considered. Also, the adsorption of metal dimers (Cu_2, Ag_2 and Au_2) on such sites is investigated for inspecting the initial stage of metal deposition on the sidewall of SWNTs. Moreover, this study can provide us the preferred adsorption site and stable geometries of deposited metal atoms and metal dimers, the nature of the metal−SWNTs bonding, and the propensity of adsorbed species to aggregate or to form metal dimers in the presence of vacancy and SW defects on the sidewall of SWNTs. It is believed that a fundamental understanding obtained by this work is of particular importance for fabricating hybrid metal−SWNT materials and for manufacturing chemical sensors.

2. Computational Details

In this work, the armchair (5,5) SWNTs were employed for exploring the adsorption of metal atoms and metal dimers. A quantum cluster model consisting of 100 carbon atoms of the nanotubes with H atoms capped at the ends of the fragment were applied to represent the SWNT structure, resulting in a $C_{100}H_{20}$ cluster model. These capped H atoms were used to avoid dangling bonds at the open ends. For the defective SWNTs, the Stone−Wales (SW) and atomic vacancy defects were generated by modifying the pristine $C_{100}H_{20}$ cluster model as shown in Figure 1. The SW defect creates a pentagon and heptagon pair by rotating a C−C bond in a hexagon by 90°. The atomic vacancy is formed by removing one carbon atom of the hexagon, consequently yielding a $C_{99}H_{20}$ cluster model. After geometry optimizations of such cluster models, the stable complexes were employed for studying the adsorptions of metal species, metal dimers, and a CO molecule on the sidewall of SWNTs.

TABLE 1: Calculated Bond Lengths r_e (M−M) (pm) and Dissociation Energies Per Atom D_e (kcal mol^{-1}/atom) of Free M_2 Dimers (M = Cu, Ag, Au)

			r_e (M−M)		D_e	
M_2	symmetry	ground state	calcd	exptl	calcd	exptl
Cu_2	$D_{\infty h}$	$^1\Sigma^+_g$	202.4	222[a]	25.6	23.2[a]
Ag_2	$D_{\infty h}$	$^1\Sigma^+_g$	261.6	248,[a] 253[b]	17.4	19.1[a]
Au_2	$D_{\infty h}$	$^1\Sigma^+_g$	256.8	247[a]	21.8	26.5[a]

[a] Reference 51 [b] References 52 and 53.

All calculations were performed based on the density functional theory (DFT), employing Becke's three-parameter hybrid exchange functional combined with the Lee, Yang, and Parr correlation functional (B3LYP)[47,48] method implemented in a Gaussian 03[49] program. The basis sets used in the calculation were 6-31G(d,p) for C, capped H, and Cu atoms. The relativistic effective core pseudopotential of Hay and Wadt was employed for Ag and Au atoms.[50] Spin-unrestricted calculations were performed for all open-shell systems.

Adsorption energies, E_{ads}, presented in this study were calculated with respect to the sum of the corresponding spin-polarized ground-state energy of a free metal species, M_1 or M_2, in its equilibrium geometry and the energy of the relaxed cluster models as follows

$$E_{ads} = E[M_n\text{−SWNTs}] - E[\text{SWNTs}] - E[M_n] \quad (1)$$

where $E[M_n\text{−SWNTs}]$ is the total energy of the metal atom (M_1) or dimer (M_2) adsorbed on the pristine or defective SWNTs, E[SWNTs] is the total energy of either pristine $C_{100}H_{20}$ or defective SWNTs, $E[M_n]$ is the total energy of the corresponding free metal species, M_1 or M_2. As we focus on the structural properties of various metal species deposited on the SWNTs as well as the dimerization of adsorbed metal atoms, the basis set superposition error (BSSE) was neglected for this study. All optimized geometries were confirmed by frequency analyses at the same level of calculation.

3. Results and Discussion

3.1. Metal Dimers. Free metal dimers (Cu_2, Ag_2, and Au_2) with a singlet ground state ($^1\Sigma^+_g$) were characterized by the density functional theory (DFT) calculation. Their experimental bond lengths[51] are 222, 248 (253[52,53]), and 247 pm for Cu_2, Ag_2, and Au_2, respectively. The corresponding experimental dissociation energies (D_e)[51] are 23.2, 19.1, and 26.5 kcal mol^{-1}/atom. Our calculated bond lengths and dissociation energies of these metal dimers are documented in Table 1. For the Cu_2 dimer, the bond length is about 20 pm shorter than the experimental value and consequently shows the overestimated dissociation energies. The calculated bond lengths of Ag_2 and Au_2 employing the ECP of Hay and Wadt somewhat overestimate the experimental values reflecting the underestimated dissociation energies.

3.2. Adsorption of Neutral Metal Atoms on the Sidewall SWNTs. In this study, the adsorptions of neutral Cu, Ag, and Au atoms on both the pristine and defective SWNTs, Stone−

TABLE 2: Calculated Parameters (bond lengths in pm, atomic charges q in electrons, and adsorption energies E_{ads} in kcal mol^{-1}) of Adsorption Complexes Concerning the Neutral Metal Atom M Deposited on the Pristine and Defective SWNTs

		pristine SWNTs	defective SWNTs	
	metal	$C_{100}H_{20}$ cluster	Stone−Wales ($C_{100}H_{20}$)	vacancy ($C_{99}H_{20}$)
$r(M-C_{sur})$[a]	Cu	203.6, 206.2, 210.5	196.7, 199.0	183.2, 185.7, 190.0
	Ag	345.3, 363.6, 365.4	240.5	212.0, 220.6, 220.8
	Au	273.5	218.5	200.6, 204.1, 210.7
q_M[b]	Cu	0.27 (−0.34, −0.31, 0.09)	0.46 (−0.44, −0.43)	0.48 (−0.23, −0.33, −0.28)
	Ag	−0.06 (0.01, 0.01)	0.00 (−0.31)	0.29 (−0.20, −0.19, −0.22)
	Au	−0.22 (−0.14, 0.06, 0.05)	−0.10 (−0.46)	0.58 (−0.36, −0.36, −0.34)
E_{ads}	Cu	−40.9	−53.8	−131.3
	Ag	−0.5	−4.0	−10.8
	Au	−4.0	−15.0	−26.3

[a] Distances between the metal atom M and nearby C_{sur} atoms. [b] Charges of the metal atom M. Values in parentheses are the charges of nearby C_{sur} atoms.

Wales (SW), and vacancy sites, are investigated. The various positions of the metal atoms deposited on the sidewall of SWNTs, cf. Figure 1, were considered for investigating the most stable geometry. For the atomic vacancy site as shown in Figure 1c, the most stable geometry of the $C_{99}H_{20}$ cluster was found to present a pentagon−enneagon defect. This defect was formed by the recombination of two dangling bonds which were generated after a removal of a C_{sur} from the $C_{100}H_{20}$ cluster. This result agrees very well with previous theoretical studies.[23,54,55] Our calculated parameters concerning the most stable adsorption complex are summarized in Table 2.

For adsorption on the pristine SWNTs ($C_{100}H_{20}$ cluster), we found that the Cu and Ag atoms preferred to adsorb over the C−C bond tilted to the tube axis (bridge site) while the Au atom adsorbs directly above the surface carbon atom, C_{sur} (on-top site). The distances of Cu−C_{sur} (203.6−210.5 pm) are shorter than those of the Au−C_{sur} (273.5 pm) and the Ag−C_{sur} (345.3−365.4 pm). This indicates that the Cu atom interacts strongly with C_{sur} atoms of the hexagon rather than the Ag and Au atoms. These results correspond with their adsorption energies, E_{ads}. The calculated adsorption energies of Cu, Ag, and Au atoms are −40.9, −0.5, and −4.0 kcal mol^{-1}, respectively. The different interaction of these three metal atoms can be explained by the transfer of electron density from the metal atom to nanotubes. On the basis of the Mulliken population analysis, the Cu atom exhibits strong positive charges (+0.27 e) while Ag and Au atoms are −0.06 e and −0.22 e, respectively. This implies that there are more electrons transferring from the Cu atom to the nanotubes which results in the stronger interaction. On the other hand, the Pauli repulsion weakens the interaction between the nanotubes and the metal atoms, particularly for the 5d metals (Au atom). Recently, the adsorption of the Cu atom on the armchair (5,5) SWNTs was studied by Zhang et al.[56] using the PBE functional[57] with the DNP basis set. Their calculated adsorption energy is −28.1 kcal mol^{-1} for the adsorption on both of the bridge and on-top sites. However, the most stable adsorption complexes found in this study were not considered in their work. Therefore, the differences of Cu−C_{sur} bonds as well as the functional considered cause a significant variation of adsorption energy. In addition, our results are in agreement with the previous periodic calculation studied by Durgun et al.[58] The interaction of the Au atom on the sidewall of pristine (6,6) SWNTs was reported to be −6.9 kcal mol^{-1}. Khongpracha et al.[34] investigated the Au atom adsorbed on the tip of a single-walled carbon nanohorn (SWNH) as well as on the tip of single-walled carbon nanotubes (SWNTs). The calculated adsorption energies with the PBE functional[57] are −10.8 and −16.2 kcal mol^{-1} for SWNH and SWNTs systems, respectively. These values are more stable than our work due to the different functional and the curvature effect. The interaction of the metal atoms was found to be even stronger on the SWNTs with high curvature.[59]

For the interaction between the metal atoms and the defective SWNTs, both of the Stone−Wales (SW) and the vacancy site were found to be the more favorable adsorption site rather than the pristine SWNTs. On the SW defect, the pyramidalization angle of the C_{sur} atom was reported to play an important factor for governing the interaction with the metal atoms.[46] In this study, the Cu atom bonded to two C_{sur} atoms which involved the highest pyramidalization angles with distances of 196.7 and 199.0 pm (cf. Figure 2). The adsorption energy was calculated to be −53.8 kcal mol^{-1}. In contrast to the adsorption complex of Cu, Ag and Au atoms bonded over a C_{sur} atom of the nanotubes. The Ag−C_{sur} and Au−C_{sur} distances are 240.5 and 218.5 pm, respectively. The corresponding adsorption energies were estimated to be −4.0 and −15.0 kcal mol^{-1}. Interestingly, the atomic adsorption on the vacancy site of SWNTs is even stronger than that on the SW defect for all metal atoms. We observed that the metal atoms prefer to be adsorbed above a position in which a C_{sur} atom was removed and form bonds with three nearby C_{sur} atoms of the nanotubes. These three C_{sur} atoms with dangling bonds are unstable and prefer to bond with the metal atom. Again, the interaction of the Cu atom on the vacancy site is stronger than that of the Au and Ag atoms, respectively. As one can see from Table 2, the Cu−C_{sur} distances are 183.2, 185.7, and 190.0 pm, which are shorter than those of the Au−C_{sur} (200.6, 204.1, and 210.7 pm) and Ag−C_{sur} (212.0, 220.6, and 220.8 pm). The estimated adsorption energies corresponding to Cu (−131.3 kcal mol^{-1}), Au (−26.3 kcal mol^{-1}), and Ag (−10.8 kcal mol^{-1}) are in accordance with the metal−C_{sur} distances. Our Cu−C_{sur} distances are similar to the work of Zhuang et al.[23] using the GGA functional in combination with periodic calculations. However, our calculated adsorption energy is more stable by ∼56 kcal mol^{-1} (∼43%). The formation energy of the vacancy is also different from our result, being more stable than their result by ∼49%. This is probably due to the difference of the exchange-correlation functional. They also employed the spin-polarized projector augmented-wave (PAW) method for describing the electron−ionic core interaction. The E_{ads} values of the metal atom on the vacancy site are about twice as strong as those on the SW defect. The M−C_{sur} distances from the adsorption complex on the vacancy site are also shorter than those on the SW defect and the pristine SWNTs. Moreover, the Mulliken population analysis confirms that the transfer of electron density from the metal atom to nearby C_{sur} atoms is greater in the defect sites. Therefore, we

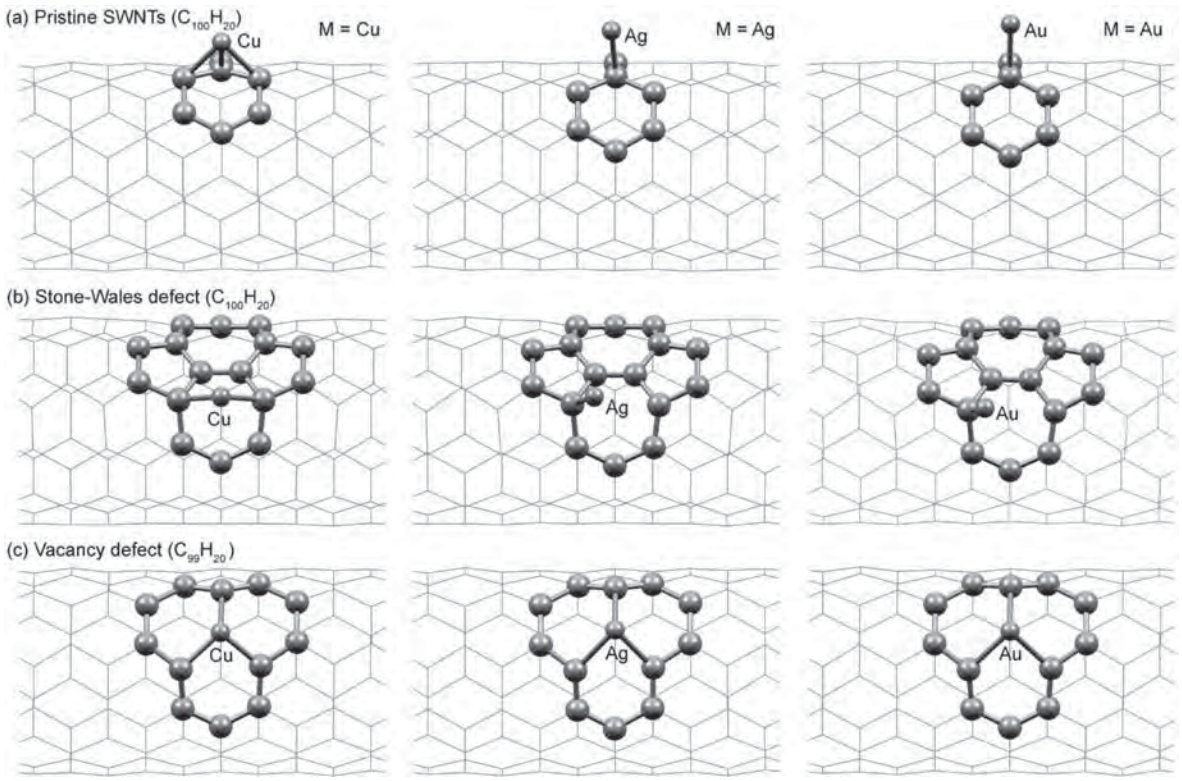

Figure 2. Adsorption complexes of M (M = Cu, Ag, and Au) species deposited on the SWNTs: (a) the pristine SWNTs ($C_{100}H_{20}$); (b) the Stone−Wales defect ($C_{100}H_{20}$); (c) the vacancy defect ($C_{99}H_{20}$).

TABLE 3: Calculated Parameters (bond lengths in pm, atomic charges q in electrons, and adsorption energies E_{ads} in kcal mol^{-1}) of Adsorption Complexes Concerning the Metal Cation M$^+$ Deposited on the Pristine and Defective SWNTs[a]

		pristine SWNTs	defective SWNTs	
	metal	$C_{100}H_{20}$ cluster	Stone−Wales ($C_{100}H_{20}$)	vacancy ($C_{99}H_{20}$)
r(M−C_{sur})	Cu^+	200.5, 202.5, 205.9	196.6, 198.3	183.6, 183.8, 189.9
	Ag^+	239.5, 278.7	229.1	209.4, 210.1, 217.3
	Au^+	221.4	214.1	200.7, 201.2, 209.5
q_M	Cu^+	0.65 (−0.35, −0.34, 0.09)	0.58 (−0.45, −0.45)	0.54 (−0.25, −0.26, −0.32)
	Ag^+	0.30 (−0.34)	0.26 (−0.39)	0.39 (−0.22, −0.28, −0.33)
	Au^+	0.05 (−0.48)	0.08 (−0.50)	0.68 (−0.36, −0.36, −0.37)
E_{ads}	Cu^+	−130.8	−154.4	−210.0
	Ag^+	−62.3	−76.0	−71.3
	Au^+	−102.8	−121.5	−128.4

[a] See Table 2 for the definitions.

conclude that the metal atoms prefer to adsorb on the defect sites, particularly on the vacancy, rather than on the pristine SWNTs.

3.3. Adsorption of Charged Metal Species on the Sidewall SWNTs. In order to describe the metal particles aggregation procedure such as the electroless deposition on the sidewall of SWNTs, the interactions of metal cation and metal anion species on the pristine and defective SWNTs were investigated. The results of these metal species are listed in Table 3 and Table 4. Most of these adsorption complexes are similar to those obtained from the neutral metal complexes as shown in Figure 2.

When the interactions of neutral metal atoms are compared, it is clear that all the metal cations bind quite strongly on the pristine and defective SWNTs. The strong interaction is in accordance with the shorter M−C_{sur} distances as well as the more positive charges of the metal. For the pristine tube, we found that the Cu^+ ion interacts on three C_{sur} atoms with distances of 200.5, 202.5, and 205.9 pm, which are shorter than those of the neutral Cu complex by about 3−4 pm. Therefore, the interaction of the Cu^+ ion and the C_{sur} bearing negative charge is stronger than that of the neutral Cu complex system. This greater electrostatic interaction contributes to the strong adsorption energy of the Cu^+ complex, −130.8 kcal mol^{-1}. Similar results are also obtained for the adsorption of Ag^+ and Au^+ ions. The Ag^+ and Au^+ ions interact directly on top of the C_{sur} atom with distances of 239.5 and 221.4 pm, respectively. As expected, the adsorptions of Ag^+ and Au^+ species on the pristine SWNTs are more favorable than those for the neutral Ag and Au atoms. The estimated adsorption energies of Ag^+ and Au^+ ions are −62.3 and −102.8 kcal mol^{-1}, respectively. For the adsorption on the SW defect, the metal cation binds strongly on the SW defect rather than on the pristine tube. The adsorption complex of the Cu^+ ion corresponds to the deposition on the bridge site with strong Cu^+−C_{sur} bonds (196.6 and 198.3 pm) whereas the adsorption complexes of Ag^+ and Au^+ ions are similar to those of the pristine SWNT system. The distances between the metal and C_{sur} shorten by about 5, 10, and 7 pm for the Cu^+, Ag^+ and Au^+ ions, respectively. Consequently, the adsorption energies are more stable by about 18−22% (Cu^+, −154.4; Ag^+, −76.0; Au^+, −121.5 kcal mol^{-1}). The interaction

TABLE 4: Calculated Parameters (bond lengths in pm, atomic charges q in electrons, and adsorption energies E_{ads} in kcal mol^{-1}) of Adsorption Complexes Concerning the Metal Anion M$^-$ Deposited on the Pristine and Defective SWNTs[a]

		pristine SWNTs	defective SWNTs	
	metal	$C_{100}H_{20}$ cluster	Stone−Wales ($C_{100}H_{20}$)	vacancy ($C_{99}H_{20}$)
r(M−C)	Cu^-	195.1, 195.1	196.7, 199.8	181.3, 184.4, 189.9
	Ag^-	343.0, 359.0	236.6	211.8, 217.2, 220.2
	Au^-	241.4	222.9	200.5, 203.0, 211.7
q	Cu^-	0.18 (−0.28, −0.28)	0.36 (−0.42, −0.41)	0.37 (−0.25, −0.26, −0.32)
	Ag^-	−0.36 (0.02, 0.02)	−0.13 (−0.31)	0.14 (−0.19, −0.20, −0.24)
	Au^-	−0.48 (−0.26)	−0.28 (−0.41)	0.43 (−0.38, −0.33, −0.36)
E_{ads}	Cu^-	−104.4	−128.2	−209.9
	Ag^-	−15.8	−24.4	−39.1
	Au^-	−8.7	−17.3	−32.3

[a] See Table 2 for the definitions.

of metal cations on the vacancy site becomes even stronger than that on the SW defect and the pristine tube. The adsorption energies were calculated to be −210.0, −71.3, and −128.4 kcal mol^{-1} for Cu^+, Ag^+, and Au^+, respectively. However, the adsorption energy of the Ag^+ ion on the vacancy site is slightly less stable than that on the SW defect by 4.7 kcal mol^{-1}. Compared with the adsorption complexes on the pristine tube, the M−C_{sur} distances shorten by 17, 27, and 17 pm for Cu^+, Ag^+, and Au^+ ions, respectively. It is worth mentioning that in this case the metal cations are the electron acceptors and the nanotubes are the electron donors. Thus, the interaction is substantially enhanced by the electron transfer from the SWNTs to the metal cations. Accordingly, we can conclude that the interaction of the metal cations on the SWNTs, both for the pristine and defective tubes, is significantly stronger than that of the neutral metal atom by about 80−100, 60−70, and 100−105 kcal mol^{-1} for Cu, Ag, and Au species, respectively.

For the metal anion species, we found that the interaction of the metal anion species is stronger than that of the neutral metal atoms on the same type of SWNTs but is weaker than that of the metal cation species. For instance, the estimated adsorption energies of Cu complexes are −40.9, −104.4, and −130.8 kcal mol^{-1} for Cu, Cu^-, and Cu^+ species, respectively. Even distances of Cu^-−C_{sur} (195.1 and 195.1 pm) are shorter than that of Cu^+−C_{sur}; the adsorption complex of the Cu^- ion is less stable than that of the Cu^+ ion which is due partly to the charge repulsion between the Cu^- ion and the electron-rich CNT as well as the electron transfer between the metal and the nanotubes. For the adsorption of the Ag^- and Au^- species, the M−C_{sur} distances lengthen by 92 and 20 pm and weaker adsorption energies are obtained (Ag^-, −15.8; Au^-, −8.7 kcal mol^{-1}) compared with the interaction of the Ag^+ and Au^+ species. For the adsorption on the SW defect, all metal anion species bind on this site more preferably than on the pristine tube. The greater electron transfer provides strong positive charges of the M species as well as more negative charges of the C_{sur} atoms as documented in Table 4. The adsorption energies of the metal anion species on the SW defect were calculated to be −128.2, −24.4, and −17.3 kcal mol^{-1} for Cu^-, Ag^-, and Au^- species, respectively. For the adsorption on the vacancy site, a stronger interaction by about 81.7 kcal mol^{-1} (Cu^- ion), 14.7 kcal mol^{-1} (Ag^- ion), and 15.0 kcal mol^{-1} (Au^- ion) is found with respect to the interaction on the SW defect. However, the interaction of metal anions is less stable than that of the metal cations on both the pristine and defective tubes by about 26, 32−52, and 93−104 kcal mol^{-1} for Cu, Ag, and Au species, respectively. Note that the estimated adsorption energies of Cu^+ and Cu^- species on the vacancy site are isoenergetic, about −210 kcal mol^{-1}. This is probably due to the very similar geometry of these two complexes. Furthermore, the transfer of electron density and the Pauli repulsion plays a major role in describing the interaction of these two species on the vacancy site. The transfer of electron density dominates over the Pauli repulsion for the vacancy site as compared with the SW defect and the pristine tube, especially for 3d metal atoms. Thus, the interaction of the Cu^- ion which provides more electrons toward the tubes is the same as that of the Cu^+ ion on the vacancy site.

3.4. Adsorption of the CO Molecule on M−SWNT Complexes. To explore the reactivity of the M−SWNTs complexes which can serve as a gas sensor as well as a catalyst, the interaction between a CO molecule and a metal atom deposited on the atomic vacancy (M−$C_{99}H_{20}$, Figure 2c) was investigated. The M−$C_{99}H_{20}$ complex was chosen as it is the most stable adsorption complex which can be presented on the sidewall of nanotubes at room temperature. Therefore, this complex can be efficiently employed for monitoring the CO molecule. The adsorptions of the CO molecule through the C atom (OC···M−$C_{99}H_{20}$) and the O atom (CO···M−$C_{99}H_{20}$) on the Cu−$C_{99}H_{20}$ complex (cf. Figure 3) were considered. Then we applied the most stable geometry obtained from the Cu−$C_{99}H_{20}$ system to study the adsorption of the CO on Ag−$C_{99}H_{20}$ and Au−$C_{99}H_{20}$ complexes. The corresponding geometrical parameters of these adsorption complexes are reported in Table 5.

The previous DFT calculations utilizing cluster and slap models reported that the adsorption of the CO molecule on the SWNTs was very weak, particularly on the pristine SWNTs.[18,36,60−62] However, the deposition of a transition metal on the sidewall of SWNTs can stabilize the CO adsorption. A similar result is obtained from our calculations. For the Cu−$C_{99}H_{20}$ complex, the adsorption of CO through the C atom (OC···M−$C_{99}H_{20}$) is more energetically favorable than through the O atom (CO···M−$C_{99}H_{20}$) by about 22 kcal mol^{-1} (cf. Table 5). This agrees reasonably well with the shortening of the Cu−C bond length (186.2 pm) as well as the lengthening of the adsorbed CO bond length (∼1 pm). We also observed a linear CO adsorption on the Cu atom (Cu−C−O angle ∼180°). On the basis of the estimated adsorption energies, the presence of Cu as well as Ag and Au atoms stabilizes the adsorption of CO on the sidewall of SWNTs. The calculated adsorption energies of CO on the Cu−$C_{99}H_{20}$, Ag−$C_{99}H_{20}$, and Au−$C_{99}H_{20}$ complexes are −26.3, −18.9, and −26.6 kcal mol^{-1}, respectively. The corresponding distances of Ag−C and Au−C are 208.9 and 198.4 pm, respectively. Moreover, the adsorption of CO affects the properties of the M−$C_{99}H_{20}$ complex. For instance, the interaction between the Cu atom and $C_{99}H_{20}$ weakens significantly, as seen from the lengthening of Cu−C_{sur} (∼5−7 pm), upon the adsorption of CO. This also results in the change of C_{sur} atomic charges which are less negative due to the reduction

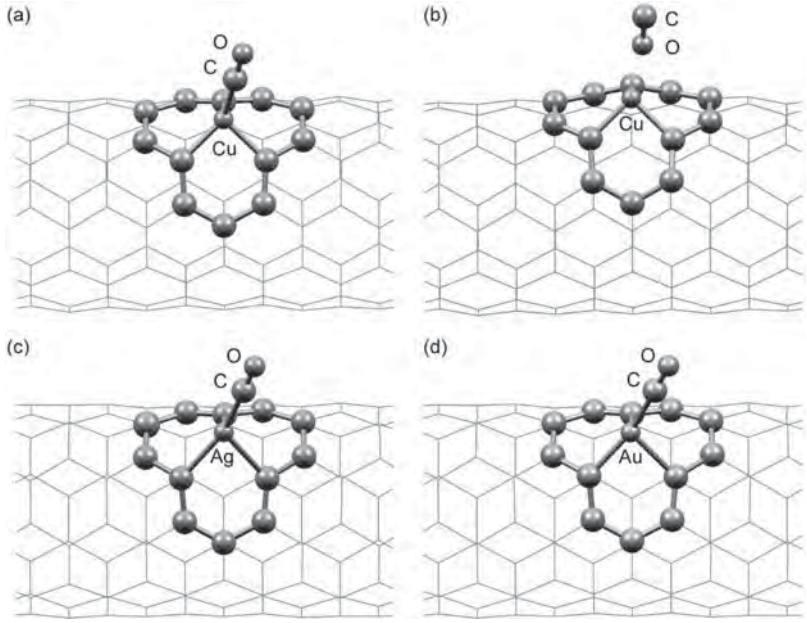

Figure 3. Adsorption of the CO molecule on the M−$C_{99}H_{20}$ (M = Cu, Ag, and Au) complexes: (a) OC···Cu−$C_{99}H_{20}$ complex; (b) CO···Ag−$C_{99}H_{20}$ complex; (c) OC···Ag−$C_{99}H_{20}$ complex; (d) OC···Au−$C_{99}H_{20}$ complex.

TABLE 5: Calculated Parameters (bond lengths in pm, atomic charges q in electrons, and adsorption energies E_{ads} in kcal mol^{-1}) of Adsorption Complexes Concerning a CO Molecule Attached on the M−$C_{99}H_{20}$ (M = Cu, Ag, and Au)

	X = Cu−$C_{99}H_{20}$		X = Ag−$C_{99}H_{20}$	X = Au−$C_{99}H_{20}$
	X−CO (Figure *3*a)	X−OC (Figure *3*b)	X−CO (Figure *3*c)	X−CO (Figure *3*d)
r(C−O)[a]	114.7	114.1	114.2	114.9
r(M−CO)[b]	186.2	237.5	208.9	198.4
r(M−C_{sur})[c]	188.6, 193.1, 197.1	185.3, 187.2, 192.7	211.9, 226.0, 228.6	202.3, 219.7, 226.9
q_M[d]	0.23 (0.36, −0.28)	0.45 (0.23, −0.17)	0.18, (0.29, −0.26)	0.50, (0.13, −0.28)
q_C[e]	−0.25, −0.22, −0.16	−0.31, −0.26, −0.21	−0.18, −0.16, −0.15	−0.39, −0.19, −0.11
E_{ads}	−26.3	−4.0	−18.9	−26.6

[a] Bond length of CO molecule. [b] Distance between the metal atom and the CO molecule. [c] Distances between the metal atom M and nearby C_{sur} atoms. [d] Charges of the metal atom M. Values in parentheses are charges of the C and O atoms of the CO molecule, respectively. [e] Charges of C_{sur} atoms surrounding the metal atom M.

of electron density of the Cu−C bond. Similar results are obtained from the OC···Ag−$C_{99}H_{20}$ and OC···Au−$C_{99}H_{20}$ complexes in which the Ag−C_{sur} and Au−C_{sur} bond lengthens by as much as 8 and 16 pm due to the adsorption of CO.

The interaction between CO and the supported M metal can be clearly explained by the classical mechanism known as the π-back-bonding mechanism.[63,64] The bonding orbitals were formed between an occupied CO orbital and an unoccupied metal orbital and between occupied metal d-orbitals and the unoccupied π*-orbital of CO. This interaction is comparable to the σ-donation from the σ orbital of CO to sd-hybrid orbitals of the metal M and π-back-donation from the d-orbitals of the metal M to π*-orbital of CO. This σ-donation forms a new bond between the metal and the C atom of the CO molecule whereas the π-back-donation weakens the CO bond due to the nature of antibonding π* orbitals. This is obvious from the lengthening of the CO bond in all adsorption complexes. For our work, we found that the CO bond lengthens by as much as 2.1 pm when it is adsorbed on the Au−$C_{99}H_{20}$ complex.

3.5. Adsorption of Metal Dimers on the Pristine and Defective SWNTs. In this section, we studied the adsorption of the Cu_2, Ag_2, and Au_2 dimers on the pristine and defective SWNTs, the Stone−Wales, and the vacancy sites. In order to inspect the most favorable geometry of a metal dimer adsorbed on the nanotubes, the metal dimers oriented parallel (mode A) and standing (mode B) to the tube axis were considered as shown in Figures 4−6. The results concerning the geometric and energetic properties are listed in Table 6 and Table 7. Combining these with the results of the metal atoms can provide us with information concerning a propensity of dimerization on the various sites of SWNTs, which is expected to be the beginning step for the nanoparticles deposited on the nanotubes.

On the pristine SWNTs, the adsorption of the Cu_2 dimer in parallel orientation (mode A) is more stable than that of the standing orientation (mode B) as shown in Figure 4a. The corresponding adsorption energies were calculated to be −35.4 and −26.6 kcal mol^{-1}/atom for mode A and mode B, respectively. The adsorption complex in mode A involves the forming of three bondings between Cu and C_{sur} atoms with distances of 192.2, 200.6, and 215.6 pm. This interaction is quite strong and leads to the reduction of electron density of the Cu−Cu bond. It is clearly seen from the lengthening of this bond (∼219.7 pm) compared with the gas phase Cu_2 (202.4 pm). In contrast to mode A, only one bonding of Cu and the C_{sur} atom is formed in the adsorption mode B. Consequently, a smaller change in the distance of Cu−Cu (210.2 pm) is obtained. The Mulliken population analysis is also consistent with the results above. Both of the Cu atoms act as electron donors in mode A but only the Cu atom bound to the C_{sur} does so for mode B. For the Ag_2 and Au_2 dimers, however, the results are different. When adsorbed on the pristine SWNTs, we found that the standing orientation of the Ag_2 and Au_2 dimers is energetically favorable

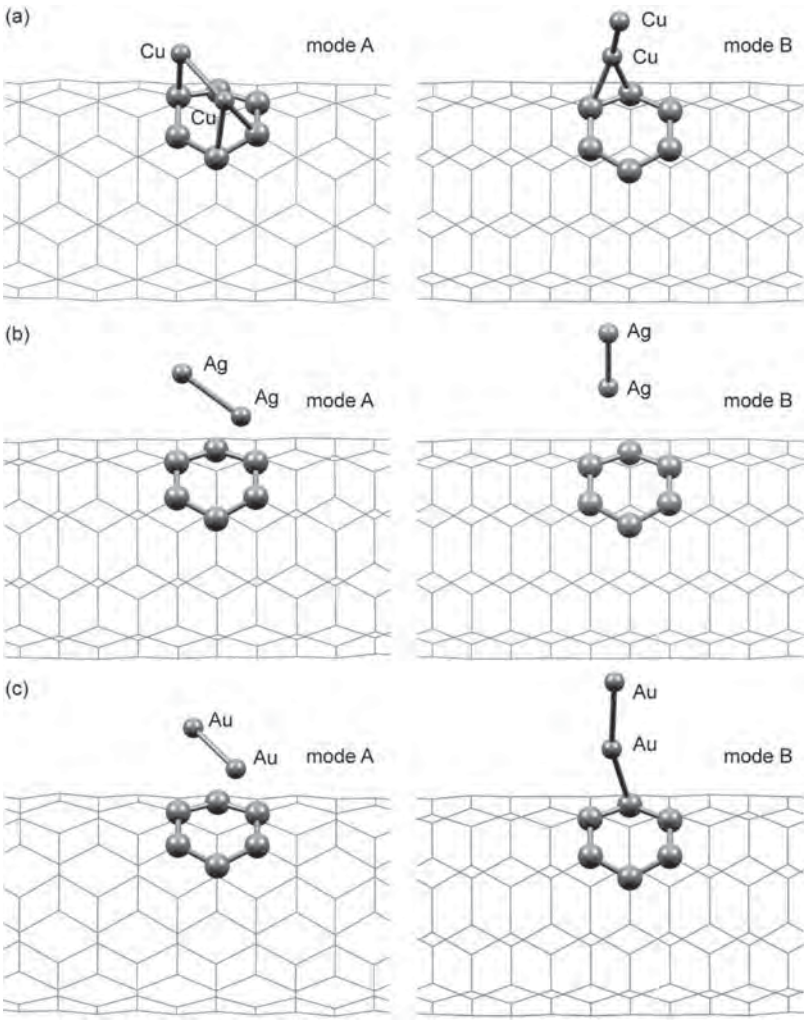

Figure 4. Adsorption complexes of the M_2 (M = Cu, Ag, and Au) dimers deposited on the pristine $C_{100}H_{20}$ cluster in adsorption mode A and mode B: (a) $Cu_2-C_{100}H_{20}$ complex; (b) $Ag_2-C_{100}H_{20}$ complex; (c) $Au_2-C_{100}H_{20}$ complex.

TABLE 6: Calculated Parameters (bond lengths in pm, atomic charges q in electrons, and adsorption energies E_{ads} in kcal mol^{-1}) of Adsorption Complexes Concerning the Metal Dimer M_2 Deposited on the Pristine SWNTs[a]

		pristine $C_{100}H_{20}$	
	metal	mode A	mode B
r(M−C)[b]	Cu	192.2, 200.6, 215.6	195.0, 198.2
	Ag	366.2, 405.9, 415.0, 423.6	276.8, 282.7
	Au	343.0, 370.6, 389.4, 398.3	241.3, 246.6
r(M−M)[c]	Cu	219.7	210.2
	Ag	261.6	261.9
	Au	257.7	257.3
q[d]	Cu	0.23 (−0.56); 0.18 (−0.33)	0.46 (−0.57, 0.07); −0.34
	Ag	−0.04 (0.0); −0.02 (0.0)	0.06 (−0.08, −0.03); −0.19
	Au	−0.07 (0.00,0.01, 0.03); −0.07	−0.02 (−0.19, −0.10); −0.19
E_{ads}	Cu	−35.4	−26.6
	Ag	−0.5	−2.0
	Au	−0.8	−6.7

[a] See Figure 4 for the definition of the adsorption modes. [b] Distances between the metal atom M and the nearby C_{sur} atom. [c] Bond length of the metal dimer M_2. [d] Charges of each atom M of the metal dimer M_2. Values in parentheses are the charges of the C_{sur} atom close to the metal atom M.

over the parallel orientation (cf. Figure 4b and Figure 4c). These results can be explained by the Pauli repulsion between the SWNTs and the metal dimers which is more pronounced than for the Cu_2 dimer system. Generally, the Pauli repulsion is less for small atoms as well as for an orientation of dimer in the standing mode. However, the interaction of the Au_2 dimer on the SWNTs is stronger than that of the Ag_2 dimer. The estimated adsorption energies of these complexes in mode B are −6.7 and −2.0 kcal mol^{-1}/atom for the Au_2 and Ag_2 dimer, respectively. The Au−C_{sur} distances are about 36 pm shorter than the Ag−C_{sur} distances. Moreover, binding on the nanotubes causes an increase of the metal−metal bond compared to the corresponding gas phase. Nevertheless, the adsorptions of the Ag_2 and Au_2 dimers on the pristine SWNTs are less stable than those on the defective sites (see below).

On the defective SWNTs, the orientations of metal dimers related to mode A and mode B were continually considered. Nevertheless, only some stable geometries were obtained as illustrated in Figure 5 and Figure 6. The adsorption complex of Cu_2 on the SW defect was found to be more stable in mode A than in mode B. The corresponding adsorption energies were calculated to be −46.0 and −30.7 kcal mol^{-1}/atom, respectively. The reason is due to the bonding between the Cu atom and the C_{sur} atoms of SWNTs as explained above. In mode A, two Cu atoms bind strongly with the C_{sur} atoms with distances of 188.3, 196.9, and 213.0 pm. Consequently, the Cu−Cu bond lengthens by 19.3 pm compared with the gas phase Cu_2 (202.4 pm). For mode B, the adsorption of the Cu_2 dimer is less stable due to

TABLE 7: Calculated Parameters (bond lengths in pm, atomic charges q in electrons, and adsorption energies E_{ads} in kcal mol^{-1}) of Adsorption Complexes Concerning the Metal Dimer M_2 Deposited on the Defective SWNTs[a]

		Stone−Wales $C_{100}H_{20}$		vacancy $C_{99}H_{20}$	
	metal	mode A	mode B	mode A	mode B
r(M−C)	Cu	188.3, 196.9, 213.0, 219.3	200.2, 205.9	181.6, 186.2, 198.4 191.7, 217.3, 220.8	
	Ag		259.4	207.5, 210.1, 229.2, 230.5	220.0
	Au		224.0	214.6, 207.1, 208.9, 201.3	202.4
r(M−M)	Cu	221.7	211.3	231.2	
	Ag		262.4	272.0	264.6
	Au		259.1	292.0	259.8
q	Cu	0.22 (−0.50, −0.21); 0.30 (−0.30, −0.13)	0.46 (−0.12, −0.21); −0.28	0.42 (−0.41, 0.10, −0.24); 0.36 (−0.21, −0.22)	
	Ag		0.04 (−0.18), −0.20	0.17 (−0.38); 0.26 (−0.23, −0.26)	0.05 (−0.26); −0.23
	Au		−0.05 (−0.44); −0.20	0.60 (−0.64, −0.36, −0.35); −0.01	0.08 (−0.42); −0.20
E_{ads}[b]	Cu	−46.0	−30.7	−79.1	
	Ag		−3.8	−0.8	−10.8
	Au		−10.6	−28.2	−23.5

[a] See Table 6 for the definitions. [b] The absence of E_{ads} indicates that metal dimers do not bind to the tubes in the corresponding adsorption mode.

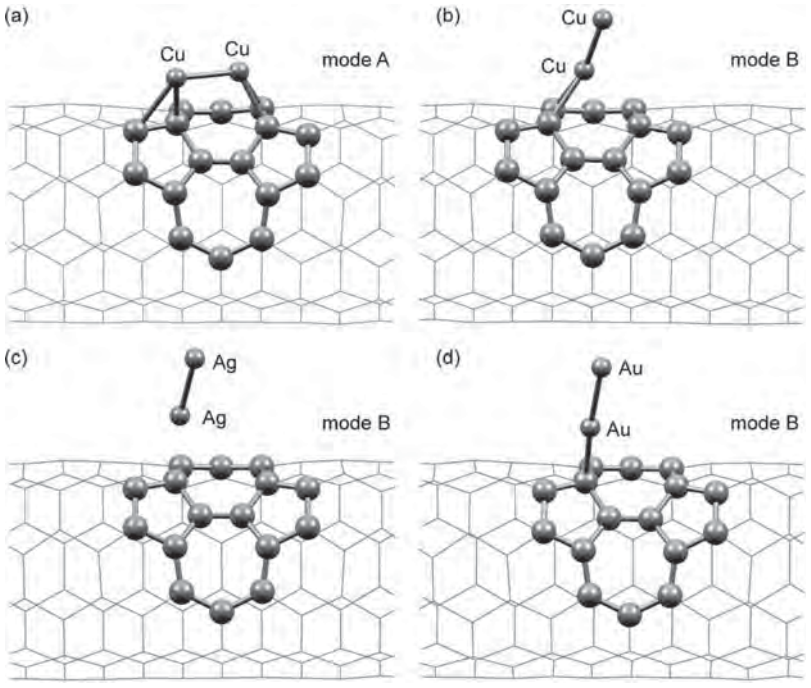

Figure 5. Adsorption complexes of the M_2 (M = Cu, Ag, and Au) dimers deposited on the Stone−Wales (SW) defect: (a) Cu_2−$C_{100}H_{20}$ complex in mode A; (b) Cu_2−$C_{100}H_{20}$ complex in mode B; (c) Ag_2−$C_{100}H_{20}$ complex in mode B; (d) Au_2−$C_{100}H_{20}$ complex in mode B.

only one Cu atom bonded to the C_{sur} atoms. As expected, longer Cu−C_{sur} distances (200.2 and 205.9 pm) are obtained from the adsorption complex in mode B. In contrast to the adsorption of the Cu_2 dimer, the optimized geometries of Ag_2 and Au_2 adsorbed on the SW defect are obtained only by the standing orientation, although various initial orientations of the dimers were applied. The strong Pauli repulsion in the parallel orientation of metal dimers probably destabilizes the adsorptions complex. As shown in Figure 5, the adsorption complex in mode B corresponds to the metal atom adsorbed directly on top of one C_{sur} atom. The Ag−C_{sur} and Au−C_{sur} distances are 259.4 and 224.0 pm, respectively. The corresponding adsorption energies were estimated to be −3.8 and −10.6 kcal mol^{-1}/atom for Ag_2 and Au_2. These results are in accordance with the smaller changes in the metal−metal bond length compared with the gas phase dimers, 0.8 pm for Ag_2 and 2.3 pm for Au_2.

Table 7 shows the results concerning the metal dimer adsorption on the vacancy site, $C_{99}H_{20}$ cluster. We found that the metal dimers adsorb more strongly on the vacancy site than on the pristine tube and on the SW defect. The most stable geometry of Cu_2 and Au_2 complexes corresponds to the strong interaction between one metal atom and the nearby C_{sur} atoms as illustrated in Figure 6. The corresponding adsorption energies of the Cu_2 and Au_2 dimers were calculated to be −79.1 and −28.2 kcal mol^{-1}/atom, respectively. This strong interaction is in accordance with the change in geometry of the metal dimer. Compared with the gas phase dimers, distances of Cu−Cu and Au−Au increase significantly by 28.8 and 45.2 pm, respectively. As described above, the electron density of such a metal−metal bond decreases dramatically. For the adsorption complex of Ag_2, the dimer interacts on the C_{suf} atom in the upright position by one Ag atom. The corresponding Ag−C_{sur} and Ag−Ag distances are 220.0 and 264.6 pm, respectively. The adsorption energy of Ag_2 was estimated to be −10.8 kcal mol^{-1}/atom. This similar mode of adsorption complex is also found for the Au_2 dimer, but it is less stable than the adsorption complex in mode A by

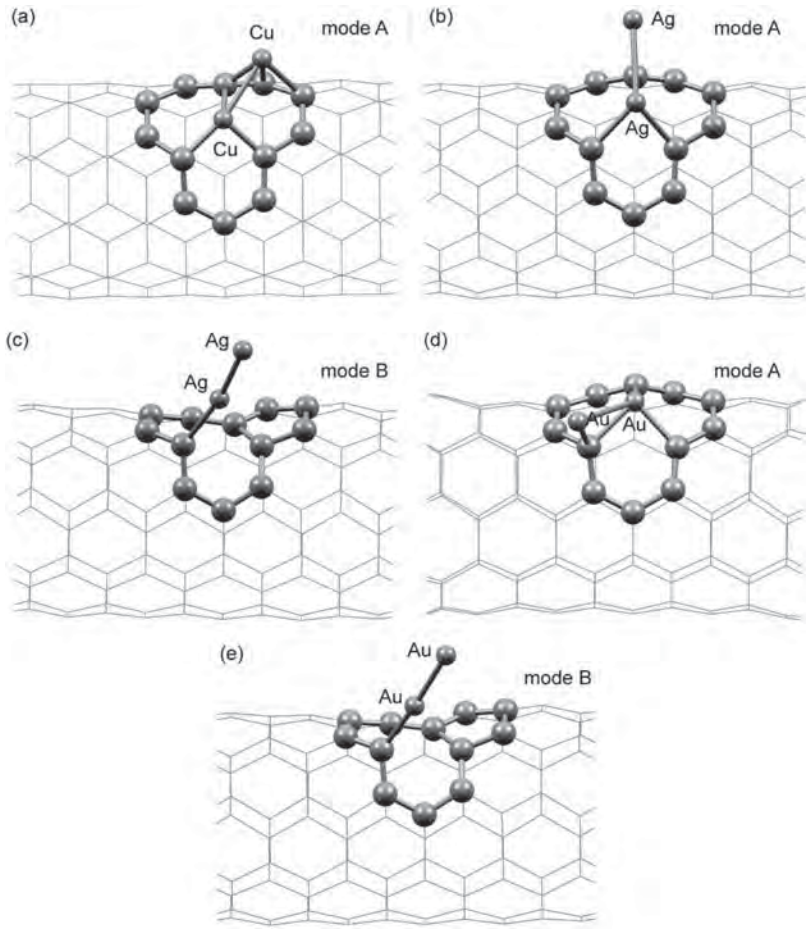

Figure 6. Adsorption complexes of the M_2 (M = Cu, Ag, and Au) dimers deposited on the vacancy defect ($C_{99}H_{20}$): (a) $Cu_2-C_{99}H_{20}$ complex in mode A; (b) $Ag_2-C_{99}H_{20}$ complex in mode A; (c) $Ag_2-C_{99}H_{20}$ complex in mode B; (d) $Au_2-C_{99}H_{20}$ complex in mode A; (e) $Au_2-C_{99}H_{20}$ complex in mode B.

about 5 kcal mol^{-1}/atom. It is worth mentioning that the orientation of the metal dimer in the upright position (mode B) diminishes the Pauli repulsion as well as the distortion in geometry of the metal dimer with respect to the other adsorption modes. Moreover, the electron transfer from the metal dimers to the SWNTs appeared from our results as the metal atom in contact with the C_{sur} atom exhibits positive charges while the charges of nearby C_{sur} atoms are negative. This implies that the transfer of electron density and the Pauli repulsion play a crucial role for determining the most stable adsorption complex.

Finally, we discuss the crucial stage as to whether indeed defect sites on SWNTs are stronger attractors for nucleation than the pristine tube. The stability of a dimer M_2 adsorbed at any site under inspection (M_2/$SWNTs_{site}$) with respect to two adatoms M, one of them bound to this site (M_1/$SWNTs_{site}$) and the other attached to the surface of the pristine SWNTs site (M_1/$SWNTs_{prist}$), is characterized by the following dimer dissociation energy on a surface site (per atom).[65,66]

$$E_{dis} = [E(M_1/SWNTs_{prist}) + E(M_1/SWNTs_{site}) - E(M_2/SWNTs_{site}) - E(SWNTs_{prist})]/2 \quad (2)$$

From Table 8, one sees that on the pristine tube E_{dis} is 17−24 kcal mol^{-1}/atom, slightly larger for Au_2 than for Cu_2 and Ag_2. These values are close to the gas phase values, D_e (Table 1). The dimer dissociation energies on all sites are not significantly different except for Ag_2 and Au_2 adsorbed on the vacancy site.

TABLE 8: Comparison of Adsorption Energies (E_{ads}) of the Neutral Metal Atom and the Metal Dimer (kcal mol^{-1}/atom) on Pristine and Defective SWNTs as Well as the Dissociation Energies (E_{dis}) of Adsorbed Dimers

site	metal	D_e[a]	E_{ads} (M_1)[b]	E_{ads} (M_2)[c]	E_{dis} (M_2)[d]
pristine tube	Cu	25.6	−40.9	−35.4	20.1
	Ag	17.4	−0.5	−2.0	17.5
	Au	21.8	−4.0	−6.7	24.5
SW defect	Cu	25.6	−53.8	−46.0	20.0
	Ag	17.4	−4.0	−3.8	19.0
	Au	21.8	−15.0	−10.6	22.9
vacancy site	Cu	25.6	−131.3	−79.1	18.6
	Ag	17.4	−10.8	−10.8	22.6
	Au	21.8	−26.3	−28.2	34.9

[a] Table 1. [b] Table 2. [c] Table 6 and Table 7. [d] $E_{dis} = [E(M_1/SWNTs_{prist}) + E(M_1/SWNTs_{site}) - E(M_2/SWNTs_{site}) - E(SWNTs_{prist})]/2$.

The stability of the adsorbed Cu_2 dimer on any sites decreases as seen from the depressing of E_{dis} by 5−7 kcal mol^{-1}/atom with respect to the gas phase value. This can be described by the strong interaction of the Cu_2 dimer on the SWNTs which causes an increase of the Cu−Cu bond length. Different results, however, are obtained for the adsorption of Ag_2 and Au_2 dimers. They are stabilized on all sites of SWNTs because the Ag_2 and Au_2 dimers which are in upright orientation do not substantially distort from the gas phase geometry. This is in accordance with the orientation of the metal dimer present in the most stable geometry (cf. Figures 4−6). Therefore, the adsorption on the SWNTs stabilizes the gas phase dimer for Ag_2 and Au_2 dimers but destabilizes for the Cu_2 dimer with respect to the gas phase

energies. Thus far, one may speculate that only Ag_2 and Au_2 dimers are stable on the sidewall of SWNTs with respect to dissociation on the surface and do not dissociate to monatomic species. In addition, the results demonstrate that the propensity for dimerization on pristine sites is virtually the same as that on SW and vacancy sites except for the Ag and Au atoms on the vacancy site. The calculated dimer dissociation energy shows that the stability of Ag and Au dimers on the vacancy site is higher than that on the pristine tube by 5.1 and 10.4 kcal mol^{-1}, respectively.

4. Conclusion

The interactions of atomic metal species and metal dimers on the different surfaces of the SWNTs was studied by means of DFT combined with the quantum cluster model representing the nanotube structure. We identified the most favorable adsorption site and geometry of adsorption complexes as well as the propensity of dimerization of the adsorbed metal atom.

For the interaction of atomic metal species on the pristine and defective SWNTs, we found that the metal cation binds more strongly than the metal anion and the neutral metal atom, respectively. The transfer of electron density between the metal species and the nanotubes as well as the electrostatic attraction, counteracted by the Pauli repulsion, mainly contributes to such strong interaction. On the pristine SWNTs, the Cu species interact strongly with several C_{sur} atoms of the nanotubes while most of the Ag and Au species bind directly on top of a C_{sur} atom. Consequently, the adsorption complexes of Cu species are more stable than those of the Au and Ag species. Moreover, the defects presented on the SWNTs affect the structural and energetic properties of the adsorption complexes. All metal species are likely to deposit on the defect sites, on the vacancy site in particular, rather than on the pristine tube. The adsorption on the vacancy site is notably stronger than that on other sites for two reasons. The Pauli repulsion between this site and metal species is lessened and the electron densities of the metal species as well as that of the vacancy are easier to polarize. The Mulliken population analysis confirms qualitatively that the transfer of electron density between the metal species and the nanotubes induces a positive charge of the metal species as well as a negative charge of nearby C_{sur} atoms. From the study of CO adsorption on the $M-C_{99}H_{20}$ complex, additionally, the metal atom deposited on the atomic vacancy is potentially used as the hybrid metal−SWNTs material for monitoring the CO molecule.

For the adsorption of metal dimers, a similar order of interaction is obtained for all types of SWNTs: $Cu_2 > Au_2 > Ag_2$. The weakness of the metal dimer bonding during the adsorption is mainly due to the transfer of electron density from the bonding of M_2 to the nanotubes. This results in the increase of the M−M distance. However, such a M−M bond does not break down reflecting that the interaction of metal−metal is stronger than that of metal−SWNTs. The effective adsorption energy per atom is also found to decrease from the metal atom to the metal dimer. On various sites of SWNTs, the adsorption complexes of the Cu_2 dimer involve the interaction of two Cu atoms on the C_{sur} atoms and consequently exhibit the strongest adsorption energy: −35.4 (pristine tube), −46.0 (SW defect), and −79.1 kcal mol^{-1}/atom (vacancy defect). In contrast to the Cu_2 dimer, most of the adsorption complexes of Ag_2 and Au_2 dimers correspond to the upright orientation of the metal dimers with respect to the tube axis. This orientation reduces the Pauli repulsion between the metal dimers and the nanotubes. However, the adsorptions of the Ag_2 and Au_2 dimers are weaker than that of the Cu_2 dimer for all sites of SWNTs.

On the basis of calculated interaction energies, we conclude that dimerization of adsorbed atoms on the SW defect is not particularly favored compared to dimerization on the pristine tube. However, the dimerization of Ag and Au atoms on the vacancy site is more stable than that on the pristine tube by 5.1 and 10.4 kcal mol^{-1}, respectively. In general, cluster growth is a complicated phenomenon; it is significantly affected by the type of metal as well as the type of sites on the sidewall of SWNTs involved in the very first stage of the metal nucleation. Therefore, high-level electronic structure calculations of adequate models are of special importance for providing information on the metal dimerization processes.

Acknowledgment. This work was supported by the Thailand Research Fund and the Commission on Higher Education (TRF-CHE: No. MRG5080253), the NSTDA Chair Professor, and NANOTEC Center of Excellence funded by the National Nanotechnology Center, the Commission on Higher Education, Ministry of Education (the "National Research University Project of Thailand (NRU)". The authors are grateful to Dr. Christian Herbst for helpful discussions.

References and Notes

(1) Iijima, S. *Nature* **1991**, *354*, 56.
(2) Iijima, S.; Ichihashi, T. *Nature* **1993**, *363*, 603.
(3) Hamada, N.; Sawada, S.; Oshiyama, A. *Phys. Rev. Lett.* **1992**, *68*, 1579.
(4) Byon, H. R.; Choi, H. C. *J. Am. Chem. Soc.* **2006**, *128*, 2188.
(5) Chen, Z.; Appenzeller, J.; Lin, Y. M.; Sippel-Oakley, J.; Rinzler, A. G.; Tang, J.; Wind, S. J.; Solomon, P. M.; Avouris, P. *Science* **2006**, *311*, 1735.
(6) Lastella, S.; Mallick, G.; Woo, R.; Karna, S. P.; Rider, D. A.; Manners, I.; Jung, Y. J.; Ryu, C. Y.; Ajayan, P. M. *J. Appl. Phys.* **2006**, *99*, 024302.
(7) Singh, K. V.; Pandey, R. R.; Wang, X.; Lake, R.; Ozkan, C. S.; Wang, K.; Ozkan, M. *Carbon* **2006**, *44*, 1730.
(8) Liu, J.; Tian, S.; Knoll, W. *Langmuir* **2005**, *21*, 5596.
(9) Jeng, E. S.; Moll, A. E.; Roy, A. C.; Gastala, J. B.; Strano, M. S. *Nano Lett.* **2006**, *6*, 371.
(10) Kose, M. E.; Harruff, B. A.; Lin, Y.; Veca, L. M.; Lu, F.; Sun, Y. P. *J. Phys. Chem. B* **2006**, *110*, 14032.
(11) Collins, P. G.; Bradley, K.; Ishigami, M.; Zettl, A. *Science* **2000**, *287*, 1801.
(12) Kong, J.; Franklin, N. R.; Zhou, C. W.; Chapline, M. G.; Peng, S.; Cho, K. J.; Dai, H. J. *Science* **2000**, *287*, 622.
(13) Rozhin, A. G.; Sakakibara, Y.; Tokumoto, M.; Kataura, H.; Achiba, Y. *Thin Solid Films* **2004**, 464.
(14) Sakakibara, Y.; Rozhin, A. G.; Kataura, H.; Achiba, Y.; Tokumoto, M. *Jpn. J. Appl. Phys.* **2005**, *44*, 1621.
(15) Cuong, N. T.; Fujiwara, A.; Mitani, T.; Chi, D. H. *Comput. Mater. Sci.* **2008**, *44*, 163.
(16) Feldman, A. K.; Steigerwald, M. L.; Guo, X.; Nuckolls, C. *Acc. Chem. Res.* **2008**, *41*, 1731.
(17) Miyata, Y.; Yanagi, K.; Maniwa, Y.; Kataura, H. *J. Phys. Chem. C* **2008**, *112*, 13187.
(18) Yeung, C. S.; Liu, L. V.; Wang, Y. A. *J. Phys. Chem. C* **2008**, *112*, 7401.
(19) Li, J.; Lu, Y.; Ye, Q.; Cinke, M.; Han, J.; Meyyappan, M. *Nano Lett.* **2003**, *3*, 929.
(20) Mercuri, F.; Sgamellotti, A. *Inorg. Chim. Acta* **2007**, *360*, 785.
(21) Wang, G.; Huang, Y. *J. Phys. Chem. C* **2008**, *112*, 9128.
(22) Durgun, E.; Dag, S.; Bagci, V. M. K.; Gülseren, O.; Yildirim, T.; Ciraci, S. *Phys. Rev. B* **2003**, *67*, 201401.
(23) Zhuang, H. L.; Zheng, G. P.; Soh, A. K. *Comput. Mater. Sci.* **2008**, *43*, 823.
(24) Lin, Y.; Watson, K. A.; Fallbach, M. J.; Ghose, S.; Smith, J. G.; Delozier, D. M.; Cao, W.; Crooks, R. E.; Connell, J. W. *Acs Nano* **2009**, *3*, 871.
(25) Guo, D.-J.; Li, H.-L. *J. Colloid Interface Sci.* **2005**, *286*, 274.
(26) Qu, L.; Dai, L. *J. Am. Chem. Soc.* **2005**, *127*, 10806.
(27) Quinn, B. M.; Dekker, C.; Lemay, S. G. *J. Am. Chem. Soc.* **2005**, *127*, 6146.
(28) Zhao, Q.; Nardelli, M. B.; Lu, W.; Bernholc, J. *Nano Lett.* **2005**, *5*, 847.
(29) Zhang, G.; Qi, P.; Wang, X.; Lu, Y.; Mann, D.; Li, X.; Dai, H. *J. Am. Chem. Soc.* **2006**, *128*, 6026.

(30) Qu, L.; Dai, L.; Osawa, E. *J. Am. Chem. Soc.* **2006**, *128*, 5523.
(31) Larciprete, R.; Petaccia, L.; Lizzit, S.; Goldoni, A. *J. Phys. Chem. C* **2007**, *111*, 12169.
(32) Okada, S. *Chem. Phys. Lett.* **2007**, *447*, 263.
(33) Inoue, S.; Matsumura, Y. *Carbon* **2008**, *46*, 2046.
(34) Khongpracha, P.; Probst, M.; Limtrakul, J. *Eur. Phys. J. D* **2008**, *48*, 211.
(35) Pannopard, P.; Khongpracha, P.; Probst, M.; Limtrakul, J. *J. Mol. Graphics Modell.* **2008**, *26*, 1066.
(36) Zhao, J.-X.; Ding, Y.-H. *Mater. Chem. Phys.* **2008**, *110*, 411.
(37) An, W.; Turner, C. H. *J. Phys. Chem. C* **2009**, *113*, 7069.
(38) Inoue, S.; Suto, H.; Wongwiriyapan, W.; Kimura, T.; Murata, Y.; Honda, S.; Katayama, M. *Appl. Phys. Express* **2009**, *2*, 035005.
(39) Ni, M. Y.; Zeng, Z.; Ju, X. *Microelectron. J.* **2009**, *40*, 863.
(40) Pannopard, P.; Khongpracha, P.; Probst, M.; Limtrakul, J. *J. Mol. Graphics Modell.* **2009**, *28*, 62.
(41) Zhao, J.-X.; Ding, Y.-h. *Mater. Chem. Phys.* **2009**, *116*, 21.
(42) Yagi, Y.; Briere, T. M.; Sluiter, M. H. F.; Kumar, V.; Farajian, A. A.; Kawazoe, Y. *Phys. Rev. B* **2004**, *69*, 075414.
(43) Charlier, J.-C. *Acc. Chem. Res.* **2002**, *35*, 1063.
(44) Li, X.; Niu, J.; Zhang, J.; Li, H.; Liu, Z. *J. Phys. Chem. B* **2003**, *107*, 2453.
(45) Ishigami, M.; Choi, H. J.; Aloni, S.; Louie, S. G.; Cohen, M. L.; Zettl, A. *Phys. Rev. Lett.* **2004**, *93*, 196803.
(46) Yang, S. H.; Shin, W. H.; Lee, J. W.; Kim, S. Y.; Woo, S. I.; Kang, J. K. *J. Phys. Chem. B* **2006**, *110*, 13941.
(47) Becke, A. D. *J. Chem. Phys.* **1993**, *98*, 5648.
(48) Lee, C.; Yang, W.; Parr, R. G. *Phys. Rev. B* **1988**, *37*, 785.
(49) Frisch, M. J. T., G. W.; Schlegel, H. B.; Scuseria, G. E.; Robb, M. A.; Cheeseman, J. R.; Montgomery, J. A., Jr.; Vreven, T.; Kudin, K. N.; Burant, J. C.; Millam, J. M.; Iyengar, S. S.; Tomasi, J.; Barone, V.; Mennucci, B.; Cossi, M.; Scalmani, G.; Rega, N.; Petersson, G. A.; Nakatsuji, H.; Hada, M.; Ehara, M.; Toyota, K.; Fukuda, R.; Hasegawa, J.; Ishida, M.; Nakajima, T.; Honda, Y.; Kitao, O.; Nakai, H.; Klene, M.; Li, X.; Knox, J. E.; Hratchian, H. P.; Cross, J. B.; Adamo, C.; Jaramillo, J.; Gomperts, R.; Stratmann, R. E.; Yazyev, O.; Austin, A. J.; Cammi, R.; Pomelli, C.; Ochterski, J. W.; Ayala, P. Y.; Morokuma, K.; Voth, G. A.; Salvador, P.; Dannenberg, J. J.; Zakrzewski, V. G.; Dapprich, S.; Daniels, A. D.; Strain, M. C.; Farkas, O.; Malick, D. K.; Rabuck, A. D.; Raghavachari, K.; Foresman, J. B.; Ortiz, J. V.; Cui, Q.; Baboul, A. G.; Clifford, S.; Cioslowski, J.; Stefanov, B. B.; Liu, G.; Liashenko, A.; Piskorz, P.; Komaromi, I.; Martin, R. L.; Fox, D. J.; Keith, T.; Al-Laham, M. A.; Peng, C. Y.; Nanayakkara, A.; Challacombe, M.; Gill, P. M. W.; Johnson, B.; Chen, W.; Wong, M. W.; Gonzalez, C.; Pople, J. A. *Gaussian 03, revision E.01*; Gaussian, Inc.: Wallingford, CT, 2004.
(50) Hay, P. J.; Wadt, W. R. *J. Chem. Phys.* **1985**, *82*, 299.
(51) Morse, M. D. *Chem. Rev.* **1986**, *86*, 1049.
(52) Simard, B.; Hackett, P. A.; James, A. M.; Langriedge-Smith, P. R. R. *Chem. Phys. Lett.* **1991**, *186*, 415.
(53) Krämer, H. G.; Beutel, V.; Weyers, K.; Demtröder, W. *Chem. Phys. Lett.* **1992**, *193*, 331.
(54) Rossato, J.; Baierle, R. J.; Fazzio, A.; Mota, R. *Nano Lett.* **2005**, *5*, 197.
(55) Lu, A. J.; Pan, B. C. *Phys. Rev. Lett.* **2004**, *92*, 105504.
(56) Zhang, B.-X.; Yang, C.; Feng, Y.-F.; Yu, Y. *Acta Phys. Sin.* **2009**, *58*, 4066.
(57) Perdew, J. P.; Burke, K.; Ernzerhof, M. *Phys. Rev. Lett.* **1996**, *77*, 3865.
(58) Durgun, E.; Dag, S.; Ciraci, S.; Gulseren, O. *J. Phys. Chem. B* **2004**, *108*, 575.
(59) Gulseren, O.; Yildirim, T.; Ciraci, C. *Phys. Rev. Lett.* **2001**, *87*, 116802.
(60) Peng, S.; Cho, K. *Nano Lett.* **2003**, *3*, 513.
(61) Star, A.; Joshi, V.; Skarupo, S.; Thomas, D.; Gabriel, J.-C. P. *J. Phys. Chem. B* **2006**, *110*, 21014.
(62) Silva, L. B.; Fagan, S. B.; Mota, R. *Nano Lett.* **2004**, *4*, 65.
(63) Blyholder, G. *J. Phys. Chem.* **1964**, *68*, 2772.
(64) Treesukol, P.; Srisuk, K.; Limtrakul, J.; Truong, T. N. *J. Phys. Chem. B* **2005**, *109*, 11940.
(65) Del Vitto, A.; Sousa, C.; Illas, F.; Pacchioni, G. *J. Phys. Chem.* **2004**, *121*, 7457.
(66) Inntam, C.; Moskaleva, L. V.; Neyman, K. M.; Nasluzov, V. A.; Rösch, N. *Appl. Phys. A: Mater. Sci. Process.* **2006**, *82*, 181.

JP109098Q

THE JOURNAL OF PHYSICAL CHEMISTRY C

ARTICLE

pubs.acs.org/JPCC

Healing of a Vacancy Defect in a Single-Walled Carbon Nanotube by Carbon Monoxide Disproportionation

Teeranan Nongnual and Jumras Limtrakul*

Laboratory for Computational and Applied Chemistry, Department of Chemistry, Faculty of Science, Center of Nanotechnology, Kasetsart University Research and Development Institute, Center for Advanced Studies in Nanotechnology and Its Applications in Chemical, Food and Agricultural Industries, and NANOTEC Center of Excellence, National Nanotechnology Center, Kasetsart University, Bangkok 10900, Thailand

ABSTRACT: We propose a new mechanism for the bimolecular healing of the vacancy defect in single-walled carbon nanotubes (SWCNTs). The mechanism is of particular importance to avoid the errors often encountered in the electronic properties of carbon nanotubes. Using density functional theory (DFT) calculations with the Perdew−Burke−Ernzerhof (PBE) functional, we investigate the reaction mechanism of the healing process of the monatomic vacancy defect in the (8, 0) SWCNT via carbon monoxide disproportionation. It is found that the proposed mechanism is theoretically possible and it has the following advantages: (1) The activation energy is only 9.37 kcal·mol^{-1} for the 4-membered-ring-opening step at high CO concentrations; (2) no catalyst is needed, and thus no purification step is needed to remove the catalyst; (3) the CO can be used as a reactant; (4) no oxygen byproduct is found; and (5) there is a high selectivity of CO for vacancy defect sites. Our finding establishes that a CNT with a vacancy defect, as it is generally obtained from the syntheses or from uses as a nanomaterial device, can be healed completely and resumes its function as a perfect CNT displaying the original electronic properties.

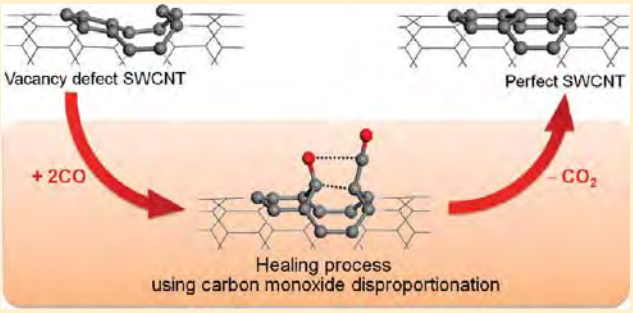

INTRODUCTION

Carbon nanotubes (CNTs) have played a crucial role in nanomaterial science since the confirmation of the discovery of single-walled carbon nanotubes (SWCNTs) by Iijima and Ichihashi[1] and Bethune et al.[2] The structure of a SWCNT can be conceptualized by wrapping a one-atom-thick layer of graphite, called graphene, into a seamless cylinder represented by a chiral vector with a pair of indices (n, m). This discovery led to the categorization of carbon nanotubes into three common types, which are zigzag, armchair, and chiral. Due to the small electronic band gap of the semiconducting single-walled carbon nanotubes (S-SWCNT) that obeys the $(n - m) \neq 3i$ rule, it is easier there than in metallic carbon nanotubes to create new impurity states within the band gap. CNT-based devices such as molecular sensors[3,4] have been created by use of this unique characteristic. Many previous studies related to S-SWCNT sensors focused on the change in the electronic properties or in the band gap after the adsorption of a molecule on the ideal nondefective pure or doped carbon nanotube.[5−8]

SWCNTs are usually studied theoretically as if they were perfectly crystalline wires even though the highest quality tubes that can be synthesized contain at least one defect per 4 μm, on average, with a distribution weighted toward areas of curvature.[9] The ozone titration method indicated that SWCNTs contain a fractional defect level of 5.5% ± 2.5%, as measured by the presence of oxidized carbon atoms at these sites.[10] Defects such as these can be created at the stage of SWCNT growth, chemical treatment, or irradiation.[11] The presence of these defects can degrade the performance and reliability of CNT-based devices. In addition, the defects can significantly cause two important errors in the sensing; essentially due to a shift of the band gap of the defect in the carbon nanotube and an under- or overbinding between the adsorbed molecule and the defect.

The crystallographic defects in carbon nanotubes can be divided into three main groups, which are native atomic rearrangements, impurities or adatoms, and atomic vacancies. This study reviews the healing techniques for these defects. The well-known atomic rearrangement defect, the Stone−Wales (SW) defect,[12] in which pentagon and heptagon pairs (5−7−7−5 rings) are observed, can be healed by a rearrangement that returns the tube back to pristine. The SW defects can be practically repaired under an applied current of 2.4 μA·nm^{-1} for thermal electronic excitation.[13] Impurity defects such as squares, three-atom protrusions, or 7−5−5−7 hillocklike defects can shed the extra atoms spontaneously under high-temperature conditions or by use of an electron beam.[14,15] H_2 adsorption on the hillocklike defect can heal it by fetching the adatoms and releasing C_2H_2 with an energy barrier of 1.26 eV.[16] O_2 and CO_2 molecules can also etch a 7−5−5−7

Received: November 6, 2010
Revised: February 5, 2011
Published: March 01, 2011

defect and an isolated C adatom, respectively, on sufficiently large CNTs, releasing two CO molecules.

Molecular dynamics simulations were used to investigate two kinds of large vacancy defects induced by compressive or torsional buckling of SWCNTs.[17] It was found that this defect was reconstructed during unloading of the external carbon sources or by increasing the temperature, forming nonhexagonal rings and SW defects, resulting in a self-healing process. Dynamic electron microscopy tracking of the healing process confirmed the closing of multivacancies of up to approximately 20 missing atoms.[15] Metallic carbon nanotubes with a monatomic vacancy (12-membered ring) induced by illumination can be electronically excited with self-healing abilities, forming 5- and 9-membered rings.[18] The defect healing process of the sp^2 carbon cap, which resulted in the removal of the 5−7, adatom, and monovacancy defects,[19,20] occurred via ring isomerization during SWCNT growth. These studies demonstrated the vacancy self-healing ability, but a perfect tube was not reached at the end. If the vacancy defect has not been healed completely, even during CNT growth, a foreign carbon atom must be introduced from external carbon sources in order to repair this defect.

A new method of SWCNT production has been introduced that uses a gas-phase catalytic process reaching 79 mol % of carbon nanotubes.[21] The carbon nanotube is grown by thermal decomposition of the catalyst, iron pentacarbonyl, in a heated flow of high-pressure carbon monoxide (known as the HiPco method). Tubes with diameters as small as 0.7 nm, the same as that of a fullerene, were produced.

A solid carbon growth mechanism was proposed, involving CO disproportionation (the Boudouard reaction) with $Fe(CO)_n$ as a catalyst.

CO disproportionation:

$$CO(g) + CO(g) \rightarrow C(s) + CO_2(g)$$

Ambient CO is used as a carbon source in the commercial HiPco method. A CO molecule can be detected by deformed CNTs but not by pristine CNTs. The radial-deformed SWCNTs change electronic properties, allowing functionalization of the tube surface to detect the presence of CO molecules.[22] In addition, metal-decorated carbon nanotubes were proposed as promising candidates for sensors: titanium-coated carbon nanotube,[23] aluminum-doped SWCNTs,[24] and Au-supported single-walled carbon nanotube and nanohorn.[25] Defect graphene sheets were also used to detect CO gas with adsorption energy of −2.33 eV, compared to that of the perfect graphene sheets of −0.12 eV.[26]

According to the need for an external carbon source for vacancy healing, we introduce an alternative mechanism of bimolecular healing by CO disproportionation without a metal catalyst, mimicking the HiPco method, in order to leave a carbon atom filling the vacancy site on the side walls of a SWCNT. In other words, the defect carbon nanotube acts as a catalyst supporting the disproportionation of two CO molecules and then heals itself by the carbon atom it produced.

METHODOLOGY

The model and periodic calculations were chosen following our recent calibration[27] with semiconducting SWCNTs with concern to computational efficiency. The (8, 0) SWCNT was chosen because it is the smallest representative S-SWCNT. Its

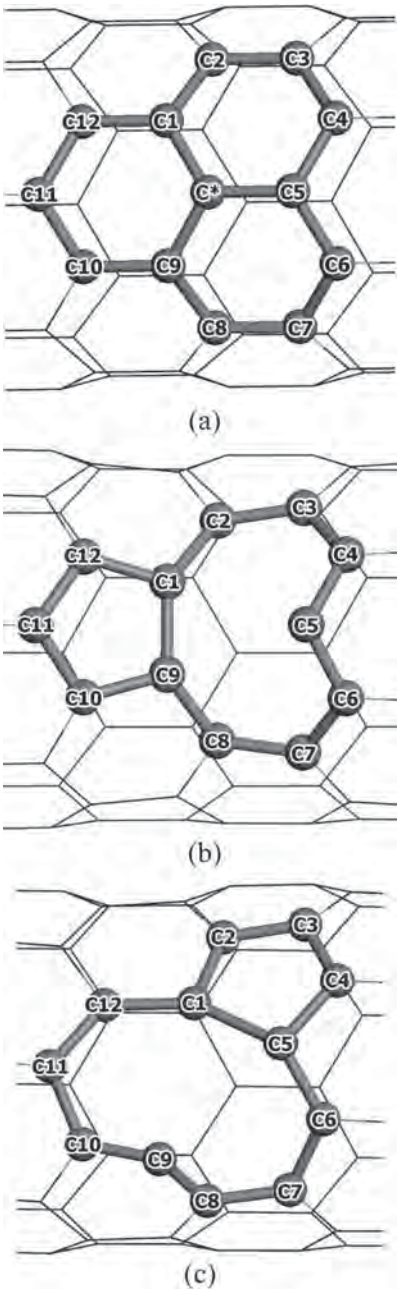

Figure 1. Optimized geometries of (a) pSWCNT, (b) symmetrical dSWCNT, and (c) asymmetrical dSWCNT labeled systematically with C1−C12, presenting the 5- and 9-membered rings at the defect site, and C*, the leaving carbon atom, leading to the defect of the SWCNT.

geometrical structure was generated in a supercell periodic box of 20 × 20 × 12.78 $Å^3$, composed of three repeated unit cells of SWCNT along the tube axis. The closest distance between two neighboring SWCNTs was set to be 13.77 Å in order to be able to ignore intertube interactions in the calculations. Since all carbon atoms in the S-SWCNT have the same topology, the monatomic vacancy defect in the (8, 0) SWCNT (dSWCNT) was built by removing one carbon atom (C* as shown in Figure 1a), resulting in the defect site called bicyclo[7,3,0]dodecane (5- and 9-membered rings) numbered C1 to C12 (Figure 1b). The distance

dx.doi.org/10.1021/jp110616c |J. Phys. Chem. C 2011, 115, 4649–4655

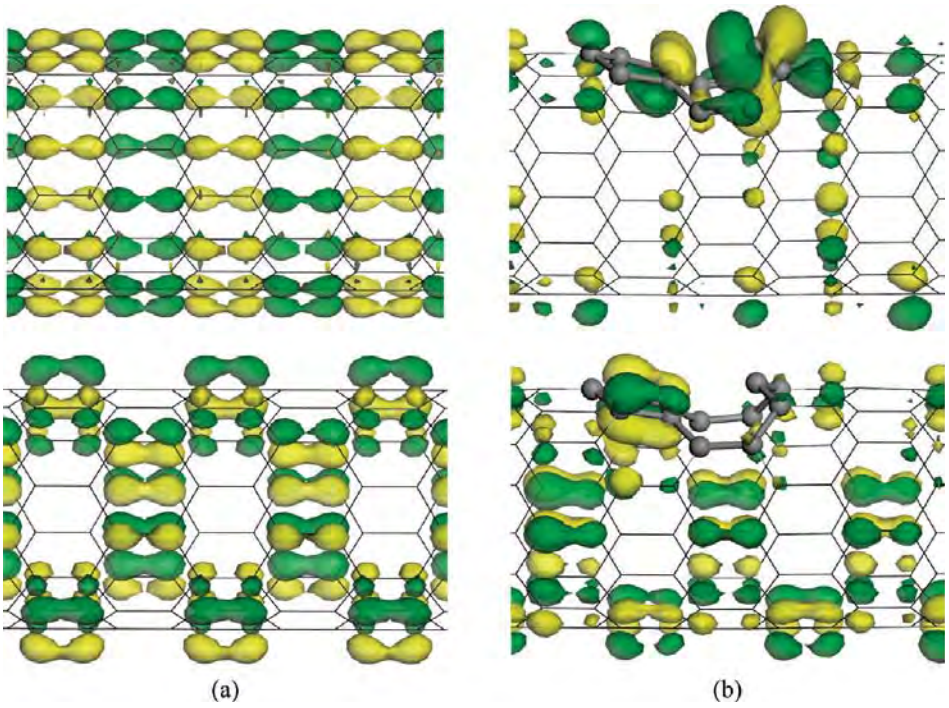

Figure 2. Lowest unoccupied molecular orbital (LUMO, top) and highest occupied molecular orbital (HOMO, bottom) of (a) pSWNCT and (b) symmetrical dSWCNT, plotted with an isovalue of ± 0.03 e·Å^{-3}.

between two adjacent defect or reaction sites on the same carbon nanotube was larger than 10 Å, in order to neglect the intermolecular interactions between defect sites. The periodic calculations were carried out by the density functional theory (DFT) method with the Perdew−Burke−Ernzerhof (PBE) functional[28] as implemented in the DMol^3 package.[29,30] The generalized gradient approximation (GGA) and an all-electron double numerical basis set plus d-functions (DND) were chosen for these spin-unrestricted computations. The DND basis set corresponds to a double-ζ quality basis set with d-type polarization functions added to heavier atoms; it is comparable to the 6-31G* Gaussian basis sets. The real-space global cutoff radius was set to be 3.70 Å. The Brillouin zone was sampled by the Monkhorst−Pack scheme.[31] For geometrical optimizations and orbital analysis, only the Γ point was considered in the Brillouin zone and all atom positions were fully optimized until all the forces on the atoms were less than 0.05 eV·Å^{-1}. In order to gain accuracy, the k points were increased to be $1 \times 1 \times 10$ to calculate the electronic properties. All possible mechanisms were searched.

The binding energy (E_b) of all reaction steps was calculated from the following equation, where n is the number of CO_x molecules (n = 0, 1, or 2; CO_x = CO or CO_2):

$$E_b(\text{dSWCNT-}n\text{CO}_x) = [E(\text{dSWCNT}) + nE(\text{CO}_x)] - E(\text{dSWCNT-}n\text{CO}_x) \quad (1)$$

RESULTS AND DISCUSSION

A new mechanism of healing the monatomic vacancy defect in dSWCNT is proposed here that uses CO disproportionation. The mechanism pathway is proposed as follows, where the perfect (8, 0) SWCNT is noted as pSWCNT:

CO adsorption process:

$$\text{dSWCNT} + 2\text{CO} \rightarrow \text{dSWCNT-CO-CO}$$

CO coadsorption process:

$$\text{dSWCNT-CO} + \text{CO} \rightarrow \text{dSWCNT-CO-CO}$$

Healing and desorption processes:

$$\text{dSWCNT-CO-CO} \rightarrow \text{pSWCNT} + \text{CO}_2$$

The electronic properties of the pSWCNT were calculated, yielding an energy gap (E_{gap}) of 0.65 eV, which is close to our recent work[27] dealing with both experimental and theoretical data. This energy gap confirms the semiconducting behavior of the zigzag (8, 0) carbon nanotube, which obeys the $(n - m) \neq 3i$ rule.

After elimination of the C* atom, the 12-membered ring remains with different initial distances, C1···C9 of 2.440 Å and C1···C5 and C1···C9 of 2.467 Å. The tube curvature distorts the 120° hybridization angle of the sp^2 C*, and the C1−C*−C9 and C5−C*−C9 angles decreased by 3.15° and 0.31°, respectively. This leads to a first-aid self-healing process forming the 5- and 9-membered rings. These 5−9 rings can be considered as two optimized configurations: a symmetrical form with the C1−C9 bond and an asymmetrical form with the C1−C5 bond (symmetrically equivalent to the C9−C5 bond). The symmetrical form is favorable due to a shorter initial distance and a lower relative energy by 29.65 kcal·mol^{-1}. Therefore, the symmetrical dSWCNT is chosen in this study.

dx.doi.org/10.1021/jp110616c |J. Phys. Chem. C 2011, 115, 4649–4655

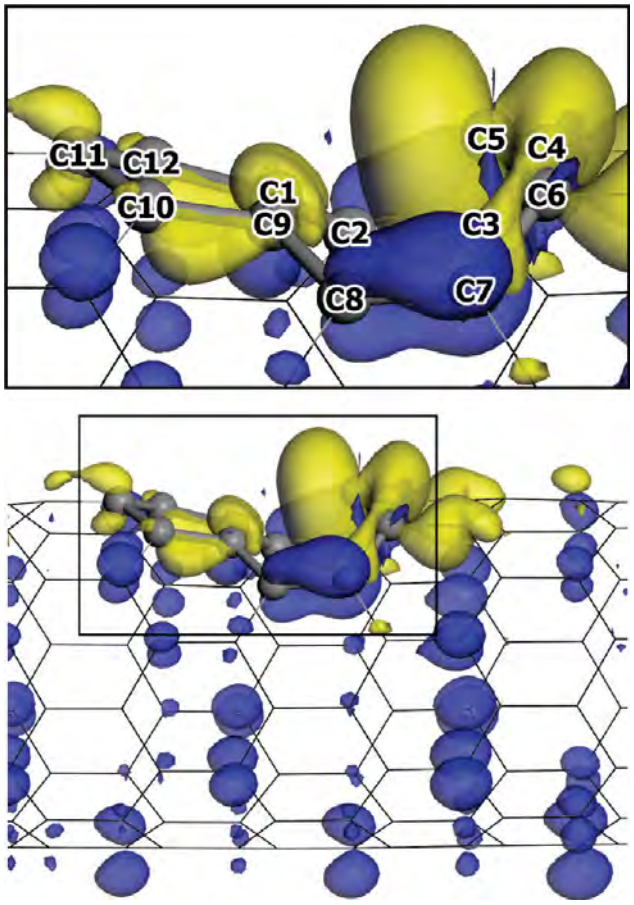

Figure 3. Nucleophilic Fukui function plot of symmetrical dSWCNT plotted with an isovalue of ±0.03 e·Å^{-3}. The plot was zoomed in and labeled as shown in the box.

The dSWCNT loses its semiconducting properties[32] with a new, metallic E_{gap} of 0.43 eV (33.8% lower than that of the pSWCNT). This is caused by new energy states of the defect sites being introduced within the band gap. The defect energy states are shown clearly in the LUMO level of the dSWCNT (Figure 2), the electrons of which occupy mostly the defect site. Therefore, the vacancy defects, even a monatomic vacancy, play an important role in the electronic properties of carbon nanotubes, confirming that a healing process is needed in order to maintain the original properties.

The nucleophilic Fukui function plots of the dSWCNT are shown in Figure 3. The strong nucleophilic zones cover mainly the defect site, particularly at the C5. Its sp hybridization lifts the C5 position away from the tube axis in order to lower its electronic repulsion with the tube atoms (Figure 4a). The plots suggest the adsorption mechanism of an incoming CO molecule. Two adsorption orientations are observed, which are dSWCNT-CO and dSWCNT-OC. dSWCNT-OC is found to be unfavorable due to a repulsive force between the nucleophilic defect site of the dSWCNT and the oxygen atom of the CO. Thus, the CO adsorption is guided by the C5, which is the main active site, and the dSWCNT-CO direction is preferable for a nucleophilic attack to the carbon atom (partial positive charge) of the CO molecule. Fortunately, the CO molecule is much less attracted to a perfect site [E_b(dSWCNT-CO) on the perfect site is 0.50 kcal·mol^{-1}]. This is caused by the low polarity of the perfect carbon nanotube and the high polarity of the CO molecule. Therefore, the CO adsorption occurs highly selectively on the defect site.

Simultaneous adsorption of two CO reactants is considered in two cases, which correspond to high and low CO concentrations in the experiment. The calculations lead us to postulate two different pathways: the associative-coadsorption pathway (ACP) and the consecutive-coadsorption pathway (CCP).

For the ACP at high CO concentration, two CO molecules (the first and second are labeled as C′O′ and C″O″, respectively) are associatively coadsorbed on each of the two nucleophilic sites (C5 and assisted C1−C9), building a coadsorption (Coads) structure at C5−C′−O′ and C1−C″(−O″)−C9. The C″O″ Coads is doubly assisted by both the C1 and C9, then breaks the C1−C9 bond in the 5-membered ring, forming a 6-membered-ring cyclization of C″−C9−C10−C11−C12−C1, as shown in Figure 4b. The C″ and C5 atoms are then bonded via the transition state TS_1 (Figure 4c) with activation energy of 2.82 kcal·mol^{-1} in order to create two new 6-membered rings, giving a more stable intermediate (Int_1) with a C″−C5 bond length of 1.539 Å, as shown in Figure 4d. This bonding also induces the O″ (partial negative charge) connected to C′ with a bond length of 1.373 Å, bringing about the 4-membered-ring cyclization of C″−O″−C′−C5. This causes a lengthening of the C″−O″, C′−C5, and C′−O′ bonds to 1.520, 1.556, and 1.198 Å, respectively. Next, the C″−O″ and C5−C′ bonds are broken with atomic distances of 2.065 and 1.655 Å, respectively, by the opening of the 4-membered-ring with an activation energy of 9.37 kcal·mol^{-1} via TS_2 (Figure 4e). This step is supported by the strong electron resonance of O″−C′−O′. The C′−O″ bond is shortened from 1.373 to 1.280 Å whereas the C′−O′ bond is lengthened from 1.198 to 1.215 Å in order to symmetrically balance the dioxide group. Finally, the carbon dioxide molecule (O″−C′−O′) as a product leaves both the defect and perfect sites of the carbon nanotube immediately without any binding energy [E_b(dSWCNT-CO_2) are 0.54 and 0.46 kcal·mol^{-1}, respectively]. The C5···C′ atomic distance is lengthened to 3.590 Å, while the remaining carbon atoms of the dSWCNT, including C″, reconstructed the pSWCNT with identical carbon−carbon bonds of 1.421 Å, as shown in Prod (Figure 4f).

At low CO concentration, the CCP can be subdivided into two subpathways called here CCP-1 and CCP-2. The proposed CCP-1 involves the C5−C′−O′ bond as shown in Ads_1 (Figure 4g). C′O′ is adsorbed strongly on C5, giving a C′−C5 bond length of 1.320 Å with an E_b of 48.47 kcal·mol^{-1}. Thus, the C′−O′ and C4−C5 (symmetrically the same as C5−C6) bonds are weakened from 1.141 to 1.176 Å and from 1.390 to 1.492 Å lengths, respectively. On the other hand, C1 (symmetrically the same as C9) can assist C5 for the adsorption, forming C1−C′(−O′)−C5 bonds and 5−6−7 fused rings, called CCP-2, as shown in Ads_2 (Figure 4h). This binding energy of the C′O′ adsorption is lower, with 43.33 kcal·mol^{-1}, than that in CCP-1, resulting in longer C′−O′ and C′−C5 bond lengths of 1.217 and 1.499 Å. The assisted C′−C1 bond is 1.538 Å in length. Even the assistance of C1 is explored; the dually assisted C1 and C9 for the C′O′ adsorption is not favorable because the C1−C9 bond of the 5-membered ring is hardly broken unless supported by the coadsorption. The C′O′ adsorption site at C5 via CCP-1 is favorable due to: the high nucleophilic C5 and the unstable sp^3 hybridization angle of C′−C1−C9 of 85.31° in the Ads_2 structure of CCP-2.

For CCP-2, no nucleophilic active site remains on the carbon nanotube defect for another CO adsorption; therefore, a subsequent

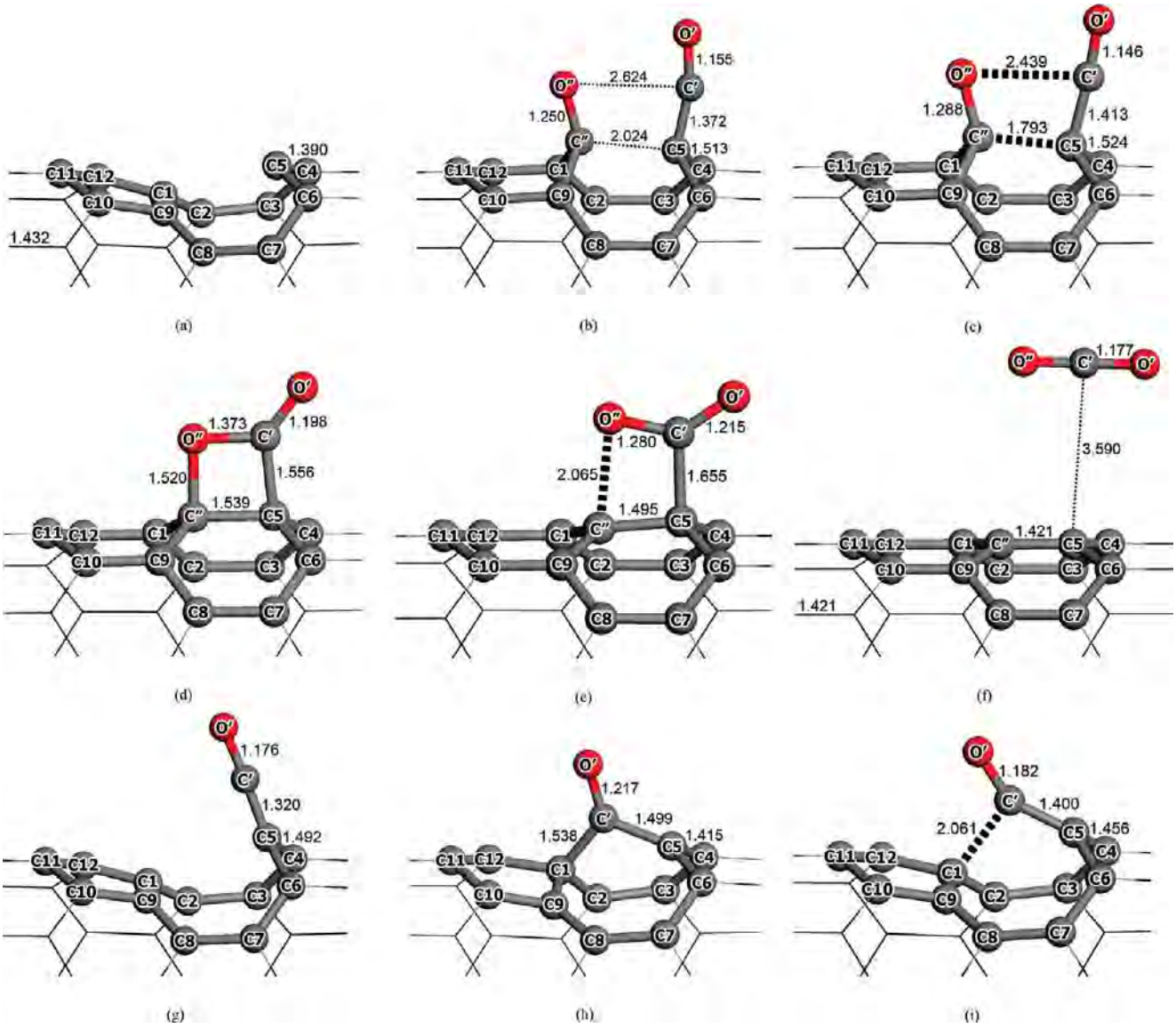

Figure 4. Optimized geometries of reaction steps in the proposed mechanisms (see Figures 5 and 6): (a) Subs; (b) Coads; (c) TS_1; (d) Int_1; (e) TS_2; (f) Prod; (g) Ads_1; (h) Ads_2; and (i) TS_3. Selected bond lengths and atomic distances are presented in angstrom units.

coadsorption from this step is impossible. Owing to the weakness of C1 in Ads_2, as described above, the C1−C′ bond is stretched with a length increasing from 1.538 to 2.061 Å. It is then broken through the transition state TS_3 (Figure 4i) by the 6-membered ring opening, forming Ads_1 with an activation energy of 14.49 kcal·mol^{-1}. In addition, this 6-membered ring opening requires a higher activation energy than that of the 4-membered ring opening in the ACP due to the lower stress in the larger ring. Surprisingly, the bypass CCP-2 merges with CCP-1 at this step. After the combination of these subpathways, the C″O″ molecule is then adsorbed on two remaining nucleophilic sites (C1 and C9), forming the same Coads structure as that in the ACP. Due to the repulsive force between the O″ and O′ atoms, the C′O′ group changes its position with a C′···O″ distance of 2.624 Å and C″···C5 distance of 2.024 Å. The C′O′ adsorption is also affected by the bond weakened from 1.320 to 1.372 Å. Thus, the reaction of the CCP continues from Coads to Prod following the ACP.

The energy profiles of the ACP and CCP are illustrated in Figures 5 and 6, respectively. For high CO concentrations, it is found that the ACP proceeds with overall activation energy of 9.37 kcal·mol^{-1} of the 4-membered ring opening as the rate-determining step. On the other hand, -1 presents a barrierless CO adsorption whereas he CCP-2 introduces a new barrier of 14.49 kcal·mol^{-1}. Although CCP-1 is kinetically controlled, CCP-2 occurs with only 5.14 kcal·mol^{-1} energy difference of the adsorption step. Therefore, for the lower CO concentration condition, a higher reaction temperature will be needed. The CCP process uses the carbon atom (C″) from the coadsorption of the second CO (C″O″) to fill in the vacancy in the healing. This mechanism thus proposes that a mole of monatomic vacancies of a SWCNT can be healed by two moles of CO, giving a mole of CO_2 as a product. In other words, the vacancy defect in the CNTs can convert two toxic CO molecules to a CO_2 molecule. Additionally, no oxygen molecule will be found as a

dx.doi.org/10.1021/jp110616c |J. Phys. Chem. C 2011, 115, 4649–4655

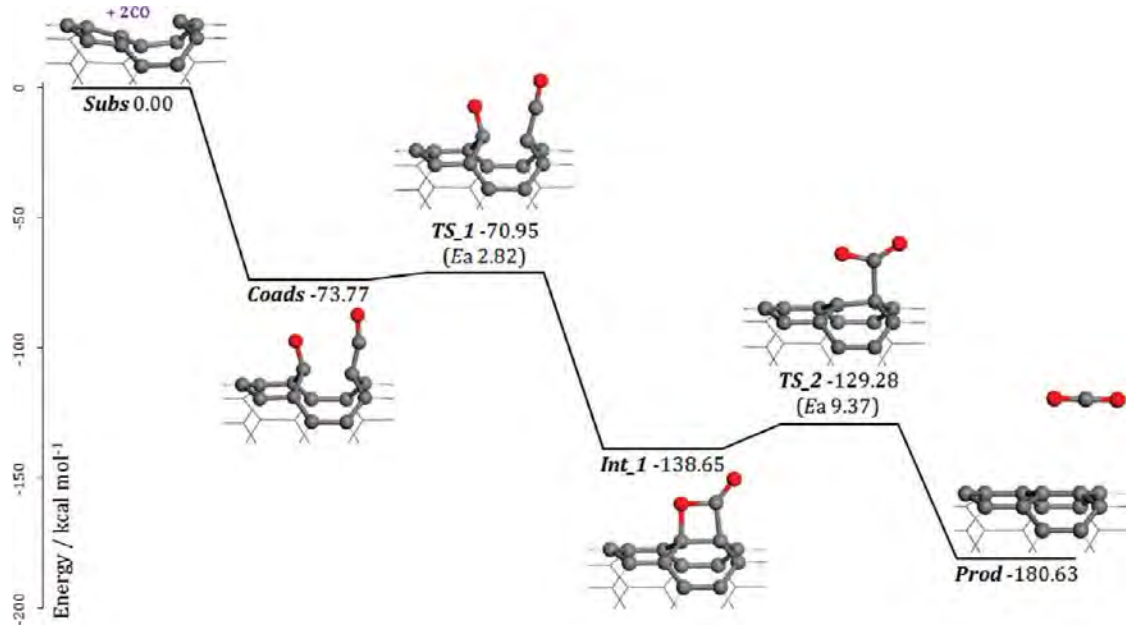

Figure 5. Energy profile of the associative-coadsorption pathway (ACP) of the healing process of the monatomic vacancy defect in the (8, 0) SWCNT by carbon monoxide disproportionation, as proposed at high CO concentrations.

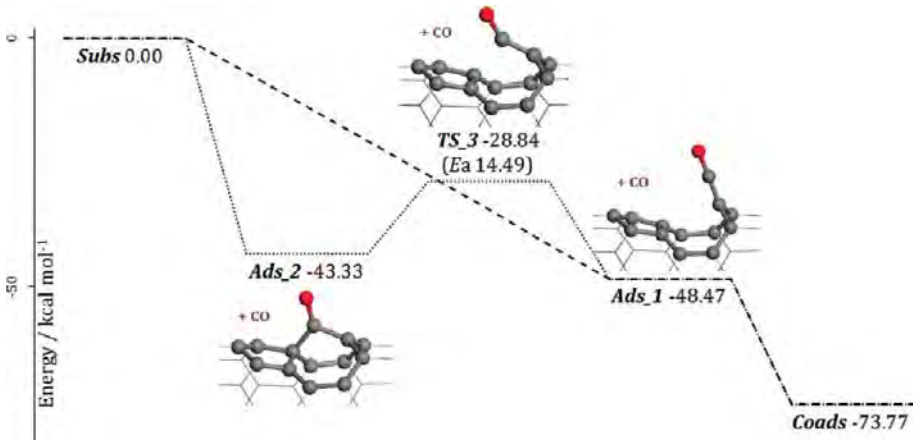

Figure 6. Energy profile of the consecutive-coadsorption pathway (CCP) of the healing process of the monatomic vacancy defect in the (8, 0) SWCNT by carbon monoxide disproportionation, as proposed at low CO concentrations. (---) CCP-1; (···) CCP-2.

byproduct. Thus, oxidation, oxidative combustion, and ozone etching of the SWCNTs can be avoided.

CONCLUSION

DFT calculations with the PBE functional are used to investigate reaction mechanisms for the healing process of a monatomic vacancy defect in SWCNT via carbon monoxide disproportionation. At high CO concentrations, the reaction can proceed via the associative-coadsorption pathway with a barrierless CO coadsorption, while at low concentrations the consecutive-coadsorption pathway introduces a new barrier of 14.49 kcal·mol^{-1}. The advantages of the healing process are: low activation energy of 9.37 kcal·mol^{-1} at the 4-membered ring opening step at high CO concentrations, no catalyst needed—thus no purification step is needed to remove the catalyst, the ambient CO can be used as a reactant, no oxygen byproduct is found, and there is high selectivity of CO for vacancy defect sites. Our findings prove that a vacancy defect in CNT, which occurs from syntheses or other uses as a nanomaterial device, can be healed to a perfect CNT holding the original electronic properties.

AUTHOR INFORMATION

Corresponding Author

*Fax +66 2562 5555, ext 2176; e-mail jumras.l@ku.ac.th.

ACKNOWLEDGMENT

This work was supported in part by grants from the National Science and Technology Development Agency (2009 NSTDA Chair Professor funded by the Crown Property Bureau under the management of the National Science and Technology Development Agency and the NANOTEC Center of Excellence funded

by the National Nanotechnology Center), Kasetsart University Research and Development Institute (KURDI), the Thailand Research Fund (TRF), the Commission on Higher Education, Ministry of Education [the "National Research University Project of Thailand (NRU)" and the "National Center of Excellence for Petroleum, Petrochemical and Advanced Materials (NCE-PPAM)"], and the Development and Promotion of Science and Technology Talents Project (DPST). The Kasetsart University Graduate School is also acknowledged. The computational calculations were supported by the Thai National Grid Center (TNGC) under the Software Industry Promotion Agency (SIPA).

REFERENCES

(1) Iijima, S.; Ichihashi, T. *Nature* **1993**, *363*, 603.
(2) Bethune, D. S.; Klang, C. H.; de Vries, M. S.; Gorman, G.; Savoy, R.; Vazquez, J.; Beyers, R. *Nature* **1993**, *363*, 605.
(3) Li, J.; Lu, Y.; Ye, Q.; Cinke, M.; Han, J.; Meyyappan, M. *Nano Lett.* **2003**, *3*, 929.
(4) Wang, J. *Electroanalysis* **2005**, *17*, 7.
(5) Krainara, N.; Nokbin, S.; Khongpracha, P.; Bopp, P. A.; Limtrakul, J. *Carbon* **2010**, *48*, 176.
(6) Kong, J.; Franklin, N. R.; Zhou, C.; Chapline, M. G.; Peng, S.; Cho, K.; Dai, H. *Science* **2000**, *287*, 622.
(7) Pannopard, P.; Khongpracha, P.; Probst, M.; Limtrakul, J. *J. Mol. Graphics Model.* **2009**, *28*, 62.
(8) Zhang, Y.; Zhang, D.; Liu, C. *J. Phys. Chem. B* **2006**, *110*, 4671.
(9) Fan, Y.; Goldsmith, B. R.; Collins, P. G. *Nat. Mater.* **2005**, *4*, 906.
(10) Mawhinney, D. B.; Naumenko, V.; Kuznetsova, A.; Yates, J. T.; Liu, J.; Smalley, R. E. *Chem. Phys. Lett.* **2000**, *324*, 213.
(11) Kang, D.; Kato, K.; Kojima, K.; Uchida, T.; Tachibana, M. *Appl. Phys. Lett.* **2008**, *93*, No. 133102.
(12) Stone, A. J.; Wales, D. J. *Chem. Phys. Lett.* **1986**, *128*, 501.
(13) Suekane, O.; Nagataki, A.; Nakayama, Y. *Appl. Phys. Lett.* **2006**, *89*, No. 183110.
(14) Tsetseris, L.; Pantelides, S. T. *Carbon* **2009**, *47*, 901.
(15) Borrnert, F.; Gorantla, S.; Bachmatiuk, A.; Warner, J. H.; Ibrahim, I.; Thomas, J.; Gemming, T.; Eckert, J.; Cuniberti, G.; Buchner, B.; Rummeli, M. H. *Phys. Rev. B* **2010**, 81.
(16) Tsetseris, L.; Pantelides, S. T. *J. Phys. Chem. B* **2009**, *113*, 941.
(17) Chen-Li, Z.; Hui-Shen, S. *J. Phys.: Condens. Matter* **2007**, *19*, No. 386212.
(18) Miyamoto, Y.; Berber, S.; Yoon, M.; Rubio, A.; Tománek, D. *Chem. Phys. Lett.* **2004**, *392*, 209.
(19) Page, A. J.; Ohta, Y.; Okamoto, Y.; Irle, S.; Morokuma, K. *J. Phys. Chem. C* **2009**, *113*, 20198.
(20) Page, A. J.; Ohta, Y.; Irle, S.; Morokuma, K. *Acc. Chem. Res.* **2010**, *43*, 1375.
(21) Nikolaev, P.; Bronikowski, M. J.; Bradley, R. K.; Rohmund, F.; Colbert, D. T.; Smith, K. A.; Smalley, R. E. *Chem. Phys. Lett.* **1999**, *313*, 91.
(22) da Silva, L. B.; Fagan, S. B.; Mota, R. *Nano Lett.* **2003**, *4*, 65.
(23) Mota, R.; Fagan, S. B.; Fazzio, A. *Surf. Sci.* **2007**, *601*, 4102.
(24) Wang, R.; Zhang, D.; Sun, W.; Han, Z.; Liu, C. *J. Mol. Struct. THEOCHEM* **2007**, *806*, 93.
(25) Khongpracha, P.; Probst, M.; Limtrakul, J. *Eur. Phys. J. D* **2008**, *48*, 211.
(26) Yong-Hui, Z.; et al. *Nanotechnology* **2009**, *20*, No. 185504.
(27) Nongnual, T.; Nokbin, S.; Khongpracha, P.; Bopp, P. A.; Limtrakul, J. *Carbon* **2010**, *48*, 1524.
(28) Perdew, J. P.; Burke, K.; Ernzerhof, M. *Phys. Rev. Lett.* **1996**, *77*, 3865.
(29) Delley, B. *J. Chem. Phys.* **1990**, *92*, 508.
(30) Delley, B. *J. Chem. Phys.* **2000**, *113*, 7756.
(31) Monkhorst, H. J.; Pack, J. D. *Phys. Rev. B* **1976**, *13*, 5188.
(32) O'Connell, M. J.; Bachilo, S. M.; Huffman, C. B.; Moore, V. C.; Strano, M. S.; Haroz, E. H.; Rialon, K. L.; Boul, P. J.; Noon, W. H.; Kittrell, C.; Ma, J.; Hauge, R. H.; Weisman, R. B.; Smalley, R. E. *Science* **2002**, *297*, 593.

Electrochimica Acta 56 (2011) 10562–10566

Contents lists available at ScienceDirect

Electrochimica Acta

journal homepage: www.elsevier.com/locate/electacta

Straightforward single-step generation of microswimmers by bipolar electrochemistry

Z. Fattah [a], G. Loget [a,1], V. Lapeyre [a], P. Garrigue [a], C. Warakulwit [b], J. Limtrakul [b], L. Bouffier [a,1], A. Kuhn [a,*,1]

[a] Université Bordeaux, ISM, ENSCBP, 33607 Pessac, France
[b] Center for Advanced Studies in Nanotechnology for Chemical, Food and Agricultural Industries, Center of Nanotechnology and Chemistry Department, Kasetsart University, Bangkok 10900, Thailand

ARTICLE INFO

Article history:
Received 19 November 2010
Received in revised form 16 January 2011
Accepted 17 January 2011
Available online 22 January 2011

Keywords:
Microswimmers
Janus particles
Bipolar electrochemistry
Carbon tubes

ABSTRACT

Autonomous microswimmers are of enormous interest not only from an academic point of view, but also for future practical applications ranging from miniaturized motors to nanomedicine. A key step for the generation of such objects is their dissymmetric modification with a catalyst particle that activates the chemical conversion of a fuel molecule, leading ultimately to the propulsion of the object. So far it has been quite difficult to synthesize such dissymmetric objects and most approaches are based on using interfaces to break the symmetry. We demonstrate here that a very simple approach based on bipolar electrochemistry allows the bulk generation of carbon microtubes that are modified selectively at one end with a Pt cluster. The presence of this metal cluster allows the catalytic decomposition of hydrogen peroxide and the resulting oxygen bubbles trigger the propulsion of the object. The type of motion can be switched from linear to circular as a function of the exact position of the Pt cluster.

1. Introduction

In the frame of the intensive current efforts to develop micro- and nanomotors, one of the most fascinating domains is the research on autonomous swimmers, able to move in fluids under the influence of external parameters, like the presence of physical fields or chemical fuels [1]. In the latter case, which is the topic of the present work, the motion is generated by the conversion of locally available chemical energy into mechanical energy with the help of catalysts that are localized on one part of the swimmer. Many reports have appeared in the literature on the synthesis of heterogeneous objects at the micrometer or nanometer scale in order to carry out catalytic reactions at their different ends [2]. These systems are of great application potential in the field of nanoscience, due to their ability to accomplish various tasks at a tiny scale, inspired for example by natural biomachines such as kinesin (a linearly progressing motor in the cell) [3] or flagellar motion [4]. The recent research in nanotechnology has focused on a variety of such micro- and nanomotors, using different design principles and various catalysts in order to induce and control their motion [5–7].

Generally there are three methods to induce the motion of these objects:

(1) Biochemical fueling which is based on the functionalization of an object with catalytically active enzymes, converting natural fuel into kinetic energy [8,9]. (2) Physical fueling which implies applying an external electric [6,10], or magnetic field [4,11]. (3) Chemical fueling for objects of different design, such as gear-like structures [5], metal nanorods [7,12], nanorotors [13,14] and millimeter-sized plates [15]. In many of the cases the structure includes a metallic segment, that acts as the catalytic site for the decomposition of hydrogen peroxide to water and oxygen gas, which in turn generates the motion either by interfacial tension gradients [5,12], or recoil from oxygen bubbles [14,15]. In this context a key step in the design of the microswimmers is the dissymmetric placement of the catalyst, which is achieved most of the time using rather complex methods such as deposition through the pores of membranes [16] or vapor deposition processes [14]. Moreover, because these processes are occurring in a two-dimensional reaction space, the yield of product is quite limited and therefore not well-adapted for large-scale production.

In this contribution we propose a straightforward single-step procedure based on bipolar electrochemistry to prepare carbon microtubes (CMTs) that are modified in a dissymmetric way with a platinum catalyst. Depending on the exact location of the catalyst cluster this allows subsequently the propulsion of these objects either on a linear or circular trajectory.

Bipolar electrochemistry occurs when a conducting object is exposed to an electric field which induces a polarization that is sufficiently high to allow oxidation and reduction reactions at the

* Corresponding author. Tel.: +33 5 40 00 65 73; fax: +33 5 40 00 27 17.
E-mail address: kuhn@enscbp.fr (A. Kuhn).
[1] ISE member.

0013-4686/$ – see front matter © 2011 Elsevier Ltd. All rights reserved.
doi:10.1016/j.electacta.2011.01.048

opposite ends of the object, in the absence of direct contact between the object and the power supply [17,18].

This principle has found several interesting applications for pattering surfaces [19,20], sensing [21], generating electrochemiluminescence [18,22,23], membrane pore functionalization [24], establishing electrical contacts [25], propulsing micro objects [6] and as a powerful bulk procedure for creating dissymmetric objects (Janus-type particles) such as single point modified carbon micro- and nanotubes [11,26]. Here we will show that the procedure can be adapted not only to the selective formation of Pt clusters at one end of a CMT, but also to influence the orientation of the metal deposit with respect to the tube axis, which gives the possibility to generate two types of motion, a linear one and a circular one.

2. Experimental

2.1. Preparation and modification of carbon microtubes

The carbon microtubes used in this study were produced by chemical vapor deposition using a porous aluminum oxide membrane serving as a template [27]. After an acidic digestion of the template, the fairly homogeneous tubes were recovered as a powder. The suspension of CMTs was obtained by the addition of CMTs (0.3 mg) to absolute ethanol (1.25 ml). The formation of the suspension was accelerated by sonicating the mixture for a short time (1 min) in order to avoid excessive breaking of the tubes. After 30 min of sedimentation, 0.5 ml of the supernatant was taken and added to 1.5 ml of a freshly prepared 60 mM H_2PtCl_6 solution in ultrapure water (hexachloroplatinic acid hexahydrate, ACS reagent grade, purchased from Sigma–Aldrich Co.). The suspension was sonicated for a few seconds to disperse the tubes and directly employed for the bipolar electrodeposition process analogous to what has been described previously [11,26]. An electric field of 30 kV/m was applied to polarize the CMTs according to the relationship:

$$\Delta V_{max} = E\,l \quad (1)$$

where ΔV_{max} is the maximum potential difference generated between both sides of the microtube, E is the total electric field and l is the length of the CMT.

2.2. Characterization of modified carbon microtubes—observation of hydrogen peroxide decomposition and CMT motion

The suspension containing the modified carbon tubes was collected after the bipolar electrodeposition experiment and observed between two glass slides with a transmission optical microscope (Zeiss, Imager M1). Before the characterization with the scanning electron microscope (Hitachi, TM-1000), the suspension was dried on a conductive substrate.

For observing the movement of the modified carbon tubes, one drop of the suspension was dried on a glass slide and the swimmers were observed with the transmission optical microscope. 5 μl of a solution of 30 wt.% hydrogen peroxide in water (purchased from Sigma–Aldrich Co.) were then added on top of the slide with the tubes. Videos were recorded using a CCD camera.

3. Results and discussion

3.1. Microswimmer preparation

Let us first consider the two redox reactions that should take place at each side of the CMT:

$$Pt^{IV}Cl_6{}^{2-}{}_{(aq)} + 4e^- \rightarrow Pt^0{}_{(s)} + 6Cl^-{}_{(aq)} \quad E^\circ = +0.73\,V/_{NHE}$$

$$2H_2O_{(l)} \leftrightarrow 4H^+{}_{(aq)} + O_{2(g)} + 4e^- \quad E^\circ = +1.23\,V/_{NHE}$$

In order to trigger both reactions at the opposite ends of the tube we assume in a first order approximation that the polarisation has to generate a potential difference which is at least equal to the difference of the formal potentials of the two redox couples. In the present case this difference is 0.5 V and, according to Eq. (1), it is clear that an electric field of at least 25 kV/m must be applied in order to induce the deposition of platinum onto a 20 μm-long CMT.

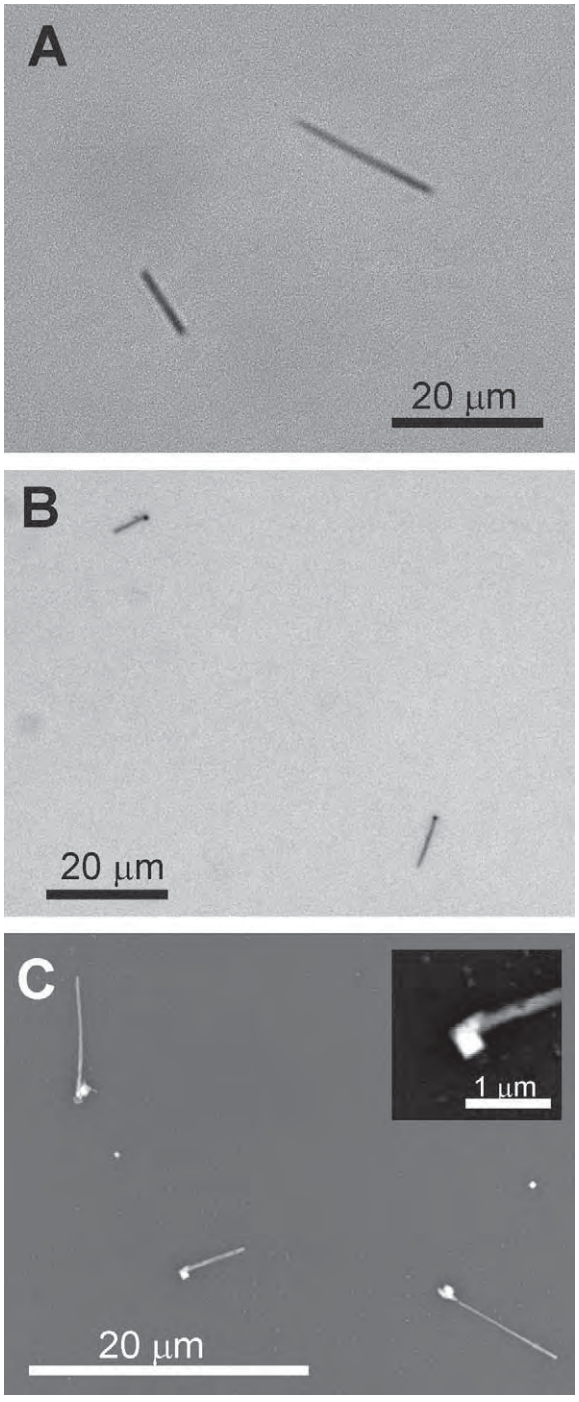

Fig. 1. Transmission optical micrograph (50 times magnification) of (A) unmodified carbon microtubes (CMTs) and (B) CMTs with either asymmetric (top left) or symmetric (bottom right) platinum deposits obtained by using bipolar electrodeposition. (C) Scanning electron microscopy image of platinum modified CMTs. Inset: magnified SEM image of the platinum deposit.

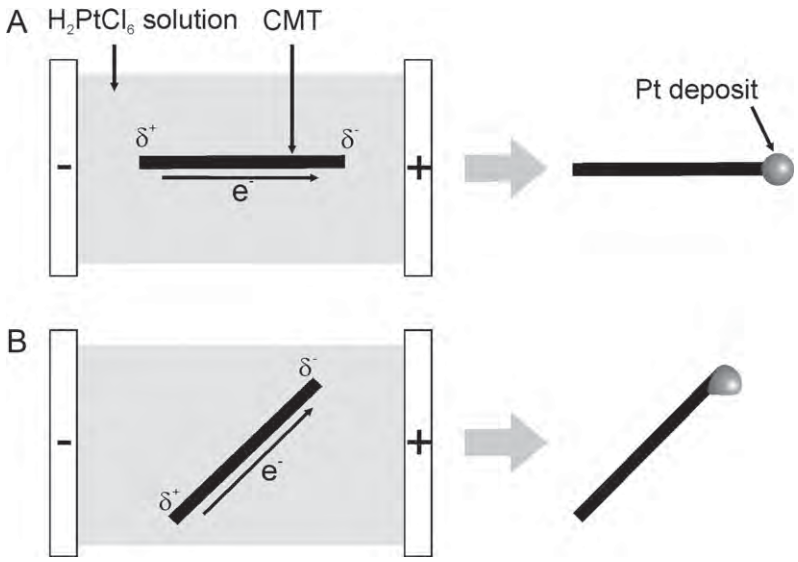

Fig. 2. Schematic illustration explaining the origin of different deposit locations obtained for CMTs as a function of their orientation in the electric field at the beginning of the electrodeposition process. (A) Aligned parallel to the electric field and (B) non-aligned with the electric field.

As reported previously, such high electric fields can be achieved with a capillary electrophoresis set-up [11]. Experimentally, we applied a slightly larger electric field (30 kV/m) to make sure that also a majority of shorter CMTs are modified. This corresponds to a good compromise because the difference of potential (ΔV) between both sides of the CMT is higher than the thermodynamic threshold value necessary for the concomitant redox reactions, but still low enough to avoid bubble formation which would disturb the experiment and cause detaching of the Pt deposit from the CMTs' extremity.

3.2. Microswimmer characterization

The major reason for choosing carbon microtubes instead of carbon nanotubes [26] in this work is the ease of visualization of the achieved modification and especially of the generated motion by standard optical microscopy. An optical micrograph of two unmodified carbon microtubes is given in Fig. 1A. Both tubes are representative of the sample containing a population of tubes with a length ranging from 5 to 20 μm. Fig. 1B has been obtained after exposing the carbon tubes to the electric field in a solution containing the platinum salt. The experiment shows clear evidence for a dissymmetric deposition of platinum at one extremity of the tubes by the bipolar electrochemistry approach. Samples have been prepared at a quite high dilution in order to avoid superposition of several tubes. Careful examination of the samples highlights two slightly different topologies. The tube (length ~ 9 μm) located at the bottom of the right side of the picture is modified in a symmetrical way with the Pt particle centered on the C2 axis of the tube. On the other hand, the shorter tube in the top left corner (length ~ 6 μm) has been modified in a non-symmetrical fashion as the particle is positioned slightly off the tube axis.

This difference might be explained on the basis of a mixed influence of two competing kinetic parameters, which are the electromechanical alignment time against the kinetic activation of the bipolar reaction. Indeed, a linear potential sweep is applied in order to reach the final working potential E_w. Theoretically, this potential ramp should last for a time long enough to allow an alignment of the tubes along the direction of the electric field before reaching the threshold value where the bipolar reaction starts taking place. In this case the experiment should lead theoretically to the formation of a symmetric electrodeposit of the Pt (Fig. 2A) with respect to the tube axis, because the nucleation point is located at the point of maximum polarization.

But the reality is more complicated because the carbon tubes of a given sample have a length distribution due to the preparation mode of the CMTs. Practically, the kinetics of alignment of a population of microtubes in a given electric field depends of three main variables: the initial orientation and the length of each tube, as well as the viscosity of the surrounding environment (the latter depending on another series of variables: solvent, temperature, nature and concentration of the supporting electrolyte). The interesting point is that these experimental conditions can be adjusted in order to tune the electrodeposition morphology (symmetrical *versus* non-symmetrical functionalization). The initial orientation of the tubes is a statistical distribution, but the subsequent alignment could be favored by applying an initial potential difference lower than the threshold value necessary for the bipolar reaction, followed by a potential step above the threshold value once the tubes are all aligned. On the other hand, the solvent choice is of first importance as the timescale of reorientation of the CMT could be either very short in water or substantially longer by adding a co-solvent with a higher viscosity. A precise tuning of the monodispersity of the tube length does not seem to be necessary as two opposite factors influence the alignment: First, the length of the tube directly influences the polarization between both extremities of the CMT. All tubes are exposed to the same electric field (30 kV/m) and that means that the polarization of a 20 μm-long carbon tube is twice as large as the polarization of a tube of 10 μm. This polarization is the driving force of the alignment, but mechanical counter forces also depend on the tube lengths. Indeed, the longer CMTs exhibit a bigger surface area in contact with the surrounding environment and are, therefore, more affected by the solvent viscosity contribution, which slows down the alignment. Experimentally we find that these two contributions do not seem to be of the same magnitude, because the longer CMTs have a higher tendency to be functionalized in a non-symmetrical fashion, meaning that they need more time to orientate in the electric field and during this time the deposition already occurs at the point of highest polarization, which in this case is not located at the center of the tube end, but at the edge. Consequently the Pt electrodeposit resulting from the reduction of H_2PtCl_6 directly grows from the most favorable nucleation site and generates an off-centered platinum/carbon tube hybrid as illustrated in Fig. 2B. One can note that

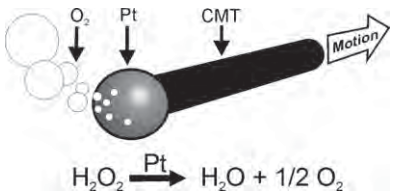

Fig. 3. Schematic illustration of the propulsion mechanism of a platinum-modified carbon tube moving in the opposite direction of the oxygen bubbles generated on the platinum catalyst.

this scenario is perfectly consistent with the extremely low surface mobility of the Pt atoms ($D_S = 10^{-18}$ cm^2 s^{-1} determined on highly oriented pyrolitic graphite, HOPG), which is several orders of magnitude lower than that of the Ag atoms for example [28].

The modified carbon tubes have also been characterized by SEM and a representative picture is given in Fig. 1C. Three successfully functionalized small tubes with a length between 5 and 8 μm can be observed and at high magnification (inset) a typical Pt particle is visible. Theoretically, the size of the platinum cluster should depend on the CMT's length, but other considerations have to be taken into account: a carbon tube which is imperfectly aligned exhibits a high polarization located at the edge of each extremity instead of the center, leading to a non-centered nucleation point. In this case the driving force is not proportional to the overall tube lengths but to the projection of the tube in the plane of the electric field lines.

Although the present study did not focus on the crystallographic structure of the Pt deposit, the observation of non-symmetrical electrodeposits is in favor of a single crystal nucleation and growth, because the alternative pathway involving several nucleation sites distributed over the whole extremity of the microtube should generate a symmetrical Pt topology.

In summary, the described characterization by optical and electron microscopy clearly demonstrates the successful electrodeposition of platinum at one extremity of the carbon tubes and therefore the controlled generation of Janus-type microobjects, which then can be used to generate a movement by applying an external stimulus.

3.3. Microswimmer propulsion

Platinum metal is a well-known catalyst which has been extensively used in organic synthesis (for example for catalytic hydrogenation) as well as in electrocatalysis. We first tested the ability of the newly prepared material to decompose hydrogen peroxide. Dioxygen bubble generation was immediately observed as

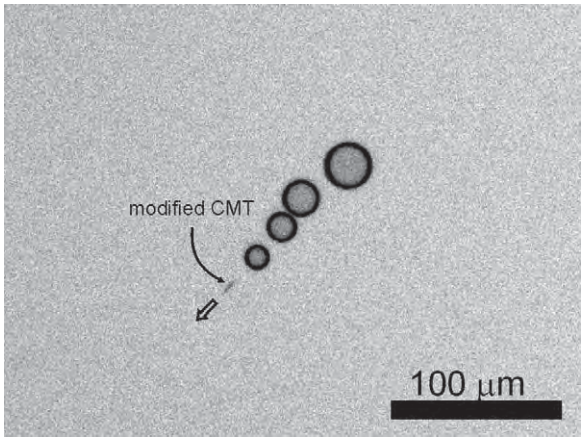

Fig. 4. Linear motion of the microswimmer leaving a bubble train behind observed under the optical microscope.

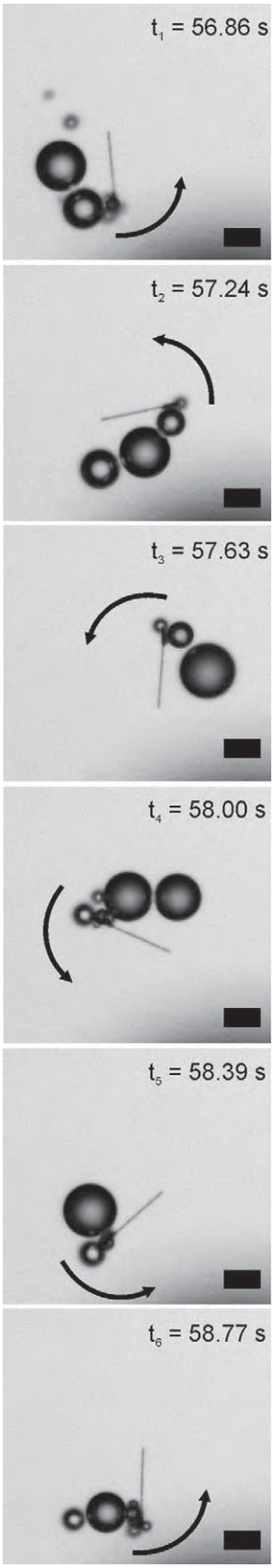

Fig. 5. Optical micrographs of a counter clockwise rotating microswimmer. Scale bar 10 μm.

soon as the Pt/CMT hybrid was in contact with the reactant solution according to the following dismutation equation:

$$H_2O_2 \rightarrow H_2O + 1/2O_2$$

The bubble production can be tuned by adjusting the hydrogen peroxide content and concentrated solutions like 30% H_2O_2 generated a very high activity. One can note that a control experiment with pure H_2O instead of H_2O_2 did never lead to any bubbles due to purely mechanical effects.

Fig. 3 gives a schematic representation of the mechanism responsible for the motion. The ideal situation corresponds to a CMT functionalized with a perfectly symmetric Pt particle at one extremity. The O_2 bubbles will generate a local mechanical perturbation and a subsequent movement of the object in the opposite direction.

The propulsion of a CMT is experimentally very challenging to image for several reasons. (1) The generation of a large quantity of bubbles is necessary to move the microhybrid, but these bubbles disturb the optical resolution by changing instantly the nature of the local environment surrounding the CMT. (2) The propulsion usually takes place in a three dimension referential (*xyz*) and the optical microscope is only able to focus on a single plane (*xy*). (3) The rate of bubble formation and the acceleration of the CMT do not take place at the same timescale and it is therefore very frequent that the CMT moves out of the focal plane of the microscope. Fig. 4 shows an optical micrograph of a CMT in motion. The four dioxygen bubbles were formed successively from right to left and this results in an efficient propulsion of the carbon tube towards the bottom–left corner of the picture. As mentioned previously, this linear mode of motion is directly linked to the morphology of the platinum deposit. A Pt particle perfectly centered at the middle of a CMT extremity results in an isotropic production of O_2 bubbles and therefore a linear motion. However a non-symmetric deposit (for example like in Fig. 1B and C) will generate bubbles anisotropically with respect to the tube axis. As a result, the mode of motion does change from a translation to a rotation. Fig. 5 shows a selection of six high magnification optical images of a CMT performing one anticlockwise turn. These data are extracted from a large set of images in which the microhybrid is spinning several times around the unfunctionalized extremity of the microtube. A time interval of 2.01 ± 0.14 s/turn was estimated from 10 full turns which allows calculating a speed of 29.9 ± 2.1 rpm (or a frequency of $\sim$0.50 Hz). The sequence of images in Fig. 5 clearly demonstrates that the driving force of the rotation is the non-symmetric O_2 formation, as the CMT is rotating in the opposite direction with respect to the bubble evolution. It is noteworthy that this rotating CMT is a particularly long one (roughly 20 μm), thus confirming that the length of the microtube seems to be one of the variables influencing the formation of a non-symmetrical Pt electrodeposit. At this stage the advantage of the present modification approach using bipolar electrochemistry with respect to other experiments, where rotational motion has been generated on purpose [14], becomes very clear. By changing the potential ramp and the solvent viscosity during the deposition experiment it is in principle possible to generate on purpose objects that can either undergo dominantly linear or rotational propulsion.

4. Conclusion

A single-step procedure based on the concept of bipolar electrochemistry has been successfully employed to create Janus-type carbon microtubes with a platinum metal deposit at one end either in a symmetric or dissymmetric orientation with respect to the tube's axis. This bulk process is straightforward and well adapted to generate microswimmers with a high efficiency, whereas the majority of the literature processes are based on the use of interfaces or surfaces to generate such swimmers. Especially for rotational motion, sophisticated synthetic procedures have usually to be employed to generate the appropriate particles. In the present study, it is possible to generate swimmers that can perform both, rotational and linear motion as a function of the position of the Pt cluster with respect to the tube axis, which catalyzes the decomposition of hydrogen peroxide. The generated oxygen bubbles drive these microobjects either in a linear or a circular motion.

Bipolar electrochemistry can be also applied to generate such micro- and nanoobjects with a variety of other materials, in order to adapt the chemistry of the propulsion process for example to bioelectrochemical mechanisms [9]. Microswimmers elaborated using this or similar approaches [29] might one day move cargo in microfluidic devices, deliver pharmaceuticals, or track toxic molecules [30].

Acknowledgments

This work is part of the CUBIHOLE project funded by the European NanoSci-Era+ action under contract ANR-08-NSCI-008-01 and has also been supported by the French Ministry of Research (MESR), CNRS, and ENSCBP. C.W. and J.L. thank the National Science and Technology Development Agency (NSTDA Chair Professor and National Nanotechnology Center NANOTEC), the Commission on Higher Education, the Ministry of Education and the Thailand Research Fund for support.

References

[1] J. Wang, K.M. Manesh, Small 6 (2010) 338.
[2] S.J. Ebbens, J.R. Howse, Soft Matter 6 (2010) 726.
[3] G.A. Ozin, I. Manners, S. Fournier-Bidoz, A. Arsenault, Adv. Mater. 17 (2005) 3011.
[4] R. Dreyfus, J. Baudry, M.L. Roper, M. Fermigier, H.A. Stone, J. Bibette, Nature 437 (2005) 862.
[5] J.M. Catchmark, S. Subramanian, A. Sen, Small 1 (2005) 202.
[6] G. Loget, A. Kuhn, J. Am. Chem. Soc. 132 (2010) 15918.
[7] T.R. Kline, W.F. Paxton, T.E. Mallouk, A. Sen, Angew. Chem. Int. Ed. 44 (2005) 744.
[8] D. Pantarotto, W.R. Browne, B.L. Feringa, Chem. Commun. (2008) 1533.
[9] N. Mano, A. Heller, J. Am. Chem. Soc. 127 (2005) 11574.
[10] P. Calvo-Marzal, S. Sattayasamitsathit, S. Balasubramanian, J.R. Windmiller, C. Dao, J. Wang, Chem. Commun. 46 (2010) 1623.
[11] G. Loget, G. Larcade, V. Lapeyre, P. Garrigue, C. Warakulwit, J. Limtrakul, M.-H. Delville, V. Ravaine, A. Kuhn, Electrochim. Acta 55 (2010) 8116.
[12] W.F. Paxton, A. Sen, T.E. Mallouk, Chem. Eur. J. 11 (2005) 6462.
[13] S. Fournier-Bidoz, A.C. Arsenault, I. Manners, G.A. Ozin, Chem. Commun. (2005) 441.
[14] L. Qin, M.J. Banholzer, X. Xu, L. Huang, C.A. Mirkin, J. Am. Chem. Soc. 129 (2007) 14870.
[15] R.F. Ismagilov, A. Schwartz, N. Bowden, G.M. Whitesides, Angew. Chem. Int. Ed. 41 (2002) 652.
[16] N.S. Zacharia, Z.S. Sadeq, G.A. Ozin, Chem. Commun. (2009) 5856.
[17] M. Fleischmann, J. Ghoroghchian, D. Rolison, S. Pons, J. Phys. Chem. 90 (1986) 6392.
[18] F. Mavré, R.K. Anand, D.R. Laws, K.-F. Chow, B.-Y. Chang, J.A. Crooks, R.M. Crooks, Anal. Chem. 82 (2010) 8766.
[19] S. Ramakrishnan, C. Shannon, Langmuir 26 (2010) 4602.
[20] C. Ulrich, O. Andersson, L. Nyholm, F. Björefors, Anal. Chem. 81 (2009) 453.
[21] K.-F. Chow, B.-Y. Chang, B.A. Zaccheo, F. Mavré, R.M. Crooks, J. Am. Chem. Soc. 132 (2010) 9228.
[22] S.E. Fosdick, J.A. Crooks, B.-Y. Chang, R.M. Crooks, J. Am. Chem. Soc. 132 (2010) 9226.
[23] F. Mavré, K.-F. Chow, E. Sheridan, B.-Y. Chang, J.A. Crooks, R.M. Crooks, Anal. Chem. 81 (2009) 6218.
[24] A. Bouchet, E. Descamps, P. Mailley, T. Livache, F. Chatelain, V. Haguet, Small 5 (2009) 2297.
[25] J.-C. Bradley, J. Crawford, K. Ernazarova, M. McGee, S.G. Stephens, Adv. Mater. 9 (1997) 1168.
[26] C. Warakulwit, T. Nguyen, J. Majimel, M.-H. Delville, V. Lapeyre, P. Garrigue, V. Ravaine, J. Limtrakul, A. Kuhn, Nano Lett. 8 (2008) 500.
[27] C. Warakulwit, Ph.D. Thesis, Kasetsart University Bangkok and University Bordeaux 1, 2007.
[28] J.L. Zubimendi, L. Vázquez, P. Ocón, J.M. Vara, W.E. Triaca, R.C. Salvarezza, A.J. Arvia, J. Phys. Chem. 97 (1993) 5095.
[29] A. Ghosh, P. Fischer, Nano Lett. 9 (2009) 2243.
[30] M. Pumera, Nanoscale 2 (2010) 1643.

Journal of Molecular Liquids 159 (2011) 38–41

Contents lists available at ScienceDirect

Journal of Molecular Liquids

journal homepage: www.elsevier.com/locate/molliq

$Au(CN)_2(CH_3NO_2)_n$ cluster anions: Energetics and geometrical features

Natcha Injan [a,b], Tünde Megyes [c], Tamas Radnai [c], Imre Bako [c], Szabolcz Balint [c], Jumras Limtrakul [b,*], Michael Probst [a,*]

[a] Institute of Ion Physics and Applied Physics, Innsbruck University, Austria
[b] Center of Nanotechnology, Chemistry Department and Center for Advanced Studies in Nanotechnology and Its Applications in Chemical, Food and Agricultural Industries Kasetsart University, Bangkok, Thailand
[c] Chemical Research Centre of the Hungarian Academy of Sciences, Budapest, Hungary

ARTICLE INFO

Available online 24 November 2010

Keywords:
Au(I) dicyano anion
Solvation shell structure
Nitromethane
Cluster calculations
Quantum chemistry
Ion solvation

ABSTRACT

Gold cyanides are widely used in chemical processes involving this coin metal since they are stable and soluble under a wide range of conditions. Nitromethane (NM) is the most widely used solvent for ionic complexes of Au. We have performed extensive quantum chemical calculations on $Au(CN)_2NM_n^-$ clusters with n = 1–10. For smaller values of n (<6), geometries with NM coordinating to the nitrogen atoms at both ends of the linear anion are the most stable ones while for higher values of n a geometrical pattern with chains or rings of NM molecules becomes competitive. We also analyze the electrostatic potentials of NM and $Au(CN)_2^-$ and the electronic structure of the anion.

1. Introduction

Gold ions in non-aqueous solution are known since the early days of gold mining but increasingly find new applications in modern technologies. Examples are the processing of electronic scrap [1], the decoration of nanomaterials with gold [2] and new types of gold clusters [3], amongst others. Due to the high complexation tendency of gold ions, bare Au(I) or Au(III) ions are normally not present in solution. CN^- forms a soluble gold complex, Dicyanoaurate(I) anion ($Au(CN)_2^-$) which is widely used in industry. This gold complex is very stable and can be prepared as an alkaline salt, ($NaAu(CN)_2$ or $KAu(CN)_2$) by cyanidation of gold clusters [4]. However, in general little is known about the microscopic details of gold complexes in solution. In this work we study the interactions between $Au(CN)_2^-$ and its preferred solvent, nitromethane, by means of quantum chemical cluster calculations.

2. Methods

2.1. Quantum chemical calculations

We performed Hartree-Fock (HF) calculations with the LANL2DZ basis set [5] for Au(I) and the D95V basis set [6] for N, O, C and H. In a previous work [7] it was found that this combination is suitable to describe such systems in which the intermolecular interactions are governed by electrostatics. Often, anions require basis sets augmented with diffuse functions. In the case of $Au(CN)_2^-$, however, the negative charge of the dicyanoaurate(I) anion is quite evenly distributed over all atoms. This makes it possible to use a more compact basis set, at least concerning energetics and geometries, which are the aim of the present work. It also allows calculations on larger $Au(CN)_2^-$–NM_n clusters which we studied with n up to 10. In many respects, calculations on the interaction of $Au(CN)_2^-$ anion with solvent molecules are less problematic than with bare Au(I) because the strong non-additive effects mentioned in [7] are not present for $Au(CN)_2^-$–NM. All quantum chemical calculations were carried out with the Gaussian 03 code [8].

3. Results and discussion

3.1. Structure and formation energy of $Au(CN)_2^-$

$Au(CN)_2^-$ itself is a linear molecule with $D_{\infty}h$ symmetry in which the C end of the cyanide group binds to Au. In order to form a $Au(CN)_2^-$ anion, one electron in a carbon sp orbital transfers to the unoccupied 6s orbital of Au(I). From an analysis of the natural populations (Table 1) it can be seen that Au(I) gains $0.36e^-$ from CN^- group group and AuCN- obtains $0.31e^-$ from the second CN^- group. Moreover, due to the strong ligand field of CN^-, only one CN^- group can fully participate in the mixing of the 6s–5d orbital of Au(I). This differs, for example, in case of bare Au(I) where two nitromethane molecules participate in

* Corresponding authors. Tel.: +43 512 507 6260.
E-mail address: michael.probst@uibk.ac.at (M. Probst).

0167-7322/$ – see front matter © 2010 Elsevier B.V. All rights reserved.
doi:10.1016/j.molliq.2010.11.008

Table 1
Atomic partial charge (NPA) and electronic configurations (NEC) of the atoms in Au(I), CN^-, AuCN and $Au(CN)_2^-$. See text for details.

	Au(I)							CN^-						
	NPA	NEC						NPA	NEC					
Au	1.00	6s	0.00	5d	10.0	6p	0.00	–	–					
C	–	–						−0.18	2s	1.56	2p	2.56	3s	0.04
N	–	–						−0.82	2s	1.62	2p	4.19	3s	0.01
	AuCN							$Au(CN)_2^-$						
	NPA	NEC						NPA	NEC					
Au	0.64	6s	0.51	5d	9.83	6p	0.02	0.33	6s	0.81	5d	9.73	6p	0.13
C	−0.20	2s	1.26	2p	2.91	3s	0.04	−0.10	2s	1.26	2p	2.77	3s	0.05
N	−0.44	2s	1.59	2p	3.84	3s	0.01	−0.57	2s	1.58	2p	3.98	3s	0.05

the mixing [7]. With the quantum-chemical methods described in 2.1, the formation energy between Au(I) cation and the first CN^- group is exothermic by 180.6 kcal/mol. The calculated Au–C and C–N distances are 1.998 and 1.160 Å, respectively. To form the $Au(CN)_2^-$ anion, the 6s orbital of Au(I) in AuCN obtains $0.31e^-$ from a sp orbital of the C atom of the second CN^- ligand. The attachment of the second cyano group releases 94.2 kcal/mol, about half as much energy as the first one, and leads to the mixing of the 6s,5d and 6p orbitals of Au. The structure of $Au(CN)_2^-$ can be compared to S–Au(I)–S complexes which have the same linear $D_{\infty}h$ – symmetry [9]. The calculated Au–C and C–N distances in $Au(CN)_2^-$ are 2.050 and 1.166 Å, respectively, in good agreement with X-ray diffraction data for the crystals $Nd[Au(CN)_2]_3 \cdot 3H_2O$ and $Am[Au(CN)_2]_3 \cdot 3H_2O$ in which the Au–C distances are 1.984 and 2.064 Å, respectively, for $Nd[Au(CN)_2]_3 \cdot 3H_2O$ and $Am[Au(CN)_2]_3 \cdot 3H_2O$. The C–N distances are 1.141 and 1.075 Å for $Nd[Au(CN)_2]_3 \cdot 3H_2O$ and $Am[Au(CN)_2]_3 \cdot 3H_2O$, respectively [10].

3.2. Electrostatic potential and electron densities

The $Au(CN)_2^-$–NM interaction is governed by the interaction of the high dipole moment (4.6 debye) of NM with the low charge density in $Au(CN)_2^-$. We use the electrostatic potentials (ESPs) of both molecules to quantify this for intermediate distances. The ESP of NM (Fig. 1a) is divided into a positive half-space (CH_3 side) and a negative one (NO_2 side). The ESP of $Au(CN)_2^-$ is negative everywhere except close to the nuclei (Fig. 1b). Consequently, the interaction of $Au(CN)_2^-$ with the NO_2 side of NM is repulsive and the one with the CH_3 side is attractive. The coordination of NM to $Au(CN)_2^-$ is described in more detail in the next section.

$Au(CN)_2^-$ consists formally of the singly positive Au(I) cation and the two singly negative cyanide ligands. The electron density (ρ) difference between $Au(CN)_2^-$ constituents was calculated according to:

$$\Delta\rho = \rho_{Total} - \rho_{Au^+} - \rho_{(CN)^-_{Right}} - \rho_{(CN)^-_{Left}} \quad (1)$$

at the optimized structure of $Au(CN)_2^-$. It reveals that the region around Au(I) gains electron density (Fig. 2) from the CN^- groups. This increase of electron density takes place in a ring-shaped region perpendicular to the axis of the anion.

3.3. $Au(CN)_2^-/NM_n$ (n = 1–10) complexes: Geometries and binding energies

Unlike in the case of the free Au(I) ion [7], the 6s orbital of gold in $Au(CN)_2^-$ is nearly fully occupied (Table 1). Therefore, it does not

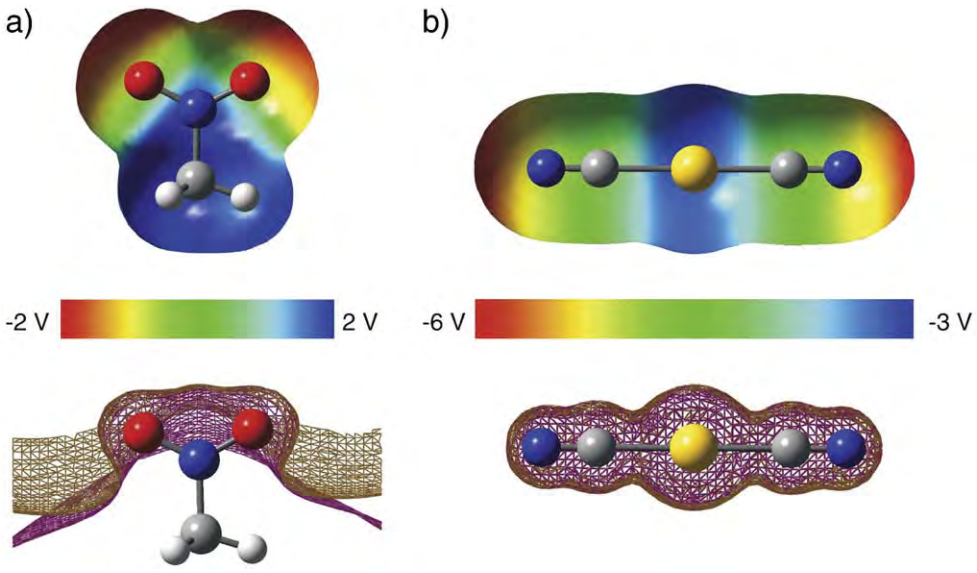

Fig. 1. Electrostatic potential (upper part) and the surface of near-zero (± 10^{-4} V)electrostatic potential (lower part) of a) nitromethane and b) $Au(CN)_2^-$.

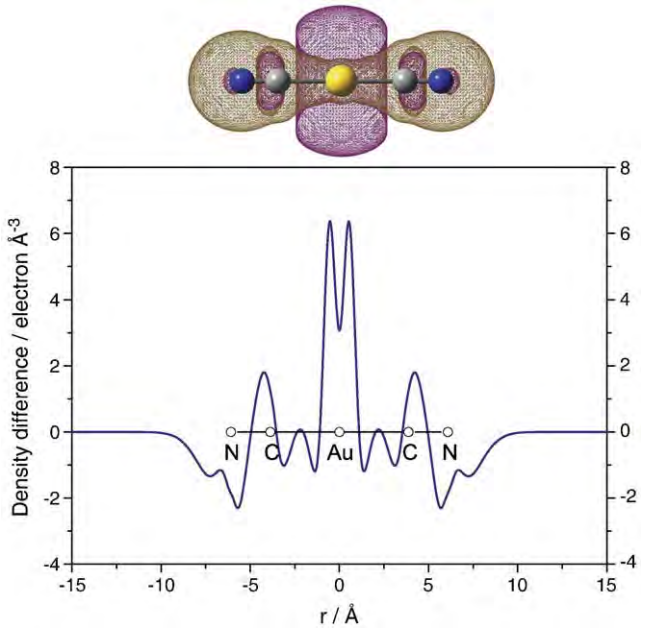

Fig. 2. Electron density difference between $Au(CN)_2^-$ complex and its constituents, Au (I) and the CN^-. Isosurface plot (upper part) and integral of $\Delta\rho(x,y,z)$ over y and z (lower part). The excess density (purple color, at $\Delta\rho = 0.4\times10^{-3}$ e/Å^3) is located around Au(I) while the CN^- groups lose some electron density. (brown color, isosurface plotted at $\Delta\rho = -0.4\times10^{-3}$ e/Å^3).

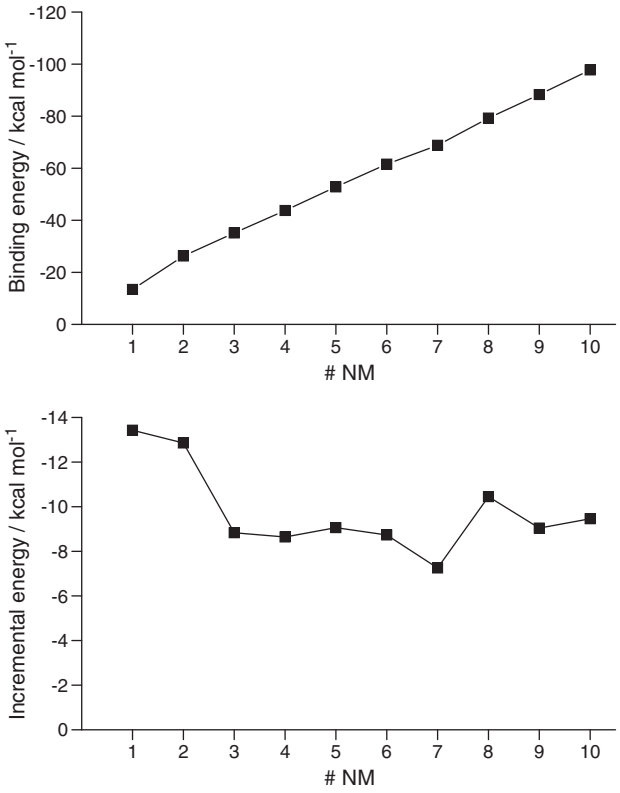

Fig. 3. (Upper) Total ligand–cation binding energies of the most stable structure defined as $E = E(Au(CN)_2^-\text{–}NM_n)\text{–}E(Au(CN)_2^-)\text{–}n\ E(NM)$ in the $Au(CN)_2^-\text{–}NM_n$ clusters with $1 \le n \le 10$. (Lower) Incremental energy defined as $\Delta E_n^{inc} = E_n^{inc} - E_{n-1}^{inc}$ where $E_n^{inc} = E(Au(CN)_2^-\text{–}NM_n)\text{–}E(Au(CN)_2^-\text{–}NM_{n-1})\text{–}E(NM)$.

change its hybridization when interacting with NM ligands. As a result, the binding energy per ligand decreases mostly (with the exception of n = 5 to 6) monotonically with the number (n) of ligands (Fig. 3) when the most stable structure for each n is considered. The optimized structures of $Au(CN)_2^-\text{–}NM_n$ with n = 1 to 10 are shown in Fig. 4. When a single NM molecule is added to $Au(CN)_2^-$, it prefers to be bound to $Au(CN)_2^-$ via end-on direction to form a linear $Au(CN)_2^-\text{–}NM$ complex. This end-on structure with a binding energy of −13.43 kcal/mol is about 5 kcal/mol more stable than the side-on structure with a T-shaped $Au(CN)_2^-\text{–}NM$ complex which is also a local minimum on the energy hypersurface. The energy difference is simply due to the fact that N in $Au(CN)_2^-$ has a higher negative partial charge than Au as is quantitatively shown in Fig. 1b. When a second NM molecule is added, $Au(CN)_2^-(NM)_2$ is formed as a linear complex with the NM molecules rather loosely bound to the anion. This linear form is 3.7 kcal/mol more stable than the one with two NM molecules binding to the same CN ligand. No local minima with NM coordinating to Au could be found for n>2 and for n = 3 we could locate only a single stable geometry. For n>3, the NM molecules can in principle either bind to the N atoms of the anion or form 'hydrogen-bonds' (we use this term simply to denote the C–H··· O pattern of arrangement between the highly polar NM molecules) to each other. From n = 4 to 7 these two geometrical patterns can be seen most clearly: The NM molecules can independently cluster on both N-sites or NM molecules can connect both sites. The respective energies are quite similar. For n>7, there are enough so that the two N binding sites of the anion are always bridged. For n = 8 and 9 half-ring structures are slightly preferred over more compact ones. Finally, for n = 10, the largest complex we investigated, a second shell of NM molecules starts to form.

The possibility of forming NM chains in the larger clusters is also reflected in the binding energies (Fig. 3). The incremental NM binding energy in the complexes with n = 8–10 is larger than for n = 7. Such a behavior is often found for solutes where solvent–solute and solvent–solvent binding energies are similar, which is the case for $Au(CN)_2(NM)_n^-$. Geometrically it reflects the competition between surface and interior states. In our system, due to the high directionality of the NM–NM interactions combined with the separation of the two N-sites of $Au(CN)_2^-$, the anion remains in the center of the complexes, at least until n = 10.

4. Conclusions

Our aim was to get an overall picture of dicyanoaurate(I) anion/nitromethane complexes. Structures and energies of clusters with up to 10 NM molecules were calculated. If less than 6 NM molecules are present, NM coordination to the nitrogen atoms at both ends of the linear is preferred while, for higher values of n, a geometrical pattern with chains or ring segments of NM molecules becomes competitive. The first solvation shell contains up to 9 NM molecules. At least for the cluster sizes we have investigated, no surface states are found with a central $Au(CN)_2^-$ being surrounded by NM molecules.

Acknowledgements

Support from the Austrian Research Fund (I200-N29), from the Austrian Ministry of Science via an infrastructure grant to the LFU scientific computing platform and from the National Science and Technology Development Agency (2009 NSTDA Chair Professor, NANOTEC Center of Excellence, CNC Consortium) the Commission on Higher Education via the "National Research University Project of Thailand" (NRU) and the University Development Council (UDC) are

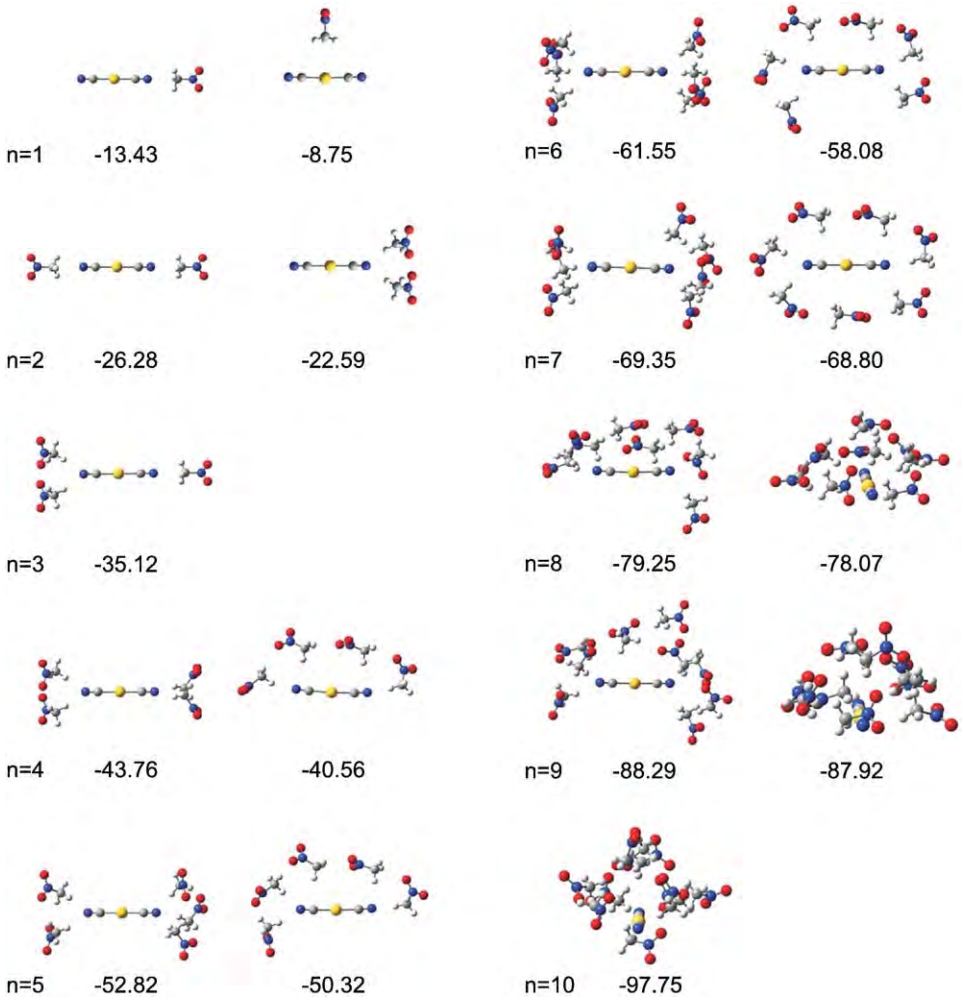

Fig. 4. Optimized geometries and binding energies of the most stable conformations of $Au(CN)_2^-$–NM_n with $1 \leq n \leq 10$ calculated at the HF level. Energies are given in kcal/mol.

acknowledged. Support from the Kasetsart University Research and Development Institute (KURDI) and the Graduate School Kasetsart University to NI is also acknowledged.

References

[1] J.R. Cui, L.F. Zhang, J. Hazard. Mater. 158 (2008) 228.
[2] C. Warakulwit, T. Nguyen, J. Majimel, M.-H. Delville, V. Lapeyre, P. Garrigue, V. Ravaine, J. Limtrakul, A. Kuhn, Nano Lett. 8 (2) (2008) 500.
[3] Z. Li, V. Ravaine, S. Ravaine, P. Garrigue, A. Kuhn, Adv. Funct. Mater. 17 (4) (2007) 618.
[4] A. Rubo, R. Kellens, J. Reddy, N. Steier, W. Hasenpusch, Ullmann's Encyclopedia of Industrial Chemistry, 'Alkali Metal Cyanides, , Wiley-VCH, Weinheim, 2006.
[5] P.J. Hay, W.R. Wadt, J. Chem. Phys. 82 (1985) 299.
[6] T.H. Dunning, P.J. Hay, in: H.F. Schaefer III (Ed.), Modern Theoretical Chemistry, Plenum Press, New York, 1976, p. 1.
[7] N. Injan, T. Megyes, T. Radnai, I. Bako, S. Balint, J. Limtrakul, D. Spangberg, M. Probst, J. Mol. Liquids 47 (2009) 64.
[8] M.J. Frisch, G.W. Trucks, H.B. Schlegel, G.E. Scuseria, M.A. Robb, J.R. Cheeseman, J.A. Montgomery Jr., T. Vreven, K.N. Kudin, J.C. Burant, J.M. Millam, S.S. Iyengar, J. Tomasi, V. Barone, B. Mennucci, M. Cossi, G. Scalmani, N. Rega, G.A. Petersson, H. Nakatsuji, M. Hada, M. Ehara, K. Toyota, R. Fukuda, J. Hasegawa, M. Ishida, T. Nakajima, Y. Honda, O. Kitao, H. Nakai, M. Klene, X. Li, J.E. Knox, H.P. Hratchian, J.B. Cross, V. Bakken, C. Adamo, J. Jaramillo, R. Gomperts, R.E. Stratmann, O. Yazyev, A.J. Austin, R. Cammi, C. Pomelli, J.W. Ochterski, P.Y. Ayala, K. Morokuma, G.A. Voth, P. Salvador, J.J. Dannenberg, V.G. Zakrzewski, S. Dapprich, A.D. Daniels, M.C. Strain, O. Farkas, D.K. Malick, A.D. Rabuck, K. Raghavachari, J.B. Foresman, J.V. Ortiz, Q. Cui, A.G. Baboul, S. Clifford, J. Cioslowski, B.B. Stefanov, G. Liu, A. Liashenko, P. Piskorz, I. Komaromi, R.L. Martin, D.J. Fox, T. Keith, M.A. Al-Laham, C.Y. Peng, A. Nanayakkara, M. Challacombe, P.M.W. Gill, B. Johnson, W. Chen, M.W. Wong, C. Gonzalez, J.A. Pople, Gaussian Inc., Wallingford CT.
[9] R.A. Bryce, J.M. Charnock, R.A.D. Pattrick, A.R. Lennie, J. Phys. Chem. A 107 (2003) 2516.
[10] Z. Assefa, K. Kalachnikova, R.G. Haire, R.E. Sykora, J. Solid State Chem. 180 (2007) 3121.

CHEMISTRY OF MATERIALS

ARTICLE

pubs.acs.org/cm

Versatile Procedure for Synthesis of Janus-Type Carbon Tubes

Gabriel Loget,[†] Véronique Lapeyre,[†] Patrick Garrigue,[†] Chompunuch Warakulwit,[‡] Jumras Limtrakul,[‡] Marie-Hélène Delville,[§] and Alexander Kuhn[†,*]

[†]Université de Bordeaux 1, ISM, ENSCBP, 33607 Pessac Cedex, France

[‡]Center of Nanotechnology and Chemistry Department, Kasetsart University, Bangkok 10900, Thailand

[§]CNRS, UPR-9048, Université de Bordeaux 1, ICMCB, 87 Avenue du Dr. A. Schweitzer, 33608 Pessac Cedex, France

ABSTRACT: A bulk procedure based on bipolar electrochemistry is proposed for the generation of Janus-type carbon tubes. The concept is illustrated with carbon tubes that are selectively modified at their ends with various metals and conducting polymers. No surface or interface is required to break the symmetry and therefore this approach could be used for the mass production of Janus micro- and nano-objects. We show evidence that the technique is very versatile, allowing the choice of the kind of material that is deposited and whether the end product is mono- or bifunctionalized.

KEYWORDS: bipolar electrochemistry, carbon tubes, capillary electrophoresis, Janus particles, dumbbell structures

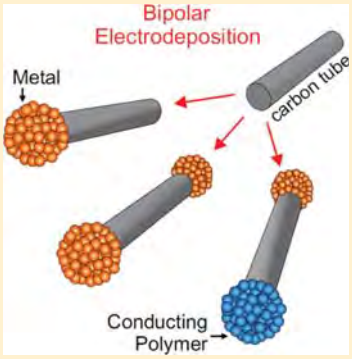

INTRODUCTION

Elaboration of functionalized micro- and nanoparticles, especially dissymmetrical Janus-type objects, is of enormous interest. These particles have high application potential in many areas such as sensing, new electronic devices, and catalysis.[1] Nevertheless, most processes, used to achieve the site-selective functionalization of a particle at this scale, require the use of an interface to break the symmetry.[2] This makes the preparation of large quantities rather difficult because the majority of the techniques usually leads to monolayer equivalents of material, as the modification occurs in a two-dimensional reaction space. Thus, there is an increasing interest in developing alternative truly three-dimensional techniques, allowing a scale-up of the production of dissymmetrical particles. Examples of such kind of approaches are based on the generation of charge carriers in semiconductors using light,[3] or antenna chemistry.[4] An elegant method reported by Banin et al. consists of the precipitation of $HAuCl_4$ to grow selectively gold tips on cadmium selenide nanorods.[5]

In this context, another attractive way to selectively modify particles in a three-dimensional reaction space is based on the concept of bipolar electrochemistry, described by Fleischmann et al.[6] This appealing approach relies on the fact that when a conducting object is placed in a strong electric field between two electrodes, a polarization occurs that is proportional to the electric field and the characteristic dimensions of the object. When this polarization is strong enough, redox reactions can be carried out at the opposite ends of the object (Scheme 1a). This interesting theoretical concept[7] has recently found applications as the driving force in electrochemiluminescent reactions,[8−11] as detection mode in capillary electrophoresis,[12] for bipolar patterning,[13,14] for membrane pore functionalization,[15] as a mechanism for propelling micro-objects,[16] and in the fields of analytical chemistry and material science in general.[11,17] The potential difference between the two ends of a conducting object under the influence of an external electric field is given by the equation

$$\Delta V = Ed \tag{1}$$

with E being the total external electric field and d the particle size. To carry out two redox reactions at the opposite sides of the object, ΔV has to be in a first-order approximation at least equal to the difference between the formal potentials of the two redox reactions. Let us consider as an example for the dissymmetrical functionalization the formal potential (E^0) of the reduction of Ni^{II} at one side

$$Ni^{II}{}_{(l)} + 2e^- \rightarrow Ni^0{}_{(s)} \tag{2}$$

and of the oxidation of water at the opposite side

$$2H_2O_{(l)} \rightarrow 4H^+{}_{(l)} + O_{2(g)} + 4e^- \tag{3}$$

From Table 1 it immediately follows that in this case the polarization has to generate a minimum potential difference of approximately

$$\Delta V_{min} = E^0_{Ni^0/Ni^{II}} - E^0_{H_2O/O_2} = 1.5\ V \tag{4}$$

This becomes an intrinsic problem of the approach when dealing with micro- or nanometer sized objects; as in this case E needs to

Received: January 17, 2011
Revised: March 29, 2011
Published: April 21, 2011

Scheme 1. (a) Concept of Bipolar Electrochemistry for the Generation of Janus-Type Objects; (b) Capillary Electrophoresis Set-up Used for the Dissymmetrical Electrodeposition

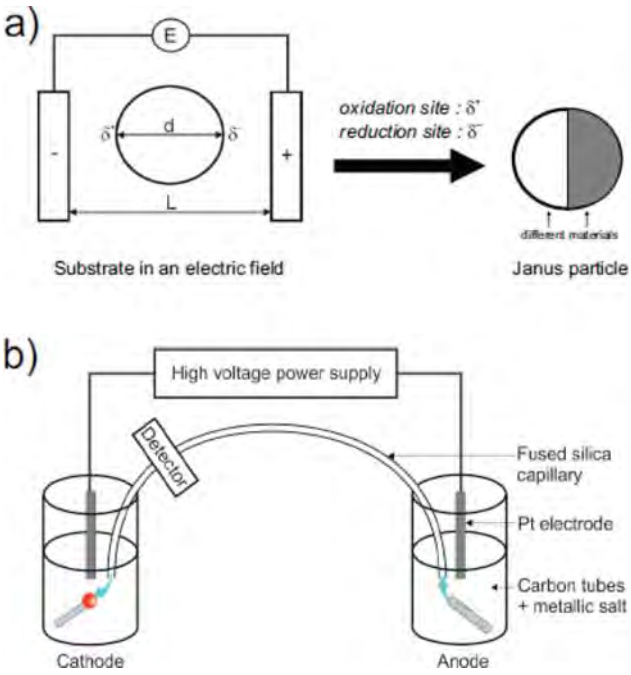

Table 1. Formal Potentials of the Redox Couples Used for the Bipolar Electrodeposition Experiments

redox couple	E^0 [V vs NHE]
$[Au^{III}Cl_4]^-/Au^0$	+0.99
Cu^I/Cu^0	+0.52
Ni^{II}/Ni^0	−0.26
Cu^{II}/Cu^I	+0.16
O_2/H_2O	+1.23

achieve values of up to MV m^{-1} (see Eq 1), conditions that seem to be incompatible with a normal laboratory environment and especially with aqueous solutions because of the intrinsic side reactions accompanied by macroscopic bubble formation at both electrodes that disturbs the orientation of the objects in the electric field. Bradley et al. could partly circumvent the problem by using organic solvents to enlarge the potential window of the electrolyte and thus it was possible to generate metal deposits in a dissymmetrical way on different objects in the micrometer and submicrometer range.[18,19] However, it was also necessary to immobilize the objects on a surface to prevent them from rotating, which means that this is again a two-dimensional and not a bulk process. We could demonstrate that it is possible to get around these problems by using a capillary electrophoresis setup to apply the high electric field (Scheme 1b).[20] In this case the bipolar electrodeposition experiment consists of imposing a strong potential (several tens of kV) between two electrodes separated by a capillary, generating an electric field in the range of 100 kV m^{-1}. Under its influence, the conductive objects become polarized, and because of the electroosmotic flow through the capillary, they are moving from the anodic reservoir to the cathodic one. Electrodeposition is achieved in this way and the modified substrates are detected at the outlet with a UV−vis detector. In this work, we describe a generalization of the approach and we have chosen to illustrate this with micrometer-sized carbon tubes (CTs) because they can be easily visualized with an optical microscope. However, the approach can also be used for nanosized objects, as has been shown for the particular case of gold deposition on CNTs.[20] The so-called CABED procedure (Capillary Assisted Bipolar ElectroDeposition) was restricted so far to metal deposition, and most importantly, only one side of the carbon (nano)tubes could be modified.[21,22]

In the present work we demonstrate that the concept can be applied not only to a variety of metal deposits but also to the deposition of conducting polymers. In contrast to what has been reported in our previous work, we show here that by choosing the right potential sequence including relaxation times, we can not only deposit a material selectively on one side of the tubes but also trigger in a single experiment the deposition at both ends of the tube, resulting in structures that are either modified on both sides with the same material or with two different materials. This is the first time that such symmetric or dissymmetrical dumbbell-like structures are synthesized by bipolar electrochemistry using a bulk approach without the need of interfaces or surfaces to break the symmetry.

EXPERIMENTAL SECTION

Preparation of Carbon Tube Suspensions. The CTs used in this study were produced by chemical vapor deposition with a porous aluminum oxide membrane serving as a template. After acid digestion of the template, the quite homogeneous tubes were recovered as a powder. For the suspensions containing Au^{III} and Ni^{II}, about 0.1 mg of CTs was added to absolute ethanol (1.5 mL). To accelerate the formation of a suspension, the mixture was sonicated, but only for a short time (1 min), to avoid excessive breaking of the tubes. After 3 h of sedimentation, 0.5 mL of the supernatant was taken and added to 0.5 mL of 10 mM $NiSO_4$ or 10 mM $HAuCl_4$ in ultrapure water. The suspension with Cu^I was prepared by adding about 0.1 mg of CTs to a solution of 10 mM CuI in acetonitrile. Suspensions with CuI and pyrrole were prepared by adding the same amount of CTs to a mixture of 10 mM CuI and freshly distilled 50 mM pyrrole in acetonitrile.

Bipolar Electrodeposition on Carbon Tubes. For electrodeposition experiments, all solutions or suspensions were introduced into the capillary by filling it manually with a syringe. The capillary used here is a fused silica capillary with a length of 24 cm and an inner diameter of 100 μm. The applied voltage was 30 kV for 5 min and the temperature was maintained at 25 °C. The CE experiment was first performed by rinsing the capillary with ultrapure water or acetonitrile. Then the CT suspension was introduced into the capillary. Because the addition of salt increases the ionic strength, it can result in the aggregation of the CTs, and therefore the suspensions were sonicated for a short time in an ultrasound bath before introduction into the capillary. For such salt concentrations, the typical currents in the electrophoresis setup were around 1 μA. The sample leaving the capillary at the cathodic side was collected directly at the outlet and transferred onto a TEM grid or another substrate, rinsed, and dried. The objects were then characterized by optical microscopy and scanning electron microscopy (SEM).

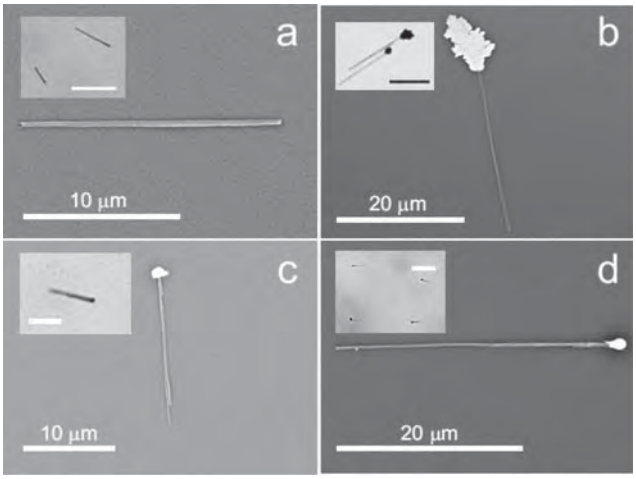

Figure 1. SEM images of CTs (a) without modification; modified at one side with (b) copper, (c) gold, and (d) nickel. Inset: optical microscope image of the modified CTs; scale bars are:(a), (b), and (d) 20 μm; (c) 10 μm.

RESULTS AND DISCUSSION

The Janus-type CTs are obtained from raw carbon tubes synthesized by chemical vapor deposition into pores of an aluminum oxide membrane. The thickness of the collected tubes is 200 nm and their length is 20−30 μm (Figure 1a). The modified CTs are collected at the outlet of the capillary after bipolar electrodeposition. Samples shown in Figure 1b−d were obtained using carbon tube suspensions in solutions of Cu^{I} (10 mM) in acetonitrile, Au^{III} (5 mM) in water, and Ni^{II} (5 mM) in water, respectively. Since copper modification was achieved in a nonaqueous solution, the reactions that occur at the tube ends are

$$Cu^{I} + e^{-} \rightarrow Cu^{0}{}_{(s)} \quad (5)$$

at one side and:

$$Cu^{I} \rightarrow Cu^{II} + e^{-} \quad (6)$$

at the opposite side. Using the E^{0} values given in Table 1, one can easily see that the overall reaction resulting from a combination of eqs 5 and 6 should occur spontaneously via a dismutation. However, the Cu^{I} species seem to be sufficiently stabilized because of the presence of I^{-} ions so that a potential difference is still needed between the two ends of the tube to drive the reaction.

Gold deposition was carried out in aqueous solution, involving the following reactions:

$$[Au^{III}C1_4]^{-} + 3e^{-} \rightarrow Au^{0}{}_{(s)} + 4Cl^{-} \quad (7)$$

and

$$2H_2O_{(1)} \rightarrow 4H^{+}{}_{(1)} + O_{2(g)} + 4e^{-} \quad (8)$$

Table 1 indicates that in this case the combination of eqs 7 and 8 is not a spontaneous reaction and therefore a minimum potential difference between the two tube ends has to be generated to achieve dissymmetrical deposition:

$$\Delta V_{min} = E^{0}_{Au^{0}/AuCl_4^{-}} - E^{0}_{H_2O/O_2} = 0.24\ V \quad (9)$$

Obviously, because the experiments are carried out in far from standard conditions in terms of pH, concentrations, and partial gas pressures, deviations from the theoretical values of the potential threshold are expected. For all these experiments the same external electric field value E = 125 kV m^{-1} was applied, which gives typically for a 30 μm object a ΔV = 3.75 V. This value is definitely high enough, compared to the theoretical ΔV_{min} values previously calculated, to drive all these redox reactions. Looking at the SEM pictures of CTs collected at the capillary outlet (Figure 1b−d), it is obvious that the corresponding metal has been deposited. Because we used the same E, the same capillary length, and an identical experiment time, the variation in deposit size can be understood via the different growth kinetics which depend essentially on (i) the required ΔV_{min} and (ii) the salt concentration. Nickel modification, which requires the highest driving force (ΔV_{min} = 1.5 V), results in the smallest deposit size because for the given overall electric field the driving force is smaller and therefore the reaction proceeds more slowly. As stated above, copper deposition should occur almost spontaneously and therefore the required minimum voltage is certainly the smallest one compared to the other metals. This means that in this case the external field generates the highest driving force and leads to the biggest deposit. Another parameter that is important for the apparent deposit size is the growth morphology and its density. Copper is growing in a much more ramified structure, which leads for the same amount of reduced metal to a much bigger deposit compared to what is obtained for nickel and gold. This new family of monofunctionalized dissymmetric particles can be used for the localized functionalization of carbon tubes with organic molecules, for binding carbon tubes to a surface and for the development of nanodevices such as nanomotors because the orientation of tubes modified with a ferromagnetic material can be controlled with a magnetic field,[21] or a decomposition reaction can be driven by a catalytically active metal present at one tube end.[22]

During these bipolar electrodeposition runs, the end of the tube opposite to the one where the metal deposition takes place is positively polarized and therefore cannot be a site of reduction. If one wants to modify in a single experiment both ends with the same metal, polarization has to be reversed after the first deposition step so that the side that was the oxidation site becomes the reduction site. Since a classic electrophoresis set-up does not allow reversal of the polarization between the electrodes, we employed another approach consisting of the introduction of a relaxation time after the first polarization (without applied potential) to induce a statistical reversal of the CTs in the capillary. The optical microscope pictures in Figure 2 were obtained with the same carbon tube dispersion and the same electric field value as for the previous dissymmetrical deposition of copper, but with a regular interruption of the potential. When the potential is continuously applied or when the relaxation time between the pulses is short (Figure 2b,d), the CTs do not have the possibility to turn around in the capillary. Actually, once these anisotropic objects are polarized in the electric field, it would cost too much energy for them to flip in the opposite direction. This means that the tubes are all aligned parallel to the electric field and will not tumble or turn during their journey through the capillary. Therefore, this results exclusively in dissymmetrical deposits. In contrast, when the pulses are sufficiently separated in time (Figure 2a,c), the tubes are no longer polarized during the relaxation period without applied field and therefore have time to statistically change their orientation, thus leading to a symmetric deposition. In this case, after the first pulse, only one end of the tube is modified with Cu^{0}, but during the 5 minutes

dx.doi.org/10.1021/cm2001573 |*Chem. Mater.* 2011, 23, 2595–2599

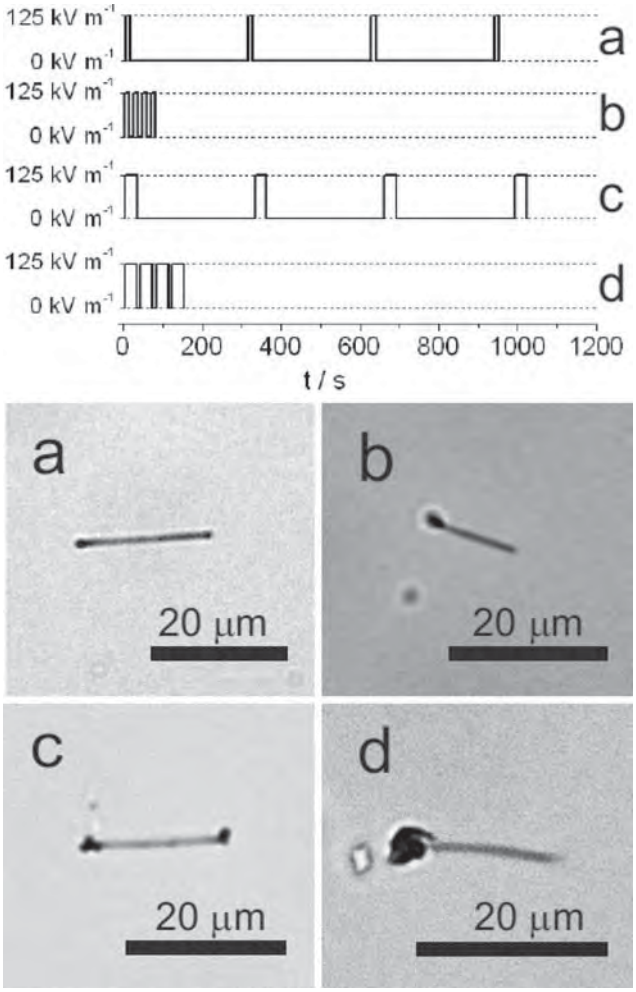

Figure 2. Pulsed bipolar electrodeposition with a suspension of CTs in 10 mM CuI in acetonitrile. The electric signal imposed between the electrodes is reported at the top and the corresponding optical microscope images of the modified carbon tubes at the bottom. The electric field was 125 kV·m. Time of potential pulses are 12 s (a and b) and 30 s (c and d); the time between the pulses are 5 min (a and c) and 10 s (b and d).

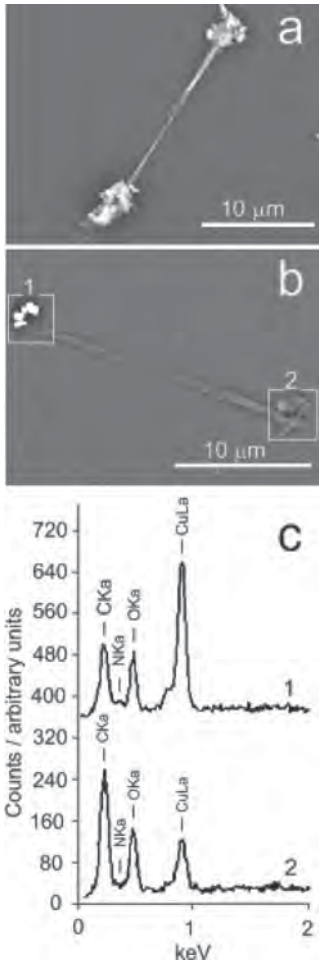

Figure 3. SEM pictures of modified dumbbell-like CTs. (a) Symmetric dumbbell-like object with copper deposits on both sides. (b) Dissymmetrical dumbbell-like object with one copper end (square 1) and one polypyrrole end (square 2). (c) EDX spectra recorded for the copper end (1) and for the polypyrrole end (2).

without polarization the tubes are allowed to reorientate in the capillary. Statistically, half of them will do so. Therefore, when the second pulse is applied, for half of the tubes the end where previously the oxidation of Cu^{I} into Cu^{II} took place becomes the reduction site where metal is formed. For these tubes, the counter reaction, which is the oxidation of Cu^{I} into Cu^{II}, now takes place at the end of the tube that had been already modified with copper during the first potential pulse. Another possible counter reaction could be the oxidation of the already present copper deposit. However, it is more difficult to oxidize Cu^{0} than Cu^{I} because the oxidation potential is more positive (see Table 1) and therefore the dominating counter reaction is $Cu^{I} \rightarrow Cu^{II}$, thus preserving the already existing metal deposit.

If this long relaxation is repeated many times, statistically all tubes have turned around several times and consequently are modified on both sides. Striking evidence for the symmetric deposition of copper at both ends of the CT is shown in the SEM image of Figure 3a. The symmetric dumbbell-like functionalization of CTs can be extended to metals other than copper and these new materials can find exciting applications for self-assembly.

In the above experiments, the oxidation that occurs at the anodic end of the CTs produces gas or other oxidation products, but the involved reactions do not lead to a modification. We were therefore looking for an additional strategy, which would make use of this oxidation reaction to deposit also a material on the positively polarized side, concomitant with the reductive metal deposition on the negatively polarized side. One obvious type of material that can be obtained by oxidation is a conducting polymer. Because of their intrinsic reactivity, the metal salt and the monomer have to be chosen carefully. A mixture of Cu^{I} and pyrrole was found to be stable in acetonitrile for at least 12 h. For longer times a brownish color that was due to the spontaneous polymerization of pyrrole appeared. CTs were added to this freshly prepared solution and bipolar electrodeposition was achieved using the same parameters that were applied for the dissymmetrical deposition of Cu^{0}. A SEM picture of a typical CT is shown in Figure 3b, the metallic end being clearly visible since the color contrast between metal and the carbon tube is very important. The polypyrrole (Ppy) end is less conductive than copper and thus exhibits a weaker contrast with respect to the

dx.doi.org/10.1021/cm2001573 |*Chem. Mater.* 2011, 23, 2595–2599

carbon tube. To make sure that the type of deposit at both ends is different, we performed, in addition, EDX experiments. The analysis has been carried out at the two opposite ends of the carbon tube. Figure 3c shows that the upper left end of the tube is characterized by a strong Cu signal around 1 keV compared to a much weaker carbon signal which originates most likely from the underlying carbon tube and the supporting grid. At the other end of the tube the carbon signal is much more prominent due to the presence of the conducting polymer. When both peaks are compared to the background oxygen signal, it becomes clear that their ratio is significantly different for the two ends of the tube, demonstrating the presence of the two different materials. However, on the Ppy side there is still a small contribution of Cu. This signal can be assigned to ionic copper species that become trapped in the polymer matrix during the pyrrole oxidation, it being known that copper forms stable complexes with polypyrrole, based on a Cu−N bond.[23]

This result opens up the way to a new family of bifunctional Janus-type materials that can be created by bipolar electrodeposition. Indeed, one can easily imagine that various metal-conducting polymer combinations can be deposited, leading to structures that could show interesting features. The pictures of Figures 1, 2, and 3 are representative of the majority of the tubes reaching the capillary outlet; however, in a more general sense, not 100% of the tubes are modified. The percentage of modified tubes obviously depends on the experimental parameters and there are several possible origins for a nonquantitative modification. The deposits might for example detach from the tube during the collection and rinsing procedure. Also, the tubes can be more or less conducting depending on their morphology and defects, which will lead to differences in polarization. When this kind of problem is minimized by careful sample handling, quantitative modification can be achieved.

CONCLUSION

In summary, we present the generalization of a new bulk method based on bipolar electrochemistry that allows the highly controlled and localized functionalization of CTs. For the first time we could synthesize with one and the same process Janus-type carbon tubes that can be divided into three families, as a function of the used experimental parameters: (i) monofunctionalized dissymmetrical tubes, (ii) symmetric dumbbell-like tubes, and (iii) dissymmetrical dumbbell-like tubes. The deposit size and location can be very easily tuned by changing the strength and time variations of the electric field. Various materials can be deposited, assigning localized features to carbon tubes, thus leading to promising materials in domains such as sensing, electronic devices, self-assembly, and catalysis. Because this process is a true bulk process, one can imagine a scale-up of the production. Although we demonstrated the validity of the approach for the particular example of carbon tubes, this technique might be adapted to a large range of other micro- and nanoparticles of various size and shape.

AUTHOR INFORMATION

Corresponding Author

*Phone: +33540006573. Fax: +33540002717. E-mail: kuhn@enscbp.fr.

ACKNOWLEDGMENT

This work has been cofunded by the French National Agency (ANR) and the European Commission in the frame of the "NanoSci-E+" transnational programme (CUBI-HOLE project, ANR's number: ANR-08-NSCI-008). It has also been supported by the French Ministry of Research, CNRS, and ENSCBP. C.W. and J.L. thank the National Science and Technology Development Agency (NSTDA Chair Professor and National Nanotechnology Center), the National Research University Project of Thailand (NRU) and the Thailand Research Fund for support.

REFERENCES

(1) Walther, A.; Muller, A. H. E. *Soft Matter* **2008**, *4*, 663–668.
(2) Pradhan, S.; Xu, L.; Chen, S. *Adv. Funct. Mater* **2007**, *17*, 2385–2392.
(3) Reiche, H.; Dunn, W. W.; Bard, A.J. *J. Phys. Chem.* **1979**, *83*, 2248–2251.
(4) Duque, J. G.; Pasquali, M.; Schmidt, H. K. *J. Am. Chem. Soc.* **2008**, *130*, 15340–15347.
(5) Mokari, T.; Sztrum, C. G.; Salant, A.; Rabani, E.; Banin, U. *Nat. Mater.* **2005**, *4*, 855–863.
(6) Fleischmann, M.; Ghoroghchian, J.; Rolison, D.; Pons, S. *J. Phys. Chem.* **1986**, *90*, 6392–6400.
(7) Duval, J.; Kleijn, J. M.; Van Leeuwen, H. P. *J. Electroanal. Chem.* **2001**, *505*, 1–11.
(8) Mavré, F.; Chow, K.-F.; Sheridan, E.; Chang, B.-Y.; Crooks, J. A.; Crooks, R. M. *Anal. Chem.* **2009**, *81*, 6218.
(9) Chow, K.-F.; Mavré, F.; Crookes, J. A.; Chang, B.-Y.; Crooks, R. M. *J. Am. Chem. Soc.* **2009**, *131*, 8364–8365.
(10) Chow, K.-F.; Mavré, F.; Crooks, R. M. *J. Am. Chem. Soc.* **2008**, *130*, 7544–7545.
(11) Mavré, F.; Anand, R. K.; Laws, D. R.; Chow, K. F.; Chang, B. Y.; Crooks, J. A.; Crooks, R. M. *Anal. Chem.* **2010**, *82*, 8766–8774.
(12) Ordeig, O.; Godino, N.; Del Campo, J.; Munos, F. X.; Nikolajeff, F; Nyholm, L. *Anal. Chem.* **2008**, *80*, 3622–3632.
(13) Ulrich, C.; Andersson, O.; Nyholm, L.; Björefors, F. *Anal. Chem.* **2009**, *81*, 453–459.
(14) Ramakrishnan, S.; Shannon, C. *Langmuir* **2010**, *26*, 4602–4606.
(15) Bouquet, A.; Deschamp, E.; Maillet, P.; Livache, T.; Chatelain, F.; Haguet, V. *Small* **2009**, *5*, 2297–2303.
(16) Loget, G.; Kuhn, A. *J. Am. Chem. Soc.* **2010**, *132*, 15918–15919.
(17) Loget, G.; Kuhn, A. *Anal.Bioanal.Chem.* **2011**, in press, DOI 10.1007/s00216-011-4862-1.
(18) Bradley, J.-C.; Chen, H.-M.; Crawford, J.; Eckert, J.; Ernazarova, K.; Kurzeja, T.; Lin, M.; Nadler, W.; Stephens, S. G. *Nature* **1997**, *389*, 268–271.
(19) Bradley, J.-C.; Ma, Z. *Angew. Chem., Int. Ed.* **1999**, *38*, 1663–1666.
(20) Warakulwit, C.; Nguyen, T.; Majimel, J.; Delville, M.-H.; Lapeyre, V.; Garrigue, P.; Ravaine, V.; Limtrakul, J.; Kuhn, A. *Nano Lett.* **2008**, *8*, 500–504.
(21) Loget, G.; Larcade, G.; Lapeyre, V.; Garrigue, P.; Warakulwit, C.; Delville, M.-H.; Ravaine, V.; Kuhn, A. *Electrochim. Acta* **2010**, *55*, 8116–8120.
(22) Fattah, Z.; Loget, G.; Lapeyre, V.; Garrigue, P.; Warakulwit, C.; Limtrakul, J.; Bouffier, L.; Kuhn, A. *Electrochim. Acta* **2011**, in press, 10.1016/j.electacta.2011.01.048.
(23) Inoue, M. B.; Nebesny, K. W.; Fernando, Q.; Castillo-Ortega, M.; Inoue, M. *Synth. Met.* **1990**, *38*, 205–212.

Structural and electronic bistability in ZnS single sheets and single-walled nanotubes

Norawit Krainara,[1,2] Jumras Limtrakul,[2] Francesc Illas,[1] and Stefan T. Bromley[1,3,*]

[1]*Departamento de Química Física & Institut de Química Teòrica i Computacional (IQTCUB), Universitat de Barcelona, Barcelona, Spain*

[2]*Department of Chemistry and Center for Advanced Studies in Nanotechnology and Its Applications in Chemical, Food and Agricultural Industries, Kasetsart University, Bangkok 10900, Thailand*

[3]*Institució Catalana de Recerca i Estudis Avançats (ICREA), Barcelona, Spain*

(Received 28 April 2011; published 30 June 2011)

We investigate a single sheet graphene analogue and a single-walled nanotube of ZnS using electronic structure calculations. Unlike the nearly perfectly flat structures of graphene and graphene analogues of other binary compounds (e.g., BN, ZnO, SiC), ZnS sheets are predicted to attain higher stability as complex, radically reconstructed structures. This predisposition to reconstruct also persists when ZnS sheets are rolled up into single-walled nanotubes. Smooth nanotubes and flat single sheets of ZnS have significantly smaller band gaps than their reconstructed counterparts, and are found to be metastable minima that are accessible from the reconstructed structures via external strain. This bistable electromechanical coupling may have significant technological potential (e.g., nanosensors, optomechanical switches).

DOI: 10.1103/PhysRevB.83.233305 PACS number(s): 61.46.Fg, 64.70.Nd, 62.23.Kn, 62.25.−g

Since the fabrication of atomically thin, nearly perfectly planar nanosheets of carbon (i.e., graphene[1]), two-dimensional (2D) materials have attracted huge scientific and technological interest. The formation of single flat sheets is facilitated in carbon, and similarly in boron nitride (BN),[2] by thermodynamic driving forces to form quasi-2D bulk crystal structures consisting of weakly interacting hexagonal ordered atomic layers (i.e., graphite and h-BN, respectively). Other technologically important materials, such as SiC, ZnO, and ZnS, exhibit fourfold-coordinated three-dimensional (3D) bulk crystal structures (i.e., zincblende or wurtzite), but these have been predicted to energetically favor layered phases[3] analogous to h-BN in thin films, which has been experimentally confirmed for ZnO.[4] Calculations have shown that isolated sheets of SiC,[5] and ZnO[6] are most stable as planar structures, just like for graphene and BN single sheets. Only for Si and Ge predicted a possible weak instability of single hexagonal planar sheets to slight puckering theory has (displacements of ±0.22 Å [Si] and ±0.32 Å [Ge] with respect to the planar sheet).[7]

Herein, using electronic structure calculations, we consider single hexagonal sheets of the II-IV semiconductor ZnS. We predict that 2D ZnS energetically prefers complex, significantly reconstructed sheets having out-of-plane displacements of ±1.95 Å. We find that these large distortions also persist even after rolling up such sheets into single-walled nanotubes (SWNTs). We further show that the application of tension/compression to 2D ZnS sheets and ZnS SWNTs can induce a structural transition between lower-energy reconstructed ZnS structures and their metastable planar/smooth forms. These structural transformations are also found to induce large band gap changes (>2 eV), showing how the mechanical and electronic properties of these systems are strongly coupled. Considering the impressive optoelectronic properties of current ZnS nanostructures[8] and the continuing advances in nanofabrication, the electronic and mechanical bistability of ZnS nanosheets and SWNTs is of potential technological importance (e.g., nanosensors, optomechanical switches).

Structures and properties were calculated using periodic density functional theory (DFT) as implemented in the Vienna Ab initio Simulation Package (VASP) code.[9] Calculations used the PW91[10] exchange-correlation potential, a plane-wave kinetic energy cutoff of 500 eV, and the projector augmented wave method.[11] Repeated image interactions were made negligible by ensuring a 15 Å separation between systems. For the nanosheets, both hexagonal cells of 32 atoms (a 4 × 4 supercell with respect to (w.r.t) the flat sheet) and rectangular 4 × 6 cells of 48 atoms (4 × 6 supercell w.r.t. the flat sheet) were employed, using 7 × 7 × 1 and 5 × 5 × 1 Monkhorst-Pack (MP)[12] meshes of k-points, respectively. In the (12,0) SWNT calculations, 48 atom supercells and 1 × 1× 9 MP k-point meshes were used. In all cases, the atomic structure of the system was fully relaxed until the forces were smaller than 0.005 eV/Å. To search for lowest-energy structures, we employed two methods. First, using a mechanical annealing technique,[13] systems were gradually compressed and stretched (up to ±30%) while optimizing the atomic positions at each stage. Every time a structural change occurred, the procedure was repeated around the newly obtained minimum energy configuration until no structural change occurred. Second, we employed microcanonical molecular dynamics with classical interatomic potentials[14] using the General Utility Lattice Program (GULP) code.[15] Systems were preheated to between 500 and 2000 K, and, during runs of 25–50 ps, sample configurations were energy-minimized and then further optimised using DFT.

We find that the strict graphene analogue of the ZnS single sheet has all atoms in a single plane with an optimized Zn-S bond distance of 2.246 Å and a 2D hexagonal supercell parameter of $a = b = 15.562$ Å. This structure is an energy minimum, with all vibrational modes having positive frequencies, and it is resilient to bending (see SWNT results below) and to small local distortions of its structure. For the latter, we prepared a number of sheets with randomly selected atoms displaced above and below the plane of the sheet, with out-of-plane displacements $\leqslant$0.03 Å, and found that the planar sheet was recovered after re-optimization.

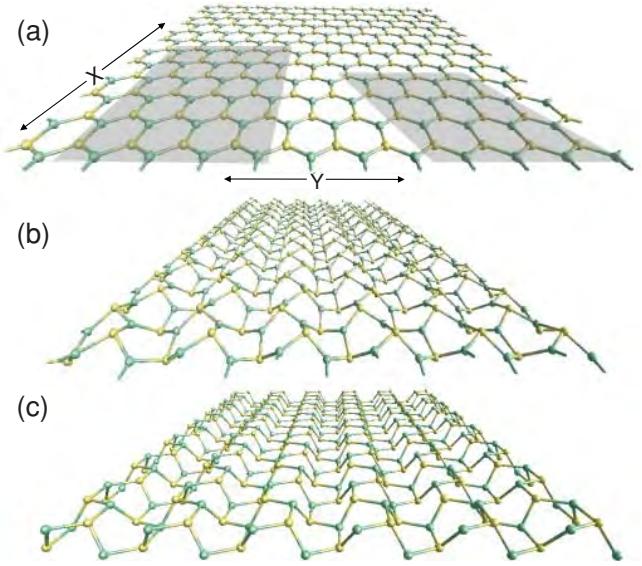

FIG. 1. (Color online) Structures of 2D ZnS systems: (a) flat sheet, (b) lowest-energy reconstructed sheet, (c) uppermost atoms of the $(11\bar{2}0)$ surface of wz-ZnS. Shaded areas show atoms in the cubic (left) and hexagonal (right) supercells. The X-Y axes in (a) relate to the applied strain directions. Lighter7darker grey balls indicate sulphur/zinc atom positions respectively.

Using a rectangular supercell (see Fig. 1), we applied strains perpendicular to in-plane directions and observed that small strains (less than ±5%) applied to the ZnS flat sheet also increased its energy, which, upon release, relaxed back to the planar minimum (see Fig 1(a)). Upon application of out-of-plane atomic distortions larger than 0.03 Å, the sheet re-optimized to a variety of lower-energy reconstructed geometries. The lowest-energy reconstructed structure found was 0.08 eV/ZnS lower in energy than the perfectly planar minimum. The significance of the magnitude of this energy difference can be appreciated by noting that it is approximately ten times larger than the calculated energy difference between zincblende ZnS (zb-ZnS) and wurtzite ZnS (wz-ZnS). This reconstructed sheet can also be obtained by increasing the in-plane compressive strain applied to the ZnS flat sheet in the *X* direction to beyond 5% (see Fig. 2(a)). The structure of the new energy minimum retains the bonding topology of the flat sheet and also exhibits all its Zn atoms in locally

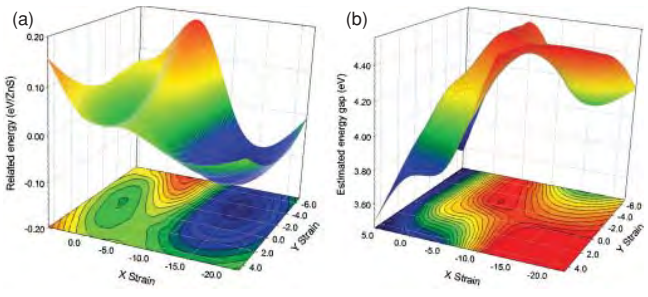

FIG. 2. (Color online) 2D ZnS flat sheet response to in-plane strain (%) with respect to: (a) relative total energy (eV/ZnS), and (b) estimated direct band gap (eV). Surfaces were generated from ∼50 *a*/*b*-constrained energy minimizations.

planar bonded configurations. The planes defined by the Zn centers and their three S nearest neighbors, however, are now not common to all Zn centers in the sheet, but instead they vary their inclination according to the alternating positions of the S atoms above and below the original plane of the flat sheet. These lateral out-of-plane atomic displacements involved in the reconstruction (up to ±1.95 Å) are found to be an order of magnitude larger than those of the relatively simple concerted buckling predicted for ZnS nanotubes (±0.1 Å)[18,20] and multilayer nanofilms (±0.265 Å),[16] with respect to corresponding perfectly planar systems. The high complexity of the reconstructed structure is reflected in the 16 atom unit cell (4 × 2) required to describe it, as compared to the two atoms per unit cell for the flat hexagonal ZnS sheet. The reconstructed structure (see Fig. 1(b)) has considerably smaller lattice supercell parameters with respect to the flat sheet (a = 14.542 Å, b = 13.971 Å), a slightly distorted near-hexagonal cell angle of 61.3°, and larger Zn-S bond distances, ranging between 2.264 and 2.278 Å. The S sublattice reconstruction is found to resemble that of the $(11\bar{2}0)$ surface of the wz-ZnS crystal (see Fig. 1(c)), which is calculated to be the most energetically stable bulk termination for ZnS.[14] The pattern of relaxation of the $(11\bar{2}0)$ wz-ZnS surface (e.g., a reduction in the S-Zn-S angles) described by Hamad *et al.*,[14] however, is much more exaggerated in 2D ZnS due to the absence of an attached underlying substrate. Other reconstructed single ZnS sheets found in our searches also resembled other bulk surfaces, such as the (110) surface of zb-ZnS, but all were found to be relatively higher in energy.

In both flat and reconstructed sheets, the Bader partitioned atomic charges are found to be very similar (flat: $Q_{Zn/S}$ = ±0.92e, reconstructed: $Q_{Zn/S}$ = ±0.90e), and, in the latter case, like those of zb-ZnS ($Q_{Zn/S}$ = ±0.90e). Thus, although some limited increase in charge transfer may occur, the main driving force behind this reconstruction is more likely to come from other influences. Assuming ZnS to be mainly covalent, we may envisage the 2D ZnS reconstruction as the result of the known tendency of S centers for sp^3 hybridization and an ensuing preference for tetrahedral coordination environments (as in "zb-ZnS"-abbreviation introduced at line). Interestingly, the reluctance of S (and Zn) to adopt more planar sp^2 hybridized multiple bonds has also been invoked in other studies to explain the relatively lower calculated energetic stability of stacks of planar ZnS sheets,[3] and smooth ZnS SWNTs[21] with respect to analogous structures in other materials (e.g., C, BN, and SiC). These studies, however, make no suggestion that sheet-based ZnS structures could thus reconstruct via sp^3 hybridization to become nonplanar to lower their energy. In a more ionic picture, we may consider the considerable mismatch between the small positive Zn ions and the considerably larger negative S ions tending to destabilize a regular hexagonal planar packing. In this picture, large, electron-rich S ions, by protruding away from the plane of the flat sheet, would be able to lower their energy through increased out-of-plane polarization. Classical interionic potentials (IPs) specifically parameterized to model S and Zn centers in tetrahedrally coordinated bulk environments in ZnS[14] also confirm that the reconstructed sheet is energetically more stable than the planar sheet. Here, this indeed occurs due to the classically incorporated polarizability of the S^{2-} ions and not via

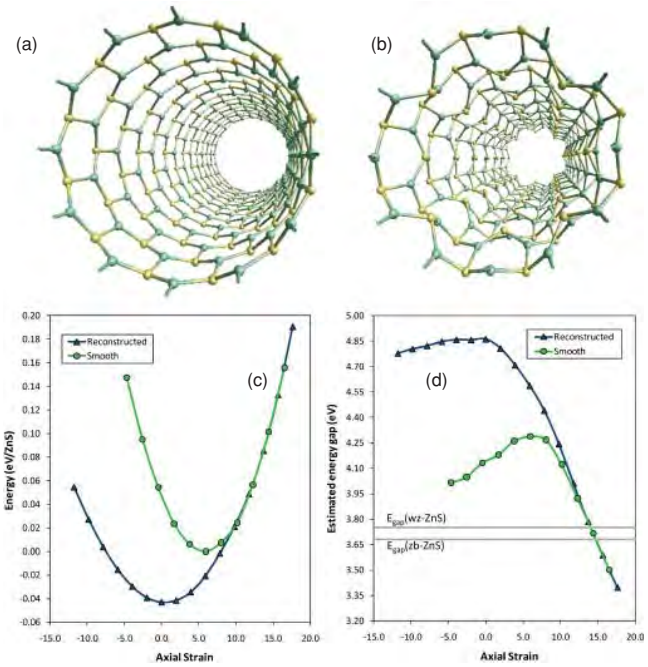

FIG. 3. (Color online) ZnS SWNT structures: (a) slightly buckled (smooth), and (b) reconstructed. Reconstructed SWNT response to axial strain (%) with respect to: (c) relative total energy, and (d) estimated direct band gap (exp. wz-ZnS and zb-ZnS band gaps also shown).

any specific directional parameters designed to promote a tetrahedral coordination environment of Zn^{2+} ions, showing that sulfur polarization may also play an important role in stabilizing reconstructed ZnS nanostructures.

Rolling up flat 2D graphene sheets gives rise to smooth carbon SWNTs. Previous theoretical studies on ZnS SWNTs have reported minor concerted atomic displacements, similar to those found in BN SWNTs,[17] whereby all relatively less electronegative (smaller) ions/atoms move slightly inward (with respect to the mid-tube axis), and the remaining more electronegative (larger) ions/atoms move slightly outward (i.e., Zn and S respectively, each by $\leqslant$0.1 Å).[18–21] This small concerted radial buckling is also predicted to be most pronounced for small-diameter SWNTs, and to quickly diminish toward zero with increasing SWNT size.[18] In strong contrast to these reports, we find that slightly radially buckled ZnS SWNTs can, like the planar ZnS sheets, significantly lower their energy via radical structural reconstruction. We find that a slightly radially buckled (12,0) SWNT (see Fig. 3(a)) has a diameter of 1.50 nm, with slightly longer Zn-S bond lengths (2.253–2.258 Å) than in the corresponding smooth sheet. Our structural search approaches both give several more energetically stable reconstructed configurations, the most stable of which is shown in Fig. 3(b). This reconstructed (12,0) ZnS SWNT has very similar Zn-S bond lengths (2.265–2.278 Å) to the reconstructed sheet, and it is 0.04 eV/ZnS lower in energy than the slightly buckled (12,0) SWNT, with a significantly reduced diameter ($\sim$1.37 nm, taken as an average of maximum and minimum diameters). Like the reconstructed sheet, the Zn centers of the reconstructed SWNT lie in almost perfectly planar environments with respect to their three neighboring S atoms protruding, that protrude inwardly and outwardly (by $\sim\pm$1.0 Å with respect to a cylindrical surface lying symmetrically between the most inner and outer S atoms). As for the 2D ZnS sheets, we also find that the application of strain (parallel to the axis of the tube) can induce an interconversion between the reconstructed and slightly buckled SWNTs. Specifically, an axial tensile strain of $\geqslant$9% applied to the reconstructed SWNT and application of $\geqslant$4% axial tensile strain to the slightly buckled SWNT lead to the same strained structure. From this elongated geometry, relaxation, or application of axial compressive strain, can lead to either of the two SWNT energy minima (see Fig. 3(c)).

Consistent with the electronic structure of bulk ZnS, and previous studies of slightly buckled ZnS SWNTs[19,20] and ZnS nanofilms,[16] our reconstructed ZnS sheets and SWNTs both have direct gamma point gaps. Although the calculated absolute band gaps are underestimated by Generalized Gradient Approach (GGA) DFT, we use the difference between the calculated (2.07 eV) and experimental (3.75 eV)[22] wz-ZnS band gaps as an approximate corrective shift, which is applied to all reported gaps. The resulting values are only intended as a rough guide to actual band gaps and should in no way be regarded as accurate quantitative predictions. At their respective minimum energy geometries, where the band gaps are largest, larger gaps are found for the reconstructed ZnS sheet (4.70 eV) and (12,0) SWNT (4.86 eV) as compared to their relatively smooth counterparts (4.21 eV and 4.28 eV, respectively), i.e., $\sim$0.5 eV difference in each case. It is thus clear that the (opto)electronic and mechanical degrees of freedom in these systems are strongly coupled. Considering strain, not only as a means to traverse between minima, but more generally as an adjustable system variable, we see that these systems also allow for large continuous and reversible band gap variation (see Figs. 2(b) and 3(d)). For example, starting with the reconstructed (12,0) SWNT at its minimum energy geometry, we may, by increasing the axial compression continuously up to 18%, decrease its band gap in a near-linear fashion, eventually inducing an overall decrease of $\sim$1.5 eV. Based upon our band gap estimates, this mechanically induced band gap engineering would allow access to a wide range of UV photon energies (approximately between 3.3 and 4.8 eV), with possible applications in tunable wide-band optoelectronic devices. We note that similar calculations (e.g., C,[23] BN,[24] SiC[25]), and experiments in the case of C,[26] on other (n,0) SWNT systems have also shown strain-induced band gap variations. Specific to ZnS, however, it is possible to employ strain to switch between two stable energy minima, each with a distinctly different gap.

ZnS sheets display a more complex nonlinear electronic response upon application of perpendicular in-plane tensile strains. In the rectangular sheet, different strains along the *a* and *b* lattice directions can combine to give a range of band gap changes with a slightly smaller range of band gap energies ($\sim$3.5–4.5 eV, see Fig. 2(b)) than in the SWNTs. In experiments, although it is possible to study unsupported single layers, it is much easier to study monolayers that are grown on supporting materials. Single wz-ZnS monolayers are often grown as passivating layers on nanostructures of other inorganic semiconductors with smaller band gaps (e.g., CdSe) in order to improve quantum yields.[27] The structures

of these single layers are, however, strongly bound to the semiconductor support and are likely to be epitaxially locked into a structure determined by that of the support.[27] Although our results suggest that epitaxial growth of ZnS may be facilitated due to its capacity to adapt its structure to better match that of a relatively rigid bulk support, once it has been prepared, this adaptiveness, and thus its elasto-optic response, will be largely diminished. From experimental and theoretical studies of single flat hexagonal sheets of BN and ZnO grown on Ag(111) metal surfaces, the sheet-support interaction seems to be relatively much weaker.[4,28,29] For a monolayer of ZnS grown on a very weakly interacting support (e.g., a suitable noble metal), we would thus expect to observe significant geometric reconstruction. By varying the sheet-support interaction strength (e.g., by varying support material, temperature, etc.), the degree of reconstruction and the electronic response could be varied. Predictive calculations as to appropriate choices of support are currently being pursued. A change in the anion in ZnS by one position in its respective group (i.e., S $\rightarrow$ O) is known to give a system (i.e., ZnO) that can only stably exhibit the flat sheet.[3–5] Our preliminary calculations for systems where a cation is exchanged for Cd and/or the anion is exchanged for Se also appear to exhibit similar bistable behavior to that found for ZnS, thus illustrating the versatility and generality of this effect.

In summary, we predict that the low-energy structures of hexagonal ordered single sheets of ZnS, and nanostructures formed thereof, exhibit strongly reconstructed geometries that are distinct from the relatively smooth structures of graphene-based systems and analogous systems of other studied AB materials (e.g., BN, SiC, ZnO). We find that application of compressive and/or tensile strain allows for reversibe passage between the reconstructed ZnS systems and smooth structured higher-lying energy minima. In both ZnS single sheet graphene analogues and SWNTs, this energetic and structural bistability is coupled to significant changes in the direct band gap. This remarkable nanoscale mechanical-electronic response may have a range of future applications, such as optoelectronic devices and sensors.

Supporting grants and institutions include FIS2008-02238, 2009SGR1041, and XRQTC, National Science and Technology Development Agency (NSTDA chair professorship, NANOTEC Center of Excellence), and the Commission on Higher Education (National Research University of Thailand, the Joint Ph.D. Program Thai doctoral degree (NK)). Computer time on MareNostrum (BSC) is acknowledged.

*Corresponding author: s.bromley@ub.edu

[1] K. S. Novoselov, A. K. Geim, S. V. Morozov, D. Jiang, Y. Zhang, S. V. Dubonos, I. V. Grigorieva, and A. A. Firsov, Science **306**, 5696 (2004).
[2] M. Corso, W. Auwärter, M. Muntwiler, A. Tamai, T. Greber, and J. Osterwalder, Science **303**, 217 (2004).
[3] C. L. Freeman, F. Claeyssens, N. L. Allan, and J. H. Harding, Phys. Rev. Lett. **96**, 066102 (2006).
[4] C. Tusche, H. L. Meyerheim, and J. Kirschner, Phys. Rev. Lett. **99**, 026102 (2007).
[5] E. Bekaroglu, M. Topsakal, S. Cahangirov, and S. Ciraci, Phys. Rev. B **81**, 075433 (2010).
[6] M. Topsakal, S. Cahangirov, E. Bekaroglu, and S. Ciraci, Phys. Rev. B **80**, 235119 (2009).
[7] S. Cahangirov, M. Topsakal, E. Aktürk, H. Şahin, and S. Ciraci, Phys. Rev. Lett. **102**, 236804 (2009).
[8] X. Fang, Y. Bando, U. K. Gautam, T. Zhai, H. Zeng, X. Xu, M. Liao, and D. Golberg, Crit. Rev. Solid State Mater. Sci. **34**, 190 (2009).
[9] G. Kresse and J. Hafner, Phys. Rev. B **47**, 558 (1993).
[10] J. P. Perdew, K. Burke, and Y. Wang, Phys. Rev. B **54**, 16533 (1996).
[11] P. E. Blöchl, Phys. Rev. B **50**, 17953 (1994).
[12] H. J. Monkhorst and J. D. Pack, Phys. Rev. B **13**, 5188 (1976).
[13] W. Sangthong, J. Limtrakul, F. Illas, and S. T. Bromley, Nanoscale **2**, 72 (2010).
[14] S. Hamad, S. Cristol, and C. R. A. Catlow, J. Phys. Chem. B **106**, 11002 (2002).
[15] J. D. Gale, Z. Kristallogr. **220**, 552 (2005).
[16] X. Zhang, H. Zhang, T. He, and M. Zhao, J. Appl. Phys. **108**, 064317 (2010).
[17] E. Hernández, C. Goze, P. Bernier, and A. Rubio, Phys. Rev. Lett. **80**, 4502 (1998).
[18] S. Pal, B. Goswami, and P. Sarkar, J. Phys. Chem. C **111**, 1556 (2007).
[19] X. Zhang, M. Zhao, S. Yan, T. He, W. Li, X. Lin, Z. Xi, Z. Wang, X. Liu, and Y. Xia, Nanotech. **19**, 305708 (2008).
[20] L. Li, M. Zhao, X. Zhang, Z. Zhu, F. Li, J. Li, C. Song, X. Liu, and Y. Xia, J. Phys. Chem. C **112**, 3509 (2008).
[21] Y. Li, Z. Zhou, Y. Chen, and Z. Chen, J. Chem. Phys. **130**, 204706 (2009).
[22] A. Ebina, E. Fukunaga, and T. Takahashi, Phys. Rev. B **12**, 687 (1975).
[23] P. K. Valavala, D. Banyai, M. Seel, and R. Pati, Phys. Rev. B, **78**, 235430 (2008).
[24] Y. Kinoshita, and N. Ohno, Phys. Rev. B **82**, 085433 (2010).
[25] Z. Wang, X. Zu, H. Xiao, F. Goa, and W. J. Weber, Appl. Phys. Lett. **92**, 183116 (2008).
[26] E. D. Minot, Y. Yaish, V. Sazonova, J.-Y. Park, M. Brink, and P. L. McEuen, Phys. Rev. Lett. **90**, 156401 (2003).
[27] B. O. Dabbousi, J. Rodriguez-Viejo, F. V. Mikulec, J. R. Heine, M. Mattoussi, R. Ober, K. F. Jensen, and M. G. Bawendi, J. Phys. Chem. B **101**, 9463 (1997).
[28] F. Müller, S. Hüfner, H. Sachdev, R. Laskowski, P. Blaha, and K. Schwarz, Phys. Rev. B **82**, 113406 (2010).
[29] R. Laskowski, P. Blaha, and K. Schwarz, Phys. Rev. B **78**, 045409 (2008).

DOI: 10.1002/cphc.201100642

Formaldehyde Encapsulated in Lithium-Decorated Metal-Organic Frameworks: A Density Functional Theory Study

Thana Maihom,[a, b] Saowapak Choomwattana,[a, b] Pipat Khongpracha,[a, b, c] Michael Probst,[d] and Jumras Limtrakul*[a, b, c]

The stability of monomeric formaldehyde encapsulated in the lithium-decorated metal-organic framework Li-MOF-5 was investigated by means of density functional calculations with the M06-L functional and the 6-31G(d,p) basis set. To assess the efficiency of Li-MOF-5 for formaldehyde preservation, we consider the reaction kinetics and the thermodynamic equilibrium between formaldehyde and its trimerized product, 1,3,5-trioxane. We propose that trimerization of encapsulated formaldehyde takes place in a single reaction step with an activation energy of 34.5 kcal mol^{-1}. This is 17.2 kcal mol^{-1} higher than the corresponding activation energy in the bare system. In addition, the reaction energy of the system studied herein is endothermic by 6.1 kcal mol^{-1} and the Gibbs free energy (ΔG) of the reaction becomes positive (11.0 kcal mol^{-1}). Consequently, the predicted reverse rate for the trimerization reaction in the Li-MOF-5 is significantly faster than the forward rate. The calculations show that the oligomerization of formaldehyde in Li-MOF-5 is a reversible reaction, suggesting that such a zeolite might be a good candidate material for preserving formaldehyde in its monomeric form.

1. Introduction

Formaldehyde, a well-known volatile organic compound (VOC), is widely used as an industrial feedstock for the production of fine chemicals, resins, and several domestic products such as paints. Nevertheless, its applicability is limited by its low boiling point of −19.5 °C. Moreover, formaldehyde rapidly self-polymerizes into chain polymers such as paraformaldehyde or into oligomers such as the cyclic trioxane. Its preservation in the monomeric form is difficult.

Na–X and Na–Y zeolites have been reported to be capable of storing formaldehyde.[1] These materials stabilize and also activate formaldehyde to undergo carbonyl–ene reactions with a variety of olefins as has also been clarified by theoretical studies.[2] In recent years, metal-organic frameworks (MOFs) were investigated as promising candidates for gas storage (e.g. CO_2 and H_2)[3] because of their flexibility and the possibility to tune their surface composition and pore structures by changing the metal center or the organic linker. Computational and experimental investigations[4–5] have shown that metal atoms or cations that either decorate the linkers or are incorporated into them can enhance the capacity of MOFs for gas storage. The most frequently used metal is Lithium (Li) because decorating MOF structures with it is especially simple. Li on MOF linkers forms an accessible open metal site that can interact well with incoming molecules. It can therefore be expected to interact with formaldehyde in a way similar to the Na cation in zeolites, which is known to prevent formaldehyde from self-polymerizing.

To the best of our knowledge, such a system has not yet been studied in detail. Therefore, we investigated it herein by means of density functional theory (DFT) calculations with the M06-L functional. We calculated the reaction mechanism and the corresponding energy profile defined by the structures of the adsorbed starting complex (three formaldehydes coordinated to Li), the transition state and the product trioxane. We also compared our findings to those obtained for the bare system.

2. Results and Discussion

2.1. Decoration of MOF-5 with Li and its Subsequent Application as Formaldehyde Adsorption Complex

Herein, MOF-5[6] (also called IRMOF-1) was chosen as host material. It consists of Zn_4O clusters connected to 1,4-benzenedi-

[a] T. Maihom, S. Choomwattana, Dr. P. Khongpracha, Prof. Dr. J. Limtrakul
Laboratory for Computational and Applied Chemistry
Department of Chemistry
Faculty of Science and Center of Nanotechnology
Research and Development Institute
Kasetsart University
Bangkok 10900 (Thailand)
Fax: (+66) 2-562-5555
E-mail: Jumras.l@ku.ac.th

[b] T. Maihom, S. Choomwattana, Dr. P. Khongpracha, Prof. Dr. J. Limtrakul
NANOTEC Center of Excellence
National Nanotechnology Center
Kasetsart University
Bangkok 10900 (Thailand)

[c] Dr. P. Khongpracha, Prof. Dr. J. Limtrakul
Center for Advanced Studies in Nanotechnology and its Applications in Chemical, Food, and Agricultural Industries
Kasetsart University
Bangkok 10900 (Thailand)

[d] Prof. Dr. M. Probst
Institute of Ion Physics and Applied Physics
University of Innsbruck
6020 Innsbruck (Austria)

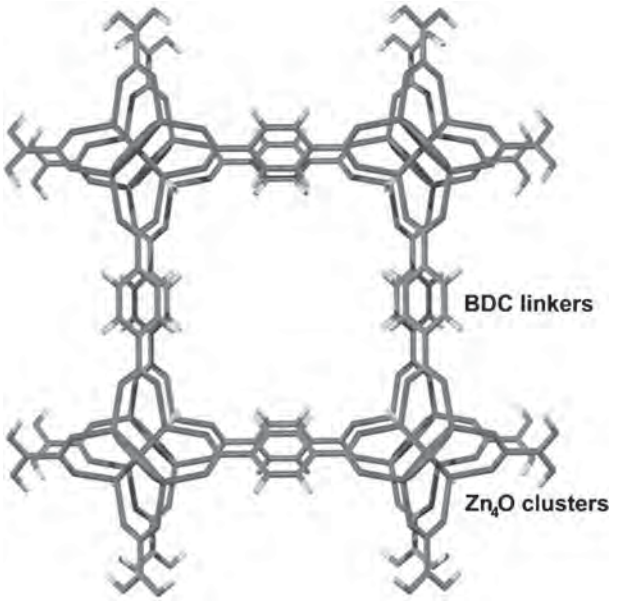

Figure 1. Unit cell of MOF-5.

carboxylate (BDC) organic linkers to form a cubic porous network with the unit formula $Zn_4O(BDC)_3$. The unit cell of MOF-5 is shown in Figure 1. Because of its large size, we used an abridged representative model to reduce the computational costs. A model consisting of two Zn_4O clusters joined by one BDC linker is the simplest one that can reasonably mimic the active site of the MOF-5 linker (Figure 2a). It is comparable to the models that have been used in previous studies.[7] The remaining BDC linkers not taken into account were replaced by hydrogen atoms. The Li ion was placed on top of the benzene ring (Figure 2b) which has been found[4a,5] to be its preferred position on hexagonal aromatic hydrocarbon structures. The Li-MOF model has the sum formula $Zn_8O_{26}C_{18}H_{14}Li$.

The geometrical parameters of selected geometrical structures of pure MOF-5 and of Li-MOF-5 are given in Table 1. In

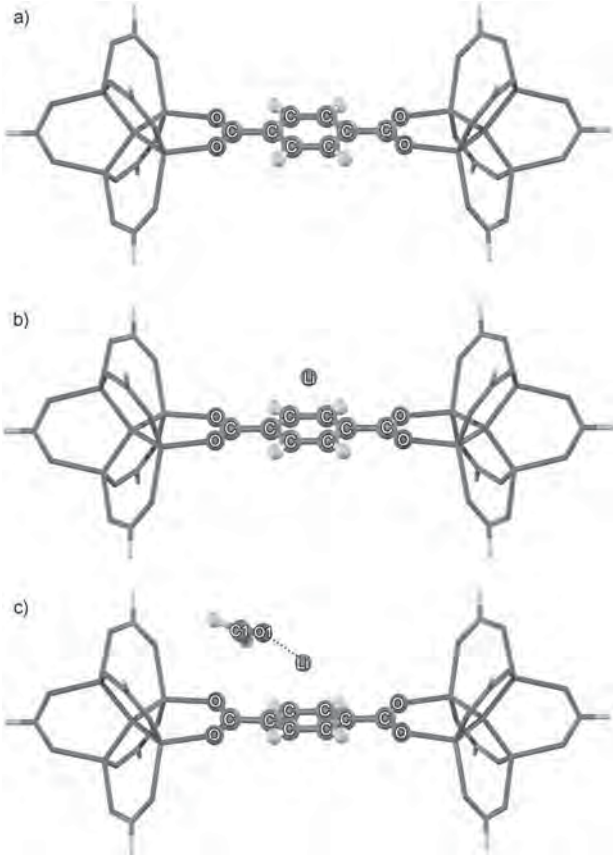

Figure 2. Optimized structures for a) pure MOF-5 (two Zn_4O clusters joined by one 1,4-benzenedicarboxylate organic linker), b) Li-MOF-5 and c) formaldehyde adsorbed on Li-MOF (Ads_MOF).

the MOF-5 cluster, the average C–C bond distance ($<C–C>_{bz}$) in the benzene ring and the C–O–C bond angle ($<C–O–C>$) are 1.40 Å and 124.6°, respectively. These values are in a good agreement with the experimental results of 1.39 Å and 126.4°, respectively.[6c] For Li-MOF-5, the Li cation coordinates symmetrically through a η^6-type interaction to the hexagonal aromatic ring of the BDC linker. The average distance between the C atoms and Li ($<Li\cdots C>$) is 2.39 Å. The adsorption of the metal cation causes the average C–C bond distance and the O–C–O angle to increase by 0.01 Å and 3.0°, respectively. The natural atomic population of Li is $+0.941\,|e|$, which is consistent with the values between $+0.5\,|e|$ to $+1.0\,|e|$ for Li-doped systems[5]. This charge transfer also explains the abovementioned increase in the geometrical parameters. The calculated adsorption energy (ΔE_{Li}) of a Li cation on MOF-5 is defined as follows in Equation (1):

Table 1. Optimized geometrical parameters of the species involved in the trimerization of formaldehyde in Li-MOF-5.

Parameter	Isolated cluster	Isolated Li-MOF-5 cluster	Formaldehyde adsorption (Ads_MOF)	Formaldehyde adsorption (Coads_MOF)	Transition state (TS1_MOF)	Trioxane product (Prod_MOF)
Distances [Å]						
$<C–C>_{bz}$	1.40	1.41	1.40	1.40	1.41	1.41
$<Li\cdots C>$	–	2.39	2.51	3.03	2.53	2.55
O1-Li	–	–	1.90	1.93	1.82	2.17
O2-Li	–	–	–	1.97	3.85	2.18
O3-Li	–	–	–	1.98	3.36	2.20
C1-O1	1.20	–	1.22	1.21	1.30	1.43
C2-O2	1.20	–	–	1.21	1.24	1.42
C3-O3	1.20	–	–	1.21	1.27	1.42
O1-C2	–	–	–	4.57	2.25	1.42
O2-C3	–	–	–	3.95	1.94	1.43
O3-C1	–	–	–	4.50	1.61	1.42
Angles [°]						
$<O–C–O>$	124.6	127.6	126.8	125.4	126.9	126.7

$$\Delta E_{Li} = E(\text{Li}-\text{MOF}) - E(\text{Li}) - E(\text{MOF}) \quad (1)$$

where *E*(Li-MOF), *E*(Li) and *E*(MOF) are the total energies of the clusters of Li-MOF (Li adsorbed), the isolated Li cation and the pure MOF-5 model, respectively. The adsorption energy of Li^+ on MOF-5 is $-32.9\,kcal\,mol^{-1}$. The difference between this value and the measured value of $-38.5 \pm 3.2\,kcal\,mol^{-1}$ for the Li^+-C_6H_6 complex[8] is explainable by a somewhat diminished π electron density over the benzene plane caused by the electrophilic nodes of the Zn_4O clusters.

The adsorption complex of one formaldehyde coordinated to the Li ion in MOF-5 (Ads_MOF) is depicted in Figure 2c and its key optimized geometrical parameters are listed in Table 1. The formaldehyde molecule interacts with the Li ion through its lone pair electrons. This conformation resembles the ones found for formaldehyde adsorbed into Na-FAU zeolites[2] and coordinated to Cu complexed in the paddlewheels of MOF-11.[9] The lone pair interaction induces the average lengthening of Li···C distances from 2.39 to 2.51 Å. The intermolecular distance between the oxygen of formaldehyde and the Li ion in the MOF is 1.90 Å. The C–O···Li-MOF angle is 138.4°. In addition, the electron transfer from O1 to the Li ion results in a slight elongation of the intramolecular carbon–oxygen bond of formaldehyde from 1.20 to 1.22 Å. The natural population analysis (NPA) revealed that the positive charge on Li is reduced from +0.941 to +0.876 $|e|$. The calculated adsorption energy of this complex is $-28.0\,kcal\,mol^{-1}$.

2.2. Reaction Mechanism of Formaldehyde Trimerization

The steric constraints in the MOF cavities prevent the polymerization of formaldehyde into a chain polymer. Therefore, we only concentrated on the trimerization reaction equilibrium between formaldehyde and trioxane in Li-MOF-5 at room temperature and compared this to the bare system. Selected geometrical parameters for this reaction step are shown in Table 1.

The trimerization is considered to proceed in a single step without intermediates. In the bare system, three formaldehyde molecules align to each other in a twisted hexagonal complex in which the interaction between a carbon atom and an oxygen atom of the next molecule causes the inter- and intramolecular C–O distances to become almost equal (Figure 3a). The complexation energy is $-7.3\,kcal\,mol^{-1}$. In the Li-MOF-5 system, the adsorbed formaldehydes' arrangement is quite different, mainly due to the effect of the Li ion. Three molecules

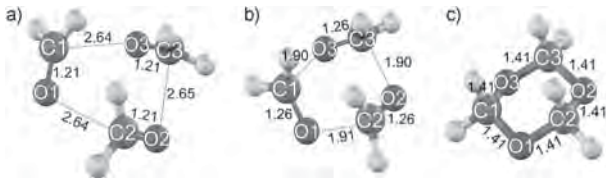

Figure 3. Optimized structures of the bare a) trimer (Complex_Bare), b) transition state (TS_Bare) and c) trioxane (Prod_Bare) for the trimerization reaction of unenclosed formaldehyde.

of formaldehyde coadsorb on the Li ion through coordination of the lone pair electrons of each formaldehyde oxygen atom to the Li ion (Figure 4a). The internuclear distances between the three formaldehyde oxygen atoms and Li^+ are 1.93, 1.97 and 1.98 Å, respectively. The coordination to Li^+ causes a slight elongation of the C=O double bonds from 1.20 in the isolated formaldehyde to 1.21 Å. The adsorption complex is additionally stabilized through hydrogen bonding from the hydrogen atoms of two formaldehyde molecules to the oxygen atoms of the linker. This causes the Li cation to shift slightly from the position above the middle of the benzene ring, as shown in Figure 4a. The total adsorption energy is -66.8 kcal mol^{-1}, indicating a considerable ability to stabilize monomeric formaldehyde.

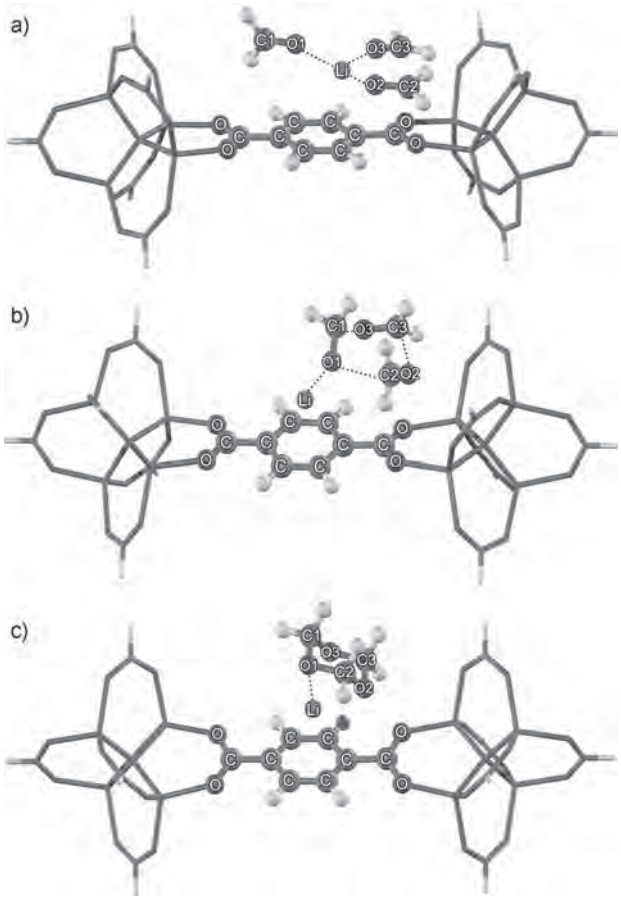

Figure 4. Optimized structures of the a) enclosed complex coordinated to Li (Coads_MOF), b) transition state (TS_MOF) and c) product (Prod_MOF) for the formaldehyde trimerization in the Li-MOF-5 system.

The cyclic trioxane product is created by the intermolecular C–O bond formation through the transition states shown in Figures 3b and 4b for the bare and the Li-MOF-5 systems, respectively. At both transition states, the intramolecular C=O double bonds of the formaldehyde molecules are stretched and the intermolecular C···O distances contract to form a new bond (Table 1). The hybridization of the formaldehyde C atoms changes from planar sp^2 to tetrahedral sp^3, as shown in Figur-

es 3b and 4b. In the bare system, the C=O double bonds increase from 1.21 to 1.26 Å while the intermolecular C···O distances decrease by about 0.75 Å. The activation barrier in this system was calculated to be 17.3 kcal mol^{-1}. Normal mode analysis reveals one imaginary frequency at 226.9*i* cm^{-1} associated with the transition state. In contrast to the bare system, the formaldehyde C=O double bonds in the MOF system are unequally increased with distances of 1.30, 1.24 and 1.27 Å for C1=O1, C2=O2 and C3=O3, respectively. This is due to effect of the Li cation. Additionally, the intramolecular C···O distances decrease to 2.25, 1.94 and 1.61 Å for C2···O1, C3···O2 and C1···O3, respectively. The transition state was confirmed by one imaginary frequency at 277.0*i* cm^{-1}. The calculated activation energy is 34.5 kcal mol^{-1}, which is higher than that of the bare system. The overall energy of the trioxane product in the bare reaction with respect to the isolated reactants is −25.3 kcal mol^{-1} which is in good agreement with a previous calculation.[2b] For Li-MOF-5, the strong interaction between the oxygens of trioxane and the Li^+ lead to an adsorption energy of −60.7 kcal mol^{-1} (see Figure 4c) with respect to the reactants.

The complete energy profiles for the formaldehyde trimerization in Li-MOF-5 and in the bare system are shown in Figure 5. The calculated thermodynamic properties and the

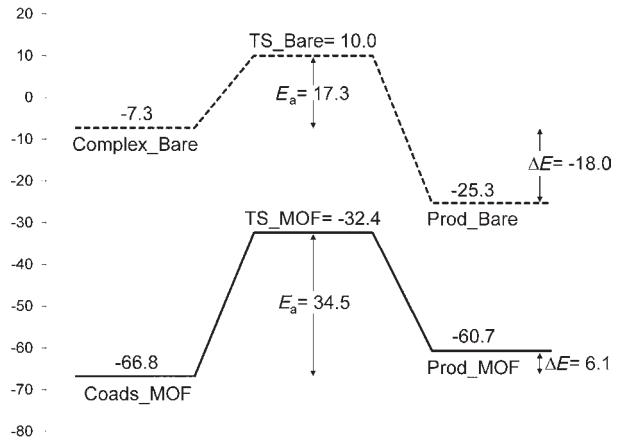

Figure 5. Energy profiles for the formaldehyde trimerization: bare system (----) and Li-MOF-5 system (——). The energies are in kcal mol^{-1}.

rate constants (k_r) are tabulated in Table 2. In the bare system, the overall reaction energy (ΔE) is exothermic by −18.0 kcal mol^{-1}. The Gibbs free reaction energy (ΔG) with respect to the isolated reactants is −2.0 kcal mol^{-1} which is close to the experimentally estimated ΔG of about −1.8 kcal mol^{-1}.[10] The overall reaction ΔG value for the trimerization is negative (−13.3 kcal mol^{-1}), as necessary for a spontaneous reaction in which the product side is favoured as can also be seen from the fact that k_r^+ outpaces k_r^-. In contrast, for the Li-MOF-5 system the reaction is endothermic and the trimerization product is thermodynamically less stable than the reactants. The reaction energy is 6.1 kcal mol^{-1} and the overall ΔG value is +11.0 kcal mol^{-1}. Therefore, the equilibrium for the Li-MOF-5 system lies strongly on the reactant side and in practice the reaction will hardly occur.

3. Conclusions

Density functional theory was used to investigate the adsorption and reaction of formaldehyde encapsulated into Li-decorated metal-organic frameworks by comparing them to the situation in the bare system. In order to demonstrate the preservation of formaldehyde in Li-MOF-5, the equilibrium between the adsorbed formaldehyde and trioxane was considered. The reaction is proposed to proceed in a single step without intermediates. The calculated activation barrier for the conversion of formaldehyde to trioxane in the Li-MOF-5 system was found to be 34.5 kcal mol^{-1}, which is 17.2 kcal mol^{-1} higher than in the bare system. The reaction energy and reaction free energy in the non-encapsulated system are negative, but positive in the Li-MOF-5 system, due to the higher adsorption energy of individual formaldehyde molecules compared to trioxane on Li^+ cations. Consequently, the rate constant of the reverse reaction is also larger than the one for the forward reaction. It can be suggested that Li-decorated MOF-5 might be a good candidate material to preserve and stabilize monomeric formaldehyde. It might also have a similar effect on other small ketones and on molecules prone to polymerize easily in general.

Computational Methods

The M06-L density functional[11] was used in all calculations. Recent studies of adsorption and reaction mechanisms in zeolites[12] and of H_2 adsorbed on light and transition metals that were doped on MOFs organic linkers[13] have been used to verify its usability. We checked this again for our systems. Single-point MP2 and M06-L calculations of the adsorption energy of Li^+ on MOF-5 give BSSE-corrected energies of −35.0 and 34.0 kcal mol^{-1}, respectively. The double-ζ 6-31G(d,p) basis set with polarization functions was employed for the H, C, O and Li atoms, while the Zn atom was described by the LANL2DZ pseudopotential and the corresponding basis set.[14] During geometry optimizations, only the 1,4-benzenedicarboxylate linker and the adsorbing molecule were allowed to relax while the rest of the structure was kept fixed at the crystallographic positions. Frequency calculations were performed at the same level of theory to identify the nature of all the stationary points and to obtain the zero point energy (ZPE) corrections. These calculations were also used to obtain thermodynamic properties. In addition, rate constants were calculated from the activation barriers and partition functions using classical transition-state theory (TST) according to Equa-

Table 2. Calculated reaction energy, thermodynamic properties and rate constant at 298.15 K for the trimerization of formaldehyde.

Systems	ΔE [kcal mol^{-1}]	ΔH [kcal mol^{-1}]	ΔG [kcal mol^{-1}]	k_r^+ [s^{-1}]	k_r^- [s^{-1}]
Bare	−18.0	−21.5	−13.3	1.86×10^{-3}	3.10×10^{-13}
Li-MOF-5	6.1	2.4	11.0	7.31×10^{-17}	8.91×10^{-9}

tion (2):

$$k_r = \frac{k_B T}{h} \frac{q_{TS}}{q_{Int}} \exp(-\Delta E_a / RT) \quad (2)$$

where ΔE_a is the activation energy, k_B is Boltzmann's constant, h is Planck's constant, T is the absolute temperature, R is the universal gas constant, and q_{TS} and q_{Int} are the total partition functions for the transition state and the adsorption or product complex, respectively, in which electronic, translational, rotational and vibrational partition functions are included. In the case of the system with Li-MOF-5, the atoms of the immobile framework do not contribute to the translational and rotational parts of the partition function. The rate constants were derived for the temperature of 298.15 K. All calculations were performed with the Gaussian 03 code[15] modified by incorporating the Minnesota Density Functionals module 3.1 by Zhao and Truhlar.[11]

Acknowledgements

This work was supported in part by grants from the National Science and Technology Development Agency (NANOTEC Center of Excellence and NSTDA Chair Professor), the Thailand Research Fund (to J.L.), the Kasetsart University Research and Development Institute (KURDI), the Commission on Higher Education, Ministry of Education ("National Research University of Thailand" and "Postgraduate Education and Research Programs in Petroleum and Petrochemicals and Advanced Materials") as well as by the program Strategic Scholarships for Frontier Research network for the Joint Ph.D. Program Thai Doctoral degree from the Office of the Higher Education Commission, Thailand (to T.M. and S.C.). M.P. acknowledges support from the Austrian Ministry of Science (infrastructure grant to the LFU scientific computing platform) and the RFBR-FWF projects I200-N29 and 09-03-91001-a. The authors thank Donald G. Truhlar and Yan Zhao for providing them with the code for the M06-L functional.

Keywords: density functional calculations · encapsulation · formaldehyde · metal-organic frameworks · zeolites

[1] T. Okachi, M. Onaka, *J. Am. Chem. Soc.* **2004**, *126*, 2306 – 2307.

[2] a) W. Sangthong, M. Probst, J. Limtrakul, *J. Mol. Struct.* **2005**, *748*, 119 – 127; b) M. Tomita, Y. Masui, M. Onaka, *J. Phys. Chem. Lett.* **2010**, *1*, 652 – 656.

[3] a) N. L. Rosi, J. Eckert, M. Eddaoudi, D. T. Vodak, J. Kim, M. O'Keeffe, O. M. Yaghi, *Science* **2003**, *300*, 1127 – 1129; b) O. M. Yaghi, M. O'Keeffe, N. W. Ockwig, H. K. Chae, M. Eddaoudi, J. Kim, *Nature* **2003**, *423*, 705 – 714; c) T. Düren, L. Sarkisov, O. M. Yaghi, R. Q. Snurr, *Langmuir* **2004**, *20*, 2683 – 2689; d) L. Pan, M. B. Sander, X. Huang, J. Li, M. Smith, E. Bittner, B. Bockrath, J. K. Johnson, *J. Am. Chem. Soc.* **2004**, *126*, 1308 – 1309; e) A. R. Millward, O. M. Yaghi, *J. Am. Chem. Soc.* **2005**, *127*, 17998 – 17999; f) J. L. C. Rowsell, E. C. Spencer, J. Eckert, J. A. K. Howard, O. M. Yaghi, *Science* **2005**, *309*, 1350 – 1354; g) S. Bourrelly, P. L. Llewellyn, C. Serre, F. Millange, T. Loiseau, G. Ferey, *J. Am. Chem. Soc.* **2005**, *127*, 13519 – 13521; h) D. J. Collins, H. C. Zhou, *J. Mater. Chem.* **2007**, *17*, 3154 – 3160; i) S. S. Han, W.-Q. Deng, W. A. Goddard III, *Angew. Chem.* **2007**, *119*, 6405 – 6408; *Angew. Chem. Int. Ed.* **2007**, *46*, 6289 – 6292; j) N. A. Ramsahye, G. Maurin, S. Bourelly, P. Lllewellyn, C. Serre, T. Loiseau, T. Devic, G. Ferey, *J. Phys. Chem. C* **2008**, *112*, 514 – 520; k) L. J. Murray, M. Dinca, J. R. Long, *Chem. Soc. Rev.* **2009**, *38*, 1294 – 1314; l) Y. H. Hu, L. Zhang, *Adv. Mater.* **2010**, *22*, E117 – E130.

[4] a) S. S. Han, W. A. Goddard III, *J. Am. Chem. Soc.* **2007**, *129*, 8422 – 8423; b) K. L. Mulfort, J. T. Hupp, *J. Am. Chem. Soc.* **2007**, *129*, 9604 – 9605; c) K. L. Mulfort, J. T. Hupp, *Inorg. Chem.* **2008**, *47*, 7936 – 7938; d) D. Zhao, D. Yuan, H. C. Zhou, *Energy Environ. Sci.* **2008**, *1*, 222 – 235; e) E. Klontzas, A. Mavrandonakis, E. Tylianakis, G. E. Froudakis, *Nano Lett.* **2008**, *8*, 1572 – 1576; f) P. Dalach, H. Frost, R. Q. Snurr, D. E. Ellis, *J. Phys. Chem. C* **2008**, *112*, 9278 – 9284; g) D. Wu, Q. Xu, D. Liu, C. Zhong, *J. Phys. Chem. C* **2010**, *114*, 16611 – 16617.

[5] a) A. Blomqvist, C. M. Araujo, P. Srepusharawoot, R. Ahuja, *Proc. Natl. Acad. Sci. USA* **2007**, *104*, 20173 – 20176; b) A. Mavrandonakis, E. Tylianakis, A. K. Stubos, G. E. Froudakis, *J. Phys. Chem. C* **2008**, *112*, 7290 – 7294.

[6] a) H. Li, M. Eddaoudi, T. L. Groy, O. M. Yaghi, *J. Am. Chem. Soc.* **1998**, *120*, 8571 – 8572; b) H. Li, M. Eddaoudi, M. O'Keeffe, O. M. Yaghi, *Nature* **1999**, *402*, 276 – 279; c) M. Eddaoudi, J. Kim, N. Rosi, D. Vodak, J. Wachter, M. O'Keeffe, O. M. Yaghi, *Science* **2002**, *295*, 469 – 472.

[7] K. Sillar, A. Hofmann, J. Sauer, *J. Am. Chem. Soc.* **2009**, *131*, 4143 – 4150.

[8] J. C. Amicangelo, P. B. Armentrout, *J. Phys. Chem. A* **2000**, *104*, 11420 – 11432.

[9] S. Choomwattana, T. Maihom, P. Khongpracha, M. Probst, J. Limtrakul, *J. Phys. Chem. C* **2008**, *112*, 10855 – 10861.

[10] Kagaku Binran, *Chemistry Handbook Basic 4th ed./Applied 5th ed.*, CSJ Publications, Maruzen, Tokyo, **2004**.

[11] a) Y. Zhao, D. G. Truhlar, *J. Phys. Chem. C* **2008**, *112*, 6860 – 6868; b) Y. Zhao, D. G. Truhlar, *Acc. Chem. Res.* **2008**, *41*, 157 – 167.

[12] a) T. Maihom, B. Boekfa, J. Sirijaraensre, T. Nanok, M. Probst, J. Limtrakul, *J. Phys. Chem. C* **2009**, *113*, 6654 – 6662; b) B. Boekfa, S. Choomwattana, P. Khongpracha, J. Limtrakul, *Langmuir* **2009**, *25*, 12990 – 12999; c) C. Kumsapaya, K. Bobuatong, P. Khongpracha, Y. Tantirungrotechai, J. Limtrakul, *J. Phys. Chem. C* **2009**, *113*, 16128 – 16137; d) T. Maihom, P. Pantu, C. Tachakritikul, M. Probst, J. Limtrakul, *J. Phys. Chem. C* **2010**, *114*, 7850 – 7856; e) B. Boekfa, P. Pantu, M. Probst, J. Limtrakul, *J. Phys. Chem. C* **2010**, *114*, 15061 – 15067; f) S. Wannakao, B. Boekfa, P. Khongpracha, M. Probst, J. Limtrakul, *ChemPhysChem* **2010**, *11*, 3432 – 3438; g) K. Bobuatong, M. Probst, J. Limtrakul, *J. Phys. Chem. C* **2010**, *114*, 21611 – 21617.

[13] a) S. J. Kolmann, B. Chan, M. J. T. Jordan, *Chem. Phys. Lett.* **2008**, *467*, 126 – 130; b) R. B. Getman, J. H. Miller, K. Wang, R. Q. Snurr, *J. Phys. Chem. C* **2011**, *115*, 2066 – 2075.

[14] P. J. Hay, W. R. Wadt, *J. Chem. Phys.* **1985**, *82*, 270 – 283.

[15] Gaussian 03, (Revision B.05), M. J. Frisch, G. W. Trucks, H. B. Schlegel, G. E. Scuseria, M. A. Robb, J. R. Cheeseman, J. A. Montgomery, Jr., T. Vreven, K. N. Kudin, J. C. Burant, J. M. Millam, S. S. Iyengar, J. Tomasi, V. Barone, B. Mennucci, M. Cossi, G. Scalmani, N. Rega, G. A. Petersson, H. Nakatsuji, M. Hada, M. Ehara, K. Toyota, R. Fukuda, J. Hasegawa, M. Ishida, T. Nakajima, Y. Honda, O. Kitao, H. Nakai, M. Klene, X. Li, J. E. Knox, H. P. Hratchian, J. B. Cross, V. Bakken, C. Adamo, J. Jaramillo, R. Gomperts, R. E. Stratmann, O. Yazyev, A. J. Austin, R. Cammi, C. Pomelli, J. W. Ochterski, P. Y. Ayala, K. Morokuma, G. A.Voth, P. Salvador, J. J. Dannenberg, V. G. Zakrzewski, S. Dapprich, A. D. Daniels, M. C. Strain, O. Farkas, D. K. Malick, A. D. Rabuck, K. Raghavachari, J. B. Foresman, J. V. Ortiz, Q. Cui, A. G. Baboul, S. Clifford, J. Cioslowski, B. B. Stefanov, G. Liu, A. Liashenko, P. Piskorz, I. Komaromi, R. L. Martin, D. J Fox, T. Keith, M. A. Al-Laham, C. Y. Peng, A. Nanayakkara, M. Challacombe, P. M. W. Gill, B. Johnson, W. Chen, M. W. Wong, C. Gonzalez, J. A. Pople, Gaussian, Inc., Wallingford, CT, **2004**.

Received: August 22, 2011
Revised: September 23, 2011
Published online on ■■ ■■, 2011

ARTICLES

*T. Maihom, S. Choomwattana, P. Khongpracha, M. Probst, J. Limtrakul**

■■ – ■■

Formaldehyde Encapsulated in Lithium-Decorated Metal-Organic Frameworks: A Density Functional Theory Study

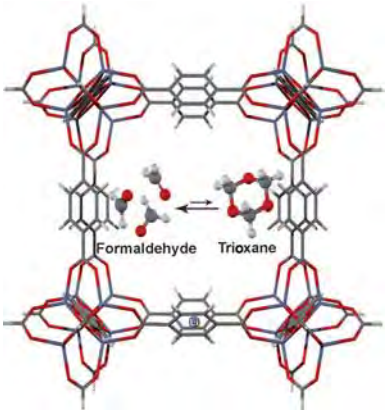

Gotcha: The equilibrium between adsorbed formaldehyde and trioxane in the Li-MOF-5 system (see picture) was investigated by means of density functional calculations with the M06-L functional.

บทความที่นำเสนอ
ในการประชุมวิชาการนานาชาติ

Nanotech Conference 2009

ณ ประเทศสหรัฐอเมริกา

ระหว่างวันที่ 3-7 พฤษภาคม 2552

จำนวน 8 เรื่อง

The Quantum Confinement Effect on the Adsorption and Reaction of Aliphatic Hydrocarbons on 'Nano Reactor' ZSM-5 Zeolite: A Newly Developed Density Functional Theory (DFT) Investigation

B. Boekfa [a,b], S. Choomwattana [a,b], P. Maitarad [a,b], P. Limtrakul [a], J. Limtrakul [a,b,*]

[a]Laboratory for Computational and Applied Chemistry, Chemistry Department, Faculty of Science, Kasetsart University, Bangkok 10900, Thailand
[b]NANOTEC Center of Excellence, National Nanotechnology Center, Kasetsart University Research and Development Institute, Thailand
[*]E-mail: jumras.l@ku.ac.th, Tel: +662-562-5555 ext 2169, Fax: +662-562-5555 ext 2176

ABSTRACT

Full quantum calculations with a newly developed functional, M06-L, on the ZSM-5 models of 5T, 12T, 34T, 46T and 128T were performed to simulate the nanoporous system. Methane and ethane are chosen to represent saturated hydrocarbons. The calculated adsorption energies are -7.0 kcal/mol for methane and -11.1 kcal/mol for ethane, which agree well with the experimental estimates of -6.7 and -9.1 kcal/mol. The M06-L method is also applied for the first time to systematically investigate the proton exchange reactions of methane and ethane within the nano-reactor of zeolite. The concerted mechanism is proposed for the reaction. The calculated activation energy of methane is 35.3 kcal/mol, which is comparable with the experimental data (33.4 kcal/mol), whereas the energy of ethane is 33.0 kcal/mol. The effect of nano-quantum confinement of the extended zeolite framework on adsorption and reaction mechanisms has been clearly demonstrated not only to better stabilize the adsorption complexes achieving the observed values but also to lower their activation energies to approach experimental benchmarking.

Keywords: zeolites, proton exchange reaction, M06-L functional, confinement effect, light alkanes

1 INTRODUCTION

In fine-chemical and pharmaceutical manufacture and in petroleum refining, zeolites, which have a combination of high stability with their excellent activity in acid-mediated reactions [1-3], have been applied in the process of heterogeneous catalysis. Especially, ZSM-5, patented in 1975, is widely used in chemical industries such as hydrocarbon cracking, isomerization, alkylation reaction and methanol to olefins (MTO) [4].

To clearly envision the structure, adsorption properties and chemical reaction mechanism, theoretical study can offer a practical tool that provides insight to the reaction mechanism complementing experimental investigations or, in certain cases, offer an understanding that is not possible by experimental investigations. Numerous experimental [5-9] and theoretical [10,11] researches have been devoted to understanding the chemistry of ZSM-5. Attempts have been made to develop the computational methodology that can precisely predict the physical and chemical properties of the zeolite itself and the reaction inside its nanocavity. The Density Functional Theory (DFT), especially B3LYP, has been widely used to study the interaction of hydrocarbons with zeolites. However, the limitation of the DFT calculations previously employed was that the contribution of dispersion interactions was not taken into account. This interaction contribution in the adsorption has been found to be essential in the chemical adsorptions and reactions inside the zeolite pore [8,12-17]. To overcome the enormous computational resource required for a DFT calculation on a large model, the ONIOM scheme combined with QM/MM calculation [18,19] is applied to such systems. This provides an acceptable balance between the accuracy of the results and the computational cost. The ONIOM scheme provides only an approximation [14,15,18-21] and, therefore, the quest for a more accurate method continues. Recently, the newly developed functional called M06-L was introduced by Zhao and coworkers [22]. It is recommended for transition metal thermochemistry, noncovalent interactions and for when a local functional is required; a local functional has a much lower cost for large systems [23-25]. With the improved combination of the computational method and the realistic model, we hypothesize that this method should be able to represent the interaction within the zeolite system.

The aim of this work is threefold: first, to present a theoretical study on the nature of the H-ZSM-5 adsorption complex of methane and ethane, second, to further describe the proton exchange reaction of methane and ethane catalyzed by the zeolite and third, to present, for the first time, the full quantum calculation application of the 'noncovalent interaction represented' M06-L method on the zeolite framework.

2 METHODOLOGY

ZSM-5 structure from the XRD data was trimmed down to become 5T, 12T, 34T, 46T and 128T cluster models (see Fig. 1). The 5T cluster ($AlSi_4O_4H_{13}$) is modeled to represent only the Brønsted active site. The T12 position was selected to be Al due to its being the most energetically favorable [26]. The 12T stands for the 10-membered-ring window of the zigzag nanochannel of the porous structure. The model was extended to 34T to cover the intersection of straight-zigzag channels, including some part of the zigzag channel. Adopted from our previous publications [12,13,20], the 46T model is similar to the 34T, but the framework

is extended surrounding the acid center in the zigzag channel. The largest model, 128T, envelops the whole model of 46T with another shell of tetrahedral subunits. The adsorption and reaction of methane and ethane on different H-ZSM-5 models are fully quantum calculated with the M06-L functional [22], along with the 6-31G(d,p) basis set. During the structure optimization on the 5T, 12T, 34T and 46T systems, the 5T portion of the active site region ($AlSi_4O_4H$) and the reacting molecule are allowed to relax while the rest is fixed at the crystallographic coordinates [27]. The transition states (TS) of the reaction were characterized by the existence of a single imaginary frequency. All calculations were performed using the Gaussian 03 code [28].

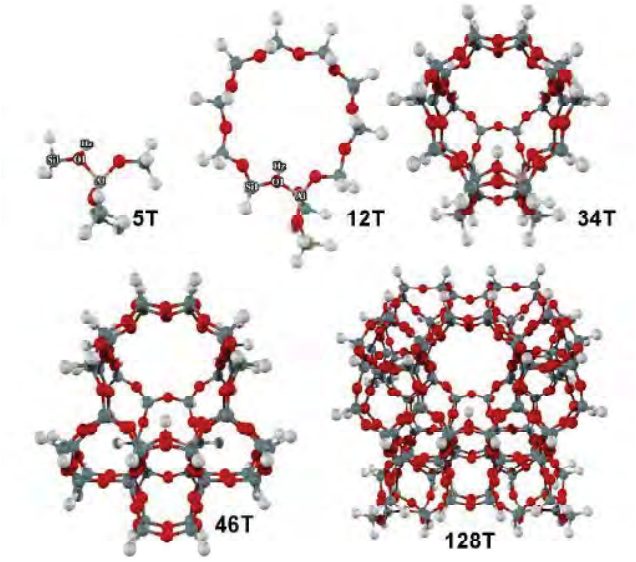

Figure 1: The evolution of H-ZSM-5 models, from the 5T unit to 128T clusters.

3 RESULTS AND DISCUSSION

3.1 Molecular Cluster and Nanocluster Models of H-ZSM-5 catalyst

The evolution of our H-ZSM-5 models, from the 5T unit to the 128T framework, is illustrated in Fig. 1. Selected structural parameters of each model are presented in Fig 2.

In the bare zeolite, one can observe the influence of the framework on the effective Brønsted acidity. From Figure 2, the acidity is insignificantly more pronounced in the extended zeolite framework according to the increased O1-Hz bond length by at most 0.2 pm. The calculated Al···H distances in the range of 234.9-237.4 pm are close to the experimental report by Klinoski of 238.0-248.0 pm of H-zeolite [29]. This good agreement confirms the validation of our models.

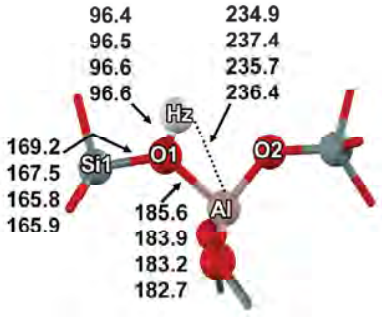

Figure 2: Optimized structure of various H-ZSM-5 models calculated with the M06-L/6-31G(d,p) method. Distance parameters shown in lines 1-4 are for 5T, 12T, 34T and 46T quantum clusters, respectively.

3.2 Adsorption of Light Alkanes on the Brønsted Acid Site

The adsorption energies of the methane and ethane complexes with various zeolite models are summarized in Table 1. As an underestimated value is expected from a small cluster, we found that the methane is bound by -2.9 kcal/mol to the acid site. This increases slightly and converges to -6.9 and -7.0 kcal/mol for the 34T and 46T, respectively. From the same zeolite models, ethane is bound by -10.8 and -11.1 kcal/mol to the acid site. The larger interaction for ethane than methane is found to agree favorably with the known adsorption trend as the molecular size increases. We also found that the adsorption energies are increased due to the presence of a larger framework effect in larger zeolite models. The experimental observation of methane and ethane adsorbed on H-ZSM-5 are -6.7 and -9.1 kcal/mol, respectively [16,17]. The calculated energies from the 34T and 46T clusters are therefore reasonably close to the experimental data.

Model	Methane	Ethane
5T	-2.9	-4.6
12T	-5.1	-7.7
34T	-6.9	-10.8
46T	-7.0	-11.1
128T [a]	-6.9	-10.7
Expt	-6.7	-9.1

[a] The adsorption energies on the 128T cluster were computed with a single point calculation on the optimized structure of the 46T cluster.

Table 1: Interaction energies (kcal/mol) calculated at M06-L/6-31G(d,p) level of theory for the adsorptions of methane and ethane on various H-ZSM-5 models.

To determine the model size of the zeolite that can well represent the adsorption in the real system, the interaction energies from the single point calculation on the large quantum cluster of 128T on the optimized structure of the 46T are used as the energy benchmark. The energies are computed to be -6.9 and -10.7 kcal/mol for methane and ethane, respectively. Since the value from

the 34T model can be considered to be the same as the 128T model, the 34T and 46T models are assumed to be large enough to include the effect of the zeolite pore on chosen nonpolar adsorbates.

From our discussion above, it can be concluded that the full quantum calculation with the M06-L method and the 6-31G(d,p) basis set on the 34T and 46T models of H-ZSM-5 zeolite is the minimal requirement to reproduce the adsorption of methane and ethane within the zeolite pore.

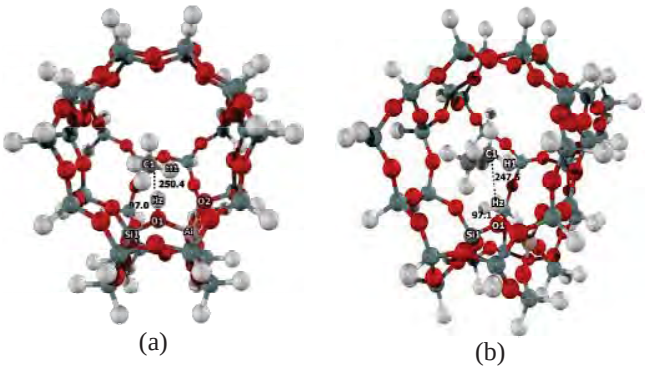

Figure 3: Optimized structure of (a) methane adsorption and (b) ethane adsorption on the 34T cluster model of H-ZSM-5 derived at the M06-L/6-31G(d,p) level of theory. Distances are in pm.

3.3 Proton Exchange Reaction of Light Alkanes

Reaction energies of the proton exchange reactions of methane and ethane with various models of H-ZSM-5 zeolite, calculated with the M06L/6-31G(d,p) method are documented in Table 2.

As for the small QM cluster of 5T, the actual activation energy for methane is computed to be 37.2 kcal/mol while the apparent activation energy is 34.3 kcal/mol. The same reaction studied on the small zeolite cluster reported the activation energy in the range of 30-40 kcal/mol [30-36]. Even the activation energies are in good agreement. The adsorption energies from this small quantum cluster are underestimated and found to be less than a half of the experimental data of 6.7 kcal/mol. With a larger zeolite model, the actual activation energies are 36.8, 35.4 and 35.2 kcal/mol, with the 12T, 34T and 46T quantum clusters, respectively. Their corresponding apparent activation energies are 31.7, 28.5, 28.2 kcal/mol. The reaction energies are considered to be 5.9, 11.0 and 10.3 kcal/mol with the 12T, 34T and 46T quantum cluster, respectively. The activation energy obtained from both the 34T and 46T clusters are virtually identical. Similar results are also derived for the single point calculation of the 128T cluster (the energy barrier of 35.2 kcal/mol and the apparent activation energy of 28.3 kcal/mol). Therefore, taking the framework effect into account improves the calculated result by increasing the underestimated adsorption energy and lowering the overestimated activation energy.

With the small quantum cluster (5T), the adsorption energy is -4.6 kcal/mol. The apparent activation energy is 32.5 kcal/mol whereas the actual one is 37.1 kcal/mol. Even though there is no experimental data for ethane on H-ZSM-5 zeolite, the calculated result is reasonable in that the reaction has a smaller energy barrier and is found to be more endothermic (about 6.5 kcal/mol). As the framework effect is considered in the 46T quantum cluster, the adsorption energy is -11.1 kcal/mol, which agrees well with the experimental data of -9.1 kcal/mol. Their corresponding actual and apparent activation energies are 32.8 and 21.7 kcal/mol, respectively. As expected, the adsorption and reaction energies calculated at the 128T model yield similar results (cf Table 2).

Model	Methane			Ethane		
	AD	TS	PR	AD	TS	PR
5T	-2.9	34.3 (37.2)	0.4	-4.6	32.5 (37.1)	-1.9
12T	-5.1	31.7 (36.8)	-0.8	-7.7	28.0 (35.7)	-2.7
34T	-6.9	28.5 (35.4)	-4.1	-10.8	22.2 (33.0)	-8.3
46T	-7.0	28.2 (35.2)	-3.3	-11.1	21.7 (32.8)	-7.7
128T[a]	-6.9	28.3 (35.2)	-2.8	-10.7	22.3 (33.0)	-10.7

[a] The adsorption energies on the 128T cluster were computed with a single point calculation on the optimized structure of the 46T cluster.

Table 2: Reaction energies (kcal/mol) of the proton exchange reactions of methane and ethane with various models of H-ZSM-5 zeolite, calculated with the M06L/6-31G(d,p) method (activation energy in parenthesis).

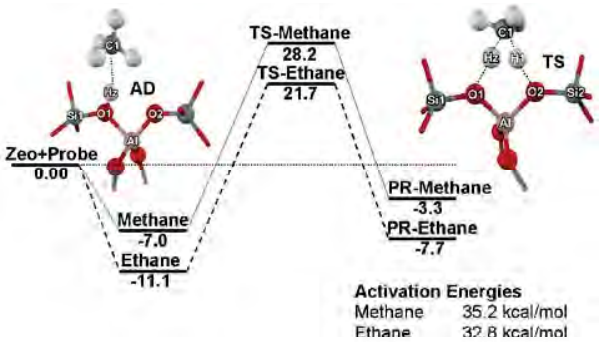

Figure 4: Energy profile for proton exchange reactions of methane and ethane on the 46T quantum cluster of H-ZSM-5, calculated with the M06-L/6-31G(d,p) method.

4 CONCLUSION

The chemical investigation on the adsorption and proton exchange reaction of methane and ethane with the H-ZSM-5 zeolite were performed with a newly developed density functional theory, M06-L. Since the dispersion interaction is included in the method, it can well reproduce the experimental estimate of the

adsorption and reaction of the nonpolar molecules, and also predict reliable information for the reactions that have not been experimentally studied. Based on the experimental report, the molecules are placed over the active site to proceed the adsorption and the reaction. With the validated combination of our 46T model and the M06L/6-31G(d,p) approach, the calculated adsorption energies of methane and ethane of -7.0 and -11.1 kcal/mol are in excellent agreement with the experimental observations of -6.7 and -9.1 kcal/mol, respectively. With the activation energy for the methane reaction calculated to be 35.2 kcal/mol, the method gives the apparent activation energy of 28.2 kcal/mol, which compares well with the experimental result. The actual and apparent activation energies for the ethane reaction are predicted to be 32.8 and 21.7 kcal/mol, respectively. To qualify our model for the prediction, we compared both adsorption and reaction results with the single point calculation for the realistic cluster model of 128T. We found that the 46T model gives virtually similar results for the reactions of both methane and ethane. Therefore, the full quantum calculation of the 46T cluster model with the newly developed functional, M06-L functional, is a practical and accurate model to systematically study the adsorption and reaction of hydrocarbons in “nano reactor” ZSM-5 zeolite.

ACKNOWLEDGEMENTS

This research was supported by grants from the National Science and Technology Development Agency (NSTDA), the Thailand Research Fund (TRF), Kasetsart University Research and Development Institute (KURDI), the Commission on Higher Education, Ministry of Education, under the Postgraduate Education and Research Programs in Petroleum and Petrochemicals, and Advanced Materials as well as the Sandwich Program in the Strategic Scholarships Fellowships Frontier Research Network (CHE-PhD-SW-SUPV to SC). The authors are grateful to Donald G. Truhlar and Yan Zhao for supporting them with the M06-L functional. The Kasetsart University Graduate School is also acknowledged.

REFERENCES

[1] B. W. Wojciechowsku and A. Corma "Catalytic Cracking: Catalysts, Chemistry, and Kinetics"; Dekker: New York, 1986.
[2] I. E. Maxwell and W. H. J. Stork "Introduction to Zeolite Science and Practice"; Elsevier: Amsterdam, 1991.
[3] G. A. Olah and A. Molnar "Hydrocarbon Chemistry"; John Wiley and Sons Inc.: New York, 1995.
[4] P. B. Venuto, Microporous Mater., 2, 297, 1994.
[5] A. Corma, J. Catal., 216, 298, 2003.
[6] E. G. Derouane and C. D. Chang, Microporous Mesoporous Mater., 35-36, 425, 2000.
[7] C. S. H. Chen and R. F. Bridger, J. Catal., 161, 687, 1996.
[8] D. J. Parrillo, C. Lee and R. J. Gorte, Appl. Catal., A, 110, 67, 1994.
[9] B. Smit and T. L. M. Maesen, Nature (London, U. K.), 451, 671, 2008.
[10] S. R. Blaszkowski, A. P. J. Jansen, M. A. C. Nascimento and R. A. van Santen, J. Phys. Chem., 98, 12938, 1994.
[11] S. R. Blaszkowski, M. A. C. Nascimento and R. A. van Santen, J. Phys. Chem., 100, 3463, 1996.
[12] J. Lomratsiri, M. Probst and J. Limtrakul, J. Mol. Graphics Modell., 25, 219, 2006.
[13] W. Panjan and J. Limtrakul, J. Mol. Struct., 654, 35, 2003.
[14] N. Injan, N. Pannorad, M. Probst and J. Limtrakul, Int. J. Quantum Chem., 105, 898, 2005.
[15] P. Pantu, B. Boekfa and J. Limtrakul, J. Mol. Catal. A: Chem., 277, 171, 2007.
[16] H. Papp, W. Hinsen, N. T. Do and M. Baerns, Thermochim. Acta, 82, 137, 1984.
[17] E. Yoda, J. N. Kondo and K. Domen, J. Phys. Chem. B, 109, 1464, 2005.
[18] S. Dapprich, I. Komiromi, K. S. Byun, K. Morokuma and M. J. Frisch, THEOCHEM, 461-462, 1, 1999.
[19] M. Svensson, S. Humbel, R. D. J. Froese, T. Matsubara, S. Sieber and K. Morokuma, J. Phys. Chem., 100, 19357, 1996.
[20] C. Raksakoon and J. Limtrakul, THEOCHEM, 631, 147, 2003.
[21] R. Rungsirisakun, B. Jansang, P. Pantu and J. Limtrakul, J. Mol. Struct., 733, 239, 2004.
[22] Y. Zhao, N. E. Schultz and D. G. Truhlar, J. Chem. Theory Comput., 2, 364, 2006.
[23] Y. Zhao and D. G. Truhlar, Theor. Chem. Acc., 120, 215, 2008.
[24] Y. Zhao and D. G. Truhlar, J. Phys. Chem. C, 112, 6860, 2008.
[25] Y. Zhao and D. G. Truhlar, Acc. Chem. Res., 41, 157, 2008.
[26] S. R. Lonsinger, A. K. Chakraborty, D. N. Theodorou and A. T. Bell, Catal. Lett., 11, 209, 1991.
[27] H. Van Koningsveld, H. Van Bekkum and J. C. Jansen, Acta Crystall. B43, 127, 1987.
[28] M. J. Frisch, et al. Gaussian 03, Revision C Gaussian, Inc., Wallingford CT, 2004.
[29] J. Klinowski, Chem. Rev., 91, 1459, 1991.
[30] E. M. Evleth, E. Kassab and L. R. Sierra, J. Phys. Chem., 98, 1421, 1994.
[31] V. B. Kazansky, M. V. Frash and R. A. van Santen, Catal. Lett., 28, 211, 1994.
[32] G. J. Kramer and R. A. van Santen, J. Am. Chem. Soc., 117, 1766, 1995.
[33] P. M. Esteves, M. A. C. Nascimento and C. J. A. Mota, J. Phys. Chem. B, 103, 10417, 1999.
[34] J. A. Ryder, A. K. Chakraborty and A. T. Bell, J. Phys. Chem. B, 104, 6998, 2000.
[35] X. Zheng and P. Blowers, J. Mol. Catal. A: Chem., 242, 18, 2005.
[36] X. Zheng and P. Blowers, J. Mol. Catal. A: Chem., 246, 1, 2006.

A Mechanistic Investigation on 1,5- to 2,6-Dimethylnaphthalene Isomerization Catalyzed by Acidic Beta Zeolite: An ONIOM Study with a Newly Developed Density Functional Theory

Chawanwit Kumsapaya [a,b], Karan Bobuatong [a,b], Saowapak Choomwattana [a,b], Pipat Khongpracha [a,b], Yuthana Tantirungrotechai [c] and Jumras Limtrakul [a,b,*]

[a]Laboratory for Computational and Applied Chemistry, Chemistry Department, Faculty of Science, Kasetsart University, Bangkok 10900, Thailand
[b]NANOTEC Center of Excellence, National Nanotechnology Center, Kasetsart University Research and Development Institute, Thailand
[c]National Nanotechnology Center (NANOTEC), NSTDA, Khongluang, Pathumthani 12120, Thailand
E-mail: jumras.l@ku.ac.th, Tel: +662-562-5555 ext 2169, Fax: +662-562-5555 ext 2176

ABSTRACT

2,6-Dimethylnaphthalene (DMN) is the key intermediate in the synthesis of poly(ethylene naphthalate) (PEN), a high-performance polymer. The detailed reaction mechanism of the catalyzed 1,5- to 2,6- DMN isomerization via 1,6-DMN by acidic beta zeolite is investigated at the ONIOM(M06-L/6-31G(d,p):UFF) level of theory. The M06-L method, a newly developed density functional theory, is applied for the first time to investigate such reaction within the nano-reactor of zeolite. The stepwise mechanism is proposed to proceed with three steps: protonation, methyl shift and proton back-donation. The methyl shift is the rate-determining step with the activation energies of 24.0 and 20.8 kcal/mol for 1,5- to 1,6-DMN and 1,6- to 2,6-DMN steps, respectively. The calculation confirmed the experiment that the 1,6-DMN formation is kinetically controlled. The calculated adsorption and activation energies are in good agreement with experimental data. Our findings demonstrate that the influence of the pore size of the beta zeolite perfectly fit for the enhancement of the isomerization of 1,5- into 2,6-DMN.

Keywords: dimethylnaphthalene, isomerization, density functional theory, zeolite, Beta

1 INTRODUCTION

A high-performance polymeric material, polyethylene naphthalate (PEN), has many more superior properties than common polyethylene terephthalate (PET) [1]. The current production process involves the condensation polymerization of ethylene glycol and dimethyl 2,6-napthalenedicarboxylate (2,6-NDC). The 2,6-NDC is in turn prepared from 2,6-dimethylnaphthalene (2,6-DMN) [2]. Its present large-scale production (30 kton/yr) is manufactured only by BP-Amoco using their patented process [3], involving four subsequent reactions in four separate reactors: alkylation, cyclization, dehydrogenation, and catalytic isomerization from 1,5- to 2,6-DMN [1, 4]. The final step is thought to be a limiting step which leads to the low availability and the high cost of 2,6-DMN [5]. The isomerization of 1,5- to 2,6-DMN occurs via an intramolecular 1,2-methyl shift [8-10]. This methyl shift is recognized as a key mechanistic step in the rearrangements of alkylbenzenes [8-9], which can be promoted by both Lewis and Brønsted acids.

Zeolite is a unique choice of catalyst for "green chemistry" industrial processes. Recently, Kraikul *et al*. conducted a catalytic activity test of H-beta, H-mordenite, and H-ZSM-5, on the isomerization of 1,5- to 2,6-DMN [5]. H-beta zeolite was found to provide the highest yield of 2,6-DMN. From further thermodynamic analysis, Kraikul *et al.* concluded that 1,5- to 1,6-DMN isomerization is the kinetically limiting step for the 1,5- to 2,6-DMN conversion. From the MD simulation to estimate the diffusional energy barrier of DMN in zeolites by Millini *et al.* [11], the diffusivity of DMN isomer is in the order 2,6-DMN > 1,6-DMN > 1,5-DMN. However, no chemical kinetics parameter is deduced from their study. Later, Suld and Stuart studied the isomerization kinetics of several alkylnapthalenes catalyzed by BF_3·HF [10]. Although there are some reports concerning the detailed investigation of this limiting step, the information of this reaction at the molecular level has not, to our knowledge, been published [1, 5-7], especially for the activation energy catalyzed by heterogeneous catalysts, zeolite in particular. In addition, although the isomerization from 1,5- into 2,6-DMN over the heterogeneous catalysts is known to occur with two methyl shift steps, the reaction mechanism has not been investigated in detail.

In this work, we report the mechanistic study of 1,5- to 2,6-DMN isomerization catalyzed by acidic beta zeolite by means of the hybrid Quantum Mechanics/Molecular Mechanics (QM/MM) approach, as well as the ONIOM (our-Own-N-layered Integrated molecular Orbital and molecular Mechanics) method [12-18]. Our several reports indicate ONIOM's good performance on the studies of adsorption and reaction in zeolite [19-29].

2 METHOD

The 120 tetrahedral subunit (120T) cluster, covering the active region, of the H-beta zeolite is used to represent the Brønsted acid site and the framework. This cluster is taken from the crystal lattice structures [30-31]. We focus on the 12T ring representing the main gateway to the intersection of two perpendicular 12T channel systems, where the reactions normally take place (see Fig. 1). A silicon atom at a T5 position in the zeolite is substituted by an aluminum atom. A proton is added to the bridging oxygen bonded

to the aluminum atom [30], labeled with O1 in this study. In the ONIOM model, an inner layer consists of a 14T cluster including the 12T and two adjacent Si atoms and a reacting molecule. An outer layer consists of the remainder of the extended framework up to 120T to take the confinement effect of the framework into account.

The ONIOM scheme consists of the inner layer of the active region calculated at the M06-L/6-31G(d,p) level and the outer layer of the framework calculated by the universal force field (UFF). M06-L, a DFT method developed by the Minnesota group [32-34]. This functional requires much less computational effort, thus it is practical for the calculation on large systems [34], such as for the interactions of the adsorbates with the acid site of zeolite. The UFF accounts for the van der Waals interaction for the framework [35], which contributes dominantly in adsorption-desorption mechanisms in zeolites [35-38]. During optimization, only the 5T region [(≡SiO)$_3$Al(OH)Si≡] was allowed to relax while the rest was fixed along the crystallographic coordinates. To obtain more reliable energies, single-point calculations at the 120T quantum cluster, i.e. 120T M06-L/6-31G(d,p)//120T ONIOM(M06-L/6-31G(d,p):UFF) are also computed. All calculations were performed using the Gaussian 03 code [39].

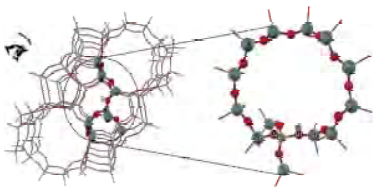

Figure 1: 120T model of H-beta zeolite. The oval dashed line encloses a nanoreactor (an intersection of two perpendicular 12MR channel systems). The 14T active region including the main gateway to the nanoreactor is shown in ball-and-stick style.

3 RESULTS AND DISCUSSION

3.1 Isomerization of 1,5- to 1,6-DMN

Fig. 2(a) summarizes the reaction mechanism of 1,5- to 1,6-DMN isomerization in the acidic beta zeolite. In this mechanism, a 1,5-DMN molecule is first adsorbed at the Brønsted acid site. Then, the adsorbed 1,5-DMN is protonated to form a σ-complex (Int_1), followed by the intramolecular methyl shift between the C5 and C6 positions. This results in the formation of a new σ-complex (Int_2) which donates proton back to the zeolite yielding a 1,6-DMN (Prod_1).

The adsorption takes place with the C5-C6 double bond interacting with the acidic proton (H1) (see Fig. 3(a)). The 1,5-DMN molecule was slightly perturbed by the zeolite cavity upon the adsorption. The C5-C6 double bond lengthens slightly. The adsorption energy of 1,5-DMN is computed to be -22.1 kcal/mol. Even though there is no report of experimental data, this value is in accord with the data of -20.4 kcal/mol for ethylbenzene in H-Y zeolites [40]. Next, the protonation in the adsorption complex, Ads_1, takes place at the C5 position. The protonated molecule is in the form of a carbenium ion in which the positive charge can delocalize over the benzene ring. At the transition state, TS_1, the zeolite proton moves toward the 1,5-DMN. The dimethylnaphthalenonium ion (Int_1) is then formed and stabilized by the resonance of the intact benzenoid nucleus [10]. The energy barrier for the protonation is 11. 7 kcal/mol and the corresponding reaction is endothermic by 5.8 kcal/mol. From Fig. 3(a), the geometry of the transition state (TS_1) is more similar to that of Int_1 than to that of Ads_1. Therefore, the reaction tends to proceed forward to the methyl shift step.

The reversible intramolecular 1,2-methyl shift moves the methyl group from α-position (C_α) to the adjacent position (C_β). The TS_2 transition structure shows the shifting methyl group located in-between with C5 and C6 atoms. At this unstable tricentric transition state, the methyl group is moving toward the C6 atom. In the Int_2 structure, the Cm-C6 bond is formed. The calculated binding energy is -15.5 kcal/mol (see Fig. 4(a)). This is slightly less stable than that of Int_1 by 0.8 kcal/mol. Therefore, the reaction is almost thermoneutral. This may be attributed to the reduction of steric hindrance between the methyl group in the naphthalene ring and the zeolitic pore. The activation energy for the DMN methyl migration is 25.7 kcal/mol.

The final stage of the 1,5- to 1,6-DMN isomerization involves the proton (H2) back-donation from the C6 position of Int_2 to the O1 of the zeolite framework to form adsorbed 1,6-DMN (see Fig. 3(a)). This stage occurs very fast as evidenced by the predicted energy barrier of 2.6 kcal/mol (see Fig. 4(a)). The reaction is exothermic by 13.0 kcal/mol. It can be interpreted that the proton prefers to sit on the zeolite. The back transferred proton forms a chemical bond with the O1 atom. The C5-C6 bond resembles a double bond. Finally, 28.4 kcal/mol is required to remove the 1,6-DMN product from the acid site.

The energy profile of the 1,5- to 1,6-DMN isomerization are in Fig. 4(a). The methyl shift was found to be the rate-determining step. It has the highest activation energy of 25.7 kcal/mol compared with 11.7 and 2.6 kcal/mol for the protonation and the back-protonation steps. These results are in good agreement with the experimental observation in which the acid-catalyzed intramolecular 1,2-methyl shift is the rate- determining step for this isomerization with the activation energy of 20.3 kcal/mol [10].

3.2 Isomerization of 1,6- to 2,6-DMN

The reaction mechanism of 1,6- to 2,6-DMN isomerization is outlined in Fig. 2(b).

NSTI-Nanotech 2009, www.nsti.org, ISBN 978-1-4398-1784-1 Vol. 3, 2009

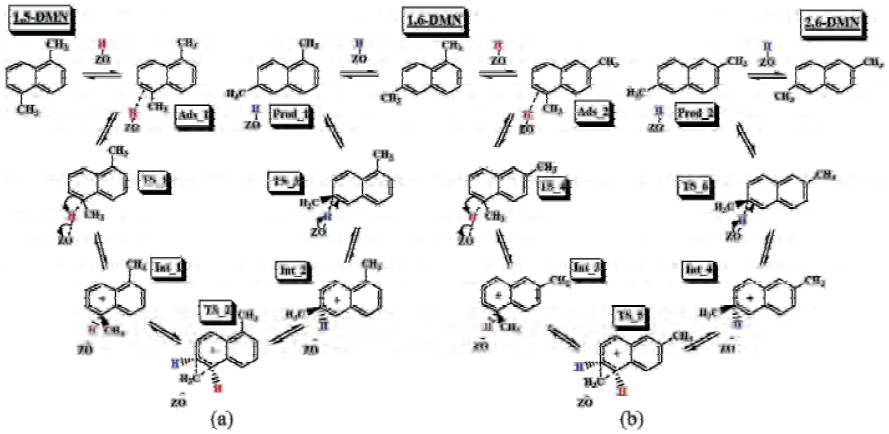

Figure 2: Reaction mechanism of (a) the 1,5- to 1,6-DMN and (b) the 1,6- to 2,6-DMN isomerization by acidic beta-zeolite. Schematically they consist of protonation, methyl shift and proton back-donation of the adsorbed species.

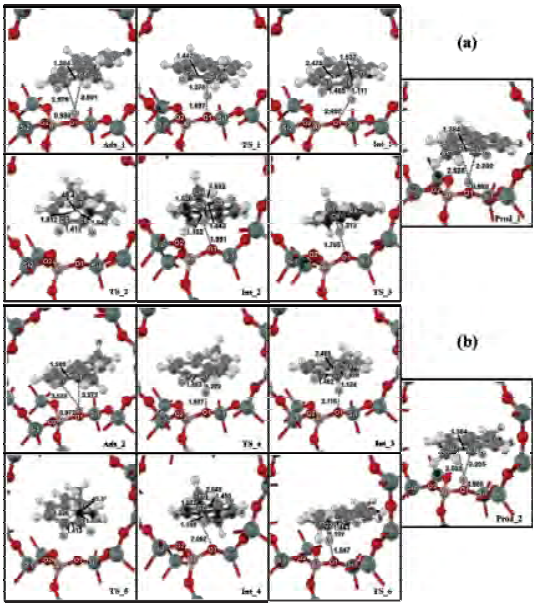

Figure 3: Optimized geometries of adsorbed reactants, transition states, intermediates and products of (a) 1,5- to 1,6-DMN and (b) 1,6- to 2,6-DMN isomerization over H-beta zeolite (14T/120T).

The energetic profiles for the overall steps of the 1,6- to 2,6-DMN isomerization are virtually similar to 1,5- to 1,6-DMN reaction and also summarized in Fig. 4(b). The methyl shift is found to be the rate-determining step for the isomerization with the energy barrier of 21.0 kcal/mol.

The isomerization from 1,5- to 2,6-DMN is shown in Fig. 2 in which is depicted the successive reactions from 1,5- to 1,6- and finally to 2,6-DMN. Comparison between the energy profiles of the 1,5- to 1,6-DMN and 1,6- to 2,6-DMN isomerizations can be made from Fig. 4. The methyl migration is the rate determining step in both reactions. The activation energy of the 1,5- to 1,6-DMN reaction is 25.7 kcal/mol, which is greater than 21.0 kcal/mol of 1,6- to 2,6-DMN reaction. This indicates that the former reaction proceeds more slowly than in the latter. The conclusion is in line with the thermodynamic observed by Kraikul *et al.* that the isomerization occurs rapidly with a higher isomerization rate [5] according to the ratio of 2,6-DMN:1,6-DMN of greater than 1. Our calculation also suggests the same trend. Although only the 14T cluster representing the active site of zeolite and the adsorbate are allowed to relax in M06-L/6-31G(d,p)//ONIOM(M06-L/6-31G(d,p):UFF) model, the information of the reaction such as adsorption and activation energies, are rational and compared well with the experimental data reports in the literature [5, 8, 10-11, 40-41].

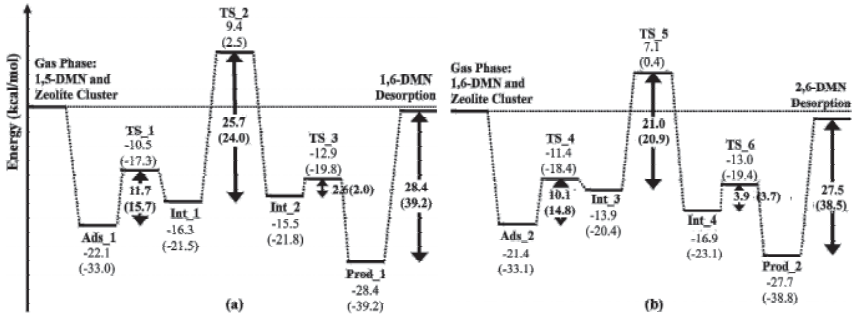

Figure 4: Overall energy profile of (a) 1,5- to 1,6-DMN and (b) 1,6- to 2,6-DMN conversions over H-beta zeolite, calculated with 120T M06-L/6-31G(d,p)//120T ONIOM(M06-L/6-31G(d,p):UFF). Values in parentheses are calculated at the ONIOM(M06-L/6-31G(d,p):UFF) method

4 CONCLUSION

The isomerization of 1,5- into 2,6-DMN over the acidic beta zeolite is investigated at the molecular level by using the 120T M06-L/6-31G(d,p)//120T ONIOM(M06-L/6-31G(d,p):UFF) method. This reaction involves two consecutive methyl shift processes through the conversion of 1,5- into 1,6-DMN and of 1,6- into 2,6- DMN, respectively. The reaction mechanism begins with the adsorption of the reactant on a Brønsted acid site of the zeolite followed by the protonation, 1,2-methyl shift and proton back-donation steps and the product desorption. The methyl shift is shown to be the rate-determining step with the 1,5- to 1,6-DMN isomerization reaction having a greater activation barrier than the 1,6- to 2,6-DMN reaction (25.7 vs. 21.0 kcal/mol). The predicted activation barriers agree with the experimental data. Under thermodynamic control, 2,6-DMN is expected to be the main product of the isomerization.

ACKNOWLEDGEMENTS

The present work was supported in part by grants from the National Science and Technology Development Agency (NSTDA Chair Professor to JL), Thailand Research Fund (TRF), Kasetsart University Research and Development Institute (KURDI), the National Nanotechnology Center (NANOTEC Center of Excellence and Computational Nanoscience Consortium), the Commission on Higher Education, Ministry of Education, under the Postgraduate Education and Research Programs in Petroleum and Petrochemicals, and Advanced Materials as well as the Sandwich Program in the Strategic Scholarships Fellowships Frontier Research Network (CHE-PhD-SW-INDV to CK and CHE-PhD-SW-SUPV to SC). The authors are grateful to Donald G. Truhlar and Yan Zhao for supporting them with the M06-L functional. The Kasetsart University Graduate School is also acknowledged.

REFERENCES

[1] L. D. Lillwitz , Appl. Catal. A Gen. 221, 337, 2001.
[2] C. Song, Cat. Tech. 6, 64, 2002.
[3] '2,6-dimethylnaphthalene (2,6-DMN): 99/00S7, Chem Systems Report', Chem Systems, 2000.
[4] K. Tanabe and W. F. Holderich, Appl. Catal. A 181, 399, 1999.
[5] N. Kraikul, P. Rangsunvigit and S. Kulprathipanja, Chem. Eng. J. 114, 73, 2005.
[6] N. Kraikul, P. Rangsunvigit, and S. Kulprathipanja, Appl. Catal. A. 312, 102, 2006.
[7] I. Ferino, R. Monaci, L. Pedditzi, E. Rombi, and V. Solinas, React. Kinet. Catal. Lett. 58, 307, 1996.
[8] D. A. McCaulay and A. P. Lien, J. Am. Chem. Soc. 74, 6246, 1952.
[9] M. Kilpatrick, J.A.S. Bett, and M. L. Kilpatrick, J. Am. Chem. Soc. 85, 1038, 1963.
[10] G. Suld and A. P. Stuart, J. Org. Chem. 29, 2939, 1964.
[11] R. Millini, F. Frigerio, G. Bellussi, G. Pazzuconi, C. Perego, P. Pollesel, and U. Romano, J. Catal. 217, 298, 2003.
[12] F. Maseras and K. Morokuma, J. Comput. Chem. 16, 1170, 1995.
[13] S. Humbel, S. Sieber, and K. Morokuma, J. Chem. Phys. 105, 1959, 1996.
[14] T. Matsubara, S. Sieber, and K. Morokuma, Int. J. Quantum Chem. 60, 1101, 1996.
[15] M. Svensson, S. Humbel, R. D. J. Froese, T. Matsubara, S. Sieber, and K. Morokuma, J. Phys. Chem. 100, 19357, 1996.
[16] M. Svensson, S. Humbel, R. D. J. Froese, T. Matsubara, S. Sieber, and K. Morokuma, J. Chem. Phys. 105, 3654, 1996.
[17] S. Dapprich, I. Komaromi, K. S. Byun, K. Morokuma, and M. J. Frisch, J. Mol. Struct. (Theochem) 461, 1, 1999.
[18] T. Vreven and K. Morokuma., J. Comput. Chem. 21, 1419, 2000.
[19] K. Bobuatong and J. Limtrakul, Appl. Catal. A 253, 49, 2003.
[20] W. Panjan and J. Limtrakul, J. Mol. Struct.(Theochem) 654, 35, 2003.
[21] C. Raksakoon and J. Limtrakul, J. Mol. Struct. (Theochem) 631, 147, 2003.
[22] S. Namuangruk, P. Pantu, and J. Limtrakul, J. Catal. 225, 523, 2004.
[23] J. Sirijaraensr, T.N. Truong, and J. Limtrakul, J. Phys. Chem. B 109, 12099, 2005.
[24] S. Namuangruk, P. Khongpracha, P. Pantu, and J. Limtrakul, J. Phys. Chem. B 110, 25950, 2006.
[25] B. Jansang, T. Nanok, and J. Limtrakul, J. Phys. Chem. B 110, 12626, 2006.
[26] W. Panyaburapa, T. Nanok, and J. Limtrakul, J. Phys. Chem. C 111, 3433, 2007.
[27] P. Pantu, B. Boekfa, and J. Limtrakul, J. Mol. Catal. A: Chem. 277, 171, 2007.
[28] B. Jansang, T. Nanok, and J, Limtrakul, J. Phys. Chem. C 112, 540, 2008.
[29] T. Maihom, S. Namuangruk, T. Nanok, and J. Limtrakul, J. Phys. Chem. C 112, 12914, 2008.
[30] A. H. de Vries, P. Sherwood, S.J. Collins, A.M. Rigby, M. Rigutto, and G. J. Kramer, J. Phys. Chem. B 103, 6133, 1999.
[31] R. Rungsirisakun, B. Jansang, P. Pantu, and J. Limtrakul, J. Mol. Struct. (Theochem) 733, 239, 2005.
[32] Y. Zhao and D. G. Truhlar, J. Chem. Phys. 125, 194101, 2006.
[33] Y. Zhao and D. G. Truhlar, Acc. Chem. Res. 41, 157, 2008.
[34] Y. Zhao and D. G. Truhlar, Theor. Chem. Acc. 120, 215, 2008.
[35] E. G. Derouane and C. D. Chang, Microporous Mesoporous Mater. 35-36, 425, 2000.
[36] A. Pelmenschikov and J. Leszczynski, J. Phys. Chem. B 103, 6886, 1999.
[37] L. A. Clark, M. Sierka, and J. Sauer, J. Am. Chem. Soc. 125, 2136, 2003.
[38] X. Rozanska, R.A. van Santen, F. Hutschka, and J. Hafner, J. Am. Chem. Soc. 123, 7655, 2001.
[39] M. J. Frisch, et al. Gaussian 03, Revision C Gaussian, Inc., Wallingford CT, 2004.
[40] D. M. Ruthven and M. Goddard, Zeolites. 6, 275, 1986.
[41] D. Barthomeuf and B. H. Ha, J. Chem. Soc., Faraday Trans. 69, 2158, 1973.

Dehydration of Ethanol into Ethylene over H-MOR: A Quantum Chemical Investigation of Possible Reaction Mechanisms in the Presence of Water

Jittima Meeprasert [a,b,c], Saowapak Choomwattana [a,b,c], Piboon Pantu [a,b,c] and Jumras Limtrakul [a,b,c] *

[a] Laboratory for Computational and Applied Chemistry, Chemistry Department, Faculty of Science, Kasetsart University, Bangkok 10900, Thailand
[b] NANOTEC Center of Excellence, National Nanotechnology Center, Kasetsart University, Bangkok 10900, Thailand
[c] Center of Nanotechnology, Kasetsart University Research and Development Institute, Bangkok
*E-mail: jumras.l@ku.ac.th, Tel: +662-562-5555 ext 2169, Fax: +662-562-5555 ext 2176

ABSTRACT

The conversion of ethanol to ethylene, which is one of the most important feed stocks for the petrochemical industry, is of particular commercial interest. Two mechanisms, stepwise and concerted, of the ethanol dehydration to ethylene in the presence of water have been investigated by the ONIOM model (14T/120T) with B3LYP/6-31g(d,p):UFF method. In the stepwise mechanism, the coadsorbed water assists the protonation of ethanol by the acidic zeolite proton to form an ethoxonium ion ($CH_3CH_2OH_2^+$). After that, the cation is dehydrated to form a surface ethoxide intermediate. The dehydration is found to be the rate-determining step with an activation barrier of 41.4 kcal/mol. The ethoxide is then deprotonated with a water molecule which results in the formation of the product of ethylene. The activation energy of the deprotonation is calculated to be 22.2 kcal/mol. The concerted mechanism differs in that the dehydration and the deprotonation occur simultaneously without the formation of the intermediate. In this mechanism, the activation barrier is higher at 54.7 kcal/mol. Therefore, we conclude that the stepwise mechanism should be the dominating one in hydrous ethanol dehydration.

Keywords: dehydration of hydrous ethanol to ethylene, H-MOR zeolite, confinement effects, ONIOM

1 INTRODUCTION

Petroleum has been and still is debatably the most important energy resource of the world. It and its derivates certainly are still needed for transportation (gasoline, diesel, jet fuel, etc.), and also have an important role in producing electricity. Of equal importance is its role as a raw material for many chemical products. Petroleum resources are inevitably becoming increasingly depleted and more expensive as consumption still continues to increase. The certainty of ever increasing scarcity of petroleum has in recent years resulted in concerted attention, efforts and research to develop alternative hydrocarbon resources.

Biomass, defined as the biological material of living organisms such as animals and plants, is becoming one such increasingly attractive alternative. Conversion of biomass can produce more valuable chemical compounds. A significant and important example of this is bio-ethanol, which is produced through the microbial fermentation of agricultural feedstock such as corn, sugarcane and cassava. Bio-ethanol has now become a highly attractive product in many countries with abundant agricultural resources.

Ethanol, in turn, used not only as a fuel, can be used also to produce more valuable hydrocarbon compounds, especially ethylene. This hydrocarbon compound is extremely important and is used industrially to synthesize a wide range of organic compounds. More than 200 years ago, acidic solution was used to be a catalyst for this reaction. Solid acid catalysts such as silica-alumina (SiO_2/Al_2O_3) and zeolites have also been used industrially, even before the twentieth century [10]. Zeolite has the advantage that it is environmentally friendly and can be reused and reactivated. Mordenite (H-MOR) and H-ZSM5 zeolite types are frequently used in ethanol dehydration [1,3,5,7,10-12]. Inaba *et al*. [6] found that H-MOR has a high selectivity for ethylene formation by intramolecular dehydration at temperatures of 400 °C, while H-ZSM-5 is effective for the formation of aromatics, parafins and C3+olefins. These results would indicate that H-ZSM-5 zeolite with a low Si/Al_2 ratio is more suitable to produce higher hydrocarbons from ethanol and, consequently, H-MOR is a more appropriate zeolite for the dehydration of ethanol into ethylene [11].

Generally, the dehydration of alcohol over zeolite is considered to start with the direct interaction of the hydroxyl group of alcohol with the Brønsted acid sites of zeolite [1-3,5,8,12]. Density functional theory (DFT) calculations with small quantum clusters were employed to study this mechanism and it is reported that ethanol dehydration proceeds via an intermediate ethoxide surface species [2]. This finding is in line with recent experimental results which confirm the presence of a stable ethoxy intermediate in this reaction [1,7]. Here, we use a 120T cluster representing the H-MOR framework and use the ONIOM (our Own N-layered-Integrated molecular Orbital and molecular Mechanics) method which recent theorectical studies [6,9,13] have shown that this method can be efficiently used for characterizing the reactivity of active sites inside zeolites.

Two different mechanisms for the dehydration of ethanol into ethylene reaction are considered. One is a concerted mechanism and the other proceeds in two steps. Moreover, we propose here that water is allowed to assist the reaction due to the fact that bio-ethanol or hydrous ethanol (a mixture of ethanol and water) is almost always used in industry and it is known from experimental studies

that water in ethanol feed enhances the catalytic activity and selectivity for ethylene formation [3,10,12].

2 MODELS AND METHODS

The structure of the 120T cluster was taken from the lattice of mordenite (H-MOR) zeolite (Figure 1). This cluster has been previously reported to be a satisfactory model for the adsorption of hydrocarbon compounds [6,9]. The ONIOM2 scheme, in which the whole model is subdivided into two layers, was adopted for computational efficiency. The inner layer is a fourteen-tetrahedral (14T) cluster consisting of the 12-membered-ring (MR) window of the straight channel of 6.5 Å × 7.0 Å where a silicon atom can be substituted by an aluminum atom to form the Brønsted acid site, which is confirmed by the occurrence of many chemical reactions in the 12MR channels of H-MOR only [9]. This layer, together with the reacting molecules, was treated with the B3LYP/6-31G(d,p) method. The rest of the model was treated with the Universal Force Field (UFF) to represent the confinement effect of the zeolite pore structure and to reduce the required computational time.

All calculations have been performed using the Gaussian 03 code. Geometry optimizations of all structures were performed at the ONIOM(B3LYP/6-31G(d,p):UFF) level of theory and allowing only the active site region 5T, $(H_3SiO)_4Al$ with the adsorbate to relax. For all transition states, vibrational spectra were calculated to ensure that only one imaginary frequency is present.

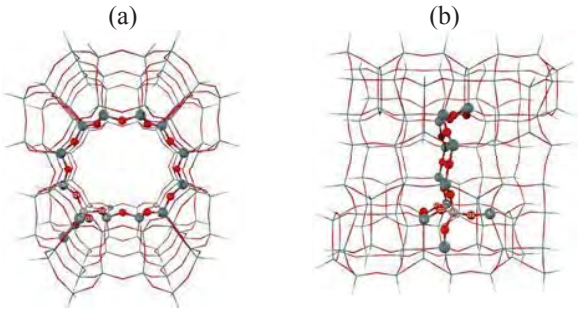

Figure 1: ONIOM model of 14T/120T cluster of H-MOR: (a) front view of the 12MR window of the straight channel and (b) side view showing the 12MR straight channel. Atoms belonging to the 14T quantum region are drawn as spheres.

3 RESULTS AND DISCUSSION

The initial step of hydrous ethanol dehydration to ethylene starts with ethanol and water molecules diffused into the pore of H-MOR zeolite and coadsorbed on the acidic and basic sites to form the coadsorption complex. The calculated adsorption energy is -24.0 kcal mol^{-1}. The value can be roughly compared with the experimental estimates of the heat of adsorption of ethanol in H-ZSM5, which is -31.1 kcal mol^{-1} [8]. The ethanol molecule is protonated by the acidic proton of zeolite to form the ethoxonium ion ($CH_3CH_2OH_2^+$) which does not occur in the case of ethanol adsorption without water. Due to the formation of three hydrogen bonds in the coadsorption complex, the structures of ethanol and the one of the active site of H-MOR zeolite change considerably. In addition to the O4-Hz hydrogen bond, H1-O5 and H5-O3 hydrogen bonds with distances of 1.47 and 1.74 Å, respectively, are formed. The C1-C2 and C1-O4 bond distances of ethanol are 1.51 and 1.48 Å, respectively while, the O2-Hz and O4-Hz bond distances are 1.48 and 1.04 Å, respectively. After the adsorption process has taken place, the ethoxonium ion is converted to ethylene via the dehydration process. This process can proceed through either a concerted or a stepwise mechanism. In this study, these mechanisms for the dehydration of ethanol in the presence of coadsorbed water are investigated.

3.1 Concerted Mechanism

In this mechanism, the reaction is initialized by the coadsorption complex (RT_C) between ethanol and water over the Brønsted acid and its adjacent Lewis basic sites of H-MOR zeolite. Then, the deprotonation and the C-O bond destruction of the ethanol molecule occur simultaneously to give the ethylene product (Eq.1):

$$C_2H_5OH + H_2O + \text{H-MOR} \rightleftharpoons C_2H_4 + 2H_2O + \text{H-MOR} \quad (1)$$

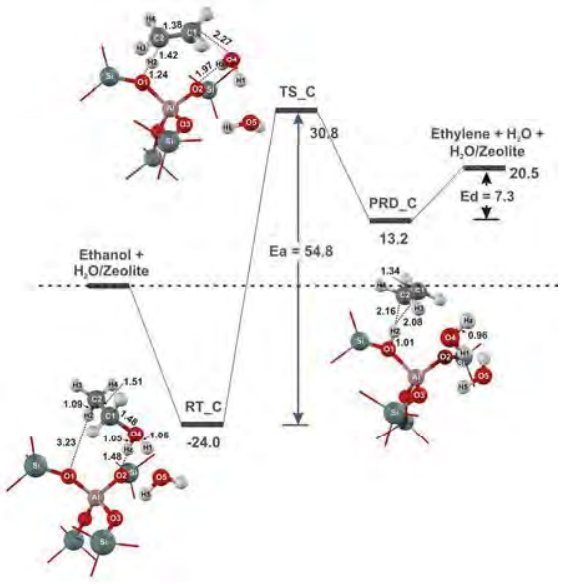

Figure 2: Calculated energy profile for the concerted mechanism of ethanol dehydration.

Figure 2 shows the optimized complexes and selected geometric parameters of the reactant, transition state and products. The coadsorbed water molecule facilitates the protonation of the ethanol molecule by the acidic proton of zeolite to form the ethoxonium ion ($CH_3CH_2OH_2^+$). The

NSTI-Nanotech 2009, www.nsti.org, ISBN 978-1-4398-1784-1 Vol. 3, 2009

adsorption energy of this complex is -48.8 kcal mol^{-1}. At the TS_C transition state configuration, the C1-O4 bond of the ethoxonium ion begins to break to form one water molecule and the ethyl group. For the formation of the latter, the C2-H2 bond distance changes from 1.09 to 1.42 Å. H2 attaches to O1 with a bond length of 1.24 Å. This transition state has one imaginary frequency at 1161.0 cm^{-1}. The activation barrier and the apparent activation energy for this step are calculated to be 54.8 and 5.9 kcal mol^{-1}, respectively. After forming the transition state, the proton (H2) of the ethyl group transfers completely from C2 to O1 to restore the acid site of zeolite and a double bond (1.38 Å) between C1-C2 is formed. The ethylene molecule remains adsorbed via the π-interaction while a water dimer is formed on the basic site of the zeolite (PRD_C). The adsorption energy of this complex is calculated to be -11.6 kcal mol^{-1}. The desorption of ethylene and one water molecule is an endothermic process which requires 7.3 kcal mol^{-1}.

3.2 Stepwise Mechanism

Alternatively, the dehydration of ethanol to ethylene can proceed in a stepwise mechanism through the formation of ethoxide intermediates that have also been observed in experiments [1,7]. The two processes involved are the dehydration of ethanol to ethoxide and the deprotonation of ethoxide to ethylene.

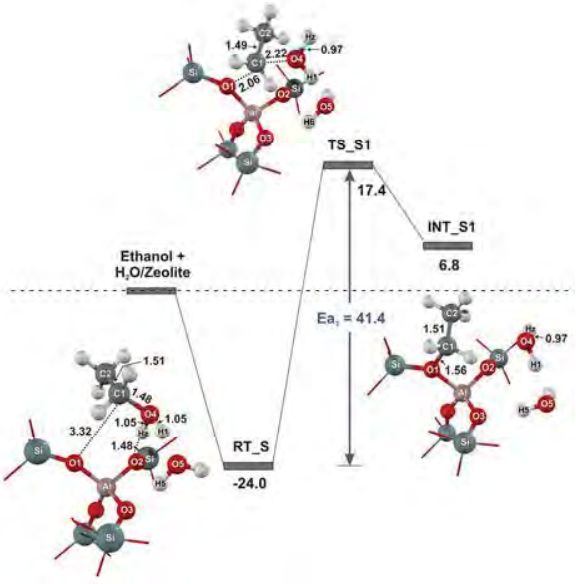

Figure 3: Calculated energy profile for the stepwise mechanism in the dehydration of ethanol to the ethoxide process.

The dehydration of ethanol to the ethoxide process: In this process, the ethanol molecule is dehydrated and an ethyl group is attached to the basic site of the zeolite. From there, the surface ethoxy species is formed within the presence of two water molecules (Eq. 2):

$$C_2H_5OH + H_2O + \text{H-MOR} \rightleftharpoons C_2H_5\text{-MOR} + 2H_2O \quad (2)$$

Figure 3 shows the optimized complexes and selected geometric parameters of the reactant, transition state and intermediates. The reaction starts with ethanol and water molecules coadsorbed on the acidic and basic sites of the zeolite, respectively. The adsorption energy of this complex is -48.8 kcal mol^{-1}. The coadsorbed water molecule facilitates the protonation of the ethanol molecule by the acidic proton of zeolite to form the ethoxonium ion ($CH_3CH_2OH_2^+$). At the TS_S1 transition state, the C1-O4 bond of ethoxonium (2.22 Å) is breaking to form a water molecule (Hz-O3-H1) while the ethyl group gets closer to the basic oxygen of zeolite with an O1-C1 distance of 2.06 Å. The O4-C1-O1 bond angle is 154.4°. The imaginary frequency of this transition state is 366.8 cm^{-1}. The activation barrier and the apparent activation energy for this step are calculated to be 41.5 and -7.7 kcal mol^{-1}, respectively. After the transition state, the intermediate of ethoxide and two water molecules (INT_S1) are formed. Their adsorption energy is -18.1 kcal mol^{-1}.

The deprotonation of ethoxide to the ethylene process: The dehydration process produces ethoxide in agreement with the experimental finding from IR spectroscopy [1,7]. In this process, the reaction starts with a surface ethoxy species and a water molecule. Then, the water-assisted deprotonation of ethoxide leads to the formation of ethylene. (Eq. 3):

$$C_2H_5\text{-MOR} + H_2O \rightleftharpoons C_2H_4 + H_2O + \text{H-MOR} \quad (2)$$

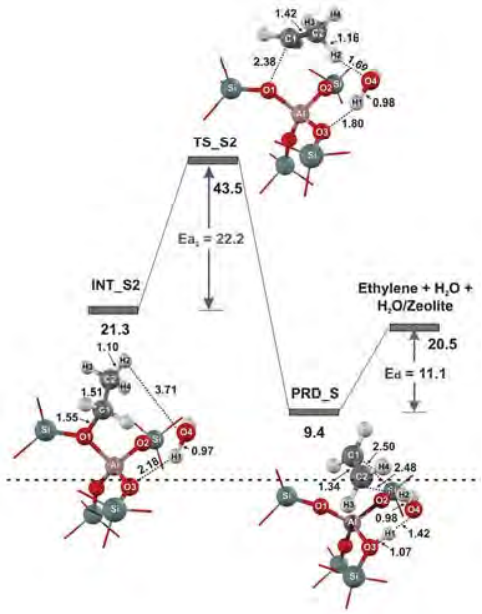

Figure 4. Calculated energy profile for the stepwise mechanism in the deprotonation of ethoxide to the ethylene process.

Figure 4 shows the optimized complexes and selected geometric parameters of the reactant, transition state and products. The reaction starts with ethoxide and water (INT_S2). This complex has an adsorption energy of -3.5 kcal mol^{-1}. In the transition state (TS_S2), the proton of ethoxide is transferred to the oxygen of the water molecule

that is hydrogen-bound to an oxygen atom of zeolite. The C1-C2 bond distance is slightly shortened by about 0.09 Å and the proton of the water molecule is transferred to the zeolite regenerating the acidic site (O3-H1 bond). This transition state has one imaginary frequency at 248.6 cm^{-1}. The calculated energy barrier and the apparent activation energy are 22.2 and 18.7 kcal mol^{-1}, respectively. The ethylene product is formed by adsorbing the water molecule via the π-interaction (PRD_S). The adsorption energy of this complex is -15.4 kcal mol^{-1}. The desorption of ethylene and water from the pore of H-MOR zeolite requires 37.5 kcal mol^{-1}. The overall reaction energy for the stepwise pathway is endothermic by 22.1 kcal mol^{-1}.

4 CONCLUSIONS

The dehydration of ethanol to ethylene over the mordenite zeolite in the presence of water has been investigated by using the ONIOM2 method. Two reaction mechanisms are considered. The stepwise mechanism occurs through the formation of ethoxide intermediates and can be separated into the dehydration of ethanol to ethoxide and the deprotonation of ethoxide to ethylene. The activation barrier of the first step is 41.5 kcal mol^{-1}, which is much higher than that of the second step (22.2 kcal mol^{-1}), and this is expected to be the rate determining step. For the concerted mechanism, without an ethoxide intermediate, the activation barrier is 54.8 kcal mol^{-1}. This is considerably higher than the barrier of the rate determining step of the stepwise mechanism (41.5 kcal mol^{-1}). On the basis of our calculations it can be concluded, therefore, that the dehydration of hydrous ethanol to ethylene over H-MOR zeolite is proceeding via a stepwise mechanism.

ACKNOWLEDGEMENTS

The present work was supported in part by grants from the National Science and Technology Development Agency (NSTDA Chair Professor to JL), Thailand Research Fund (TRF), Kasetsart University Research and Development Institute (KURDI), the National Nanotechnology Center (NANOTEC Center of Excellence and Computational Nanoscience Consortium), the Commission on Higher Education, Ministry of Education, under the Postgraduate Education and Research Programs in Petroleum and Petrochemicals, and Advanced Materials as well as the Sandwich Program in the Strategic Scholarships Fellowships Frontier Research Network (CHE-PhD-SW-SUPV to SC). The Kasetsart University Graduate School is also acknowledged.

REFERENCES

[1] R. Barthos, A. Széchenyi and F. Solymosi, "Decomposition and Aromatization of Ethanol on ZSM-Based Catalysts," J. Phys. Chem. B., 110, 21816-21825, 2006.

[2] S. R. Blaszkoski and R. A. van Santen, "Theoretical Study of C-C Bond Formation in the Methanol-to-Gasoline Process," J. Am. Chem. Soc., 119, 5020-5027, 1997.

[3] E. Costa, A. Ugeles, J. Aguado and P. J. Hernăndes, "Ethanol to Gasoline Process: Effect of Variables, Mechanism, and Kinetics," Ind. Eng. Chem. Process Des. Dev., 24, 239-244, 1985.

[4] F. Haase and J. Sauer, "Interaction of Methanol with Bronsted Acid sites of Zeolite Catalysts: An ab Initio Study," J. Am. Chem. Soc., 117, 3780-3789, 1995.

[5] M. Inaba, K. Murata, M. Saito and I. Takahara, "Ethanol Conversion to Aromatic Hydrocarbons over Several Zeolite Catalysis," React. Kinet. Catal. Lett., 88, 135-142, 2006.

[6] B. Jansang, T. Nanok and J. Limtrakul, "Interaction of Mordenite with an aromatic hydrocarbon: An embedded ONIOM study," Journal of Molecular catalysis A., 164, 33-39, 2007.

[7] J. N. Kondo, K. Ito, E. Yoda, F. Wakabayashi and K. Domen, "An Ethoxy Intermediate in Ethanol dehydration on Brønsted Acid Sites in Zeolite," J. Phys. Chem. B., 109, 10969-10972, 2005.

[8] C. C. Lee and R. J. Gorte, "Calorimetric Study of Alcohol and Nitrile Adsorbtion Complexes in H-ZSM-5," J. Phys. Chem. B., 101, 3811-3817, 1997.

[9] P. Pantu, B. Boekfa and J. Limtrakul, "The adsorption of saturated and unsaturated hydrocarbons on nanostructured zeolites (H-MOR and H-FAU): An ONIOM study," Journal of Molecular Catalysis A., 277, 171–179, 2007.

[10] C. B. Phillips and R. Datta, "Production of Ethylene from Hydrous Ethanol on H-ZSM-5 under Mild Conditions," Ind. Eng. Chem. Res., 36, 4466-4475, 1997.

[11] I. Takahara, M. Saito, M. Inaba and K. Murata, "Dehydration of ethanol into ethylene over solid acid catalysts," Catalysis Letters, 105, 249-252, 2005.

[12] A. K. Talukdar, K. G. Bhattacharyya and S. Sivasanker, "H-ZSM-5 Catalysed Conversion of Aqueous Ethanol to Hydrocarbons," Applied Catalysis A, 148, 357-371, 1997.

[13] T. Maihom, S. Namuangrak, T. Nanok and J. Limtrakul, "Theorectical Study on Structures and Reaction Mechanisms of Ethylene Oxide Hydration over H-ZSM-5: Ethylene Glycol Formation," J. Phys. Chem. C., 112, 12914-12920, 2008.

The Theoretical Investigation of Oxidative Dehydrogenation of Ethane to Ethene over Fe-ZSM-5: A QM/MM Study

Karan Bobuatong [a,b], Jakkapan Sirijaraensre [a,b,c], Pipat Khongpracha [a,b], Piboon Pantu [a,b,c] and Jumras Limtrakul [a,b,c*]

[a] Laboratory for Computational and Applied Chemistry, Chemistry Department, Faculty of Science, Kasetsart University, Bangkok 10900, Thailand
[b] NANOTEC Center of Excellence, National Nanotechnology Center, Kasetsart University, Bangkok 10900, Thailand
[c] Center of Nanotechnology, Kasetsart University Research and Development Institute, Bangkok
*E-mail: jumras.l@ku.ac.th, Tel: +662-562-5555 ext 2169, Fax: +662-562-5555 ext 2176

ABSTRACT

The complete detailed reaction mechanism for the oxidative dehydrogenation of ethane over Fe-ZSM-5 zeolite has been systematically investigated by means of the ONIOM(MP2/6-31G(d,p):UFF)//ONIOM(B3LYP/6-31G(d,p):UFF) scheme. Two types of reaction mechanisms for the oxidative dehydrogenation of ethane have been suggested: stepwise and concerted. The concerted mechanism, the concurrent abstraction of two hydrogen atoms from ethane was found to be unattainable. Two routes of the stepwise pathway were proposed. The reaction at the straight channel takes place via the alkoxide intermediate, while the key intermediate of the reaction occurring at the sinusoidal channel is an "ethyl radical" one. The activation energies of the reaction observed at the straight channel are 12.4 and 54.9 kcal/mol, which is quantitatively higher than those at the sinusoidal channel (10.3 and 4.8 kcal/mol). The stepwise reaction taking place via the radical intermediate has been proved to be a dominant step in generating the ethene molecule.

Keywords: ethene, Fe-ZSM-5 zeolite, ONIOM, oxidative dehydrogenation, ethane

1 INTRODUCTION

Ethene is one of the most important basic chemicals in the petrochemical industry as a feedstock for the production of ethylene oxide, ethylene dichloride, vinyl acetate, ethyl alcohol and other petrochemical products. Conventionally, ethane is produced in the petrochemical industry by stream cracking. This process occurs at a high temperature (750-950 ^{0}C) [1]. Since the conventional production of ethylene has a high-energy consumption, much effort has been devoted to find an efficient route for the selective production of light olefins. Currently, the oxidative dehydrogenation of ethane is an alternative route to produce ethylene. This route carries on at a low temperature which would essentially reduce the formation of coke and also extend the lifetime of catalysts.

A range of heterogeneous catalysts have been used in this reaction for the purpose of achieving energy savings and increasing productivity. These include: metal oxides [3,4], zeolites [5,6], and metal-doped mesoporous materials [7,8].

The iron-modified zeolite of the MFI structure, Fe-ZSM-5, is proven to be one of the potential catalysts for the dehydrogenation of ethane. Held *et al*. [6] found that the ethane oxidation over the iron-modified zeolites; Y, MOR and ZSM-5 zeolites. They found that Fe-ZSM-5 provided the highest selectivity towards ethylene formation (in the range of 55% to 87%), whilst the Fe-MOR and Fe-FAU zeolite provides mainly the complete oxidation process. These results showed that the zeolite structure plays a key role in the catalytic activity of iron species for oxidative dehydrogenation reaction. However, the reaction mechanism of this reaction inside the pore of ZSM-5 zeolite has not been fully investigated.

The purpose of the present study is to analyze the reaction mechanisms of the oxidative dehydrogenation of ethane to ethene over Fe-ZSM-5 zeolite by means of the ONIOM (our-Own-N-layer Integrated molecular Orbital + molecular Mechanics) method. The results of this study may be helpful for understanding the fundamentals of how the oxidative dehydrogenation of ethane over zeolite works.

2 METHOD

The model of ZSM-5 zeolite, the 232T cluster, which covers the 10T active region and three different channel structures (the channel intersection, the straight channel, and the zigzag channel) where the reaction normally takes place, is taken from the lattice structure of the ZSM-5 zeolite [9]. The ONIOM2 scheme, in which the whole model is subdivided into two layers, is adapted. The active region, shown in Figure 1, consists of the 12T cluster, which is considered to be the smallest unit required for representing the reaction site of zeolite and the reactive molecules, is treated with the B3LYP level of theory using the 6-31G(d,p) basis set for H, C, O, Al and Si atoms and the effective core potential basis of Stuttgart and Bonn for the Fe atom [10]. In view of there being several reports that the sextet spin state was the most stable electronic configuration for the theoretical study on Fe-ZSM-5 [11-12], the total spin of the system was maintained at this state throughout all calculations. In order to obtain more reliable interaction energies, the single-point energy calculations at the ONIOM(MP2/6-31G(d,p):UFF)//ONIOM(B3LYP/6-31G(d,p):UFF) level were carried out. The rest of the extended framework is treated with the less demanding UFF force field [13]. It is

considered that these selected models for the ZSM-5 zeolites are large enough to cover all the important framework effects that act on both the active site and on the adsorbates.

All calculations have been performed using the Gaussian 03 code [14]. During the structure optimization, the 5T portion of the active site region and the adsorbate are allowed to relax while the rest of the active region is fixed at the crystallographic coordinates.

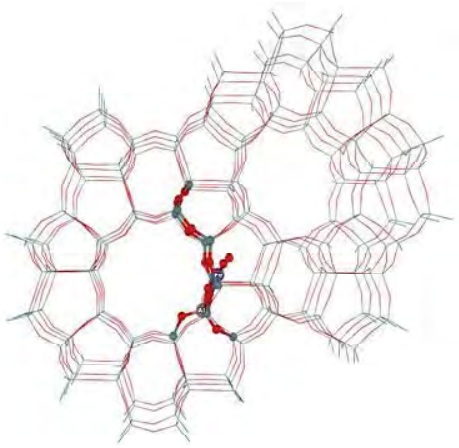

Figure 1: ONIOM2 layer of the 232T cluster model of Fe-ZSM-5. Atoms belonging to the12T quantum cluster are drawn as balls and sticks.

3 RESULTS AND DISCUSSION

3.1 Stepwise mechanism for ethane oxidative dehydrogenation

Due to the ZSM-5 zeolite consisting of two different types of pore: straight channel and sinusoidal channel, it is of interest to investigate the oxidative dehydrogenation of ethane taking place in different environments in order to get more insight into the role of the confinement effect of zeolite on the reaction.

Effect of straight channel within the nanoreactor on chemical reactions, Stepwise I: The reaction taking place in the straight channel at the junction of the sinusoidal channel and the straight one, molecular adsorption of ethane on the α-oxygen of Fe-ZSM-5, is observed by the mean of the ONIOM2 scheme. The adsorption complex of ethane (Ads_1) causes the slight lengthening of Fe-O1 and Fe-O2 bond distances by 0.001 Å. The computed adsorption energy is -8.5 kcal/mol. Dunne *et al*. [15] studied the calorimetric heats of adsorption and adsorption isotherm of methane and ethane on the silicalite which has the same crystal structure as ZSM-5 zeolite. The heat of adsorption of methane and ethane on the silicalite zeolite is 5.0 and 7.5 kcal/mol, respectively. This result shows that the difference of the energy is caused by the confinement effect of the zeolitic pore. In comparing the adsorption energy for the interaction of ethane and methane over the Fe-ZSM-5, the difference of values is 2.4 kcal/mol which is consistent with the difference in the adsorption from experimental data [15]. It can be concluded that the adsorption energy of ethane is qualitatively reliable. At the C-H cleavage transition state (TS_1), the activation energy required during the process of the (C1-H1 cleavage is 12.4 kcal/mol lower than the activation energy required during the C-H cleavage of methane over the Fe-ZSM-5 zeolite (15.3 kcal/mol) reported in previous work. The lowering of the activation energy is consistent with the weakening of the C-H bond of methane and ethane. The C-H bonding energy of methane is higher than that of ethane (435 vs. 420 kJ/mol). Therefore, cleavage of the C-H of ethane is preferable. After this step, the ethoxide and hydroxyl groups are formed. The alkoxide intermediate (Ads_2) is located in the intersection space and the H1-O1 bond also points to the direction of the free space in the intersection channel. The obtained ethoxide intermediate is much more stable than the initial state by 75 kcal/mol. The subsequent migration of hydrogen from the alkoxide group to the adjacent hydroxyl group (TS_2) leads to the formation of ethylene and water molecules. These indicate the migrating of

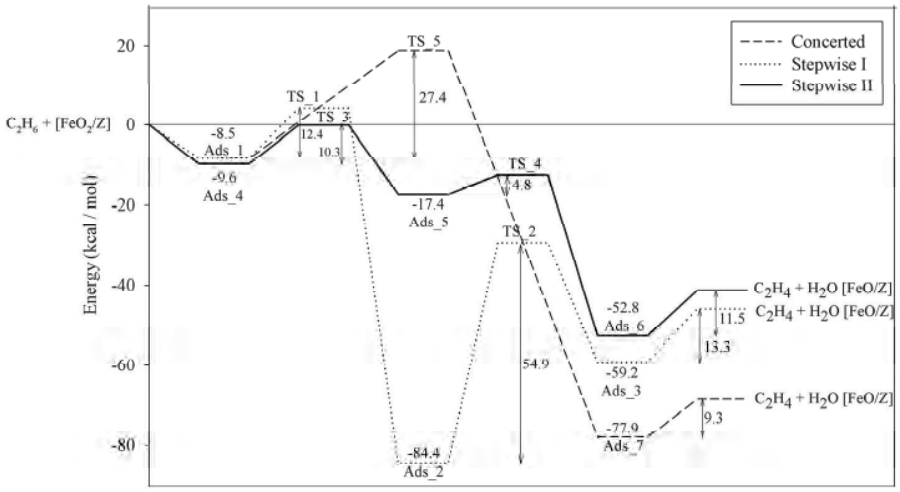

Figure 3: Compared energy profile for stepwise mechanism in the intersection, sinusoidal channel and concerted mechanism.

NSTI-Nanotech 2009, www.nsti.org, ISBN 978-1-4398-1784-1 Vol. 3, 2009

the C-H bond and the formation of the O-H bond, forming the ethylene and water molecules. This process is exothermic by 59.2 kcal/mol with a high-energy barrier of 54.9 kcal/mol.

Effect of the sinusoidal channel within the nanoreactor on chemical reactions, Stepwise II: The pathway of the oxidative dehydrogenation of ethane inside the sinusoidal channel is similar with that inside the straight channel in general, but their main differences will be highlighted. The reaction is initiated at the O2 site pointing toward the sinusoidal channel. The adsorption energy of ethane (Ads_5) in this channel is -9.6 kcal/mol. At the H abstraction transition state (TS_3), the energy barrier is calculated to be 10.3 kcal/mol, which is slightly lower than that of the C-H cleavage inside the straight channel. Variation of pore dimension at the transition state is shown to affect the direction of the reaction. Obviously, barrier height is decreased by about 30%. Comparison of the TS_1 in the straight channel shows that the form of the intermediate complex is affected by the pore shape. At this channel, the ethyl radical (Ads_6) is stabilized inside the sinusoidal channel. This phenomenon is called "intermediate shape selectivity" [16]. The ethyl radical intermediate is slightly more stable than the initial state by 7 kcal/mol. The formation of ethylene yields via the second H-abstraction by migrating one of the C-H bonds at the methyl site of the ethyl radical to the hydroxyl group bound on the iron site to form a water molecule. The coadsorption between water and ethylene molecules (Ads_6) are reached after the TS_4 requires only 4.8 kcal/mol, which is significantly lower than the activation energy for the corresponding step in the straight channel (TS_2). This result reveals that the ethyl radical is much more active than the alkoxide complex (Ads_2). The Ads_6 has the lowest energy, having the energy difference of about 35 kcal/mol with respect to Ads_5. Removal of water and propene from Ads_6 requires only 11.5 kcal/mol. The rate-limiting step of the reaction is the first H-abstraction step yielding the ethyl radical that reacts with the hydroxyl group attaching to the Fe site (Ads_5).

3.2 Concerted mechanism for ethane oxidative dehydrogenation

In addition to the stepwise mechanism in the formation of ethylene, we consider now the reaction pathway through a cyclic mechanism involving the simultaneous hydrogen abstraction of two hydrogen atoms from ethane to the iron oxygen atoms, yielding the $Fe(OH)_2$ site and the ethylene molecule. In this hypothesis, the ethane is coordinated on the α-oxygen atoms by a bidentate complex.

Such a TS is expected to involve double hydrogen abstractions with the breaking of the C-H bonds and the making of O-H bonds, leading to the formation of ethylene. However, in spite of intensive search, we were not able to locate the related cyclic minimum whilst the corresponding transition state structure (TS_5) is observed in which two hydrogen atoms are eliminated from the ethane to the α-oxygen atoms of the Fe site. In the bidentate complex, the ethane is twisted into an eclipsed conformation less stable than the minimum form: the staggered conformation, by

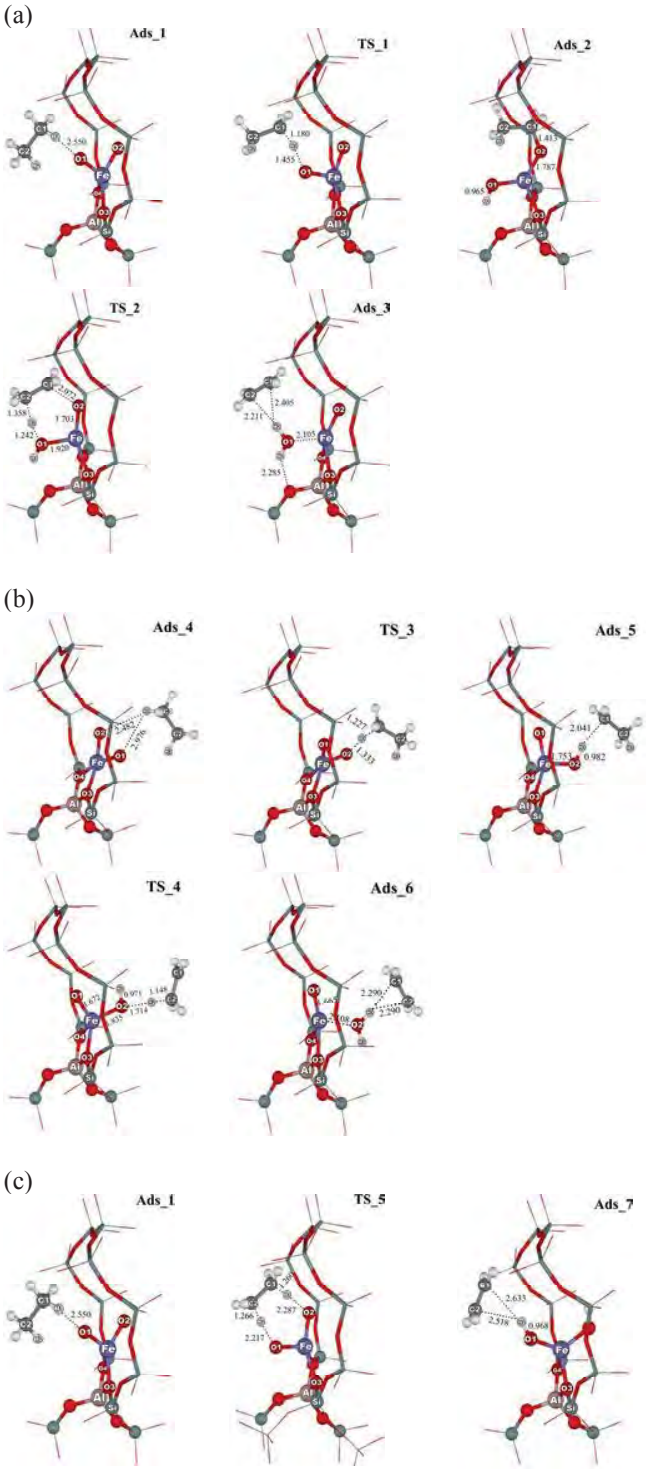

Figure 2: Optimized structures of adsorbed reactants, transition structures and products of (a) the stepwise mechanism in the intersection channel, Stepwise I, (b) the stepwise mechanism in the sinusoidal, Stepwise II, (c) the concerted mechanism.

3 kcal/mol [17]. Due mainly to steric hindrance, the interaction between eclipse-formed ethane and the α-oxygen atoms does not exist The route via the TS_5 yields ethylene attached to the $Fe(OH)_2$ site. The exothermicity of the reaction is -77.9 kcal/mol. The subsequent desorption of ethylene is weakly endothermic by 9.3 kcal/mol. These results suggest that only the single site of Fe is not favorable to perform the ethylene via a single step by abstracting two hydrogen atoms from ethane simultaneously. Formation of ethylene should be carried out via the stepwise mechanism.

4 CONCLUSION

The oxidative dehydrogenation reaction of ethane over Fe-ZSM-5 zeolite has been investigated using the ONIOM2 model. Two mechanisms, stepwise and concerted, have been evaluated. The concerted mechanism was found to be unfavorable. Our finding reveals that the stepwise mechanism taking place via the ethyl radical intermediate dominates the overall reaction of the oxidative dehydrogenation of ethane. However, this process competes against another plausible stepwise reaction that can proceed through the "alkoxide intermediate" at the straight channel. For the stepwise reaction with a radical intermediate occurring at the sinusoidal channel, it starts with the hydrogen abstraction of the ethane molecule to form the ethyl radical complex. The ethylene is generated via the second hydrogen abstraction in the second step. The activation energy of the first step is 10.3 kcal/mol, two fold higher than that of the second step (4.8 kcal/mol). These activation energies are quantitatively lower than those of the reaction via the alkoxide intermediate taking place at the straight channel (12.4 and 54.9 kcal/mol for the first and second H-abstractions, respectively). From calculated results, the activity of Fe ions is highly affected by the spaces in the vicinity of the active site. The ethane locating along the narrow channel would be readily dehydrogenated to ethylene faster than that on the open channel.

ACKNOWLEDGEMENTS

The present work was supported in part by grants from the National Science and Technology Development Agency (NSTDA Chair Professor to JL), Thailand Research Fund (TRF), Kasetsart University Research and Development Institute (KURDI), the National Nanotechnology Center (NANOTEC Center of Excellence and Computational Nanoscience Consortium), the Commission on Higher Education, Ministry of Education, under the Postgraduate Education and Research Programs in Petroleum and Petrochemicals, and Advanced Materials. The Kasetsart University Graduate School is also acknowledged.

REFERENCES

[1] L. Kniel, O. Winter, K. Stork, Ethylene: Keystone to the Petrochemical Industry, Marcel Dekker, New York, 1980.
[2] M. A. Banares, Catal. Today. 51 (1999) 319.
[3] M. Huff, L. D. Schmidt, J. Phys. Chem. 97 (1993) 11815.
[4] E. Jagielska, R. Mostowicz, S. Szarlik, Chemiczny 86 (2007) 340.
[5] N. Mimura, M. Okamoto, H. Yamashita, S. T. Oyama, K. Murata, J. Phys. Chem. B 110 (2006) 21764.
[6] A. Held, J. Kowalska, K. Nowinska, Appl. Catal. B 64 (2006) 201.
[7] Bi, Y.-L, V. C. Corberan, H. Zhuang, K. –J. Zhen, Stud. Surf. Sci. Catal. 153 (2004) 343.
[8] H. Yang, S. Liu, L. Xu, S. Xie, Q. Wang, L. Lin, Stud. Surf. Sci. Catal. 147 (2004) 697.
[9] H. van Koningveld, H. van Bekkum, H, J. C. Jansen, Acta Crystallogr. B 43 (1987) 127.
[10] J. A. Ryder, A. K. Chakraborty, A. T. Bell, J. Phys. Chem. B 106 (2002) 7059.
[11] W. Liang, A. T. Bell, M. Head-Gordon, A. K. Chakraborty, J. Phys.Chem. B 108 (2004) 4362.
[12] J. A. Ryder, A. K. Chakraborty, A. T. Bell, J. Catal. 220 (2003) 84.
[13] A. K. Rappe, C. J. Casewit, K. S. Colwell, W. A. Goddard, W. M. Skiff, J. Am. Chem. Soc. 114 (1992) 10,024.
[14] M. J. Frisch, et al. Gaussian 03, Revision C Gaussian, Inc, Wallingford CT, 2004.
[15] J. A. Dunne, R. Mariwala, M. Rao, S. Sircar, R. J. Gorte, A. L. Myers, Langmuir 12 (1996) 5888.
[16] L. A. Clark, M. Sierka, J. Sauer, J. Am. Chem. Soc. 126 (2004) 936.
[17] V. Pophristic, L. Goodman, Nature 411 (2001) 565.

Mechanism of MOF-505 and Cu-ZSM-5 Promoted Mukaiyama Aldol Reaction: An ONIOM study

Sudarat Yadnum [a,b], Saowapak Choomwattana [a,b], Pipat Khongpracha [a,b], and Jumras Limtrakul [a,b*]

[a]Laboratory for Computational and Applied Chemistry, Chemistry Department,
Faculty of Science, Kasetsart University, Bangkok 10900, Thailand
[b]NANOTEC Center of Excellence, National Nanotechnology Center,
Kasetsart University Research and Development Institute, Thailand
*E-mail: jumras.l@ku.ac.th, Tel: +662-562-5555 ext 2169, Fax: +662-562-5555 ext 2176

ABSTRACT

Density-functional theory (B3LYP/6-31G(d,p)) and ONIOM(B3LYP/6-31G(d,p):UFF) have been employed to investigate the reaction of the Mukaiyama aldol reaction and compare the catalytic efficiency between the metal-organic framework (MOF-505) and Cu-exchanged ZSM-5 zeolite. The Mukaiyama aldol reaction of encapsulated formaldehyde and silyl enol ether was studied on three model systems: (1) bare model: $O{=}CH_2/H_3SiOHC{=}CH_2$; (2) MOF-505: MOF-505/$O{=}CH_2/H_3SiOHC{=}CH_2$; and (3) Cu-exchanged zeolite: Cu-ZSM-5/$O{=}CH_2$ /$H_3SiOHC{=}CH_2$. The reaction is proposed to take place in a single concerted reaction step. It is found that both catalysts make the carbon atom in formaldehyde more electrophilic which leads to a lower energy barrier of the reaction as compared to the bare model system. For the comparison of the catalytic efficiency, it is found that Cu-ZSM-5 reduces the activation energy (6.3 kcal/mol) to be lower than that for MOF-505 (11.0 kcal/mol).

Keywords: Cu-ZSM-5 zeolite, Mukaiyama aldol reaction, confinement effects, metal-organic framework (MOF-505), ONIOM

1 INTRODUCTION

The Mukaiyama aldol reaction, an acid-catalyzed aldol reaction between a silyl enol ether and a carbonyl compound, has been an important and versatile tool in organic and biochemical domains [1]. For instance, Takasu et al. [2] reported the preference reaction on a [2+2] cycloaddition over the Mukaiyama aldol reaction in their study of the Lewis acid-catalyzed reactions between silyl enol ethers and α,β-unsaturated ethers. In the aspect of organic chemistry, formaldehyde is well known as one of the most versatile carbon electrophiles. However, its application is often limited because it rapidly tends to polymerize to solid paraformaldehyde and trioxane. In order to obtain formaldehyde monomer, thermal or Lewis acid pretreatment is therefore used to depolymerize paraformaldehyde or trioxane. Environmentally friendly porous materials such as zeolites were found to be promising candidates for the storage of molecular formaldehyde. For the reaction with larger molecules, porous materials like metal-organic frameworks (MOFs) become more advantageous because of the accessible variation of freely designed pore dimension and chemistry inside the cavity. As porous materials, MOFs also find applications in catalysis [3-7]. We approach the reaction mechanisms on a molecular level by means of quantum chemical calculations. Because both zeolites and MOFs are micro-mesoporous materials, the computational methods and schemes used for MOFs can be adopted from the ones used in the study of zeolites. Like in zeolites [8-11], only a small part of the framework affects the electronic properties of the reactive site, thus facilitating modeling using quantum chemical methods. To include the contribution of the environmental framework on the adsorption of the reactants, hybrid methods such as embedded cluster or combined quantum mechanics/ molecular mechanics (QM/MM) methods [12-19] as well as the ONIOM schemes are well suited to such systems. In this work, we study the reaction mechanism of the Mukaiyama aldol reaction between an encapsulated formaldehyde molecule and silyl enol ether on MOF-505 and Cu-ZSM-5 zeolite.

2 COMPUTATIONAL METHOD

Both Cu-ZSM-5 and MOF-505 structures are obtained from the XRD data. In the ONIOM model, the system is separated into two parts. The inner cluster consists of the active region, typically modeled in a small cluster calculated with density functional theory, to account for the interactions of adsorbates with the porous structure and their chemical reactions. The outer layer represents the environmental framework, described by a molecular mechanics force field, to account for the van der Waals interactions due to the extended structure. In this study, we study the reaction mechanism of the Mukaiyama aldol reaction between encapsulated formaldehyde molecule and silyl enol ether on MOF-505 and Cu-ZSM-5 zeolite. We have employed the ONIOM2 (B3LYP/6-31G(d,p):UFF) method to investigate the reaction on Cu-ZSM-5 and MOF-505. Since the active paddle wheel unit of MOF-505 is the effective part of the molecules of the system because formaldehyde can easily enter between the 3,3',5,5'-biphenyltetra-carboxylic

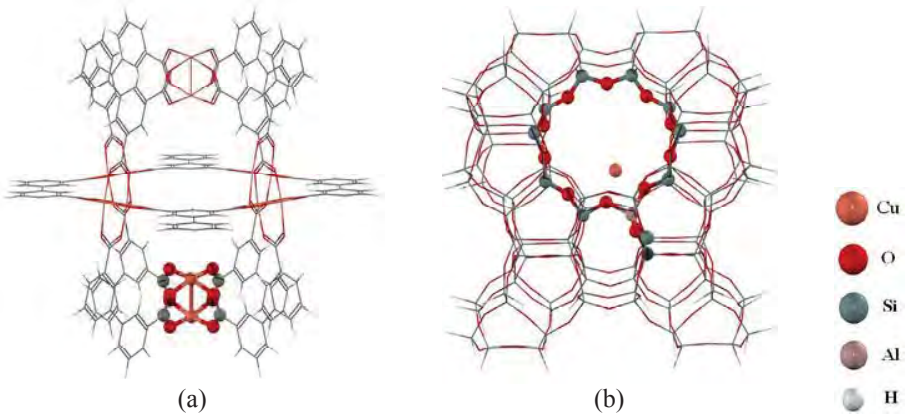

(a) (b)

Figure 1: Geometry of (a) MOF-505 and (b) Cu-ZSM-5
where the high layer (DFT region) is represented in ball-bond view and the low layer (UFF) is represented by line view.

acid unit, it is the inner ONIOM layer. The framework environment constitutes the outer ONIOM layer. For the ZSM-5 crystal structure (MFI framework), there are 12 symmetrically nonequivalent tetrahedral framework positions known as T-sites. The active region, consists of the 10T ring, representing the acidic site of zeolite and that of the reactive molecules whereas the rest of the framework is included into the calculation with the universal force field.

3 RESULTS AND DISCUSSION

We separate the topics into sections: 3.1-3.3. In the first section, we discuss the reaction without any Lewis acid catalyst. In section 3.2, the existence and reactivity of encapsulated formaldehyde in the MOF-505 ($O=CH_2$ @MOF-505) is described. We predict the interactions of MOF-encapsulated formaldehyde with silyl enol ether ($O=CH_2$ @MOF-505/$H_3SiOHC=CH_2$). In section 3.3, we describe the proposed mechanism of the Cu-ZSM-5 catalyzed reaction ($O=CH_2$@MOF-505/$H_3SiOHC=CH_2$). Finally, we make the comparison of the two catalyzed cases with the reaction without any Lewis acid catalyst.

3.1 The Mukaiyama aldol reaction between formaldehyde and silyl enol ether without a Lewis acid catalyst

For the mechanism of the uncatalyzed Mukaiyama aldol reaction of the parent system, the concerted pathway has been examined previously by Gung et al. [20] and Denmark et al. [21]. In agreement with results obtained by Gung et al., a boat-shaped six-membered-ring transition state is located for the concerted pathway. This concerted transition state involves a simultaneous C-C bond formation and the silicon group transfer. In the present work the reaction is predicted to be exothermic, by -26.6 kcal/mol. The reaction coordinate (the normal mode that has an imaginary frequency) indicates again the concerted mechanism of the Mukaiyama aldol reaction. The activation energy is 13.7 kcal/mol.

3.2 MOF encapsulated formaldehyde ($O=CH_2$@MOF-505) and the Mukaiyama aldol reaction between MOF-505 encapsulated formaldehyde and silyl enol ether ($O=CH_2$@MOF-505/$H_3SiOHC=CH_2$

The Cu unit (Cu_1-Cu_2) is barely changed upon the adsorption of formaldehyde (0.084 Å and 5° for changes in the Cu_1-Cu_2 bond distance and the O-Cu-O bond angle, respectively). According to the interaction between the hydrogen atoms of formaldehyde and the oxygen atoms of the framework, the corresponding distance between the formaldehyde oxygen and the Cu atom of MOF-505 active site is 2.32 Å. The carbon-oxygen bond of formaldehyde is elongated from 1.21 to 1.22 Å. For the Mukaiyama aldol reaction, a concerted mechanism was proposed in which the bond between the carbon atom of formaldehyde (C) and the silyl enol ether (C1) is found and the silicon group transferred. We suggest the fundamental step of the reaction as follows:

$$CH_2=O + \text{MOF-505} \rightarrow CH_2=O@\text{MOF-505} \quad (1)$$

$$SiH_3O\text{-}CH=CH_2 + CH_2=O@\text{MOF-505} \rightarrow O=CHCH_2CH_2OSiH_3@\text{MOF-505} \quad (2)$$

$$O=CHCH_2CH_2OSiH_3@\text{MOF-505} \rightarrow O=CHCH_2CH_2OSiH_3 + \text{MOF-505} \quad (3)$$

Initially, formaldehyde adsorbs over the paddlewheel active site of MOF-505 via a lone pair electron interaction with an adsorption energy of -14.3 kcal/mol. Then, the encapsulated formaldehyde interacts with silyl enol ether via a π interaction with a coadsorption energy of -23.2 kcal/mol, followed by the chemical reaction in order to produce 3-silyloxy-propanal. The activation energy is 11.0 kcal/mol. The transition structure of the proposed concerted pathway is confirmed with its mode of imaginary frequency which belongs to the C-C bond formation and the silicon group transfer. The product formation is exothermic by -46.8 kcal/mol. The adsorbed

NSTI-Nanotech 2009, www.nsti.org, ISBN 978-1-4398-1784-1 Vol. 3, 2009

propanal needs 20.2 kcal/mol to desorb from the active site in the final step (3). From our calculation, we propose MOF-505 to be a potential catalyst for the Mukaiyama aldol reaction of formaldehyde and silyl enol ether.

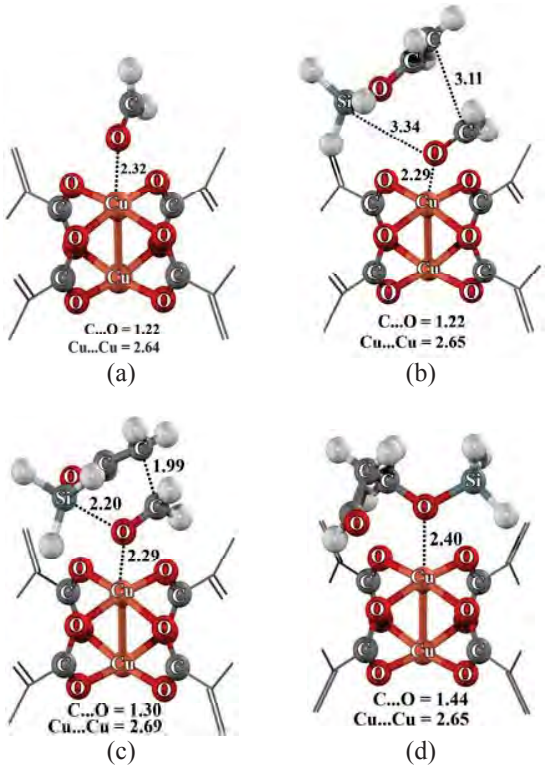

Figure 2: Optimized structures of (a) O=CH_2@MOF-505 (b) coadsorption complex (c) transition state and (d) product adsorption.

3.3 Cu-ZSM-5 encapsulated Formaldehyde (O=CH_2 @Cu-ZSM-5) and the Mukaiyama aldol reaction between Cu-ZSM-5 encapsulated formaldehyde and silyl enol ether (O=CH_2@Cu-ZSM-5/$H_3SiOHC=CH_2$)

Formaldehyde first interacts with the active Lewis acid site by its lone pair electron. The carbon-oxygen bond of formaldehyde is consequently elongated from 1.21 Å to 1.22 Å. The intermolecular distance, measured between the formaldehyde oxygen and the Cu atom of zeolite, is 1.89 Å and the corresponding adsorption energy for the complex is -31.8 kcal/mol. The C-O···Cu-ZSM-5 angle is 138.0°. We propose the reaction proceeds through the same mechanism that was previously described in the section 3.2. The reaction is initiated by the coadsorption of silyl enol ether on the encapsulated formaldehyde at the active site of the zeolite. The silyl enol ether molecule diffuses over the adsorbed formaldehyde on the Cu-ZSM-5 with a coadsorption energy of -52.7 kcal/mol. The activation energy is 6.3 kcal/mol. These results demonstrate that the zeolite framework contributes a larger effect on the stabilization of the adsorption and transition state than the one on the MOF structure. The adsorbed 3-silyloxy-propanal product is exothermic, -66.3 kcal/mol. The product desorption requires 39.6 kcal/mol in the final step. Therefore, Cu-ZSM-5 zeolite can be used as a catalyst in the Mukaiyama aldol reaction.

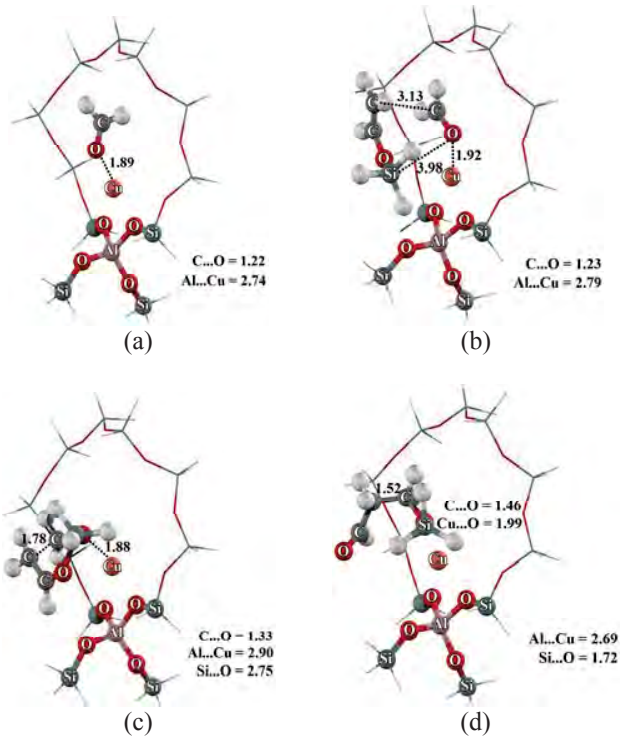

Figure 3: Optimized structures of (a) O=CH_2@Cu-ZSM-5 (b) coadsorption complex (c) transition state and (d) product adsorption.

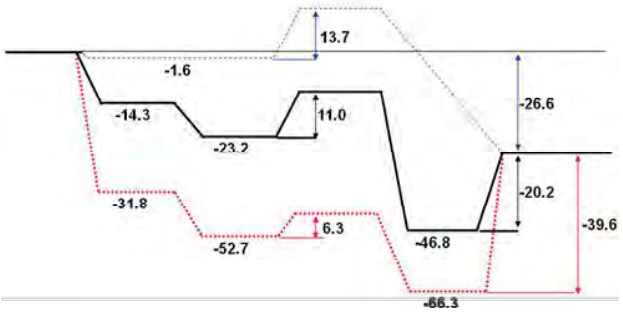

Figure 4: Calculated energy profile (kcal/mol) for the Mukaiyama aldol reaction between formaldehyde and silyl enol ether in the MOF-505 system (black solid line), the Cu-ZSM-5 system (red dot line) and the bare system (blue dash line).

The energy diagram of all three systems, i.e. uncatalyzed, MOF-505 and Cu-ZSM-5 catalyzed, were plotted in Fig. 4. For the bare system, the activation energy of the reaction is 13.7 kcal/mol whereas the barriers of the MOF-505 and the Cu-ZSM-5 systems are 11.0 and 6.3 kcal/mol, respectively. MOF-505 and Cu-ZSM-5 reduce the activation energy to be lower than that in the bare system. Cu in both catalysts induces the oxygen of formaldehyde to be more electronegative, which can be attacked by carbon nucleophile such as carbon in silyl enol ether.

4 CONCLUSIONS

Density-functional theory and the ONIOM approach are used for comparing the catalytic efficiency between the metal-organic framework (MOF-505) and the zeolite structure (Cu-ZSM-5) on the Mukaiyama aldol reaction of formaldehyde and silyl enol ether. The reaction mechanism is proposed to be intermediate-free concerted, consisting of the silicon group transfer and carbon-carbon bond formation. Both MOF-505 and Cu-ZSM-5 contain a Cu ion which behaves as a Lewis acid. Not only the acid in both catalysts is predicted to reduce the energy barrier, it was also found that environmental inclusion of the metal organic framework and zeolite has an effect on the structure and energetics of the adsorption complexes. As a consequence, it leads to a lower energy barrier (ΔE_{act} = 11.0 and 6.3 kcal/mol) of the reaction as compared to the bare model system (13.7 kcal/mol). The results indicate that Cu-exchanged ZSM-5 and MOF-505 can preserve formaldehyde in a monomeric form and also act as a Lewis acid which catalyzes the Mukaiyama aldol reaction of formaldehyde with olefin without the presence of potentially harmful acidic chemicals.

ACKNOWLEDGEMENTS

This research was supported by grants from the National Science and Technology Development Agency (NSTDA), the Thailand Research Fund (TRF), Kasetsart University Research and Development Institute (KURDI), the Commission on Higher Education, Ministry of Education, under the Postgraduate Education and Research Programs in Petroleum and Petrochemicals, and Advanced Materials as well as the Sandwich Program in the Strategic Scholarships Fellowships Frontier Research Network (CHE-PhD-SW-SUPV to SC). The Kasetsart University Graduate School is also acknowledged.

REFERENCES

[1] (a) R. Mahrwald, "Modern Aldol Reactions", Wiley-VCH: New York, 2004. (b) K. Miura and A. Hosomi, "In Main Group Metals in Organic Syntheses", 409-592, 2004.
[2] K. Takasu, M. Ueno, K. Inanaga and M. Ihara, J. Org. Chem. 69, 517, 2004.
[3] S. Hasegawa, S. Horike, R. Matsuda, S. Furukawa, K. Mochizuki, Y. Kinoshita and S. Kitagawa, J. Am. Chem. Soc. 129, 2607, 2007.
[4] M. Casarin, C. Corvaja, C. diNicola, D. Falcomer, L. Franco, M. Monari, L. Pandolfo, C. Pettinari, F. Piccinelli and P. Tagliatesta, Inorg. Chem. 43, 5865, 2004.
[5] L. Alaerts, E. Seguin, H. Poelman, F. Thibault-Starzyk, P. A. Jacobs and D. E. De Vos, Chem. Eur J. 12, 7353, 2006.
[6] B. Xiao, H. Hou and Y. Fan, J. Organomet Chem. 692, 2014, 2007.
[7] S. Choomwattana, T. Maihom, P. Khongpracha, M. Probst and J. Limtrakul, J. Phys. Chem. C. 112, 10855, 2008.
[8] J. Sauer, Chem. Rev. 89, 199, 1989.
[9] J. Sauer, P. Ugliengo, E. Garrone and V. R. Saunders, Chem. Rev. 94, 2095, 1994.
[10 J. Limtrakul, Chem. Phys. 193, 79, 1995.
[11] J. Limtrakul, P. Treesukol, C. Ebner, R. Sansone and M. Probst, Chem. Phys. 215, 77, 1997.
[12] J. Limtrakul, S. Jungsuttiwong and P. Khongpracha, J. Mol. Struct. 525, 153, 2000.
[13] P. E. Sinclair, A. De Vries, P. Sherwood, C. R. A. Catlow, and R. A. Van Santen, J. Chem. Soc. Faraday Trans. 3401, 1998.
[14] M. Braendle and J. Sauer, J. Am. Chem. Soc. 120, 1556, 1998.
[15] S. P. Greatbanks, I. H. Hillier, N. A. Burton, P. J. Sherwood, Chem. Phys. 105, 3770, 1996.
[16] R. Z. Khaliullin, A. T. Bell and V. B. Kazansky, J. Phys. Chem. A. 105, 10454, 2001.
[17] J. Limtrakul, T. Nanok, S. Jungsuttiwong, P. Khongpracha and T. N. Truong, Chem. Phys. Lett. 349, 161, 2001.
[18] A. H. De Vries, P. Sherwood, S. J. Collins, A. M. Rigby, M. Rigutto and G. J. Kramer, J. Phys. Chem. B. 103, 6133, 1999.
[19] M. Svensson, S. Humbel, R. D. J. Froese, T. Matsubara, S. Sieber and K. Morokuma, J. Phys. Chem. 100, 19357, 1996.
[20] B. W. Gung, Z. Zhu and R. A. Fouch, J. Org. Chem. 60, 2860, 1995.
[21] S. E. Denmark, B. D. Griedel, D. M. Coe and M. E. Schnute, J. Am. Chem. Soc. 116, 7026, 1994.

Dissymmetric Metal Deposition on Carbon Nanotubes

C. Warakulwit[1,3], M.-H. Delville[2], V. Ravaine[1], J. Limtrakul[3], A. Kuhn[1]*

[1]Université Bordeaux 1, ISM, ENSCPB, Pessac, France, kuhn@enscpb.fr
[2]ICMCB, CNRS, Pessac, France, delville@icmcb-bordeaux.cnrs.fr
[3]Chemistry Department, Kasetsart University, Bangkok, Thailand, jumras.l@ku.ac.th

ABSTRACT

Dissymmetric nanoobjects are of enormous interest in many areas ranging from molecular electronics to targeted drug delivery. So far it has been quite difficult to synthesize dissymmetric objects at the nanoscale and most approaches have been based on using interfaces to break the symmetry. Only a few bulk procedures are known so far to produce these Janus-type objects. We report here a simple approach for the bulk generation of dissymmetric nanoobjects, especially carbon nanotubes (CNTs), based on electrochemical principles. A stabilized suspension of nanotubes is introduced in a capillary containing an aqueous metal salt solution and a high electric field is applied to orientate and polarize the individual tubes. During their transport through the capillary under sufficient polarization each nanotube is the site of water oxidation at one end, and of metal ion reduction at the other one. The method can be generalized for very different types of deposits such as other metals, semiconductors or polymers. The approach therefore opens up the way to a whole new family of experiments leading to complex nanoobjects with an increasingly sophisticated design.

Keywords: Janus particles, bipolar electrochemistry, carbon nanotubes, capillary electrophoresis

1 INTRODUCTION

Dissymmetric functionalization of micro- and nanoobjects is of major importance to study, for example, directed self-assembly, but also for many applications ranging from electronic paper to sensing and catalysis. Various approaches to generate dissymmetric particles have been reported in the recent literature. These Janus-type particles have been obtained either by protection/deprotection mechanisms [1], focused laser-induced reactions [2], co-jetting of parallel polymer solutions under the influence of an electrical field [3], anisotropic electroless deposition [4], or with microfluidic techniques [5]. However, so far most of the methods used to generate such objects need to break the symmetry by introducing interfaces like in the case of sputtering [6,7], stamp coating [8,9], and Langmuir-Blodgett-based techniques [10]. This makes the preparation of large quantities rather difficult.

Thus, there is an increasing interest in developing alternative methods to replace the two-dimensional approaches by truly three-dimensional techniques allowing a scale-up of the production of Janus objects to larger quantities by using bulk procedures [11].

In this context an attractive method that uses the concept of bipolar electrochemistry [12] has been reported by Bradley et al. and allows generating metal layers in a dissymmetric way on different substrates [13,14]. In brief, when a conducting object is placed in a strong electric field between two electrodes a polarization occurs that is proportional to the electric field *E* and the characteristic dimension *r* of the object.

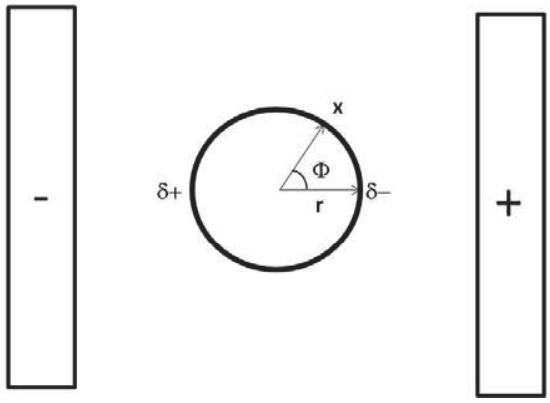

Figure 1. *Polarization of a conducting spherical particle in an electric field.*

The simple equation governing this polarization also immediately illustrates the practical problems that will arise when applying this concept to nanoobjects.

$$\eta_x = E\ r\ \cos\Phi \qquad (1)$$

With η_x being the polarization at a given point x at the surface of the nanoobject, one can easily calculate that the maximum potential difference between the two opposite sides of the object is given by:

$$\Delta V_{max} = 2\ E\ r \qquad (2)$$

In order to carry out two different redox reactions at the opposite sides of the nanotube (oxidation at the left side and reduction at the right side) ΔV_{max} has to be at least equal to the difference of the formal potentials of the two redox reactions. Two typical redox reactions that could take place in an aqueous environment might be the following ones:

$$[AuCl_4]^-_{(aq)} + 3e^- \rightarrow Au^0_{(s)} + 4Cl^-_{(aq)} \qquad E° = +0.99\ V$$

$$2H_2O_{(l)} \leftrightarrow 4H^+_{(aq)} + O_{2(g)} + 4e^- \qquad E° = +1.23\ V$$

It immediately follows that the polarization has to generate a potential difference of at least 0.24 V. In order to achieve this difference on an object with *r* in the nanometer range, *E* reaches values of the order of MV/m. These conditions seem to be incompatible with a normal laboratory environment and especially with an aqueous solution. This might be partly the reason why previous work has been focused on objects in the micrometer or submicrometer range and the experiments had to be carried out in organic solvents [13, 14]. We show in this contribution that the approach can be extended to nanoobjects like carbon nanotubes, modified in aqueous solutions when a capillary electrophoresis set-up is used to apply the high electric field. This capillary assisted bipolar electrodeposition (CABED) process represents, therefore, an original alternative to generate dissymmetric nanoobjects of various compositions [15].

2 EXPERIMENTAL

2.1. Preparation of the nanotube suspensions

Aqueous suspensions of CNTs can be produced analogous to what has been reported for other types of carbon [16, 17]. The raw sample of carbon nanotubes used for this study was multi-wall carbon nanotubes produced by catalytic chemical vapor deposition (ARKEMA). About 0.1 mg of MWNTs was added to a polyoxometalate (POM) solution (10 mM $H_3PMo_{12}O_{40}$/0.1 M H_2SO_4). This solution was prepared from phosphomolybdic acid hydrate, $H_3PMo_{12}O_{40}.xH_2O$ (FLUKA) in 0.1 M H_2SO_4. The suspension was sonicated with a high intensity ultrasonic processor. After 1 hour of sonication a stable suspension of shortened CNTs is formed that can be further processed by fractionated centrifugation in order to select nanotubes with a quite narrow size distribution [18].

2.2. Bipolar gold deposition on carbon nanotubes

The starting solution used for the capillary electrophoresis (CE) experiment is an aqueous CNT/$HAuCl_4$ (1 mM) suspension. For CE experiments, all solutions or suspensions were introduced into the capillary by filling it manually with a syringe. The capillary used here is a fused silica capillary with a length of 45 cm and an inner diameter of 100 μm. The distance from the capillary inlet (left side in Figure 2) to the detection window (right side) in this case was 41 cm. The applied voltage was 30 kV whilst the temperature was maintained at 25°C. The CE experiment was first performed by rinsing the capillary with ultrapure water. Then the diluted aqueous suspension of the shortened, POM-modified carbon nanotubes was introduced into the capillary. The reason for using a diluted suspension for the CE experiment is due to the narrow capillary (100 μm). Introducing suspensions that are too concentrated leads to clogging of the capillary. The combination of migration and electroosmotic flow determines the transport of the CNTs through the capillary. The flow characteristics were determined by recording the absorbance variations in the UV detector (254 nm) as a function of time.

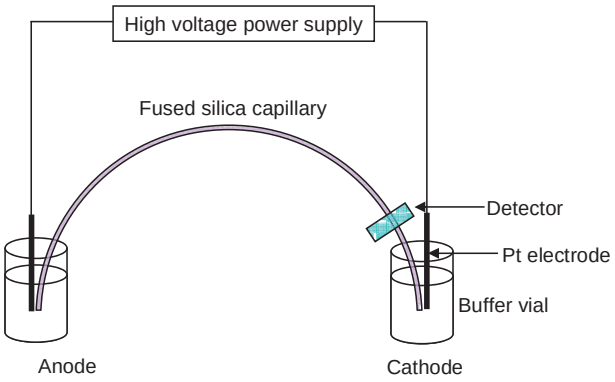

Figure 2. *Schematic illustration of the capillary electrophoresis set-up.*

The bipolar electrochemical gold deposition on CNTs is achieved by introducing the CNT/$HAuCl_4$ (1mM) suspension into the capillary at the anodic side. Because the addition of acid ($HAuCl_4$ here) can result in the aggregation of the POM-modified CNTs, the suspension has to be sonicated for 1 minute in an ultrasound bath in order to maintain the CNTs being well dispersed before introduction into the capillary.

The sample leaving the capillary at the cathodic side was collected directly at the outlet. This collected sample drop was put on a TEM grid and dried. Because the suspension still contains the gold salt ($AuCl_4^-$), drying of the suspension on the grid leads to gold salt crystallization

NSTI-Nanotech 2009, www.nsti.org, ISBN 978-1-4398-1782-7 Vol. 1, 2009

which extremely disturbs the further TEM analysis. Therefore, after the suspension was dropped onto the TEM grid, the solution still containing $HAuCl_4$ was soaked through the grid by placing a cleaning tissue under the grid. After that, the remaining particles on the grid were washed three times with ultrapure water using the same procedure. The washed particles were then characterized by TEM.

3 RESULTS AND DISCUSSION

The potentials given in the above redox equations are standard potentials and as the experiment is carried out far from standard conditions in terms of concentrations and partial gas pressures, large deviations from the threshold value of 0.24 V can be expected. This also means that the calculated electric fields in the MV range might be different, especially when somewhat longer objects like the CNTs are used. Using carbon nanotubes for this proof-of-principle experiment also has the advantage that, due to their anisotropy the polarization induces at the same time an orientation parallel to the electric field, that the nanotubes preserve during their whole journey through the capillary. Thus, it will be easier to perform such a bipolar electrochemical deposition with CNTs compared to spherical objects that might change their orientation during the experiment and in this way lead to random metal deposition at the object's surface.

The experiment has been carried out at the maximum potential difference that can be delivered by the capillary electrophoresis set-up, which is 30 kV. When this potential difference is applied between the two ends of a capillary with a total length of 45 cm, an electric field of 67 kV/m is generated in the capillary. The nanotube pieces obtained by the above mentioned sonication procedure have an average length of 500 nm [18]. One can therefore easily calculate that the maximum polarization that can be obtained between the two ends of a nanotube is of the order of 50 mV. This value is smaller than the minimum potential difference necessary for driving the two redox reactions when the calculation is based on the standard potentials and, therefore, no bipolar electrodeposition should occur under these conditions. Performing the experiment shows, however, striking evidence for a dissymmetric deposition of gold nanoparticles at one end of the nanotubes (see Figure 3). We explain this not only by the conditions that are far from the standard conditions used to define the E° values, but most likely the presence of adsorbed polyoxometalate molecules at the CNT surface has also an influence on the potential values as they can undergo complexation reactions with metal ions [19].

The pictures of Figure 3 are representative of the majority of the nanotubes reaching the capillary outlet; however, not 100% are modified. There are several possible origins for a non-quantitative modification. First of all, the gold deposit can detach from the tube during the collection and rinsing procedure, as seems to be the case for the small particles that can be seen in Figure 3A. Second, nanotubes can be more or less conducting depending on their morphology and defects. In the extreme case of an isolating tube, no deposition can occur and even for conducting tubes the conductivity has to be better than that of the surrounding electrolyte to induce a sufficient potential difference. The third reason is that the potential drop scales with the length of the tube, and therefore shorter tubes might experience a potential difference between the two ends that is below the threshold value.

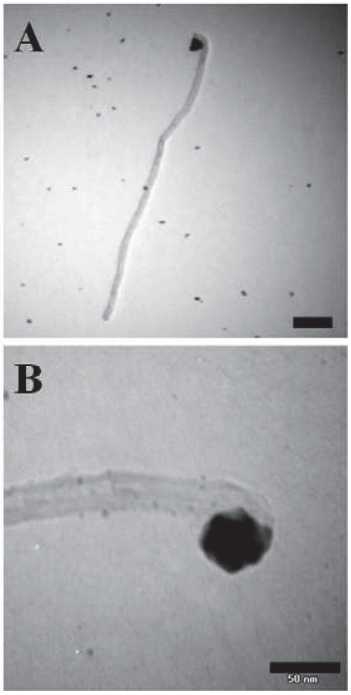

Figure 3. *Site selective bipolar electrodeposition of gold at one end of a carbon nanotube* ***A****) TEM image of a selected nanotube from a very diluted sample* ***B****) Magnification of the modified end of a nanotube; scale bars are 100 and 50 nm respectively.*

It is important to note that, in contrast to the former experiments [13, 14], in this set-up the high voltage is not a problem, although we don't use organic solvents but water, because the electrodes are positioned at the outside of the capillary. This means that an eventual macroscopic hydrogen or oxygen evolution at the cathode or anode respectively doesn't perturb the experiment as it take place in the bulk solution and not in the capillary. Furthermore the currents are in the nA range because there is no supporting electrolyte present and thus the total amount of developed gas is rather low.

4 CONCLUSION

In summary, the concept of bipolar electrochemistry has been adapted to modify in a dissymmetric way multiwall carbon nanotubes with a gold cap as illustrated in Figure 4. The method employed to create these Janus-type objects is based on a slightly modified capillary electrophoresis experiment, (i) allowing the application of the mandatory high voltages (ii) without having to use organic solvents and (iii) especially avoiding gas bubble formation in the reaction chamber, which otherwise would completely prevent the alignment of the nanotubes in the electric field.

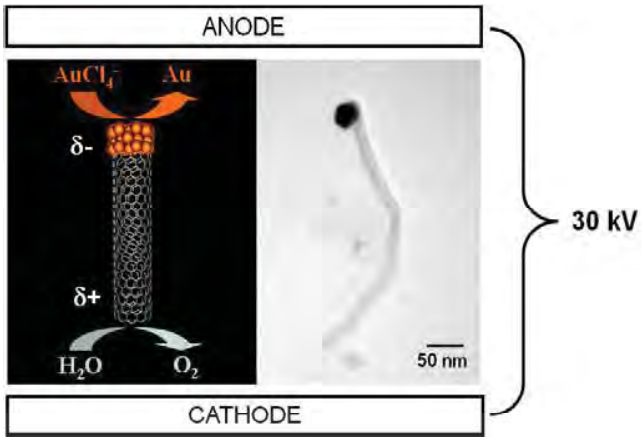

Figure 4. *Reaction scheme for the site selective generation of a metal cluster* ***(left)*** *and TEM image of a MWCNT, modified at one end with a gold cluster(****right)****.*

Most importantly, the procedure uses a real bulk-phase reaction in contrast to most of the literature methods based on interfaces to break the symmetry. This makes the method very attractive to scale-up the production of such dissymmetric objects.

Looking to the future, the CABED process can be generalized to other types of nanoobjects and also deposits of a very different nature such as other metals, semiconductors, or polymers. The approach therefore opens up the way to a whole new family of experiments leading to complex nanoobjects with an increasingly sophisticated design allowing original applications. In addition, the procedure reported here could also be adapted to sort conducting, semiconducting, and insulating carbon nanotubes, as the latter ones will not be modified with metal, whereas the first two categories of species will undergo a potential-dependent metal modification.

Acknowledgment. This work is supported by the French Ministry of Research, CNRS, and ENSCPB. We thank P. Poulin for various CNT samples. C.W. and J.L. also thank the National Science and Technology Development Agency (NSTDA), the Thailand Research Fund (TRF), Commission on Higher Education, Ministry of Education, the Kasetsart University Research and Development Institute (KURDI).

REFERENCES

[1] Perro, A.; Reculusa, S.; Pereira, F.; Delville, M.-H.; Mingotaud, C.; Duguet, E.; Bourgeat-Lami, E.; Ravaine, S. J. Chem. Soc., Chem. Comm. 2005, 44, 5542.
[2] Hugonnot, E.; Delville, M.-H.; Delville, J.-P. Appl.Surf.Sci 2005, 248, 470.
[3] Roh, K.-H.; Martin, D. C.; Lahann, J. Nature Mat. 2005, 4, 759.
[4] Cui, J.-Q.; Kretzschmar, I. Langmuir 2006, 22, 8281.
[5] Nisisako, T.; Torii, T.; Takahashi, T.; Takizawa, Y. Adv.Mater. 2006, 18, 1152.
[6] Takei, H.; Shimizu, N. Langmuir 1997, 13, 1865.
[7] Lu, Y.; Xiong, H.; Jiang, X.; Xia, Y.; Prentiss, M.; Whitesides, G. M. J.Am.Chem.Soc. 2003, 125, 12724.
[8] Cayre, O.; Paunov, V. N.; Velev, O. D. J.Mater.Chem. 2003, 13, 2445.
[9] Paunov, V. N.; Cayre, O. J. Adv.Mater. 2004, 16, 788.
[10] Fujimoto, K.; Nakahama, K.; Shidara, M.; Kawaguchi, H. Langmuir 1999, 15, 4630.
[11] Hong, L.; Cacciuto, A.; Luijten, E.; Granick, S. Nano Lett. 2006, 6, 2510.
[12] Fleischmann, M.; Ghoroghchian, J.; Rolison, D.; Pons, S. J.Phys.Chem. 1986, 90, 6392.
[13] Bradley, J.-C.; Chen, H.-M.; Crawford, J.; Eckert, J.; Ernazarova, K.; Kurzeja, T.; Lin, M.; McGee, M.; Nadler, W.; Stephens, S. G. Nature 1997, 389, 268.
[14] Bradley, J.-C.; Zhongming, M. Angew. Chem.Int.Ed. 1999, 38, 1663.
[15] Warakulwit, C.; Nguyen, T.; Majimel, J.; Delville, M.-H. ; Lapeyre, V. ; Garrigue, P. ; Ravaine, V. ; Limtrakul, J. ; Kuhn, A. NanoLett. 2008, 8, 500.
[16] Garrigue, P.; Delville, M.-H.; Labrugère, C.; Cloutet, E.; Kulesza, P. J.; Morand, J. P.; Kuhn, A. Chem.Mater. 2004, 16, 2984.
[17] Fattakhova, D.; Kuhn, A. Carbon 2006, 44, 1942.
[18] Warakulwit, C.; Majimel, J.; Delville, M.-H. ; Garrigue, P. ; Limtrakul, J. ; Kuhn, A. J.Mater.Chem. 2008, 18, 4056
[19] Martel, D. ; Kuhn, A. ; Kulesza, P.J. ; Galkowski, M.T. ; Malik, M.A. Electrochim.Acta 2001, 46, 4197

Electron Hopping Process in SWCNT-Mediated Redox Reaction: An Evidence Observed by DFT Theory

T. Nongnual[a,b,c], S. Choomwattana[a,b,c], S. Nokbin[a,b,c], P. Khongpracha[a,b,c], and J. Limtrakul[a,b,c*]

[a]Chemistry Department, Faculty of Science, Kasetsart University, Bangkok 10900, Thailand
[b]NANOTEC Center of Excellence, National Nanotechnology Center, Kasetsart University
[c] Center of Nanotechnology, Kasetsart University Research and Development Institute, Bangkok
*E-mail: jumras.l@ku.ac.th, Tel: +662-562-5555 ext 2169, Fax: +662-562-5555 ext 2176

ABSTRACT

The electron hopping mechanism in SWCNT-mediated redox reaction of anthraquinonnyl (AQH_2-) and 4-arylhydroxyl amine (4AHA-) groups is systematically studied by DFT for the first time. It was found that electrons from the oxidized AQH_2 group can transfer to the oxidizing 4AHA group at the other end of the nanotube by the hopping process through the mediating SWCNT confirmed by the non-localized distribution of the hopping electrons. The electron density and Hirshfeld partial charges analysis shows that SWCNT can hold 87% of the extra electron density of the hypothetical negative intermediate forming by the oxidation of the AQH_2 process. Chemical attachments of these two redox reagents to the SWCNT also caused new impurity states within the band gap, thereby introducing more metallic characteristics to the system. These findings provide a detailed understanding of the electron hopping process and agree well with the previous experimental study.

Keywords: electron hopping process, SWCNT-mediated redox reaction, generalized gradient approximation (GGA), Perdew-Burke-Ernzerhof (PBE) method, carbon nanotube

1 INTRODUCTION

Among all nanoscale morphologies of carbon, multiwalled carbon nanotubes (MWCNTs) were first observed under transmission electron microscopy (TEM) by Iijima in 1991[1]. After that, single-walled carbon nanotubes (SWCNTs) were produced independently by Iijima[2] and Bethune[3] in 1993. Since their discoveries of the low-dimensional carbon nanostructures, carbon nanotubes (CNTs) have attracted much interest in modern nanoscience and nanotechnology due to their novel and structure-dependent properties. Over the years, the physical and chemical properties of CNTs have been well-documented as the results of more sophisticated methods. Novel properties of these CNTs endow their nanoscale applications as nanoelectronic devices[4], sensors[5], field emission sources[6], and composite materials[7], The CNTs also function as nanowires to transport electrons between the underlying electrode and electroactive protein chemically attached on each end of the tube[8]. The transport distances, controlling the rate of electron transfer, are greater than 150 nm from the enzymatic active center to the electrode[9].

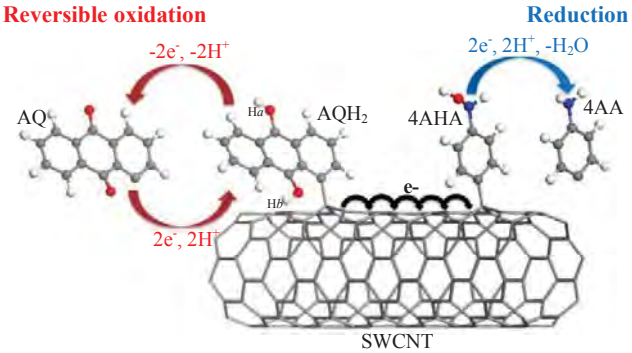

Figure 1: Proposed mechanism for the SWCNT-mediated redox reaction, consisting of the reversible oxidation and the irreversible reduction reactions. The SWCNT accepts electrons from the AQH_2 species and then donates the electrons to the 4-arylhydroxyl amine.

The chemical functionalization reactions for CNTs are categorized into three methods, which are: direct attachment to the graphitic surface, ester linkage, and covalent binding using diazonium reagents with high selectivity. The diazonium media method was also developed by Compton's group to initiate chemisorptions of aryl diazonium salts by direct reduction with hypophosphorous acid in the presence of carbon powder[10-12]. The method was further extended to the application on MWCNTs with anthraquinone-1-diazonium chloride and 4-nitrobenzenediazonium tetrafluoroborate, resulting in the synthesis of 1-anthraquinonyl-MWCNTs (AQ-MWCNTs) and 4-nitrophenyl-MWCNTs (NB-MWCNTs)[13].

Recently, Wong *et al.*[14] reported a redox reaction on the same nanovessel MWCNT for the first time. This MWCNT is functionalized from two redox-active species directly attached by the diazonium salt method. The 4-arylhydroxyl amine (4AHA) and AQH_2 species are generated in the first oxidation cycle from NO_2–C_6H_4–MWCNT and AQ–MWCNT, respectively. This redox reaction consists of a reversible oxidation and an irreversible reduction studied by the cyclic voltammetry technique. They proposed the redox reaction mechanism, where AQH_2 is an oxidizing agent while NHOH–C_6H_4 is a reducing group.

$$AQH_2 - \mathbf{MWCNT} - C_6H_4 - NHOH \rightarrow AQ - \mathbf{MWCNT} - C_6H_4 - NH_2 + H_2O$$

Structure	Hirshfeld charge				Energy gap / eV	Relative energy / kcal mol^{-1}
	Partial charge			Total		
pristine SWCNT	-	-	-	-	0.62 D	-
substrate	AQH_2 = **0.05**	SWCNT = **-0.07**	4AHA = **0.03**	0.01	0.00	-
intermediate-1-a	AQH = **-0.06**	SWCNT = **-0.91**	4AHA = **-0.02**	-0.99	0.04 D	0.00
intermediate-1-b	AQH = **-0.16**	SWCNT = **-0.81**	4AHA = **-0.02**	-0.99	0.04 I	-0.95
intermediate-2	AQ = **-0.19**	SWCNT = **-1.73**	4AHA = **-0.07**	-1.99	0.10 I	-
intermediate-3	AQ = **-0.07**	SWCNT = **-0.77**	Ph-NH = **-0.16**	-1.00	0.16 I	-
product	AQ = **-0.01**	SWCNT = **-0.03**	4AA = **0.05**	0.01	0.00	-

Table 1: Hirshfeld partial charge, energy gap (eV), and relative energy (kcal mol^{-1}) calculated with the PBE method and DNP basis set for pristine SWCNT, substrate, intermediate, and product states. (D = direct, I = indirect energy gap)

The mechanistic pathway of electron transfer from AQH_2 to the 4-arylhydroxyl amine group is also investigated, to determine whether it is intermolecular electron tunneling between reagents or by electron hopping via the CNT. Nevertheless, the hopping was proposed to be more favorable because of the shorter distance in the electron transfer. Such phenomenon is unique for both oxidizing and reducing groups confined on the same CNT.

Herein, we report the theoretical study on the possibility and the process of the electron hopping between two redox reagents that are functionalized on the same CNT. Even mediating MWCNT in the real system is simplified to the semiconducting SWCNT for computational efficiency; the periodic calculations are performed improve the electronic results so that they are more reasonable. In addition, we focus only on the redox reaction instead of the chemical attachment and the preparation steps. Thus, this redox reaction from AQH_2–**SWCNT**–4AHA terminated at AQ–**SWCNT**–4AA is proposed in the reversible oxidation and the irreversible reduction, where 4AA (4-arylamine) is noted.

Total reaction:

AQH_2 – **SWCNT** – 4AHA
$\rightarrow$ AQ – **SWCNT** – 4AA + H_2O

Oxidation:

AQH_2 – **SWCNT** – 4AHA
$\leftrightarrow$ AQ – **SWCNT** – 4AHA + $2H^+$ + $2e^-$

Reduction:

AQ – **SWCNT** – 4AHA + $2H^+$ + $2e^-$
$\rightarrow$ AQ – **SWCNT** – 4AA + H_2O

2 MODELS AND METHODOLOGY

The periodic calculations were carried out using the density functional theory (DFT) method as implemented in the DMol3 package[15,16]. The generalized gradient approximation (GGA) in the various methods and an all-electron double numerical basis set with polarized function (DNP) were chosen for the spin-unrestricted DFT computation. The real space global cutoff radius was set to be 3.70 Å. For geometrical optimization, the forces on all atoms were optimized to be less than 0.05 eV.Å^{-1}. The Brillouin zone was sampled using the Monkhorst-Pack scheme[17].

2.1 Diameter calibration of SWCNTs

Zigzag SWCNTs are calibrated in different diameters from (6,0) to (12,0). Each initial structure is generated in a supercell periodic box with $20 \times 20 \times 8.52$ Å^3 composed of two unit cells of SWCNT. The nearest distance between two neighboring SWCNTs is greater than 10 Å for ignoring an intertube interaction. The calibrations are performed by the GGA in the Perdew-Burke-Ernzerhof (PBE)[18], Becke's exchange and Lee, Yang, and Parr's correlation functional (BLYP)[19,20], and non-local exchange-correlation functional (PW91)[21] with *k* point $1 \times 1 \times 40$.

2.2 Redox system

An (8,0) SWCNT, the smallest semiconducting zigzag providing an acceptable energy gap, was chosen to be functionalized by two redox groups which were more than 12 Å

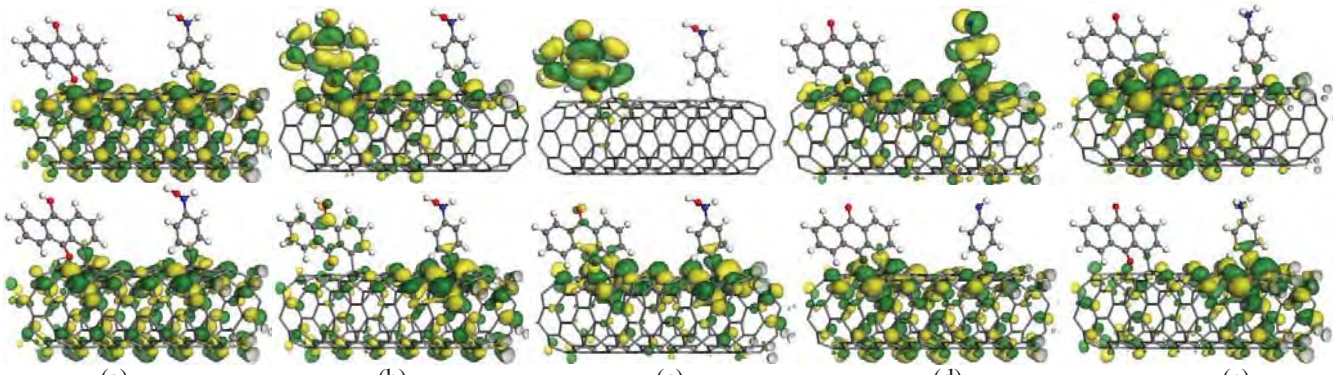

(a) (b) (c) (d) (e)

Figure 2: LUMO (top) and HOMO (bottom) plots of *subs* (a), *int-1-b* (b), *int-2* (c), *int-3* (d), and *prod* (e).

distant from each other to neglect an intermolecular interaction of these two species. A supercell with 40 × 40 × 24.15 Å^3 comprised of six periodic lengths for the zigzag SWCNT was adopted in the calculation with the PBE function. Each supercell consists of two redox groups, which are covalently bonded to the sidewall of the SWCNT. The nearest distance between two neighboring SWCNTs is greater than 30 Å. Only Γ point was considered in the Brillouin zone for the geometric optimization and orbital analysis but *k* points 1 × 1 × 10 was sampled to calculate electronic properties of the redox system. Even though the individual processes in the overall redox reaction take place concurrently, we simplify the problem by dividing the redox pathway into five hypothetical states, which are AQH_2-SWCNT-4AHA (substrate: *subs*), $[AQH\text{-}SWCNT\text{-}4AHA]^{1}$ (intermediate-1), $[AQ\text{-}SWCNT\text{-}4AHA]^{2-}$ (intermediate-2: *int-2*), $[AQ\text{-}SWCNT\text{-}Ph\text{-}NH]^{1-}$ (intermediate-3: *int-3*) and AQ-SWCNT-4AA (product: *prod*) (AQ = anthraquinonyl, 4AHA = 4-arylhydroxyl amine, 4AA = 4-arylamine, SWCNT = (8,0) zigzag SWCNT). The intermediate-1 state can be considered in two configurations, which are intermediate-1-a (*int-1-a*) and intermediate-1-b (*int-1-b*) for H*a* and H*b* removal, respectively.

3 RESULTS AND DISCUSSION

The diameter of carbon nanotubes and the periodic calculation with three functionals (PBE, BLYP, and PW91) was calibrated for searching a zigzag SWCNT suited to our models. Although all methods of investigating (n,0) zigzag SWCNTs give the same energy gap results, the PBE functional is chosen in our calculations following the previous theoretical studies. Moreover, it was found that the (6,0), (9,0), and (12,0) SWCNTs obey the $n - m = 3i$ metallic rule with *E*gap = 0.00, 0.17, and 0.14 eV, respectively. The (7,0) SWCNT presents as a semi-metallic character with a 0.15 eV energy gap. Fortunately, the (8,0) SWCNT is the first smallest zigzag carbon nanotube that provides semiconducting behavior with an acceptable 0.62 eV energy gap. Therefore, the SWCNT-mediated redox models in this paper are generated from the (8,0) SWCNT and calculated by periodic calculations with PBE method.

The electronic properties of the redox system are reported in Table 1. The results show the difference of relative energy of *int-1*, resulting in the *int-1-b* being more favorable than *int-1-a* due to the less steric effect between the hydrogen atom of AQH group and the nanotube media. Thus, the proposed mechanism pathway of the redox reaction starts with the *subs* configuration and forwards to *int-1-b*, *int-2*, *int-3*, and *prod*, respectively. Chemical attachments of these two redox reagents to the SWCNT cause new impurity states within the band gap, thereby introducing more metallic characteristics to the system. These properties lead to the ease of electron delocation among the modified system.

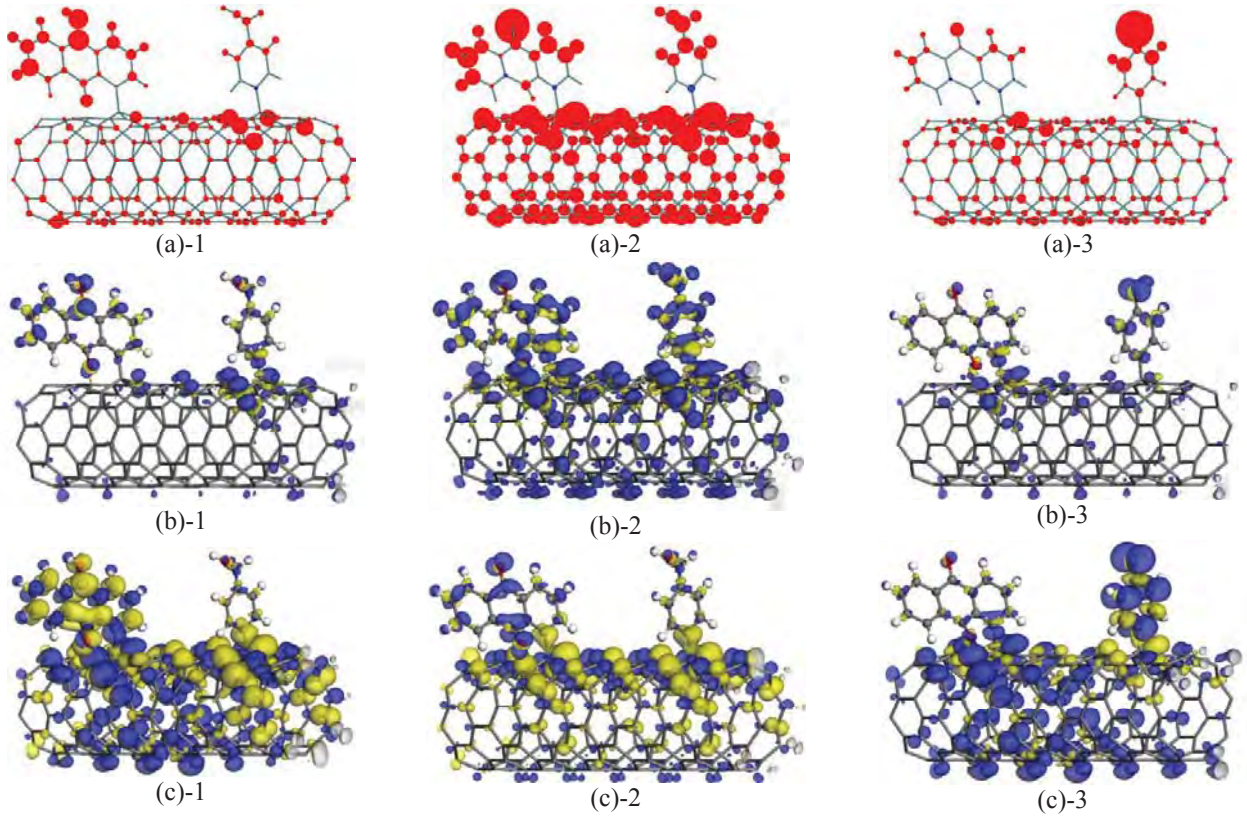

Figure 3: **Hirshfeld charge difference** of *int-1-b* (a)-1, *int-2* (a)-2, and *int-3* (a)-3 where the red color is a negative charge and the blue color is a positive charge. **Electron density difference** of *int-1-b* (b)-1, *int-2* (b)-2, and *int-3* (b)-3 is plotted for an isovalue of ±0.004 e/Å^3, where the blue and yellow color is represented for the electron accumulation and electron depression zones, respectively. **Nucleophilic Fukui function plot** of *int-1-b* (c)-1, *int-2* (c)-2, and *int-3* (c)-3.

The electron density difference and Hirshfeld partial charges analyses show that SWCNT can hold 87% of the extra electron density of the hypothetical negative intermediate forming that forms by the oxidation of the AQH_2 process.

The explanation of how an electron transfers from AQH_2 to 4AHA via SWCNT is illustrated in Figure 2. First, an electron ionization and reception occurs at SWCNT, which can be clearly observed at both the HOMO and LUMO for the substrate. At the intermediate steps, an electronic connection between the AQ and the 4AHA molecules on the SWCNT is shown clearly at the HOMO levels. An electron in the *int-1-b* and *int-2* that strongly remained at the AQ part can reversely reduce the AQ to AQH_2. Electrons move to the 4AHA side result in a reduction reaction, and the HOMO of the product shows that the electrons distribute mostly at 4AA and no longer occupy the AQ side. The opposite trend is observed for the LUMO of the product.

Hirshfeld charge density difference plots are presented in Figure 3(a). An electron in the intermediate states has a high occupation at the AQH, leading to the reverse reduction of AQH to AQH_2. Two electrons in the *int-2* step have a high occupation at the AQ, 4AHA, and the bridge in the nanotube media as shown in Figure 3(a)-2. Therefore, the AQ and 4AHA groups can be reduced to AQH_2 and 4AA, respectively. In Figure 3(b), the calculations are performed from the difference of the electron density between the negative-charge structure and its neutralized geometry, resulting in the density of only the negative charge. It is clearly presented about the negative charge from the reducing group connecting to the oxidizing group. The electron density obviously occupies only the redox molecules and their junction in the SWCNT media. The nucleophilic Fukui function plots as demonstrated in Figure 3(c) strongly confirmed the electron hopping process of the redox reaction via nanotube. The mechanism starts with high nucleophilic character at AQ and the connection. Then, the reducing negative behavior at AQ leads to the increase at 4AHA. Therefore, the electron transfer between two redox groups can occur apparently by electron hopping via the SWCNT.

4 CONCLUSIONS

The the PBE functional using the DFT calculation is used to investigate the reaction mechanism of electron hopping in the SWCNT-mediated redox reaction of anthraquinonnyl (AQH_2-) and 4-arylhydroxyl amine (4AHA-) groups. Our findings can be summarized into three main points. First, the electron density and Hirshfeld partial charges analysis shows that SWCNT can hold 87% of the extra electron density of the hypothetical negative intermediate forming by the oxidation of AQH_2 process. Second, chemical attachments of these two redox reagents to the SWCNT also caused new impurity states within the band gap, thereby introducing more metallic characteristics to the system. Third, the electrons from the oxidized AQH_2 group can transfer to the oxidizing 4AHA group at the other end of the nanotube by the hopping process through the mediating SWCNT. The mechanism is confirmed by the non-localized distribution of the hopping electrons. These findings provide a detailed understanding of the electron hopping process and agree well with the previous experimental study. This work is not only complementing experimental study by giving a fundamental interpretation but also demonstrating one other promising application of the CNT materials in the nanotechnology field.

ACKNOWLEDGEMENTS

This research was supported by grants from the National Science and Technology Development Agency (NSTDA Chair Professor and NANOTEC Center of Excellence, National Nanotechnology Center), the Thailand Research Fund (TRF), Kasetsart University Research and Development Institute (KURDI), the Commission on Higher Education, Ministry of Education, under the Postgraduate Education and Research Programs in Petroleum and Petrochemicals, Advanced Materials as well as the Sandwich Program in the Strategic Scholarships Fellowships Frontier Research Network (CHE-PhD-SW-SUPV to SC), and the Development and Promotion of Science and Technology Talents Project (DPST). The Kasetsart University Graduate School is also acknowledged.

REFERENCES

[1] S. Iijima, Nature. 354, 56, 1991.
[2] S. Iijima and T. Ichihashi, Nature. 363, 603, 1993.
[3] D. S. Bethune, C. H. Klang, M. S. de Vries, G. Gorman, R. Savoy, J. Vazquez and R. Beyers, Nature. 363, 605, 1993.
[4] S. J. Tans, A. R. M. Verschueren and C. Dekker, Nature. 393, 49, 1998.
[5] J. Kong, N. R. Franklin, C. Zhou, M. G. Chapline, S. Peng, K. Cho and H. Dai, Science. 287, 622, 2000.
[6] W. A. de Heer, A. Châtelain and D. Ugarte, Science. 270, 1179, 1995.
[7] R. H. Baughman, A. A. Zakhidov and W. A. de Heer, Science. 297, 787, 2002.
[8] J. J. Gooding, R. Wibowo, J. Q. Liu, W. Yang, D. Losic, S. Orbons, F. J. Mearns, J. G. Shapter and D. B. Hibbert, J. Am. Chem. Soc. 125, 9006, 2003.
[9] F. Patolsky, Y. Weizmann and I. Willner, Angew. Chem. Int. Ed. 43, 2113, 2004.
[10] M. Pandurangappa, N. S. Lawrence and R. G. Compton, Analyst. 127, 1568, 2002.
[11] G. G. Wildgoose, M. Pandurangappa, N. S. Lawrence, L. Jiang, T. G. J. Jones and R. G. Compton, Talanta. 60, 887, 2003.
[12] H. C. Leventis, I. Streeter, G. G. Wildgoose, N. S. Lawrence, L. Jiang, T. G. J. Jones and R. G. Compton, Talanta. 63, 1039, 2004.
[13] G. G. W. Charles G. R. Heald, Li Jiang, Timothy G. J. Jones, Richard G. Compton,, ChemPhysChem. 5, 1794, 2004.
[14] E. L. S. Wong and R. G. Compton, J. Phys. Chem. C. 112, 8122, 2008.
[15] B. Delley, J. Chem. Phys. 92, 508, 1990.
[16] B. Delley, J. Chem. Phys. 113, 7756, 2000.
[17] H. J. Monkhorst and J. D. Pack, Phys. Rev. B. 13, 5188, 1976.
[18] J. P. Perdew, K. Burke and M. Ernzerhof, Phys. Rev. Lett. 77, 3865, 1996.
[19] A. D. Becke, Phys. Rev. A. 38, 3098, 1988.
[20] C. Lee, W. Yang and R. G. Parr, Phys. Rev. B. 37, 785, 1988.
[21] J. P. Perdew and Y. Wang, Phys. Rev. B. 45, 13244, 1992.

Comparing the Stabilities of Nanoclusters and Cluster-based Materials: Alkali Halides and the First Row Element Compounds

W. Sangthong [a,b,c], S.T. Bromley [c,d], F. Illas [c] and J. Limtrakul [a,b] *

[a] Department of Chemistry, Kasetsart University, Bangkok 10900, Thailand
[b] Center of Nanotechnology, Kasetsart University, Bangkok 10900, Thailand
[c] Departament de Química Física & Institut de Química Teòrica i Computacional (IQTCUB), Universitat de Barcelona, Cl Martí i Franquès 1, E-08028 Barcelona, Spain
[d] Institució Catalana de Recerca i Estudis Avançats (ICREA), 08010 Barcelona, Spain
E-mail: jumras.l@ku.ac.th, Tel: +662-562-5555 ext 2169, Fax: +662-562-5555 ext 2176

ABSTRACT

We present state-of-the-art plane wave periodic density functional (DF) calculations aimed to unravel the structure and electronic properties of polymorphs of LiF, BeO, BN and C obtained by assembling LiF_{12}, BeO_{12}, BN_{12} and C_{24} C_{12} building blocks with cage structure. Specifically, a nanoporous analogue of the sodalite zeolite (SOD) structure can be obtained in this way. The energy difference between the ground state phases and the SOD bulk polymorphs (per LiF, BeO, BN or C_2 unit; hereafter referred to simply as unit) was found to increase across the LiF, BeO, BN and C series with $\Delta E_{SOD\text{-}stab}$ = 0.05, 0.17, 0.68 and 1.07 eV/unit, respectively. The different electron distribution on each cluster is illustrated by the ELF analysis. The electronic properties results demonstrate that the cage-based polymorphs of these materials have band gaps significantly different from those in the most stable state phase, which could be interesting for nanotechnology applications.

Keywords: nanoclusters, sodalite, first row elements and density functional theory

1 INTRODUCTION

The appearance of pores in materials leads to a large number of applications as compared to the more dense bulk phases, zeolites being a paradigmatic example. Although experiments are now able to effectively maintain negative pressure conditions to explore the existence of phases with density lower than the ground state, this technique does not yet allow one to investigate a wide class of very low density porous crystalline materials. Nanoporous materials could be synthesized via a bottom-up route. Ultra-stable nanoclusters aggregation may result in various types of nanoporous materials. Hence, low density materials may possibly be obtained by aggregation of stable nanoclusters.

Assembling cage clusters, through edge to edge interactions, results in nanoporous materials similar to zeolites which are broadly used in industry. Recently, some of us reported on the prediction of low density nanoporous polymorphs of alkali halides [1], MgO, ZnO [2] and SiO_2 [3] based on the assembly of highly stable nanoclusters. The LiF, BeO, BN and C compounds formed from first row elements of the periodic table only provide simple models to expand the study about the stability of this type of zeolitic-like nanoporous materials.

Rock salt is the ground state phase of highly ionic LiF whereas BeO crystallizes in a wurtzite structure. Hexagonal structures are found to be stable in BN and C also appears in the form of graphite. In the present work, we report DF calculations aimed to study the geometry and electronic structure of the LiF_{12}, BeO_{12}, BN_{12} and C_{24} cage clusters of first row elements and to explore the stability of the new low density phases formed by assembling these building blocks relative to the ground state phase.

2 COMPUTATIONAL DETAILS

Two sets of plane wave density functional calculations have been carried out to explore the possibility of low density phases of the binary compounds of the first row elements (LiF, BeO, BN) and of C. The first one involves the stability of the LiF_{12}, BeO_{12} BN_{12} and C_{24} cage clusters, whereas the second one concerns extended bulk systems built from these units. Energies, structures, and electronic states of cluster isomers and bulk phases of these compounds were calculated using the PW91 exchange-correlation potential [4-5] and the VASP code [6-8]. The PAW method [9] was used to represent the effect of the atomic cores and a 415 eV energy cutoff was used for the plane wave expansion. For the discrete systems, a large enough box has been constructed so that the distance between repeated clusters is larger than 1 nm. For the solids, the unit cell is defined by the crystal structure. The integrations in the reciprocal space is accomplished by using Monkhorst-Pack grids of special *k* points (7×7×7 for rock salt, wz, BN and graphite, 3×3×3 for low dense phases and Γ point for isolated clusters). For bulk phases the volume versus energy data was fitted using the Birch-Murnaghan EOS [10].

3 RESULTS & DISCUSSION

3.1 Stability of $(AB)_{12}$ cage clusters

The main purpose of the present work is to analyze the possible existence of low density bulk phases of the first row element binary compounds and their relative stability

with respect to the ground state phases. First, we analyze the possible structure of LiF_{12}, BeO_{12}, BN_{12} and C_{24} cage clusters consisting of 6 square faces and 8 hexagons. The geometry of these cage clusters is shown in Figure 1 and the optimized parameters are reported in Table 1.

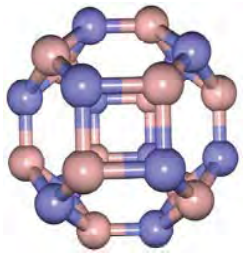

Figure 1: Geometry of LiF_{12}, BeO_{12} and BN_{12} cage clusters.

The geometry of these cage clusters is shown in Figure 1 and the optimized parameters are reported in Table 1.

Parameters	LiF	BeO	BN	C
d (sq-hex), Å	0.168	0.159	0.149	0.149
d (hex-hex), Å	0.163	0.153	0.144	0.138
∠ABA (sq),°	95.0 (Li)	98.3 (Be)	98.4 (B)	90.0
	84.9 (F)	80.8 (O)	80.3 (N)	90.0
∠ABA (hex), °	122.0 (Li)	124.9 (Be)	125.8 (B)	120.0
	117.4 (F)	112.4 (O)	110.9 (N)	120.0
LUMO, eV	-0.87	-1.22	-1.48	-3.89
HOMO, eV	-7.72	-6.96	-6.46	-5.10
E. Gap, eV	6.85	5.74	4.98	1.21
E./unit, eV	-9.28	-13.44	-16.24	-16.28

Table 1: Structural parameters and electronic features of the LiF_{12}, BeO_{12}, BN_{12} and C_{24} cage clusters.

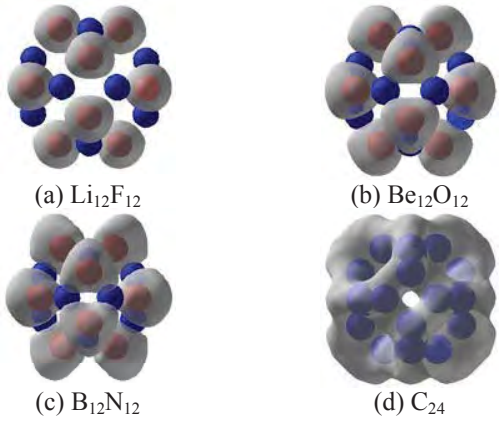

(a) $Li_{12}F_{12}$ (b) $Be_{12}O_{12}$

(c) $B_{12}N_{12}$ (d) C_{24}

Figure 2: Electron density map of LiF_{12}, BeO_{12}, BN_{12} and C_{24} cage clusters.

The geometry optimization results in a slight deviation of the molecular structure from a regular configuration except for the C24 cluster. These deviations result from charge transfer and ionicity in the chemical bond of the heteroatomic clusters. The bond distances increase with increasing ionicity. Bond angles are slightly different from the expected regular value because of the inhomogeneous electron localization. The energy gap, ΔE, between the HOMO and the LUMO and energy per unit for all cage clusters decreases from LiF to C.

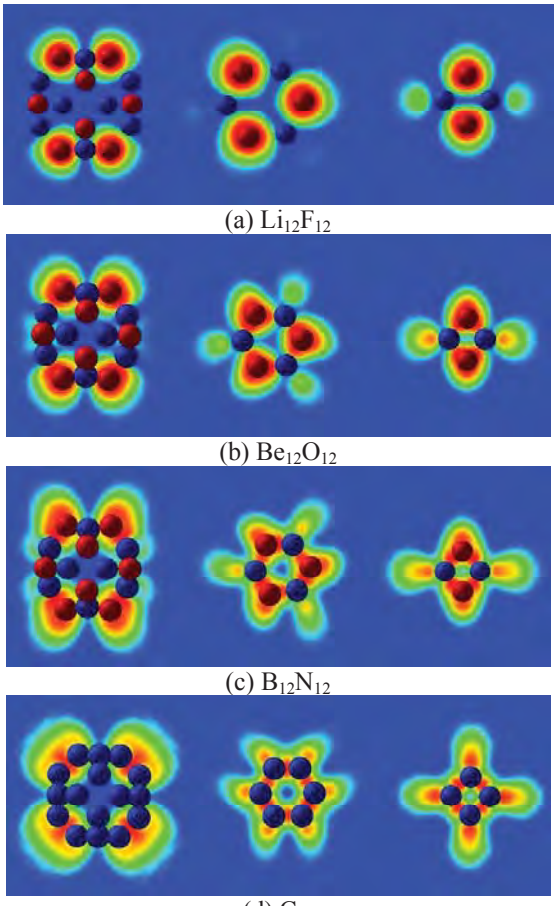

(a) $Li_{12}F_{12}$

(b) $Be_{12}O_{12}$

(c) $B_{12}N_{12}$

(d) C_{24}

Figure 3: Electron density maps in the three planes passing through $(AB)_{12}$ cage clusters.

To obtain additional detailed insight into the bonding and ionic polarization in the cage clusters, we have also analyzed the changes in the electronic structure upon increasing the formal cation/anion radii ratio using the Electron Localization Function (ELF). In the case of the first row element clusters, the chemical bonding is highly ionic in LiF and decreases when moving to C. From the ELF maps shown in Figure 2 one can note that when going from the extremes of LiF to CC, through BeO and BN as intermediate cases, interesting changes emerge. The ELF maps for the LiF cluster show rather spherical ELF basins, which are indicative of a highly ionic character, and they are increased and noticeably deformed when going from heteroatomic cages LiF, BeO, BN

to the case of C. In fact, for the carbon cage cluster the situation is rather different, the ELF maps are largely deformed from the symmetric spherical shape, the electron pair are clearly distributed all around the cluster. This is a clear indication that, in spite of a similar structure, the chemical bond between atoms in cage clusters is different, as expected, from chemical intuition.

A clear difference exists in the chemical bond of the first row element cage structures, which is further confirmed by the ELF maps in each plane reported in Figure 3

3.2 Relative stability of the sodalite phase

In order to compare the stability of the sodalite phase to that of the most stable polymorph and other possible phases, we explicitly considered other phases and determined the optimized parameters using the Birch-Murnaghan EOS. From the optimized parameters reported in Table 3 we find that the optimized volume per unit of the sodalite phase is larger than that of the ground state phase of LiF and BeO by 53% and 20%, respectively, whereas for for BN and C the volume of the most stable phase per unit is larger than that of the sodalite phase by 38% and 35%, respectively.

Phase-AB	E0	ΔE0	V0	B0
RS-LiF (exp)			16.32[a]	69.9[b]
RS-LiF (present work)	-9.73	0.00	16.85	68.6
SOD-LiF	-9.68	0.05	25.87	41.7
WZ-BeO (exp)[c]	-12.73		13.79	212
WZ-BeO (present work)	-14.38	0.00	14.02	210.4
SOD-BeO	-14.21	0.17	17.05	168.34
HEX-BN (exp)[d]				36.7
HEX-BN (present work)	-17.67	0.00	19.37	39.82
SOD-BN	-16.99	0.68	14.61	290.05
Graphite-C (exp)[e]			35.15	42
Graphite-C (exp)[f]			35.12	33.8
Graphite-C (present work)	-18.49	0.00	18.98	39.01
SOD-C	-17.42	1.07	14.04	328.41

[a] Ref. 11, [b] Ref. 12, [c] Ref. 13, [d] Ref. 14, [e] Ref. 15, [f] Ref. 16

Table 2: Properties for various polymorphs (per unit) of LiF, BeO, BN and C as calculated from the EOS fits to the GGA-DFT calculated data: E0 is the minimum total energy (eV), ΔE_0 the total energy differences (eV), V0 the volume at minimum energy ($Å^3$) and B0 the bulk modulus (GPa). V0 and B0 are compared with available experimental values.

In order to find the trend on the stability of the sodalite phase relative to the other phases considered in the present work, we plot in Figure 4 the energy difference (per unit) between the total energy of sodalite and the total energy of the most stable polymorph. From Figure 4 a clear monotonous trend is observed which makes it undoubtedly clear that the stability of the sodalite phase decreases along the LiF, BeO, BN and C series or that increasing covalent character of the chemical bond destabilizes the low density polymorph with respect to the more dense phases corresponding to the most stable polymorph. These results indicate that the sodalite form is likely to be easily synthesized from highly ionic compounds where for the remaining studied systems this will face increasing difficulties.

3.3 Electronic properties

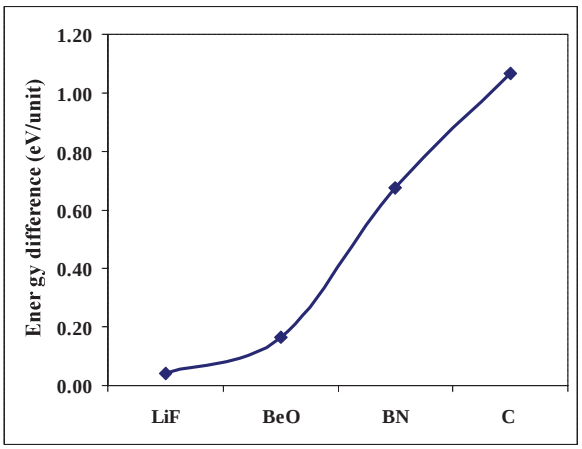

Figure 4: The energy differences between the sodalite phase and the ground state phase.

In order to investigate the electronic structures of the different polymorphs of LiF, BeO, BN and C more precisely, we have calculated the total density of states using the standard procedure. All band energies are given with respect to the Fermi energy (E_F) and shown in Figure 5. The Fermi energy is located at the top of the valence bands which is located at the Γ point and is set to zero. The DOS plots for rock salt and sodalite phases of LiF are presented in Figures 5a1 and 5a2, respectively. Below zero, there is a broad range of F states below the top of the valence band, whereas the conduction band consists of F and Li states. The difference between the maximum of the F valence band and the minimum of the Li conduction band results in a band gap of 8.83 eV and 6.36 eV for rock salt and sodalite phases, respectively. The band gap for the rock salt phase is underestimated with respect to the experimental value of 13.6 eV. This is a well known failure of the GGA functional. Nevertheless, one expects that the relative trends are well reproduced. The DOS plots of BeO for wurtzite and sodalite phases (Figures 5b1 and 5b2) display the same trend, the valence regions are mainly composed of O states while the conduction bands originate predominantly from Be states. The calculated energy gaps are 7.22 eV and 5.18 eV for wurtzite and sodalite phases, respectively. Again the band gap for wurtzite is underestimated with respect to the experimental value of 10.6 eV. The DOS for the two polymorphs of BN phases are reported in Figures 5c1 and 5c2 and also show that the top and the low energy part of the valence band is predominantly formed by the states of nitrogen atoms. The upper conduction band is dominated by contributions from both B and N states. The calculated band gap for hexagonal BN is 4.37 eV (experimental value = 5.4 eV) while the

calculated value for the sodalite phase is 4.38 eV. For the graphite phase (Figure 5d1), the DOS for the unit cell shows two groups of peaks with a band gap of 1.43 eV between them. The Fermi energy is placed at the top of the valence band (VB) so all states below it have two electrons per orbital, and all states above it are unoccupied. The energy gap of the sodalite form of carbon is calculated to be 2.44 eV.

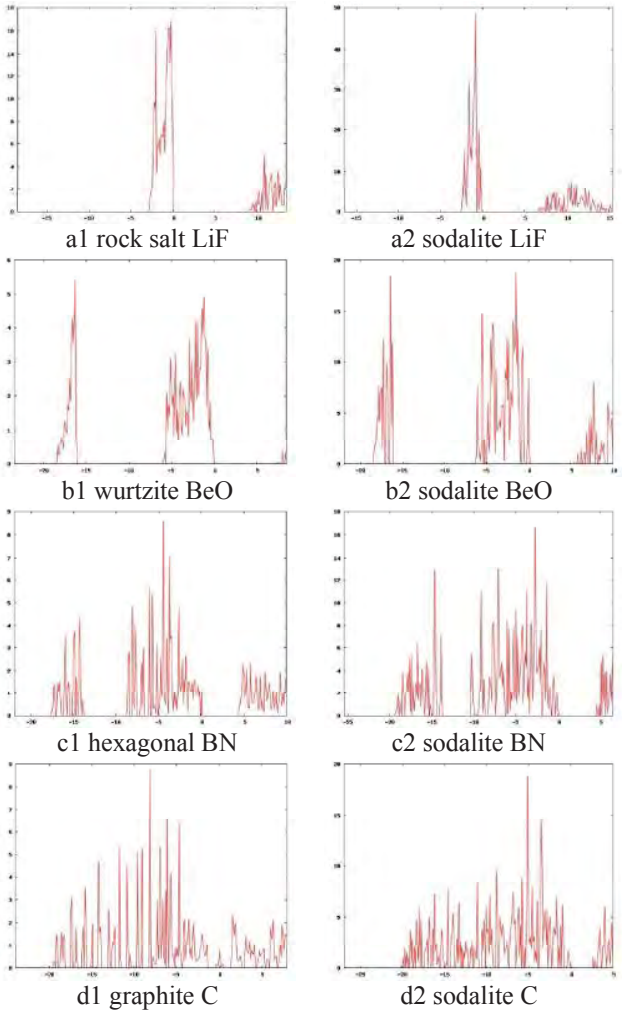

Figure 5: Total density of states of bulk phases of LiF, BeO, BN and C.

4 CONCLUSION

A bottom up approach and state-of-the-art plane wave periodic density functional calculations were utilized to investigate the possible existence of low density phases of the LiF, BeO, BN first row element binary compounds and of C. The existence of stable $(AB)_{12}$ or C_{24} cage clusters, where AB= LiF, BeO, BN, suggest that these could act as building blocks to form novel nanoporous materials. The calculated HOMO-LUMO gaps of all clusters decreases along the LiF, BeO, BN, C series and can be understood from the ELF analysis. In fact, the ELF analysis of the bare cage clusters explains the difference in optimized geometry and electron distribution on each cluster. Bulk materials constructed from the cages may exhibit a sodalite structure; the total energy difference (per unit) between the most stable and the sodalite polymorphs was found to increase when going from LiF to C ($\Delta E_{SOD\text{-}stab}$=0.05, 0.17, 0.68, 1.07 eV/unit for LiF, BeO, BN and C, respectively). The calculated HOMO-LUMO gaps and electronic structure of all predicted nanoporous phases are different from those of the corresponding ground state phases. Merging state of the art density functional calculations and a bottom-up strategy provides a complementary way to motivate further synthesis and applications of new predicted nanoporous phases.

ACKNOWLEDGEMENTS

This work was supported in part by grants from the National Science and Technology Development Agency (NSTDA), KURDI the Thailand Research Fund (to WS. and JL.) and the Commission on Higher Education, Ministry of Education under Postgraduate Education and Research Programs in Petroleum and Petrochemicals, and Advanced Materials. This study has been supported in part by the Spanish Ministerio de Ciencia e Innovacion grant FIS2008-02238/FIS.

REFERENCES

[1] W. Sangthong, J. Limtrakul, F. Illas and S. T. Bromley, J. Mater. Chem., 2008, 18, 5871.
[2] J. Carrasco, F. Illas and S. T. Bromley, Phys. Rev. Lett., 2007, 99, 235502.
[3] J. C. Wojdel, M. A. Zwijnenburg and S. T. Bromley, Chem. Mater., 2006, 18, 1464.
[4] J. P. Perdew, J. A. Chevary, S. H. Vosko, K. A. Jackson, M. R. Pederson, D. J. Singh and C. Fiolhais, Phys. Rev. B, 1992, 46, 6671.
[5] J. A. White and D. M. Bird, Phys. Rev. B, 1994, 50, 4954.
[6] G. Kresse and J. Hafner, Phys. Rev. B, 1993, 47, 558.
[7] G. Kresse and J. Furthmu¨ ller, Comput. Mater. Sci., 1996, 6, 15.
[8] G. Kresse and J. Furthmu¨ ller, Phys. Rev. B, 1996, 54, 11169.
[9] P. E. Blöchl, Phys. Rev. B, 1994, 50, 17953.
[10] F. Birch, Phys. Rev., 1947, 71, 809.
[11] V. A. Streltsov, V. G. Tsirelson, R. P. Ozerov and O. A. Golovanov, Kristallografiya, 1987, 33, 90.
[12] C. V. Briscoe and C. F. Squire, Phys. Rev., 1957, 1175, 106.
[13] Hazen R M and Finger L W, J. Appl. Phys., 1986, 59, 3728.
[14] S. Bohr, R. Haubner, B. Lux, Diamond Relat. Mater., 1995, 4, 714.
[15] Y.X. Zhao and I.L. Spain, Phys. Rev. B, 1989, 40, 993.
[16] M. Hanfland, H. Beister, and K. Syassen, Phys. Rev. B, 1989, 39, 12 598.

American Chemical Society National meeting & Exposition ครั้งที่ 239

ณ ประเทศสหรัฐอเมริกา

ระหว่างวันที่ 21-25 มีนาคม 2553

จำนวน 11 เรื่อง

918 - Propane cracking reaction over different types of nanostructured zeolites: A newly developed DFT approach

Sarawoot Impeng, Thana Maihom, Pipat Khongpracha, Dr. Somkiat Nokbin, Dr. Jumras Limtrakul, Prof. Dr. . Department of Chemistry, Faculty of Science, Kasetsart University Laboratory for Computational & Applied Chemistry, Physical Chemistry Division Chatuchak Bangkok Thailand, Center of Nanotechnology, Kasetsart University Research and Development Institute Chatuchak Bangkok Thailand, NANOTEC Center of Nanotechnology, National Nanotechnology Center, Kasetsart University Chatuchak Bangkok Thailand

Propane cracking over different types of zeolites was investigated using the realistic nanocluster of 120T performed at the M06L/6-31G(d,p)//14T ONIOM(M06L/6-31G(d,p):UFF) level of theory. The adsorption energies of propane were predicted to be -7.6 and -9.9 kcal/mol for H-FAU and H-MOR, respectively. Using the experimental adsorption energies as the benchmark, our combined ONIOM scheme is found to represent the interaction of propane with zeolites. After adsorption, the zeolite's proton was inserted into a C-C bond of a propane molecule and yielded a methane and ethoxide intermediate. The intermediate was then deprotonated to form the ethylene product. The first step was found to be rate-determining with actual activation energies of 43.7 and 41.3 kcal/mol for H-FAU and H-MOR, respectively. The activation energies for the second step were 24.7 and 18.5 kcal/mol for H-FAU and H-MOR, respectively. Our findings suggested that the propane cracking was insensitive to the zeolite structure.

Tuesday, March 23, 2010 07:00 PM

Inorganic Catalysts (07:00 PM - 09:00 PM)

Close Window

919 - Adsorption of a basic probe molecule over nanostructured zeolitic catalysts (H-FAU, H-MOR and H-MCM-22): A newly developed density functional M06-2X study

Supalak Khueanphet*, Bundet Boekfa, Dr. Tanin Nanok, Dr. *Jumras Limtrakul*, Prof. Dr. . Department of Chemistry, Faculty of Science, Kasetsart University Laboratory for Computational & Applied Chemistry, Physical Chemistry Division Chatuchak Bangkok Thailand, Center of Nanotechnology, Kasetsart University Research and Development Institute Chatuchak Bangkok Thailand, NANOTEC Center of Nanotechnology, National Nanotechnology Center, Kasetsart University Chatuchak Bangkok Thailand, Department of Chemistry Faculty of Liberal Art and Science, Kasetsart University Kamphaeng Saen Campus Nakhon Pathom Thailand

The confinement effect on the adsorption of ammonia on different types of zeolite (H-FAU, H-MOR and H-MCM-22) has been studied with the newly developed Density Functional Theory, M06-2X, with 6-31G(d,p) basis set. The nanoporous zeolites, where chemical reactions take place, are represented by a small cluster of 14T up to a nanocluster of 120 tetrahedral atoms (T is Si or Al atoms). The adsorption energies of ammonia on H-FAU, H-MOR and H-MCM-22 are predicted to be -35.0, -41.1 and -41.7 kcal/mol, respectively, which are in the range of experiment observation of -35.9 kcal/mol for H-FAU and -38.2 kcal/mol of H-MOR. Therefore, the full quantum calculation with the new density functional theory, M06-2X/6-31G(d,p), is a practical and accurate model to study the confinement effect on the adsorption of the polar molecule in different pore sizes of zeolites.

Keywords: Confinement effect, Zeolites, Ammonia adsorption, M06-2X functional

Tuesday, March 23, 2010 07:00 PM

Inorganic Catalysts (07:00 PM - 09:00 PM)

Close Window

917 - Skeletal isomerization of 1-butene over ferrierite zeolite: A quantum chemical analysis of structures and reaction mechanisms

Chularat Wattanakit*, Bundet Boekfa, Dr. Somkiat Nokbin, Dr. Piboon Pantu, Asst. Prof. *Jumras Limtrakul*, Prof. Dr. . Department of Chemistry, Faculty of Science, Kasetsart University Laboratory for Computational & Applied Chemistry, Physical Chemistry Division Chatuchak Bangkok Thailand, Center of Nanotechnology, Kasetsart University Research and Development Institute Chatuchak Bangkok Thailand, NANOTEC Center of Nanotechnology, National Nanotechnology Center, Kasetsart University Chatuchak Bangkok Thailand, Department of Chemistry Faculty of Liberal Art and Science, Kasetsart University Kamphaeng Saen Campus Nakhon Pathom Thailand

The skeletal isomerization of 1-butene to isobutene has been investigated by a full quantum calculation using M06L/6-31G(d,p) method with a 37T H-FER cluster. The adsorption energies for 1-butene and isobutene, respectively, are predicted to be -22.0 and -16.7 kcal/mol. The monomolecular acid-catalyzed formation of isobutene has been considered. The mechanism starts with the protonation of the adsorbed 1-butene by an acidic proton to produce a surface secondary alkoxide intermediate and is subsequently transformed into primary alkoxide via the cyclic transition state. The isobutoxide is then altered to the isobutene product through *tert*-butyl cation. The activation barriers are 9.0 and 20.9 kcal/mol for the sequent first and second steps, respectively. For the third step, the barrier is 30.2 kcal/mol and is considered to be the rate-determining step, which agrees well with experiment,~30 kcal/mol. The shape selectivity due to the “nano-confinement” effect of the zeolite framework has been clearly demonstrated.

Tuesday, March 23, 2010 07:00 PM

Inorganic Catalysts (07:00 PM - 09:00 PM)

Close Window

STRUCTURES AND REACTION MECHANISMS OF GLYCEROL DEHYDRATION OVER H-ZSM-5 ZEOLITE

Kanokwan Kongpatpanich [a, b, c], *Tanin Nanok* [a, b, c], *Bundet Boekfa* [b, c] *and Jumras Limtrakul* [a, b, c*]

[a] Laboratory for Computational and Applied Chemistry, Chemistry Department, Faculty of Science, Kasetsart University, Bangkok 10900, Thailand.
[b] Center of Nanotechnology, Kasetsart University Research and Development Institute, Kasetsart University, Bangkok 10900, Thailand.
[c] NANOTEC Center of Excellence, National Nanotechnology Center, Bangkok 10900, Thailand.

Introduction

The global energy crisis that has been brought about by the continuing depletion of petroleum resources and the increase of environmental problems is acknowledged by researchers as a serious problem. This has led to the search for new, alternative and renewable resources. Biodiesel, an alternative non-toxic and biodegradable diesel fuel, can offer one alternative energy supply. At the present time, biodiesel costs are still higher than petroleum-based diesel mainly because of the cost of raw materials and the large amount of waste generated within the processes. Therefore, approaches that can utilize the waste from the processes are of particular interest. Several researches have been focused on new approaches for converting this valueless waste derived from biomass to higher value chemicals.[1]

Glycerol, a by-product from biodiesel production, has a relatively low global demand with a low market price which has a negative impact on biodiesel economics.[2] Since the demand for glycerol is outpaced by biodiesel production, a solution has to be found to increase the value of glycerol. One solution is to convert it to a more valuable chemical.[3] Acrolein or 2-propenal is a value-added chemical readily prepared from the catalytic dehydration of glycerol under a mild condition. Acrolein is an essential and versatile starting intermediate material widely used in the production of acrylic acid, DL-Methionine, super absorber polymers, and detergents.[4] For many years, acrolein has been produced by the oxidation of propylene over Bi/Mo mixed oxide catalysts, but the production is limited by the continuously increasing price of propylene.[5] Avoiding this route by using alternative carbon sources from biomass would be a green alternative for the chemical industry. Moreover, this route could improve the sustainability in environmental care and also is an economically attractive one.

Zeolite, with its selective properties, high thermal stability and intrinsic acidity[6] is one of the most important solid acid catalysts widely used in petroleum refinery industries and for the production of fine chemicals. Several studies have been conducted describing the dehydration of glycerol over different solid acids, for example Nb_2O_5, heteropoly acids, silica-supported heteropoly acids, and zeolites.[7-12] H-ZSM-5 zeolite has been found to have high catalytic activity and selectivity for the dehydration of glycerol into acrolein.[10-12] However, the reaction mechanism is still not clearly understood. Although there have been some theoretical studies of glycerol dehydration over homogeneous catalysts[13] but, as far we know, there are no theoretical studies reported about the detailed reaction mechanism of glycerol dehydration over solid acid, which may offer a different mechanism from the conventional ones.

In the present work, the full quantum chemical calculation was employed to study the dehydration of glycerol over H-ZSM-5 zeolite in order to better understand its chemistry and further control the industrial operating conditions.

Methods

The structure of the 128T cluster model taken from the lattice structure of the ZSM-5 zeolite was employed to study the reaction mechanism. The cluster covers the straight channel, the zigzag channel, and the channel intersection. The intersection of the two channels allows a large space for the reaction to take place. Previous studies from our group indicate that the M06-2X functional developed by the Minnesota group[14, 15] show reliable results for the study of the interaction of organic molecules in the zeolite system.[16-18] Geometry optimizations were done over the 12T cluster at the M06-2X/6-31G(d,p) level of theory, with only the 5T cluster of the active site region and the adsorbing molecules being allowed to relax to reduce the required computational time. The frequency calculations were performed at the same level to verify that the transition state structure has only one imaginary frequency. Single-point calculation of the 128T cluster was done on the optimized structures to represent the confinement effect of the zeolite framework and to obtain more accurate energies. The standard enthalpy (ΔH) and Gibbs free energy changes (ΔG) of all structures in the first dehydration step were obtained from the frequency calculations. These data were used to predict the rate constants and the equilibrium constants. The rate constants were evaluated over the temperature range of 200-500 °C with the interval of 50 °C using a simple transition state theory (TST).[19] All calculations were performed using the Gaussian 03 code[20] incorporated with the Minnesota Density Functionals module 3.1 by Zhao and Truhlar.

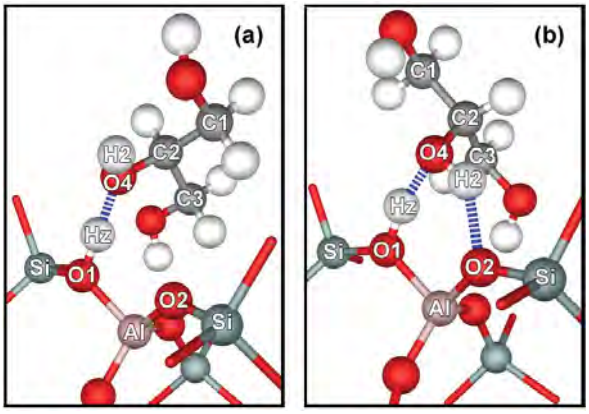

Figure 1. Optimized structures of (a) the side-on and (b) the end-on glycerol adsorption structures.

Results and discussion

Glycerol is a highly flexible C_3 molecule containing three hydroxyl groups. In the gas phase, it preferably forms a cyclic structure of intramolecular hydrogen bonds between three hydroxyl groups termed gG'gg'Gg(γγ) as the most stable conformer.[21] Therefore, we have chosen this conformer as a starting geometry for studying its entire reaction in the H-ZSM-5 zeolite. Prior to the exploration of the reaction mechanism for glycerol conversion to acrolein, the search for the adsorption structures leading to acrolein formation has been established. The protonation at the secondary hydroxyl group (OH) is placed for the crucial adsorption structures. Figures 1a and b show the side-on and end-on adsorption structures of glycerol adsorbed onto the Brønsted active site of H-ZSM-5. Glycerol has a completely different conformation from that found in the isolated gas phase. The cyclic intramolecular hydrogen bonding between the three hydroxyl groups has been separated and liberally stabilized by the partially negative-charged oxygen atoms of the zeolite framework. For the side-on structure, the secondary OH group interacts with the Brønsted proton via the lone-pair electron of its oxygen center and the OH group points away from the lattice oxygens of the zeolite framework. The lateral hydrogen bonding of the secondary OH group with the basic lattice oxygen is found, additionally, in the end-on structure. The adsorption energies for the side-on and end-on structures are estimated to be exothermic by 52.7 and 51.1 kcal/mol, respectively. These values are considerably larger than the experimental measurement for the exothermic methanol adsorption of 27.5 kcal/mol.[22] The effects of zeolite confinements and a number of hydrogen bondings experienced by glycerol are accountable for the highly exothermic adsorption energy. The strongest hydrogen bonding between the secondary OH group and the zeolite Brønsted active site results in the significant elongation of the O1-Hz zeolite bond distance from 0.97 Å to 1.06 and 1.07 Å for the side-on and end-on structures, respectively. The three-centered hydrogen bond angle, O1-Hz-O4, is close to a linear angle (177.2˚ and 165.0˚, for the side-on and end-on adsorption structures, respectively) and the O1-O4 distance is calculated to be 2.46 Å in both cases.

As mentioned above, the selective activation at the secondary OH group is substantially the initial reaction for acrolein production. We, thus, follow the schematic diagram of the reaction mechanisms guided by the previous infrared spectroscopic (IR) study.[12] The transformation of glycerol to acrolein can be consecutively divided into three main steps as follows:

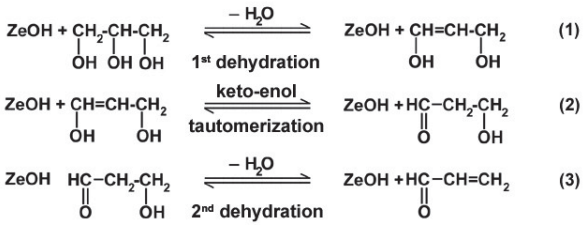

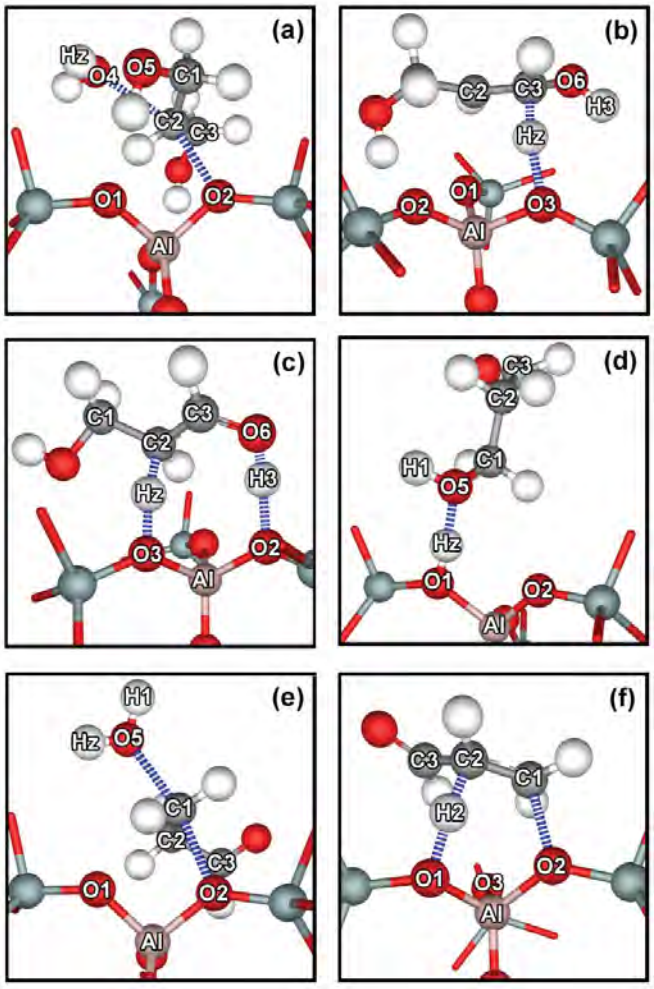

Figure 2. Optimized structures of the transition states and a stable intermediate (3-hydroxypropanal) along the reaction pathway for glycerol transformation to acrolein (a) ts_dehyd_1 (b) ts_alk_1 (c) ts_tauto_1 (d) keto_OH (e) ts_alk_2 and (f) ts_acrolein.

(1) The first dehydration. The protonation at the secondary OH group of glycerol is the key step for activating the first dehydration reaction. This process results in the weakening of the glycerol C2-O4 bond at the secondary position and, hence, promoting the OH group to be a good leaving group. To prevent the reversible proton back donation to the zeolite, that can occur readily under normal experimental conditions, we proposed the activated complex as shown in Figure 2a as the transition state structure, **ts_dehyd_1**, for the first dehydration reaction. The protonated glycerol molecule is oriented to have the secondary carbon C2 located in the middle, between the protonated OH group and the zeolite lattice oxygen O2. The strongly active mode of an imaginary frequency vibration of the transition state complex resembles the S_N2 mechanism in which the C2-O2 bond formation and the C2-O4 bond cleavage occur in the concerted fashion. When considering

the geometric parameters, it can be seen that a water molecule is completely developed (C2-O4 = 2.40 Å) during the formation of an alkoxide (C2-O2 = 2.28 Å). Therefore, this activated complex is considered as the late transition state complex which requires the activation energy of 41.4 kcal/mol with respect to the side-on adsorption complex. According to the well-known Hammond-Leffler postulate[23], any reaction that proceeds through the product-like transition state is likely to be the endothermic reaction. As expected, the reaction is endothermic by 25.5 kcal/mol. The secondary surface alkoxide species **alk_1** and a water molecule are the products of this reaction step. To shift the reaction forwards, it is necessary to desorb the water molecule from the system. The calculated desorption energy required for the removal of a water molecule adsorbed nearby the surface alkoxide is 16.4 kcal/mol. After the water molecule is eliminated from the system, the surface alkoxide can readily undergo the proton back donation to regenerate the zeolite Brønsted active site by returning a proton attached to the primary carbon C1 back to the basic zeolite oxygen O3 and releasing 1,3-dihydroxypropene **hyd_enol_1** as a resulting product. The reaction proceeds through the transition state **ts_alk_1** (see Figure 2b) and requires the activation energy of 25.0 kcal/mol. 1,3-dihydroxypropene has an enol-form structure and it can strongly adsorb onto the zeolite Brønsted active site via the hydrogen bonding interaction using its vinyl hydroxyl group.

(2) The keto-enol tautomerization. In order to tautomerize 1,3-dihydroxypropene, an enol form, into its keto form, the orientation of an adsorbed molecule is readjusted to interact with the Brønsted proton via the loosely bound π-bonding interaction, **pi_enol_1**. The π-bonding adsorption structure of the enol form can, then, easily tautomerize to the keto form 3-hydroxypropanal through a nearly barrierless transition state **ts_tauto_1** (see Figure 2c). The imaginary frequency vibration of the transition state demonstrates that the acidic proton that attached to the zeolite O3 transfers to the C2 of glycerol at the same time that the hydroxyl proton on the glycerol O5 transfers back to the zeolite O2 to regenerate the acidic site. The tautomerization from the enol to keto form is the exothermic reaction. The keto-product strongly adsorbs onto the Brønsted acid site via the hydrogen bonding using its carbonyl group, **keto_CO**.

(3) The second dehydration. The protonation at the primary OH group of 3-hydroxypropanal is the key activating process for the second dehydration reaction. Therefore, the adsorption structure of 3-hydroxypropanal (see Figure 2d) **keto_OH** via its OH group with the Brønsted acid site is adopted to be the starting geometry of this second dehydration step. Similar to the first dehydration step, the OH group is protonated by zeolite and acts as a leaving group. At the transition state **ts_alk_2** (see Figure 2e), the attack of the 3-hydroxypropanal primary carbon by the basic zeolite oxygen takes place in concomitance with an elimination of a water molecule. This step requires an activation energy of 38.6 kcal/mol. The primary alkoxide

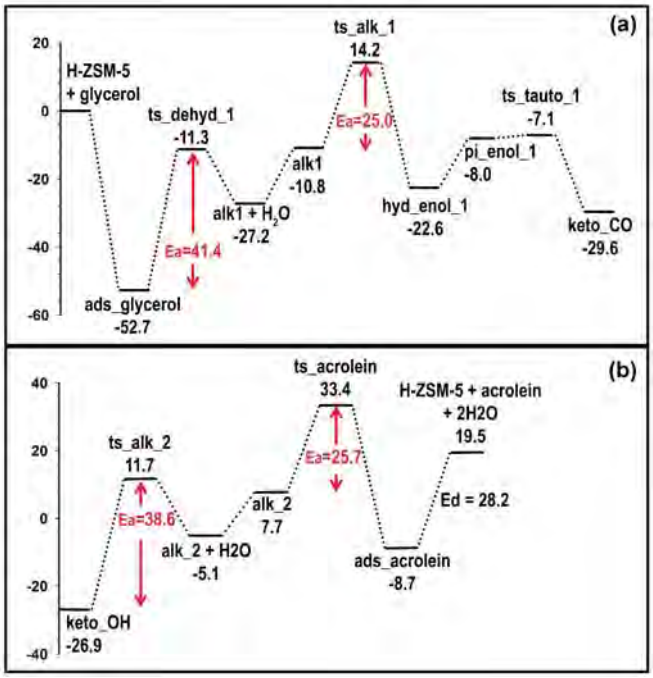

Figure 3. Relative energy profiles of (a) the first dehydration step and the keto-enol tautomerization and (b) the second dehydration step. Energies are in kcal/mol.

intermediate **alk_2** generated from this step is solvated by a single water molecule. To remove an adsorbed water molecule from the alkoxide species, it requires the desorption energy of 12.8 kcal/mol. The dehydrated alkoxide species undergoes proton back donation from the secondary carbon to the basic zeolite oxygen leading to the acrolein product formation. The transition state **ts_acrolein** (see Figure 2f) for acrolein formation requires an activation energy of 25.7 kcal/mol. Desorbing acrolein from the zeolite surface requires the desorption energy of 28.2 kcal/mol.

The overall energy profile for glycerol conversion to acrolein shown in Figures 3a and b indicates that the production of acrolein from glycerol over H-ZSM-5 is an endothermic process. The dehydration reaction is considered as the rate limiting step of the overall reaction because it requires the highest activation energy to overcome the reaction barrier. Instead, the hydration reaction which goes in the opposite direction of the dehydration reaction is found to be thermodynamically and kinetically favoured. Therefore, in order to shift the reaction from the left to the right, it is necessary to introduce a sufficiently high temperature to the system because the dehydration reaction is generally favoured at high temperature whereas the hydration reaction can readily occur at a low temperature.[11, 24] Table 1 shows the calculated rate constants (k_{for} and k_{rev}) and the equilibrium constants (K) for the first dehydration reaction step over the temperature range of 200-500 °C. The rate constant increases with increasing the temperature. This behaviour is in good accordance with the typical endothermic reaction. Since the water molecule generated by the dehydration process

Table 1. Calculated rate constants (k_{for} and k_{rev}) and the equilibrium constants (K) for the first dehydration reaction step over the temperature range of 200-500 °C.

T (°C)	$k_{forward}$	$k_{reverse}$	K_{eq}
200	4.23×10^{-6}	4.43×10^{4}	9.55×10^{-11}
250	3.72×10^{-4}	3.39×10^{5}	1.10×10^{-9}
300	1.52×10^{-2}	1.83×10^{6}	8.33×10^{-9}
350	3.47×10^{-1}	7.58×10^{6}	4.58×10^{-8}
400	5.01×10^{0}	2.55×10^{7}	1.96×10^{-7}
450	5.03×10^{1}	7.30×10^{7}	6.90×10^{-7}
500	3.77×10^{2}	1.83×10^{8}	2.06×10^{-6}

can readily react with the active alkoxide intermediate, the continuous removal of water from the system is another crucial point for preventing the backward reaction. From the overall energy diagram, it can be concluded that 3-hydroxypropanal is a stable intermediate in acrolein production. Several works have reported that 3-hydroxypropanal is able to be dehydrated into acrolein when the temperature is increased and acrolein can be readily hydrated into 3-hydroxypropanal at lower temperatures.[25, 26]

Conclusions

The structures and reaction mechanisms of glycerol dehydration over the H-ZSM-5 zeolite have been investigated using the newly developed density functional theory with the M06-2X functional. Three main reaction steps have been proposed to take place consecutively. The selective dehydration of glycerol at the secondary OH group is proved to be the first important step leading to acrolein formation. Even though the transition state of this step requires a relatively high activation energy compared to the other steps along the reaction pathway, the large amount energy released by glycerol adsorption could make the reaction becoming more efficient. Among several intermediates involved in the reaction, 3-hydroxypropanal is found to be the most stable intermediate. With respect to the gas phase glycerol, the acrolein formation is an endothermic reaction. In addition to increasing the reaction temperature, the removal of developed water from system could favor the forward reactions. The rate constants for the first dehydration over the temperature range of 200-500 ˚C are provided for comparing with future available kinetic experiments. Our findings are important for understanding the chemistry of glycerol dehydration over acidic zeolites.

Acknowledgements. This work was supported in part by grants from the National Science and Technology Development Agency (2009 NSTDA Chair Professor funded by the Crown Property Bureau under the management of the National Science and Technology Development Agency and NANOTEC Center of Excellence funded by the National Nanotechnology Center), The Thailand Research Fund, the Commission of Higher Education, Ministry of Education ("National Research University of Thailand" and "Postgraduate Education and Research Programs in Petroleum and Petrochemicals and Advanced Materials"). The support from the Kasetsart University Research and Development Institute (KURDI) and Graduate School Kasetsart University are also acknowledged. The authors are grateful to Donald G. Truhlar and Yan Zhao for their support with the M06-2X functional.

References

(1) Corma Canos, A.; Iborra, S.; Velty, A., *Chem. Rev.* **2007,** *107*, 2411.
(2) Pagliaro, M.; Ciriminna, R.; Kimura, H.; Rossi, M.; Della Pina, C., *Angew. Chem. Int. Ed.* **2007,** *46*, 4434.
(3) Zheng, Y.; Chen, X.; Shen, Y., *Chem. Rev.* **2008,** *108*, 5253.
(4) Katryniok, B.; Paul, S.; Capron, M.; Dumeignil, F., *ChemSusChem* **2009,** *2*, 719.
(5) Pudar, S.; Oxgaard, J.; Chenoweth, K.; van Duin, A. C. T.; Goddard, W. A., *J. Phys. Chem. C* **2007,** *111*, 16405.
(6) Van Santen, R. A.; Kramer, G. J., *Chem. Rev.* **1995,** *95*, 637.
(7) Chai, S. H.; Wang, H. P.; Liang, Y.; Xu, B. Q., *J. Catal.* **2007,** *250*, 342.
(8) Atia, H.; Armbruster, U.; Martin, A., *J. Catal.* **2008,** *258*, 71.
(9) Tsukuda, E.; Sato, S.; Takahashi, R.; Sodesawa, T., *Catal. Commun.* **2007,** *8*, 1349.
(10) Zhou, C. J.; Huang, C. J.; Zhang, W. G.; Zhai, H. S.; Wu, H. L.; Chao, Z. S., *Stud. Surf. Sci. Catal.* **2007,** *165*, 527.
(11) Corma, A.; Huber, G. W.; Sauvanaud, L.; O'Connor, P., *J. Catal.* **2008,** *257*, 163.
(12) Yoda, E.; Ootawa, A., *Appl. Catal. A : General* **2009,** *360*, 66.
(13) Nimlos, M. R.; Blanksby, S. J.; Qian, X.; Himmel, M. E.; Johnson, D. K., *J. Phys. Chem. A* **2006,** *110*, 6145.
(14) Zhao, Y.; Truhlar, D. G., *Acc. Chem. Res.* **2008,** *41*, 157.
(15) Zhao, Y.; Truhlar, D. G., *Theor. Chem. Acc.* **2008,** *120*, 215.
(16) Maihom, T.; Boekfa, B.; Sirijaraensre, J.; Nanok, T.; Probst, M.; Limtrakul, J., *J. Phys. Chem. C* **2009,** *113*, 6654.
(17) Kumsapaya, C.; Bobuatong, K.; Khongpracha, P.; Tantirungrotechai, Y.; Limtrakul, J., *J. Phys. Chem. C* **2009,** *113*, 16128.
(18) Boekfa, B.; Choomwattana, S.; Khongpracha, P.; Limtrakul, J., *Langmuir* **2009**, DOI: 10.1021/la901841w.
(19) Choomwattana, S.; Maihom, T.; Khongpracha, P.; Probst, M.; Limtrakul, J., *J. Phys. Chem. C* **2008,** *112*, 10855.
(20) Frisch, M. J. T., G. W.; Schlegel, H. B.; Scuseria, G. E.; Robb, M. A.; Cheeseman, J. R.; Montgomery, Jr., J. A.; Vreven, T.; Kudin, K. N.; Burant, J. C.; Millam, J. M.; Iyengar, S. S.; Tomasi, J.; Barone, V.; Mennucci, B.; Cossi, M.; Scalmani, G.; Rega, N.; Petersson, G. A.; Nakatsuji, H.; Hada, M.; Ehara, M.; Toyota, K.; Fukuda, R.; Hasegawa, J.; Ishida, M.; Nakajima, T.; Honda, Y.; Kitao, O.; Nakai, H.; Klene, M.; Li, X.; Knox, J. E.; Hratchian, H. P.; Cross, J. B.; Bakken, V.; Adamo, C.; Jaramillo, J.; Gomperts, R.; Stratmann, R. E.; Yazyev, O.; Austin, A. J.; Cammi, R.; Pomelli, C.; Ochterski, J. W.; Ayala, P. Y.; Morokuma, K.; Voth, G. A.; Salvador, P.; Dannenberg, J. J.; Zakrzewski, V. G.; Dapprich, S.; Daniels, A. D.; Strain, M. C.; Farkas, O.; Malick, D. K.; Rabuck, A. D.; Raghavachari, K.; Foresman, J. B.; Ortiz, J. V.; Cui, Q.; Baboul, A. G.; Clifford, S.; Cioslowski, J.; Stefanov, B. B.; Liu, G.; Liashenko, A.; Piskorz, P.; Komaromi, I.; Martin, R. L.; Fox, D. J.; Keith, T.; Al-Laham, M. A.; Peng, C. Y.; Nanayakkara, A.; Challacombe, M.; Gill, P. M. W.; Johnson, B.; Chen, W.; Wong, M. W.; Gonzalez, C.; and Pople, J. A. *Gaussian 03, revision B.05*, Gaussian, Inc., Wallingford CT, 2004.
(21) Chelli, R.; Gervasio, F. L.; Gellini, C.; Procacci, P.; Cardini, G.; Schettino, V., *J. Phys. Chem. A* **2000,** *104*, 11220.
(22) Lee, C. C.; Gorte, R. J.; Farneth, W. E., *J. Phys. Chem. B* **1997,** *101*, 3811.
(23) Hammond, G. S., *J. Am. Chem. Soc.* **2002,** *77*, 334.
(24) Izumi, Y., *Catal. Today* **1997,** *33*, 371.
(25) Pressman, D.; Lucas, H. J., *J. Am. Chem. Soc.* **2002,** *64*, 1953.
(26) Clacens, J. M.; Pouilloux, Y.; Barrault, J., *Appl. Catal. A : General* **2002,** *227*, 181.

Application of newly developed M06-2X functional for identifying a suitable industrially important petrochemical zeolite catalyst for a particular reaction

Bundet Boekfa [a,b,c] *, Piboon Pantu* [a,b]*, Pailin Limtrakul* [a]*, Michael Probst* [a,b]*, and Jumras Limtrakul* [a,b*]

[a] Laboratory for Computational & Applied Chemistry, Physical Chemistry Division, Department of Chemistry, Faculty of Science, Kasetsart University, Bangkok 10900, Thailand
[b] Center of Nanotechnology, Kasetsart University Research and Development Institute, Kasetsart University, Bangkok 10900, Thailand
[c] Chemistry Department, Faculty of Liberal Art and Science, Kasetsart University Kamphaeng Saen Campus, Nakhon Pathom 73140, Thailand

Introduction

Zeolite, aluminosilicate materials with regular pore structure of molecular dimensions, is one of the most important heterogeneous catalysts widely used for environmental, pertrochemical and industrial applications.[1-7] Their activity and selectivity make them stand out from other catalysts in petrochemical industries. The aldol condensation is one of the C-C bond forming organic reactions that are widely used in the production of solvents and plasticizers, and in the synthesis of intermediates for perfumes and pharmaceuticals.[5,8,9] Acetone tautomerization to enol form is an important initial step of aldol condensation and C-C coupling. The activity of tautomerization (also known as enolization) is found to be dependent on the acidity and the ionic strength of the reaction media. [10-12]

Theoretical studies on keto-enol tautomerization of acetaldehyde and acetone over uncatalyzed and zeolite catalysts have reported that the bifunctional features of Brønsted acid and Lewis basic sites on H-ZSM-5 drastically reduce the barrier height for the tautomerization of acetaldehyde and acetone.[22,23] In addition, the interaction between the zeolite framework and an adsorbed molecule, which is generally called confinement effect,[13] also plays an important role for the adsorption and reactions on zeolites.[14-21] Therefore, the details of interactions between the reactants and the active site in the zeolite's framework and the influence of the topology close to the active site are important to completely understand the reaction mechanism inside zeolite pores. Recently, with the new density functional M06-2X, the role of the confinement effect on reactions of unsaturated aliphatic, aromatic and heterocyclic compounds has been studied by using full quantum calculations. [20,21]

The aim of this work is to study the confinement effect of the zeolite framework (H-ZSM-5) on the adsorption and reaction mechanism of acetone tautomerization using the M06-2X density functional. The effect of the quantum cluster size on the energy profile of the reaction will also be discussed.

Methodology

Three different clusters were employed to model the H-ZSM-5 zeolite. First, the 5T cluster, $AlSi_4O_4H_{13}$, was the smallest cluster used to represent only the Brønsted acid site of zeolite. Second, 12T the quantum cluster was used to include the 10-membered-ring window over the acid site of the H-ZSM-5. A silicon atom was substituted with an aluminum atom at the most favorable position (T12). The last and most realistic model for this study was the 34T quantum cluster. This model includes the structure of the intersection cavity where the straight pore channel and the zigzag channel are crossed (Figure 1). In our previous works, the 34T quantum cluster was found to be sufficient to cover the non covalent effect of the zeolite.[20,21]

The M06-2X density functional was used in all calculations.[24,25] During geometry optimizations, only the 5T active region of ≡SiOHAl$(OSi)_2$OSi≡ and the probe molecule were allowed to relax while the rest of the structure was kept fixed at the crystallographic coordinates.[26] For geometry optimizations, the 6-31G(d,p) basis set was used. In order to get more accurate interaction energies, the single point calculations with the 6-311+G(2df,2p) basis set were carried out. Transition state structures were checked to verify that they had one imaginary frequency corresponding to the reaction coordinate. All calculations were performed with the Gaussian 03 code[27] modified to incorporate the Minnesota Density Functional module 3.1 by Zhao and Truhlar.

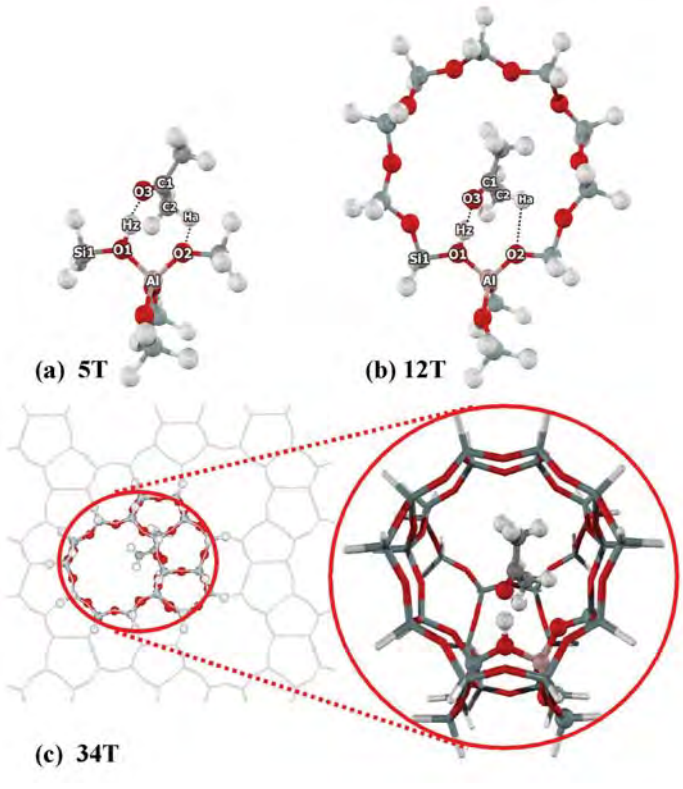

Figure 1. Quantum clusters used for modeling acetone adsorption and tautomerization on H-ZSM-5 zeolite (a) 5T, (b) 12T and (c) 34T model.

Results and Discussion

Nanocluster Models of Zeolite and Adsorption of Acetone. All cluster models of H-ZSM-5 of zeolite, from the 5T unit to the 34T framework, are shown in Figure 1. The Brønsted acid O1-Hz bond lengths are 0.968, 0.970 and 0.970 Å, for the 5T, 12T and 34T cluster, respectively. The acidity is insignificantly changed with the O1-Hz bond length about 0.002 Å. The Al···Hz distances are between 2.33 – 2.36 Å, which compares well with the experimental values (2.38 – 2.48 ± 0.04 Å). [28,29]

The optimized structure of acetone adsorbed on the acid site at the intersection cavity of H-ZSM-5 zeolite is shown in Figure 2. An acetone molecule forms a hydrogen bond between its carbonyl oxygen atom, O3, and the Brønsted acidic proton, Hz, of zeolite. A weak interaction between a methyl hydrogen atom of acetone, Ha, and the adjacent oxygen atom, O2, is also present. Increasing the cluster sizes increases the interactions between acetone and the zeolite framework as evidenced by the increase of the O1-Hz bond distance from 0.97 Å to 1.05, 1.08 and 1.11 Å for the 5T, 12T and 34T, respectively and the increase of the C1-O3 double bond distance from 1.21 Å to 1.23 Å. The O1-Hz···O3 angle is near-linear (178.4, 179.1 and 177.6 degrees, respectively).

The adsorption energy of acetone on H-ZSM-5 was calculated at the M06-2X/6-311+G(2df,2p)//6-31G(d,p) level of theory. For the small 5T model, the adsorption energy is calculated to be -18.9 kcal/mol, which is much lower than the experimental report of -31.1 kcal/mol.[30] Increasing the cluster size results in higher adsorption energy. The calculated adsorption energies are -23.6 and –28.1 kcal/mol for the 12T and the 34T model respectively. The more realistic model, 34T gives the adsorption energy that agrees well with the experimental result. Solans-Monfort et al.[23] used ONIOM(B3LYP:MNDO) and ONIOM(B3LYP:AM1) approaches to study the interaction and reaction of acetaldehyde in ZSM-5 zeolite and reported the adsorption energy to be -7.4 and -9.3 kcal/mol, respectively. We also have tried the ONIOM(B3LYP/6-31G(d,p):UFF) and found the adsorption energy of acetone on the 12T/128T model of H-ZSM-5 is -26.3 kcal/mol. Although, the ONIOM model, with the right combination of high and low level methods, can give a good estimation of adsorption energy, it cannot account for all the non covalent effects of the zeolite because it uses a low level of calculations to represent the zeolite framework. The M06-2X, however, can account for all interactions with the zeolite framework quantum mechanically and the results show that the larger the quantum cluster size results the better they agree with the experimental result.

Tautomerization of Acetone on H-ZSM-5 zeolite. As discussed in the previous section, acetone is adsorbed on the active site of H-zeolite by strong hydrogen bonding. The reaction mechanism occurs concerted in one step in which the Brønsted acid proton is transferred to the carbonyl oxygen atom of acetone and the methyl C-H bond of acetone is dissociated giving a proton back to the negatively charged framework oxygen of zeolite, as shown in Figure 3. The enol product interacts with the zeolite via the π-adsorption complex. In all models, the transition state structure resembles the product structure. Figure 3 presents the energy profiles for the acetone tautomerization for the 34 quantum cluster of H-ZSM-5 zeolite. Selected geometric parameters of the intermediates and transition state are tabulated in Table 2 and are shown in Figures 4 and 5.

In the 34T cluster of ZSM-5 zeolite (Figure 3), the tautomerization reaction of acetone occurs in the intersection cavity of the 10T channel. The acetone molecule adsorbs by forming two hydrogen bonds, O1-Hz ··· O3 and C2-Ha ··· O2, with the zeolite acid site. The reaction proceeds via the concerted mechanism. The transition state structure (Figure

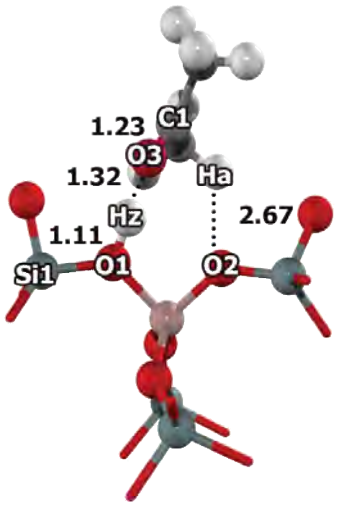

Figure 2. Optimized structure of the adsorption complex of acetone on the 34T cluster model of H-ZSM-5. For clarity atoms far from the acid site are omitted. Distances are in Å.

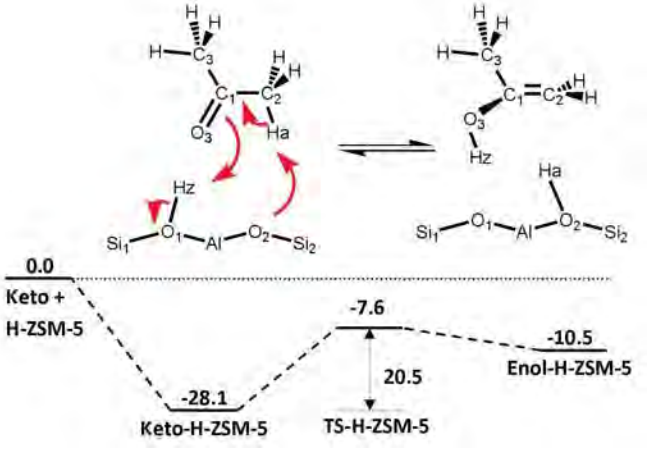

Figure 3. Potential energy diagram (kcal/mol) of the tautomerization of acetone on the 34T quantum cluster of H-ZSM-5.

4) is closer to the product structure. At the transition state, the hydroxyl Hz-O3 is already formed and the hydrogen atom of the methyl group (Ha) is dissociated and the C1-C2 double bond is formed. On the zeolite active site, the Brønsted O1-Hz bond is completely dissociated (O1-Hz distance =1.80 Å) and the O2-Ha bond is forming (O2-Ha distance =1.25 Å). An imaginary frequency at 917i cm^{-1} associated with the transition state was found. Its vibrational motion corresponds to the moving of the Brønsted proton to the O3 of acetone and the proton Ha at the methyl group of acetone to the O2, oxygen of zeolite. The enol product (Figure 5) interacted with zeolite through the hydrogen bond between the Brønsted acid (Ha) and the π bond of enol (C1-C2). The unsymmetrical distances between Ha ··· C1 (2.25 Å) and Ha ··· C2 (1.76 Å) are found indicating a weak π interaction.

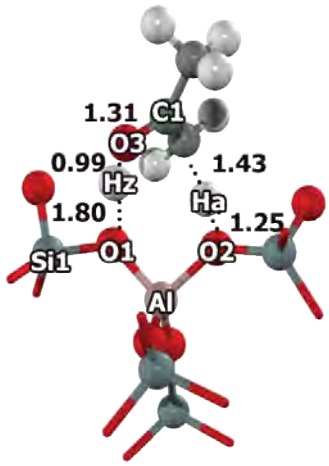

Figure 4. Optimized structure of the transition state complex of acetone on the 34T cluster model of H-ZSM-5. Distances are in Å.

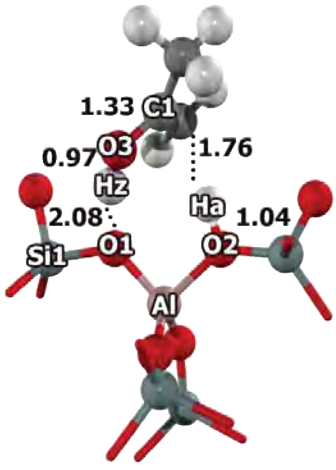

Figure 5. Optimized structure of the enol form of acetone on the 34T cluster model of H-ZSM-5. Distances are in Å.

Table 1. Reaction energies (kcal/mol) of the tautomerization reaction of acetone with various models of H-ZSM-5 zeolite, calculated with the M06-2X/6-311+G(2df,2p)//M06-2X/6-31G(d,p) level of theory (activation energy is in parenthesis).

Model	Keto	TS	Enol
5T	-18.9	0.9 (19.8)	-3.9
12T	-23.6	-2.6 (21.0)	-6.7
34T	-28.1	-7.6 (20.5)	-10.5

Table 2. Structure parameters for the tautomerization reaction of acetone on the 34T cluster of H-ZSM-5 (distances are in Å and angles are in degrees).

	Bare	Keto	TS	Enol
Distance				
Si1-O1	1.65	1.63	1.59	1.58
Si2-O2	1.59	1.57	1.62	1.64
Al -O1	1.82	1.78	1.71	1.69
Al -O2	1.68	1.69	1.77	1.80
Al-Oavg	1.71	1.71	1.71	1.71
Al···Hz	2.35	2.45	3.19	3.52
O1-Hz	0.97	1.11	1.80	2.08
Hz···O3		1.32	0.99	0.97
O1···O3		2.42	2.74	2.52
O3-C1	1.21	1.23	1.31	1.33
C1-C2	1.52	1.49	1.38	1.36
C2-Ha	1.09	1.10	1.43	1.76
C1···Ha	2.14	2.10	2.07	2.25
Ha···O2		2.67	1.25	1.04
Angle				
Al-O1-Si1	130.6	128.4	127.6	127.4
Al-O2-Si2	133.3	135.8	133.0	133.0
O1-Hz-O3		177.6	156.8	142.0
O1-Al-O2	90.4	93.1	93.7	92.4

The calculated activation energy of acetone tautomerization in ZSM-5 zeolite is 20.5 kcal/mol. Previous MP2 studies reported that in the gas phase (isolated) acetone tautomerization required a high activation energy of 64.0 - 69.2 kcal/mol. [31,32] In the zeolite framework, the activation energy is greatly reduced. A similar result has been reported by using the ONIOM calculation.[23] It is interesting to note that in this study the activation energy of reverse reaction (enol to keto form) is also drastically reduced to only 2.9 kcal/mol (in the 34T model). For isolated acetone, the activation energy for the change from enol to the keto form is 52.4 kcal/mol and with the catalyzing effect of water molecules this energy is reduced to 20.9 kcal/mol.[32] The low activation energy for the enol to keto reaction is due to the interactions with the framework zeolite that can stabilize the transition state. This result was not observed in the previous ONIOM calculations.[23] Increasing the quantum cluster size results in the higher stabilization of adsorbed intermediates and the transition state and, thus, the lower activation energy.

Conclusions

The effect of the zeolitic confinement on the adsorption and tautomerization of acetone has been studied by the new density functional theory, M06-2X. The adsorption energies are calculated to be -18.9, -23.6 and -28.1 kcal/mol for the 5T, 12T and 34T quantum cluster, respectively. We found that the extended framework significantly enhances the stabilities of adsorbed intermediates and the transition state. The large 34T model results in a better estimation of adsorption energy that is close to the experimental report of -31.1 kcal/mol. For the tautomerization of acetone on H-ZSM-5 zeolite, activation barriers are calculated to be 19.8, 21.0 and 20.5 kcal/mol, respectively. The reaction energies are 15.0, 16.9 and 17.6 kcal/mol, respectively. Moreover, the activation energy for the reverse reaction is also greatly reduced to 4.8, 4.1, 2.9 kcal/mol, respectively. The results obtained from this study indicate that the confinement effect from the large zeolite framework described by M06-2X functional is important to account for the interactions with the zeolite framework that lead to the stabilization of the transition state of the reaction mechanism.

Acknowledgement. This work was supported in part by grants from the National Science and Technology Development Agency (2009 NSTDA Chair Professor funded by the Crown Property Bureau under the management of the National Science and Technology Development Agency and NANOTEC Center of Excellence funded by the National Nanotechnology Center), The Thailand Research Fund, the Commission of Higher Education, Ministry of Education ("National Research University of Thailand" and "Postgraduate Education and Research Programs in Petroleum and Petrochemicals and Advanced Materials"). The support from the Kasetsart University Research and Development Institute (KURDI) and Graduate School Kasetsart University are also acknowledged. The authors are grateful to Donald G. Truhlar and Yan Zhao for their support with the M06-2X functional.

References

(1) Wojciechowsku, B. W.; Corma, A. *Catalytic Cracking: Catalysts, Chemistry, and Kinetics*; Dekker: New York, 1986.
(2) Olah, G. A.; Molnar, A. *Hydrocarbon Chemistry*; John Wiley and Sons Inc.: New York, 1995.
(3) Maxwell, I. E.; Stork, W. H. J. *Introduction to Zeolite Science and Practice*; Elsevier: Amsterdam, 1991.
(4) Venuto, P. B. *Microporous Mater.* **1994**, *2(5)*, 297-411.
(5) Corma, A.; Garcia, H. *Chem. Rev. (Washington, DC, U. S.)* **2003**, *103(11)*, 4307-4365.
(6) Corma, A. *J. Catal.* **2003**, *216(1-2)*, 298-312.
(7) Hunger, M. *Microporous Mesoporous Mater.* **2005**, *82(3)*, 241-255.
(8) Panov, A. G.; Fripiat, J. J. *J. Catal.* **1998**, *178(1)*, 188-197.
(9) Biaglow, A. I.; Sepa, J.; Gorte, R. J.; White, D. *J. Catal.* **1995**, *151(2)*, 373-384.
(10) Flego, C.; Perego, C. *Appl. Catal., A* **2000**, *192(2)*, 317-329.
(11) Xu, T.; Munson, E. J.; Haw, J. F. *J. Am. Chem. Soc.* **1994**, *116(5)*, 1962-1972.
(12) Xu, M.; Wang, W.; Hunger, M. *Chem. Commun. (Cambridge, U. K.)* **2003,** *(6)*, 722-723.
(13) Derouane, E. G.; Chang, C. D. *Microporous Mesoporous Mater.* **2000**, *35-36*,425-433.
(14) Kasuriya, S.; Namuangruk, S.; Treesukol, P.; Tirtowidjojo, M.; Limtrakul, J. *J. Catal.* **2003**, *219(2)*, 320-328.
(15) Namuangruk, S.; Pantu, P.; Limtrakul, J. *J. Catal.* **2004**, *225(2)*, 523-530.
(16) Namuangruk, S.; Pantu, P.; Limtrakul, J. *ChemPhysChem* **2005**, *6(7)*, 1333-1339.
(17) Maihom, T.; Boekfa, B.; Sirijaraensre, J.; Nanok, T.; Probst, M.; Limtrakul, J. *J. Phys. Chem. C* **2009**, *113(16)*, 6654-6662.
(18) Pantu, P.; Boekfa, B.; Limtrakul, J. *J. Mol. Catal. A: Chem.* **2007**, *277(1-2)*, 171-179.
(19) Kumsapaya, C.; Bobuatong, K.; Khongpracha, P.; Tantirungrotechai, Y.; Limtrakul, J. *J. Phys. Chem. C* **2009**, *113(36)*, 16128-16137.
(20) Boekfa, B.; Choomwattana, S.; Khongpracha, P.; Limtrakul, J. *Langmuir* **2009**, DOI: 10.1021/la901841w.
(21) Boekfa, B.; Choomwattana, S.; Maitarad, P.; Limtrakul, P.; Limtrakul, J. *Nanotech Conference & Expo 2009* **2009**, *3*,268-271.
(22) Rodriguez-Santiago, L.; Vendrell, O.; Tejero, I.; Sodupe, M.; Bertran, J. *Chem. Phys. Lett.* **2001**, *334(1,2,3)*, 112-118.
(23) Solans-Monfort, X.; Bertran, J.; Branchadell, V.; Sodupe, M. *J. Phys. Chem. B* **2002**, *106(39)*, 10220-10226.
(24) Zhao, Y.; Truhlar, D. G. *J. Phys. Chem. C* **2008**, *112(17)*, 6860-6868.
(25) Zhao, Y.; Truhlar, D. G. *Acc. Chem. Res.* **2008**, *41(2)*, 157-167.
(26) Van Koningsveld, H.; Van Bekkum, H.; Jansen, J. C. *Acta Crystallogr., Sect. B: Struct. Sci.* **1987**, *B43(2)*, 127-132.
(27) Frisch, M. J.; Trucks, G. W.; Schlegel, H. B.; Scuseria, G. E.; Robb, M. A.; Cheeseman, J. R.; Montgomery, J. A., Jr.; Vreven, T.; Kudin, K. N.; Burant, J. C.; Millam, J. M.; Iyengar, S. S.; Tomasi, J.; Barone, V.; Mennucci, B.; Cossi, M.; Scalmani, G.; Rega, N.; Petersson, G. A.; Nakatsuji, H.; Hada, M.; Ehara, M.; Toyota, K.; Fukuda, R.; Hasegawa, J.; Ishida, M.; Nakajima, T.; Honda, Y.; Kitao, O.; Nakai, H.; Klene, M.; Li, X.; Knox, J. E.; Hratchian, H. P.; Cross, J. B.; Adamo, C.; Jaramillo, J.; Gomperts, R.; Stratmann, R. E.; Yazyev, O.; Austin, A. J.; Cammi, R.; Pomelli, C.; Ochterski, J. W.; Ayala, P. Y.; Morokuma, K.; Voth, G. A.; Salvador, P.; Dannenberg, J. J.; Zakrzewski, V. G.; Dapprich, S.; Daniels, A. D.; Strain, M. C.; Farkas, O.; Malick, D. K.; Rabuck, A. D.; Raghavachari, K.; Foresman, J. B.; Ortiz, J. V.; Cui, Q.; Baboul, A. G.; Clifford, S.; Cioslowski, J.; Stefanov, B. B.; Liu, G.; Liashenko, A.; Piskorz, P.; Komaromi, I.; Martin, R. L.; Fox, D. J.; Keith, T.; Al-Laham, M. A.; Peng, C. Y.; Nanayakkara, A.; Challacombe, M.; Gill, P. M. W.; Johnson, B.; Chen, W.; Wong, M. W.; Gonzalez, C.; Pople, J. A. *Gaussian 03, revision B.05; Gaussian, Inc.: Pittsburgh, PA*, 2003.
(28) Klinowski, J. *Chem. Rev.* **1991**, *91(7)*, 1459-1479.
(29) Freude, D.; Klinowski, J.; Hamdan, H. *Chem. Phys. Lett.* **1988**, *149(4)*, 355-362.
(30) Sepa, J.; Lee, C.; Gorte, R. J.; White, D.; Kassab, E.; Evleth, E. M.; Jessri, H.; Allavena, M. *J. Phys. Chem.* **1996**, *100(47)*, 18515-18523.
(31) Lee, D.; Kim, C. K.; Lee, B.; Lee, I. *J. Comput. Chem.* **1997**, *18(1)*, 56-69.
(32) Zakharov, M.; Masunov, A. E.; Dreuw, A. *J. Phys. Chem. A*, **2008**, *112(41)*, 10405-10412.

QUANTUM-CHEMICAL ANALYSIS OF REACTIONS BETWEEN PYRIDINE AND THE INDUSTRIALLY IMPORTANT PETROCHEMICAL ZEOLITE CATALYST

Pemikar Srifa[a,b,c], *Somkiat Nokbin*[a,b], *Bundet Boekfa*[b,c,d] *and Jumras Limtrakul*[a,b,c*]

[a] Laboratory for Computational & Applied Chemistry, Physical Chemistry Division, Department of Chemistry, Faculty of Science, Kasetsart University, Bangkok 10900, Thailand
[b] Center of Nanotechnology, Kasetsart University Research and Development Institute, Kasetsart University, Bangkok 10900, Thailand
[c] NANOTEC Center of Nanotechnology, National Nanotechnology Center, Kasetsart University, Bangkok 10900, Thailand
[d] Chemistry Department, Faculty of Liberal Art and Science, Kasetsart University Kamphaeng Saen Campus, Nakhon Pathom 73140, Thailand

Introduction

Acidic-Faujasite (H-FAU), one of the aluminosilicate zeolites containing the protonate sites, has been frequently used as the heterogeneous acid catalyst for petrochemical processes, especially the heavy oil cracking[1-3]. Due to its primitive building unit which is the fusion of two supercages[4,5], the large molecules such as heavy oil can be trapped by forming a strong hydrogen bond between those guest molecules and Brønsted bridging hydroxyl groups Si-OH-Al within the porous intersection of the catalyst before being reformed to smaller molecules. The catalytic properties of acidic sites around the area are thus a significant process to find out the catalytic proficiency of this zeolitic 'nanoreactor'.

Generally, zeolite acidity can be investigated by the adsorption of basic probe molecules on the Brønsted acidic site of zeolite using many straightforward methods such as microcalorimetry, temperature-programmed desorption (TPD), Nuclear Magnetic Resonance Spectroscopy (NMR) or other appropriate methods[6-11]. In the aspect of using pyridine as the probe molecule, these experiments explain that the pyridinium complex (PYH^+) first occurred during the adsorption process and is then stabilized by interacting with anionic zeolite (Z^-)[12-14].

In order to study the hidden agenda of these steps, theoretical investigation and experimental data have been combined, since it clearly provides not only the information on the proton transfer from the zeolite active site to an adsorbate but also the confinement effect of the framework: how the physical geometry, excluding the active site with the long range interaction of zeolite, affect the measured adsorption enthalpies[15,16]. Several theoretical elucidations using the quantum cluster calculation of pyridine adsorbed on zeolites have been reported[17-21]. Among these studies, there are some reports of our group related to the adsorption energy and geometry changes when pyridine adsorbed on different zeolitic cluster sizes using the embedded-ONIOM method[20,21] in which the long-range electrostatic interactions are represented on the outer layer of the calculated model. Although the results of this hybrid method are usually in agreement with experiments, the imbalance of the van der Waals interaction represented by the two methods combined in the ONIOM scheme may create an error, so the accuracy of system studied for the selected methods must be carefully checked. In the present study, to avoid the weakness of the proposed model, we thus employ full quantum methods with the newly developed hybrid density functional M06-2X, which cover the important weak interactions[22,23], for investigation of the interaction between pyridine and different model sizes of H-FAU. The effects of the infinite zeolitic framework on the cluster model are also included by a set of point charges generated by the embedded nanocluster model.

The goals of this study are to study the confinement effect from the zeolite on the adsorption properties of pyridine, and to demonstrate the combined interactions between the newly developed density functional theory, M06-2X, and the extended point charge. We will discuss the behavior of the different sizes of zeolite framework.

Methods

Five different sizes of H-FAU model clusters, 5T, 14T, 38T, 54T and 120T cluster (T represents tetrahedral of Si or Al atoms) were employed to investigate the adsorption of pyridine, as shown in Figure 1. The most energetically favored Si position, T1, was replaced by an Al atom and used in all cluster sizes[24] to generate the Brønsted acid site. The 5T quantum cluster, $AlSi_4O_4H_{13}$, is considered as the smallest unit required to represent the Brønsted acid site of zeolite. The larger 14T cluster which covers the 12 membered-ring (12 MR) at the intersection window of the two supercages of H-FAU is then considered. The model was extended to 38T to cover the other shell of the Si unit around the 12MR. The

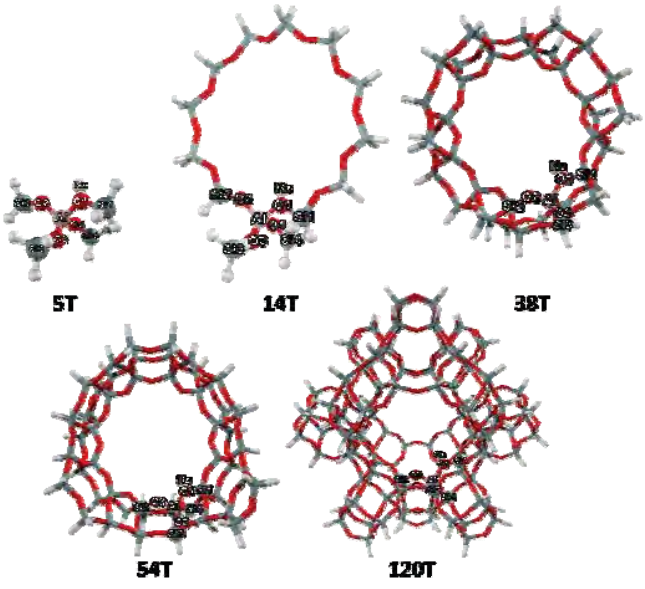

Figure 1. Presentation of H-FAU models in different sizes. Relaxation atoms are shown in balls, whereas the rest is symbolized with wireframes.

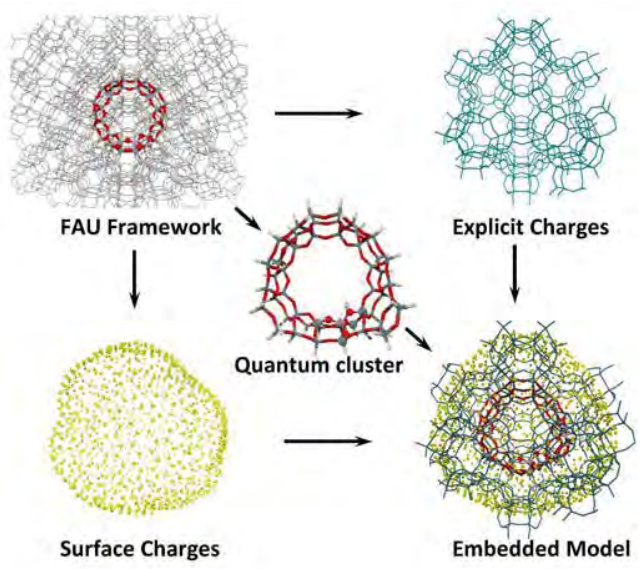

Figure 2. Surface charge representation of External electrostatic potential scheme.

54T is similar to the 38T, but the framework is more extended. Considered, in order to account for the important confinement effect of the zeolite, is that the larger model, 120T, acts as a nanoscopic reaction vessel which covers the two supercages in H-FAU. It can be expected that the largest 120T cluster represents the entire solid network of H-FAU.

The adsorptions of pyridine on different H-FAU models are calculated with the M06-2X functional and 6-31G(d,p) level of theory. Geometry optimizations are carried out for the 5T, 14T and 38T clusters with the criterion that the active region 5T and the probe molecule are allowed to relax while the rest remain fixed at the crystallographic positions. To determine the model size that can best represent the interaction properties, single-point energy calculations of the 54T and 120T at the M06-2X/6-31G(d,p) level were carried out to get more accurate energies, including the confinement effect of H-FAU.

To study the electrostatic contribution of the extended framework, the Madelung potential from the extended lattice is reproduced by point charges enclosed around the 54T cluster, as shown in Figure 2 (see ref. 21 for more details). The M06-2X calculation and the optimized electrostatic point charges method, called "embedded M06-2X approach", has been successfully applied to study the adsorption and reaction mechanism of unsaturated aliphatic, aromatic and heterocyclic compounds on H-ZSM-5 zeolites[25]. The calculated adsorption energies were obtained from the difference between the total energy of the complex and the isolated species in each system as described by $\Delta E_{ads} = E_{(Complex)} - E_{(Zeolite)} - E_{(Pyridine)}$. All quantum cluster calculations were performed by using the Gaussion 03 program[26] incorporated with the Minnesota Density Functionals module 3.1 by Zhao and Truhlar[22,23].

Results and Discussion

Molecular cluster and adsorption structure of pyridine on H-FAU zeolite. The selected geometrical parameters for 5T, 14T and 38T models are shown in Table 1. The lengthening of the O1-Hz bond, as a function of the cluster size, from 0.960 Å (5T) → 0.970 Å (14T) → 0.971 Å (38T) indicates the influence of the zeolite framework on acidity. The Al-O1-Si1 angle, one of the significant parameters for considering zeolite acidity, is found to be slightly increased from the 5T model by 0.4 and 1.7 degrees for the 14T and the 38T, respectively, demonstrated that the acidity values were increased as with the larger model. The calculated Al···Hz distances are measured in the range of 2.450-2.532 Å, which agree well with reported experimental observations by Klinoski of 2.380 - 2.480 Å[27], indicated the validation of the calculation models.

At the adsorption step, the pyridine adsorptions on H-FAU are clearly demonstrated the effects of the framework on the existence of adsorbate/adsorbent species in the system. For the small 5T cluster, we found only a simple hydrogen-bonded pyridine/zeolite complex in which the pyridine is held over the Brønsted acid site of H-FAU zeolite. The significant lengthening of the O1-Hz bond compared with the bare zeolite system can be observed (from 0.960 to 1.320 Å). The intermolecular distance between pyridine and zeolite, N-O1, is 2.489 Å. The N-Hz-O1 bond angle is found to be near-linear (178.6 degree), which describes the quite strong hydrogen bond interaction in the adsorbing complex. A weaker interaction between the hydrogen of pyridine, H1, and the adjacent oxygen, O2, is also presented. The changes of the zeolites structures are in accordance with Gutmann's rules[28,29], i.e., a lengthening of the O1-Hz bond, a shortening of the Al-O1 bond and, a lengthening of the Al-O2 bond.

Table 1. Geometrical Parameters of Pyridine Adsorbed on Three Sizes of H-FAU Models. (Distances in Å, Angles in Degrees).

Parameter	System					
	5T		14T		38T	
	Isolated	Complex	Isolated	Complex	Isolated	Complex
O1-Hz	0.960	1.320	0.970	1.574	0.971	1.634
O2-Hz	2.692	2.489	2.822	2.864	3.004	3.058
O2-H1	-	2.196	-	2.162	-	2.127
Al-O1	1.926	1.850	1.946	1.812	1.968	1.821
Al-O2	1.710	1.728	1.716	1.758	1.724	1.774
Al-O3	1.709	1.718	1.711	1.730	1.718	1.737
Al-O4	1.700	1.711	1.703	1.725	1.710	1.731
Al-Hz	2.450	2.525	2.499	2.789	2.532	2.865
N-O1	-	2.489	-	2.649	-	2.685
N-Hz	-	1.357	-	1.074	-	1.063
<Al-O1-Si1	130.6	128.3	130.9	128.5	132.3	131.0
<Al-O1-Hz	111.3	113.5	113.6	110.8	114.6	112.4
<Al-O2-H1	-	120.4	-	122.0	-	115.9
< N-Hz-O1	-	178.6	-	179.2	-	175.0

By enlarging the model to 14T, an ion-pair complex can be found. Increasing the model cluster was found to enhance the protonation of the Brønsted acidic site of zeolites to pyridine resulting in the formation of the pyridinium ion pair complex [PYH^+] by increasing of the O1-Hz bond to 1.574 Å corresponds with decreasing the N-Hz bond to 1.074 Å. The ion-pair interaction is also found on the more realistic 38T model, as shown in Figure 3. The longest O1-Hz bond (1.634 Å) and the shortest N-Hz bond (1.063 Å) indicate a stronger interaction between pyridine and H-FAU zeolite. The N-O1 intermolecular distances, on the one hand, are found to increase the model, expanding it from 2.489 Å (5T) to 2.685 Å (38T) while the O2···H1 distances, on the other hand, are decreased from 2.196 Å (5T) to 2.127 Å (38T). These suggest the greater stability of the adsorption complex in the larger cluster model. As a result, the interaction between pyridine and H-FAU is more stable as a function of the cluster size.

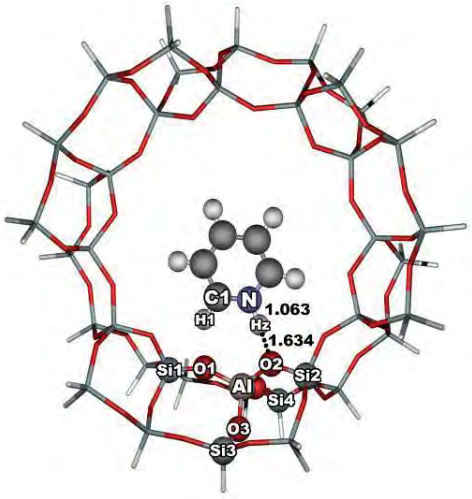

(a)

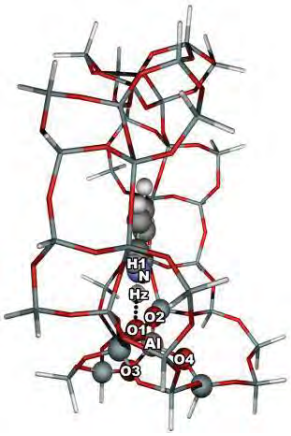

(b)

Figure 3. Presentation of the Pyridine interacting with the 38T model of H-FAU zeolite through the 12MR channel **(a)** and the side view **(b)**. All bond lengths are in angstroms.

The energetic of pyridine on H-FAU zeolite. All calculated pyridine adsorption energies have been summarized in Table 2. As expected, the interaction energy is stronger if the ion-pair is more pronounced. In energy features, the small cluster (5T unit) gives the adsorption energy of -24.9 kcal/mol, which is lower than the experimental data of -43.1 kcal/mol[30]. This is due to the rather weak interaction of the hydrogen-bonded configuration of the adsorption complex existing in the system. As for the 14T and 38T models, the adsorption energy increases considerably to -41.7 and -42.7 kcal/mol, respectively, resulting from the more stable ion-pair configuration of [PYH^+]/[FAU^-]. The adsorption energy slightly changes to -43.5 and -44.1 kcal/mol, respectively, by increasing the model sizes to 54T and 120T. The adsorption energy from the 54T model gives virtually the same results as the 120T model. This indicates that the 54T cluster is a good compromise between accuracy and the practical computational time.

Since the ion-pair complex existed in the larger model studied, the electrostatic potential from the infinite lattice of zeolite might play a bigger role on the ion-pair interaction of pyridine on H-FAU. Therefore, the "embedded M06-2X method" the combination between the M06-2X functional and the embedded approach was considered to examine the electrostatic potential effect. The optimized point charges are embedded into the quantum cluster 54T as shown in Figure 2. From Table 2, the adsorption energies from the M06-2X on 38T and the embedded M06-2X on 54T are -42.7 and -44.4 kcal/mol, respectively. The latter value agrees well with both the largest quantum cluster, 120T (-44.1 kcal/mol) and the experimental value (-43.1 kcal/mol). This suggests that the embedded M06-2X is more practical and accurate to study the adsorption of pyridine on zeolite. The embedding of the optimized point charges causes the adsorption energy obtained from the 54T cluster to be nearly identical with those of the120T cluster.

Table 2. Comparison of Adsorption Energies (kcal/mol) of Pyridine on Various Model Sizes of H-FAU.

Model	Method	Adsorption Energy
5T[a]	M06-2X	-24.9
14T[a]	M06-2X	-41.7
38T[a]	M06-2X	-42.7
54T[b]	M06-2X	-43.5
120T[b]	M06-2X	-44.1
54T[b]	Embedded M06-2X	-44.4
Experimental value		-43.1

[a] Energies calculated from full quantum optimization using the M062X/6-31G(d,p) level of theory.
[b] Energies obtained from single point calculation using geometries from 38T model clusters treated with the same method and basis set.

Conclusions

The effect of the zeolitic nanocage on the adsorption properties of the important heterocyclic base, pyridine, of different sizes of H-FAU has been investigated by the M06-2X density functional with the 6-31G(d,p) basis set. The zeolitic 'nanoreactor' porous intersection, where chemical reactions take place, is represented by a small cluster of 5T up to a realistic nanocluster of 120 tetrahedral atoms. The adsorption energies were calculated to be -24.9, -41.7, -42.7, -43.5 and -44.1 kcal/mol for 5T, 14T, 38T, 54T and 120T, respectively and compare with the experimental value of -43.1 kcal/mol The results demonstrate that the newly developed hybrid density functional M06-2X is able to cover important weak interactions, especially the van der Waals interaction which is essential for describing the nano-confinement effect from the zeolite framework. Then, the adsorption energies are more accurate if the embedded nanocluster model is used. The effects of the infinite zeolitic framework on the cluster model are also included by a set of point charges generated by the embedded nanocluster model. The energy for the adsorption of pyridine on an embedded nanocluster model is predicted to be -44.4 kcal/mol, which is very close to experimental observations. The nano-confinement effect of the extended zeolite framework has been clearly demonstrated not only to stabilize the pyridine/zeolite complexes but also to improve their corresponding adsorption energies to approach the experimental benchmark. All results, for the model considered in this study, confirm that the embedded M06-2X method can be used effectively to study the reaction between the pyridine molecule and other zeolites for further comparison of the acidity of various zeolites.

Acknowledgement. This work was supported in part by grants from the National Science and Technology Development Agency (2009 NSTDA Chair Professor funded by the Crown Property Bureau under the management of the National Science and Technology Development Agency and NANOTEC Center of Excellence funded by the National Nanotechnology Center), the Commission of Higher Education, Ministry of Education ("National Research University of Thailand" and "Postgraduate Education and Research Programs in Petroleum and Petrochemicals and Advanced Materials"). The support from the Kasetsart University Research and Development Institute (KURDI) is also acknowledged. The authors are grateful to Donald G. Truhlar and Yan Zhao for their support with the M06-2X functional.

References

(1) Ng, S.; Zhu, Y.; Humphries, A.; Zheng. L; Ding, F.; Yang, L.; Yui, S. *Energy Fuels* **2002**, *16*, 1196.
(2) Kuznicki, S. M.; McCaffrey, W. C.; Bian, J.; Wangen, E.; Koenig, A.; Lin, C. H. *Microporous Mesoporous Mater*. **2007**, *105*, 268-272.
(3) Stoyanov, S. R.; Gusarov, S.; Kuznicki, S. M.; Kovalenko, A. *J. Phys. Chem. C*. **2008**, *112*, 6794-6810.
(4) Breck, D. W. *U.S. Patent 3*, **1964**, 130,007.
(5) Costenoble, M. L.; Mortier, W. J.; Uytterhoeven, J. B. *J. Chem. Soc., Faraday Trans. I*. **1976**, *72*, 1877-1883.
(6) Gorte, R. J. *Catal. Today* **1996,** *28*, 405-414.
(7) Auroux, A. *Top. Catal*. **2002,** *19*, 3–4.
(8) Mishin, I. V.; Brueva, T. R.; Kapustin, G. I. *Adsorpt. Sci. Technol*. **2005,** *11*, 415–424.
(9) Jia, C.; Massiani, P.; Barthomeuf, D. *J. Chem. Soc. Faraday Trans*. **1993,** *89(19)*, 3659-3665.
(10) van Santen, R. A.; Kramer, G. J. *Chem. Rev*. **1995**, *95*, 637-660.
(11) Gorte, R. J. *Catal. Lett*. **1999**, *62*, 1–13.
(12) Parrillo, D. J.; Lee, C.; Gorte, R. J.; White, D.; Farneth, W. E. *J. Phys. Chem*. **1995**, *99*, 8745.
(13) Kubelkova, L.; Kotrla, J.; Florian, J. *J. Phys. Chem*. **1995**, *99*, 10285.
(14) Savitz, S.; Myers, A. L.; Gorte, R. J.; White, D. *J. Am. Chem. Soc*. **1998**, *120*, 5701.
(15) Derouane, E. G.; Fripiat, J. G. *J. Phys. Chem*. **1987**, *91*, 145.
(16) Derouane E.G.; Chang C. D. *Microporous Mesoporous Mater*. **2000**, *35*, 425–433.
(17) Rozanska, X.; van Santen, R. A.; Hutschka, F. *J. Catal*. **2001**, *200*, 79.
(18) Komiyama, M.; Kobayashi, M. *J. Phys. Chem. B* **1999**, *103*, 48.
(19) Ventura, M. C.; Akacem, Y.; Kassab E. *J. Phys. Chem. C* **2008**, *112*, 19045–19054.
(20) Lomratsiri, J.; Probst, M.; Limtrakul, J. *J. Mol. Graph. Model.* **2006,** *25*, 219–225.
(21) Injan, N.; Pannorad, N.; Probst, M.; Limtrakul, J. *Int J. Quantum Chem.* **2005**, 105, 898.
(22) Zhao, Y.; Truhlar, D. G. *J. Phys. Chem .C* **2008,** *112(17)*, 6860-6868.
(23) Zhao, Y.; Truhlar, D. G. *Theor. Chem. Acc*.**2008**, *120*, 215-241.
(24) Suzuki, K.; Noda, T.; Sastre, G.; Katada, N.; Niwa, M. *J. Phys. Chem. C* **2009**, *113*, 5672–5680.
(25) Boekfa, B.; Choomwattana, S.; Khongpracha, P.; Limtrakul, J. *Langmuir* **2009**, DOI: 10.1021/la901841w.
(26) Frisch, M. J. T.; Trucks, G. W.; Schlegel, H. B.; Scuseria, G. E.; Robb, M. A.; Cheeseman, J. R.; Montgomery, Jr., J. A.; Vreven, T.; Kudin, K. N.; Burant, J. C.; Millam, J. M.; Iyengar, S. S.; Tomasi, J.; Barone, V.; Mennucci, B.; Cossi, M.; Scalmani, G.; Rega, N.; Petersson, G. A.; Nakatsuji, H.; Hada, M.; Ehara, M.; Toyota, K.; Fukuda, R.; Hasegawa, J.; Ishida, M.; Nakajima, T.; Honda, Y.; Kitao, O.; Nakai, H.; Klene, M.; Li, X.; Knox, J. E.; Hratchian, H. P.; Cross, J. B.; Bakken, V.; Adamo, C.; Jaramillo, J.; Gomperts, R.; Stratmann, R. E.; Yazyev, O.; Austin, A. J.; Cammi, R.; Pomelli, C.; Ochterski, J. W.; Ayala, P. Y.; Morokuma, K.; Voth, G. A.; Salvador, P.; Dannenberg, J. J.; Zakrzewski, V. G.; Dapprich, S.; Daniels, A. D.; Strain, M. C.; Farkas, O.; Malick, D. K.; Rabuck, A. D.; Raghavachari, K.; Foresman, J. B.; Ortiz, J. V.; Cui, Q.; Baboul, A. G.; Clifford, S.; Cioslowski, J.; Stefanov, B. B.; Liu, G.; Liashenko, A.; Piskorz, P.; Komaromi, I.; Martin, R. L.; Fox, D. J.; Keith, T.; Al-Laham, M. A.; Peng, C. Y.; Nanayakkara, A.; Challacombe, M.; Gill, P. M. W.; Johnson, B.; Chen, W.; Wong, M. W.; Gonzalez, C.; and Pople, J. A.;. *Gaussian 03, revision B.05*, Gaussian, Inc., Wallingford CT, 2004.
(27) Klinowski, *J. Chem. Rev*. **1991**, *91*, 1459.
(28) Gutmann, V. *The Donor–Acceptor Approach to Molecular Interaction*, Plenum Press, New York, **1978**.
(29) Gutmann, V.; Resch, G.; Linert, W. *Coord. Chem. Rev.***1982**, *43*, 133–164.
(30) Parrillo, D. J.; Gorte, R. J. *J. Phys. Chem.* **1993**, *97*, 8786.

WOXIDATIVE DEHYDROGENATION OF PROPANE OVER A VO2-EXCHANGED MCM-22: A NEWLY DEVELOPED DFT STUDY

Sippakorn Wannakao[a,b], Bundet Boekfa[b,c], Pipat Khongpracha[a,b] and Jumras Limtrakul[a,b]*

[a] Laboratory for Computational & Applied Chemistry, Physical Chemistry Division, Department of Chemistry, Faculty of Science, Kasetsart University, Bangkok 10900, Thailand
[b] Center of Nanotechnology, Kasetsart University Research and Development Institute, Bangkok 10900, Thailand
[c] Chemistry Department, Faculty of Liberal Arts and Science, Kasetsart University Kamphaeng Saen Campus, Nakhon Pathom 73140, Thailand

Introduction

Propene is one of the most important starting materials in many chemical industry processes, for example, polymer synthesis processes. With the continuing scarcity of natural resources, the demand for propene will increase significantly in the near future. Concerted efforts to find inexpensive ways to produce propene are now high on research priority lists. Among those, oxidative dehydrogenation of the lower cost raw material, propane, is an outstanding method for the production of propene due to its lower energy consumption, lower coke and CO_x byproducts and high selectivity to the desired product compared to the conventional dehydrogenation process.[1-3]

Vanadia supported catalysts have been proven to be active and selective for this reaction.[1-14] Silica supported vanadium oxide catalysts are highly propene selective catalysts because they do not favor direct combustion of the propane reactant to CO_x species, compared to alumina and titania supports.[13,14] Zeolites and mesoporous silicas which are industrially important catalysts can also be used as the silica support catalysts.[14-18] Even though many theoretical studies of the propane oxidative dehydrogenation over vanadium oxides and silica supported catalysts were conducted, i.e., gas phase[19,20], cluster[21-23] and periodic[24,25] systems, to the best of our knowledge, porous silica supported vanadia catalysts have never been studied theoretically for the propane oxidative dehydrogenation reaction. For studying systems in the confined space, van der Waals interaction plays an important role in adsorption and catalysis processes. In our previous calculations on various reactions in zeolites, ONIOM (B3LYP:UFF) was found to reproduce the experimental data. Even due to the compensation between the overestimated framework confinement effect and the underestimated interaction in the active region, this method is accurate and economic in computational cost.[26-34] Recently, Zhao and Truhlar have developed a new type of DFT (M06-series) in which the dispersion force was taken into account.[35,36] In our recent studies, this method has been proved to be one of the useful methods for studying adsorption and reaction mechanisms of the van der Waals dominant species over zeolite systems.[37-39]

To understand the reaction which occurs in a confined space, a well calibrated VO_2-exchanged-MCM-22 (VO_2-MCM22) model which was recently experimentally studied[17], was used for studying the propane ODH reaction. In this work, M06-DFT has been employed to study the reaction mechanism of the propane oxidative dehydrogenation reaction over the catalyst. The reaction can be divided into two main steps, 1) methylene (-CH_2-) hydrogen activation and 2) propene formation. A reoxidation of the catalyst was not considered because it is not the rate limiting step for the propane oxidative dehydrogenation reaction.[40]

Methods

The structure of the MCM-22 zeolite cluster was obtained from the crystal structure[41], represented by clusters of 14T (T = tetrahedral of Si or Al atoms). The cluster covers the 12-membered ring at the intersection of two channels which is considered to be an appropriate active site of the catalyst (see Figure 1). An Al atom was located at the T1 position, the most stable configuration of this model.[42] The Vanadium oxide specie $[VO_2]^+$ is placed at the highly accessible Brønsted acid site. All geometry optimizations were performed by the M06-L functional using the 6-31G(d,p) level of theory for H, C, O, Al and Si atoms, while the effective core potentials (ECP) of Stuttgart and Born[43] were employed for the V atom. To cover the confinement effect from the zeolite framework, the model is extended to a 120T structure. The 120T includes a supercage of MCM-22 where the adsorbates are trapped inside. During the optimization, only the active site of the catalyst ($VO_2/AlSi_4O_4$) and probe molecule were allowed to relax, while the rest was kept fixed as the original crystal structure. Normal mode analysis of the transition states have only one imaginary frequency whose mode corresponds to the designated reaction. The total spin was kept constant at the singlet state which was found to be the most stable state among the considered reaction steps.[19] All calculations were performed by the Gaussian 03 package[44] incorporated with the Minnesota Density Functionals module 3.1 by Zhao and Truhlar.

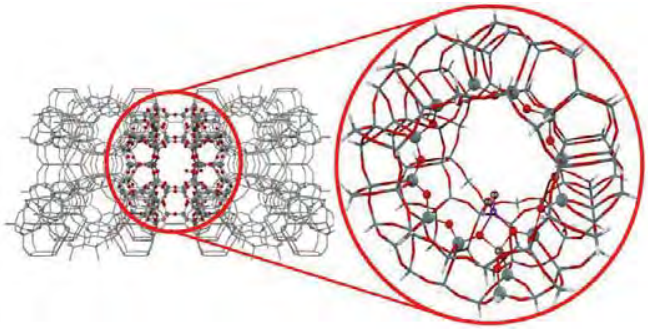

Figure 1. Illustration of the selected structure of VO_2-MCM-22. Balls represent the fully optimized quantum 14T cluster